The Development of High-Performance Post-Tensioned Rocking Systems for the Seismic Design of Structures

Dion Marriott

A thesis presented for the degree of

Doctor of Philosophy

in

Civil Engineering

at the

University of Canterbury

Christchurch, New Zealand

February 2009

This thesis is dedicated to my grandparents

Anne & Harold Marriott,

Jean & Malcolm Whall

Abstract

It is not economical, nor practical, to design structures to remain elastic following a major earthquake event. Therefore, traditional seismic design methodologies require structures to respond inelastically by detailing members to accommodate significant plasticity ("plastic hinge zones"). It can be appreciated that, while life-safety of the occupants is ensured, structures conforming to this traditional design philosophy will be subjected to excessive physical damage following an earthquake. Thus, the direct costs associated with repair and the indirect costs associated with business interruption are expected to be great. Adding to this, structures located within a near-field region, close to a surface rupture, can be subjected to large velocity pulses due to a ground motion characteristic known as forward directivity in which a majority of the earthquake's energy arrives within a very short period of time. Conventionally constructed systems are, in general, unable to efficiently deal with this ground motion.

In the last two decades, advanced solutions have been developed to mitigate structural damage utilising unbonded post-tensioning within jointed, ductile connections, typically combined with hysteretic damping. While there is a growing interest amongst the engineering fraternity towards more advanced systems, their implementation into mainstream practice is slow due to the lack of understanding of unfamiliar technology and the perceived large construction cost. However, even considering such emerging construction technology, these systems are still susceptible to excessive displacement and acceleration demands following a major velocity-pulse earthquake event.

In this research, the behaviour of advanced post-tensioned, dissipating lateral-resisting systems is experimentally and analytically investigated. The information learned is used to develop a robust post-tensioned system for the seismic protection of structures located in zones of high seismicity within near-field or far-field regions.

A series of uniaxial and biaxial cyclic tests are performed on 1/3 scale, post-tensioned rocking bridge piers, followed by high-speed cyclic and dynamic testing of five 1/3 scale, post-tensioned rocking walls with viscous and hysteretic dampers. The experimental testing is carried out to develop and test feasible connection typologies for post-tensioned rocking systems and to improve the understanding of their behaviour under cyclic and dynamic loading.

Insights gained from the experimental testing are use to extensively refine existing analytical modelling techniques. In particular, an existing section analysis for post-tensioned rocking connections is extended to assess the response of post-tensioned

viscous systems and post-tensioned connections under biaxial loading. The accuracy of existing macro-models is further improved and a damping model is included to account for contact damping during dynamic loading.

A Direct-Displacement Based Design (DDBD) framework is developed for post-tensioned viscous-hysteretic systems located in near-field and far-field seismic regions. The single-degree-of-freedom (SDOF) procedure is generic and has applications in new design and retrofit, while the multi-degree-of-freedom (MDOF) procedure is developed specifically for continuous bridge systems. Detailed design guidelines and flow-charts are illustrated to encourage the knowledge transfer from this report and to promote the use of emerging technology.

Combining the information gathered from experimental testing, modelling and design, a probabilistic seismic hazard analysis is performed on three post-tensioned viscous-hysteretic bridge systems. In all cases, the post-tensioned bridge systems are shown to be more feasible than a traditional monolithic ductile bridge. Furthermore, while a post-tensioned hysteretic bridge is shown to be the most economic solution, the viscous-hysteretic system becomes more advantageous as the cost of fluid-viscous-dampers reduces.

Acknowledgements

There are a large number of people who I owe thanks to, who have supported me during my years of post-graduate studies.

I would first like to thank my principal supervisor Dr Stefano Pampanin whose knowledge on everything seismic is unsurpassed. His constant support and encouragement during my studies has been greatly appreciated. I would also like to thank and acknowledge the support provided by my co-supervisors Dr Alessandro Palermo and Prof. Des Bull for their unrivalled technical support and for helping me to steer my research to where it ended up.

I would also acknowledge my many post-graduate colleagues who supported me extensively throughout my studies, in particular: Umut Akguzel, Alejandro Amaris, Brendon Bradley, Weng Yuen Kam, Mike Newcombe and Didier Pettinga. Not to mention the many past students including Matthew Ireland, James Jensen and Tobias Smith. An awesome social atmosphere developed over the years and many became flat-mates, gym-mates, squash-mates, soccer-mates and “travelling though Europe and China”-mates.

Finally, I am immensely appreciative of the support provided by mother, father and brother during my entire time at university.

Table of Contents

Abstract……..v

1. Introduction and Scope of the Research 1.1
   1.1. Introduction 1.1
   1.2. Research Motivation 1.3
   1.3. Objectives and Scope of the Research 1.3
   1.4. Overview 1.4
   1.5. References 1.5

2. Recent Investigations into the Behaviour of Jointed, Precast, Post-Tensioned Rocking Structures 2.1
   2.1. The Joint U.S.-Japan PRESSS Research Program 2.1
   2.2. Post-Tensioned, Precast Wall Systems 2.5
   2.3. Post-Tensioned Masonry Wall Systems 2.7
   2.4. Post-Tensioned Precast Bridge Pier Systems 2.8
   2.5. Conclusions 2.10
   2.6. References 2.11

3. A Discussion on Existing Performance-Based Design Philosophies and Analysis Techniques for Post-Tensioned Rocking Systems 3.1
   3.1. Introduction 3.1
   3.2. Performance-Based Design Framework 3.1
   3.3. Direct-Displacement-Based Design (DDBD) Priestley et al. [2007] 3.2
      3.3.1. An Overview of the DDBD Procedure, Priestley et al. [2007] 3.4
      3.3.2. Comparison Between FBD and DDBD 3.6
      3.3.3. The Structural Performance Factor S_p within DDBD 3.9
   3.4. Rocking Behaviour of Rigid Bodies 3.11
      3.4.1. The Behaviour of Inverted Pendulum Structures, Housner [1963] 3.11
      3.4.2. Conclusions Specific to the Rocking Response of Rigid Blocks 3.16
   3.5. Modelling Techniques for Post-Tensioned Rocking Systems 3.16
      3.5.1. Lateral Response of Post-Tensioned Connections 3.16
      3.5.2. Section Analysis Methods for Post-Tensioned Rocking Connections 3.18
      3.5.3. Cyclic Modelling Techniques for Post-Tensioned Rocking Connections 3.25
      3.5.4. Conclusions on Modelling Post-Tensioned Rocking Systems 3.30
   3.6. References 3.31

4. Uniaxial and Biaxial Quasi-Static Testing of Post-Tensioned Bridge Piers.....4.1
4.1. Introduction.....4.1
4.2. Design of the prototype bridge pier system.....4.1
4.3. Structural Details and Construction of the Bridge Pier Test Specimens 4.3
4.3.1. Monolithic, Ductile Benchmark Pier: MON.....4.4
4.3.2. Hybrid Bridge Pier with Internal, Grouted, Reinforcement: HBD1 ...4.5
4.3.3. Hybrid Bridge Pier with Internally Grouted & Threaded, Reinforcement: HBD2 .....4.8
4.3.4. Post-Tensioned Bridge Pier with Internal, Semi-Replaceable Dissipaters: HBD3 .....4.10
4.3.5. Post-Tensioned Bridge Piers with External Replaceable Dissipaters: HBD4 and HBD5 .....4.12
4.4. Fabrication and Testing of the External Mild Steel Dampers.....4.15
4.5. Experimental Laboratory Test Set-Up 4.19
4.5.1. Uniaxial Quasi-Static Laboratory Test Set-Up 4.19
4.5.2. Biaxial Quasi-Static Laboratory Test Set-Up 4.22
4.6. Material Properties.....4.24
4.6.1. Mild Steel Reinforcement 4.24
4.6.2. Post-tensioned Reinforcement 4.24
4.6.3. Concrete 4.25
4.7. Discussion on the Experimental Results.....4.26
4.7.1. Monolithic Benchmark Bridge Pier 4.26
4.7.2. Post-Tensioned Only Bridge Piers.....4.28
4.7.3. Post-Tensioned Bridge Pier Testing with Internal Dissipation: HBD1 ... .4.31
4.7.4. Post-Tensioned Bridge Pier Testing with Internal Dissipation: HBD2 ... .4.32
4.7.5. Post-Tensioned Bridge Pier Testing with Internal Dissipation: HBD3 ... .4.34
4.7.6. Post-Tensioned Bridge Pier Testing with External Dissipation: HBD4 .. ..4.35
4.7.7. Post-Tensioned Bridge Pier Testing with External Dissipation: HBD5 .. ..4.37
4.7.8. Area-Based Equivalent Viscous Damping.....4.40
4.7.9. Performance Evaluation of the Post-Tensioned Bridge Piers.....4.44
4.7.10. Bi-Axial Moment Interaction.....4.48
4.8. Conclusions.....4.50
4.9. References.....4.51

5. High-Speed Cyclic Testing of Post-Tensioned Precast Walls with Viscous and Hysteretic Dissipation.....5.1
5.1. introduction 5.1
5.2. design of the prototype specimen.....5.1
5.3. Details of the Post-Tensioned Wall, test specimens 5.1
5.3.1. Damper Details 5.3
5.4. Construction of the Post-Tensioned Wall 5.6
5.5. Experimental High-Speed Set-Up and Instrumentation.....5.7
5.5.1. Laboratory Test Set-Up.....5.7
5.5.2. Instrumentation 5.7
5.6. High-Speed Control Using the Shake-Table.....5.9

5.6.1. Description of the Shake-Table 5.9
5.6.2. Shake-Table Capacity 5.10
5.6.3. Acquisition System 5.10
5.6.4. Displacement Protocol and Control Algorithm 5.10
5.7. Material Properties 5.14
5.7.1. Mild Steel Reinforcement 5.14
5.7.2. Prestressed Reinforcement (Post-Tensioned Reinforcement) 5.15
5.7.3. Laminated Veneer Lumber (LVL) 5.15
5.7.4. Viscous Dampers 5.18
5.8. Experimental Results 5.22
5.8.1. Wall 1: Post-Tensioned Only 5.22
5.8.2. Wall 2: Post-Tensioned with Fluid Viscous Dampers 5.23
5.8.3. Wall 3: Post-Tensioned with Fluid Viscous Dampers and Mild Steel Dampers 5.25
5.8.4. Wall 4: Post-Tensioned with Mild Steel Dampers (High Mild Steel Reinforcement Content) 5.27
5.8.5. Wall 5: Post-Tensioned with Mild Steel Dampers (Low Mild Steel Reinforcement Content) 5.29
5.9. Discussions 5.30
5.9.1. Equivalent Viscous Damping 5.30
5.9.2. Effectiveness of the Fluid Viscous Dampers 5.30
5.9.3. Strain-Rate Effects 5.31
5.10. Conclusions 5.33
5.11. References 5.34

6. Dynamic Testing of Post-Tensioned Precast Concrete Walls with Viscous and Hysteretic Dissipation 6.1
6.1. Introduction 6.1
6.2. Details and Construction of the Prototype Post-Tensioned Wall 6.1
6.3. Laboratory Test Set-Up and Instrumentation 6.4
6.3.1. Experimental Test Set-Up 6.4
6.3.2. Driving Mass 6.4
6.3.3. Instrumentation 6.7
6.4. Experimetnal Program 6.8
6.4.1. Selection and Scaling of the Ground Motions 6.9
6.5. Shake Table Control 6.10
6.5.1. Record Modification to Avoid Velocity Saturation 6.10
6.5.2. Similitude Scaling for Dynamic Testing 6.15
6.5.3. Performance and Tuning of the Shake Table 6.15
6.6. Experimental response 6.19
6.6.1. Free Vibration Release Tests 6.19
6.6.2. Energy Balance Considerations 6.23
6.6.3. Earthquake Excitation 6.26
6.7. Strain-Rates 6.30
6.8. Horizontal Accelerations During Rocking Impact 6.30
6.9. Vertical Accelerations During Rocking Impact 6.32
6.10. Estimating the Equivalent Viscous Damping Associated with Contact Damping 6.35
6.10.1. Equivalent Viscous Damping Based on Pure Free-Vibration 6.35

6.10.2. Equivalent Viscous Damping Considering an Energy Balance Approach 6.36
6.11. Conclusions 6.40
6.12. References 6.41

7. Modelling the Monotonic, Cyclic and Dynamic Response of Post-Tensioned Rocking Systems 7.1
7.1. Introduction 7.1
7.2. Modeling the Monotonic Response of Post-Tensioned Rocking Systems 7.1
7.2.1. The Revised Monolithic Beam Analogy for Post-Tensioned Rocking Systems with Internally Grouted Mild Steel, Palermo [2004] 7.2
7.2.2. Comparison of an Analytical Monotonic Backbone Model with Experimental Test Results 7.20
7.2.3. An Analytical Model for Post-Tensioned Systems Subjected to Biaxial Bending 7.53
7.3. A Cyclic Macro-Model for Post-Tensioned Rocking Systems 7.67
7.3.1. Cyclic Material Models for Use within a Multi-Spring Macro Model 7.68
7.3.2. Calibration of the Axial Stiffness of a Multi-Spring Element via a Moment-Rotation Section Analysis 7.69
7.3.3. Additional Modelling Issues to be Considered when Dealing with a Multi-Spring Macro-Model 7.72
7.3.4. An Analytical Macro-Model for LVL Wall 4 with Hysteretic Dampers. 7.77
7.3.5. An Analytical Macro-Model for LVL Wall 2 with Non-Linear Viscous Dampers 7.78
7.3.6. A 3-Dimensional Macro-Model for Post-Tensioned Rocking Systems 7.80
7.4. Modelling the Dynamic Response of Post-Tensioned Rocking Systems 7.83
7.4.1. Modelling the Contact Damping in Post-Tensioned Rocking Systems 7.83
7.5. Conclusions 7.89
7.6. References 7.91

8. Direct Displacement-Based Design of Post-Tensioned Rocking Systems, Part I: SDOF Rocking Systems with Viscous Dampers 8-1
8.1. Introduction 8-1
8.1.1. Design Issues for Post-Tensioned Rocking Systems with Viscous Dampers 8-1
8.2. Development of A Damped Design Spectra for Systems with Non-Linear Viscous Damping 8-4
8.2.1. Description of the SDOF System and THA Model Parameters 8-5
8.2.2. Selection and Scaling of the Earthquake Ground Motions 8-6
8.2.3. Spectral Reduction Factors for Linear Viscous Dampers 8-11
8.2.4. Spectral Reduction Factors for Non-Linear Viscous Dampers 8-15
8.2.5. Modification of the Spectral Reduction Factors to Account for a Bilinear Backbone Envelope 8-18
8.3. Relating Local Supplementary Damping Properties to Global Structural Damping Properties 8-25

8.4. A Viscous Direct Displacement-Based Design (Viscous-DDBD) Procedure. 8-36
8.5. Time History Design verification 8-42
8.6. Accounting for Elastic Deformations in the Design of Post-Tensioned Viscous Systems 8-44
8.6.1. Design Parameters to be used Considering Elastic Deformations....8-48
8.6.2. Design Considerations for Equivalent Viscous Damping of a System with Elastic Deformations 8-49
8.7. Conclusions....8-50
8.8. References....8-51

9. Direct Displacement-Based Design of Post-Tensioned Rocking Systems, Part II: SDOF Systems with Viscous and Hysteretic Dampers 9-1
9.1. Introduction....9-1
9.2. Direct Displacement-Based Design of Post-Tensioned Rocking Systems with Hysteretic Damping....9-1
9.3. DDBD of Post-Tensioned Rocking Systems with Viscous and Hysteretic Damping....9-3
9.3.1. Elastic Damping Component of EVD, ξ_{el}....9-4
9.3.2. Viscous Damper Component of EVD, ξ_{vd}....9-4
9.3.3. Hysteretic Component of EVD, ξ_{hyst} 9-6
9.3.4. Modifying the Hysteretic Component of EVD for Near-Field Seismicity....9-6
9.3.5. Combining the Components of EVD....9-7
9.3.6. Design Displacement for Post-Tensioned Viscous-Hysteretic systems 9-7
9.3.7. Bilinear Base Shear Reduction Factor, $\phi_{BL,sys}$ 9-8
9.4. Time History Design Verification 9-10
9.5. Design Methods 9-13
9.6. Conclusions....9-18
9.7. References....9-19

10. Direct Displacement-Based Design of Post-Tensioned Rocking Systems, Part III: MDOF Systems with Viscous and Hysteretic Dampers....10-1
10.1. Introduction....10-1
10.2. An Overview of DDBD for Conventional MDOF RC Continuous Bridge Systems 10-1
10.3. DDBD of Post-Tensioned Hybrid Continuous Bridge Systems....10-4
10.4. DDBD of Post-Tensioned rocking continuous Bridge Systems with Viscous and hysteretic Dampers....10-5
10.4.1. Elastic Damping Component, ξ_{el} 10-5
10.4.2. Viscous (Supplementary) Damper Component of EVD, ξ_{vd}....10-7
10.4.3. Hysteretic Component of EVD, ξ_{hyst} 10-9
10.4.4. Combining the Components of EVD....10-10
10.4.5. Design Displacement for Post-Tensioned Viscous-Hysteretic systems 10-11
10.4.6. Bilinear Base-Shear Reduction Factor, $\phi_{BL,sys}$ 10-11
10.5. Design Procedure for MDOF Continuous Bridge Systems with Viscous and Hysteretic Dampers....10-13
10.6. Verification of the MDOF Viscous-DDBD Procedure using THA....10-16

10.6.1. Description of the Prototype Bridges 10-16
10.6.2. Bridge Modelling Issues 10-16
10.6.3. Design Verification 1: Continuous Bridge Systems with Supplementary Viscous Dampers 10-17
10.6.4. Design Verification 2: Continuous Bridge Systems with Supplementary Viscous and hysteretic Dampers 10-20
10.7. Conclusions 10-23
10.8. References 10-24

11. The Feasibility of Advanced Post-Tensioned Bridge Systems Considering a Probabilistic Seismic Loss Assessment 11.1
11.1. Introduction 11.1
11.2. Geometry of the Prototype Bridge Systems 11.1
11.3. Design of the Prototype Bridges 11.3
11.3.1. Seismic Design Hazard 11.3
11.3.2. Direct Displacement-Based Design (DDBD) Bridge Summary 11.4
11.4. Design Details of the Bridge Systems 11.6
11.4.1. Bridge 1: Monolithic Ductile Benchmark 11.6
11.4.2. Bridge 2: Traditional Post-Tensioned Hybrid Bridge 11.6
11.4.3. Bridge 3: Advanced Hybrid Bridge AFS1. ..... 11.9
11.4.4. Bridge 4: Advanced Hybrid Bridge AFS2. ..... 11.10
11.4.5. Cost Estimation 11.11
11.5. Loss Assessment within a Performance-Based Seismic Assessment Framework 11.13
11.5.1. Expected Annual Loss (EAL) Formulation 11.14
11.6. Seismic Hazard Model and Ground Motions for the Loss Assessment 11.14
11.6.1. Loss Assessment Hazard Model 11.14
11.6.2. Scaling of the Selected Ground Motions 11.15
11.7. Structural Performance Limits, Performance Objectives and Design Criteria 11.18
11.7.1. Material Limit States 11.18
11.7.2. Structural Performance Levels 11.19
11.7.3. Performance Objectives 11.21
11.8. Damage States and Loss Ratios 11.22
11.8.1. Damage States and Loss Ratios for Monolithic, Ductile Bridge Systems 11.22
11.8.2. Damage States and Loss Ratios for Hybrid, Post-Tensioned Bridge Systems 11.23
11.9. Modelling the Bridge Systems 11.27
11.9.1. Ductile, Benchmark Bridge 11.28
11.9.2. Post-Tensioned Hybrid Bridge 11.29
11.9.3. AFS1 Bridge 11.30
11.9.4. AFS2 Bridge 11.31
11.10. Results of the Probabalistic Seismic Loss Assessment 11.33
11.10.1. Bridge Response Considering the 2/3MCE (Design level) and MCE (Ultimate level) Seismic Intensity 11.33
11.10.2. Intensity-Drift (IM-EDP) Relationship 11.35
11.10.3. Annual Rate of Exceedance 11.37

11.10.4. Loss-Hazard Relationship 11.37
11.10.5. Expected Annual Loss 11.39
11.10.6. Expected Annual Loss Including Initial Cost of Construction ... 11.40
11.10.7. Loss Associated with Downtime 11.41
11.11. Loss Assessment of an Irregular Bridge 11.43
11.12. Results of the Probablistic Seismic Loss Assessment: Irregular bridge 11.45
11.12.1. Irregular Bridge Response when Subjected to the 2/3MCE (Design level) and MCE (Ultimate level) Seismic Intensity 11.45
11.12.2. Annual Rate and Probability of Global Collapse 11.46
11.12.3. Loss-Hazard Relationship 11.47
11.12.4. Expected Annual Loss 11.48
11.13. Discussions 11.49
11.13.1. Feasibility of Post-tensioned Bridge Systems 11.49
11.13.2. Superstructure, Abutments and Bearing Related Losses 11.50
11.13.3. Feasibility of an Alternative Post-tensioned Bridge Systems 11.50
11.13.4. The Option to Build High Performance Structures 11.51
11.14. Conclusions 11.52
11.15. References 11.54

Appendix A A.1
A1. Displacement-Based Design of the Prototype Bridge Pier A.1
A2. Displacement-Based Assessment Procedure to Evaluate the Seismic Performance of an experimental test A.4
A3. references A.7

Appendix B B.1
B1. Instrumentation B.1
B2. Marriott, D., Pampanin, S. and Bull, D. (2007). "Improving the Seismic Performance of Existing Reinforced Concrete Buildings using Advanced Rocking Wall Solutions." NZSEE, Palmerston North, New Zealand. B.3

Appendix C C.1
C1. Precast Wall Construction Drawings C.1
C2. Record Modification, Method A C.3
C3. Record Modification, Method B C.5
C4. Energy Formulations C.8
C5. References C.10

Appendix D D.1
D1. Comparison Between the Experimental Testing and the Multi-Spring Macro Model D.1
D2. Stress Block Factors for Confined Concrete D.14

Appendix E E.1
E1. Formulation of the Bilinear, Base shear Reduction Factor ϕ_{BL} E.1
E2. Damped Response Spectra for Post-Tensioned Systems with Non-Linear Dampers, α = 0.15-0.75 ..... E.3
E3. Derivation of the Internal Lever Arm to the Resultant Supplementary Damper Force E.5

E4. Derivation of the Net Velocity of the Supplementary Viscous Dampers .. E.7
E5. Design Example of a Post-Tensioned Wall System with Viscous Dampers ... E.9
E6. References ... E.22

Appendix F ... F.1
F1. Manipulation of the Spectral Reduction Factor for Near-Field Compatibility ... F.1
F2. Design Example of a Post-Tensioned Rocking System with Viscous and Hsyteretic Dampers ... F.2
F3. References ... F.16

Appendix G ... G.1
G1. Design Example of a Post-Tensioned Rocking Bridge System with Viscous and Hysteretic Dampers ... G.1
G2 Derivation of the Weighting Function to Determine the System Damping Coefficient C_{VD} ... G.8
G3. Details and Formulation of an Elastic Damping, Dashpot Model ... G.10
G4. References ... G.13

Nomenclature

a	βc
$a(t)$	System acceleration at time t
A_e	Area of effectively confined core
A_{cc}	Area bound by the centreline of the peripheral hoops (confined core)
A_g	Gross area of the section
A_{pt}	Area of prestressing tendon
A_r	Aspect ratio of the section (H_e/l_w)
A_{shx}	Transverse reinforcement ratio providing confinement in the x-direction
A_{shy}	Transverse reinforcement ratio providing confinement in the y-direction
b_{ex}	Length of effectively confined core in the x-direction
b_{ey}	Length of effectively confined core in the y-direction
B	Width of a rectangular section
c	Neutral axis depth
c_{vd}	Damping coefficient of the supplementary viscous damper (local element level)
C_c	Resultant concrete compression force
C_c	Critical damping
C_{VD}	Damping coefficient of the system (global level) due to the supplementary viscous devices.
$C_{VD,i}$	Damping coefficient of DOF i
C_e	Confinement effectiveness coefficient
d_{vd}	Distance from centreline of section to damper group
$d_{pt,i}$	Distance from the centreline of the section to the post-tensioned tendon
d_{pt}	Distance from the centreline of the section to the post-tensioned tendon
D	Depth of a rectangular section or diameter of a circular section
E_{ms}	Young's modulus of elasticity of mild steel reinforcement

E_{pt}	Young's modulus of elasticity of prestressing reinforcement
E_c	Young's modulus of elasticity of concrete
E_{sec}	Secant modulus of elasticity of confined concrete to peak confined concrete stress
f_{yh}	Yield stress of transverse/hoop reinforcement
$f_{s,ms}$	Stress in mild steel reinforcement
f_c	Longitudinal concrete compression stress (confined or unconfined)
f'_c	Maximum unconfined concrete compressive stress
f'_{cc}	Maximum confined concrete compressive stress
f_l	Lateral confining stress
$f_{l,e}$	Lateral confining stress within the effectively confined core
$f_{l,i}$	Lateral confining stress within the ineffectively confined core
$f_{l,m}$	Lateral confining stress within the ineffectively confined core due to perimeter cover protection providing a moderate level of confinement.
$f_{pt,i}$	Stress in the post-tensioned tendon
$f_{pt,y}$	Yield stress of prestressing reinforcement
f_{ms}	Mild steel stress
$f_{y,ms}$	Mild steel stress at yield
$f_{u,ms}$	Mild steel ultimate stress
$f_{x,ms}$	Mild steel stress at a strain of $\varepsilon_{x,ms}$
f_{pt}	Post-tensioned steel stress
$f_{y,pt}$	Post-tensioned steel stress at yield
$f_{u,pt}$	Post-tensioned steel ultimate stress
$f_{x,pt}$	Mild steel stress at a strain of $\varepsilon_{x,pt}$
F	Applied lateral load
F_{vd}	Force in the viscous damper element
$F_{VD,sys}$	Equivalent viscous damper force at the effective height of the SDOF substitute structure
F_{vd}	Force in viscous damper element (local level)
$F_{VD,sys}$	Equivalent system force due to viscous damper elements
$F_{damp,i}$	Viscous damper force of damper group *i*
F_1	Larger lateral confining stress of two directions
F_2	Smaller lateral confining stress of two directions
h_w	Height of the section (vertical plan)
h_{cx}	Length between centreline of peripheral hoops in x-direction
h_{cy}	Length between centreline of peripheral hoops in y-direction
H	Clear cantilever height

H_e	Height to effective mass
H_i	Height at level *i*
H_n	Height of structure at level *i*=*n*
I_e	Effective second moment of area of the section i.e. $I_e=\kappa I_g$
$jd_{0.5lw}$	Internal lever arm to the centreline of the section
jd_{approx}	Approx internal lever arm of the section
$jd_{pt,i}$	Internal lever arm to the post-tensioned tendon duct *i*
jD	Internal lever arm to the centroid of the viscous damper forces
$jd_{vd,i}$	Internal lever arm to viscous damper group *i*
$k_{pt,i}$	Axial stiffness of post-tensioned tendon group *i*
K_e	Effective stiffness of the SDOF system at the target displacement
K_{red}	Tendon axial stiffness modification factor to account for elastic shortening of the precast element
l_{sp}	Strain penetration length
l_{ub} or $l_{ub,pt}$	Unbonded length of the post-tensioned tendons
$l_{ub,ms}$	Unbonded length of the mild steel reinforcement
l_w	Section length (depth in the horizontal plane specific to a wall section)
L_p	Plastic hinge length
m_e	Effective mass
m_i	Mass at level i
M	Applied Moment
M_n	Nominal moment capacity of the rocking section
$M_{n,pc}$	Nominal moment capacity of the precast element
M_i	Moment demand
M_{dec}	Decompression section moment
M_{vd}	Viscous damper moment contribution of the section
n_{vd}	Total number of supplementary viscous dampers within the section
$n_{vd,i}$	Total number of viscous dampers at location *i*
n_{vis}	Total number of viscous damper groups
n_{pt}	Total number of post-tensioning tendons in section
$n_{pt,i}$	Total number of post-tensioning tendons at duct *i*
n_{duc}	Total number of tendon ducts (groups)
N	Axial load

P	Lateral load
P_i	Applied load at DOF i
P	Power factor describing the non-linear strain-hardening curve of steel
R_ξ	Damping constant used within the EVD formulation
s	Spacing of the transverse reinforcement sets (centre to centre spacing)
$S_{\xi\%}$	ξ% damped, spectral response: displacement, velocity or acceleration
$S_{5\%}$	5% damped, spectral response: displacement, velocity or acceleration
t_w	Section width
t	time
T	Period of the system
T_e	Effective period of the SDOF system at the target displacement
$T_{pt,0}$	Total initial post-tensioning force within the section
$T_{pt,req}$	Total post-tensioning force required at the design displacement/rotation
T_{pt}	Total post-tensioning force within the section
$v(T,\xi)$	Damped spectral velocity
$v(T,5\%)$	5% damped spectral velocity
v_r	Design velocity of the SDOF system at the effective height (global) when $\Delta(t)=\Delta_r$
v_d	Pseudo-spectral velocity of the SDOF system corresponding to Δ_d
v_{vd}	Velocity of the viscous damper element
$\bar{v}_{vd}$	Average velocity of all viscous dampers in the section
$v(t)$	Velocity at time t
V_b	Design base shear of the system

α	Concrete stress block factor (Whitney Stress Block Analogy)
α	Spectral displacement damping reduction power coefficient for DDBD
α	Viscous damper velocity power coefficient
α_1	Confinement factor
α_2	Confinement factor
β	Concrete stress block, length factor
β_{vd}	Ratio between the system damping coefficient and the local damping coefficient, $\beta_{vd} = C_{vd}/c_{vd}$
$\beta_{vd,i}$	Ratio between the damping coefficient at the top of the pier and the local damping coefficient, $\beta_{vd,i} = C_{vd,i}/c_{vd}$
χ	Dimensionless neutral axis depth $\chi=c/D$
δ_i	Normalised displacement at level i
Δ_i	Displacement of level *i*
$\dot{\Delta}_{vd,i}$	Velocity of viscous damper group *i*
Δ_e	Elastic displacement
Δ	Displacement
$\Delta(t)$	System displacement at time t
Δ_d	Design displacement at the effective height
$\Delta_{d,\xi}$	Target/design displacement of the SDOF substitute
$\Delta\varepsilon_{pt,i}$	Strain increment due to tendon elongation
Δ_i	Displacement at level i
$\Delta_{pt,i}$	Displacement elongation of the post-tensioned tendon
Δ_{ls}	Limit state displacement
Δ_y	Yield displacement
Δ_r	Design displacement of the SDOF system for post-tensioned viscous systems
$\Delta T_{pt,i}$	Total tendon force increment due to tendon elongation
$\Delta_{vd,i}$	Displacement of the viscous damper group *i*
Δ_{vd}	Viscous damper displacement at centroid of viscous damper force
ε_c	Concrete compression strain at the extreme edge of the section
ε_{cc}	Concrete compression strain corresponding to the peak confined compressive stress
ε_{co}	Concrete compression strain corresponding to the peak unconfined compressive stress
ε_{sp}	Spalling strain of concrete
$\varepsilon_{dc,c}$	Concrete compression limit for the damage control limit state

$\varepsilon_{dc,c}$	Concrete compression limit for the damage control limit state
$\varepsilon_{c,ls}$	Limit state strain of concrete in compression
$\varepsilon_{s,ls}$	Limit state strain of steel in tension
ε_s	Steel strain
ε_s'	Steel strain in compression
ε_{su}	Steel strain at the ultimate stress
$\varepsilon_{x,ms}$	Mild steel strain on strain-hardening portion of monotonic curve
ε_{ms}	Mild steel strain
$\varepsilon_{y,ms}$	Mild steel strain at yield
$\varepsilon_{sh,ms}$	Mild steel strain hardening
$\varepsilon_{u,ms}$	Mild steel strain at ultimate stress
ε_{pt}	Post-tensioned steel strain
$\varepsilon_{y,pt}$	Post-tensioned steel strain at yield
$\varepsilon_{u,pt}$	Post-tensioned steel strain at ultimate stress
$\varepsilon_{x,pt}$	Post-tensioned steel strain on strain-hardening portion of monotonic curve
$\varepsilon_{sh,app}$	Apparent strain hardening due to cyclic loading
ϕ_{dec}	Decompression curvature
ϕ_o	Section over-strength action due to material over-strength characteristics
ϕ	Bridge displaced shape
$\phi_{ls,c}$	Curvature corresponding to concrete compression limit state
$\phi_{ls,s}$	Curvature corresponding to reinforcement tension limit state
ϕ_y	Yield curvature
ϕ_{BL}	Base shear reduction factor to account for a bilinear loading envelope
Φ_{1-2}	Geometric relationship between damper forces within group 1 and 2
Φ_{2-3}	Geometric relationship between damper forces within group 2 and 3
γ_{vd}	Geometric constant relating system velocity to damper velocity
Γ_Δ	Rigid body displacement/rotation reduction factor
η	Spectral reduction factor
η_{disp}	Spectral displacement reduction factor
η_{vel}	Spectral velocity reduction factor
k_ϕ	Yield curvature coefficient
λ	Moment ratio defined as $\lambda = \left(M_{pt} + M_N\right) / M_{ms}$. Also referred as the re-centring ratio.

λ	Constant to convert secant stiffness damping to tangent stiffness damping in DDBD.
μ	Dimensionless moment demand
μ_Δ	Displacement ductility
ρ_v	Transverse reinforcement ratio
ρ_{ax}	Transverse reinforcement ratio providing confinement in the x-direction
ρ_{ay}	Transverse reinforcement ratio providing confinement in the y-direction
θ	Base rotation of the section (assuming rigid cantilever action) or lateral drift of the system $\theta = \Delta_d/H_e$
θ_d	Design inter-storey drift or building drift ratio
θ^{rb}	Design base rotation of the section reduced to account for elastic displacements (rigid body rotation)
θ_r	Design base rotation, reduced for non-zero velocity
θ_Δ	P-Δ stability index
ω	Circular natural frequency or angular velocity
Ω	Ratio of the supplementary damping coefficient $\boldsymbol{C_{vd}}$ to the critical damping $\boldsymbol{C_c}$ of the system, defined as the Supplementary Damping Ratio (SDR), $\Omega = C_{vd}/C_c$
ξ_{el}	Elastic component of equivalent viscous damping ratio
ξ_{vd}	Viscous damper component of equivalent viscous damping ratio
ξ_{hyst}	Hysteretic component of equivalent viscous damping ratio
ξ_{eq}	Equivalent viscous damping ratio
ξ_{eq}^{disp}	Equivalent viscous damping ratio appropriate to the damped displacement
ξ_{eq}^{vel}	Equivalent viscous damping ratio appropriate to the damped velocity
ξ_{ss}	Equivalent viscous damping ratio of the superstructure
ξ_i	Equivalent viscous damping at DOF i
$\xi_{el,i}$	Elastic damping at DOF i

1. Introduction and Scope of the Research

1.1. INTRODUCTION

The importance for design engineers to provide modern societies with structures that have a superior level of performance for resisting a major earthquake event has become widely accepted. Engineers are required to design structures, which will not only remain operational after a major earthquake event, but should also limit direct costs associated with repair and indirect financial loss associated with business operation and downtime.

As seismological research continues to create a better understanding of the energy characteristics of earthquakes, the objective stated above becomes more difficult to achieve. For example, ground motions recorded within 10-20km of an earthquake's rupture surface are shown to contain an earthquake characteristic known as forward directivity, where a majority of the earthquake's energy arrives to a site in a very short period of time (Somerville [2005]). One such condition for forward directivity exists when a strike-slip rupture (such as the San Andreas Fault in California) propagates towards a site. The surface waves arriving at the site located perpendicular to the fault surface (fault normal) can contain one or two large velocity pulses (Somerville et al. [1997]). An example of this is the 1992 Landers earthquake in California's Yucca Valley where peak ground velocities upwards of 1300mm/s were recorded at the Lucerne Station located 1.1km from the surface rupture. These ground motions are termed "near-field" events.

In light of the growing demand for high-performing structures, major developments to the construction of seismic resisting systems utilising dry, jointed, ductile connections within precast concrete structures have been heavily researched over the last two decades. Precast jointed systems are constructed with unbonded post-tensioned tendons to induce a controlled rocking mechanism in place of a region of significant plasticity ("plastic hinge"). This controlled rocking confines all of the deformation to a number of "gap openings" throughout the structure, as opposed to the inelastic response of multiple plastic hinge zones (PHZ) in traditional monolithic concrete construction, precast concrete emulation of monolithic concrete construction. This significantly reduces direct costs associated with structural repair and indirect costs associated with downtime and business disruption.

Research conducted within the United States PREcast Seismic Structural Systems (PRESSS) program in the late 1990's demonstrated the seismic performance of post-tensioned jointed systems through a number of structural sub-assembly tests,

concluding with the construction of a 5-storey, precast, post-tensioned frame and wall building tested at the University of California, San Diego (Priestley et al. [1999]). The findings from this research program led to this technology being recognised within seismic design provisions within the United States (ACI-T1.2-03 [2003]) and New Zealand, (NZS3101 [2006]), while design guidelines are available in Europe (EC8 [2004]) and Japan (AIJ [2004]). Several buildings have been built world-wide utilising this technology, with the tallest being the 39-storey Paramount Apartment Building in San Francisco, California (Englekirk [2002]). In Italy, several on site applications, specific to gravity-load-dominated frames, have developed a variation of PRESSS technology adopting a draped tendon configuration, referred to as a "Brooklyn System" (Pagani [2001], Pampanin et al. [2004]). The Dominican Republic, in central America, presented the first building in literature constructed using post-tensioned coupled walls (Stanton et al. [2003]). Industry interest is also developing in New Zealand, where currently one multi-storey building is under construction in Wellington adopting post-tensioned frames in one direction and post-tensioned coupled walls in the other (Cattanach and Pampanin [2008]).

Post-tensioned systems are inherently suited to displacement-based design methods, as damage is directly correlated to displacement. Displacement-based design has been developed extensively, culminating in the following state-of-the-art publications: fib [2003] and Priestley et al. [2007]. While in their infancy, current seismic design codes are slowly adopting displacement-based design methods (EC8 [2004]). Further evidence is given by Appendix B of NZS3101 [2006], which permits the use of a displacement-based design approach for the design of post-tensioned jointed systems.

In spite of the developments involving precast, post-tensioned construction, the seismic risk is still significant considering velocity-pulse ground motion characteristics. An alternative means of dealing with excessive earthquake demands is to alter the input energy by removing/dissipating, or modifying the structural response, with the addition of supplementary dampers. Fluid viscous dampers, steel hysteretic elements and friction devices are typically used as supplementary damping; the latter being experimentally implemented into post-tensioned systems (Kurama [2004]). More recently, a combination of hysteretic and viscous devices have emerged as the new generation, seismic-resisting system for the protection of structures located in seismic regions whose hazard is consistent with the near-field characteristics mentioned above (Kam et al. [2007]).

However, with this in mind, the use of emerging seismic-resisting systems and materials into engineering practice faces inevitable inertia from industry. Typically, the design community is slow to adopt solutions that are less common in mainstream engineering: especially those falling outside the current building code, those that require detailed *prescriptive design guidelines* and independent peer review. Furthermore, in general, insurance companies do not recognise building performance as a means of assessing premiums. It is to this end that the decision to use advanced technology comes down to the engineer's ability to convey the benefits to the client and the client's risk adversity to the type of investment the structure represents.

Considering the extensive experimental validation, design provisions/guidelines and on-site applications, it is likely that a broad use of this technology will be embraced in the near future.

1.2. RESEARCH MOTIVATION

Current technology is widely available to satisfy the growing demand required of engineers to provide communities with superior levels of structural performance during an earthquake. As more advances are made in seismic engineering, the available technology becomes more cost-competitive when compared to traditional construction practice: further financial benefits can be associated with the improved response of the system considering the seismic risk applied over the working life of the structure. High performing systems will be designed to operate more efficiently as they are tuned to their direct application. As a result, the seismic demand imposed onto a structure (maximum displacements and accelerations) can be significantly reduced, thereby reducing material costs and construction time. However, in developing this new technology, design recommendations are required to ensure the technology is appropriately utilised.

1.3. OBJECTIVES AND SCOPE OF THE RESEARCH

The objective of this research is to provide a refined understanding on the experimental response, modelling, design and feasibility aspects of post-tensioned rocking systems implementing viscous and hysteretic damping for systems located in regions of high seismicity. The objectives required to meet this demand are be listed below into four areas

1 The research aims to experimentally understand the cyclic and dynamic characteristics of post-tensioned, viscous-hysteretic systems through scaled subassembly tests. Attention is given to investigate alternative connection typologies for post-tensioned connections to maximise their efficiency.

2 Existing analytical models are extensively refined to describe the monotonic, cyclic and dynamic behaviour of post-tensioned viscous-hysteretic systems

3 Displacement-based design procedures are developed for single-degree-of-freedom (SDOF) and multi-degree-of-freedom (MDOF) post-tensioned hysteretic-viscous systems and extensively verified against a number of prototype bridge examples.

4 The feasibility of these advanced solutions is studied using a probabilistic seismic loss assessment of three advanced prototype system located in a region of high seismicity in New Zealand.

1.4. OVERVIEW

Chapter 2 presents a number of recent experimental and analytical investigations undertaken on post-tensioned rocking systems. While the list is relatively exhaustive, little literature exists on dynamic testing and developing robust connection details. A detailed discussion is presented in Chapter 3 on existing performance-based design methodologies and Direct Displacement-Based Design. The mechanics of rigid rocking blocks are discussed, following with a description of current modelling techniques for post-tensioned rocking systems.

Chapter 4 presents a series of uniaxial and biaxial cyclic test results on 1/3 scale post-tensioned bridge piers. Chapter 5 follows with high-speed cyclic testing on five post-tensioned walls with hysteretic and viscous dampers. Chapter 6 concludes the experimental testing with free-vibration and shake-table testing of five post-tensioned precast concrete walls.

The information gathered from the experimental testing is compiled in Chapter 7 to refine existing monotonic, and cyclic modelling techniques. In both cases, uniaxial and biaxial modelling techniques are discussed and found to compare very well to the experimental.

Chapter 8, 9 and 10 develop a detailed displacement-based design framework for single-degree-of-freedom (SDOF) and multi-degree-of-freedom (MDOF) post-tensioned systems with viscous and hysteretic damping located in regions of high seismicity.

Finally, in Chapter 11 a prototype bridge system is developed and a detailed probabilistic seismic loss assessment is performed to determine the feasibility of advanced post-tensioned rocking bridge systems.

1.5. REFERENCES

ACI-T1.2-03. (2003). *Special Hybrid Moment Frames Composed of Discretely Jointed Precast and Post-Tensioned Concrete Members*.

AIJ. (2004). "Guidelines for performance evaluation of earthquake resistant reinforced concrete buildings (Draft)." *Architectural Institute of Japan (in Japanese)*.

Cattanach, A. and Pampanin, S. "21st Century Precast: The detailing and manufacture of NZ's first multi-storey PRESSS building." *New Zealand Concrete Industry Conference*, Rotorua, New Zealand.

EC8. (2004). "Eurocode 8: Design of structures for earthquake resistance - Part 1: General rules, seismic actions and rules for buildings." CEN/TC 250, Brussels, Belgium.

Englekirk, R. E. (2002). "Design-Construction of The Paramount-A 39 Story Precast Prestressed Concrete Apartment Building." *PCI Journal*.

fib. (2003). *Displacement Based Seismic Design of Reinforced Concrete Buildings*, International Federation for Structural Concrete, Lausanne, Switzerland.

Kam, W. Y., Pampanin, S., Carr, A. J. and Palermo, A. "Advanced Flag-Shape Systems for High Seismic Performance including Near-Fault Effects." *NZSEE 2007*, Palermston North.

Kurama, Y. (2004). "A Friction Damper for Post-Tensioned Precast Concrete Moment Frames." *PCI*, 49(4), 112-133.

NZS3101. (2006). "Concrete Structures Standard: Part 1-The Design of Concrete Structures." Standards New Zealand, Wellington.

Pagani, C. (2001). "Four is better than two - the principle of cable-stayed bridges applied to bridge beams." *Elite Journal*, 4, 50-69.

Pampanin, S., Pagani, C. and Zambelli, S. "Cable-stayed and suspended post-tensioned solutions for precast concrete frames "The Brooklyn System"." *New Zealand Concrete Industry Conference*, Queenstown.

Priestley, M. J. N., Calvi, G. M. and Kowalsky, M. J. (2007). *Displacement-Based Seismic Design of Structures*, IUSS, Pavia.

Priestley, M. J. N., Sritharan, S., Conley, J. R. and Pampanin, S. (1999). "Preliminary results and conclusions from the PRESSS five-story precast concrete test building." *PCI Journal*, 44(6), 42-67.

Somerville, P. "Engineering Characterization of Near Fault Ground Motions." *New Zealand Society of Earthquake Engineering Conference*.

Somerville, P. G., Smith, N. F. and Graves, R. W. (1997). "Modification of Emperical Strong Ground Motion Attenuation Relations to Include the Amplitude and Duration Effects of Rupture Directivity." *Seismological Research Letters*, 68(1), 199-222.

Stanton, J., Pizano-Battle, V. and Pizano-Thomen, V. "Design of the Cala Building using PRESSS technology." *Concrete Structures in Seismic Regions: FIB 2003 Symposium*.

2. Recent Investigations into the Behaviour of Jointed, Precast, Post-Tensioned Rocking Structures

2.1. THE JOINT U.S.-JAPAN PRESSS RESEARCH PROGRAM

The collaboration of the joint U.S.-Japan research program in the early 1990's under the title of the PREcast-Seismic-Structural-Systems (PRESSS) program was a major force in the development of jointed ductile precast connections, Priestley [1991]. The intent of this major research program was to improve the inelastic response, analytical modelling, design recommendations, and to improve the understanding of "ductile" precast buildings. The US.PRESSS program was divided into three phases (Priestley [1991]); Phase I was concerned with the conceptual development and evaluation of newly proposed structural concepts, specifically concerning practicality, economy and seismic performance (ductility and dissipation capabilities). This was followed by Phase II involving detailed experimental studies of precast components and sub-assemblages, paralleled with analytical studies. Phase III involved the testing of a 60% scale, multi-storey precast building having both structural moment resisting frames and shear wall elements.

Phase II and III of the research program deals entirely with experimental confirmation and analytical modelling. As part of the inter-program co-ordination of the US.PRESSS program, the National Institute of Standards and Technology (NIST), carried out numerous experimental tests related to Phase II. One of the earlier tests carried out by the PRESSS program is discussed in Priestley and Tao [1993]. They present the experimental results of a pre-stressed, pre-cast beam-column-joint sub-assembly with fully grouted post-tensioned tendons carried out at NIST. While comparable ductility demands to monolithic reinforced concrete elements could be achieved, the response was subjected to extensive stiffness degradation, pinching and hence unreliable energy dissipation. Furthermore, as the tendons are likely to exceed the limit of proportionality (yielding in tension), the shear transfer mechanism at the beam interface may be lost, resulting in a loss in the gravity load carrying capacity. Priestley and Tao [1993] then proposed the idea of partially unbonded post-tensioning tendons, whereby the tendon would be debonded for some length either side of the beam-column joint. This would reduce the strains in the tendon, and provide a non-linear elastic response with a marked increase in stability. The system however would have relatively little energy dissipation and be the subject of large concrete compressive strains. It is for this reason special detailing at the beam end region, consisting of spiral reinforcement, was suggested. Based on a number of non-linear time-history analyses (NLTHA), and the force-displacement relationships adopted, they stated that the difference in displacement response between a non-linear elastic

pre-stressed concrete frame with unbonded tendons, and an equivalent reinforced concrete frame, may be less than 38%.

The natural progression within phase II of the PRESSS program was to provide a similar system with fully debonded (unbonded) tendons. Thus, Priestley and MacRae [1996] constructed and tested a 67% scale pre-cast, post-tensioned interior and exterior beam-column joint subassembly with unbonded tendons. While the experimental results indicated a stable force-displacement response up to 4% of inter-storey drift, the units were subjected to significant stiffness degradation (initial stiffness reduced by approx 65% at a design inter-storey drift ratio of 2.5%). It is likely this degradation resulted from crushing of the beam cover concrete and inelastic compression stresses in the concrete at the beam end region, in addition to cracking within the column, joint and beam elements. The beam end regions were detailed with special spiral confinement reinforcing (2.5% by volume), while joint transverse reinforcement was keep to a minimum as it was envisaged that joint shear would be resisted entirely by a single diagonal strut from corner to corner of the joint due to the pre-stressed nature of the system. Diagonal shear cracking developed within the joint, but stabilised as the lateral load reached a maximum - this was in addition to yielding of the transverse reinforcement. It is for these reasons that the authors suggest to adopt a more conservative design approach for the design of the joint transverse reinforcement.

The inter-program co-ordination of the PRESSS program allowed a number of experimental tests to run in parallel. Cheok and Stone [1994] tested a total of twenty 33% scale, precast beam-column joint subassemblies consisting of both post-tensioned tendons (bonded, partially debonded and fully unbonded) and mild steel reinforcement (bonded, partially debonded or fully unbonded). This work was also reported in similar publications by Stone et al. [1995] and Stanton et al. [1997]. Of the 20 tests conducted, 4 specimens were accepted for a second round of proof testing and are discussed in detail. The four specimens comprised of two mild steel reinforcement ratios and two different material types: grade 60 (f_y = 414MPa) and a ductile grade of stainless steel (f_y = 304MPa). All four specimens had partially grouted post-tensioned tendons, grouted over a length equal to 37.7% of the bay length. Furthermore, the mild steel was either fully bonded or de-bonded over a length equal to 50mm at the connection interface. The mild steel units were found to perform well, with first rupture of the mild steel occurring at 2.9% for one unit and 3.5% for the second unit, with the tendons remaining elastic in both tests. The stainless-steel units did not perform well as the strain capacity of the stainless steel was reduced because deformed ribs were machined along the bar to help improve bond performance. In one test, rupture occurred at a lateral drift ratio of 2.0% while in the second test bond failure occurred at lateral drift ratio of 2.0% due to a relatively optimistic anchorage length. In all cases the tendons remained elastic except for the test unit having bond failure which was tested to 6.0% of lateral drift. Losses within the tendon load were recorded in all four specimens as a result of strain penetration within the grouted portion of the tendon (in addition to yielding of the tendons for one specimen), reducing the average strain over the unbonded length. However, given the reduction in tendon load, it was concluded that the gravity load carrying capacity (due to friction) could still be maintained.

El-Sheikh et al. [1999] presented two analytical models to model the experimental lateral response of a single NIST beam-column joint test, one being a fibre element model, the second being a lumped plasticity spring model. In general, both models were able to accurately capture the experimental response – including the initial stiffness and lateral strength. El-Sheikh et al. [1999] divided the push-over response of a post-tensioned frame into three (displacement) limit states. These three limit states were defined via a tri-linear representation of the moment-rotation behaviour of the beam-column connections; 1) the linear limit state, defining a reduction in lateral stiffness from the initial elastic stiffness of the system; 2) the yield limit, corresponding to yielding of the unbonded post-tensioned tendons; 3) the ultimate limit state, being failure of the confined concrete due to rupture of the spiral reinforcement (or rupture of the post-tensioned reinforcement). A design procedure is outlined by associating the three displacement limit states with three corresponding seismic design intensities (elastic, design and survival). The proposed design adopts an equivalent lateral force procedure (as per BSSC [1997]) and is based on the equal displacement principle for ductile structures in order to respect the three structural displacement limit states. The elastic design spectrum is reduced by the response modification factor, $\boldsymbol{R} = 8$ for "special moment resisting frames with ductile connections". However, the non-linear time-history analyses revealed that the equal displacement principle violated the design requirements for frame structures located on medium or soft soil conditions in regions of high seismicity.

In addition to pre-cast beam-column joints, the PRESSS program also investigated the behaviour of pre-cast, post-tensioned walls within Phase II. Much of this work was carried out at Lehigh University, Pennsylvania. The experimental results of Mueller [1986], presented by Armouti [1993], were used to validate a fibre model used within the DRAIN-2DX program reported by Kurama et al. [1998]. Mueller [1986] constructed and tested five precast, concrete walls of 1/3 scale; one wall being representative of an unbonded, post-tensioned precast concrete wall appropriate for an analytical comparison with a fibre model. The precast wall comprised of 3 segments, where only the pre-stressing bars crossed each precast wall panel. That is, the only form of inelastic deformation would come from material nonlinearity of the concrete and post-tensioning steel in addition to friction within the PVC grouted ducts (assumed to be unbonded). That is, the longitudinal reinforcement was curtailed within each precast element and did not pass between the precast wall panels. The precast wall was constructed with spiral reinforcement around the toe regions to confine the concrete under excessive axial strains. It was for this reason that the concrete was modelled as a multi-linear inelastic spring using the confinement model of Mander et al. [1988]. The experimental results exhibited a significant amount of stiffness degradation and material non-linearity (with an appreciable amount of energy dissipation). The fibre model accurately captured the cyclic behaviour, albeit for under predicting the loading branch: this was attributed to errors in accurately recording the experimental lateral load. Kurama et al. [1998] concluded that while the experimental test verification was not based on unbonded tendons (the tendons were grouted within smooth electrical conduits), the fibre model required further verification with more experimental tests to fully confirm its accuracy.

Kurama et al. [1999] proposed a seismic design approach for precast concrete walls with unbonded post-tensioned tendons. A performance-based design approach was developed, incorporating structural limit states and a seismic hazard based on the

equivalent lateral force method in BSSC [1997]. In particular Kurama et al. [1999] provided a number of structural limit states that should be satisfied considering two seismic design intensities. For a design level event (corresponding to an immediate occupancy performance level) the yield displacement (and lateral capacity) of the wall should not be exceeded: this corresponds to yielding of the post-tensioned tendons. Furthermore, inter-storey displacements should be limited to prevent damage to the non-structural elements. For the survival limit state (corresponding to the collapse prevention performance level) yielding of the tendons can be accepted, however, the self-centring capability of the system should be preserved to some extent. The displacement should not exceed the maximum displacement capacity of the wall (corresponding to fracture of the special confinement reinforcement) and crushing of the precast panel should be avoided (in those regions of concrete not having special confinement reinforcement). Furthermore, at the survival limit state, shear slip of the precast wall panel units is to be avoided and the lateral displacements of the gravity-load carrying elements should be controlled to ensure their vertical load carrying capacity is not compromised.

Using a fibre-element model, Kurama et al. [1999] investigated the lateral load behaviour of precast walls with unbonded post-tensioned tendons by varying a number of structural parameters. The initial post-tensioned force, amount of prestressed reinforcement, wall length, location of the post-tensioning tendons, unbonded length and the confinement reinforcement ratio were investigated. Kurama et al. [1999] commented on the effect these parameters have on three design limit states corresponding to: 1) onset of softening; 2) yielding of the prestressed reinforcement; and 3) rupture of the confinement reinforcement. Kurama et al. [1999] concludes by stating that the equal displacement assumption provides some correlation to time history analysis for walls located on stiff soil sites only and noted that further research is required to improve this estimation. The base shear was found to be significantly influenced by higher modes for post-tensioned walls due to the elongation of the modal periods when the structure entered the non-linear range.

Further analytical studies were also carried out by Kurama [2000] investigating the application of unbonded post-tensioned walls utilising linear viscous dampers connected to adjacent column braces. A fibre model was verified against a finite element model using nonlinear rectangular plane-stress elements in addition to gap/contact elements within the finite element program ABAQUS. Kurama [2000] proposed a design procedure using an Acceleration Displacement Response Spectrum (ADRS), combined with non-linear time-history analyses subjected to increasing white noise intensity.

As part of Phase III of the PRESSS program, a 60% scale, five-storey precast test building was designed and tested at the University of California, San Diego (UCSD). The test building comprised of precast moment resisting frames in one direction and post-tensioned coupled walls in the orthogonal direction, as reported in Priestley et al. [1999] and pictured in Figure 2.1. In particular, the coupled walls provided strength and dissipation through the use of U-Shaped Flexure Plates (UFP) fixed between the two walls and activated via the relative vertical displacement incompatibility between the two wall elements. This form of dissipation was found to be extremely stable and efficient following component testing carried out under the NIST program and reported in Priestley [1996]. The building was tested under a pseudo-dynamic loading

protocol, simulating the response to real earthquake excitation. Furthermore, as the earthquake intensity was increased, push-over tests were carried out after each major event to determine the structure flexibility and energy dissipation characteristics. Three design intensity earthquake records were run through the structure with a fourth record equal to 150% of the design intensity to represent the response under a maximum credible event. The structure experienced only minor damage to the cover concrete at the toe of the coupled wall, along with some cracking and deformation of the adjoining precast floor units at each floor level. In general, a simple macro model (using lumped plasticity modelling techniques) was able to accurately model the time history response, however, higher modes associated with contact stiffness at the base-foundation rocking interface were sensitive to the spring stiffness adopted in the model, Conley et al. [1999]. Furthermore, it was found that in order to return a proper agreement between the experimental results and the analytical model, the inclusion of an external column element was required to represent the out-of-plane stiffness of the orthogonal frames. It was concluded that the use of UFP plates provided an outstanding level of structural performance, while the performance of the structure further verified the displacement-based design methodology for precast buildings.

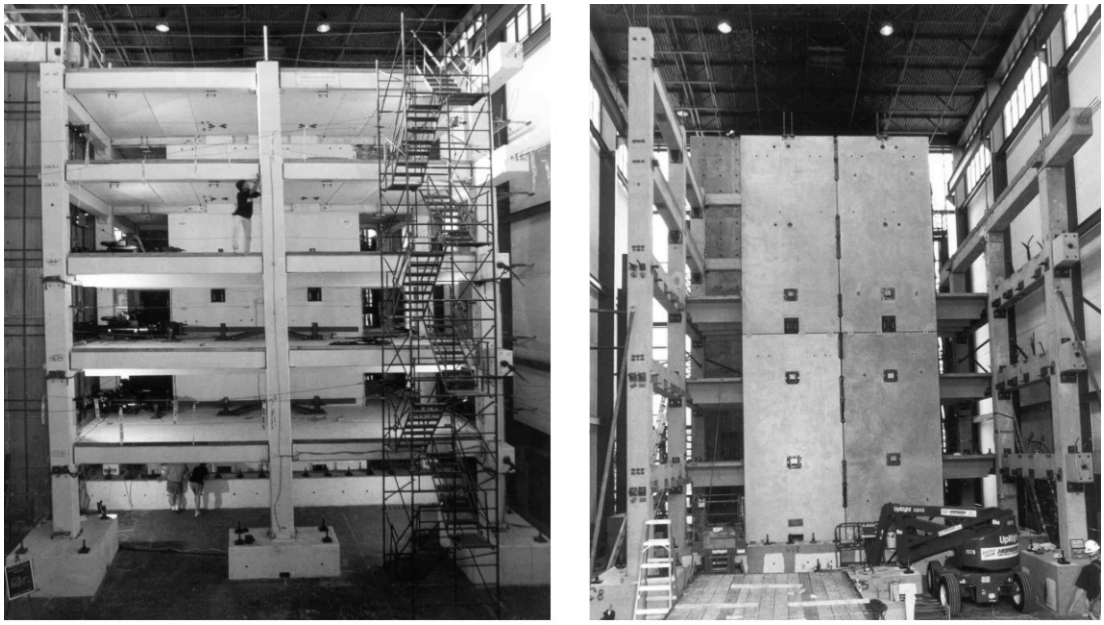

(a) Post-tensioned hybrid frame (b) Post-tensioned coupled walls

Figure 2.1 Five storey precast post-tensioned frame building tested at the University of California, San Diego (Priestley et al. [1999])

2.2. POST-TENSIONED, PRECAST WALL SYSTEMS

A significant amount of experimental and analytical work on precast concrete systems with unbonded post-tensioning has been investigated outside of the PRESSS program. In particular, Rahman and Restrepo [2000] tested three half scale unbonded post-tensioned precast concrete wall units at the University of Canterbury, Figure 2.2. The

post-tensioned walls were tested with and without grouted mild steel reinforcement. Unit-1 was detailed with two unbonded post-tensioned tendons each stressed to approximately 95kN. The experimental response was very stable, with some stiffness degradation as a result of crushing of the cover concrete and tendon losses. The toe regions were adequately detailed for the expected high concrete compression strains. This limited damage to crushing of the cover concrete. Unit-2 was detailed with two unbonded post-tensioned tendons each stressed to approximately 95kN in addition to two grouted mild steel reinforcing bars. The mild steel bar had a machined diameter of 12mm over a length of 200mm to confine the inelastic strain to the machined region. The experimental response was very stable with some stiffness degradation due to damage to the cover concrete and losses within the post-tensioning tendons. Furthermore, rupture of one dissipater occurred at 3% of drift. Unit 3 was identical to unit 2 except for a more heavily detailed toe region, anticipating higher concrete strains resulting from a) 16mm diameter mild steel dissipaters, b) 200kN additional post-tensioning representing gravity loading. The experimental response was stable with almost no strength deterioration but significant stiffness degradation. Furthermore, residual deformations were almost completely non-existent. Again, damage was limited to loss of cover concrete and minor flexural cracking.

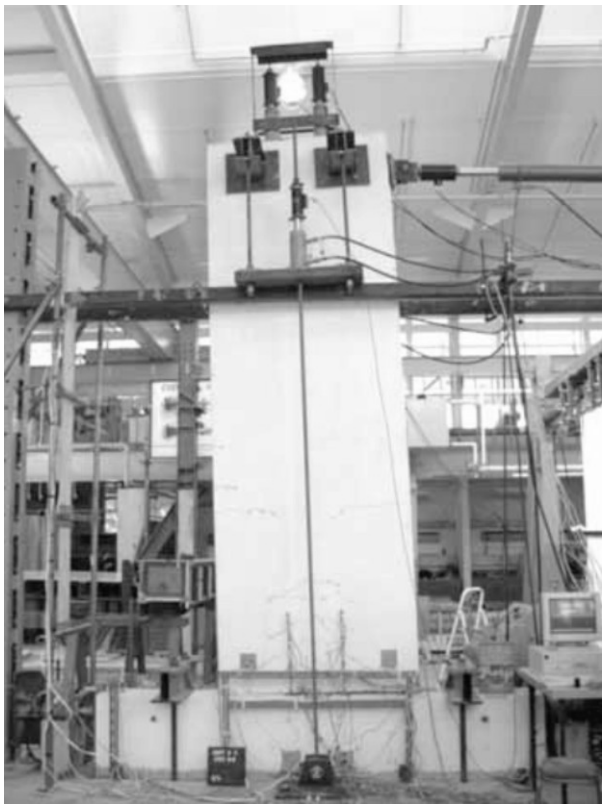

Figure 2.2 Post-tensioned rocking wall tested at University of Canterbury, Rahman and Restrepo [2000]

Similar work by Holden [2001], also carried out at the University of Canterbury, investigated the cyclic response of two precast concrete wall specimens. One wall unit combined unbonded post-tensioned tendons (using carbon fibre tendons) and grouted

mild steel reinforcement, with details being similar to the walls tested by Rahman and Restrepo [2000]. This hybrid wall was detailed with steel base plates at the toe of the wall welded to a diagonal strut made from steel bars which met at the middle of the wall, Figure 2.3. The steel diagonal strut was designed to resist the large compression forces as the wall rocked from toe to toe. The second specimen was an emulation of a cast-in-place monolithic wall: this was used as a benchmark to compare the response of the hybrid wall. The experimental response of the hybrid specimen was found to have very little energy dissipation, significant stiffness degradation and significant pinching. Holden [2001] concluded that the poor behaviour was associated with a combined bearing/push-out failure of the internal steel dissipaters beneath the foundation block. This prevented the mild steel from yielding in compression, limiting the equivalent viscous damping to approximately 3.5%-8% for the 3rd and 1st cycle respectively. The hybrid unit sustained virtually no cosmetic damage, and residual deformations were negligible.

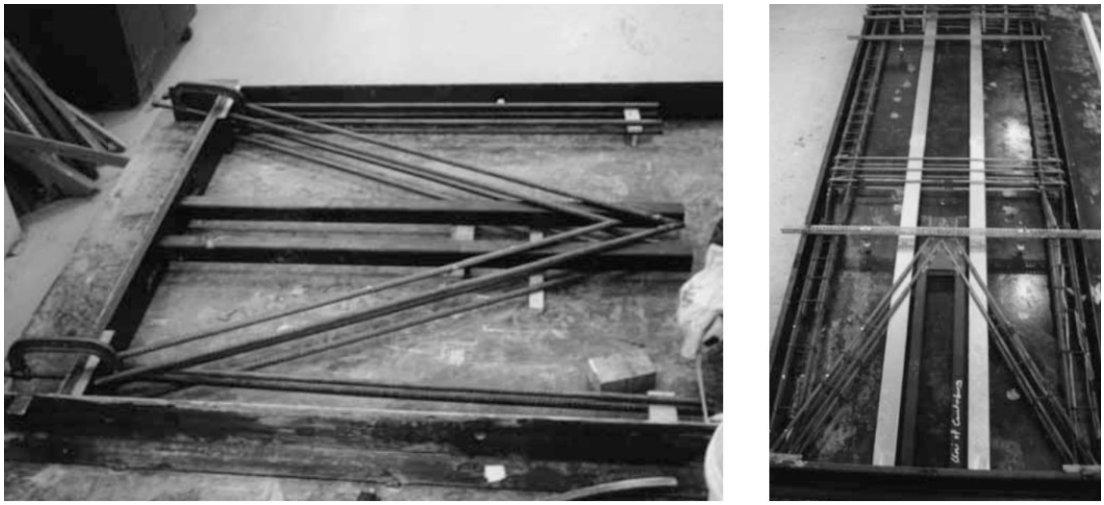

(a) Steel diagonal struts to resist compression (b) Wall configuration

Figure 2.3 Detailing of a post-tensioned wall, providing load paths for the high compression forces during rocking, Holden [2001]

2.3. POST-TENSIONED MASONRY WALL SYSTEMS

Further work at the University of Canterbury investigated the response of a masonry infilled wall coupled to an adjacent reinforced concrete frame. Toranzo-Dianderas [2002] designed and tested a three-story, 40% scale, masonry infilled frame upon the shake-table at the University of Canterbury which was designed to rock at the top of the foundation. The shake-table test is pictured in Figure 2.4 (a). The infilled frame was designed to behave as a rocking wall, coupled to an adjoining frame. The coupled frame was detailed to allow for pin-like behaviour of the ground floor columns and slab-beam elements. This minimised damage to the adjacent frame. The rocking wall incorporated one of two types of energy dissipation; the first being a confined bar yielding in tension and compression, while the second was a machined flexural arm located at the rocking interface of the confined masonry wall, Figure 2.4 (b). The

confined bar did not guarantee dependable behaviour as a result of buckling. The flexure device was very stable; however, it required a larger cross-section to in order to achieve the desired section capacity. Toranzo-Dianderas [2002] noted that when the lateral drift exceeded 1.10%, the stiffness of the system increased due to the stiffening effects of the slab-beams. This stiffening effect, combined with higher mode effects, resulted in base shears in the order of 2-3 times greater than the design base shear. Furthermore, the system was designed to insure the over-turning moment due to gravity was greater than the steel damper moment capacity: this ensured re-centring was always achieved, limiting damage to flexural hinging of the slab-beams (and column base), without compromising their gravity load carrying capacity. Unbonded post-tensioned tendons were not used, axial load comprised of gravity loading alone.

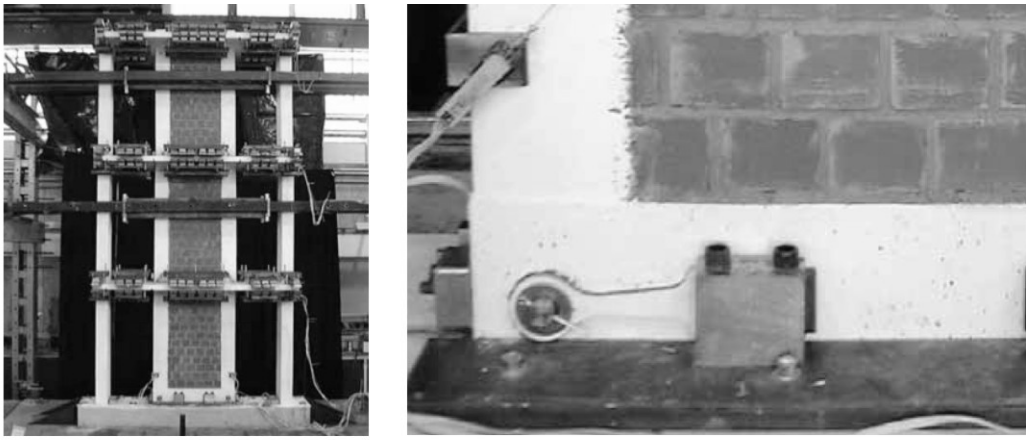

(a) Rocking, masonry-infilled frame (b) Flexural dampers at base of masonry wall

Figure 2.4 Dynamic testing of a rocking confined-masonry wall tested at the University of Canterbury, Toranzo-Dianderas [2002]

Additional research on rocking masonry wall structures was carried out by Wight et al. [2006] at North Carolina State University (NCSU). A total of four post-tensioned, masonry wall elements were tested on the shake-table at NCSU Constructed Facilities Laboratory. The voids within the concrete masonry walls were partially grouted and the tendons were unbonded over their entire length. Wight et al. [2006] found that the response of the systems was found to be very desirable for seismic performance due to the non-linear elastic response and the low damage each of the wall systems sustained. Wight et al. [2006] concluded by stating that the initial post-tensioning of the tendons had a significant influence on the maximum response of the masonry wall. In particular it was noted an 84% reduction in the peak response was achieved for a 37% increase in the initial post-tensioning – although, this study on the effects of initial post-tensioning was limited to a single earthquake excitation.

2.4. POST-TENSIONED PRECAST BRIDGE PIER SYSTEMS

Similar post-tensioning concepts have been investigated for the seismic design of bridge structures; more specifically, bridge pier systems. Mander and Cheng [1997]

tested near full scale rocking bridge pier specimens designed to rock from toe to toe under lateral displacements at the State University of New York, Buffalo. The pier unit was located on a steel angle beneath each toe to directly engage rocking about each corner. A number of post-tensioning configurations were tested (constant axial load, with and without unbonded post-tensioned tendons). While no form of dissipating mechanism was directly activated due to rocking of the pier, a 9.5mm thick rubber pad was sandwiched between each steel toe of the pier and the steel foundation angles. With the exception of the rubber insert, each of the five configurations tested had a very stable force-displacement behaviour, little energy dissipation and negligible residual deformations. The rubber insert increased the energy dissipation slightly but suffered degradation due to damage of the rubber pads. Equivalent viscous damping of less than 5% for the post-tensioned only solutions was achieved whereas 10% damping was achieved having a rubber interface. Analytical predictions were based on over-turning moments taken about the toe of the pier: these predictions could accurately capture the lateral push-over response of the pier. Mander and Cheng [1997] also proposed a design strategy for rocking bridge pier systems using a capacity spectrum/push-over approach. Energy dissipation is assumed to consist of contact/radiation damping related to a coefficient-of-restitution. A relationship between the coefficient-of-restitution and pier geometry allows an estimate of the equivalent viscous damping to be determined, with and without post-tensioning. A spectral demand curve (acceleration vs. displacement: ADRS curve) is computed based on a damped response spectra (a function of viscous damping) and compared with the lateral capacity of the pier system. The intersection of the capacity with the demand defines the performance point of the system. Furthermore, an iterative procedure was developed which computes the expected maximum displacement response for a given peak ground acceleration (PGA).

The lateral response of precast post-tensioned bridge piers was investigated at the University of California, San Diego by Hewes and Priestley [2001]. Four circular hollow precast segmental bridge piers were constructed and tested (each pier was tested twice) with steel confining jackets located around the segments at the foundation rocking interface. Lateral drift ratios of 6.0% were achieved with minimal damage. Rocking was not confined entirely to the foundation: in fact, rocking was also measured between the first and second precast segments above the foundation. As a result, some spalling of the cover concrete was observed within the unconfined precast segment not having any steel jacket.

Numerical work on bridge piers was carried out by Palermo [2004]. A Displacement-Based Design approach (DBD) was developed for the seismic design of bridge structures incorporating unbonded post-tensioned tendons and mild steel dissipation. An already existing member compatibility approach (Pampanin et al. [2001]) was modified to define the lateral push-over capacity of “controlled rocking” bridge pier connections with unbonded post-tensioned tendons. The modified member compatibility approach was validated against a beam-column joint test carried out at NIST during Phase II of the PRESSS program discussed above. This member compatibility approach was implemented within a FORTRAN code and design tables were created to relate section properties (moment-rotation, neutral axis position, steel stress) to a number of performance limit states (as a function of the section geometry).

2.5. CONCLUSIONS

While there is a general acceptance regarding the desirable behaviour of precast systems with unbonded post-tensioned systems, the degree of damage sustained to the structural elements and the efficiency (and stability) of the energy dissipation lies within the detailing and design of the critical rocking regions. Detailing of the rocking toe region, anchorage of the dissipation (either internally or externally) and tendon details appear to vary from test to test. A standardised method is required to maximise the efficiency of precast systems with unbonded post-tensioned tendons.

To a greater extent, while significant analytical and experimental work has been carried out on precast systems with unbonded post-tensioned tendons (with or without energy dissipation), little work to confirm the dynamic response has been carried out. A significant amount of analytical work has focused on relatively complex fibre-element models in addition to simple macro-models (discussed in greater detail in the following chapter). While the complex modelling techniques are very accurate, they require a degree of competency to be used correctly. Simple macro models appear extremely attractive as they can achieve comparable accuracy at a fraction of the computational cost.

Moreover, while supplementary viscous dampers have been investigated within precast systems, little work has been devoted to experimental testing and to the development of adequate and simple design procedures. The combination of both hysteretic and viscous dampers has great potential for the seismic protection of structures located in either near-field or far field seismic regions. Furthermore, precast systems with unbonded post-tensioning appear to be an attractive solution in which to implement this hysteretic-viscous combination.

2.6. REFERENCES

Armouti, N. (1993). "Seismic Preformance of Precast Concrete Structural Walls," Lehigh University, Bethlehem.

BSSC. (1997). *NEHRP Recommended Provisions for the Development of Seismic Regulations for New Buildings*, Federal Emergency Management Agency, Washington, D.C.

Cheok, G. S. and Stone, W. C. (1994). "Performance of 1/3 Scale Model Precast Concrete Beam-Column Connections Subjected to Cyclic Inelastic Loads." Report No 4: NISTIR 5436, N. I. o. S. a. Technology, ed.

Conley, J., Sritharan, S. and Priestley, M. J. N. (1999). "Precast Seismic Structural Systems PRESSS-3: The Five Story Precast Test Building Vol. 3-1: Wall Direction Response." Report No. SSRP-99/19, Department of Structural Engineering, University of California, San Diego.

El-Sheikh, M. T., Sause, R., Pessiki, S. and Lu, L. (1999). "Seismic behavior and design of unbonded post-tensioned precast concrete frames." *PCI Journal*, 44(3), 54-71.

Hewes, J. and Priestley, M. J. N. (2001). "Seismic design and performance of precast concrete segmental bridge columns." University of California, San Diego, San Diego.

Holden, T. J. (2001). "A Comparison of the Seismic Performance of Precast Wall Construction: Emulation and Hybrid Approaches." Research Report 2001-04, University of Canterbury, Christchurch.

Kurama, Y. C. (2000). "Seismic design of unbonded post-tensioned precast concrete walls with supplemental viscous damping." *ACI Structural Journal*, 97(4), 648-658.

Kurama, Y. C., Pessiki, S., Sause, R., Lu, L. and El-Sheikh, M. T. (1998). "Analytical Modelling and Lateral Load Behavior of Unbonded Post-Tensioned Precast Concrete Walls." PRESSS Report No. 98/02, P. S. S. S. PRESSS, ed., Lehigh University.

Kurama, Y. C., Sause, R., Lu, L. and Pessiki, S. (1999). "Seismic Behaviour and Design of Unbonded Post-Tensioned Precast Concrete Walls." *PCI Journal*, 44(3), 72-89.

Mander, J. B. and Cheng, C.-T. (1997). "Seismic Resistance of Bridge Piers Based on Damage Avoidance Design." Technical Report NCEER-97-0014, University of Buffalo, New York.

Mander, J. B., Priestley, M. J. N. and Park, R. (1988). "Theoretical Stress-Strain Model for Confined Concrete." *Journal of Structural Engineering*, 114(8), 1804-1826.

Mueller, P. (1986) "Hysteretic Behaviour of Precast Panel Walls." *U.S.-Japan Seminar on Precast Concrete Construction in Seismic Zones*, Tokyo, Japan.

Palermo, A. (2004). "The Use of Controlled Rocking in the Seismic Design of Bridges," Technical University of Milan, Milan.

Pampanin, S., Priestley, M. J. N. and Sritharan, S. (2001). "Analytical Modelling of the Seismic Behaviour of Precast Concrete Frames Designed with Ductile Connections." *Journal of Earthquake Engineering*, 5(3), 329-367.

Priestley, M. J. N. (1991). "Overview of PRESSS research program." *PCI Journal*, 36(4), 50-57.

Priestley, M. J. N. (1996). "PRESSS program - current status and proposed plans for phase III." *PCI Journal*, 41(2), 22-40.

Priestley, M. J. N. and MacRae, G. A. (1996). "Seismic tests of precast beam-to-column joint subassemblages with unbonded tendons." *PCI Journal*, 41(1), 64-80.

Priestley, M. J. N., Sritharan, S., Conley, J. R. and Pampanin, S. (1999). "Preliminary results and conclusions from the PRESSS five-story precast concrete test building." *PCI Journal*, 44(6), 42-67.

Priestley, M. J. N. and Tao, J. R. (1993). "Seismic response of precast prestressed concrete frames with partially debonded tendons." *PCI Journal*, 38(1), 58-69.

Rahman, A. M. and Restrepo, J. I. (2000). "Earthquake Resistant Precast Concrete Buildings: Seismic Performance of Cantilever Walls Prestressed Using Unbonded Tendons." Research Report 2000-5, University of Canterbury, Christchurch.

Stanton, J. F., Stone, W. C. and Cheok, G. S. (1997). "A hybrid reinforced precast frame for all seismic regions." *PCI Journal*, 42(2), 20-32.

Stone, W. C., Cheok, G. S. and Stanton, J. F. (1995). "Performance of hybrid moment-resisting precast beam-column concrete connections subjected to cyclic loading." *ACI Structural Journal (American Concrete Institute)*, 92(2), 229.

Toranzo-Dianderas, L. A. (2002). "The Use of Rocking Walls in Confined Masonry Structures: A Performance-Based Approach," University of Canterbury, Christchurch.

Wight, G. D., Ingham, J. M. and Kowalsky, M. J. (2006). "Shaketable Testing of Rectangular Post-Tensioned Concrete Masonry Walls." *ACI Structural Journal. Vol. 103, no. 4, pp. 587-595. July-Aug. 2006.*

3. A Discussion on Existing Performance-Based Design Philosophies and Analysis Techniques for Post-Tensioned Rocking Systems

3.1. INTRODUCTION

This introductory chapter presents existing Performance-Based Earthquake Engineering (PBEE) design methodologies, with an emphasis on Direct Displacement-Based Design (DDBD). PBEE has been widely accepted as a means of quantifying the performance of a system over the working life of a structure. Traditional seismic design will typically consider two performance objectives 1) an ultimate limit state considering strength, and to a lesser extent displacements and 2) the serviceability limit state considering deflection, cracking and vibration etc. PBEE identifies multiple performance objectives (generally three or more) to encompass a set of anticipated hazards over the working life of the structure. PBEE will be presented in the context of post-tensioned rocking systems, which is the focus of this thesis. Following from a discussion on existing design procedures, the mechanics of rigid rocking blocks is presented. Finally, existing section analysis and modelling techniques for post-tensioned connections are presented in the form of lumped plasticity modelling methods or more complex distributed plasticity models.

3.2. PERFORMANCE-BASED DESIGN FRAMEWORK

Performance-based earthquake engineering (PBEE), assigns a series of structural performance levels to a set of seismic hazards; SEAOC [1999], FEMA [2003], fib [2003a], Priestley et al. [2007]. This technique is summarised in Figure 3.1 (a) where individual *material strain limits* are first defined. Each material limit state defines a specific *structural limit state* i.e. yielding, spalling of the cover concrete etc. Each *structural performance level* groups together a number of material limit states of similar damage. From here, each structural performance level is associated with a specific *seismic hazard* such that the expected level of structural/non-structural damage has some probability of being exceeded within the working life of the structure: this is defined as a *performance objective*. The earthquake intensity at a site is related to the annual rate of such an event being exceeded. Common intensity measures include peak ground acceleration (PGA) or spectral acceleration at the fundamental period of the structure (Shome and Cornell [1999]). The relationship between earthquake shaking and the annual rate of exceedance defines the seismic hazard. Generally three or more performance objectives are defined for the structure, from frequent events causing little damage to very rare events causing significant damage: this is known as a *performance matrix*. An example of such a performance

matrix is presented in Figure 3.1 (b), reproduced from the Californian SEAOC manual (SEAOC [1999]). In this example, three sets of performance objectives are illustrated for structures of various importance levels (Basic to Safety-Critical). Similar design philosophies have been incorporated into design guidelines in the United States for the design of new structures (FEMA [2003]) and for the rehabilitation of existing structures (FEMA [1997], FEMA [2000]). In addition to these documents a number of documents have been published refining the performance-based philosophy to its current state-of-the-art; Kurama et al. [1999], El-Sheikh et al. [1999], fib [2003a], fib [2003b], Priestley et al. [2007].

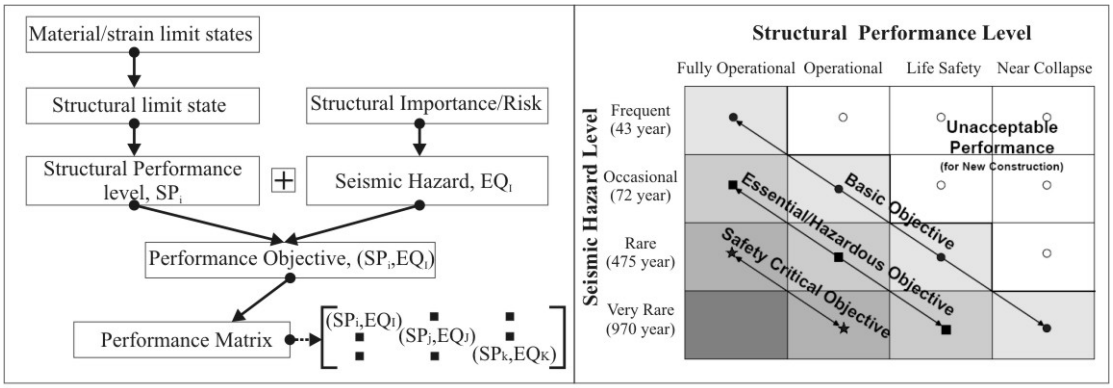

(a) Flow diagram summarising PBEE (b) Performance matrix, SEAOC 1999

Figure 3.1 Basic concepts of performance-based earthquake engineering

3.3. DIRECT-DISPLACEMENT-BASED DESIGN (DDBD) PRIESTLEY ET AL. [2007]

Direct displacement-based design (DDBD) falls under the umbrella of Performance-Based Earthquake Engineering (PBEE). As per PBEE, a performance level within DDBD is defined as an explicit level of structural (and non-structural) damage corresponding to an earthquake intensity having a specific probability of exceedance. Damage is generally related to displacements, which in turn, are related to member curvatures and hence, material strains. The DDBD procedure was developed recognising that damage is primarily related to displacements, resulting in a more intuitive design methodology. Modern Force-Based Design (FBD) is a rather developed procedure (over a period of decades) originally adopted as it appeared compatible with conventional gravity load analysis; that is, both dealt directly with forces. FBD was developed, somewhat incorrectly, on the premise that inelastic (ductile) structures are subjected to displacements equal (or at least similar) in magnitude to an elastically responding system: this defines the equal displacement approximation (Newmark [1960]). Various researches have shown this relationship rather loosely, if at all, fits this trend (Carr [2003], Priestley et al. [2007]). The maximum displacement response from a series of time history analyses (THA) are presented in Figure 3.2 for three different hysteresis rules, each having the same loading envelope; a Flag-shaped hysteresis, a Takeda hysteresis, and an inelastic

bilinear rule. Each of the three systems were designed to the EC8 loading spectrum for a force reduction factor of four (***R***=4, note in EC8 this factor is defined as the behaviour factor ***q***). Seven spectrum compatible ground motions were subjected to each system for elastic periods ranging from 0.25-2.5sec. The maximum displacement is presented as a ratio to the average peak elastic displacement. The following can be concluded from Figure 3.2

The equal displacement rule states that each of the three systems should have a value of 1.0. This rule is increasingly violated for systems with decreasing hysteretic energy dissipation (area-enclosed within the force-displacement response). It can be seen that the displacement response is heavily dependant on the type of structural system; the use of a single global force reduction factor, let alone one based on a rather crude approximation, should not be considered. The equal-displacement relationship is increasingly violated for periods less than 0.75sec. In fact, some seismic loading codes (such as New Zealand, NZS1170.5 [2004]; Europe, Eurocode:8 [2003] and the United States, FEMA [2003]) recognise this period dependency and define force reduction factors based on an equal-energy (or an equal acceleration) rule within this period range.

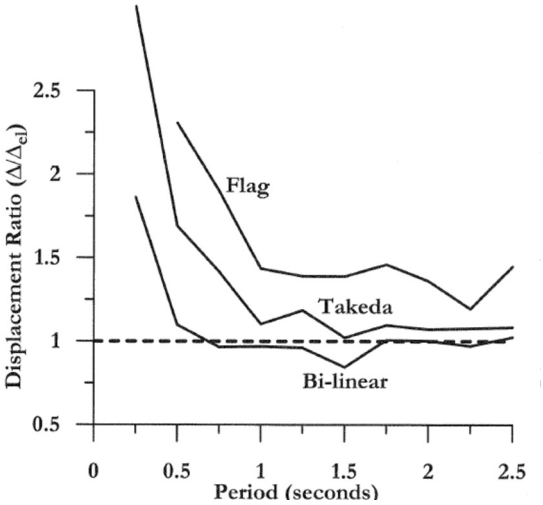

Figure 3.2 Ratio of inelastic to elastic displacement for different hysteresis rules (Priestley et al. [2007])

Further inconsistencies between structural behaviour and Force-Based Design (FBD) are evident in the manner in which the relationship between strength and stiffness is treated in FBD. It can be shown that the stiffness of a reinforced concrete (R.C) section is proportional to its strength. FBD adopts effective member stiffness based almost entirely on geometry; for beams, the New Zealand Concrete Standard suggests effective section stiffness modifiers of 0.32-0.40, while for columns the range is 0.3-0.8 depending on the level of axial load acting on the section. In hind site, these values represent typical reinforcement ratios: relationships are provided for reinforcement ratios outside the norm. The fundamental structural period is generally estimated, either by empirical equations, or by modal/structural analysis based on the above stiffness modification factors. The structural period determines the lateral

design coefficient and the loads to be applied to the structure. As the lateral loads define the internal design actions, iteration is clearly required as the reinforcement content, which dictates both the strength and stiffness of the section, is not known prior to the analysis. When it comes to distributing lateral forces throughout the structure, FBD will proportion them relative to the effective (cracked) elastic stiffness of each structural element. In contrast, DDBD intuitively recognises that the forces applied to a ductile system should be proportioned according to the relative strength of each structural element. Proportioning forces according to relative strength will result in a more consistent (and regular) distribution of reinforcement and utilise the full strength of each structural element.

3.3.1. An Overview of the DDBD Procedure, Priestley et al. [2007]

An outline of DDBD is presented in Figure 3.3, highlighting four key steps. The first two steps (a) and (b) convert the multi-degree-of-freedom (MDOF) system into an equivalent single-degree-of-freedom (SDOF) system. The inelastic first mode shape δ_i describes the displacement profile of the MDOF system at the design drift. The DDBD procedure will be presented in terms of a low-rise frame building below. The mode shape δ_i is a function of the structural system (frames, walls, dual systems etc): for a low-rise frame building (less than five levels) the normalised mode shape is assumed be linear with height where H_i is the height to level i and H_n is the total height of the structure.

$$\delta_i = f\left(\frac{H_i}{H_n}\right) = \frac{H_i}{H_n} \qquad \textbf{3.1}$$

Given the displacement profile δ_i, the displacement Δ_d of the effective mass can be determined

$$\Delta_d = \frac{\sum_{i=1}^{n} m_i \Delta_i^2}{\sum_{i=1}^{n} m_i \Delta_i} \qquad \textbf{3.2}$$

The effective mass m_e and the effective height H_e are determined from the following

$$m_e = \frac{\sum_{i=1}^{n} m_i H_i}{\Delta_d} \qquad \textbf{3.3}$$

$$H_e = \frac{\sum_{i=1}^{n} m_i \Delta_i H_i}{\sum_{i=1}^{n} m_i \Delta_i} \qquad \textbf{3.4}$$

The next step (c), relates energy dissipation to the peak displacement response. The energy dissipation is computed from the system ductility μ which in turn is computed from an estimation of the yield displacement Δ_y. The energy dissipation is heavily

dependant on the type of structural element within the system i.e. walls, frames, RC, steel etc. The system ductility μ is used to evaluate the Equivalent Viscous Damping (EVD) ξ_{eq} of the structural system. This is used to estimate the expected reduction in peak displacement response (when compared to an elastic system). In Eq.(3.5) the elastic displacement response spectrum $\Delta_{d,5\%}(T)$ is reduced by the factor η, which accounts for the equivalent viscous damping within the system ξ_{eq} during the excursion to the peak displacement.

$$\Delta_{d,\xi}(T) = \Delta_{d,5\%}(T) \cdot \eta \qquad \textbf{3.5}$$

Where η is defined as

$$\eta = \sqrt{\frac{7}{2+\xi_{eq}}} \qquad \textbf{3.6}$$

Finally, in Step (d) the effective period T_e, being the *secant* period to the target displacement Δ_d, is inferred from the reduced displacement spectrum $\Delta_{d,\xi}(T_e)$. The stiffness of the equivalent elastic SDOF system K_e is computed.

$$K_e = 4\pi^2 \frac{m_e}{T_e^2} \qquad \textbf{3.7}$$

The design base shear V_b is then calculated.

$$F = V_b = K_e \Delta_d \qquad \textbf{3.8}$$

The base shear is proportioned up the height of the structure according to the inelastic mode shape δ_i and the mass at each level m_i.

$$F_i = V_b \frac{m_i \Delta_i}{\sum_{i=1}^{n} m_i \Delta_i} \qquad \textbf{3.9}$$

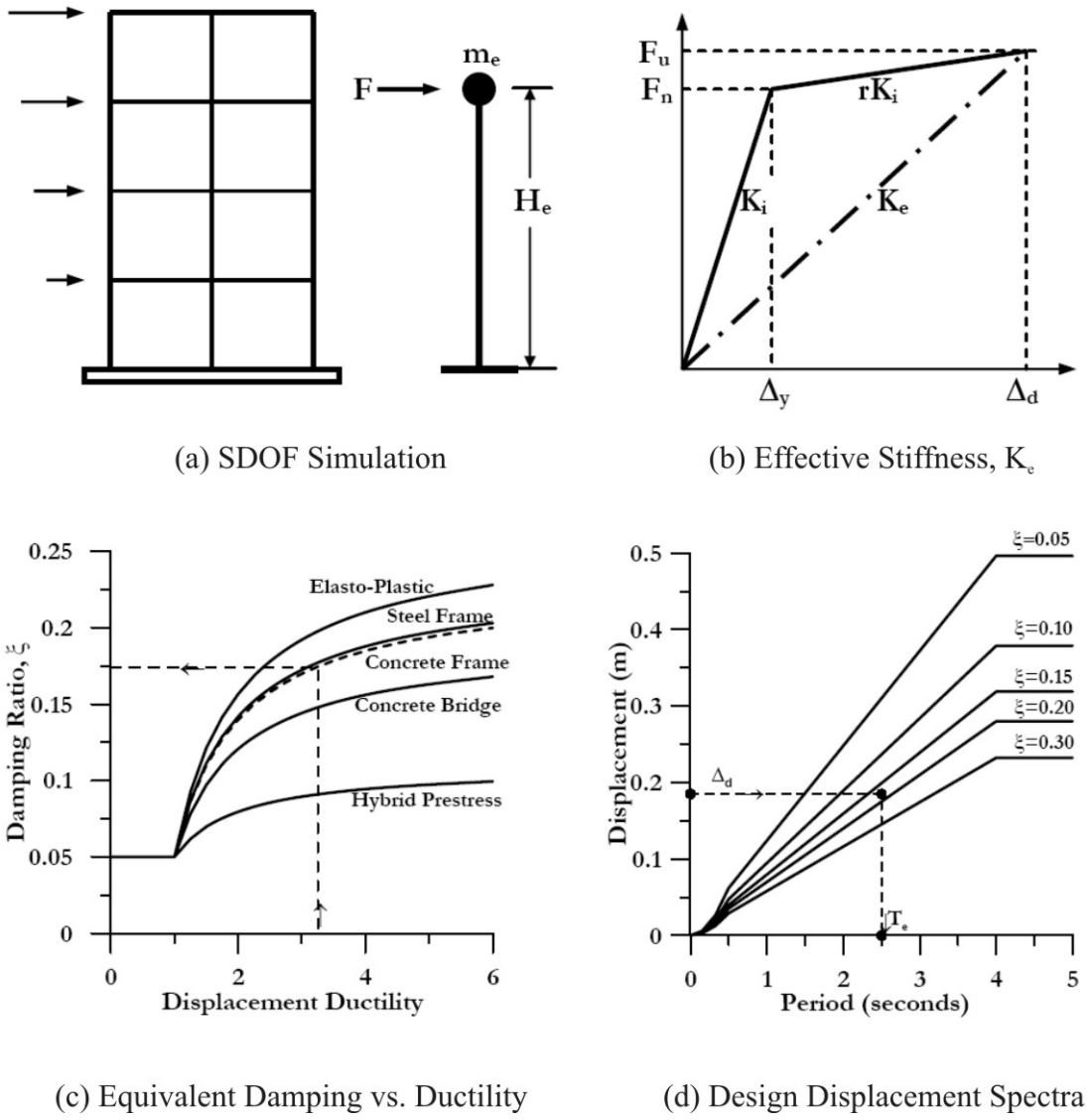

Figure 3.3 DDBD procedure for seismic resisting systems (Priestley et al. [2007])

3.3.2. Comparison Between FBD and DDBD

This section will provide an example of the design parameters and response of four single-degree-of-freedom (SDOF) systems, each designed to DDBD and FBD. Following the design, each system is subjected to 15 recorded far-field ground motions that are later used in the thesis. The four SDOF systems include two elastic periods ($T_1 = 0.4$sec and $T_1 = 1.5$sec) and two ductility levels ($\mu = 1.25$ and $\mu = 4$). The New Zealand seismic loadings code NZS1170.5 [2004] is used to define the elastic design spectrum. For DDBD the elastic spectrum is reduced according to η in Eq.(3.6), while for FBD the elastic spectrum is reduced according to the ductility reduction factor k_μ following the seismic provisions of NZS1170.5 [2004]. The design is carried out for a seismic hazard having a zone factor $z = 0.28$, risk factor $R = 1$, near-fault factor $N(T_1,D) = 1$, soil class C, and for consistency all systems include a structural performance factor of $S_p = 1.0$. The resulting design peak ground acceleration is $S_a(T = 0) = 0.372$g.

For FBD the elastic response spectrum is reduced according to Eq.(3.10) and Eq.(3.11) below, depending on the fundamental period of the structure T_1.

For $T_1 \geq 0.7$s (for soil class C)

$$k_u = \mu \tag{3.10}$$

For $T_1 < 0.7$s (for soil class C)

$$k_u = \frac{(\mu - 1)T_1}{0.7} + 1 \tag{3.11}$$

For DDBD the elastic response spectrum is reduced according to η in Eq.(3.6), where the EVD ξ_{eq} is computed from Eq.(3.12) below (the constant in Eq.(3.12) is specific to an R.C frame structure).

$$\xi_{eq} = 0.05 + 0.565\left(\frac{\mu - 1}{\mu\pi}\right) \tag{3.12}$$

A summary of the key design parameters are presented in Table 3.1 comparing each of the four systems designed to FBD and DDBD. The common structural properties between the FBD and DDBD system is the design ductility μ, the fundamental period T_1 and the system mass m_e. This example gives some insight into whether FBD or DDBD will result in a larger design base shear V_b. While FBD has a large spectral reduction at the fundamental period, DDBD has a small spectral reduction at the effective period. The following conclusions are made

- DDBD tends to require a lower base shear for short periods of any ductility level.
- For medium-long periods and high ductility, DDBD requires a larger base shear
- For nominally elastic structures (limited ductility) DDBD requires a reduction in base shear when compared to FBD regardless of the fundamental period.
- As the ductility approaches $\mu = 1$ (elastic design) DDBD reduces to an elastic design compatible with FBD having $\mu = 1$.

A summary of the model parameters and time history analysis (THA) response is presented in Table 3.2. The mean peak displacement response, when subjected to 15 ground motions Δ_{THA}, is compared to the expected design displacement Δ_{des} resulting from FBD and DDBD. The following conclusions are made;

- DDBD results in a more uniform and predictable response when compared to FBD for all short and medium-long periods of any ductility.
- For medium-long periods designed with large ductility, FBD underestimates the base shear considerably. As a result, the THA displacements are 41% larger than that estimated from the design. On the other hand, DDBD requires a larger base shear for the same system; the THA displacements are within 9% of the design displacement.

- For medium-long period structures with limited ductility, both the FBD and DDBD return maximum displacements that are comparable with the design.
- By comparing the design base shear with the THA response, it can be seen that DDBD is a more consistent design methodology providing structures with more uniform risk.

Table 3.1 Seismic design summary for four systems considering FBD and DDBD

		System 1	System 2	System 3	System 4
	μ	**4**	**4**	**1.25**	**1.25**
	T_1 [sec]	**0.4**	**1.5**	**0.4**	**1.5**
	m_e [tonne]	750	750	750	750
FBD	k_μ	2.71	4.00	1.14	1.25
	$1/k_\mu$	0.368	0.250	0.875	0.800
	K_i [kN/m]	184969	13173	184794	13159
	$V_b/w_t = C_d(T_1)$ [g]	0.244	0.061	0.579	0.197
	Δ_y [m]	0.010	0.034	0.023	0.110
	$\mu\Delta_y$ [m]	0.039	0.136	0.029	0.138
DDBD	Δ_d [m]	0.037	0.161	0.025	0.125
	Δ_y [m]	0.010	0.040	0.020	0.100
	ξ_{eq}	0.185	0.185	0.086	0.086
	η[1]	0.585	0.585	0.813	0.813
	T_e [sec]	0.8	3.0	0.45	1.68
	$V_b/w_t = C_d(T_e)$ [g]	0.230	0.072	0.496	0.179
	V_{DDBD}/V_{FBD}	*0.943*	*1.181*	*0.856*	*0.908*

[1] No lower limit was applied to the spectral reduction factor η

Table 3.2 Time history analysis summary of four systems designed to FBD and DDBD

		System 1	System 2	System 3	System 4
	μ	**4**	**4**	**1.25**	**1.25**
	T_1 [sec]	**0.4**	**1.5**	**0.4**	**1.5**
	m_e [tonne]	750	750	750	750
	V_{DDBD}/V_{FBD}	*0.943*	*1.181*	*0.856*	*0.908*
FBD	Δ_y [m]	0.010	0.034	0.023	0.110
	K_i [kN/m]	184969	13173	184794	13159
	F_y [kN]	1795	449	4260	1449
	$\Delta_{des} = \mu\Delta_y$ [m]	0.039	0.136	0.029	0.138
	Δ_{THA} [m]	0.035	0.192	0.024	0.142
	$\Delta_{THA}/\Delta_{des}$	0.894	1.411	0.846	1.032
	Error	*-10.6%*	*41.1%*	*-15.4%*	*3.2%*
DDBD	Δ_y [m]	0.010	0.040	0.020	0.100
	K_i [kN/m]	184969	13173	184794	13159
	F_y [kN]	1693	530	3646	1316
	$\Delta_{des} = \Delta_d$ [m]	0.037	0.161	0.025	0.125
	Δ_{THA} [m]	0.038	0.176	0.024	0.139
	$\Delta_{THA}/\Delta_{des}$	1.036	1.090	0.969	1.111
	Error	*3.6%*	*9.0%*	*-3.1%*	*11.1%*

3.3.3. The Structural Performance Factor S_p within DDBD

This section on DDBD concludes with a discussion on the correct use of the structural performance factor S_p within a DDBD framework. The New Zealand seismic loading standard (NZS1170.5 [2004]) incorporates a structural performance factor S_p to reduce the elastic design spectrum for ductile structures. NZS1170.5 [2004] accounts for the poor relative performance of brittle/low ductile structures by increasing their design loads by a factor of 1/0.7 (Page 9, NZS1170.5 [2004] commentary). Considering a design at the *Ultimate Limit State* (defined by NZS1170.5 [2004]) S_p is a function of the system's design ductility μ and construction material. For steel structures with $\mu > 1.25$ and for R.C. structures with $\mu > 3$ S_p is equal to 0.7, otherwise S_p is equal to 0.9. For R.C. structures with $\mu < 3$, S_p can be relaxed to a value of 0.7 provided the potential plastic hinge regions are detailed as ductile elements. Unless specified in the appropriate materials code, NZS1170.5 [2004] specifies that the structural performance factor S_p is equal to 0.7 unless $1.0 < \mu < 2.0$, in which case is, S_p is defined by Eq.(3.13).

$$S_p = 1.3 - 0.3\mu \qquad \textbf{3.13}$$

In general, ductile structures will be designed such that the elastic design spectrum is reduced by 30% (S_p reduction) in addition to the reduction associated with ductility. In NZS1170.5 [2004] S_p is incorporated within the calculation of the design base shear by reducing the design acceleration spectrum in Eq.(3.14)

$$C_d(T_1) = \frac{Z \cdot C(T_1) S_p}{k_\mu} \qquad \textbf{3.14}$$

Where;

- $C_d(T_1)$ = horizontal design coefficient
- Z = site hazard factor [g]
- $C(T_1)$ = elastic hazard spectrum
- S_p = structural performance factor
- k_μ = ductility reduction factor

For DDBD, and considering steady-state harmonic motion, the elastic (5% damped) displacement spectrum is computed from the acceleration design spectrum of Eq.(3.14) as follows

$$\Delta_{NZS,5\%}(T) = \frac{C_d(T, \mu = 1) \cdot T}{4\pi^2} = \frac{Z \cdot C(T) \cdot S_p \cdot T}{4\pi^2} \qquad \textbf{3.15}$$

Hence, the (effective) period is proportional to the inverse of S_p,

$$T(\Delta_{NZS,5\%}) = \frac{\Delta_{NZS,5\%} 4\pi^2}{Z \cdot C(T) \cdot S_p} \qquad \textbf{3.16}$$

For DDBD the base shear is proportional to the inverse of the effective period squared. Therefore, the base shear will be proportional to S_p squared. That is, for DDBD the S_p reduction is accounted for twice in the base shear calculation.

$$V_b = K_e \Delta_d = \frac{4\pi^2 m_e}{T_e^2} \Delta_d = f(S_p^2, Z^2 ...) \quad \textbf{3.17}$$

It follows, considering a DDBD of two systems on two different sites (defined by two seismic hazards) having the same effective period, the base shear is proportional to the square of the peak ground acceleration (Z) of the two sites, i.e. Eq.(3.18), Priestley [2002].

$$\frac{V_{b2}}{V_{b1}} = \left(\frac{Z_2}{Z_1} \right)^2 \quad \textbf{3.18}$$

Similarly, a FBD of two systems on two different sites having the same elastic period (and ductility), the base shear is proportional to the peak ground acceleration (Z) of the two sites as follows

$$\frac{V_{b2}}{V_{b1}} = \frac{Z_2}{Z_1} \quad \textbf{3.19}$$

For DDBD to be seen as compatible (or competitive) with FBD, the S_p factor should be retained when computing the base shear V_b. However, the author understands that the S_p reduction is a base shear reduction factor, not a seismic hazard reduction factor. It is for this reason, specific to DDBD, the S_p factor should not be used to reduce the elastic response spectrum $C_d(T_1)$ of Eq.(3.14), but added to the base shear calculation of Eq.(3.20) as follows,

$$V_b = S_p K_e \Delta_d = S_p \frac{4\pi^2 m_e}{T_e^2} \Delta_d \quad \textbf{3.20}$$

In doing so, the elastic design displacement spectrum of Eq.(3.21) is no longer reduced by S_p, but is accounted for when computing the base shear V_b.

$$\Delta_{NZS,5\%}(T) = \frac{Z \cdot C(T) \cdot T}{4\pi^2} \quad \textbf{3.21}$$

3.4. ROCKING BEHAVIOUR OF RIGID BODIES

3.4.1. The Behaviour of Inverted Pendulum Structures, Housner [1963]

The mechanics of a rigid block was first investigated in detail by Housner in 1963. By equating moments about point **O** in Figure 3.4, the free-vibration equation of motion can be written as Eq.(3.22).

$$I_0\ddot{\theta} = -WR \cdot \sin(\alpha - \theta) \qquad \textbf{3.22}$$

Where

I_0 = mass moment of inertia about point **O**

$\ddot{\theta}$ = angular acceleration of the block in rad/s^2

All other terms are defined in Figure 3.4.

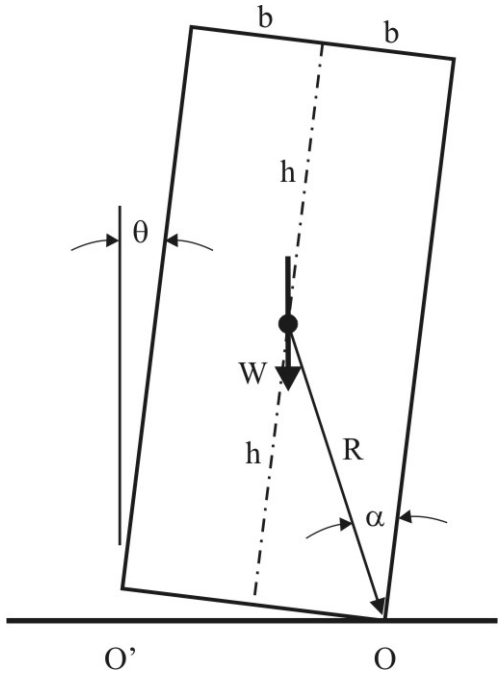

Figure 3.4 Housner's rocking block

The response of a rigid block under free vibration is highly non-linear; the period of the system is highly dependant on the rotation amplitude θ. The relationship describing the period is shown in Figure 3.5 (a), where θ_0 represents the release amplitude. As the release amplitude θ_0 approaches α, the period extends to infinity before over-turning. The period is equal to zero when the release amplitude is zero (assuming a rigid block). By equating moments about the rocking toe **O**, the lateral response, in terms of overturning moment versus base rotation is easily computed and shown in Figure 3.5 (b). Intuitively, the negative bilinear stiffness of the system implies a highly non-linear, unstable system.

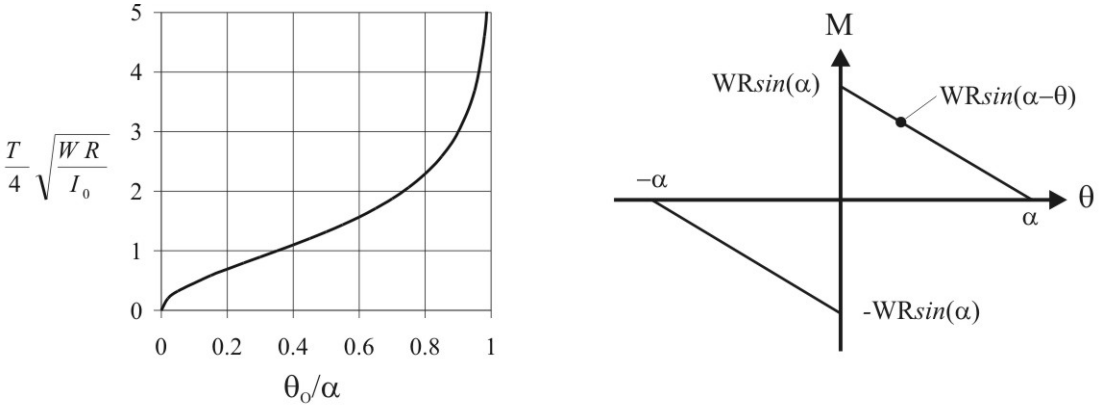

(a) Rocking period of vibration with amplitude θ_0

(b) Moment rotation response of rocking block

Figure 3.5 Mechanical properties of a rigid rocking block

If there is no energy lost during rocking, the system would oscillate indefinitely at the period defined by the release amplitude. In reality, some energy is lost during rocking defined as contact damping. Housner expresses this energy loss as the ratio of the kinetic energy before and after impact and assumes the impact is purely inelastic, i.e. no elastic rebound force occurs (no bouncing)

$$r = \left(\frac{\dot{\theta}_2}{\dot{\theta}_1}\right)^2 \qquad \textbf{3.23}$$

The coefficient of restitution ***e*** is defined by Eq.(3.24)

$$e = \frac{\dot{\theta}_2}{\dot{\theta}_1} \qquad \textbf{3.24}$$

Where

$\dot{\theta}_2$ = angular velocity immediately after impact

$\dot{\theta}_1$ = angular velocity immediately before impact

Housner went on to show that by equating moment equilibrium immediately before and after impact, the change in kinetic energy is related entirely to the geometry of the block

$$r = \left(1 - \frac{MR^2}{I_0}\left[1 - \cos(2\alpha)\right]\right) \qquad \textbf{3.25}$$

A relationship is derived relating the amplitude $\boldsymbol{\theta}$ after ***n*** successive rocking impacts when released from an initial amplitude $\boldsymbol{\theta_o}$.

$$\phi_n = 1 - \sqrt{1 - r^n \left[1 - (1 - \phi_0)^2\right]} \qquad \textbf{3.26}$$

Where

n = number of impacts from release

ϕ = dimensionless amplitude, $\phi = \frac{\theta}{\alpha}$, where ϕ_0 defines the dimensionless release amplitude and ϕ_n is the dimensionless amplitude after n impacts.

In a later publication, Priestley et al. [1978] related this reduction in kinetic energy to equivalent viscous damping derived considering free-vibration of rocking blocks.

$$\xi_{eq} = \frac{1}{n\pi} \ln\left(\frac{\theta_0}{\theta_n}\right) \qquad \textbf{3.27}$$

Eq.(3.27) can be approximated with the following empirical equation

$$\xi_{eq} = -0.34 \ln(r) \qquad \textbf{3.28}$$

Tso and Wong [1989a] note that the highly non-linear nature of rocking blocks gives rise to complicated dynamic characteristics during forced or earthquake excitation. Makris and Konstantinidis [2001] and Makris and Konstantinidis [2003] dispute the use of Eq.(3.28) for the design of rocking blocks. They argue that the dynamic characteristics of a rocking system are not compatible with a response spectrum derived from either a single-degree-of-freedom inelastic bilinear oscillator or an elastic damped oscillator. The conclusion that the rocking response is quite different to that of a traditional elastic or ductile structural response has been supported by Aslam et al. [1980] and was further confirmed after experimental tests were found difficult to repeat. Makris supported his argument with numerical analyses indicating that at a 1.6% change in the excitation amplitude resulted in a 125% change in displacement (rotation) response, whereas similar increases to the response of a bilinear oscillator would be minimal. Following these studies by Makris and Konstantinidis [2001] the use of a rocking spectrum was suggested as a design tool for rocking blocks.

Experimental studies have shown that the reduction in kinetic energy predicted by Eq.(3.24) is almost always greater than that observed during testing. Housner's theorem states that the impact must be purely inelastic; however, free-vibration studies have shown that some energy is returned to the rocking system via elastic bouncing during impact, Evison [1977]. On the contrary, other experimental studies noted other sources of energy dissipation, such as friction within the system, resulting in greater energy loss than that predicted by Eq.(3.24), Tso and Wong [1989b].

Aslam et al. [1980] provided a practical extension of the pure rocking block by locating prestressed tendons within the centre of the rocking block to increase the stability of the system (Figure 3.6).

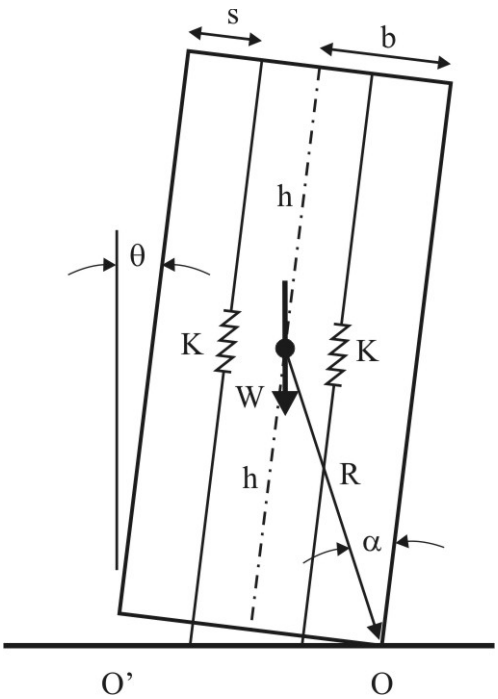

Figure 3.6 Aslam et al. [1980] post-tensioned rocking block

The addition of the post-tensioned tendons dramatically improves the overturning response of the block. Figure 3.7 compares the lateral response of a post-tensioned block with a pure rocking block. In Figure 3.7 the distance from the rocking toe to each post-tensioned tendon group is defined as d_i, the total (initial) prestressing force is denoted as $T_{PT,0}$, while the stiffness of each tendon group is defined as K.

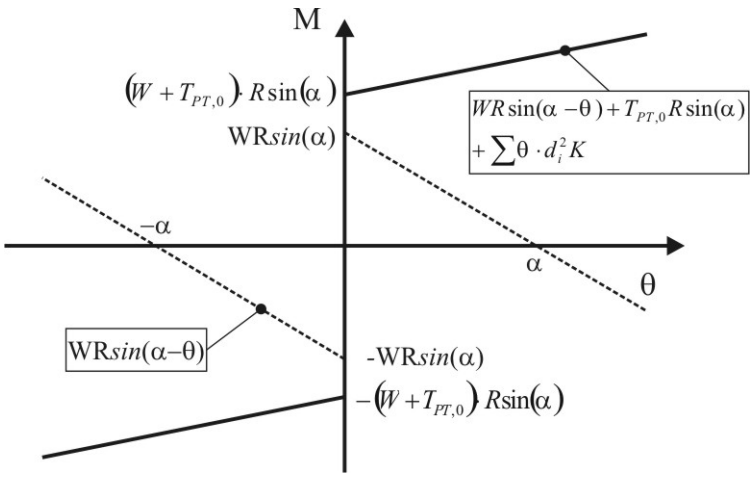

Figure 3.7 Moment rotation response of a post-tensioned rigid block

The addition of prestressed tendons has two key advantages; first, the bilinear stiffness is significantly increased: if the tendon stiffness K is large enough the bilinear stiffness will be positive. Second, toppling of the block is prevented. While

the system is still non-linear, the dynamic characteristics are now more consistent with traditional ductile systems. In the case of a prestressed rocking block, the rocking spectrum is no longer appropriate and the use a traditional response spectrum can be adopted for design.

Another extension to the free-standing block was carried out by Makris and Zhang [1999] by adding ductile elements at the edge of the rocking section (Figure 3.8). The addition of the ductile elements adds strength and energy dissipation to the section, increasing the overall stability. Makris and Zhang [1999] found that the ductile restrainers provided only a marginal improvement to the response under a sine-pulse acceleration time history (representing a simplified near-fault ground motion). Under these ground motion events the level of mechanical damping has little relevance, rather the strength and stiffness of the loading envelope is of greater importance. The lateral response of Figure 3.8 is graphically illustrated in Figure 3.9.

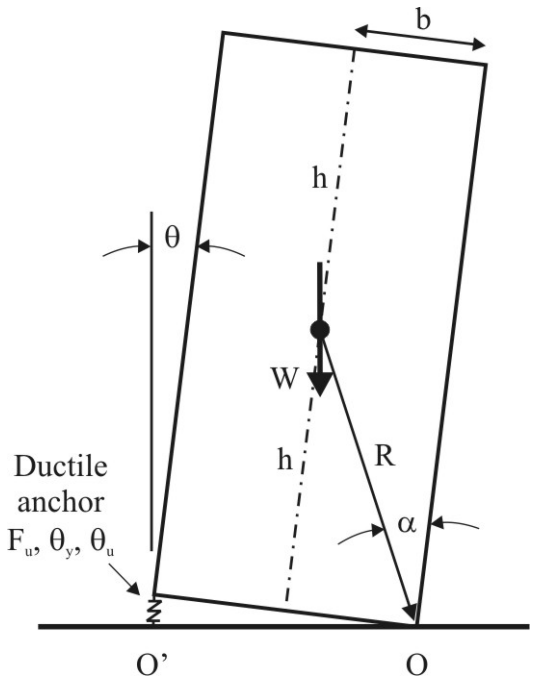

Figure 3.8 Makris and Zhang [1999] restrained post-tensioned rocking block

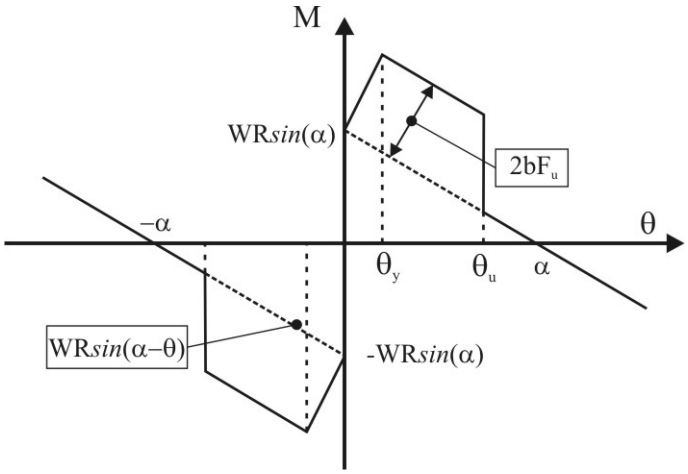

Figure 3.9 Makris and Zhang [1999], moment rotation response of a restrained post-tensioned rigid block

3.4.2. Conclusions Specific to the Rocking Response of Rigid Blocks

This thesis is concerned with post-tensioned rocking systems. The peculiarities of free-standing blocks are of little relevance to post-tensioned systems whose dynamic characteristics are more akin to that of traditional ductile systems. Post-tensioned systems have a larger bilinear stiffness: this increases the stability of the system by mitigating/preventing toppling. Hence, this suggests that a conventional response spectrum, as opposed to a rocking spectrum, is more appropriate.

The coefficient of restitution (defining the energy lost during impact) is a useful concept when modelling rocking blocks based on the fundamentals of block mechanics, i.e. by numerically solving the equation of motion for an inverted pendulum. A more practical alternative for design and modelling is to equate this energy loss to equivalent viscous damping (EVD). While it is argued that the coefficient of restitution can not be related to EVD for free-standing rocking blocks, such a relationship may be valid for post-tensioned systems whose dynamic characteristics are similar to traditional ductile systems.

3.5. MODELLING TECHNIQUES FOR POST-TENSIONED ROCKING SYSTEMS

3.5.1. Lateral Response of Post-Tensioned Connections

The lateral response of a generic post-tensioned system is discussed below and illustrated in Figure 3.10. The lateral response is characterised by a number of discrete points.

Decompression is the deformation state where the strain at the outer most fibre approaches zero and uplift (rotation) of the base is initiated. The neutral axis depth is located at the edge of the section ($c = L_w$) and is characterised by a sudden reduction in stiffness when compared to the initial (gross) section stiffness.

Geometric non-linearity occurs when the neutral axis of the section approaches the mid height of the section ($c = L_w/2$) and defines a further reduction in stiffness.

Yielding of the mild steel reinforcement can occur either before or after the geometric non-linearity point depending on the section dimensions and location of the steel reinforcement within the section. While some stiffness is lost the system still retains significant post-yield stiffness due to the elongation of the prestressed reinforcement along the rocking interface.

Yielding of the prestressed reinforcement will result in a total loss in stiffness. Prestressing tendons are inherently brittle with minimal strain ductility. The re-centring capacity of the section can be jeopardised if the prestressed reinforcement yields: this reduces the effective tendon prestressing force. Some permanent displacements may be tolerated for very rare earthquake events. A reduction in the prestress force can be detrimental in some cases, such as a beam-column joint relying on shear transfer through friction at the rocking beam interface.

Rupture of the mild steel reinforcement can generally be manipulated or controlled for hybrid sections by specifying an appropriate yielding region (unbonded length). Rupture of the mild steel will, in general, not equate to a total loss in stability as a significant proportion of strength is provided by the post-tensioned tendons (and possibly additional mild steel reinforcement that has not yet ruptured). For this reason rupture of the mild steel may be tolerated for rare events. This is especially the case if the dissipation is in the form of external (replaceable) devices where the full structural integrity can be reinstated immediately following a major earthquake event.

Rupture of the prestressed reinforcement or confinement reinforcement will result in a sudden loss of lateral stability and defines the ultimate limit of the structure.

Other structural performance limit states include sliding of the rocking interface, shear failure of the precast wall panels and sliding shear between the precast wall panels; however, these can be prevented or minimised considering higher mode effects and over-strength actions during design.

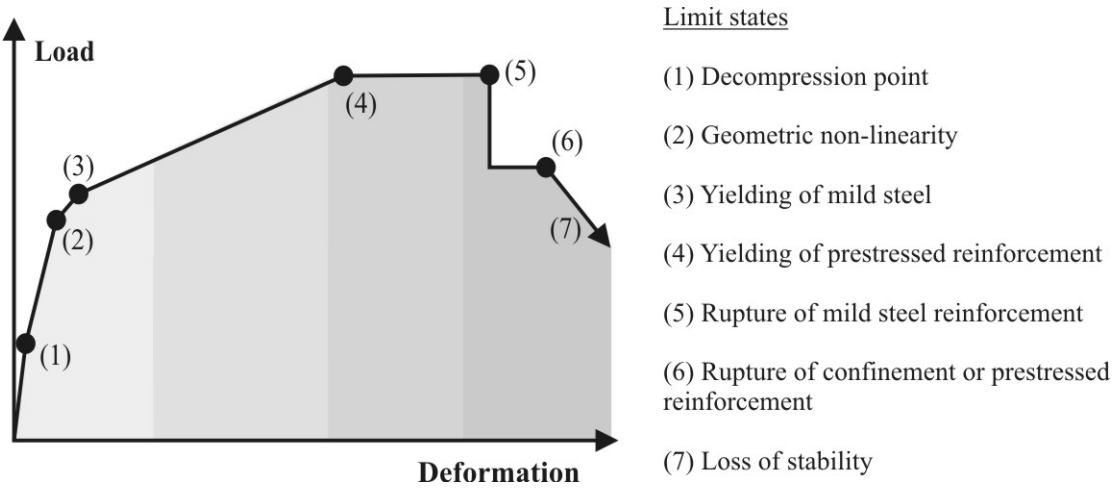

Figure 3.10 Structural limit states of a post-tensioned rocking system

3.5.2. Section Analysis Methods for Post-Tensioned Rocking Connections

The curvature at a rocking interface is infinite, violating Bernoulli theory that "plane sections remain plane". Therefore, a moment-curvature analysis of a post-tensioned rocking system is not applicable; rather, a moment-rotation analysis is performed. Furthermore, due to the unbonded nature of the post-tensioned tendons and the partially unbonded region along the grouted mild steel reinforcement, strain compatibility between the concrete and steel is violated. This incompatibility requires the introduction of an alternative compatibility condition at a global (member) level. A full step-by-step method to compute the moment-rotation response of a jointed ductile connection (post-tensioned, rocking, dissipating) was developed as part of the PRESSS program by Pampanin et al. [2001]. This was later implemented within fib [2003b], the New Zealand Concrete Design Standard, NZS3101 [2006] and the American Concrete Manual, ACI:T1.2-03 [2007]. This procedure considers a global member-compatibility condition and is referred to as the Monolithic Beam Analogy (MBA). The MBA analogy illustrated in Figure 3.11 assumes that the lateral displacement of a post-tensioned (PT) ductile connection Δ_{pt} is equal to that of an Equivalently Reinforced Monolithic (EM) connection Δ_{mono} for the same lateral load, Eq.(3.29).

$$\Delta_{pt} = \Delta_{mono} \tag{3.29}$$

If the geometry and reinforcement between the two elements is also identical the elastic displacements will be equal: leaving only the plastic (rigid) displacement. The rigid plastic displacement components of a post-tensioned (PT) and monolithic (EM) connection are equated, Eq.(3.30)

$$\theta_{imp} L_{cant} = \left(\phi_{mono} - \phi_y\right) L_p \left(L_{cant} - 0.5 L_p\right) \tag{3.30}$$

Where

θ_{imp} = rotation at the rocking interface
L_{cant} = cantilever length of the element
L_p = plastic hinge length of the monolithic element

An equivalent concrete strain ε_c can be computed within the PT connection by rearranging Eq.(3.30) and recognising that the curvature of the section is given by $\phi = \varepsilon_c / c$,

$$\varepsilon_c = \left[\frac{\theta_{imp} L_{cant}}{\left(L_{cant} - 0.5 L_p\right) \cdot L_p} + \phi_y \right] \cdot c \tag{3.31}$$

Where

ε_c = hypothetical concrete strain within the precast, post-tensioned system

c = depth of the neutral axis at the rocking interface

The plastic hinge length can be approximated below from Priestley et al. [2007]

$$L_p = kL_{cant} + L_{sp} \geq 2L_{sp} \quad \textbf{3.32}$$

Where

k = a measure of the spread of plasticity, $k = 0.2\left(f_u / f_y - 1\right) \leq 0.08$

$\boldsymbol{L_{sp}}$ = the length of strain penetration, $L_{sp} = 0.022 f_y d_b$

$\boldsymbol{f_y}$ = yield stress of the longitudinal reinforcement

$\boldsymbol{f_u}$ = ultimate stress of the longitudinal reinforcement

$\boldsymbol{d_b}$ = diameter of the longitudinal reinforcement

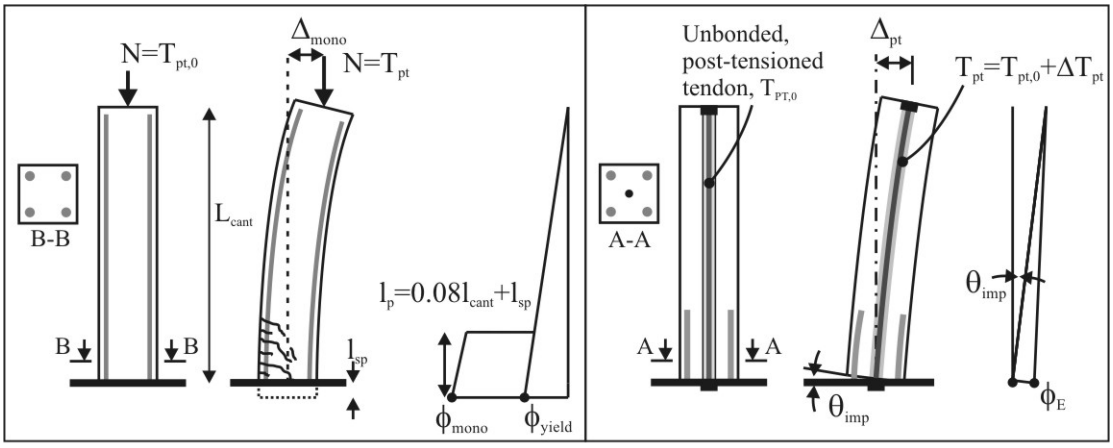

(a) Displacement components of a monolithic connection

(b) Displacement components of a post-tensioned connection

Figure 3.11 The Monolithic Beam Analogy (MBA)

This analogy was later revisited by Palermo [2004] forming the revised Monolithic Beam Analogy (rMBA). The revised analogy recognises that the post-tensioned system is inherently more flexible than the Equivalent Monolithic (EM) element. Consider the two elements in Figure 3.11 having a lateral load (less than yield) applied to the top of the cantilever. The elastic displacement of both cantilevers will be the same if the geometry and reinforcement is identical for both; however, the PT system has additional flexibility due to the gap opening at the rocking interface. The principle behind the rMBA is that prior to the decompression displacement the concrete strain distribution is identical within the two sections. For lateral loads greater than the decompression displacement the additional monolithic displacement (beyond decompression) is equal to the rigid rotation displacement of the post-tensioned element. Palermo [2004] discretely divides the analogy into three regions which is explained with the aid of Figure 3.12

The first region relates strains of a EM connection to a PT connection for curvatures less than the yield displacement Δ_y of the EM section. In this region, the maximum

concrete strain at the extreme fibre within the hybrid post-tensioned element $\varepsilon_{c,pt}$ and the monolithic element $\varepsilon_{c,mono}$ are identical and given by Eq.(3.33).

$$\varepsilon_{c,pt} = \varepsilon_{c,mono} = \varepsilon_0 + \phi_{mono} \cdot \frac{D}{2} \qquad \textbf{3.33}$$

Where

ε_0 = initial compression strain within the section due to the presence of axial load and/or initial post-tensioning.
D = depth of the section
ϕ_{mono} = curvature in the EM section at the base of the cantilever due to the applied load F

The system is linear up until decompression, requiring only a single calculation at the onset of rotation where $\theta = 0$. The force, displacement and concrete strain at decompression are given by Eq.(3.34), (3.35) and (3.36) respectively.

$$F_{dec} = \frac{M_{dec}}{L_{cant}} = \frac{\left(N + T_{PT,0}\right) \cdot D}{6L_{cant}} \qquad \textbf{3.34}$$

$$\Delta_{dec} = \frac{\phi_{dec} \cdot L_{cant}^2}{3} = \frac{2\left(N + T_{PT,0}\right)L_{cant}^2}{3E_c BD^2} \qquad \textbf{3.35}$$

$$\varepsilon_{c,dec} = 2\varepsilon_0 = \frac{2\left(N + T_{PT,0}\right)}{E_c BD} \qquad \textbf{3.36}$$

Where

M_{dec} = decompression moment
N = applied axial load
$T_{PT,0}$ = initial post-tensioning force
ϕ_{dec} = decompression curvature
B = width of the rectangular section
E_c = elastic modulus of concrete

The second region relates compression strains within an EM connection to the strains within a PT connection between the decompression and the yield displacement of the EM system. The lateral displacement of the PT element Δ_{pt} is given by

$$\Delta_{pt} = \theta_{imp} \cdot L_{cant} + \Delta_e \qquad \textbf{3.37}$$

Where

Δ_e = elastic flexural displacement of the cantilever element
θ_{imp} = rotation at the rocking interface
L_p = plastic hinge length of the monolithic element

The displacement of the monolithic element is given by

$$\Delta_{mono} = \frac{\phi_{mono} \cdot L_{cant}^2}{3} \quad \textbf{3.38}$$

For a given lateral load, the displacement of a post-tensioned system will be greater than an equivalent monolithic system with identical geometry and reinforcement, i.e. $\Delta_{pt} > \Delta_{mono}$. Applying the rMBA theory: "the additional displacement beyond the decompression displacement Δ_{dec} of a monolithic element is equal to the rigid rotation displacement $\theta_{imp}L_{cant}$ of a post-tensioned system", yields Eq.(3.39) below

$$\theta_{imp} \cdot L_{cant} = \Delta_{mono} - \Delta_{dec} = \frac{\phi_{mono} \cdot L_{cant}^2}{3} - \frac{\phi_{dec} \cdot L_{cant}^2}{3} \quad \textbf{3.39}$$

By rearranging Eq.(3.39) the hypothetical concrete strain at the extreme edge of the PT connection is given by

$$\varepsilon_c = \left[\frac{3\theta_{imp}}{L_{cant}} + \phi_{dec} \right] c \quad \textbf{3.40}$$

The rotation limits about which this strain relationship is valid for can be derived from Eq.(3.39) and is given by

$$0 < \theta_{imp} < \left(\phi_y - \phi_{dec}\right) \frac{L_{cant}}{3} \quad \textbf{3.41}$$

The third region relates compression strains within the EM connection to those within the PT connection for displacements greater than yield of the EM connection. The displacement of the PT system remains unchanged from Eq.(3.37) above, while the displacement of the monolithic element is given by

$$\Delta_{mono} = \frac{\phi_y \cdot L_{cant}^2}{3} + \left(\phi_{mono} - \phi_y\right) \cdot L_p \cdot \left(L_{cant} - \frac{L_p}{2} \right) \quad \textbf{3.42}$$

Referring again to the rMBA analogy above, the displacement increment is equated

$$\theta_{imp} \cdot l_{cant} = \Delta_{mono} - \Delta_{dec} = \frac{\left(\phi_y - \phi_{dec}\right) \cdot L_{cant}^2}{3} + \left(\phi_{mono} - \phi_y\right) \cdot L_p \cdot \left(L_{cant} - \frac{L_p}{2} \right) \quad \textbf{3.43}$$

By rearranging Eq.(3.43) the hypothetical concrete strain at the rocking base of the hybrid connection can be computed below

$$\varepsilon_c = \left[\frac{\frac{3\theta_{imp}}{L_{cant}} - \left(\phi_y - \phi_{dec}\right)}{\frac{3L_p}{L_{cant}}\left(1 - \frac{L_p}{2L_{cant}}\right)} + \phi_y \right] \cdot c \qquad \textbf{3.44}$$

This strain relationship is applicable within the following range of θ_{imp}.

$$\left(\phi_y - \phi_{dec}\right)\frac{L_{cant}}{3} < \theta_{imp} < \frac{\left(\phi_y - \phi_{dec}\right)\cdot L_{cant}}{3} + \left(\phi_u - \phi_y\right)\cdot \frac{L_p}{L_{cant}} \cdot \left(L_{cant} - \frac{L_p}{2}\right) \qquad \textbf{3.45}$$

As mentioned, strain compatibility is violated at the rocking interface; therefore, the steel strains are computed from the imposed displacements along the rocking interface, Palermo [2004]. If the steel strain is less than yield ε_y then the following equation is adopted

$$\varepsilon_{ms,i} = \frac{\theta_{imp}\left(d_{ms,i} - c\right)}{l_{ub,ms} + 4/3 l_{sp}} \qquad \textbf{3.46}$$

Where;

$\varepsilon_{ms,i}$ = strain in the i^{th} mild steel layer.
$d_{ms,i}$ = distance from the compression edge of the section to the i^{th} mild steel layer
$l_{ub,ms}$ = unbonded length of the mild steel

When the strain in the mild steel exceeds the yield strain ε_y, the following expression is adopted.

$$\varepsilon_{ms,i} = \frac{\theta_{imp}\left(d_{ms,i} - c\right) + 2/3 l_{sp}\alpha_i \varepsilon_y}{l_{ub,ms} + 2l_{sp}} \qquad \textbf{3.47}$$

Where α_i is an elastic strain ratio defined as

$$\alpha_i = \frac{f_{ms,i}}{E_s \cdot \varepsilon_y} \qquad \textbf{3.48}$$

Because α_i is a function of the actual mild steel stress $f_{ms,i}$, iteration between Eq.(3.47) and (3.48) is required. The value of α_i is generally not much greater than 1.0 and α_i converges rapidly. Alternatively, recognising that the second term ($2/3 l_{sp}\alpha_i\varepsilon_y$) in the numerator of Eq.(3.47) is very small in comparison to the first term, Eq.(3.47) can be simplified to the following expression

$$\varepsilon_{ms,i} = \frac{\theta_{imp}\left(d_{ms,i} - c\right)}{l_{ub,ms} + 2l_{sp}} \qquad \textbf{3.49}$$

Similarly, the strain in the post-tensioned tendons is computed from

$$\varepsilon_{pt,i} = \varepsilon_{pt,0} + \frac{n \cdot \theta_{imp}\left(d_{pt,i} - c\right)}{l_{ub,pt}} \qquad \textbf{3.50}$$

Where

$\varepsilon_{pt,0}$ = strain in the tendons due to the initial post-tensioning
n = number of gap openings along the tendon unbonded length
$d_{pt,i}$ = distance from the compression edge of the section to the i^{th} tendon layer
$l_{ub,pt}$ = unbonded length of the tendon

Once the strains can be defined throughout the section any non-linear (or linear) stress-strain relationship can be adopted for the concrete and steel to compute the resultant compression force within the concrete, mild steel stresses and tendon forces to satisfy translation equilibrium (force equilibrium). The moment capacity of the section can be computed at each rotation increment to define the entire loading envelope for the section. When computing the moment capacity of the section, it is typically computed about the centroid of the concrete compression region. In doing so, the relative moment contributions from the mild steel and post-tensioning can be computed to define the re-centring ratio λ.

$$\lambda = \frac{M_{PT} + M_N}{M_{ms}} \qquad \textbf{3.51}$$

Where

M_{PT} = post-tensioned tendon moment contribution
M_N = axial load moment contribution
M_{ms} = mild steel moment contribution

The re-centring ratio gives an indication of residual deformations and the energy dissipation capacity of the section. A larger re-centring ratio will guarantee minimal residual displacements; however, less energy will be dissipated leading to larger maximum displacements. In fact, this re-centring ratio has been incorporated within two design codes; the Appendix of the New Zealand concrete design standard (NZS3101 [2006]) and, although in a slightly different form ($\beta = M_{ms}/M_{total}$), the American ACI manual of concrete practice (ACI:T1.2-03 [2007]). In the New Zealand concrete design standard, hybrid post-tensioned systems are to be designed to ensure the re-centring ratio is greater than α_0. The factor α_0 accounts for a possible increase of the mild steel moment due to strain hardening and is equal to 1.15, i.e. $\lambda \geq 1.15$. The ACI manual of concrete practice specifies that the mild steel (special reinforcement) moment contribution must not exceed 50% of the total moment capacity of the section in both directions, i.e., $M_{ms}/M_{total} \leq 0.5$, or $\lambda \geq 1.0$.

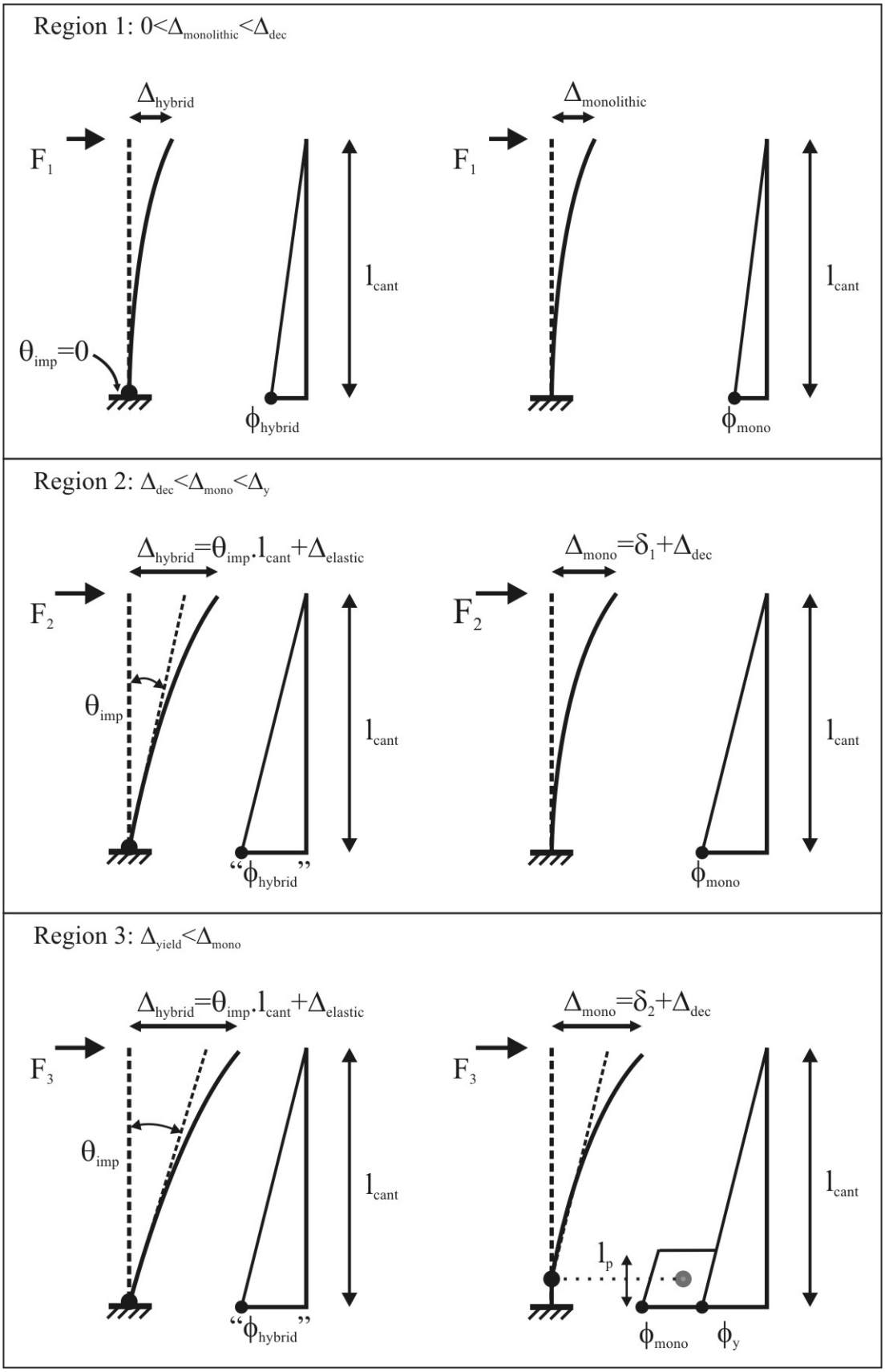

Figure 3.12 Three regions of the revised monolithic beam analogy (RMBA)

3.5.3. Cyclic Modelling Techniques for Post-Tensioned Rocking Connections

A variety of modelling techniques exists for post-tensioned rocking systems ranging from simple lumped plasticity models to complex finite element models. A summary of the current methods are presented.

(a) Lumped Plasticity Models

Lumped plasticity models, comprising of rotation springs in parallel, have been extensively developed to model the moment-rotation response of post-tensioned rocking systems, Pampanin et al. [2001], fib [2003b], Palermo et al. [2005a]. The physical layout of such a model is illustrated in Figure 3.13 having two rotational springs in parallel of zero length located at the rocking interface. The column/beam/wall element is modelled as an elastic Giberson frame element with appropriate (effective/cracked) section properties. Macro models of this sort require a proper understanding of the physical problem to yield sensible results. To start with, a section analysis (described in Section 3.5.2) must be carried out. In doing so, the various moment-rotation components of the section can be disaggregated into the mild steel contribution and prestressed (and/or axial load) contribution. An appropriate non-linear hysteresis rule is calibrated to each of the moment components. Generally a bilinear or trilinear non-linear elastic hysteresis rule is used to model the tendon/axial moment response. For the mild steel, the type of non-linear inelastic hysteresis model depends on the type of dissipation adopted. For internally grouted reinforcement a Modified Takeda (Otani [1974]) hysteresis rule can be used to account for bond degradation between the mild steel and concrete. The non-linear rule in Figure 3.13 is a Ramberg-Osgood steel rule (Ramberg and Osgood [1943]) representative of a system with external dissipaters.

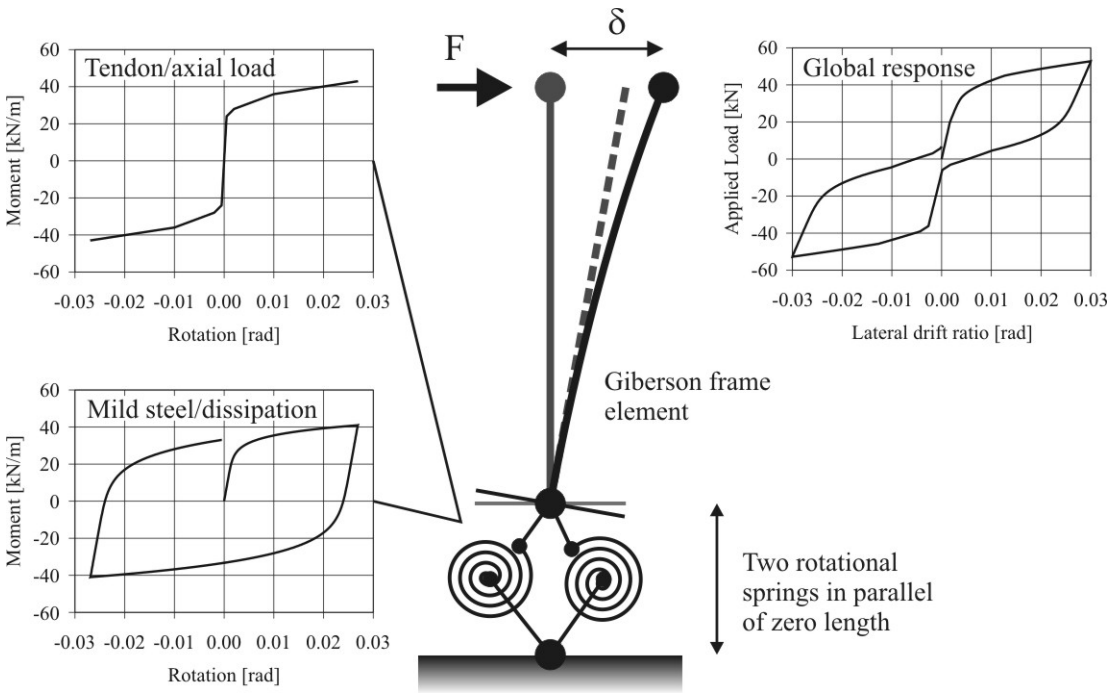

Figure 3.13 Lumped plasticity model consisting of two rotational springs in parallel

(b) Multi(axial)-Spring Models

An early version of a multi-axial spring model consisted of two axial springs positioned along the rocking interface of a post-tensioned coupled wall system. The model in Figure 3.14 represents two post-tensioned wall systems coupled with U-Shaped flexural plates, Conley et al. [1999]. Two elastic compression-only springs are located beneath each of the precast walls and located at the centroid of the resultant compression force (one spring is located at each end of the wall and positioned within the contact region during uplift). This method is an approximation of the actual rocking response of each wall as the base is assumed to pivot about the centroid of the compression block. In reality the "pivot" point is located at the neutral axis within the section; hence, the tendon elongation and internal moment can be non-conservatively overestimated.

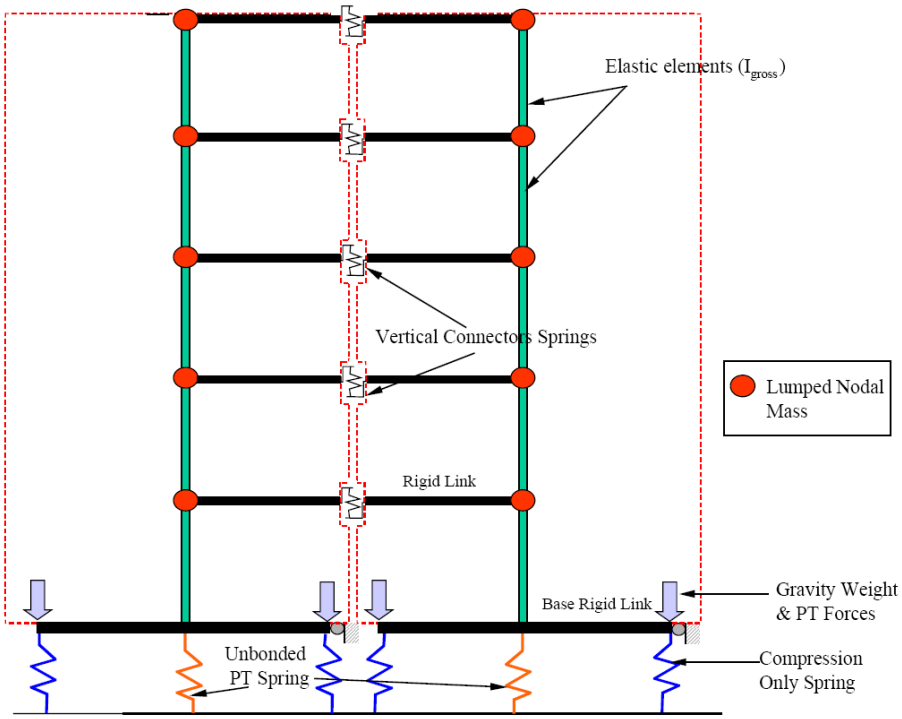

Figure 3.14 Two spring model of a precast, post-tensioned coupled wall, Conley et al. [1999].

More detailed macro-models utilising multiple axial springs located along the rocking interface of a post-tensioned connection have been investigated by Kim [2002], Spieth et al. [2004], Palermo et al. [2005b]. Kim implemented a multi-spring element that was available in the computer program DRAIN-2DX (Prakash et al. [1993]). This element had nine uniformly distributed spring elements of equal strength and stiffness located along the rocking interface in Figure 3.15 (only two of the nine springs is pictured for clarity). The axial springs were modelled as compression-only, elastic-perfectly plastic springs having a yield displacement corresponding to a strain of 0.004. The elongation of the mild steel, tendons and beam elongation is inherently captured within such a model. The mild steel is modelled as a simple bilinear relationship with discrete springs located at the rocking interface. The tendons are

modelled as truss elements, where the ends are attached to the anchorage points in the real system. The initial post-tensioned force in the tendon is accounted for by pretensioning the truss element in the computer program. The beam and column elements are modelled as elastic frame elements with appropriate section properties while the joint is modelled as rigid bar elements.

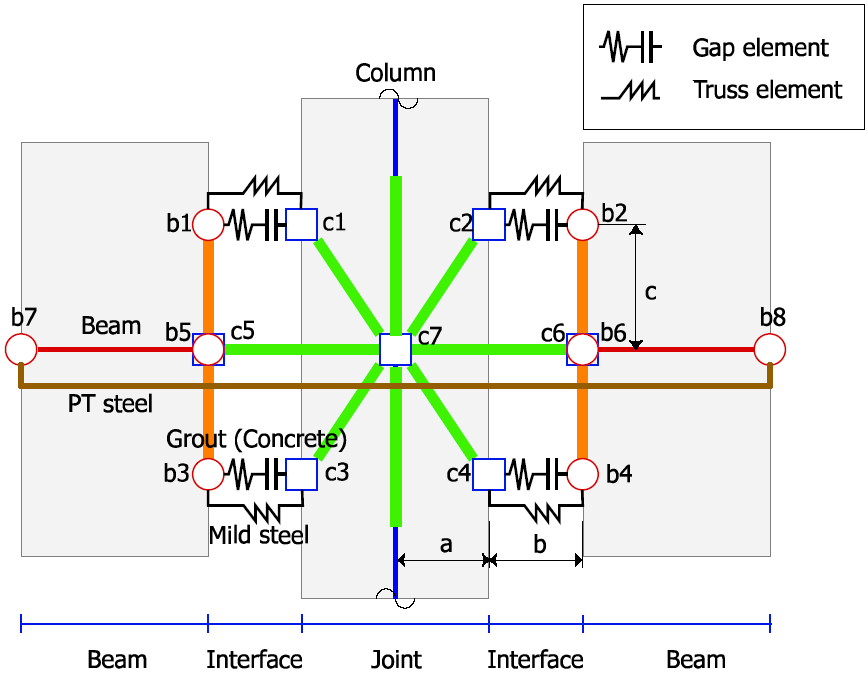

Figure 3.15 DRAIN-2DX model for a hybrid joint, Kim [2002]

Spieth et al. [2004] carried out a finite element analysis to determine the required length of the cantilever element that can be used to define the axial stiffness of the multi-spring element. The analysis studied the strain distribution within the element to determine the depth of the disturbed strain region. A value of one quarter of the element depth was found to give reliable results with the response being relatively insensitive to an increase in length of 200%. During this work a multi-spring element was added within the element library of the finite element program, Ruaumoko (Carr [2005]). This element has the option of 2-10 individual springs in addition to various weighting options for spring stiffness and spring distribution within the element. This multi-spring model was also used to model a post-tensioned concrete wall and beam column joint, providing further validation of the model, Palermo et al. [2005b].

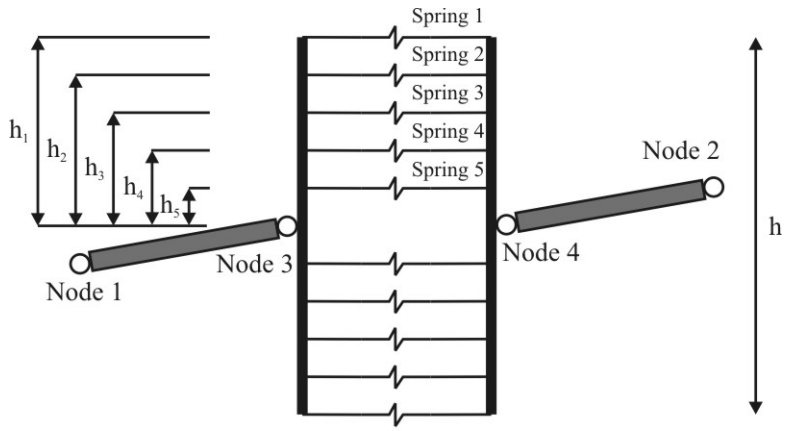

Figure 3.16 Multi-spring element within Ruaumoko, Carr [2005].

(c) Fibre Element and Finite Element Models

Fibre element models have been used to capture the response of unbonded post-tensioned beam-column joint subassemblies, El-Sheikh et al. [1998] and post-tensioned walls, Kurama et al. [1998]. Both studies were concerned with unbonded post-tensioned tendons only, i.e. there was no partially grouted mild steel reinforcement passing the rocking interface. A fibre element model divides an element into a number of segments along its length. Each segment consists of a number of discrete fibre layers. Each fibre represents either concrete or bonded steel reinforcement and associates an appropriate uniaxial material stress-strain relationship with each fibre. The number of segments and fibres can be increased to improve the accuracy of the analysis. The stress and strain at each fibre is monitored about the mid-section of each segment. The fibre element adheres to the principle that plane sections remain plane; therefore, (strictly-speaking) are unable to capture the rocking/uplift mechanism of a post-tensioned system. Rather, the uplift/gap-opening of a rocking system is accounted for by the integration of the tension strain throughout the segment length. A fibre element segment is located adjacent to the column with zero tension strength and stiffness and no bonded reinforced steel elements. One of the key input parameters required for a fibre element model (besides the material stress-strain relationships) is the length of this "rocking" segment $\boldsymbol{L_{cr}}$. This "rocking" segment length $\boldsymbol{L_{cr}}$ differs to the plastic hinge length $\boldsymbol{L_p}$ in reinforced concrete. El-Sheikh proposed that the crushing length $\boldsymbol{L_{cr}}$ is equal to twice the depth of the concrete stress block (less the depth of the unconfined concrete), but not greater than the confined depth of the member between the outer confinement reinforcement. The influence of $\boldsymbol{L_{cr}}$ on the moment-rotation response of a beam-column joint analysis is shown in Figure 3.18; five multiples of $\boldsymbol{L_{cr}}$ are shown from 0.25 to 2.7. A variation of ±100% makes a significant difference to the strength and ultimate displacement capacity of the section. In a similar study on post-tensioned walls, Kurama used a length $\boldsymbol{L_{cr}}$ equal to the thickness of the confining spiral reinforcement (at the rocking toe) and also recognised that the strength and displacement capacity was dependant on this length.

Finite element models have been used to model the response of post-tensioned precast walls by Kurama [2000] and Allen and Kurama [2002] using the ABAQUS package.

Gap/contact elements are located at the rocking interface between the foundation and wall elements to allow uplift. The finite element model compared well to an equivalent fibre element model, where the lateral response and the uplift and contact during rocking were well in agreement.

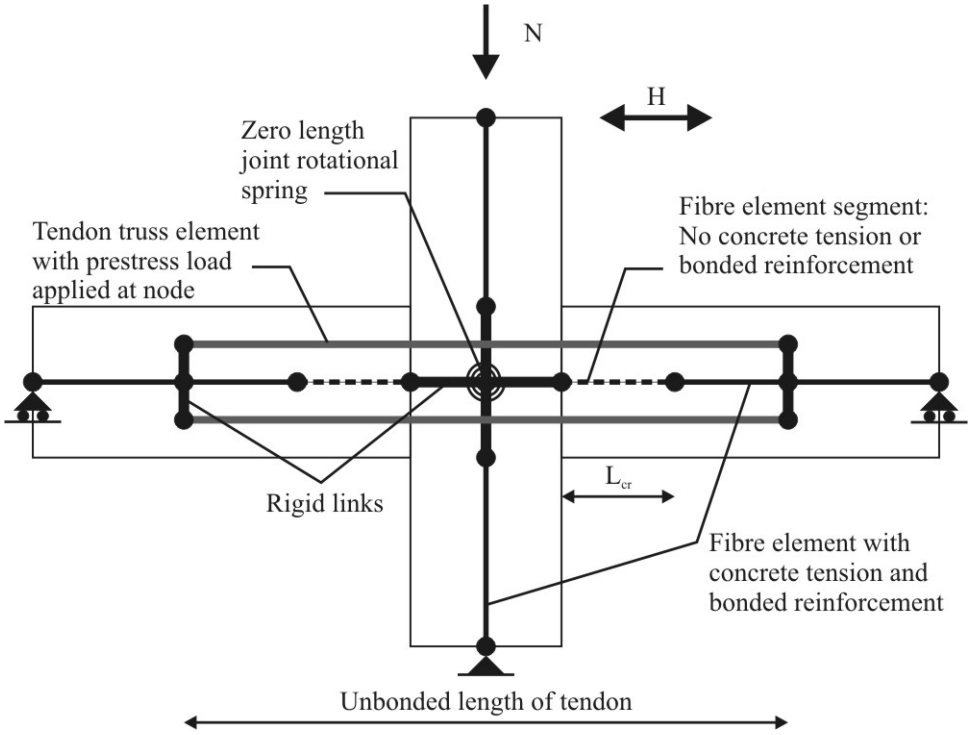

Figure 3.17 Fibre element model of a post-tensioned beam-column joint subassembly (modified from El-Sheikh et al. [1998])

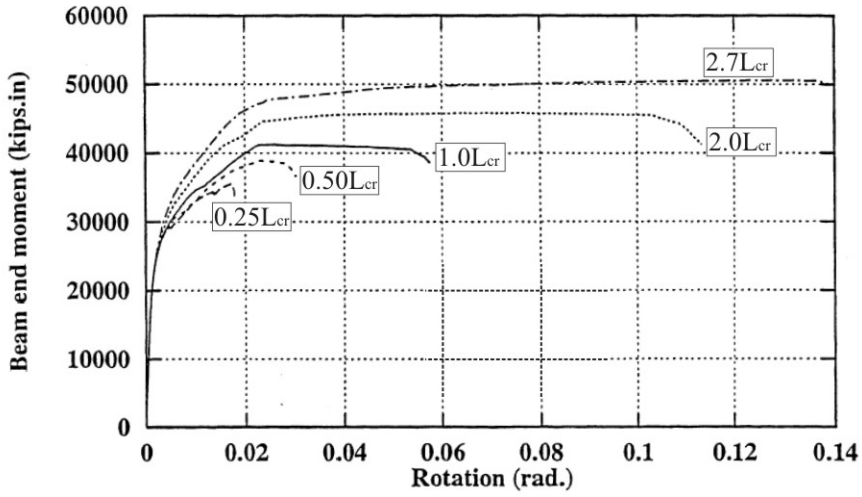

Figure 3.18 Influence of the length of the "rocking" fibre segment on the moment-rotation response

3.5.4. Conclusions on Modelling Post-Tensioned Rocking Systems

Three types of modelling techniques for post-tensioned rocking/dissipative systems were presented above. The first technique presented was a moment-rotation section-analysis approach to evaluate the monotonic lateral response of post-tensioned systems considering a global member-compatibility requirement known as the Monolithic Beam Analogy (MBA). This technique is capable of being implemented into an Excel spreadsheet or Matlab code. The second type of model was a lumped plasticity macro model considering either rotational springs in parallel or multiple axial, compression only springs located along the rocking interface. These macro-models are developed to capture the non-linear cyclic response of post-tensioned rocking systems. Both macro models must be calibrated to a monotonic section-analysis; however, they are simple to implement and very fast computationally. A distributed plasticity fibre or finite element model was also discussed. These models can be accurate; however, with respect to the fibre element method, rocking and gap opening is accounted for via a homogeneous concrete fibre segment (no bonded reinforcement). While recommendations exist regarding the length of this segment, the value is relatively arbitrary and the response is sensitive to what length is used in the analysis. The finite element model is likely to provide the most accurate solution as there is minimal ambiguity; the user simply enters the appropriate material relationship in addition to setting up the geometry of the model. The downside is the large computational cost of such an exercise to set up the model in addition to the time needed to carry out the analysis.

It is for this reason that the multi-spring macro-model appears to be the most attractive solution. The accuracy that can be achieved is very high and the speed at which the model can be created and run is unsurpassed. The only unknown parameter within the model is the axial stiffness of the multi-spring unit. A technique is developed within this thesis to define this axial stiffness via calibration to a monotonic section-response. A similar calibration could be carried out for a fibre-element model; however, the accuracy achieved with a macro model is likely to be similar.

3.6. REFERENCES

ACI:T1.2-03. (2007). *ACI Manual of Concrete Practice-Special Hybrid Moment Frames Composed of Discretely Jointed Precast and Post-Tensioned Concrete Members*.

Allen, M. and Kurama, Y. (2002). "Design of rectangular openings in precast walls under combined vertical and lateral loads." *PCI*, 47(2), 58-83.

Aslam, M., Godden, W. G. and Scalise, D. T. (1980). "Earthquake rocking response of rigid bodies." *Journal of the Structural Division, ASCE*, 106(ST2), 377-392.

Carr, A. (2003) "The generation of in-elastic response spectra for earthquake acceleration records." *2003 Pacific Conference on Earthquake Engineering*, New Zealand.

Carr, A. (2005). "RUAUMOKO." Christchurch, Inelastic Dynamic Analysis.

Conley, J., Sritharan, S. and Priestley, M. J. N. (1999). "Precast Seismic Structural Systems PRESSS-3: The Five Story Precast Test Building Vol. 3-1: Wall Direction Response." Report No. SSRP-99/19, Department of Structural Engineering, University of California, San Diego.

El-Sheikh, M. T., Sause, R., Pessiki, S. and Lu, L. (1999). "Seismic behavior and design of unbonded post-tensioned precast concrete frames." *PCI Journal*, 44(3), 54-71.

El-Sheikh, M. T., Sause, R., Pessiki, S., Lu, L. and Kurama, Y. (1998). "Seismic analysis, behavior and design of unbonded post-tensioned precast concrete frames." PRESSS report no 98/04, Lehigh University, Bethlehem.

Eurocode:8. (2003). "Design of Structures for Earthquake Resistance." CEN/TC 250, Brussels.

Evison, R. J. (1977). "Rocking foundations," University of Canterbury, Christchurch.

FEMA. (1997). *NEHRP Guidelines for the Seismic Rehabilitation of Buildings: FEMA 273*, Washington, D.C.

FEMA. (2000). "Prestandard and Commentary for the Seismic Rehabilitation of Buildings: FEMA 356." Washington, D.C.

FEMA. (2003). *NEHRP Recommended Provisions for Seismic Regulations for New Buildings and Other Structures: FEMA 450*, Washington, D.C.

fib. (2003a). *Displacement Based Seismic Design of Reinforced Concrete Buildings*, International Federation for Structural Concrete, Lausanne, Switzerland.

fib. (2003b). *Seismic Design of Precast Concrete Building Structures*, International Federation for Structural Concrete, Lausanne, Switzerland.

Housner, G. (1963). "The Behaviour of Inverted Pendulum Structures During Earthquakes." *Bulletin of the Seismoligical Society of America*, 53(2), 403-417.

Kim, J. (2002). "Behavior of hybrid frames under seismic loading," University of Washington.

Kurama, Y. C. (2000). "Seismic design of unbonded post-tensioned precast concrete walls with supplemental viscous damping." *ACI Structural Journal*, 97(4), 648-658.

Kurama, Y. C., Pessiki, S., Sause, R., Lu, L. and El-Sheikh, M. T. (1998). "Analytical Modelling and Lateral Load Behavior of Unbonded Post-Tensioned Precast Concrete Walls." PRESSS Report No. 98/02, P. S. S. S. PRESSS, ed., Lehigh University.

Kurama, Y. C., Sause, R., Lu, L. and Pessiki, S. (1999). "Seismic Behaviour and Design of Unbonded Post-Tensioned Precast Concrete Walls." *PCI Journal*, 44(3), 72-89.

Makris, N. and Konstantinidis, D. (2001). "The Rocking Spectrum and the Shortcomings of Design Guidelines." PEER report 2001/07, University of California, Berkeley.

Makris, N. and Konstantinidis, D. (2003). "The rocking spectrum and the limitations of practical design methodologies." *Earthquake Engineering & Structural Dynamics*, 32(2), 265-289.

Makris, N. and Zhang, J. (1999). "Rocking response and overturning of anchored equipment under seismic excitation." Peer report 99/06, University of California, Berkeley.

Newmark, N. (1960). "A development in the modeling of far-field intensities for New Zealand earthquakes." *Bulletin of NZSEE*, 28(3), 196-217.

NZS1170.5. (2004). "Structural Design Actions, *Part 5: Earthquake actions*." Standards New Zealand, Wellington.

NZS3101. (2006). "Concrete Structures Standard: Part 1-The Design of Concrete Structures." Standards New Zealand, Wellington.

Otani, S. (1974). "SAKE, A Computer Program for Inelastic Response of R/C Frames to Earthquakes." Report UILU-Eng-74-2029, University of Illinois, Urbana-Champaign.

Palermo, A. (2004). "The Use of Controlled Rocking in the Seismic Design of Bridges," PhD.Thesis, Technical University of Milan, Milan.

Palermo, A., Pampanin, S. and Calvi, G. M. (2005a). "Concept and Development of Hybrid Solutions for Seismic Resistant Bridge Systems." *Journal of Earthquake Engineering. Vol. 9, no. 6, pp. 899-921. Nov. 2005*.

Palermo, A., Pampanin, S. and Carr, A. J. (2005b). "Efficiency of Simplified Alternative Modelling Approaches to Predict the Seismic Response of Precast Concrete Hybrid Systems." fib symposium, Budapest.

Pampanin, S., Priestley, M. J. N. and Sritharan, S. (2001). "Analytical Modelling of the Seismic Behaviour of Precast Concrete Frames Designed with Ductile Connections." *Journal of Earthquake Engineering*, 5(3), 329-367.

Prakash, V., Powell, G. and Campbell, S. (1993). "DRAIN-2DX base program description and user guide." Technical report UCB/SEMM-93-17, University of California, Berkeley.

Priestley, M. J. N. (2002). "Direct Displacement-Based Design of Precast/Prestressed Concrete Buildings." *PCI*, 6.

Priestley, M. J. N., Calvi, G. M. and Kowalsky, M. J. (2007). *Displacement-Based Seismic Design of Structures*, IUSS, Pavia.

Priestley, M. J. N., Evison, R. J. and Carr, A. J. (1978). "Seismic response of structures free to rock on their foundations." *Bulletin of the New Zealand National Society for Earthquake Engineering*, 11(3), 141-150.

Ramberg, W. and Osgood, W. R. (1943). "Description of Stress-Strain Curves by Three Parameters." National Advisory Committee on Aeronautics, Technical Note 902.

SEAOC. (1999). *Recommended Lateral Force Requirements and Commentary*, Structural Engineers Association of California.

Shome, N. and Cornell, A. (1999). "Probabilistic seismic demand analysis of nonlinear structures." Report No. RMS-35, RMS Program, Stanford University, Stanford, CA.

Spieth, H. A., Carr, A. J., Pampanin, S., Murahidy, A. G. and Mander, J. B. (2004). "Modelling of Precast Prestressed Concrete Frame Structures with Rocking Beam-Column Connections." University of Canterbury Research Report 2004-01, N. t. c. o. r. n. o. p. r. thesis, ed., University of Canterbury, Christchurch.

Tso, W. K. and Wong, C. M. (1989a). "Steady state rocking response of rigid blocks, part 1: analysis." *Earthquake Engineering & Structural Dynamics*, 18(1), 89-106.

Tso, W. K. and Wong, C. M. (1989b). "Steady state rocking response of rigid blocks, part 2: Experiment." *Earthquake Engineering & Structural Dynamics*, 18(1), 107-120.

4. Uniaxial and Biaxial Quasi-Static Testing of Post-Tensioned Bridge Piers

4.1. INTRODUCTION

This chapter presents the experimental response of seven 1:3 scale post-tensioned bridge piers with internal and external mild steel dissipaters (tension-compression-yielding dampers). The bridge piers are tested under uni-directional and bi-directional quasi-static cyclic loading. The cyclic response of the post-tensioned bridge piers are compared to a benchmark monolithic ductile pier having comparable reinforcement and lateral strength. One of the outcomes is to investigate a number of post-tensioned rocking connection typologies including internal, external and replaceable mild steel yielding elements.

The experimental testing indicates that a) each of the post-tensioned bridge piers suffer a marked reduction in damage when compared to the monolithic pier, and b) the post-tensioned piers can achieve similar levels of maximum lateral displacement during an earthquake.

4.2. DESIGN OF THE PROTOTYPE BRIDGE PIER SYSTEM

The prototype bridge system is illustrated in Figure 4.1. The single cantilever bridge pier forms part of a large span bridge system. While the bridge system has a relatively short span and pier height, the numbers represent an example for a proof of concept only: little attention should be given to the actual geometric details. The single-degree-of-freedom (SDOF) equivalent prototype pier has a height of 4.8m and a total participating gravity deck load of 1800kN.

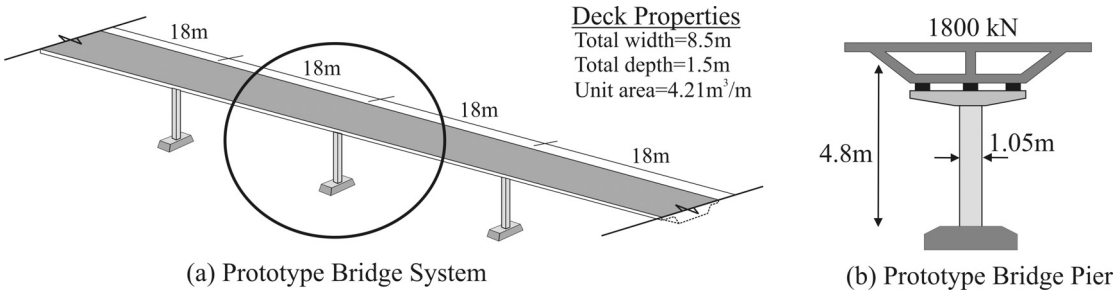

Figure 4.1 Prototype bridge system

The prototype bridge pier is designed to a Direct Displacement-Based Design (DDBD) methodology (Priestley et al. [2007]). DDBD uses an equivalent elastic single degree of freedom substitute structure with secant stiffness to the target displacement. Three displacement objectives were chosen during design, corresponding to three seismic hazard levels (return periods): 1000 years, 1425 years and 2000 years. The design objectives are summarised in Figure 4.2(a) & (c) via a Demand-Capacity spectra (note that the spectral ordinates are damped spectral ordinates). The NZS1170.5 [2004] seismic hazard parameters (corresponding to a 2000 year return period) are tabulated in Figure 4.2(b). It should be recognised that P-Δ loads are not accounted for in design as the experimentally applied axial load did not induce second order moment demands. A summary of the design calculations is presented in Appendix A for a return period of 2000 years.

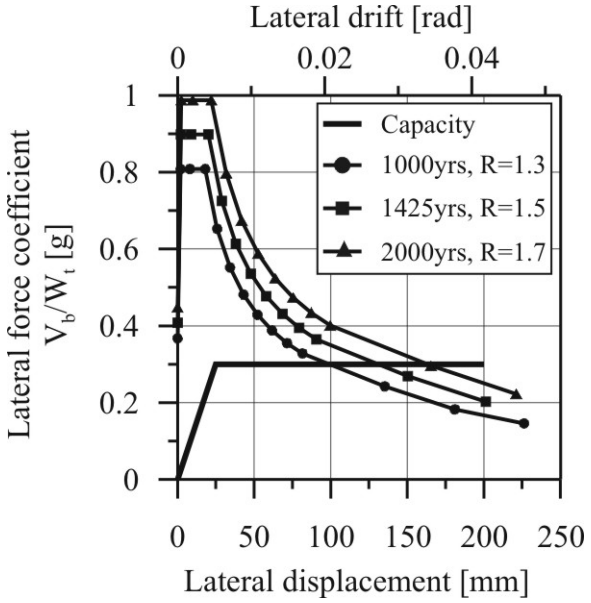

(a) Demand-Capacity spectra

NZS1170.5 [2004] Hazard Parameter	
Z	0.334
Soil	C
T_R	2000 years
R	1.7
D	20km
$N(T_1,D)$	1.0
S_p	1.0
$C_d(T_1=0)$ = PGA	0.578

(b) Seismic hazard parameters

Return Period [years]	Design Drift [Δ_d/L_{cant}]
1000	2.0%
1425	2.6%
2000	3.4%

(c) Design displacement objectives

Figure 4.2 Displacement-Based Design summary of the benchmark bridge pier

A benchmark monolithic ductile pier (MON) was designed to achieve the performance objectives tabulated in Figure 4.2 above of 0.3g: corresponding to a lateral capacity of 60kN for the test specimen. In general the post-tensioned (PT) piers were designed to achieve a similar objective; that is, a lateral capacity of 60kN; however, the strength of a PT system is highly dependant on the target displacement due to the high post-yield stiffness. The lateral strength of the PT piers was chosen to correspond to a value of 60kN at a lateral drift of 2.0%. From a displacement-based design point of view this would account for the lower level of hysteretic damping inherent of a PT system: at drift ratios exceeding 2.0%, the lateral capacity continues to increase, compensating for the lower level of equivalent viscous damping. To add to this, one post-tensioned pier (HBD4) was designed to be under-strength by approximately 15% to recognise the larger displacement capacity of a PT system.

4.3. STRUCTURAL DETAILS AND CONSTRUCTION OF THE BRIDGE PIER TEST SPECIMENS

A total of seven post-tensioned bridge piers and three benchmark bridge piers were tested. Details of each specimen are summarised in Table 4.1, where QS refers to Quasi-Static testing, 2D refers to uniaxial and 3D refers to biaxial testing.

Each of the post-tensioned bridge piers was tested from a single precast pier element. Each end of the precast element was specifically constructed to allow both ends to be tested with a number of different rocking connection details. One end of the post-tensioned pier had a concrete surface (pier specimens HBD1, HBD2 & PT1), while the other end had a steel surface (pier specimens HBD3-HBD5 & PT2). The steel interface was created by casting a 25mm steel plate into the base of the pier, welded to the longitudinal reinforcement.

Table 4.1 Bridge pier details

Test	Description	Axial load /Initial post-tensioning	Mild steel dissipaters	Testing protocol
MON	Benchmark ductile pier	200kN, constant axial load control	Cast-in-place construction: 16-D10 grade 300MPa reinforcement.	2D QS 3D QS
HBD1	Hybrid, internally grouted	200kN: 2 tendons at 100kN each ($0.538f_{pu}$)	4-D16 longitudinal bars grouted with 50mm unbonded length	2D QS
HBD2	Hybrid, internally grouted and threaded	300kN: 4 tendons at 75kN each ($0.403f_{pu}$)	4-12.5mm diameter machined reinforcement (Grade 500MPa) with 50mm fuse length. Threaded into foundation, grouted into pier.	2D QS
HBD3	Hybrid, internally threaded (semi-replaceable)	300kN: 4 tendons at 75kN each ($0.403f_{pu}$)	4-13.5mm diameter machined, internally-located bars. Threaded into pier, bolted to underside of foundation.	2D QS
HBD4	Hybrid, external dissipation (replaceable)	300kN: 4 tendons at 75kN each ($0.403f_{pu}$)	4-10mm diameter mild steel machined dissipaters (Grade 300MPa). 75mm machined fuse length.	2D QS
HBD5	Hybrid, external dissipation (replaceable)	300kN: 4 tendons at 75kN each ($0.403f_{pu}$)	8-8mm diameter mild steel machined dissipaters (Grade 300MPa). 115mm machined fuse length.	2D QS 3D QS
PT1	HBD1, with no dissipation	200kN: 2 tendons at 100kN each ($0.538f_{pu}$)	-	2D QS
PT2	HBD4, with no dissipation	300kN: 4 tendons at 75kN each ($0.403f_{pu}$)	-	2D QS 3D QS

4.3.1. Monolithic, Ductile Benchmark Pier: MON

The benchmark specimen represented a well designed bridge pier designed according to the New Zealand Concrete Design Standard: NZS3101:2006 [2006].

The prototype bridge pier had an 1800kN tributary deck weight, 4.8m pier height and 1.05m square cross-section as shown in Figure 4.1. The test specimen, therefore, required an axial load of 200kN, a cantilever length of 1.6m and a square cross-section of 0.35m. During the experimental test, the axial load was monitored and was maintained at 200kN.

The pier was detailed with 16-D10 (10mm diameter, Grade 300MPa, deformed bars) longitudinal reinforcement and R6 (6mm diameter, Grade 300MPa, smooth bars) transverse reinforcement spaced at 50mm centres (each stirrup set consists of three rectangular hoops, resulting in four legs in both directions): refer Figure 4.3. Construction of the benchmark specimen was carried out in two stages. First, the foundation was cast, then after one week the pier element was cast. The concrete on the surface of the foundation was roughened prior to curing. This was to encourage a bond to develop between the "old" and "new" concrete during casting of the pier in the second pour. While a single pour would prevent the formation of a "cold joint", it was more practical to cast the pier in two stages (Figure 4.4).

Three monolithic piers were construction: one for unidirectional testing, one for bidirectional testing and a third pier for future pseudo-dynamic testing.

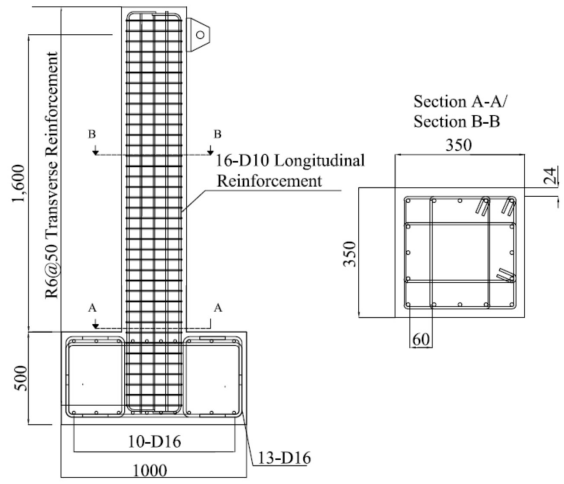

(a) Construction drawings

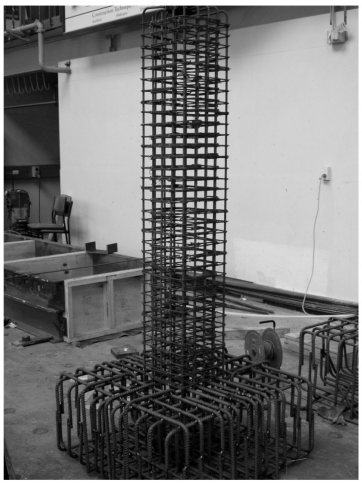

(b) Pier and foundation reinforcement

Figure 4.3 Monolithic bridge pier, geometry and reinforcement details

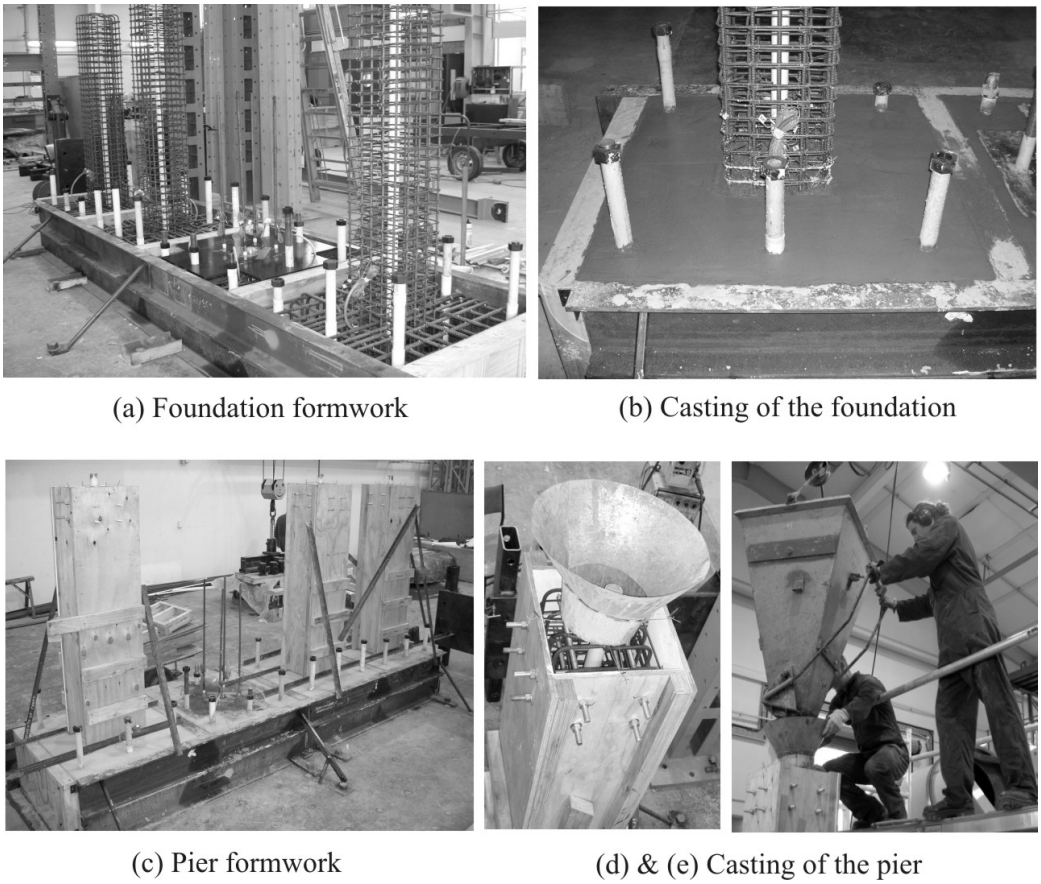

Figure 4.4 Construction of the monolithic bridge pier

4.3.2. Hybrid Bridge Pier with Internal, Grouted, Reinforcement: HBD1

The post-tensioned pier HBD1 is detailed with 4-D16 internally grouted mild steel reinforcement. The 4-D16 longitudinal bars were cast into the foundation as starter bars and then grouted within the pier once lowered onto the foundation. Two post-tensioned tendons were located in the centre of the pier ($\boldsymbol{A_{pt}}$ = 100mm^2 per tendon), to provide a total post-tensioned force of 200kN ($0.538f_{pu}$ per tendon; $\boldsymbol{f_{pu}}$ = 1860MPa). The initial post-tensioned force of 200kN corresponds to the gravity deck load of the prototype test specimen and, hence, represents unstressed tendons within the full-scale prototype post-tensioned pier. The structural details of HBD1 and images of the as-built test specimen are presented in Figure 4.5. A 30mm steel angle (2mm wall thickness) was cast around the toe of the precast pier element to provide protection of the highly strained cover concrete during rocking. Figure 4.7 illustrates how the steel angle assembly was embedded into the precast element: a total of eight reinforcing bars were welded to the angle assembly. Shear transfer between the pier and foundation was primarily resisted by friction and dowel action of the grouted mild steel bars; however, a metallic semi-spherical ball was mechanically fixed to the top of the foundation and a socket was match-cast within the centre of the precast pier (refer Figure 4.6 and Figure 4.9 (b) & (d)). This spherical key would help to relocate the pier to its original position during unloading but provided no shear transfer during uplift of the pier unless significant sliding occurred. Additional shear keys were located at each corner of the pier to control torsion induced by differential yielding of the mild steel elements. These shear keys, shown in Figure 4.6 (b), were particularly

important for the post-tensioned piers with external mild steel elements (construction details presented later) as torsion-sliding was difficult to prevent when relying on dowel action alone.

The reinforcement within the precast pier element (above the rocking interface) was identical to the reinforcement within the monolithic pier (Figure 4.4), but did not cross the rocking interface. The foundation was constructed with a 20mm steel plate cast into the top surface (Figure 4.8 (d)) to give the rocking surface sufficient robustness for a large number of tests. The precast pier was lowered into position on the foundation after it was fixed to the laboratory strong floor (Figure 4.9). When in place, the tendons were post-tensioned and the starter bars were grouted.

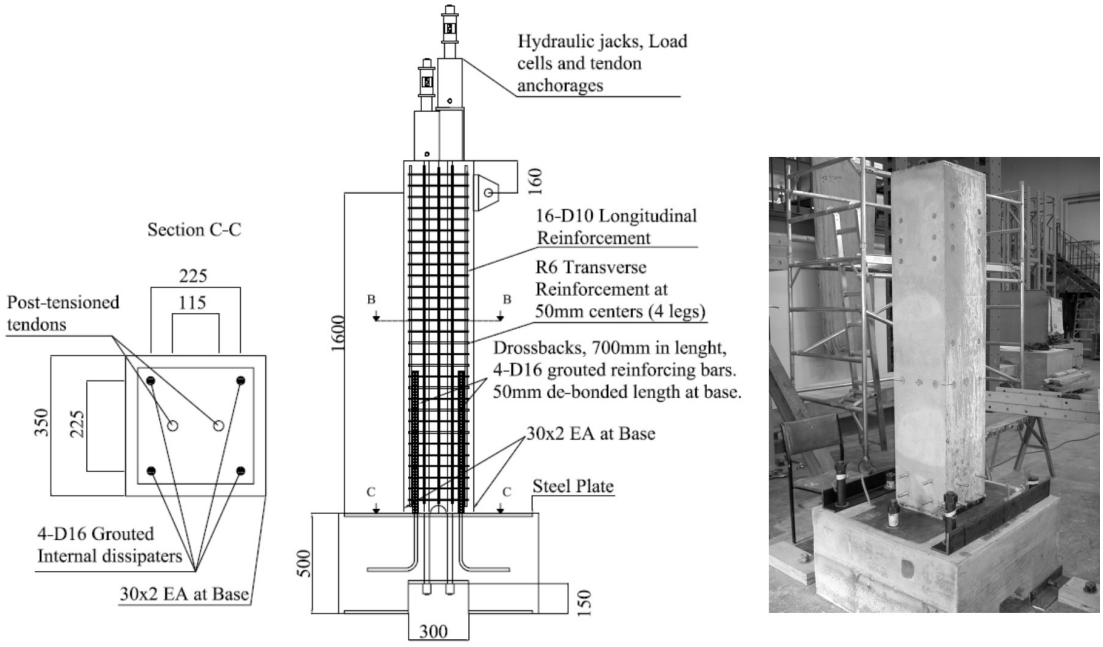

(a) Construction drawings (b) As-built specimen

Figure 4.5 Post-tensioned pier HBD1 structural details

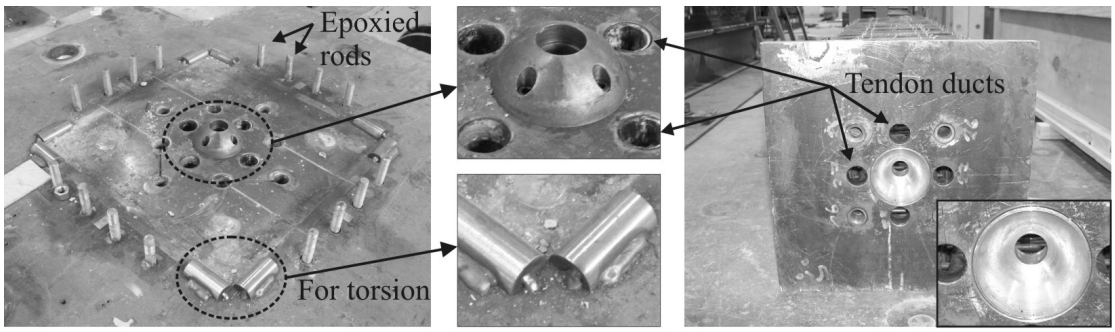

a) Footprint of rocking interface b) Shear keys c) Socket, underside of pier

Figure 4.6 Shear transfer mechanism and torsion control for the post-tensioned piers

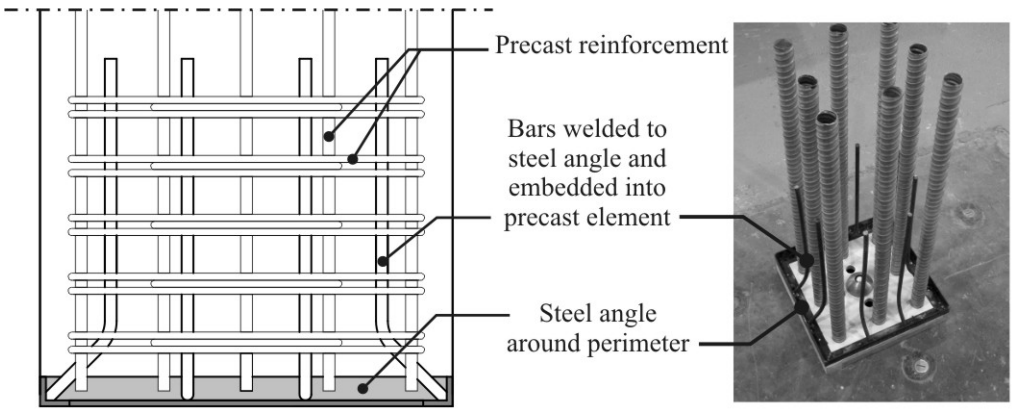

(a) Confinement detail showing steel confining angle and precast reinforcement (Drossbachs omitted for clarity)

(b) As-built steel angle detail ready to be inserted into precast reinforcement cage

Figure 4.7 Steel angle assembly at the base of the rocking pier to prevent damage to the cover concrete

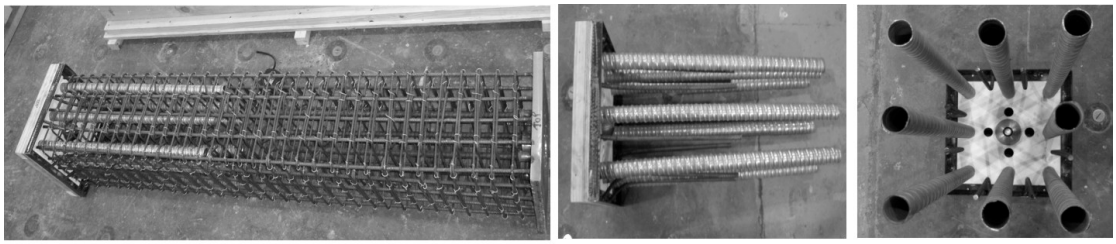

(a) Pier reinforcement

(b) & (c) Pier drossbachs

(d) Foundation reinforcement

(e) Foundation starter bars (showing de-bonded length) and spherical shear key

Figure 4.8 Reinforcement details of the foundation and pier elements

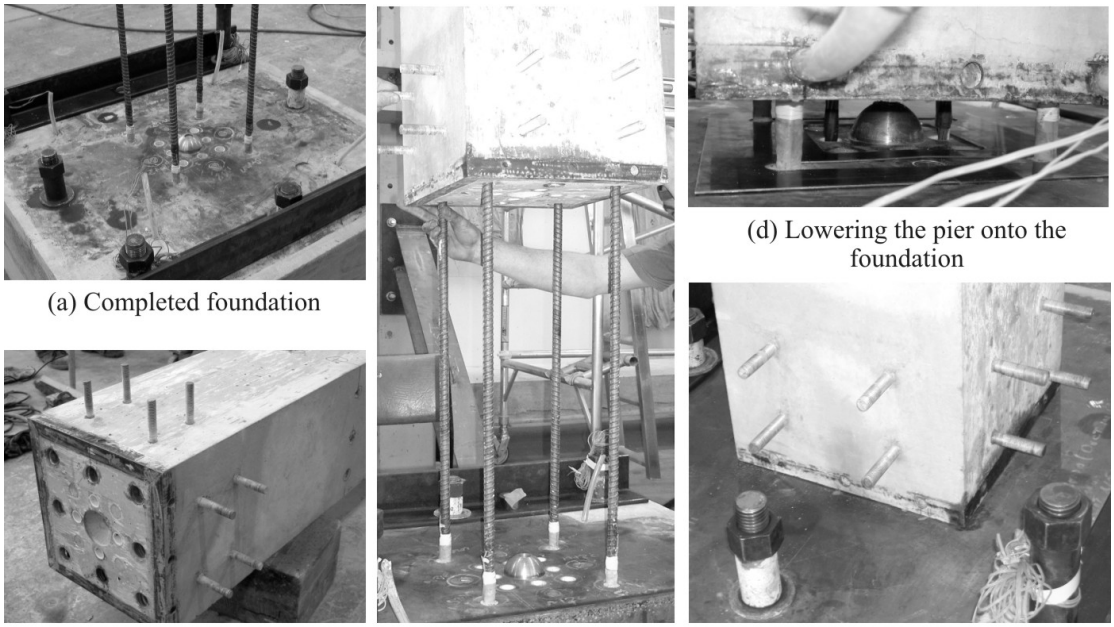

(a) Completed foundation

(b) As-built pier

(c) Locating the starter bars within the precast pier

(d) Lowering the pier onto the foundation

(e) Final position

Figure 4.9 Assembly of HBD1

4.3.3. Hybrid Bridge Pier with Internally Grouted & Threaded, Reinforcement: HBD2

The post-tensioned pier HBD2 was identical to HBD1 with the exception that the mild steel bars were threaded into foundation concrete inserts (not grouted within the pier as cast in-situ starter bars). Furthermore, four post-tensioned tendons provided a total initial post-tensioned force of 300kN (four tendons at $0.403f_{pu}$), refer Figure 4.10 (a). The mild steel bars were 4-HD20 (20mm diameter, Grade 500MPa) longitudinal reinforcement with a reduced diameter of 12.5mm over a length of 50mm (Figure 4.10 (b)). A thread was created at one end of the mild steel bars so they could be threaded into the cast in-situ foundation inserts (M20 TCM concrete inserts). After the mild steel bars were threaded into the foundation, the precast pier was lowered into position on the foundation and post-tensioned (Figure 4.11). The mild steel bars were then grouted within the precast pier (Figure 4.12). The idea behind threaded dissipaters was to improve the level of flexibility during design. The machined portion of the mild steel bar allows for greater control over the mild steel moment contribution.

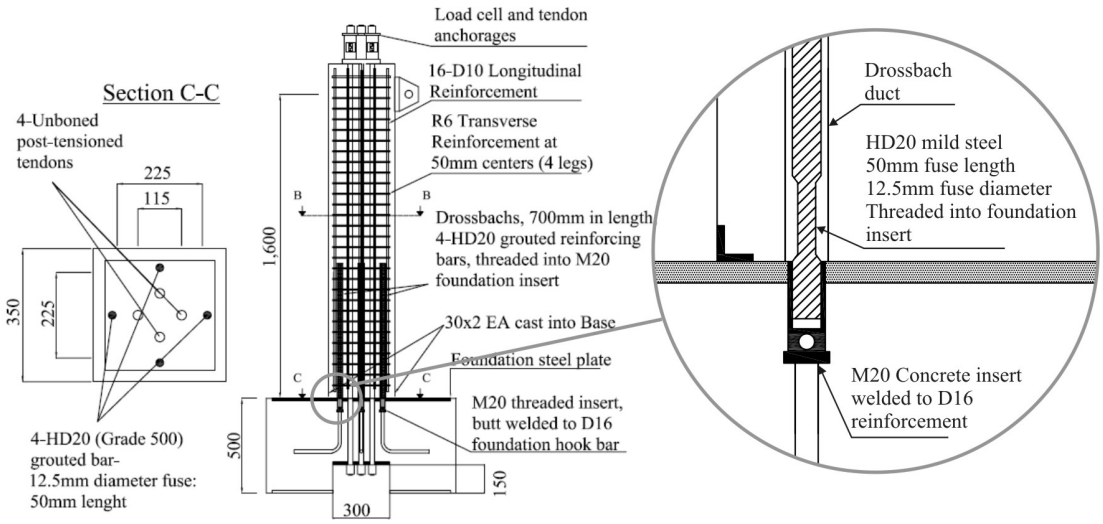

Figure 4.10 Post-tensioned pier HBD2 structural details

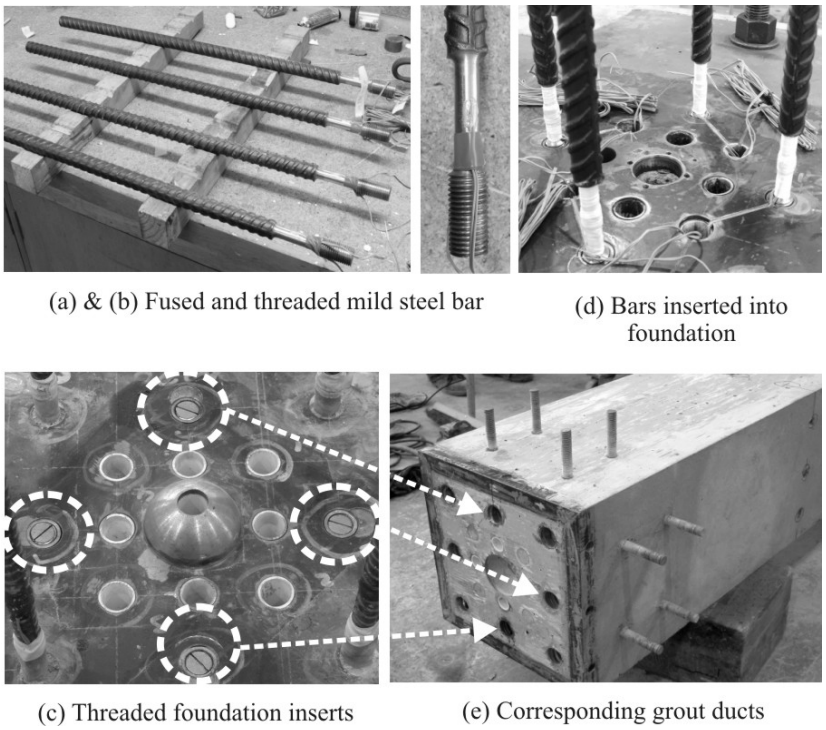

Figure 4.11 Details of the threaded dissipaters, HBD2

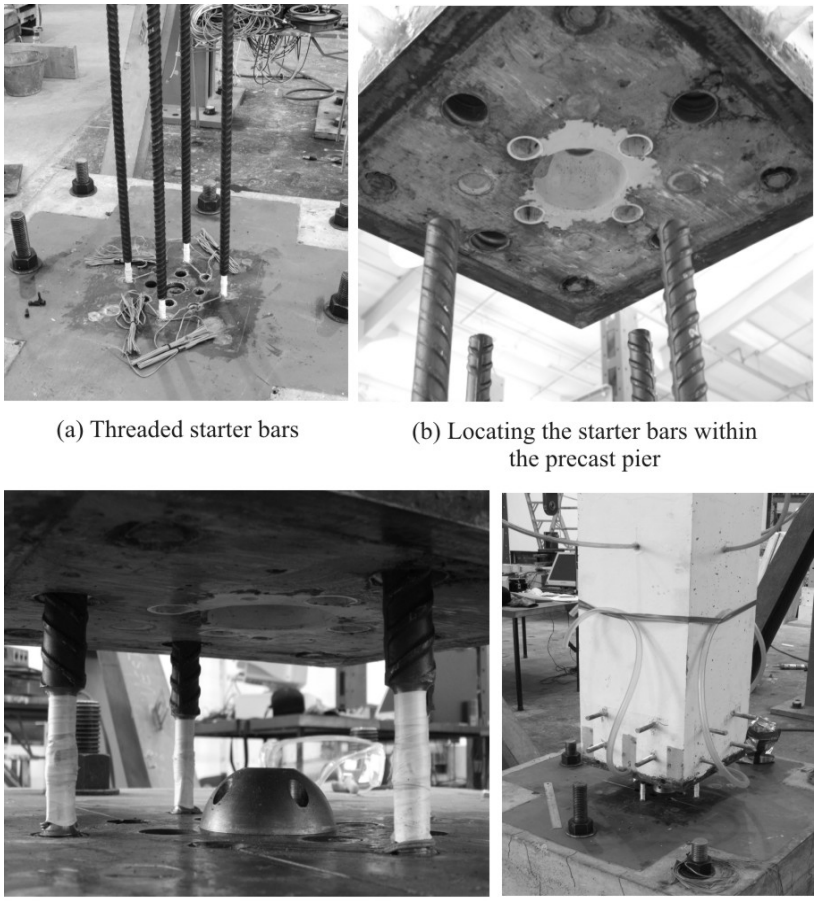

(a) Threaded starter bars

(b) Locating the starter bars within the precast pier

(c) & (d) Lowering the precast pier onto the foundation

Figure 4.12 Assembly of HBD2

4.3.4. Post-Tensioned Bridge Pier with Internal, Semi-Replaceable Dissipaters: HBD3

The third post-tensioned pier (HBD3) was constructed with semi-replaceable dissipaters located internal to the foundation. One end of the mild steel dissipater was threaded into the underside of the precast pier, while the other end was bolted to a connection located on the underside of the foundation. Four post-tensioned tendons were again stressed to a total initial post-tensioning force of 300kN: $0.403f_{pu}$ per tendon (Figure 4.13). The mild steel bars were considered semi-replaceable because, in their current configuration, the pier would need to be de-stressed and uplifted from the foundation in order to remove and replace the mild steel bars.

The internal dissipaters were fabricated from 20mm mild steel bar and had a fused region in the middle of the bar to control/confine the inelastic steel strains. The fused region had a diameter of 13.5mm over a length of 75mm. The length of the fused region was chosen to limit the strain in the mild steel and prevent premature rupture. Little attempt was made to prevent buckling of the internal dissipaters: the 20mm diameter mild steel bars were located within the foundation within 25mm diameter PVC ducts. Ideally, the entire PVC duct should have been epoxy injected; however, this was too difficult to achieve. The mild steel bars were threaded at each end; one

end was screwed into a concrete insert located on the underside of the pier (Figure 4.15 (a)). With the mild steel bars protruding from the underside of the pier, it was lowered onto the foundation. Each mild steel bar passed through a PVC duct within foundation and was bolted to the underside of the foundation after the post-tensioning load was applied (Figure 4.15 (d)).

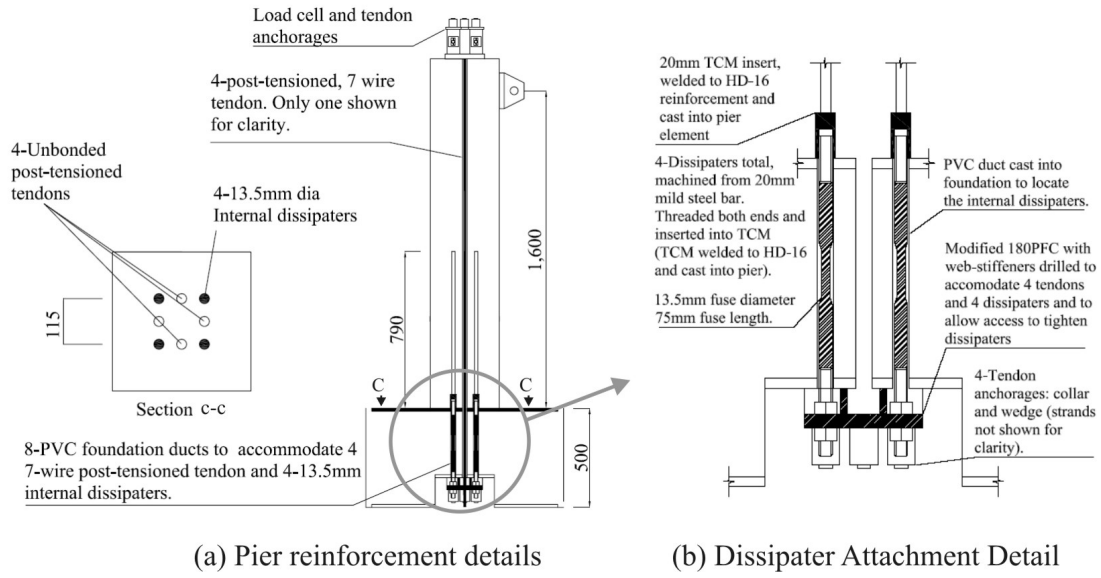

(a) Pier reinforcement details (b) Dissipater Attachment Detail

Figure 4.13 Post-tensioned pier HBD3 structural details

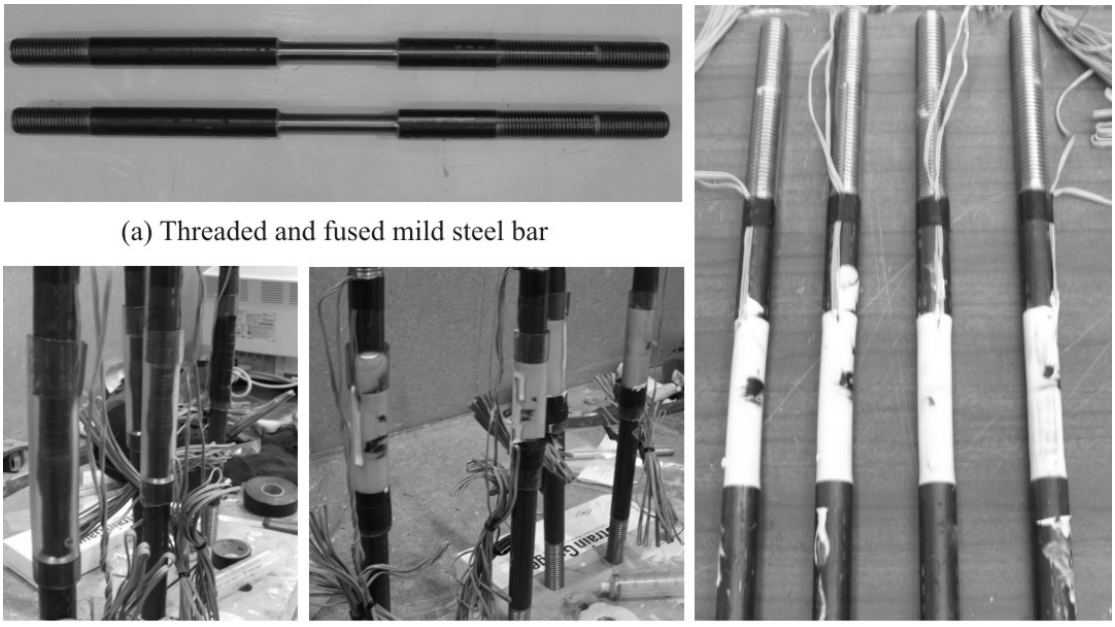

(a) Threaded and fused mild steel bar

(b) & (c) Epoxy injection

(d) Dissipaters ready for installation

Figure 4.14 Internal mild steel dissipaters of HBD3

(a) Bars threaded into precast pier

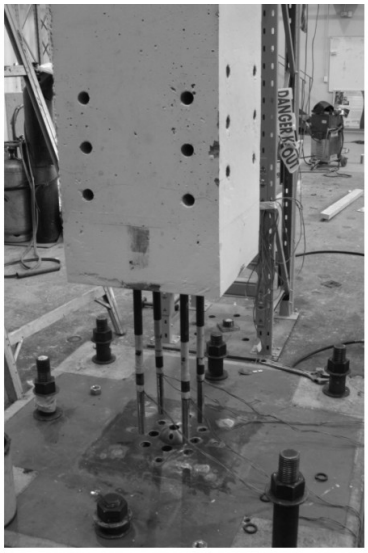

(b) locating bars into foundation ducts

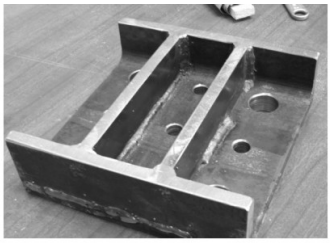

(c) Foundation dissipater/ tendon anchorage bracket

(d) Dissipater and tendon anchorage, foundation underside

Figure 4.15 Assembly of HBD3

4.3.5. Post-Tensioned Bridge Piers with External Replaceable Dissipaters: HBD4 and HBD5

Two post-tensioned bridge piers were constructed with external replaceable tension-compression-yielding (TCY) dampers. The two piers differed in the number of external TCY dampers that were attached to the pier. HBD4 had four TCY devices attached to the pier while HBD5 had eight TCY devices (refer Figure 4.16 and Figure 4.17). Four post-tensioned tendons were each stressed to 75kN ($0.403f_{pu}$): Figure 4.16 (a) shows the details of the generic pier section, while the two different damper arrangements are shown in Figure 4.16 (b). Details relating to the fabrication and testing of the TCY dampers are discussed in Section 4.4.

The TCY dampers were fabricated from 20mm mild steel bar with a yielding region of specific diameter and length. Specific to HBD4, the TCY dampers had a fused diameter of 10mm over a length of 75mm. For HBD5 the TCY dampers had a fused diameter of 8mm over a length of 115mm. The installation procedure of the dampers into the pier is shown in Figure 4.18. Strain-gauges allowed the strain to be monitored while the dampers were bolted into position to ensure they were not pre-yielded before testing.

The TCY dampers were connected to a steel bracket mounted to the side of the precast pier (Figure 4.16 (a)). A total of eight 25mm diameter, high-strength, threaded rods held a steel bracket to each of the four faces. Relying on shear friction to transfer force can be extremely unpredictable, hence, the steel and concrete were roughened and a film of high strength epoxy (Hilti RE500) was applied to the surface of the concrete and steel prior to installation. This ensured that there was no movement of the steel bracket relative to the concrete surface. The foundation end of TCY damper was bolted to a block on top of the foundation. The steel block was bolted to the

foundation with 12mm, 880MPa threaded rods epoxy-cast into the foundation to an embedment depth of 250mm.

The steel plate detail at the rocking interface of HBD4 & HBD5 is illustrated in Figure 4.19. A 25mm steel plate was welded to the longitudinal reinforcement of the precast pier.

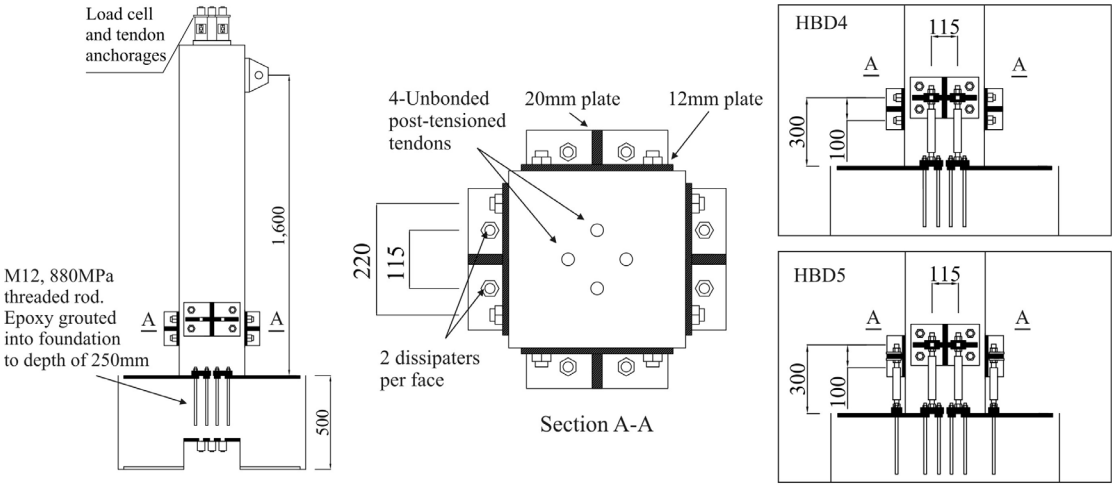

(a) Pier geometry and section detail at the rocking interface (b) Dissipater attachment detail

Figure 4.16 Structural details for post-tensioned piers HBD4 and HBD5

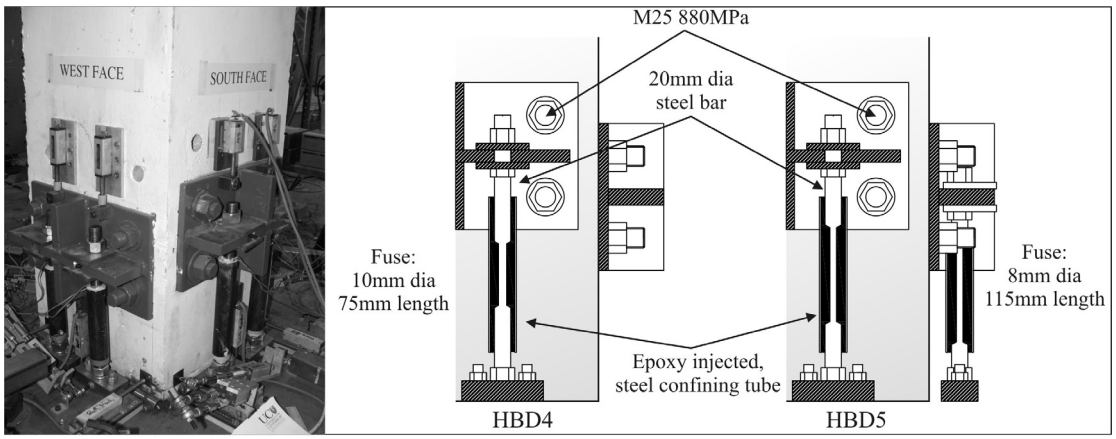

(a) As-built pier (b) Dissipater attachment detail

Figure 4.17 Dissipater connection details for HBD4 and HBD5

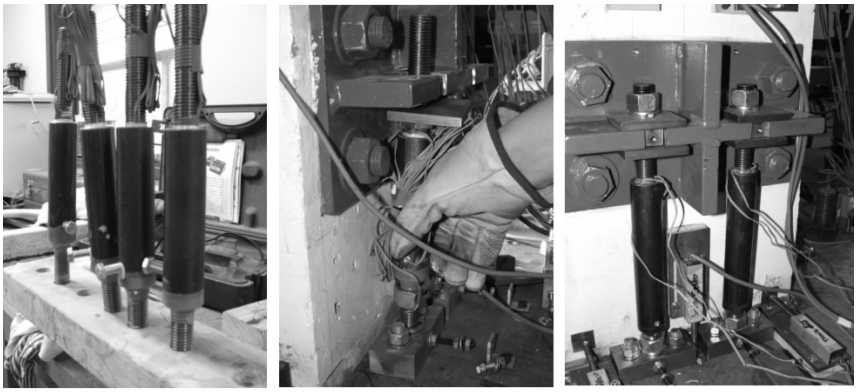

(a) Dissipater elements ready for installation

(b) Installing the dissipaters

(c) Ready for testing

Figure 4.18 Installation of the external dissipaters

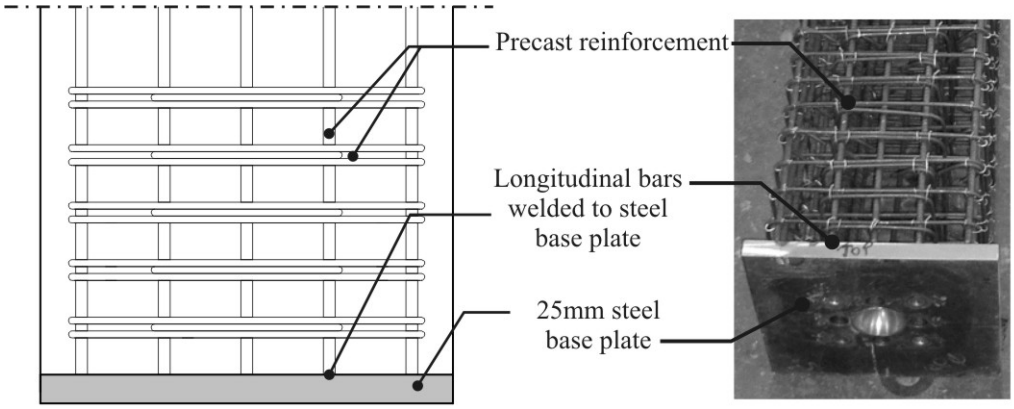

(a) Rocking steel plate detail (Special reinforcement and PVC ducts omitted for clarity)

(b) As-built steel plate detail prior to casting

Figure 4.19 Steel plate detail at the rocking base of HBD4 and HBD5

4.4. FABRICATION AND TESTING OF THE EXTERNAL MILD STEEL DAMPERS

The tension-compression-yielding (TCY) dampers were fabricated at the Civil Engineering Laboratory at the University of Canterbury from 20mm diameter mild steel bar. A yielding region is machined along bar with a reduced diameter over a specified length. The process is illustrated in Figure 4.20: the bar was first placed in a lathe and fused length was "turned" to the desired diameter. Next, the steel dissipater was strain gauged (for instrumentation purposes only). A 34mm (outside diameter) tube, with a wall thickness of 2mm, was located over the machined area of the steel bar and temporarily fixed in place. Epoxy was then injected into a hole located at the bottom of the steel tube to ensure all the air was expelled out of the opening at the top. The fabrication process was relatively simple and cheap, the most time consuming and expensive exercise was strain gauging (which is not required in practical applications).

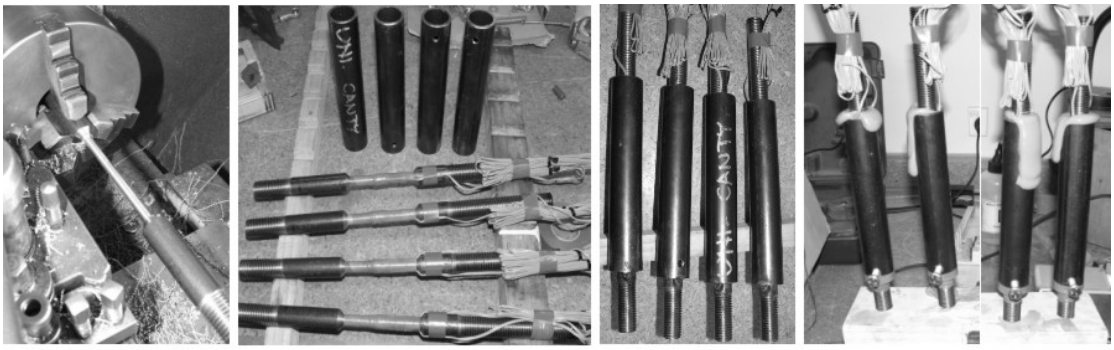

(a) Machining process in lathe (b) Strain guaging (c) Anti-buckling tube installed (d) Epoxy injection

Figure 4.20 TCY damper manufacturing process

Prior to the pier testing, the dampers were individually tested to characterise their stability under cyclic loading and energy dissipation capacity. The test setup for the TCY damper is shown in Figure 4.21 (a). A 250kN Instron test-rig was used to impose a displacement time-history similar to what was expected when tested within the actual bridge pier, Figure 4.21 (b). Three different TCY dampers, with varying fuse diameters, were tested to determine the effectiveness of the anti-buckling tube (Table 4.2).

Four TCY damper tests (damper Group C) are presented in Figure 4.23 plotting the axial force versus axial displacement cyclic response. The four damper specimens were identical in terms of geometry but fabricated from different steel batches. The response is very stable and capable of providing a large amount of dependable energy dissipation. Furthermore, the anti-buckling system worked well: pinching is not evident and the response is very stable.

Consider the response of the two TCY damper tests C3 and C4 (Figure 4.23 (c) & (d) respectively). These two dampers were subjected to net negative displacements.

Negative displacements were expected for the TCY dampers located on the external faces of the post-tensioned pier HBD5. The test results indicate a sudden increase in stiffness when the damper is subjected to negative displacement demands. This can be explained with the illustration in Figure 4.22. As the damper is compressed into the negative range, the larger diameter of the bar comes into contact with the surrounding epoxy increasing the stiffness of the damper in compression. In Figure 4.22 k_1 refers to the elastic stiffness of the mild steel bar alone, while k_2 refers to the additional stiffness provided by the epoxy. The elastic stiffness in compression is the sum of k_1 and k_2 until compression yielding occurs, in which case the stiffness in compression reduces to k_2, the stiffness attributed to the epoxy alone.

The typical failure mechanism of the TCY damper was rupture of the mild steel within the fused region due to low-cycle fatigue (Figure 4.21 (c)). While buckling is observed, the buckled length is very short (Figure 4.21 (c) indicates an effectively buckled length of approximately 3-3.5 bar diameters). This allowed the damper to yield efficiently in compression during unloading.

Multiple cyclic dissipater tests revealed that the strain at rupture typically occurred in the region of 100×10^{-3}-140×10^{-3}mm/mm.

Table 4.2 Details of the TCY damper test groups

	TCY damper detail	Corresponding test
Group A	13.5mm fuse diameter, 75mm fuse length	-
Group B	10.0mm fuse diameter, 75mm fuse length	HBD4
Group C	8.0mm fuse diameter, 115mm fuse length	HBD5

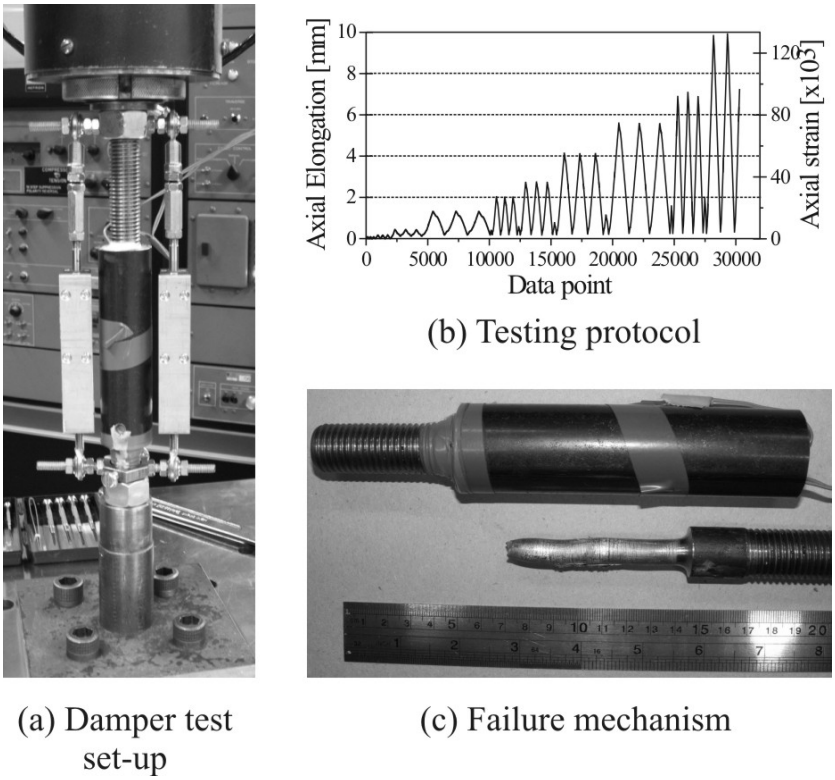

Figure 4.21 TCY damper testing

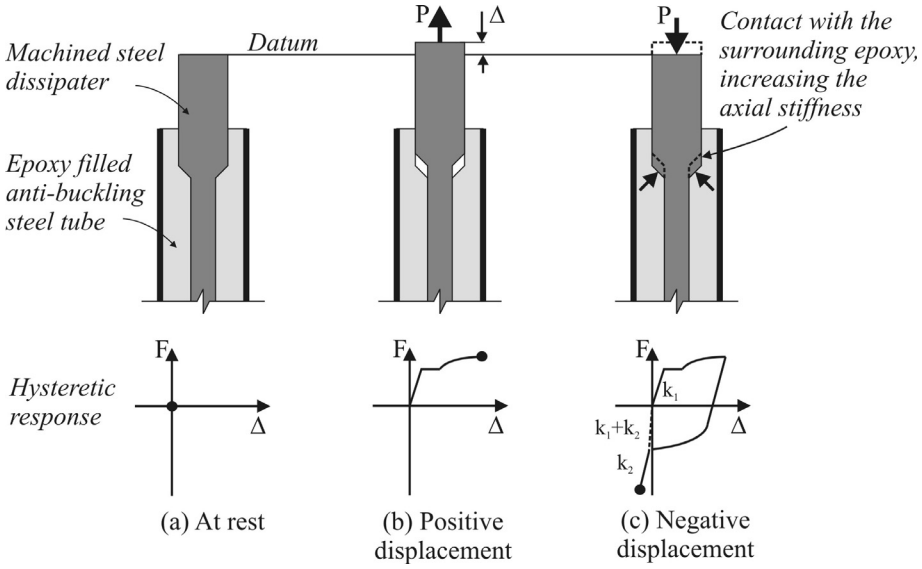

Figure 4.22 The effect of the epoxy, anti-buckling system increasing the axial stiffness of the TCY dampers in compression

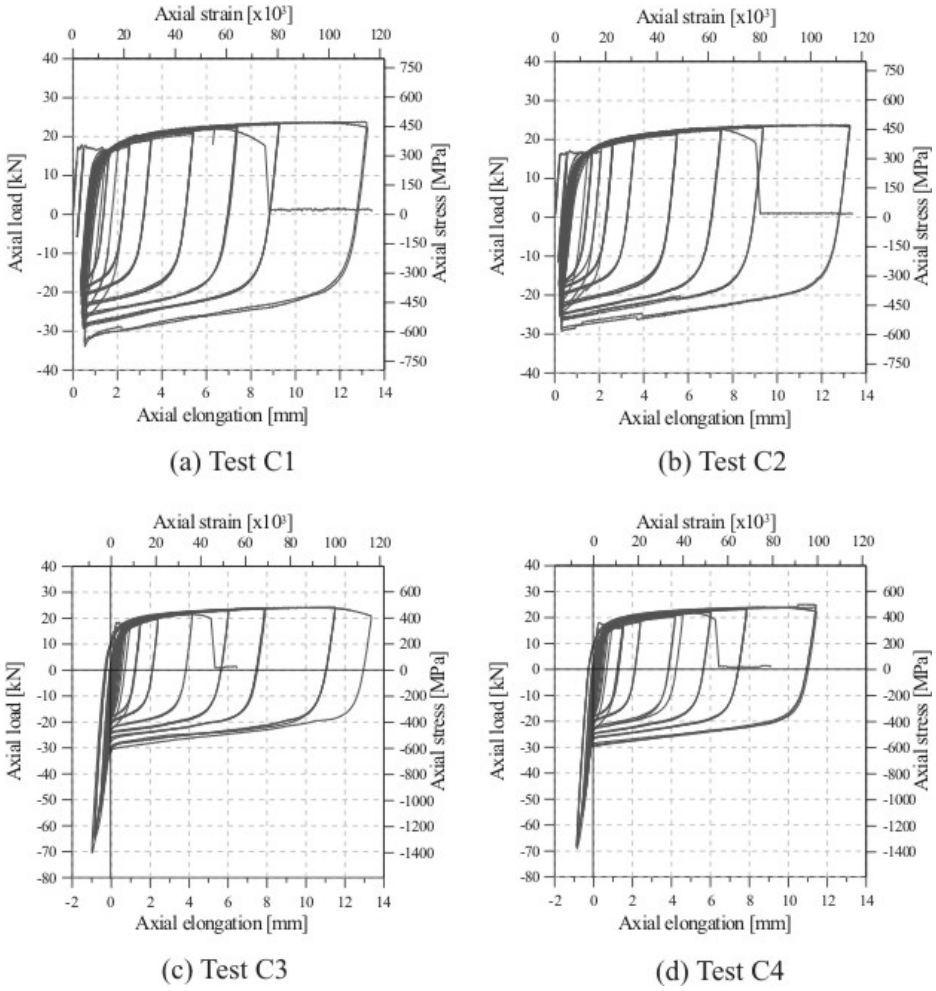

Figure 4.23 Cyclic testing of TCY dampers (Group C). Test specimen C1 & C2 positive displacements only, Test specimens C3 & C4 positive and negative displacements

4.5. EXPERIMENTAL LABORATORY TEST SET-UP

4.5.1. Uniaxial Quasi-Static Laboratory Test Set-Up

The experimental cantilever test pier is illustrated in Figure 4.24. The test set-up was identical for both the post-tensioned (PT) and the monolithic test specimens. Specific instrumentation schemes were adopted depending on whether rotation or curvature was measured during each test. During testing of the monolithic benchmark pier (MON) the 200kN axial load was kept constant to represent the gravity deck load. For the PT test specimens the initial post-tensioning represented the summation of the gravity deck load and the initial post-tensioned force within the prototype pier. As the PT piers displaced laterally the axial load increased as a result of tendon elongation due to the gap opening along the rocking interfaced.

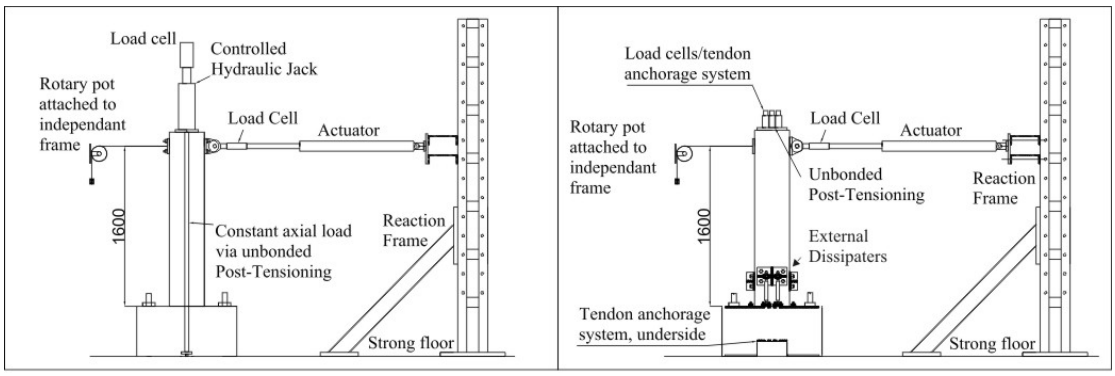

(a) Monolithic pier set-up (b) Post-tensioned pier set-up

Figure 4.24 Experimental test set-up

The quasi-static loading regime consisted of three cycles at each specified lateral drift ratio, followed by a single intermediate cycle at a small drift ratio (Figure 4.25 (b)). The procedure defining the loading protocol was adopted from the ACI recommendations "Acceptance criteria for moment frames based on structural testing" ACI [2001]. This standard defines the minimum experimental evidence that must be satisfied to construct structural systems outside the requirements of ACI 318-99. The document provides a number of prescriptive pass/fail criteria. On completion of the 3rd and final cycle at a drift ratio not less than 3.5% (being the typical MCE displacement demand for moment resisting frames), the system must satisfy the following

- The peak force in any given loading direction must exceed 75% of the maximum force in the same loading direction.
- The relative energy dissipation (ratio of energy dissipated to an equivalent elasto-plastic system) shall exceed 1/8 (0.1275).
- The secant stiffness from -3.5% to 3.5% of lateral drift shall exceed 0.05 times the initial stiffness of the system (determined from the elastic cycles at the beginning of the test protocol).

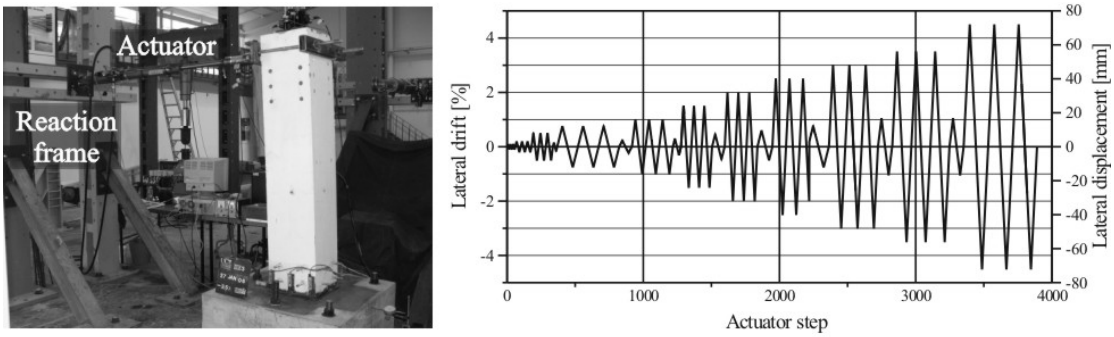

(a) As-built test set-up (b) Displacement time-history

Figure 4.25 Quasi-static test-rig and displacement controlled testing protocol

(a) Measuring Lateral Displacements

Lateral displacements at the top of the pier were measured by rotary potentiometers fixed to independent steel frames, located in line with the hydraulic actuators.

(b) Measuring Lateral and Axial Loads

The lateral load was directly measured via a 150kN load cell attached at the end of the hydraulic actuator. The tendon loads were measured using 150kN load cells that were specifically fabricated to fit beneath each tendon anchorage.

(c) Computing Curvatures and Rotation

Curvatures were not directly measured up the height of the monolithic pier, rather rotations were measured at 200mm intervals up the height of the pier to a distance of 800mm above the foundation (Figure 4.26 (a)).

With respect to the instrumentation up the height of the monolithic bridge pier in Figure 4.26 (a), the rotation relative to points 1 and 2 is given by Eq.(4.1). All linear potentiometers were arranged such that extension recorded a positive numeric value.

$$\theta_{mon}^{1-2} = \frac{\Delta_A - \Delta_B}{x} \qquad \textbf{4.1}$$

It follows that the average curvature between points 1 and 2 is computed from Eq.(4.2)

$$\phi_{mon}^{1-2} = \frac{\theta_{1-2}}{h_{1-2}} \qquad \textbf{4.2}$$

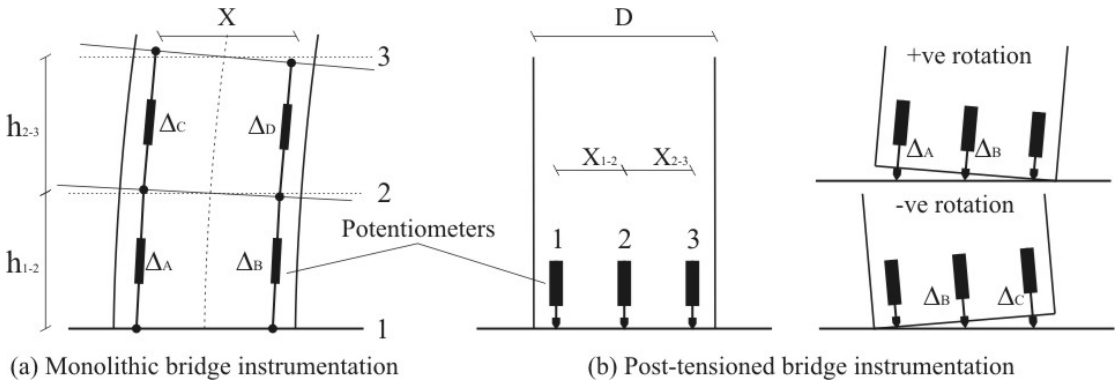

Figure 4.26 Instrumentation to record rotation

The rotation at the base of the post-tensioned bridge piers can be determined by Eq.(4.3) for positive rotations in Figure 4.26 (b) and Eq.(4.4) for negative rotations.

$$\theta_{PT}^{+ve} = \frac{\Delta_A - \Delta_B}{x_{1-2}} \quad \textbf{4.3}$$

$$\theta_{PT}^{-ve} = \frac{\Delta_C - \Delta_B}{x_{2-3}} \quad \textbf{4.4}$$

(d) Computing the Neutral Axis Depth

It was not necessary to define the neutral axis depth within the monolithic bridge pier. However, the neutral axis depth ***c*** could be readily computed along the base of the post-tensioned piers from the instrumentation layout in Figure 4.26 (b). For positive rotations the neutral axis depth can be computed from Eq.(4.5), while for negative rotations Eq.(4.6) is used. The formulation of Eq.(4.5) and Eq.(4.6) is presented as a ratio of the section depth $\chi = c/D$. The behaviour of the neutral axis depth provides a better understanding of the section response for analytical modelling purposes.

$$\frac{c}{D} = \chi_{+ve,\theta} = 0.5 - \frac{x_{1-2}}{D}\frac{\Delta_B}{\Delta_A - \Delta_B} \quad \textbf{4.5}$$

$$\frac{c}{D} = \chi_{+ve,\theta} = 0.5 - \frac{x_{2-3}}{D}\frac{\Delta_B}{\Delta_C - \Delta_B} \quad \textbf{4.6}$$

4.5.2. Biaxial Quasi-Static Laboratory Test Set-Up

The uniaxial test-rig was extended to two directions for biaxial testing in Figure 4.28. The uniaxial ACI protocol described in Section 4.5.1 was used to determine the lateral drift amplitudes in both the N-S and E-W direction during biaxial testing. The combined displacement time-history of both the N-S & E-W actuators results in a clover displacement path shown in Figure 4.27. The radius ***r*** at any point is described by the function $r(\theta) = R \cdot \sin(2\theta)$. The magnitude of the maximum displacement at each cycle is defined by ***R*** and located at an angle of 45 degrees to the principal axis. The ***x*** and ***y*** co-ordinates are therefore given by $x(\theta) = r(\theta) \cdot \cos(\theta)$ and $y(\theta) = r(\theta) \cdot \sin(\theta)$ respectively. The largest ***x*** and ***y*** displacement component occurs at an angle less than 45 degrees: approximately equal to 36 degrees. Three complete cycles of the clover-shape were circumscribed during each specified drift level. This was quite a demanding loading protocol as the pier was subjected to a total of six excursions into the positive and negative x-axis and y-axis during each specified drift level.

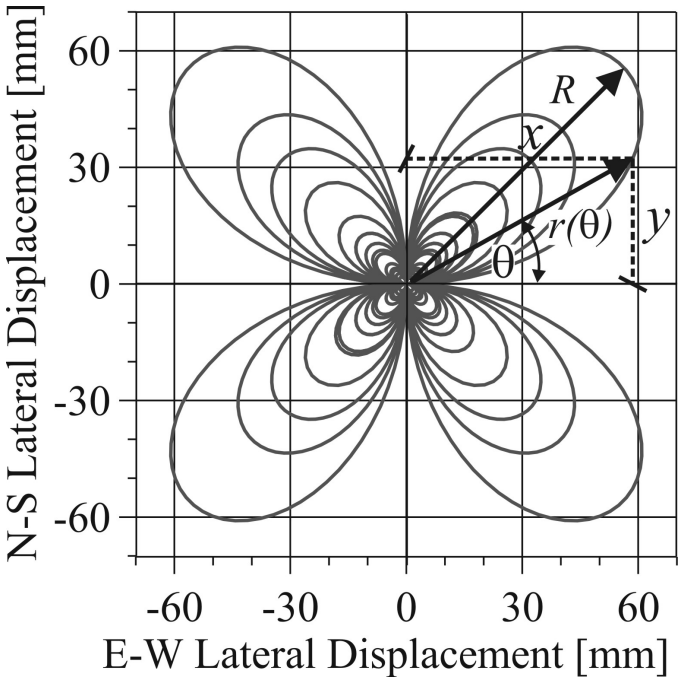

Figure 4.27 Biaxial displaced profile

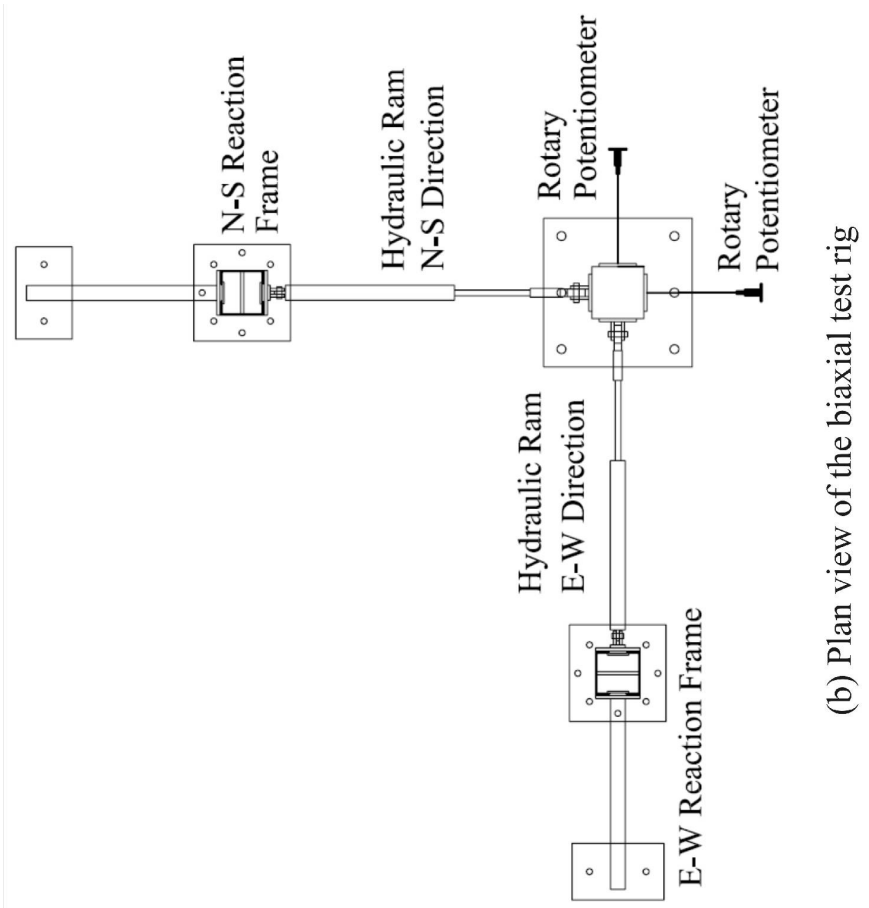

(b) Plan view of the biaxial test rig

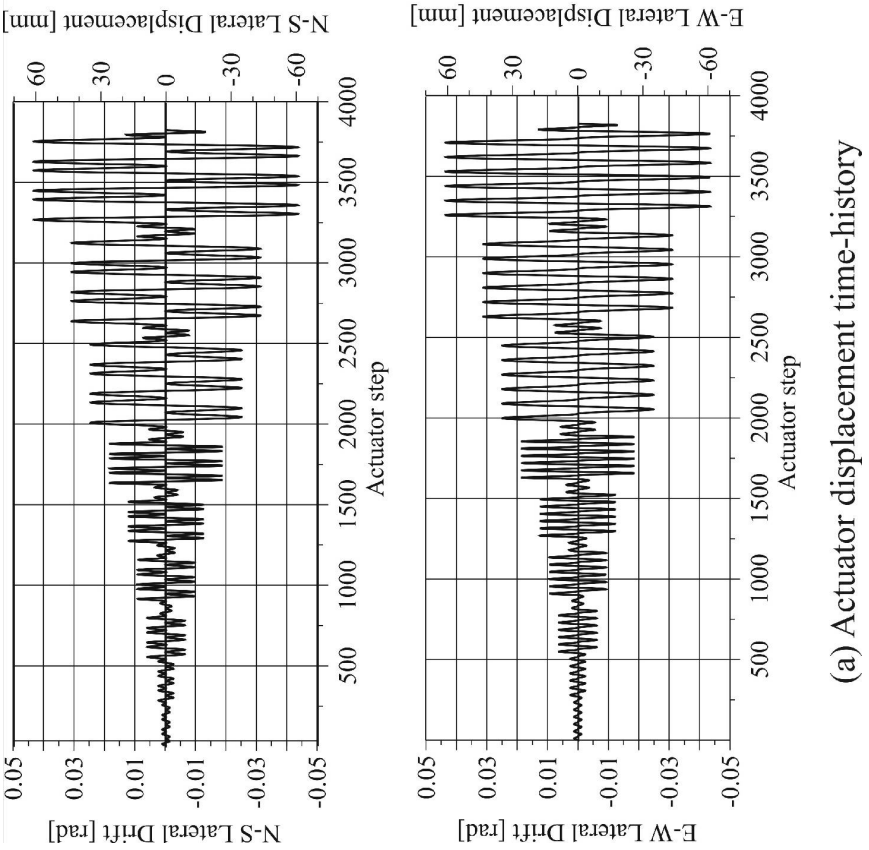

(a) Actuator displacement time-history

Figure 4.28 Bi-directional loading protocol and test rig

4.6. MATERIAL PROPERTIES

4.6.1. Mild Steel Reinforcement

Monotonic tension testing was carried out on the five types of mild steel reinforcement used as dissipaters within the post-tensioned piers as well as the longitudinal reinforcement within the monolithic (MON bridge pier. The mild steel is listed below

- Longitudinal reinforcement within MON (and the precast longitudinal reinforcement within the PT pier)
- Grouted longitudinal reinforcement used in HBD1
- Grouted, fused longitudinal reinforcement used in HBD2
- Mild steel bar used in HBD3 and HBD4
- Mild steel bar used in HBD5

At least three test specimens were selected from each steel group, with the average material properties summarised in Table 4.3.

Table 4.3 Average mild steel material properties

	E	f_y	f_u	ε_y	ε_{sh}	ε_u
MON	187000MPa	317MPa	433MPa	0.00170	0.030	0.20
HBD1	194000MPa	304MPa	450MPa	0.00157	0.022	0.20
HBD2	218500MPa	568MPa	704MPa	0.00260	0.016	0.08
HBD3	190000MPa	320MPa	460MPa	0.00170	0.026	0.20
HBD4	190000MPa	320MPa	460MPa	0.00170	0.026	0.20
HBD5	193000MPa	320MPa	461MPa	0.00165	0.025	0.20

4.6.2. Post-tensioned Reinforcement

The prestressed/post-tensioned reinforcement used was 0.5 inch (12.7mm) diameter, 7-wire strands (A_{pt} = 100mm^2). While monotonic testing was carried out, the strands were not tested to rupture. Additional material tests were carried out by the steel distributor, which allowed the ultimate strength to be determined. The properties are listed below in Table 4.4.

Table 4.4 Post-tensioned reinforcement material properties

	E	f_y	f_u	ε_y	ε_u
7-wire strand	197100MPa	1560MPa	1850MPa	0.00792	NA

4.6.3. Concrete

Unconfined concrete compression tests were carried out on the concrete material used in the construction of the monolithic and post-tensioned piers. The 28 day and lead-up compressive strengths are recorded in Table 4.5.

Table 4.5 Concrete compressive strengths

	Monolithic pier	**PT pier**
7 day compressive strength	52.6MPa	40.6MPa
28 day compressive strength	66.5MPa	49.5MPa
Strength at first day of testing	65.9MPa	54.1MPa

4.7. DISCUSSION ON THE EXPERIMENTAL RESULTS

4.7.1. Monolithic Benchmark Bridge Pier

(a) Uniaxial Quasi-Static Cyclic Test Results

The lateral load-displacement response of the monolithic benchmark bridge pier (MON) is graphed in Figure 4.29 (a). Typical of a well detailed section, the response is very stable with large inelastic cycles developing a large amount of energy dissipation; however, at a consequence of large static residual deformations. Significant pinching occurs due to the 200kN applied axial load representing the gravity deck load of the bridge pier. Cyclic stiffness degradation occurs due to degradation of the mechanical bond around the mild steel reinforcement. There is no loss in strength up to a lateral drift ratio of 4.5%.

As a result of the "cold-joint" (the bridge pier in two stages: first the foundation, followed by the pier, as per typical construction practice), damage was confined to a few wide cracks (Figure 4.29 (b) & (c)). The wider cracks were located primarily at the foundation-pier interface and to a lesser extent, up to a height approximately equal to the depth of the pier. Due to the high compressive strength of the concrete (f'_c = 66.5MPa at 28 days) spalling was not observed until the lateral drift ratio exceeded 4.5%; thereafter, spalling was initiated by buckling of the longitudinal reinforcement.

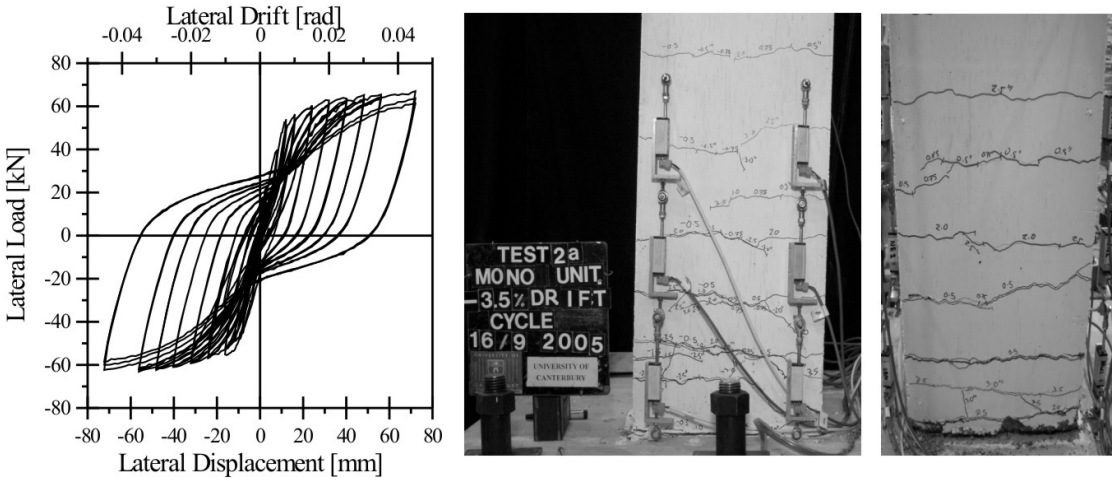

(a) Lateral response (b) & (c) Damage at 3.5% drift

Figure 4.29 Experimental force-displacement response and photos indicating damage of the benchmark monolithic pier at a lateral drift ratio of 3.5%.

(b) Biaxial Quasi-Static Cyclic Test Results

The biaxial cyclic load-displacement behaviour of the monolithic bridge pier is presented in Figure 4.30 (a). The biaxial response is similar to the uniaxial response in that the system is relatively stable and has a large amount of energy dissipation capacity. Spalling was initiated at a lateral drift ratio of 1.5% at each corner of the pier and becomes more wide spread (up to a height of 200-300mm) at a lateral drift of 2%. Cyclic stiffness degradation is initiated by bond deterioration and progressive spalling of the unconfined cover concrete and continues to degrade as the displacement ductility increases. The reduction in strength during the second cycle at 3.5% lateral drift within the S-E quadrant resulted from rupture of the N-W and S-W longitudinal reinforcing bars. Prior to rupture of the longitudinal reinforcement no strength degradation was observed. Large static residual deformations were apparent due to the non-recoverable inelastic strains within the longitudinal reinforcement.

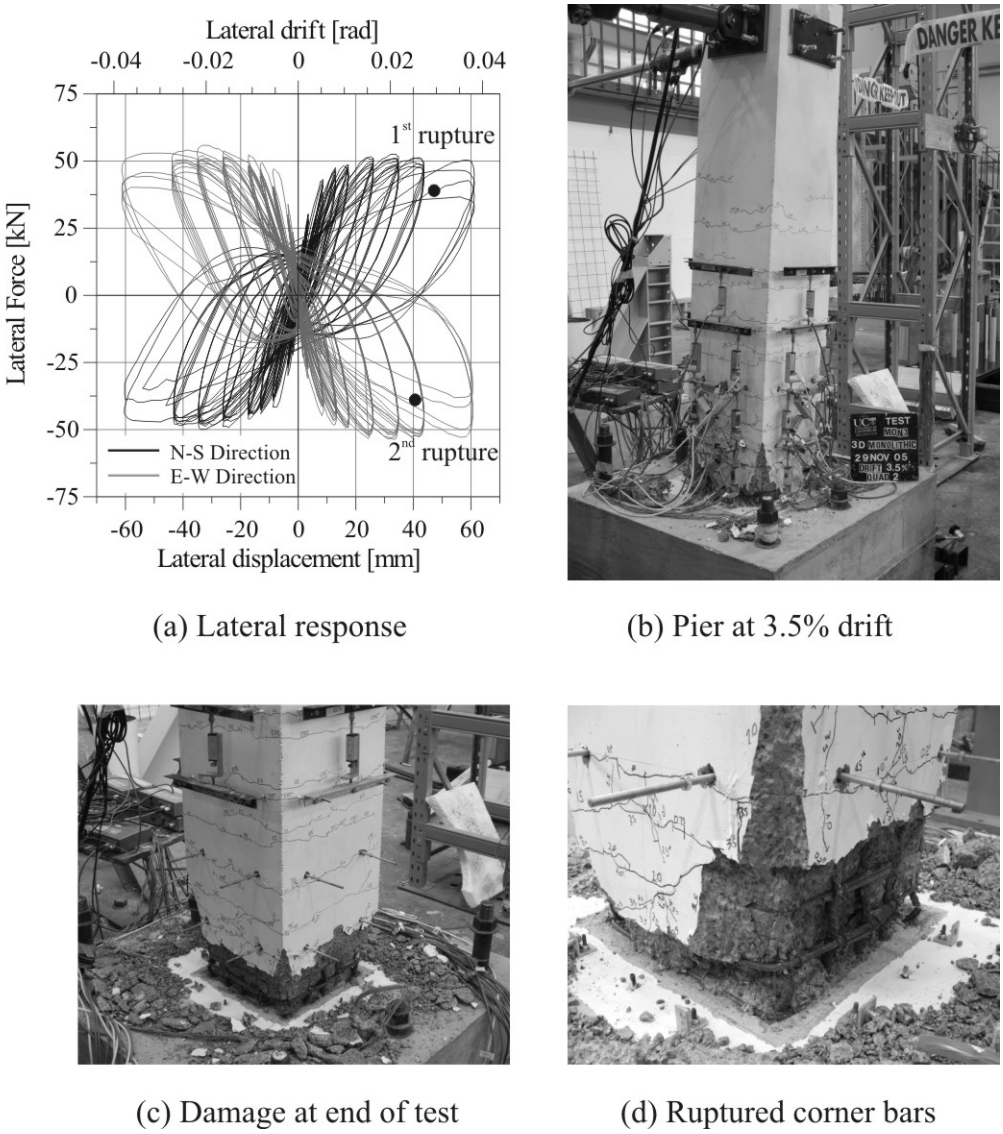

Figure 4.30 Performance of the monolithic bridge pier under bi-directional cyclic loading

First-buckling of the longitudinal reinforcement was observed at a lateral drift of 2.5%; thereafter, the stiffness began to degrade significantly. This was followed by a marked reduction in strength after rupture of the corner reinforcing bars occured. Damage was extensive, being entirely confined to a region approximately equal to the depth of the pier section (the length of the plastic hinge): Figure 4.30 (b), (c) & (d). It should be appreciated that the structural integrity would be difficult and costly to reinstate in this case.

4.7.2. Post-Tensioned Only Bridge Piers

(a) Uniaxial Quasi-Static Cyclic Test Results

The uniaxial, quasi-static lateral response of two post-tensioned only piers is presented in Figure 4.31 and Figure 4.32. The post-tensioned pier PT1 in Figure 4.31 is the same as the post-tensioned pier PT2 in Figure 4.32 the difference being the type of material at the rocking interface. PT1 had a concrete rocking surface; in fact, PT1 and HBD1 were the same specimen, PT1 was tested before the internal mild steel reinforcement was grouted within the precast pier (this defined HBD1). It is for this reason that PT1 was only tested to a lateral drift of 0.75% to protect the mild steel reinforcement from damage. PT2 had a steel rocking surface and was the same specimen as the post-tensioned hybrid pier HBD4 without any external TCY damper elements connected.

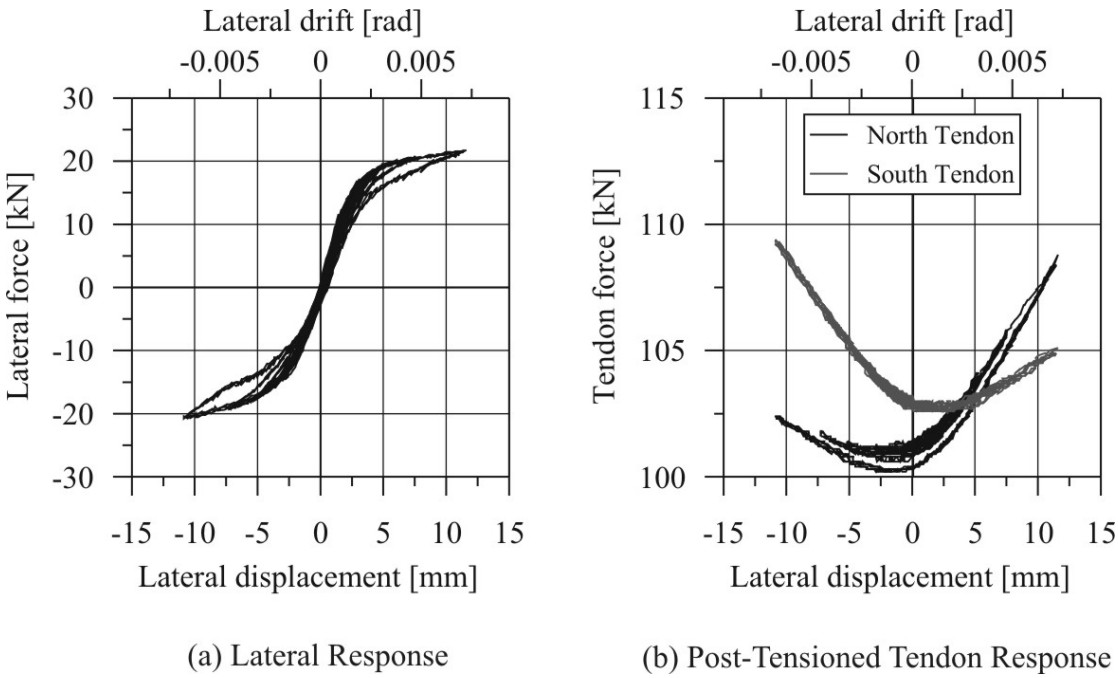

Figure 4.31 PT1 (post-tensioned only pier) quasi-static cyclic response

The force-displacement behaviour of both PT tests is essentially characterised by a non-linear elastic response. Some energy dissipation (and minor stiffness degradation) is observed for PT1, primarily related to a reduction of the initial post-tensioned load due to mechanical take-up of the tendon anchorages as the load in the tendon

increased. In contrast, the tendon anchorages in PT2 were pre-loaded to a load greater than that expected during testing. Therefore, no tendon losses were observed in this test, resulting in an almost completely elastic response.

The non-linear point describing the transition between the initial and the bi-linear stiffness in Figure 4.31 (a) and Figure 4.32 (a) corresponds to a geometric non-linearity point due to the sudden relocation of the neutral axis position within the section. This is not a material non-linearity point. This geometric non-linearity is an inherent property of post-tensioned rocking systems. The behaviour of the neutral axis is discussed in more detail in Chapter 7.

At the completion of both tests, no damage was observed, albeit for minor flexural cracking up the height of the pier. On unloading, the thickness of the residual crack widths were of hairline due to the post-tensioned force acting on the pier.

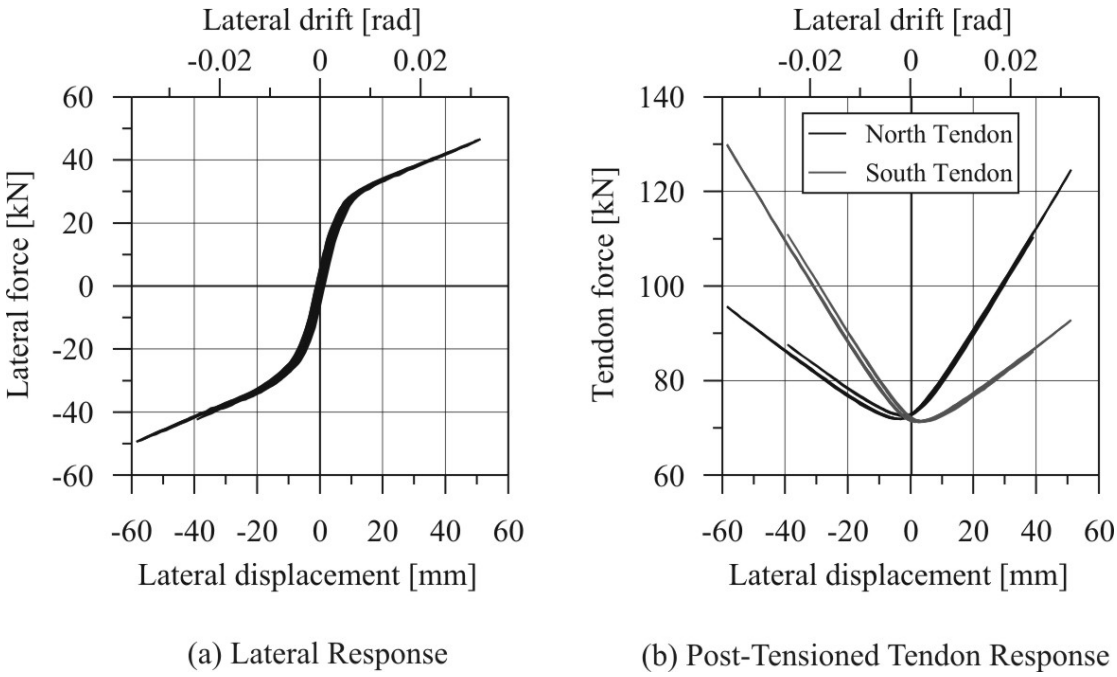

Figure 4.32 PT2 (post-tensioned only pier) quasi-static cyclic response

(b) Bi-Directional Quasi-Static Cyclic Test Results

The N-S and E-W bi-directional lateral response of PT2 is presented in Figure 4.33 showing the lateral force-displacement response (a) and the tendon behaviour (b). Some stiffness degradation is observed in Figure 4.33 (a) due to minor damage around the corner of the rocking toe. Photos of this damage are shown Figure 4.34: the damage is primarily superficial spalling of the cover concrete combined with some flexural yielding of the 25mm steel base plate at each corner. As the bridge pier rocks about the corner toe large compression strains can be expected. As the plate yields and some cover concrete is lost, a reduction in lateral stiffness is expected for following loading cycles due to a reduction in length of the internal lever-arm defining the

moment capacity of the section. In fact, the test was terminated at a drift ratio of 1.5% to preserve the bridge pier for subsequent tests.

The clover-shaped tendon load response in Figure 4.25 is related to the biaxial displacement loading protocol. There were no tendon losses observed during or after testing as the tendons and tendon anchorages were pre-loaded prior to testing.

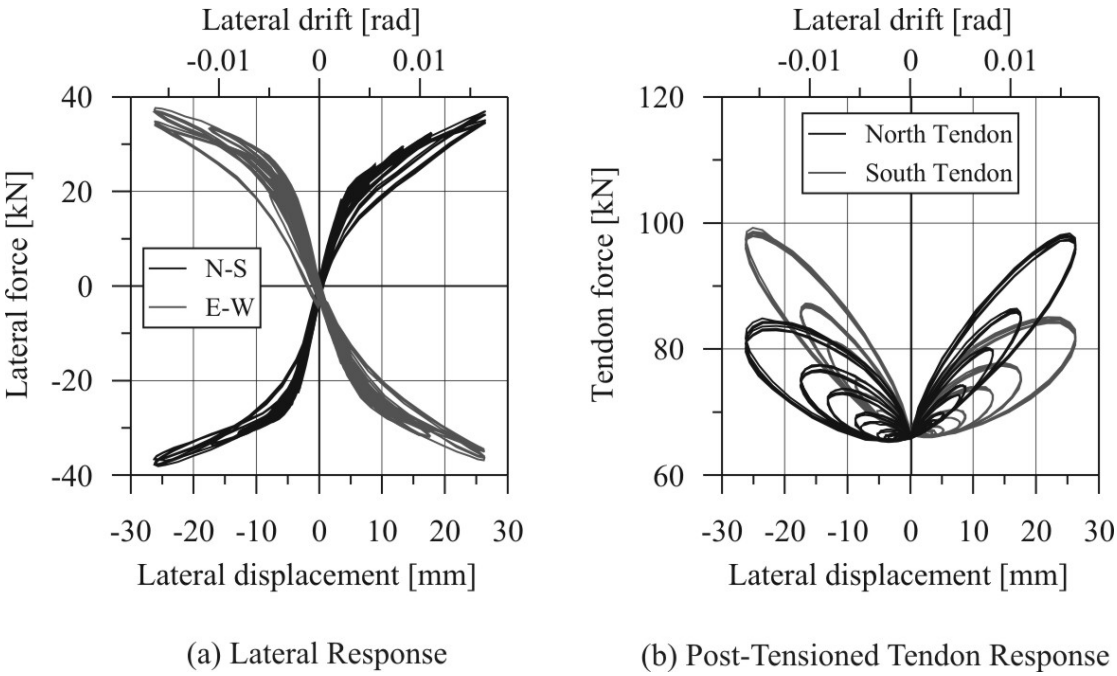

Figure 4.33 PT2 (post-tensioned only pier) biaxial quasi-static cyclic response

(a) Gap opening at the rocking interface (b) & (c) Minor loss of cover concrete to pier toe

Figure 4.34 Damage of PT2 under biaxial cyclic testing

4.7.3. Post-Tensioned Bridge Pier Testing with Internal Dissipation: HBD1

(a) Uni-Directional Quasi-Static Cyclic Test Results

The cyclic testing of HBD1 (post-tensioned pier with internally grouted mild steel reinforcement) is plotted in Figure 4.35 (a) and shows a very stable lateral response. Some cyclic stiffness degradation is evident due to deterioration of the bond around the grouted mild steel reinforcement. The strength is very stable up until the test is terminated at a lateral drift ratio of 3.0%.

The tendons remained completely elastic (f_y = 156kN). Minor tendon losses were observed due to pull-in of the wedges within the tendon anchorage in Figure 4.35 (b). The apparent "hysteresis" response of the post-tensioned tendons in Figure 4.35 (b) is not related to yielding of the tendons; rather, the elongation of the tendon differs considering both the loading and unloading cycle. The depth of the neutral axis is larger during the loading cycle when compared to unloading cycle as the extreme mild steel layers go from being loaded in tension to being loaded in compression.

Damage was confined to yielding of the mild steel reinforcement and flexural cracking up the height of the pier (Figure 4.36). Upon unloading, a majority of the cracks were of hairline thickness. Spalling of the cover concrete was prevented by the cast-in steel angle assembly located around the perimeter of the base.

Some static residual deformations were evident during the test. The ratio of the axial load plus prestressed reinforcement moment (M_N+M_{pt}) to the non-prestressed reinforcement moment (M_{ms}) was approximately equal to 1.0, i.e. with reference to Eq.(4.7), $\lambda \approx 1.0$. When this is the case, static residual deformations are expected considering over-strength of the mild steel (strain-hardening). However, even considering material over-strength, the system will still return low residual deformations following an earthquake due to dynamic re-centring and the high bilinear stiffness of the system.

$$\lambda = \frac{M_{pt} + M_N}{M_{ms}} \qquad \textbf{4.7}$$

Technically, HBD1 failed the ACI acceptance criteria (refer Section 4.5.1) as the peak lateral drift ratio did not equal or exceed 3.5%; however, one could infer from the stability of the test results that a lateral drift of 3.5% could be easily achieved. The *relative energy dissipation* was equal to 0.332 for the 3rd cycle at 3.0% lateral drift, with a ratio of the secant stiffness (at 3.0% lateral drift) to the initial stiffness of 0.145. No reduction in strength was observed.

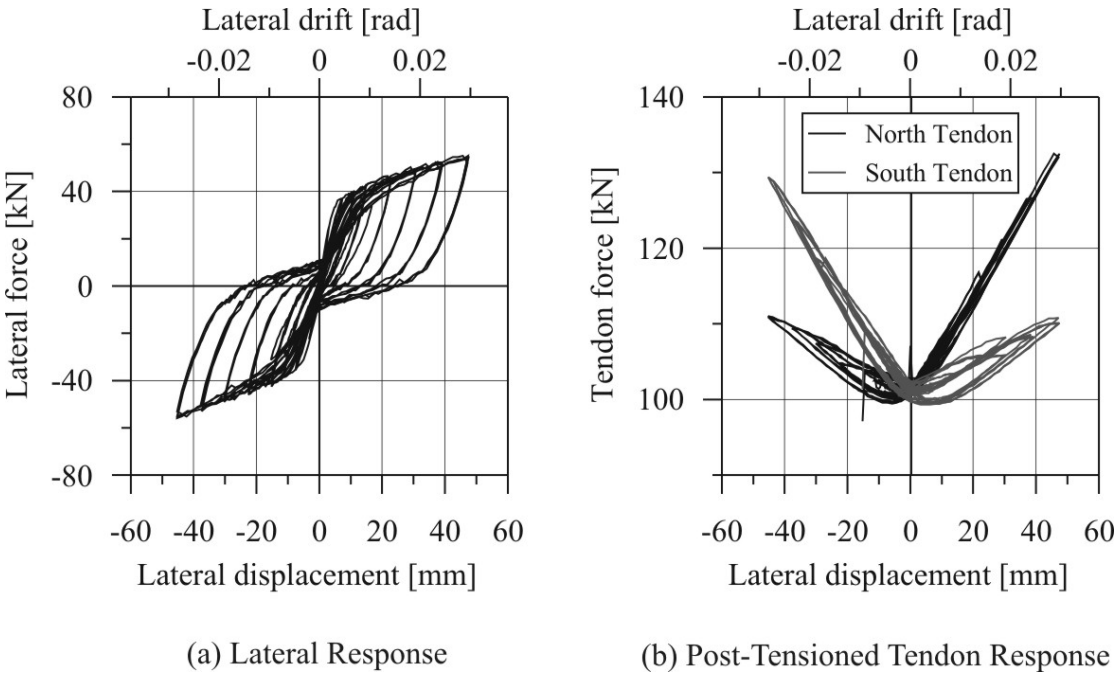

Figure 4.35 HBD1 quasi-static cyclic response

(a) & (b) Pier at a lateral drift of 2.0% and 3.0% respectively

(c) Flexural cracking on North face

Figure 4.36 Damage of HBD1

4.7.4. Post-Tensioned Bridge Pier Testing with Internal Dissipation: HBD2

(a) Uniaxial Quasi-Static Cyclic Test Results

The cyclic response of the post-tensioned bridge pier HBD2 is similar to HBD1 in that the response is very stable with a large amount of dependable energy dissipation

capacity (Figure 4.37 (a)). There is less cyclic stiffness degradation present in HBD2 due to the nature of the mild steel reinforcement: strain penetration and bond deterioration is significantly reduced when a fuse region is located along the mild steel bar.

The larger initial post-tensioned force of 300kN acting on the section led to larger concrete compression strains during rocking. The consequence of this was minor (superficial) spalling of the cover concrete directly above the cast-in steel angle assembly located around the base of the pier (Figure 4.38). The larger tendon load also increased the moment ratio of the section to approximately $\lambda = 1.5$ (at a lateral drift of 2%): this reduced the static residual deformations after testing.

Due to laboratory complications during testing, only one cycle at the final drift ratio of 3.5% was recorded. However, considering the stability of the system up until this point the remaining two cycles would have been completed without any issues.

Again, technically HBD2 failed the ACI acceptance criteria as laboratory issues prematurely ended the testing, allowing only a single drift cycle at 3.5% to be recorded. A *relative energy dissipation* ratio of 0.311 (>0.1275), for the 1st cycle at a lateral drift ratio of 3.5%, was achieved with a ratio of the secant stiffness (at 3.5% lateral drift) to the initial stiffness of 0.266. No strength degradation was observed.

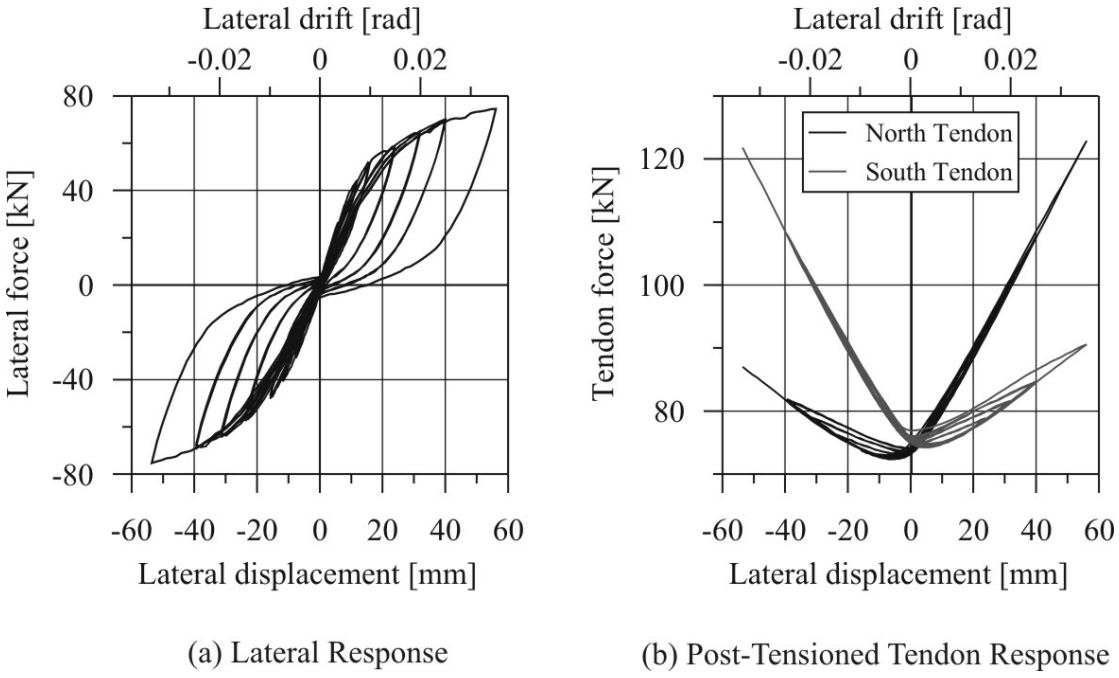

Figure 4.37 HBD2 quasi-static cyclic response

(a) & (b) Damage to HBD2 at the end of testing: minor loss of cover concrete

Figure 4.38 Damage of HBD2 at the end of testing indicating superficial spalling of the cover concrete above the cast in-situ steel angle assembly

4.7.5. Post-Tensioned Bridge Pier Testing with Internal Dissipation: HBD3

(a) Uniaxial Quasi-Static Cyclic Test Results

The cyclic force-displacement response of HBD3 was characterised by significant pinching and stiffness degradation in Figure 4.40 (a). The internal mild steel dissipaters, which pass through PVC ducts located within the foundation, prematurely buckled and prevented efficient yielding in compression. The buckled dissipaters are pictured in Figure 4.39 (a) after being removed from the pier at the end of the test. Some tendon losses were observed but were minimal and related to anchorage pull-in of the wedges in Figure 4.40 (b).

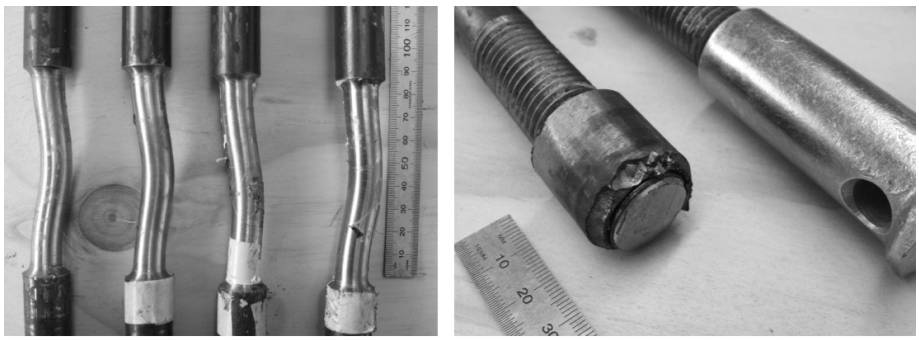

(a) Buckled internal dissipaters (b) Failure of a foundation insert

Figure 4.39 Buckled internal dissipaters and rupture of a pier threaded-insert

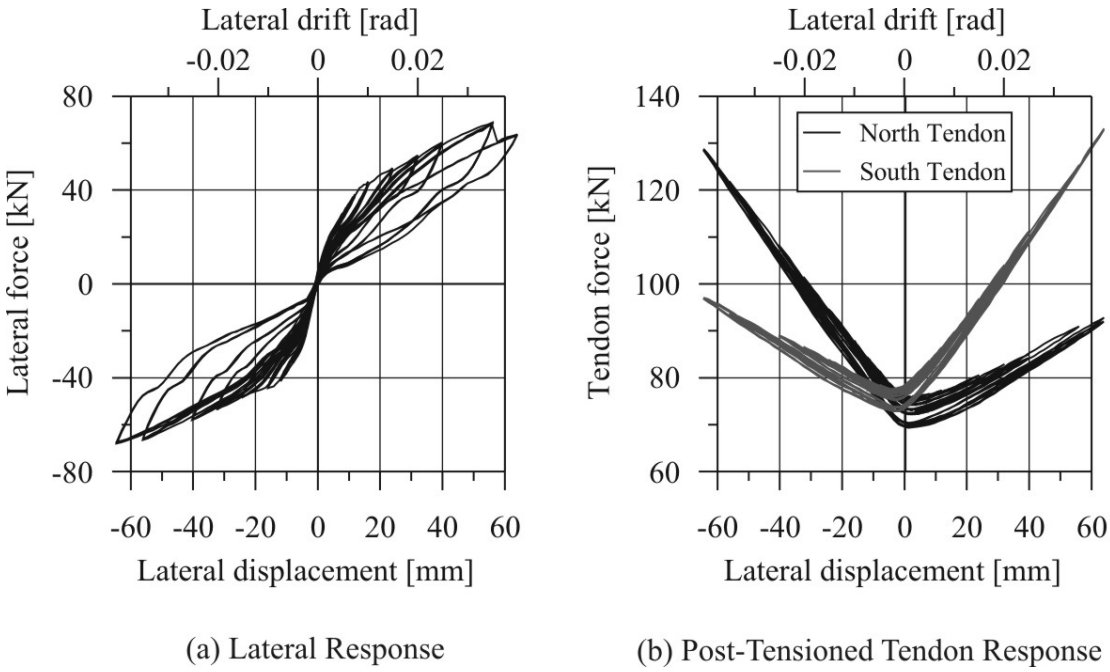

Figure 4.40 HBD3 quasi-static cyclic response

During the final cycle approaching a lateral drift ratio of 4% a sudden reduction in strength was observed. This strength reduction resulted from fracture of one of the threaded-inserts. The inserts were cast into the precast pier: the dissipaters were later threaded into the inserts. The rupture plane was located at the location of a temporary construction weld. This weld contained a region of brittle material encouraging rupture.

The entire ACI acceptance criteria were achieved for HBD4. Three cycles at a lateral drift of 3.5% was recorded. A *relative energy dissipation* ratio of 0.135 (>0.1275) at the 3rd cycle at a lateral drift ratio of 3.5%, was achieved with a ratio of the secant stiffness (at 3.5% lateral drift) to the initial stiffness of 0.194. The reduction in strength did not fall below 75% of the peak load in the same direction.

4.7.6. Post-Tensioned Bridge Pier Testing with External Dissipation: HBD4

(b) Uniaxial Quasi-Static Cyclic Test Results

The cyclic response of the post-tensioned pier with external TCY dampers (HBD4) was the most stable of all the tests reported herein. The entire cyclic response was extremely stable: the only stiffness degradation resulted from Bauschinger effects of the mild steel TCY dampers in Figure 4.41 (a). Damage was limited to flexural cracking up the height of the pier: when the lateral load was removed the cracks were of hairline thickness.

The imposed displacement demands acting on the steel TCY dampers was in the order of 6.5mm at a lateral drift of 3.5%. These displacement demands are highlighted in

Figure 4.42 (b). The entire inelastic deformation was concentrated to the sacrificial and replaceable dampers.

The steel brackets supporting the externally mounted dampers provided essentially zero slip along the connection interface: this maximised the efficiency of the TCY dampers. Furthermore, the tendons remained elastic and rupture of the dissipaters was avoided up to a lateral drift of 3.5%. All three ACI acceptance criteria were met with a *relative energy dissipation* ratio equal to 0.16 (>0.1275) for the final cycle at a lateral drift of 3.5% and a secant-to-initial stiffness ratio of 0.22 at 3.5% lateral drift.

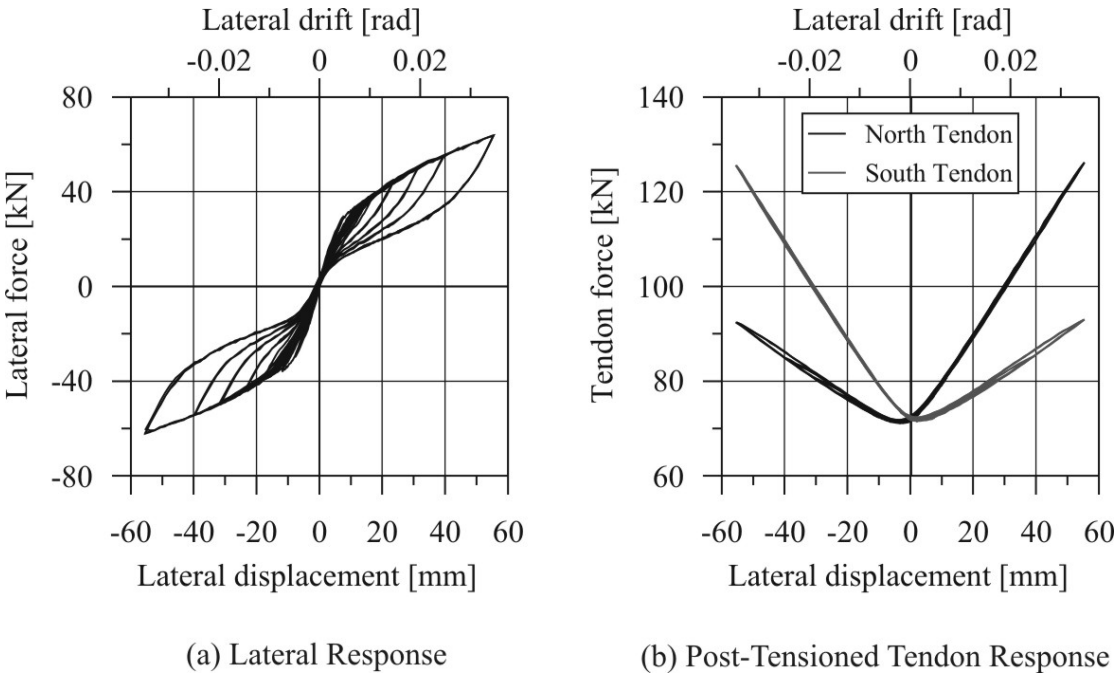

Figure 4.41 HBD4 quasi-static cyclic response

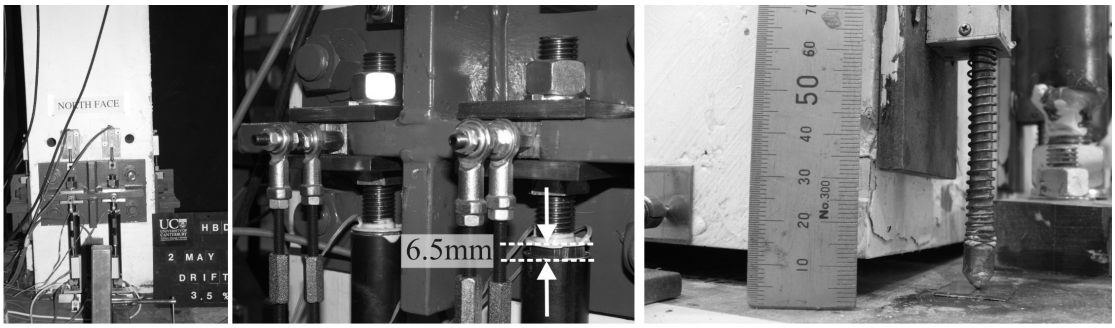

(a) HBD4 at 3.5% drift (b) Extension of the external dampers (c) Uplift of the rocking interface

Figure 4.42 Rocking response of HBD4 at 3.5% lateral drift

4.7.7. Post-Tensioned Bridge Pier Testing with External Dissipation: HBD5

(a) Uniaxial Quasi-Static Cyclic Test Results

As was the case for HBD4, the cyclic response of the post-tensioned pier HBD5 was found to be very stable, Figure 4.43. Premature rupture of one dissipater occurred in each direction during loading to the final cycle at a lateral drift of 3.5%. It is worth noting that rupture was mainly due to an inadequate fuse length of 115mm: this length was constrained by the available length at the base of the rocking connection. While monotonic tensile testing of the mild steel bars indicated available mild steel strain capacities in the order of $200\text{x}10^{-3}$mm/mm (Table 4.3), cyclic testing suggested that the available strain capacity would reduce by as much as 35-50% due to low-cycle fatigue (refer Figure 4.21). Cyclic dissipater tests indicated that the strain at rupture typically occurred in the region of 100×10^{-3} to $140\times10^{-3}\,mm/mm$. The strain demand acting on the TCY dampers that were located on the outside face of the pier section was in the order of $120\text{x}10^{-3}$mm/mm at a lateral drift of 3.5%, so it was of no surprise that rupture to one or more of the mild steel dissipaters occurred during the final drift cycles.

With this in mind, the collapse-prevention design objective at the MCE limit state was not completely satisfied for HBD5 as two out of a total of eight dampers ruptured. Details of the design objectives at the 2/3MCE and MCE are discussed in Section 4.2. However, given that two out of a total of eight dampers had ruptured the lateral stability was not compromised due to high level of redundancy within the system: as well as the remaining dampers, the post-tensioned tendons are still fully contributing to the lateral capacity of the system (in fact, the tendons will, in general, contribute to at least 50% of the lateral capacity). Furthermore, the entire vertical load bearing capacity of the system is still maintained after any number of dissipaters rupture.

The higher percentage of energy dissipation is clearly evident for HBD5 when compared to HBD4: this resulted in minor static residual deformations for HBD5. As expected, the damage to HBD5 was limited to flexural cracking of the precast pier and inelastic yielding of the steel dissipaters. All three ACI acceptance criteria were met; only a 10% loss in strength occurred as a result of one dissipater rupturing in each direction, a *relative energy dissipation* ratio equal to 0.27 (>0.1275) and a secant-to-initial stiffness ratio of 0.14 was measured at a lateral drift of 3.5%.

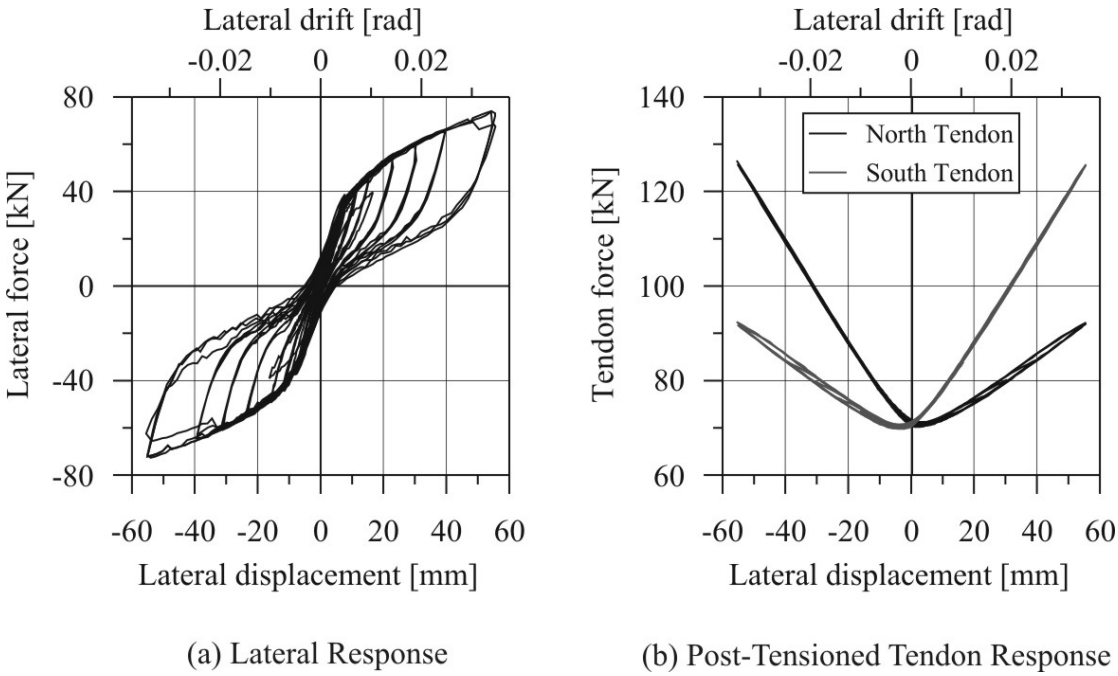

Figure 4.43 HBD5 quasi-static cyclic response

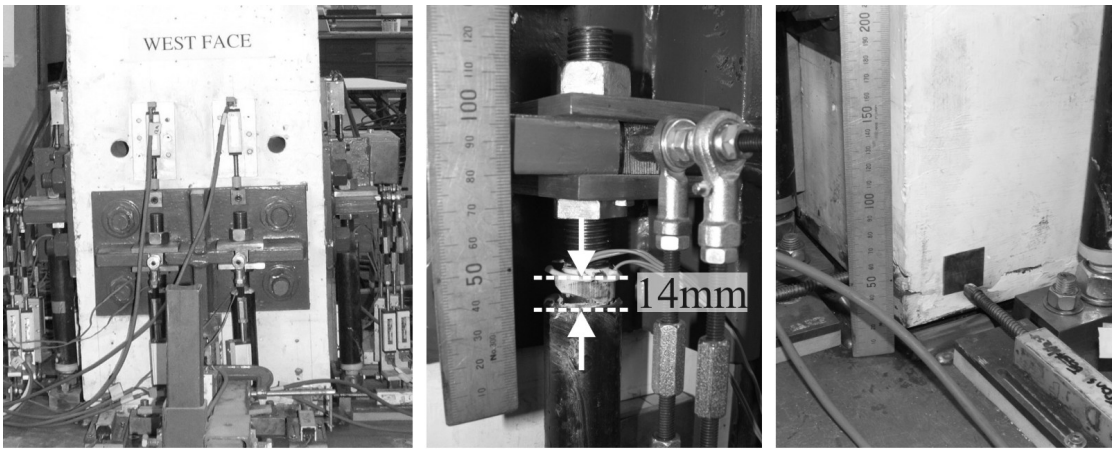

(a) HBD4 at 3.5% drift

(b) Extension of the external dampers

(c) Uplift of the rocking interface

Figure 4.44 Rocking response of HBD5 at 3.5% lateral drift

(b) Bi-Directional Quasi-Static Cyclic Test Results

Figure 4.45 (a) presents the N-S and E-W lateral response of the post-tensioned, hybrid bridge pier HBD5. The response was stable with very little stiffness and strength degradation until rupture of the 1st TCY damper at a lateral drift ratio approaching 2.5%. Two more dampers ruptured during subsequent drift ratios at 2.5%: this is indicated by the significant drop in strength and stiffness to the system in the cycles to follow. Given that three out of eight dissipaters had ruptured, significant residual strength and stiffness could still be relied upon due to the post-tensioned

tendons and the five remaining TCY dampers. Some spalling occurred at the base of the pier around each corner: concrete spalling was accompanied by flexural yielding of the steel plate (Figure 4.45 (c) & (d)).

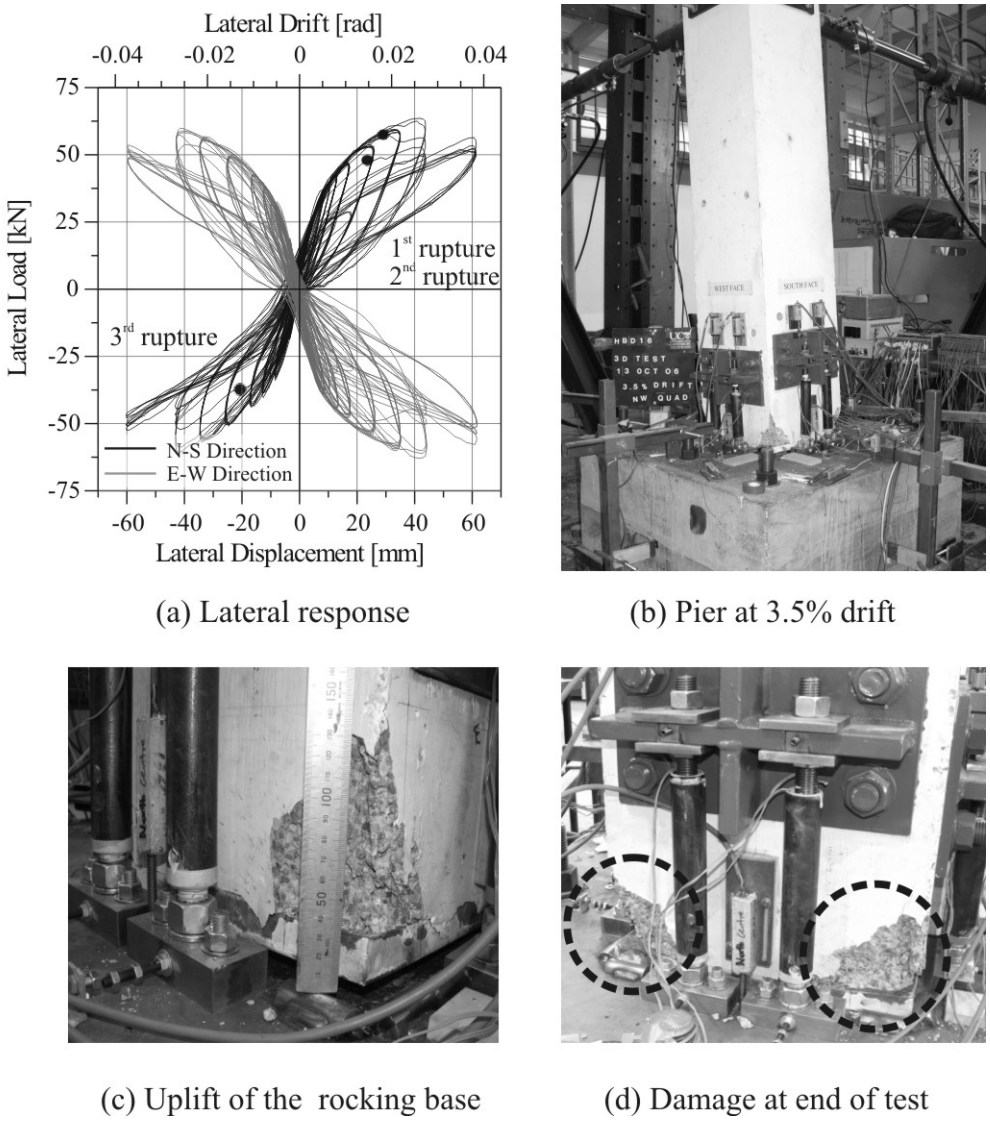

Figure 4.45 Performance of the HBD5 bridge pier under biaxial cyclic loading

4.7.8. Area-Based Equivalent Viscous Damping

With reference to Figure 4.46, the area-based equivalent viscous damping (area-based EVD) can be computed from Eq.(4.8).

$$\xi = \frac{1}{4\pi}\frac{E_D}{E_s} \qquad \textbf{4.8}$$

Where:

$\boldsymbol{E_D}$ = total energy dissipated during one complete cycle

$\boldsymbol{E_S}$ = equivalent strain energy at the maximum displacement of the cycle

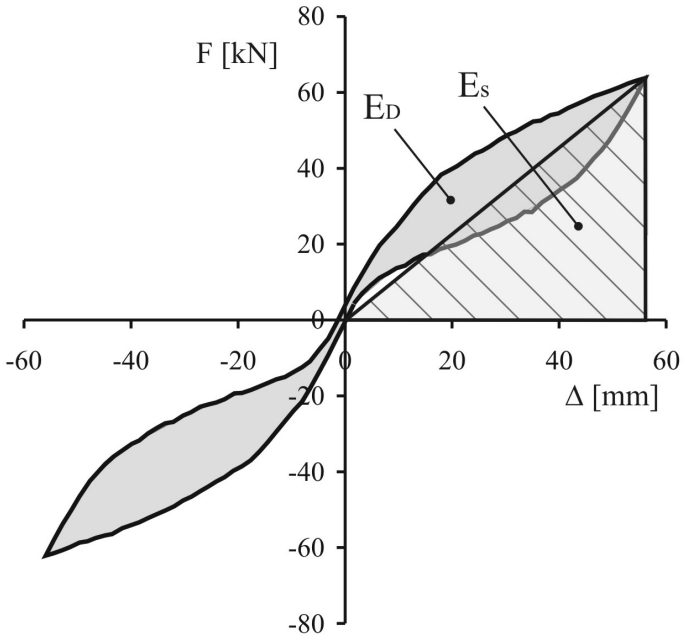

Figure 4.46 Area-based, Equivalent Viscous Damping calculation

The equivalent viscous damping (EVD) was computed for each post-tensioned bridge pier and compared with the ductile monolithic pier in Figure 4.47 as a benchmark. The EVD is plotted showing the 3rd cycle at each drift level. The horizontal axis at the top of each graph indicates the ductility demand of the monolithic pier.

Each post-tensioned pier was able to dissipate an appreciable amount of energy. HBD1 indicated a very high damping ratio was possible; however, some residual deformations could be expected following an earthquake due to the low proportion of prestressed to non-prestressed reinforcement within the section. On the contrary, HBD3 returned quite a low level of damping. This was as a result of buckling of the internal mild steel dampers. If buckling had of been prevented the damping capacity would have improved significantly.

The EVD of each bridge pier is graphed in Figure 4.48 and Figure 4.49 for each displacement cycle. These graphs allow the EVD of each pier to be compared at each cycle and to investigate the degradation associated with bond deterioration or bar buckling. First, considering the ductile monolithic bridge pier, there is surprisingly

little degradation of area-based damping following each drift cycle. The lateral cyclic response of Figure 4.29 suggests that the degradation that occurs between each cycle to the same drift is minimal: the stiffness degradation appears to be largely dependant on the current maximum ductility demand and less dependant on the total number of displacement cycles. Similar conclusions can be made with regards to HBD1.

The decrease in area-based damping from the 1st cycle to subsequent cycles for HBD3 is attributed to buckling of the internal mild steel bars. After bar-buckling has occurred within the first cycle, the damping stabilises during subsequent cycles. The degradation associated with HBD4 and HBD5 is primarily attributed to the Bauschinger material effect of the external TCY dampers: in fact the difference in area-based damping between the first and third cycles for these tests is minimal. This highlights the stability of a post-tensioned system with external TCY dampers.

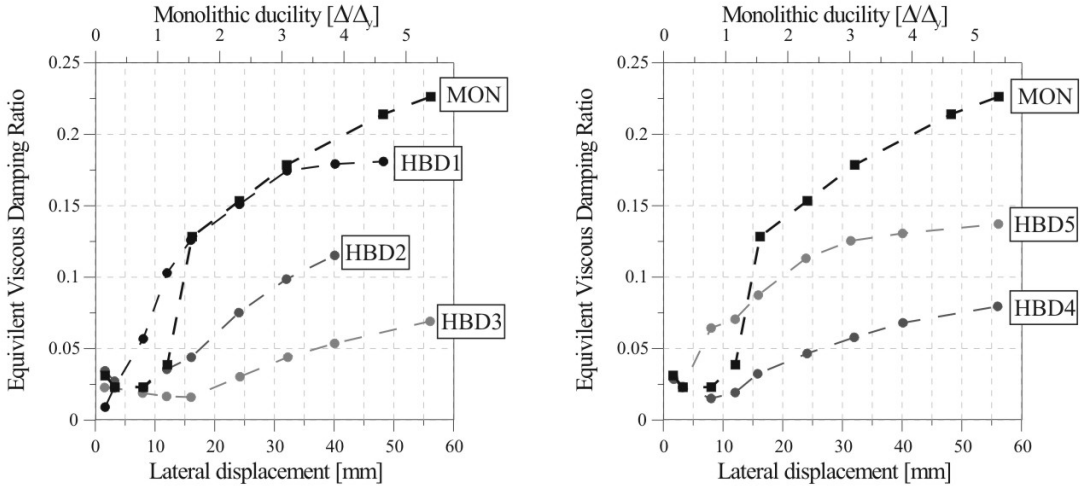

Figure 4.47 Equivalent viscous damping comparison (3rd cycle at each drift)

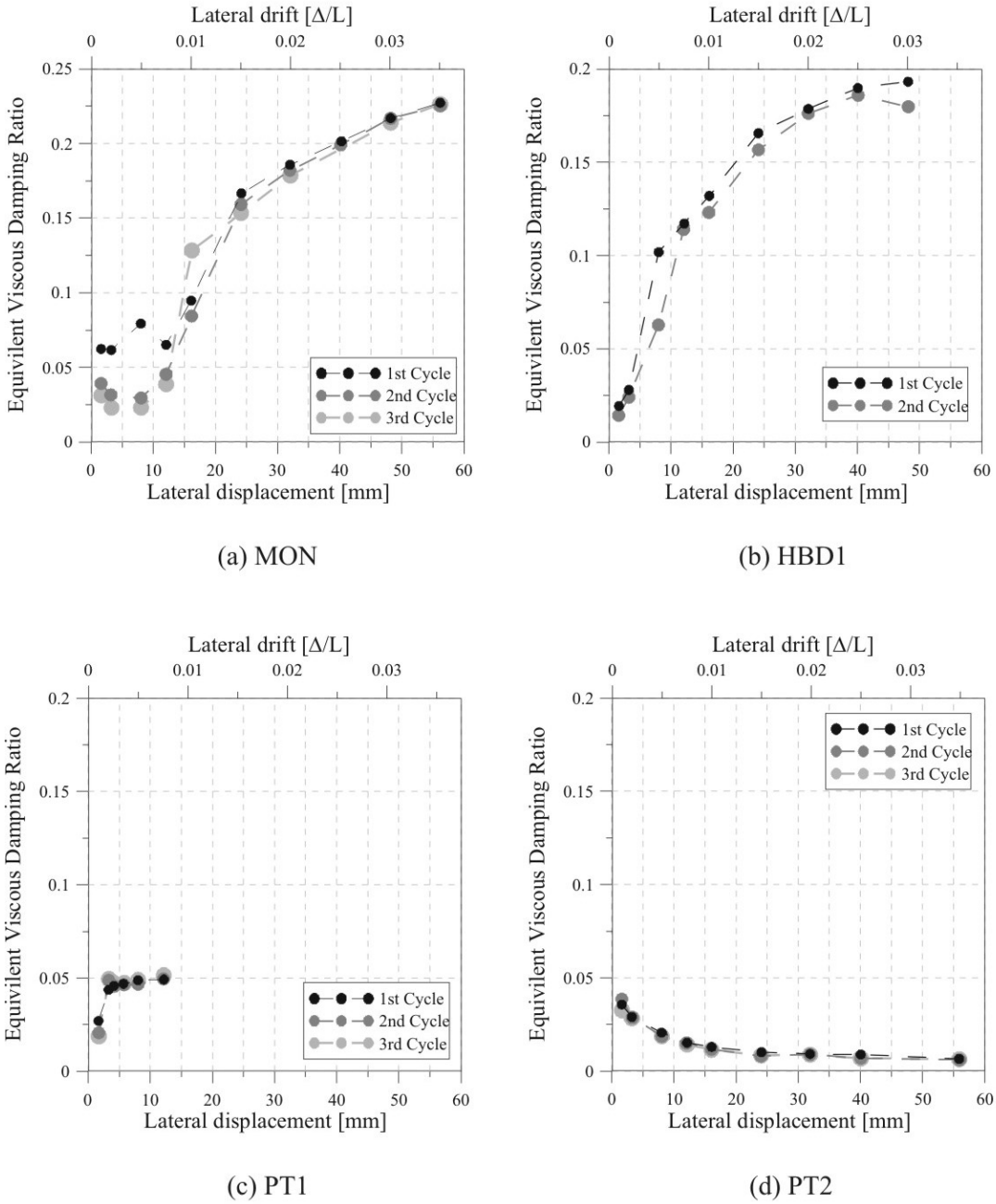

Figure 4.48 Comparison of equivalent viscous damping (EVD) between MON, HBD1, PT1 & PT2

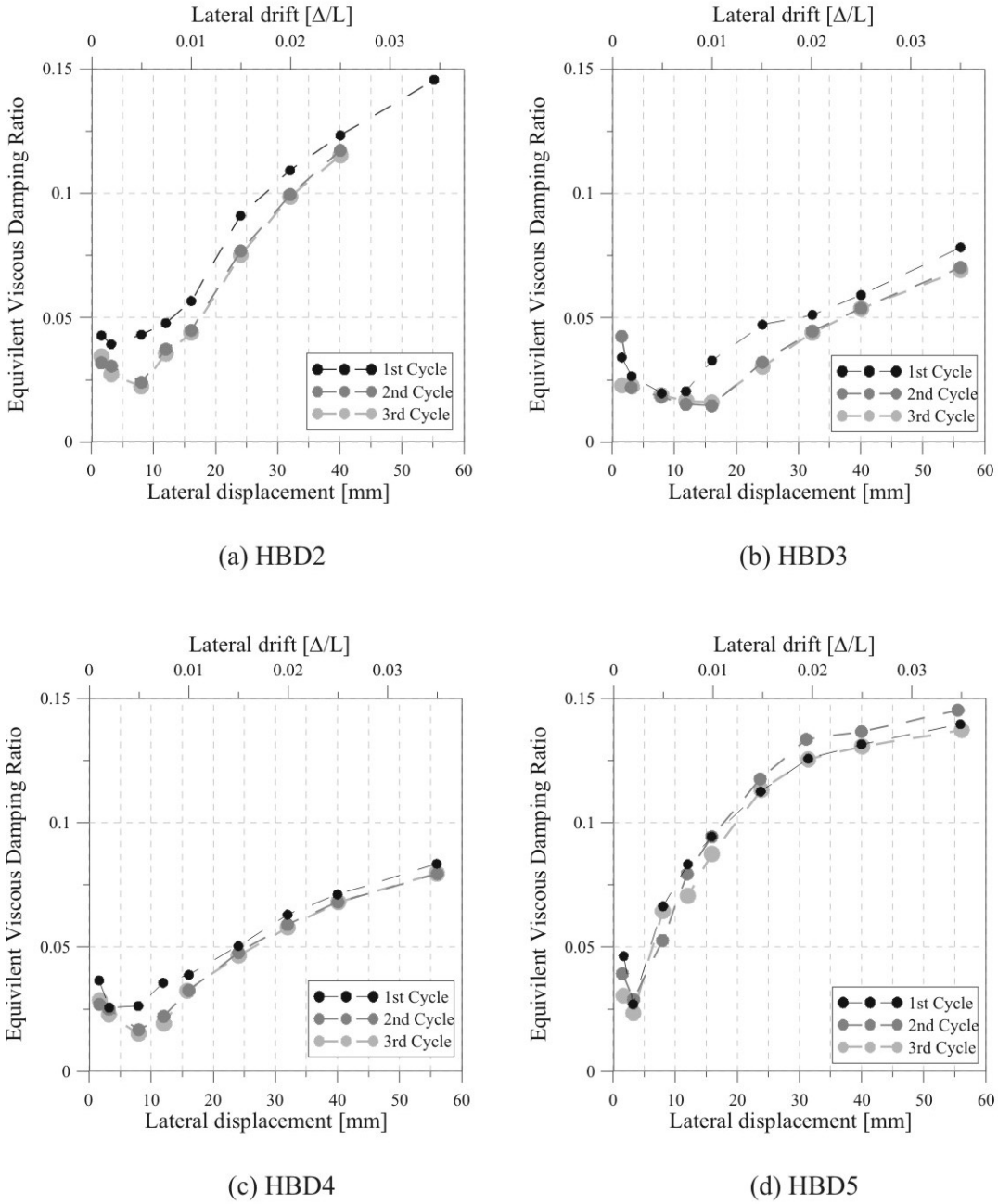

Figure 4.49 Comparison of equivalent viscous damping (EVD) between HBD2-HBD5

4.7.9. Performance Evaluation of the Post-Tensioned Bridge Piers

In order to determine the performance of each bridge pier, considering the expected displacement demand under a specific seismic intensity, the experimental area-based damping relationships plotted in Section 4.7.9 are used within a displacement-based assessment. The full assessment procedure is described in detail in Appendix A. The New Zealand seismic loading standard NZS1170.5 [2004] was used as the seismic hazard in determining the performance objectives of each bridge pier

The performance of MON is shown in Figure 4.50. The solid black lines represent the seismic hazard at increasing levels of intensity, considering a return period of 100 years ($\boldsymbol{R} = 0.5$) to a return period of 2000 years ($\boldsymbol{R} = 1.7$). Each seismic hazard ($\boldsymbol{R}$ value) has been reduced from the 5% elastic hazard according to the level of equivalent viscous damping (EVD) that would be achieved at each displacement objective. The experimental EVD-displacement relationship for each pier presented in Figure 4.48 and Figure 4.49 allows a unique damping value to be determined for any lateral displacement (up to the peak lateral displacement measured during testing). When computing the numerical value of EVD the 2nd cycle was used to conservatively allow for some degradation within the system following the initial smaller cycles of an earthquake ground motion.

Figure 4.50 illustrates that a lateral drift demand of approximately 3.41% can be expected considering a return period of 2000 years ($\boldsymbol{R} = 1.7$). This compares well with the 3.4% design drift stipulated in Section 4.2 and summarised in Appendix A.

The performance objectives are summarised in Table 4.6 considering the entire range of seismic hazard levels (return period of 100 years to 2000 years). It is interesting to note that the lateral drift demand does not increase in proportion to the seismic intensity: generally, the drift demands increase at a greater rate than the seismic intensity.

This displacement-based assessment was also carried out on each of the post-tensioned bridge piers HBD1-HBD5 and PT2. The assessments are of these bridge piers are illustrated in Figure 4.51. This evaluation procedure allows each system to be compared relative to one another. Of all the post-tensioned piers, only HBD2 and HBD5 provide test results to indicate information for a 2000 year earthquake event.

The performance of each bridge system in Figure 4.51 is also summarised in Table 4.6. The lateral drift demand ($\boldsymbol{\Delta / l_{cant}}$) is shown considering all five seismic intensities $\boldsymbol{R}$. Table 4.6 also lists the interpolated area-based damping $\boldsymbol{\xi_{area\text{-}based}}$ from the experimental data in Figure 4.48 and Figure 4.49. The equivalent viscous damping for design $\boldsymbol{\xi_{eq}}$ is also presented in Table 4.6: it is this damping value that is used to reduce the 5% elastic design spectrum. *NA* indicates that the expected lateral drift exceeds the maximum recorded experimental lateral drift considering that particular seismic hazard level.

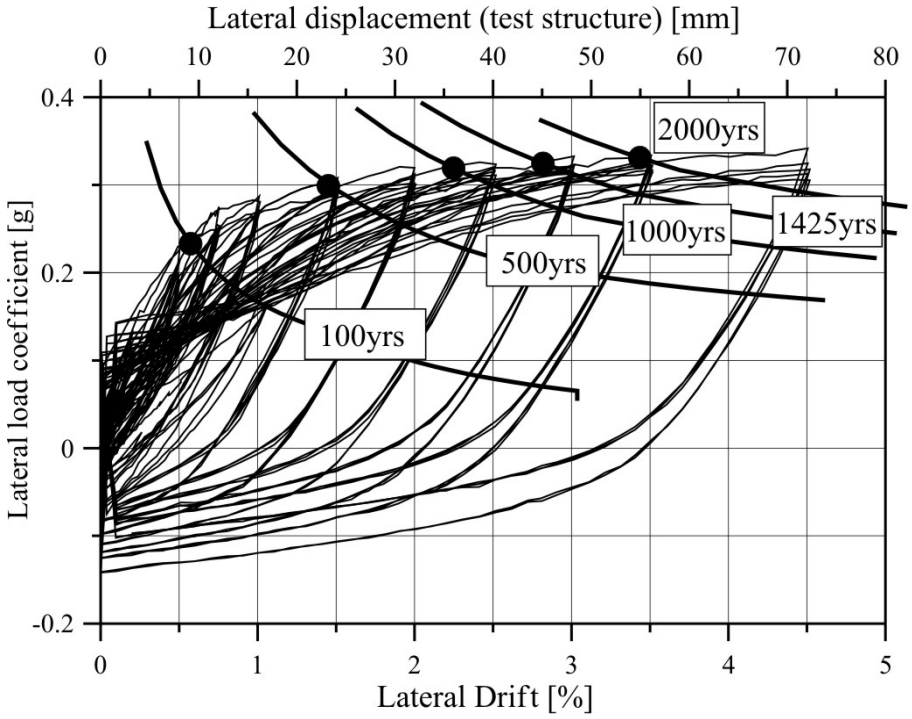

Figure 4.50 Performance evaluation of MON

While HBD1 was under-strength by approximately 18% when compared to MON, the performance between both systems was comparable. Larger displacements are expected for HBD1; however, the damage sustained to HBD1 is minimal in comparison to MON. Given that testing of HBD1 ended at a lateral drift ratio of 3%, the stability indicates that the section could very easily sustain the 1425 year seismic design intensity.

The pinched response of HBD3 returned slightly less area-based damping when compared to HBD4 (Figure 4.47). The internal mild steel bars within HBD3 buckled, whereas HBD4 was characterised by a more stable response due to the buckling-restrained mild steel dampers. The reduction in area-based damping for HBD3 is balanced by the slight increase in lateral strength when compared to HBD4. The net result is that the two systems have comparable performance. This suggests that a post-tensioned system that is expected to experience some pinching and stiffness degradation (due to buckled mild steel dissipaters) will achieve similar performance to a more stable system by providing only a modest increase to the lateral strength.

It is interesting to find that the performance of the post-tensioned specimen, HBD5, surpassed that of the benchmark pier, MON. In particular, while the displacements were similar in magnitude between the two systems (HBD5 actually returned lower displacements for $\boldsymbol{R} > 1.3$), the damage sustained to HBD5 was very minimal when compared to MON: damage of HBD5 comprised of minor flexural cracking and yielding of the sacrificial external TCY dampers, whereas large plastic rotations developed at the base of MON.

Table 4.6 Performance evaluation of each bridge pier

		Seismic Hazard, Return Period (Risk factor, R)				
		100yrs (0.5)	**500yrs (1.0)**	**1000yrs (1.3)**	**1425yrs (1.5)**	**2000yrs (1.7)**
MON	Δ/l_{cant}	0.59%	1.47%	2.22%	2.84%	3.41%
	$\xi_{area\text{-}based}$	3.5%	15.3%	18.9%	21.1%	22.4%
	ξ_{eq}	7.8%	13.5%	16.0%	18.1%	19.9%
HBD1	Δ/l_{cant}	0.59%	1.75%	2.56%	3.00%	
	$\xi_{area\text{-}based}$	8.2%	16.6%	18.5%	18.0%	NA
	ξ_{eq}	10.1%	15.5%	18.8%	19.8%	
HBD2	Δ/l_{cant}	0.69%	1.72%	2.44%	2.94%	3.44%
	$\xi_{area\text{-}based}$	3.4%	8.7%	11.5%	12.7%	13.8%
	ξ_{eq}	7.4%	10.2%	12.6%	14.0%	15.5%
HBD3	Δ/l_{cant}	0.78%	2.38%	3.31%		
	$\xi_{area\text{-}based}$	1.5%	5.1%	6.7%	NA	NA
	ξ_{eq}	6.1%	7.7%	9.3%		
HBD4	Δ/l_{cant}	0.94%	2.38%	3.25%		
	$\xi_{area\text{-}based}$	3.0%	6.6%	7.7%	NA	NA
	ξ_{eq}	6.3%	9.3%	11.1%		
HBD5	Δ/l_{cant}	0.63%	1.63%	2.25%	2.75%	3.19%
	$\xi_{area\text{-}based}$	6.6%	12.3%	13.5%	13.9%	14.3%
	ξ_{eq}	9.1%	13.0%	15.1%	16.6%	18.0%
PT2	Δ/l_{cant}	1.31%				
	$\xi_{area\text{-}based}$	1.0%	NA	NA	NA	NA
	ξ_{eq}	4.3%				

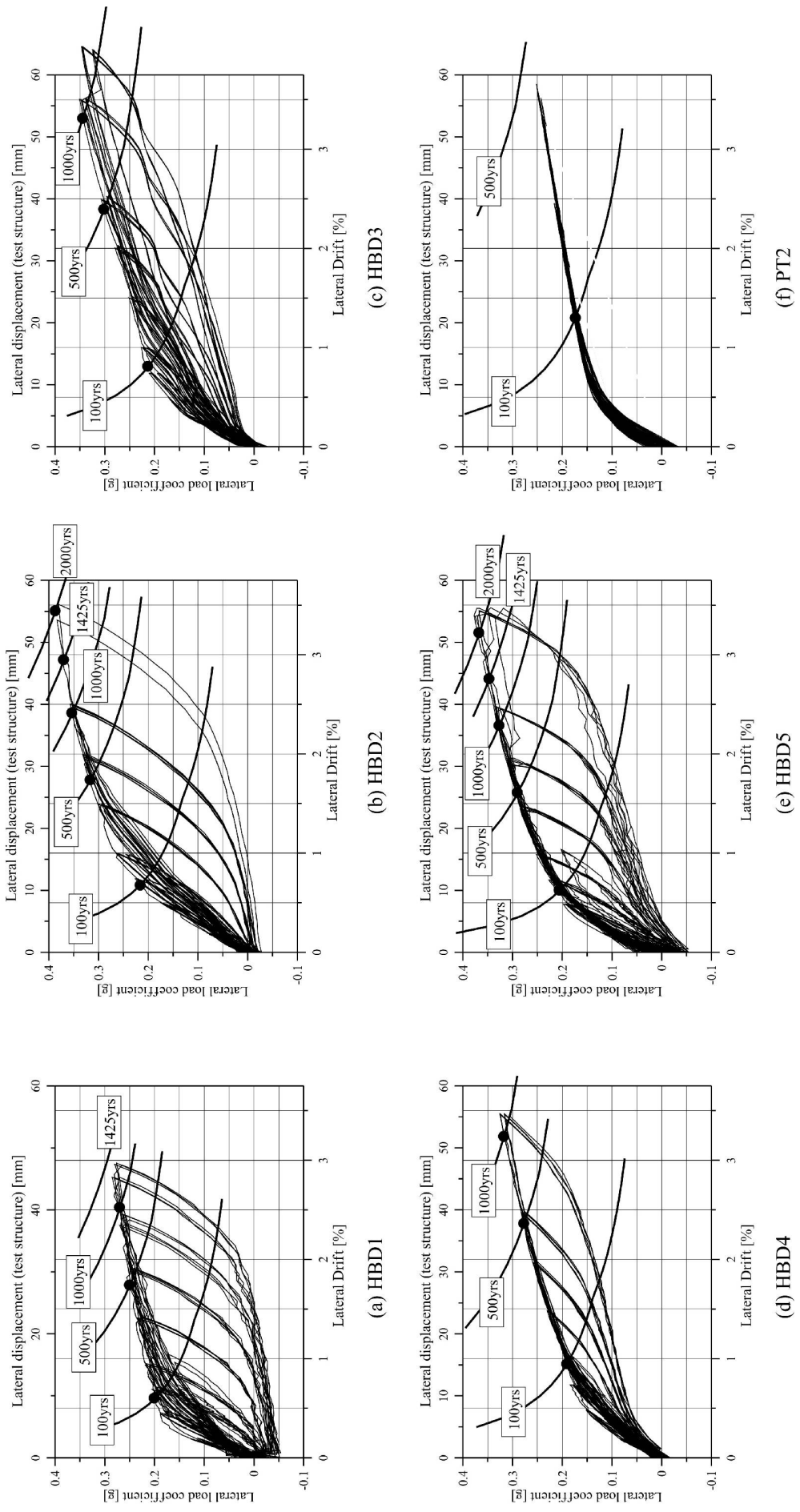

Figure 4.51 Performance evaluation of HBD1-HBD5 and PT2

4.7.10. Bi-Axial Moment Interaction

The biaxial response of MON (Section 4.7.1) and HBD5 (Section 4.7.7) is compared to the uniaxial testing of the same pier specimen in Figure 4.52. For the biaxial response in Figure 4.52 the lateral load represents the principal component of lateral load in one of the two directions: being symmetric, only one principal component is plotted.

In both graphs the design objective, corresponding to a 1000 year seismic hazard, is indicated for the monolithic pier (black dashed line). In Section 4.2 this was shown to correspond to a target strength of 60kN (0.3g) at a lateral displacement of 32mm (lateral drift of 2.0%). The lateral strength under biaxial bending is reduced when compared to an equivalent uniaxial response. This reduction is related to geometric issues in addition to the greater damage sustained to the section under biaxial bending. This may lead to higher than expected displacements under a design level event considering a two component earthquake loading.

The reduction in lateral capacity due to biaxial bending is more significant for the monolithic pier when compared to the post-tensioned pier. This is because the monolithic pier suffers significantly more damage than the post-tensioned pier: greater damage leads to a reduced internal lever arm within the section, reducing the lateral capacity. On average, the reduction in lateral capacity of the monolithic pier due to biaxial bending was approximately 15%. This compares with a reduction of approximately 7% for the post-tensioned pier. The reduction in lateral strength is more significant for the monolithic pier if cyclic stiffness degradation is also considered. Contrary to this, the stiffness degradation of the post-tensioned pier was significantly reduced due to the nature of the external dissipaters. Moreover, the strength and stiffness of a post-tensioned pier can increase under biaxial bending as the tendons (and dissipaters) are subjected to a greater elongation. This increases the moment capacity (and tangent stiffness) of the section.

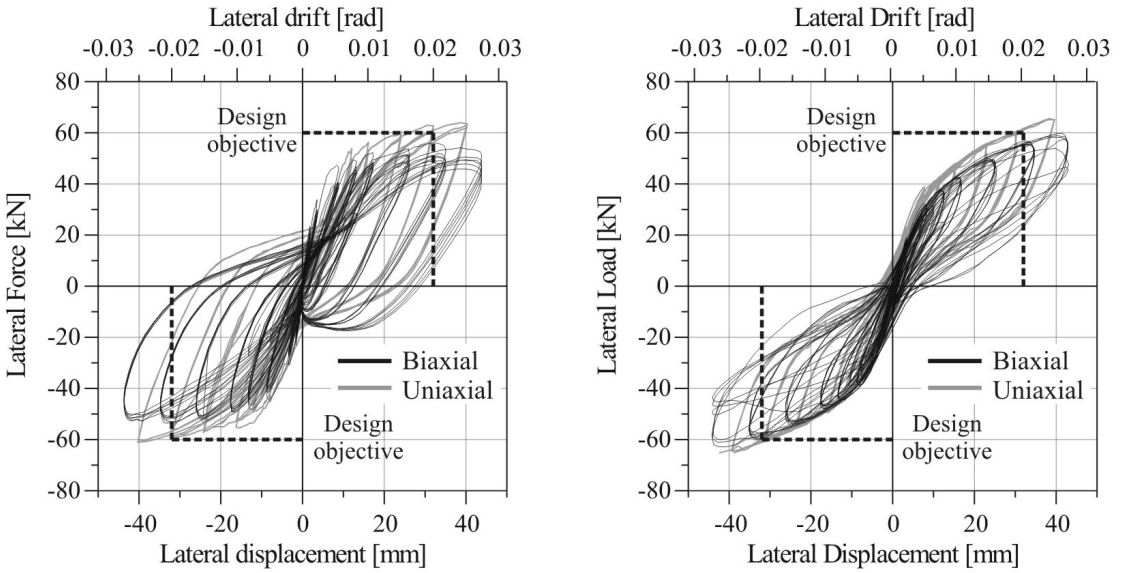

a) Ductile, monolithic pier, MON

b) Post-tensioned, hybrid pier, HBD5

Figure 4.52 Bi-directional quasi-static testing and comparison with uni-directional testing

The uniaxial and biaxial area-based equivalent viscous damping (EVD) for the ductile pier MON and the hybrid pier HBD5 are compared in Figure 4.53. The damping ratio is plotted given the 2nd cycle of uniaxial testing, while the average of the two directions (N-S and E-W) during the 2nd clover cycle is plotted for biaxial testing. For the ductile pier MON only a small increase in damping is observed under biaxial bending when compared to the uniaxial response in Figure 4.53. In contrast, there is very little difference in damping between the unaxial and biaxial response of the post-tensioned pier HBD5. A sudden reduction in damping is observed under biaxial bending when the drift ratio exceeds 2.5% as some of the external TCY dampers begin to rupture. Given the similarity between the 2D and 3D displacement-damping curves in Figure 4.53, existing 2-dimensional damping-ductility relationships within Direct Displacement-Based Design (DDBD) can be confidently used when considering orthogonal earthquake loading.

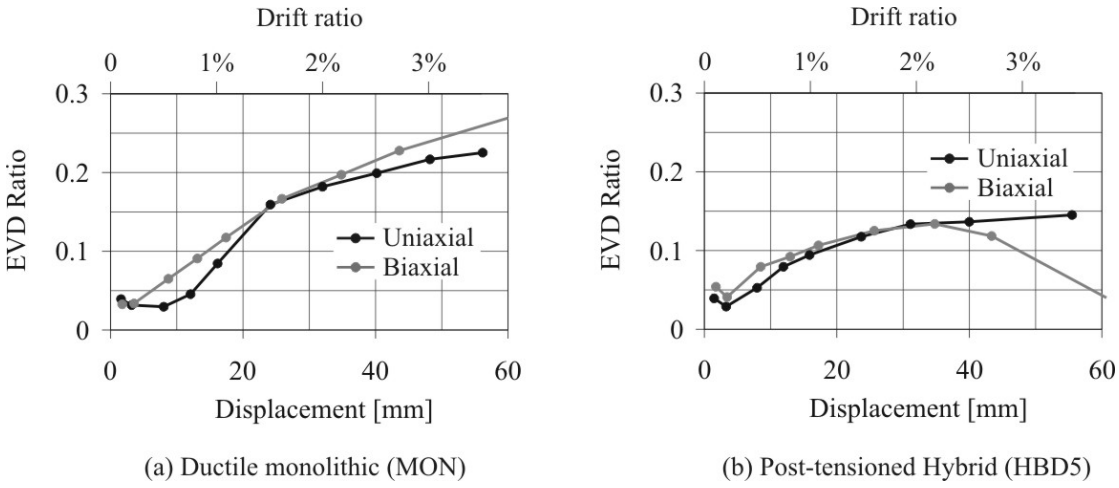

Figure 4.53 Equivalent viscous damping: comparison between uniaxial and biaxial bending. Damping ratio for uniaxial testing presented for 2nd cycle, while the average of the two directions during the 2nd clover cycle is presented for the biaxial tests.

4.8. CONCLUSIONS

The experimental testing of seven post-tensioned rocking, cantilever bridge systems was presented. The testing was conducted under uniaxial and biaxial quasi-static loading to understand the behaviour of rocking systems and to compare their performance against an equivalent monolithic ductile pier. A number of unique damper options were explored including internally grouted, fused mild-steel bars, semi-replaceable internal dampers. However, the most successful option was a post-tensioned bridge pier system with fully-replaceable, external dampers, owing to the ease in which they can be replaced following a major earthquake event; combined with the stability of the dampers under repeated cyclic loading.

In all cases, damage of the post-tensioned piers was limited to flexural cracking up the height of the pier: at the end of testing the cracks were of hairline thickness due to the post-tensioned clamping force. In contrast, the damage sustained to the equivalent ductile pier suffered extensive cracking and spalling. Damage was relatively confined to a few large cracks at the base due to the "cold-joint" located between the pier and foundation during construction. This contrast in damage was more pronounced following biaxial testing. The post-tensioned pier suffered some superficial damage at the rocking toe; however, a majority of the damage was confined to the sacrificial external dampers. While some dampers ruptured prior to the end of the test, a significant proportion of lateral resistance could be relied upon by the post-tensioned tendons and the remaining dampers. This is in contrast to the equivalent ductile pier whose damage was very extensive, comprising of ruptured and buckled longitudinal reinforcing bars and spalling of the cover concrete. The structural integrity was greatly compromised and following a major earthquake event, could be very difficult and costly to reinstate. The results of the biaxial testing also concluded that the damping-displacement relationship between uniaxial and biaxial bending is similar, if not conservative considering both a post-tensioned and conventional bridge pier system.

A novel method was presented to assess the relative performance of each of the post-tensioned bridge piers. The assessment uses the area-based energy dissipation computed from experimental testing, combined with an iterative displacement-based assessment technique. The experimental response was presented in an acceleration-displacement-response-spectrum (ADRS) allowing the lateral capacity to be compared directly with the seismic demand. It was shown that a post-tensioned bridge pier can achieve similar, if not, better performance than an equivalent ductile pier owing to the reduced damage associated with each performance level. It was also concluded that the larger displacement capacity of a post-tensioned bridge pier can allow larger displacements to be targeted during design: this may result in a reduction to the design strength.

4.9. REFERENCES

ACI. (2001). "Acceptance Criteria for Moment Frames Based on Structural Testing (T1.1-01) and Commentary (T1.1R-01)." A. I. T. G. 1, ed., Farmington Hills, Michigan.

NZS1170.5. (2004). "Structural Design Actions, *Part 5: Earthquake actions*." Standards New Zealand, Wellington.

NZS3101:2006. (2006). "Concrete Structures Standard: Part 1-The Design of Concrete Structures." Standards New Zealand, Wellington.

Priestley, M. J. N., Calvi, G. M. and Kowalsky, M. J. (2007). *Displacement-Based Seismic Design of Structures*, IUSS, Pavia.

5. High-Speed Cyclic Testing of Post-Tensioned Precast Walls with Viscous and Hysteretic Dissipation

5.1. INTRODUCTION

This chapter presents the experimental testing of five post-tensioned walls tested under high-speed cyclic push-pull displacement control. The aim of this particular study was to investigate the effects of velocity dependant dampers and to further understand the behaviour of precast rocking systems.

5.2. DESIGN OF THE PROTOTYPE SPECIMEN

In this experimental phase a post-tensioned wall was designed and tested which represented a retrofit solution for an existing frame building. A prototype frame structure was developed with the intention to be retrofitted with an external post-tensioned wall following a proposed Direct Displacement-Based Retrofit procedure (DDB-Retrofit). The design procedure defines the required strength of the post-tensioned wall in order to limit the deformation of the building to acceptable limit states. The deformation limit states include joint shear deformations and member curvatures within critical beam and column elements. While the DDBD-retrofit procedure is not presented in detail in this thesis, details of the design philosophy can be found in Appendix B, Marriott et al. [2007]. Details of the prototype frame structure are illustrated in Figure 5.1 (a) while the retrofit intervention is presented in Figure 5.1 (b).

5.3. DETAILS OF THE POST-TENSIONED WALL, TEST SPECIMENS

The 1/3 scale post-tensioned wall specimens were constructed from laminated vaneer lumber (LVL). LVL is an engineered wood composite made from 3mm thick veneers peeled from a timber log. The veneers are glued together such that the grain is orientated parallel to the member length. The compressive strength of LVL (parallel to the grain) is comparable to concrete; however, the stiffness is about 1/3 of concrete.

LVL was chosen to explore alternative materials for post-tensioned seismic-resisting systems, but to also speed up the construction time. The response of the wall was expected to be almost material independent: that is, whether the wall was constructed from concrete or LVL simply dictated the constitutive relationship of the material at

the rocking interface. A single LVL wall was constructed from 2-600x63 and 4-90x45 hySPAN beams supplied by Carter Holt Harvey (Figure 5.2).

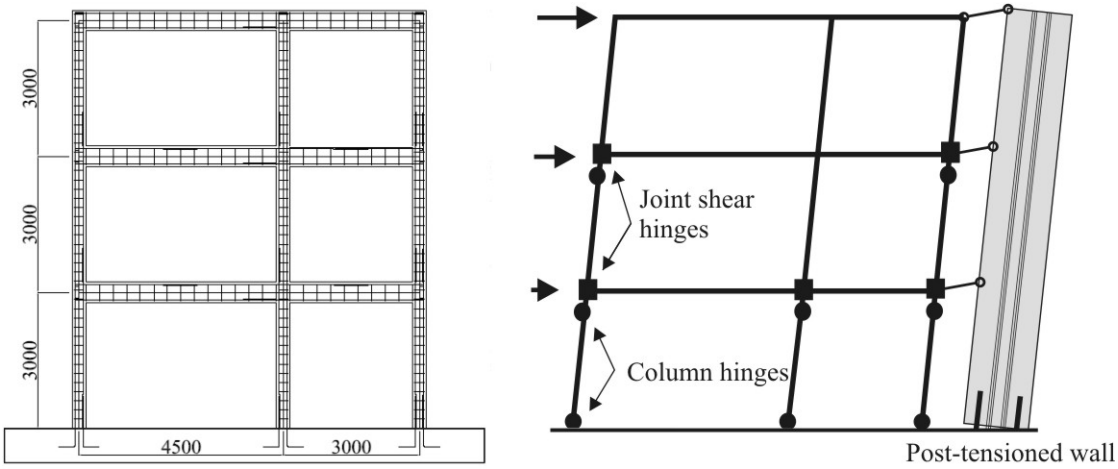

(a) Existing prototype frame building (a) Idealised retrofit behaviour

Figure 5.1 Prototype frame structure and retrofit intervention

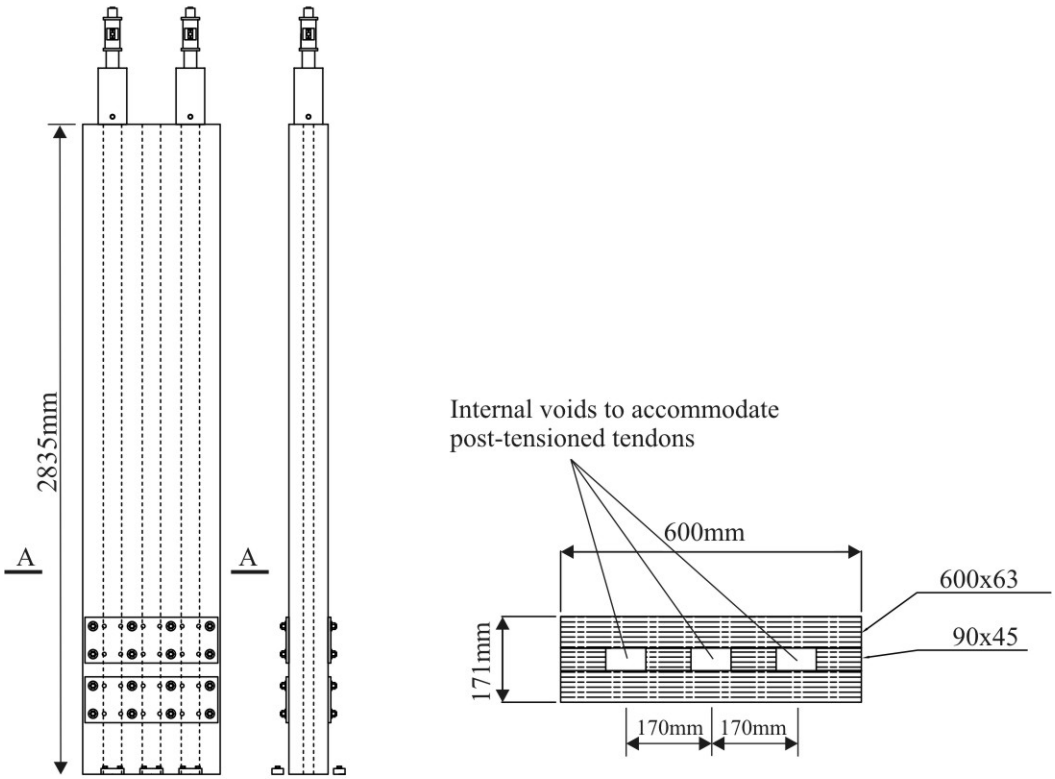

(a) Front and end elevation (b) Wall section A-A

Figure 5.2 Geometry of the post-tensioned wall

Two steel plates were attached to both sides of the LVL wall. This provided six locations to attach the external dampers to. A total of five wall specimens were tested with a slight variation to the type and amount of external dampers and post-tensioning. A summary of the post-tensioning and damper details of each wall is listed in Table 5.1 while further details can be found in Figure 5.4.

Table 5.1 Post-tensioned steel and damper details for each wall

Specimen	Initial Post-Tensioning	Dissipation
Wall 1	Two tendons stressed to 50kN each ($0.321f_{py}$)	None
Wall 2	Two tendons stressed to 30kN each ($0.192f_{py}$)	4 fluid viscous dampers
Wall 3	Two tendons stressed to 20kN each ($0.128f_{py}$)	4 fluid viscous dampers and 2-7mm diameter TCY dampers
Wall 4	Two tendons stressed to 30kN each ($0.192f_{py}$)	4-7mm diameter TCY dampers
Wall 5	Two tendons stressed to 40kN each ($0.256f_{py}$)	2-7mm diameter TCY dampers

5.3.1. Damper Details

The performance of two external dampers was investigated: a mild steel tension-compression-yielding (TCY) damper and a fluid viscous damper (FVD). The TCY damper was fabricated at the University of Canterbury's Civil Engineering Laboratory (fabrication details and cyclic behaviour were discussed in Chapter 4). The FVD was supplied courtesy of *FIP Industriale*[1].

(a) Mild Steel Dampers (TCY)

The TCY dampers used within the testing of the post-tensioned walls discussed herein were identical to that used in the post-tensioned bridge pier tests discussed in Chapter 4. The only difference being the diameter and length of the yielding region within the dissipater: Figure 5.3 (a) & (b). Two TCY dampers were used within the post-tensioned walls tested herein: both have the same fuse diameter, but differ in the length of the fuse region.

(b) Fluid Viscous Dampers (FVD)

Four FVDs were supplied by *FIP Industriale*: the geometry of the FVDs is illustrated in Figure 5.3 (c). The dampers were fabricated from a high-grade stainless steel alloy in Italy. Spherical bearings were located at each end of the damper to ensure only axial load could be transmitted to the dampers. The dampers have a maximum stroke of ±60mm and a maximum rated velocity of 400mm/s.

[1] FIP *Industriale* contact person, Dr Cabriella Castellano

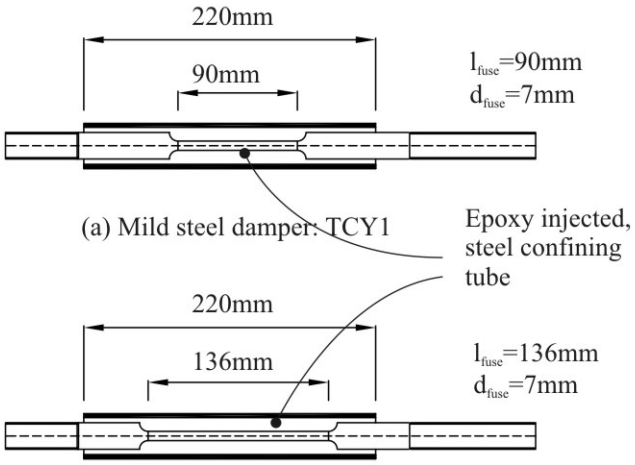

(a) Mild steel damper: TCY1

(b) Mild steel damper: TCY2

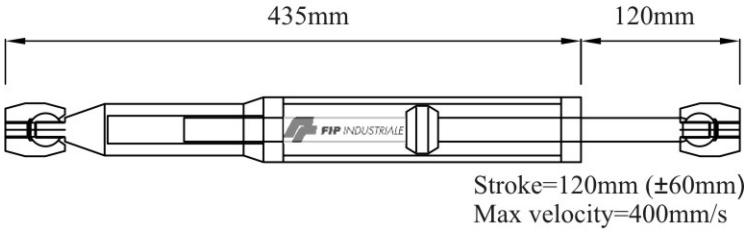

(c) *fip industriale* fluid viscous damper: FVD

Figure 5.3 Details of the external damper elements

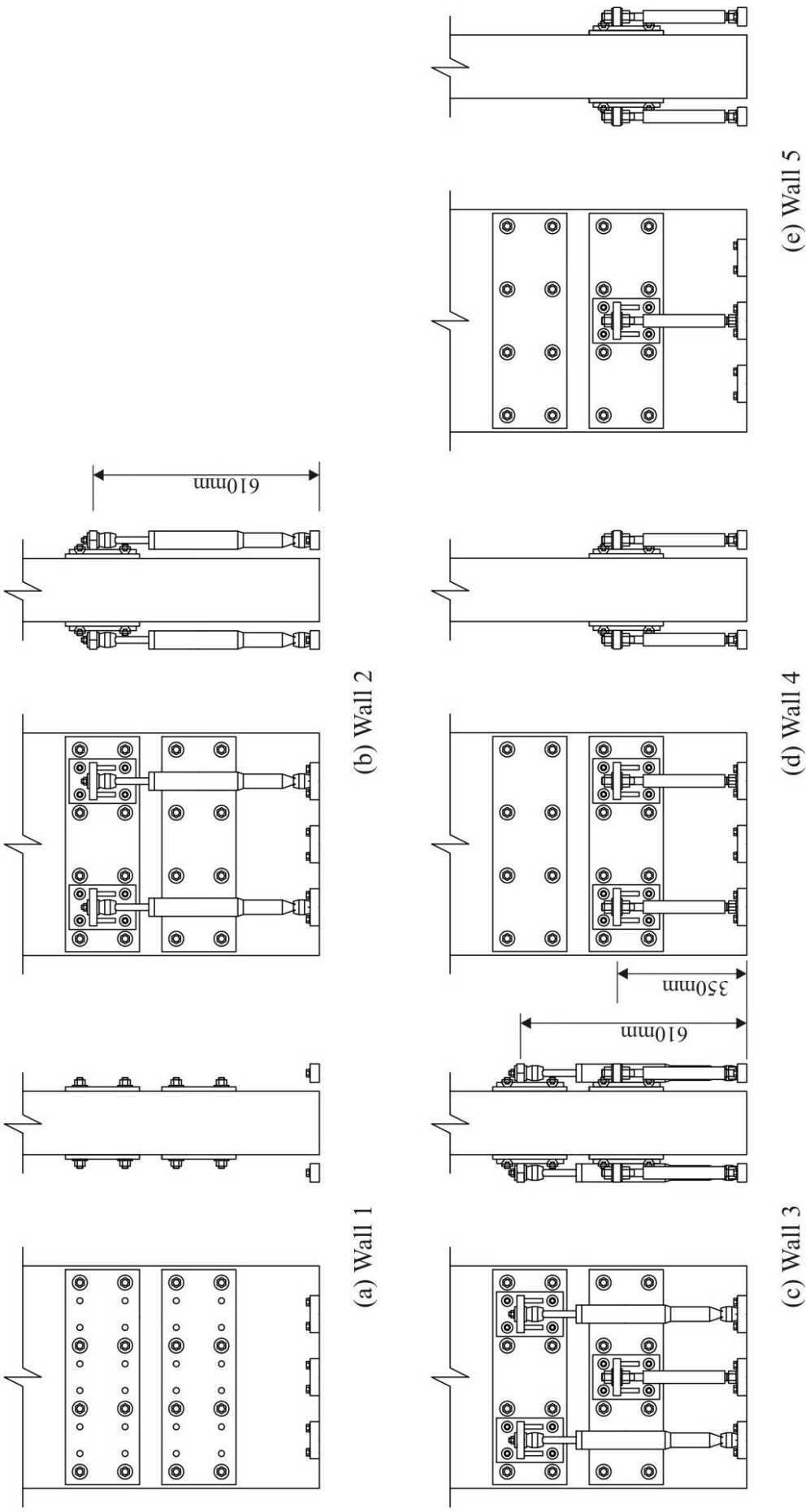

Figure 5.4 Details of the post-tensioned wall units

5.4. CONSTRUCTION OF THE POST-TENSIONED WALL

The LVL timber wall was constructed by Carter Holt Harvey and came assembled to the university without the steel plates as pictured in Figure 5.2. The LVL wall was formed from individual hySPAN units and joined using an industrial epoxy adhesive. Additional nails were driven around the wall (in addition to the epoxy) to ensure a good connection existed between each of the hySPAN sections. After fabrication the ends of the LVL wall were cut square to guarantee a flat rocking surface.

The damper connections were specifically designed to prevent any slipping between the connection and the damper. The intent was to confine all of the rocking uplift to displacement of the external dampers: this improves the efficiency and stability of the system.

Two 12mm steel plates were attached to each side of the LVL wall in Figure 5.5. These steel plates were used to attach the external dampers to the wall. Prior to fixing the plates to the wall, both the steel and LVL surfaces were roughened with horizontal saw cuts at 20mm intervals to a depth of approx 5mm (Figure 5.5 (a)). A film of heavy duty epoxy (Hilti Hit RE500) was applied to the steel plate and the LVL surface in Figure 5.5 (b). When the 12mm plates were located in position, 8-M20 high-tensile (880MPa yield strength) threaded rods were tightened in position either side of the wall to permanently hold the steel plate in position (Figure 5.5 (c)). This procedure was repeated for the second set of steel plates.

Each external damper was attached to the wall via a (near-rigid) fabricated steel bracket pictured in Figure 5.6 (b). The fabricated brackets were bolted to the steel plates that were fixed on each side of the LVL wall using counter-sunk bolts that were tightened to a specified torque of 205Nm. The foundation-end of the external dampers were attached to a heavy steel block that was securely bolted to the foundation, Figure 5.6 (c).

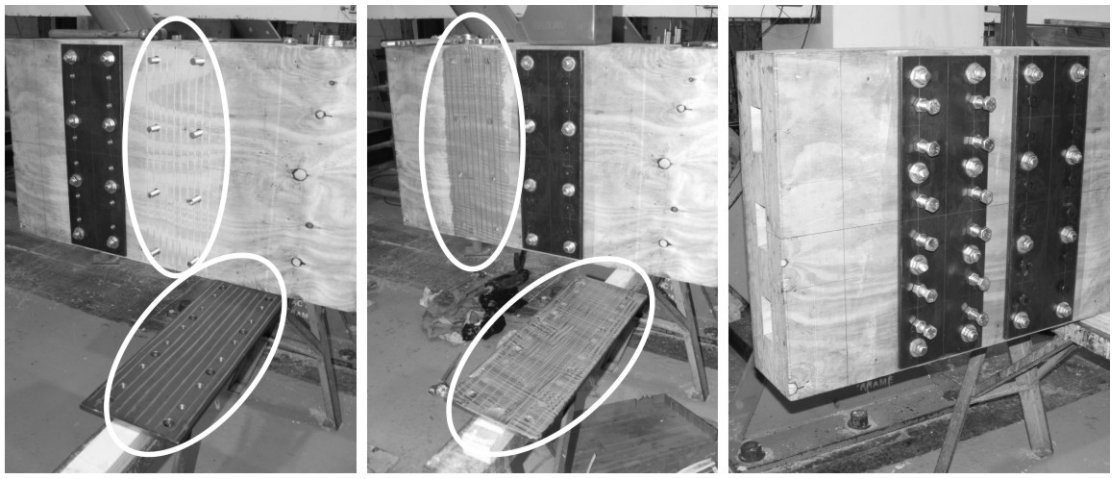

(a) Preparation of the two surfaces, both surfaces roughened

(b) Application of the epoxy to both surfaces

(c) Steel plates located in place and threaded rods tightened

Figure 5.5 Assembly process of the steel plates located on each side of the LVL wall

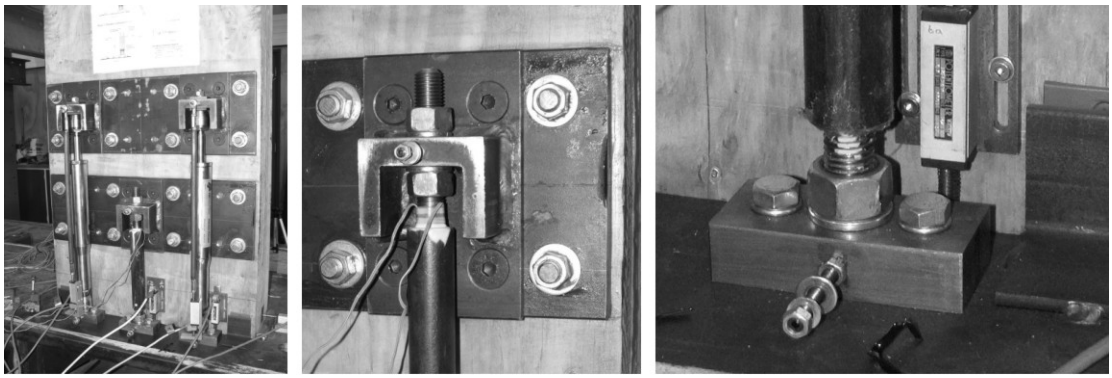

(a) Completed connection: Wall 3 shown including instrumentation

(b) Wall mount detail

(c) Foundation mount detail

Figure 5.6 External damper connection detail

5.5. EXPERIMENTAL HIGH-SPEED SET-UP AND INSTRUMENTATION

5.5.1. Laboratory Test Set-Up

As a high-speed actuator was not currently available at the University of Canterbury, the high-speed cyclic testing was performed on the shake-table. The experimental test set-up is illustrated in Figure 5.7. The top of the wall was fixed to a steel reaction frame at a height of 2100mm above the foundation. A load cell was located between the steel brace and the LVL wall. Lateral displacements were imposed to the wall by horizontal translation of the shake-table.

Out-of-plane movement of the wall was prevented by a steel channel located either side of the wall (only one is shown in Figure 5.7 for clarity). A near frictionless sliding surface was provided between the LVL wall and the steel channels with the use of lubricated Formica Board.

The steel brace/load-cell that linked the wall to the reaction frame was fixed at each end with specially fabricated expanding steel pins. The expanding pins were necessary to avoid hammering at high-speed due to clearances within the pins.

The LVL wall was located on top of a heavy steel foundation: this in turn was bolted to the shake-table. The steel foundation was fabricated from 40mm steel plate spanning between 200x100x9 RHS at 762mm centres (refer Figure 5.7). 20mm stiffeners were welded between the RHS and the 40mm steel plate to further prevent bending of the steel foundation during testing.

5.5.2. Instrumentation

The position of the major instrumentation is shown in Figure 5.7. A complete list of instrumentation is listed in Appendix B.

(a) Shake-table instrumentation

The displacement of the shake table was measured via a Linear Variable Displacement Transducer (LVDT) while table acceleration was measured by an accelerometer attached directly to the table.

(b) Foundation instrumentation

Potentiometers were installed adjacent the foundation to measure sliding of the foundation relative to the table. Potentiometers were also located on the underside of the foundation to measure the rotational flexibility of the foundation.

(c) Precast wall instrumentation

Three linear potentiometers were installed on both sides of the wall at the base of the wall to allow the base rotation and the neutral axis to be determined. Sliding of the wall relative to the foundation was also monitored. Potentiometers were located at each damper to measure damper elongation during uplift of the base. Furthermore, each TCY steel damper was fitted with two strain gauges.

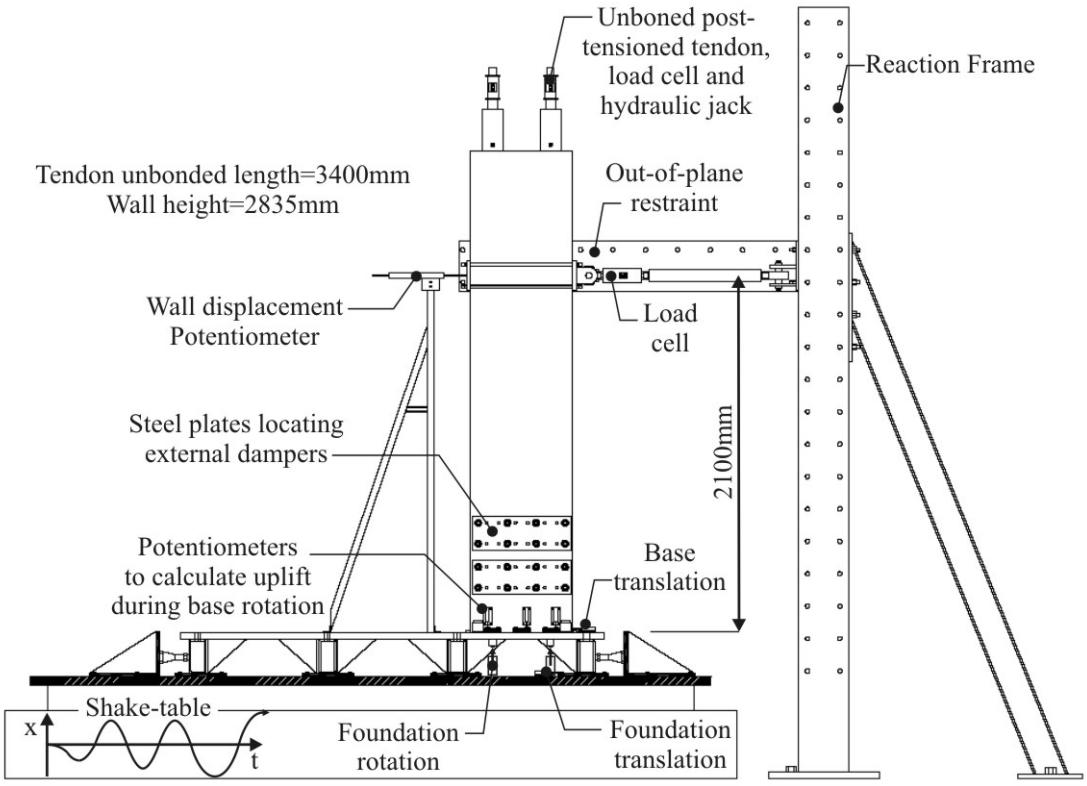

Figure 5.7 High-speed experimental test set-up and instrumentation

5.6. HIGH-SPEED CONTROL USING THE SHAKE-TABLE

5.6.1. Description of the Shake-Table

The shake-table at the University of Canterbury is a uniaxial earthquake ground motion simulator. The table has a plan area of 2m wide by 4.5m in length. The table top is constructed from 12mm steel plate connected on top of 4-410UB54 steel sections running the length of the table. In the transverse direction 12mm steel plate stiffeners are welded between all four 410UB sections at intervals of 500mm. Connected to the web of the exterior 410UB sections are 4-100DU115 steel housings which accommodate a series of Teflon bearings. The Teflon bearings slide along a 100mm diameter Bright steel shaft; each shaft sits on top of a 250UB37 steel beam bolted to the laboratory strong floor. Further details and construction drawings can be found in Ghee [1985]. The shake-table has an unloaded mass of 2500kg.

A 300Hp motor operating at 4000psi powers a 280kN double acting hydraulic actuator which drives the shake-table. A set of Moog E072-054 servovalves control the hydraulic actuator and are capable of supplying 232 lpm, Chase et al. [2005].

The servovalves are controlled by a TestStar control system from MTS Systems Corporation. The MTS control is a closed servo loop using proportional, integral and derivative feed-forward adjustment. By altering the amount of proportional and/or integral gain, the tracking of the table can be manipulated. A table command is given to the system as a displacement time history, doubly integrated from the desired acceleration time-history.

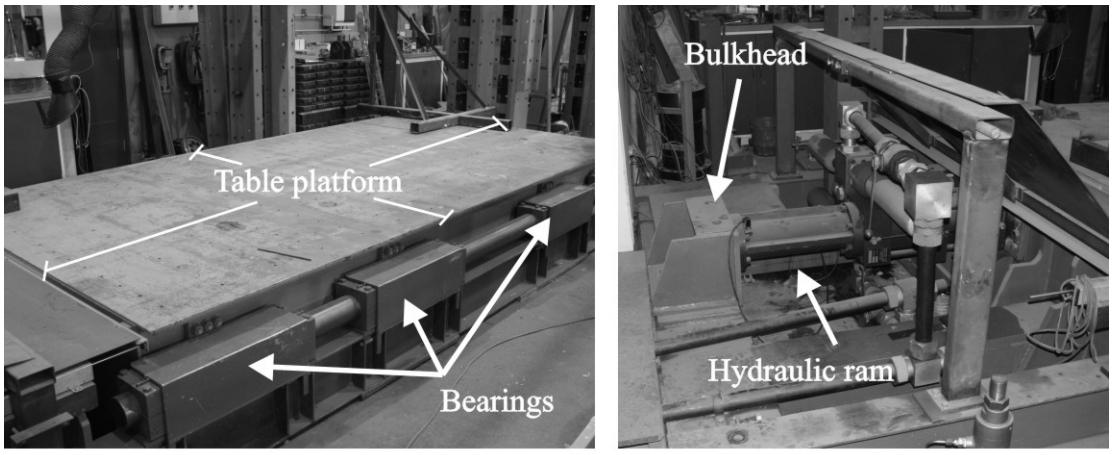

(a) Shake-table platform (b) Shake-table hydraulic ram and bulkhead

Figure 5.8 University of Canterbury Shake-Table

5.6.2. Shake-Table Capacity

The shake-table has a payload capacity of 20 tonnes and displacement amplitude of 130mm (total stroke of 260mm). The capacity of the servovalves limits the velocity of the table to approximately 242mm/s. This is defined as the saturation velocity of the table, and in all cases, should be avoided. As the table reaches saturation, the velocity gradient suddenly reaches zero, resulting in large table accelerations. These acceleration spikes can be very significant and, in many cases, can be much greater than that expected from the desired acceleration command.

5.6.3. Acquisition System

Shake-table data acquisition was collected via a high speed logger and computer arrangement. A total of 64 channels could be logged at any one time. The logger unit had an in-built analogue filter buried within the software. This analogue filter had a passband of 200Hz, that is, at 200Hz the normalised passband voltage was equal to 0.707 (refer Figure 5.9).

Data could be sampled from as low as 1Hz to upwards of 1000Hz. While, the full effect of sampling at 1000Hz would not be felt due to the analogue filter, it was used in order to have a sufficient sample size for filter options during post-processing. The displacement command supplied to the MTS control unit was in time steps of $\Delta t = 0.005$ to maximise the resolution: this was the smallest time step that could be recognised by the control unit.

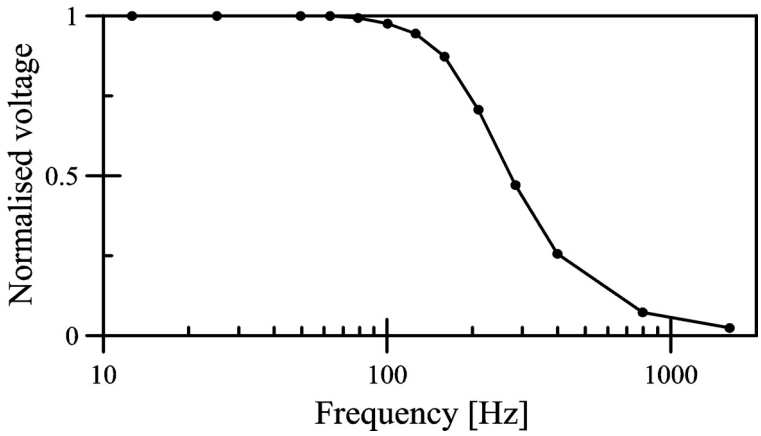

Figure 5.9

5.6.4. Displacement Protocol and Control Algorithm

A sinusoidal displacement command of varying amplitude and frequency was imposed to the shake-table. While generating the command signals, consideration was given to the limitations of the shake-table. In particular, the velocity limit of 242mm/s (a safe velocity limit of around 235mm/s was targeted) and the maximum

displacement stroke of ±130mm could not be exceeded. The sinusoidal displacement ***x(t)***, velocity ***v(t)*** and acceleration ***a(t)*** time-history is expressed in Eq.(5.1), (5.2) & (5.3) respectively.

$$x(t) = A \cdot \sin(\omega \cdot t) \quad \textbf{5.1}$$

$$v(t) = A \cdot \omega \cdot \cos(\omega \cdot t) \quad \textbf{5.2}$$

$$a(t) = -A \cdot \omega^2 \cdot \sin(\omega \cdot t) \quad \textbf{5.3}$$

Where,

A = maximum displacement amplitude within the cycle
ω = angular frequency of excitation, where $\omega = 2\pi f$ in units of rad/s
f = excitation frequency in units of Hz.

Four frequency ranges were investigated: ***f*** = 0.1Hz, 0.5Hz, 1.0Hz and 2.0Hz. Quasi-static cyclic testing was essentially defined as testing at 0.1Hz. This frequency range was felt to be appropriate considering the frequency content within recorded strong ground motions (and also considering the physical limitation dictated by the shake-table). By defining the target excitation frequency ***f***, the maximum displacement amplitude ***A*** was limited by the velocity saturation limit of 235mm/s. The maximum excitation velocity is given by Eq.(5.4): by setting ***v*** = 235mm/s the maximum displacement amplitude ***A*** at each level of excitation frequency ***f*** could be determined.

$$v_{table} = A \cdot 2\pi \cdot f \quad \textbf{5.4}$$

For each frequency, a sinusoidal displacement protocol was created comprising of two cycles at each drift level. A summary of the displacement amplitudes and the corresponding peak velocity during each cycle is listed in Table 5.2. In all cases velocity saturation of the table was avoided by limiting the displacement amplitude ***A*** to Eq.(5.4).

Table 5.2 Displacement command steps and corresponding maximum table velocity

0.1Hz			**0.5Hz**			**1.0Hz**			**2.0Hz**		
Drift	Displ [mm]	Vel [mm/s]	Drift	Displ [mm]	Vel [mm/s]	Drift	Displ [mm]	Vel [mm/s]	Drift	Displ [mm]	Vel [mm/s]
0.20%	4.2	2.6	0.20%	4.2	13.2	0.20%	4.2	26.4	0.20%	4.2	52.8
0.50%	10.5	6.6	0.50%	10.5	33.0	0.50%	10.5	66.0	0.50%	10.5	131.9
0.75%	15.8	9.9	0.75%	15.8	49.5	0.75%	15.8	99.0	0.75%	15.8	197.9
1.00%	21.0	13.2	1.00%	21.0	66.0	1.00%	21.0	131.9	0.90%	18.9	237.5
1.50%	31.5	19.8	1.50%	31.5	99.0	1.50%	31.5	197.9			
2.00%	42.0	26.4	2.00%	42.0	131.9	1.75%	36.8	230.9			
2.50%	52.5	33.0	2.50%	52.5	164.9						
3.50%	73.5	46.2	3.50%	73.5	230.9						

The shake-table input command comprised of two steady-state displacement cycles for each drift amplitude in Figure 5.10. Each steady-state set was preceded and followed by a single transition cycle. The transition cycle was required to prevent acceleration spikes entering the command due to the sudden change in displacement gradient. The transition cycle is described by Eq.(5.5).

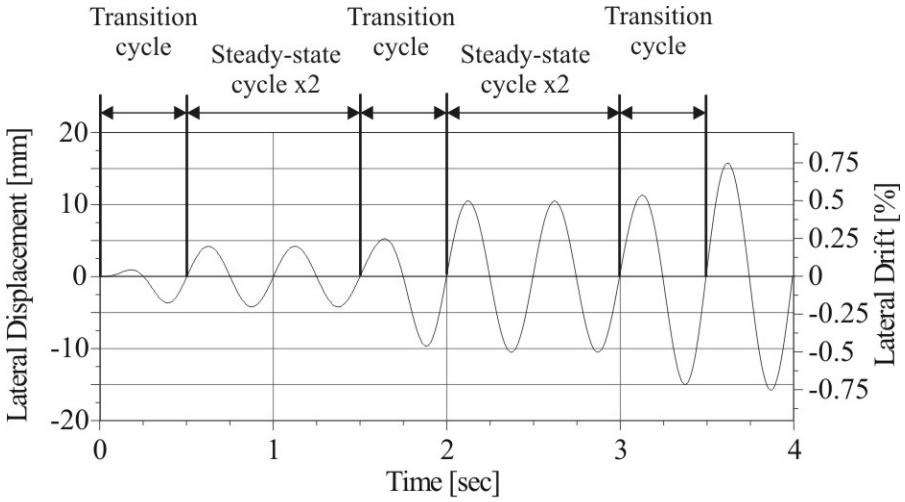

Figure 5.10 Displacement command signal: steady-state and transition cycles

$$x(t) = \left(A_1 + \left[A_2 - A_1\right] \cdot t \cdot f\right) \cdot \sin\left(\omega \cdot t\right) \qquad \textbf{5.5}$$

Where

A_1 = maximum displacement amplitude of the i^{th} steady state cycle
A_2 = maximum displacement amplitude of the $i^{th}+1$ steady state cycle
f = excitation frequency
t = time, starting from zero at the end of the i^{th} cycle and equal to $1/f$ at the beginning of the $i^{th}+1$ cycle

The transition cycle essentially created a linear ramp between successive steady-state cycles. A transition cycle was also required at the beginning of the record ($A_1 = 0$) and at the end of the record ($A_2 = 0$). Each displacement command signal is plotted in Figure 5.11 at excitation frequencies of 0.1Hz, 0.5Hz, 1.0Hz and 2.0Hz.

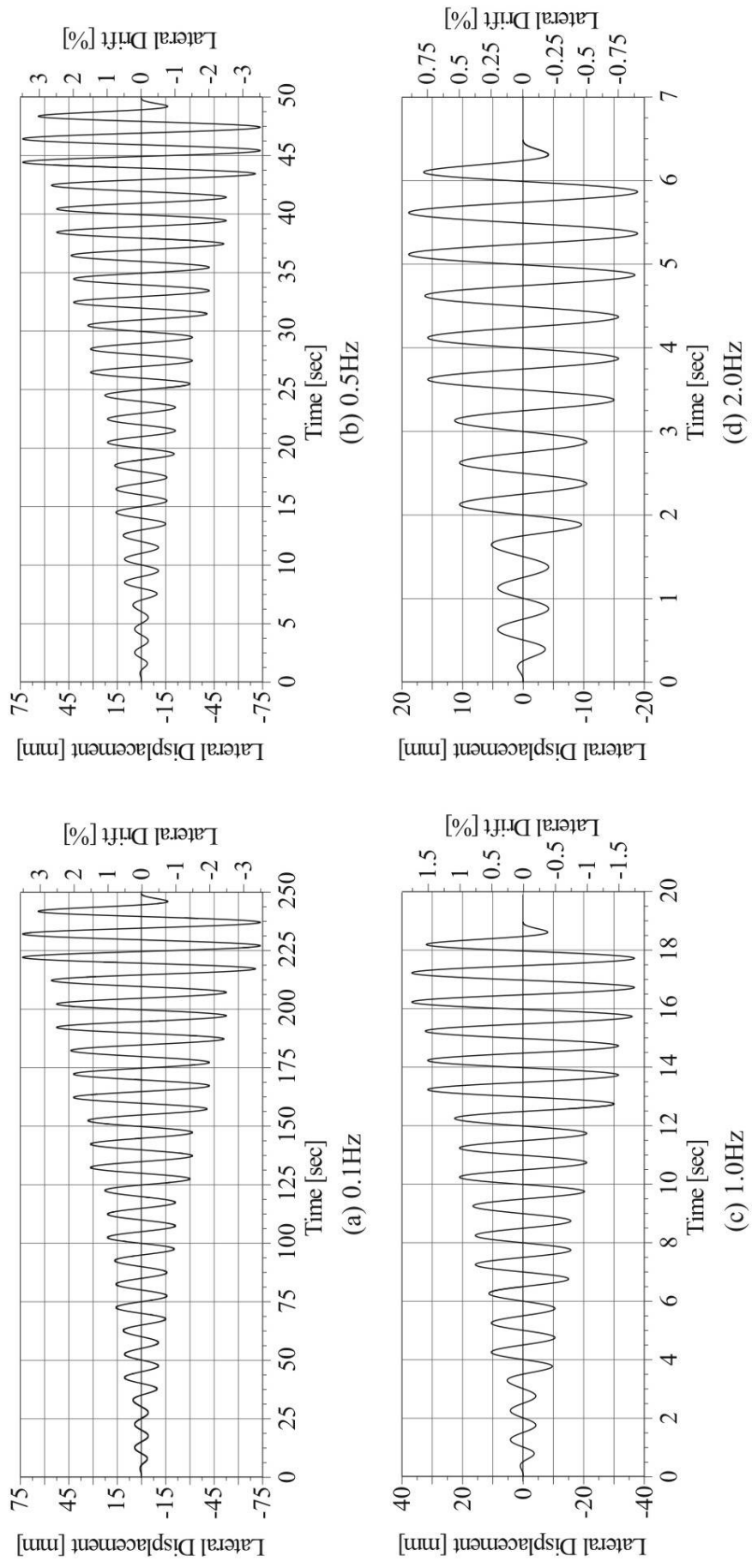

Figure 5.11 Shake-table displacement command for high-speed cyclic testing at excitation frequencies of 0.1, 0.5, 1.0 & 2.0Hz

5.7. MATERIAL PROPERTIES

5.7.1. Mild Steel Reinforcement

The only mild steel used in the high-speed cyclic testing was the material used in the fabrication the TCY dampers. Monotonic and cyclic testing was carried out on the TCY dampers and is discussed in a later section.

(a) Monotonic Testing of the Mild Steel Reinforcement

A total of six material specimens were tested from the batch of mild steel bar used. The average monotonic material properties are listed in Table 5.3.

Table 5.3 Average mild steel material properties following monotonic tension testing

	E	f_y	f_u	ε_y	ε_{sh}	ε_u
TCY	205150MPa	322MPa	457MPa	0.0016	0.0264	0.20

(b) Cyclic Testing

Two 7mm TCY dampers were fabricated with two different fuse lengths: 90mm and 136mm to replicate the dampers that were installed within the post-tensioned wall. Cyclic testing of six TCY dampers was carried out: average damper properties are listed in Table 5.4. The strain-hardening displacement was not recorded as it was difficult to ascertain and has little relevance to the cyclic behaviour of steel. Details of the TCY damper test set-up and instrumentation were discussed in Chapter 4.

Table 5.4 Average TCY damper properties following cyclic testing

TCY	$k_{elastic}$	F_y	F_u	Δ_y	Δ_{sh}	Δ_u
90mm	79.86×10^3kN/m	13.06kN	18.61kN	0.164mm	-	9.3mm
136mm	57.31×10^3kN/m	12.94kN	18.65kN	0.226mm	-	13.6mm

The cyclic damper properties in Table 5.4 were converted to equivalent stress-strain properties in Table 5.5. The dimensions of the dissipaters were accurately measured prior to testing to allow the conversion of force-displacement to stress-strain. These properties can be compared to the monotonic properties in Table 5.3: it is worth noting the large reduction in available strain ductility considering cyclic testing.

Table 5.5 Equivalent stress-strain properties for the TCY dampers following cyclic testing

TCY	E	f_y	f_u	ε_y	ε_{sh}	ε_u
90mm	186800MPa	339MPa	484MPa	0.00183	-	0.1033
136mm	202500MPa	336MPa	485MPa	0.00167	-	0.1000

5.7.2. Prestressed Reinforcement (Post-Tensioned Reinforcement)

The prestressed reinforcement that was used to post-tension each of the walls was 0.5 inch 7-wire strands (A_{pt} = 100mm^2). While monotonic testing of the prestressing steel was carried out, the strands were not tested to rupture. However, the prestressing steel was tested to rupture by the steel supplier: the yield and ultimate material properties are recorded below in Table 5.6.

Table 5.6 Stress-strain properties of the prestressed reinforcement

	E	f_y	f_u	ε_y	ε_{sh}	ε_u
7-wire strand	197100MPa	1560MPa	1850MPa	0.00792	NA*	NA*

*NA = Not applicable

5.7.3. Laminated Veneer Lumber (LVL)

LVL material testing was carried out after the high-speed cyclic testing of the post-tensioned wall. LVL material test specimens were cut from the as-tested wall, refer Figure 5.12. Three test specimens were extracted from the wall (Figure 5.12) for monotonic compression testing to failure. A further three specimens were cut from the left over material to carry out cyclic testing within the elastic range of the LVL (loads less than the maximum compressive load of the material). Each material test specimen was machined on all six sides to ensure a perfectly flat testing surface and to allow the dimensions of each specimen to be accurately determined.

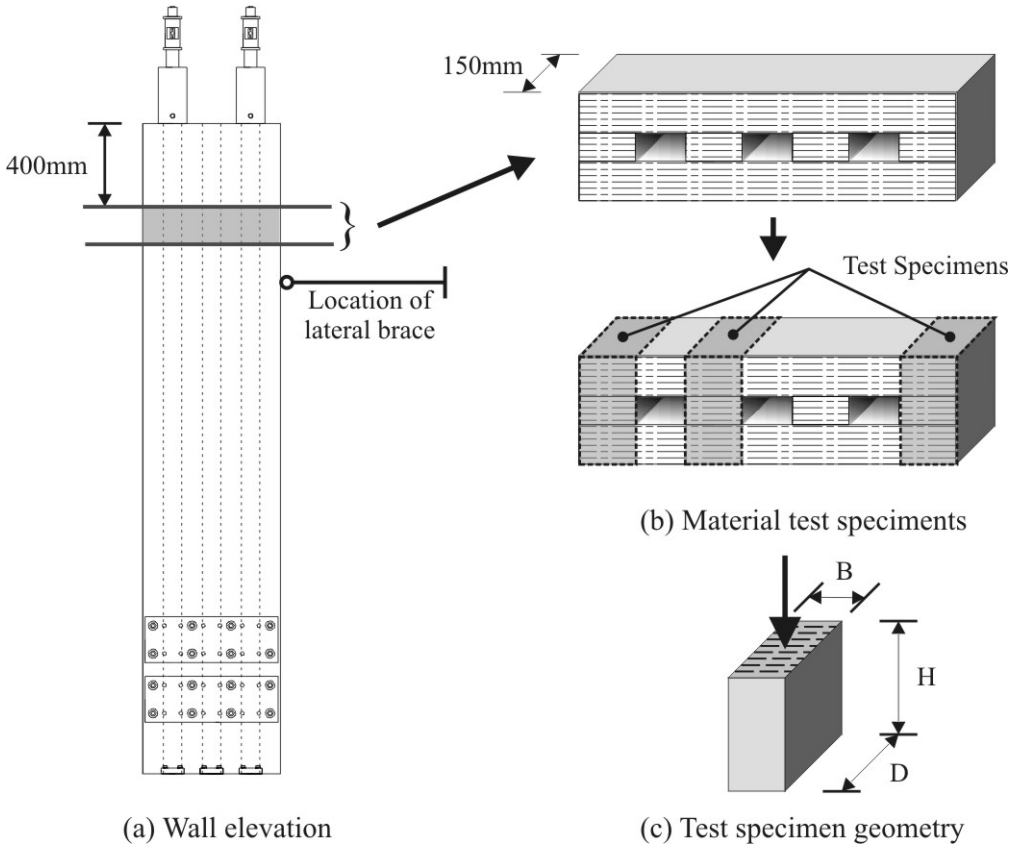

Figure 5.12 LVL material test specimens used for monotonic compression testing to failure

The dimensions of the each LVL material test specimen are listed in Table 5.7. The first three specimens (LVL 1 to LVL 3) were monotonically loaded to failure, while the other three specimens were cycled within the elastic range

Table 5.7 LVL test specimen geometry

	B [mm]	D [mm]	H [mm]
LVL 1	89.1	174.5	148.2
LVL 2	89.1	174.8	149.4
LVL 3	88.9	174.8	148.8
LVL 4	64.3	73.5	150.8
LVL 5	72.1	65.0	151.6
LVL 6	65.0	68.8	151.6

(a) Monotonic Compression Testing of LVL

The monotonic test was load controlled and included a single unloading and re-loading cycle at an axial strain of approximately 0.01. The stress-strain behaviour of the three material test specimens are plotted in Figure 5.13 (a)-(c). A comparison of all three specimens prior to unloading is presented in Figure 5.13 (d).

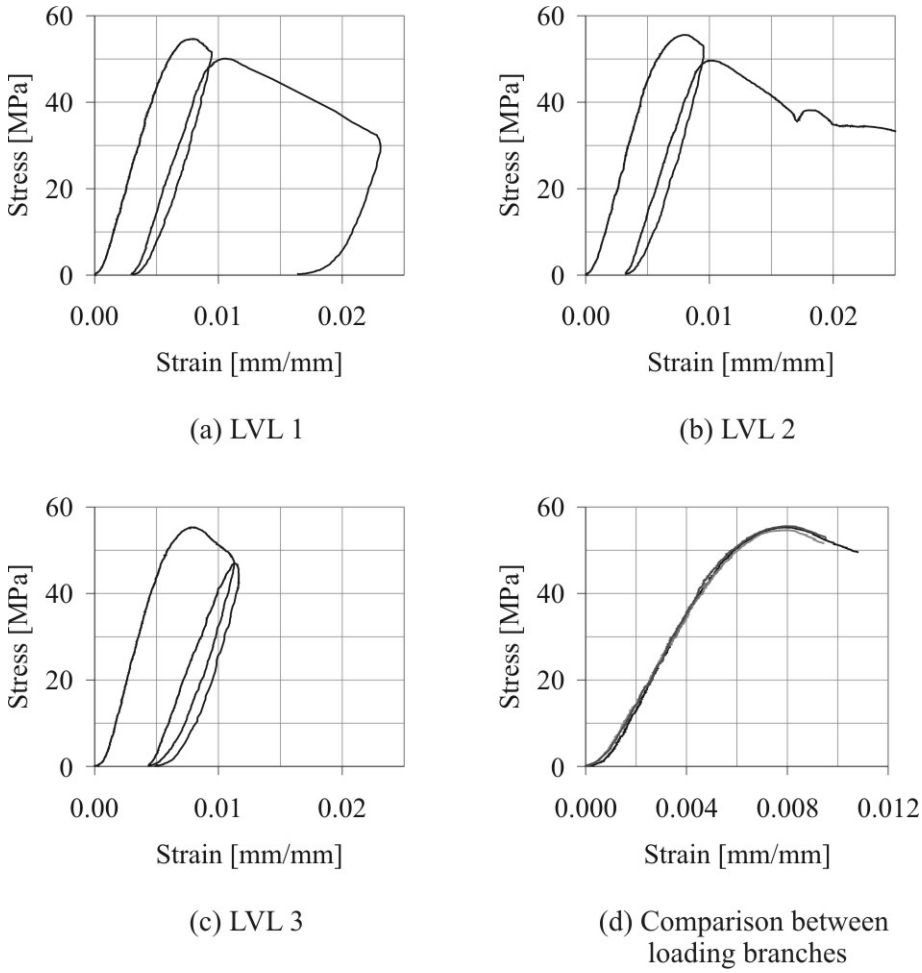

Figure 5.13 Monotonic axial compression testing of the LVL material

The monotonic stress-strain curves in Figure 5.13 (d) indicate an initial softened response followed by elastic behaviour up until approximately 50% of the peak load. For loads greater than about 50% of the peak load the material begins to soften and become increasingly non-linear. The maximum load occurs at an axial strain of approximately 0.0075. The average ultimate stress of the LVL material is f'_{LVL} = 54MPa, with an elastic modulus parallel to the grain of E_{LVL} = 10,600MPa.

(b) Cyclic Load Testing of LVL within the Elastic Range

The cyclic tests comprised of three load reverses at approximately 20%, 40% and 60% of the peak compressive load. The material test specimens of LVL 5 & 6 included a fourth load reversal to approximately 75% of the peak load. Even within the elastic range, the response had some non-linearity and permanent plastic strains developed within the material. Therefore, even after low amplitude rocking of the post-tensioned wall permanent deformations can be expected around the rocking toe region.

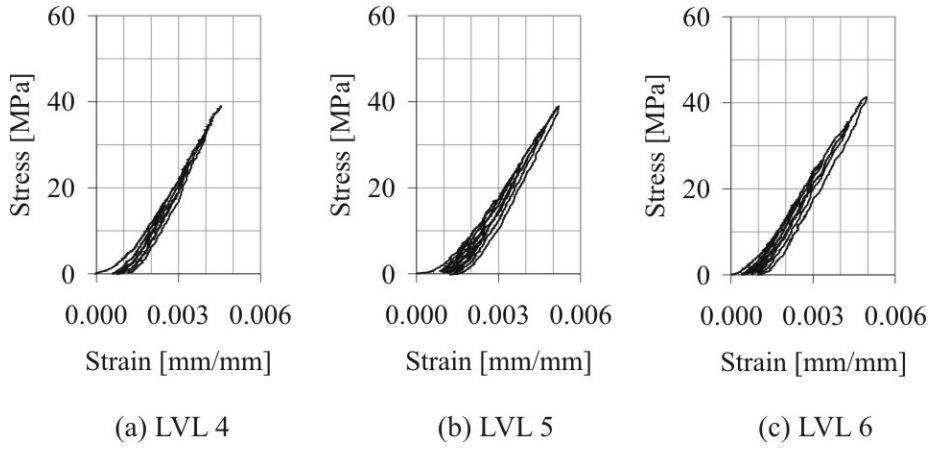

Figure 5.14 Cyclic testing within the elastic range of the LVL material

5.7.4. Viscous Dampers

High-speed cyclic testing was conducted on all four of the fluid viscous dampers (FVDs). The Civil Engineering Laboratory was not equipped to test the FVDs at high-speed; therefore, the testing was carried out in the Mechanical Engineering Laboratory. The four FVDs were each number 1 to 4 (referred to as Damper 1, etc)

(a) High-Speed Test rig

The testing facility at the Mechanical Engineering Laboratory employed a high-speed MTS testing system (Figure 5.15). The MTS was controlled via a high-speed dSpace computer controller and logger capable of recording data at 1MHz. Axial loads and displacements were directly measured through the MTS system, requiring no external instrumentation.

Figure 5.15 High-speed MTS system ready to test the fluid viscous dampers in the Mechanical Engineering Laboratory

(b) Damper testing protocol

The imposed damper displacement protocol was identical in mathematical form to that described in Section 5.6.4 used to control the shake-table. That is, two steady-state cycles were carried out at each displacement amplitude. This was preceded and followed by one transition cycle. A summary of the displacement amplitudes and the corresponding maximum expected damper velocity is tabulated in Table 5.8. In all cases, the maximum rated damper velocity was not exceeded.

It was possible to estimate the maximum likely velocity demand that the FVDs would be subjected to during shake-table testing. The bold values in Table 5.8 represent the maximum velocity expected during each amplitude of high-speed cyclic testing. The italic values in Table 5.8 are outside the operating range of the shake-table; however, testing was still carried out to properly identify the characteristics of each fluid viscous damper.

Table 5.8 Damper displacement amplitudes and corresponding maximum damper velocity imposed during the high-speed damper testing

0.1Hz		**0.5Hz**		**1.0Hz**		**2.0Hz**	
Displ [mm]	Vel [mm/s]	Displ [mm]	Vel [mm/s]	Displ [mm]	Vel [mm/s]	Displ [mm]	Vel [mm/s]
2	**1.3**	**2**	**6.3**	**2**	**12.6**	**2**	**25.1**
5	**3.1**	**5**	**15.7**	**5**	**31.4**	*5*	*62.8*
10	**6.3**	**10**	**31.4**	*10*	*62.8*	*10*	*125.7*
15	*9.4*	*15*	*47.1*	*15*	*94.2*	*15*	*188.5*
20	*12.6*	*20*	*62.8*	*20*	*125.7*		
25	*15.7*	*25*	*78.5*	*25*	*157.1*		

(c) Experimental response of the fluid viscous dampers

The force-displacement response of two FVDs (Damper 1 and Damper 3) is shown in Figure 5.16 at two levels of maximum displacement amplitude: 5mm and 15mm. While the capacity of the damper has some dependency on frequency, it is minimal. More importantly, some of the dampers indicated some slipping within the hysteretic response due to mechanical clearances within the ball-joint connection at each end of the damper. This is evident within Damper 3 in Figure 5.16 (a), indicating almost 2mm of slip. As the velocity of the damper increases the slipping became less noticeable; either due to the momentum developed within the shaft of the FVD counteracting the slip, or due to filtering of the experimental data.

The mathematical relationship describing the force-velocity behaviour was determined from the measured force-displacement response of each damper. The force in a non-linear FVD is described by Eq.(5.6). For linear FVDs the velocity exponent α is equal to 1.

$$F_{vd} = c_{vd} \cdot (v_{vd})^{\alpha} \qquad \textbf{5.6}$$

Figure 5.17 plots the relationship between the damper force and excitation velocity. The mathematical relationship of Eq.(5.6) was fitted to this experimental data.

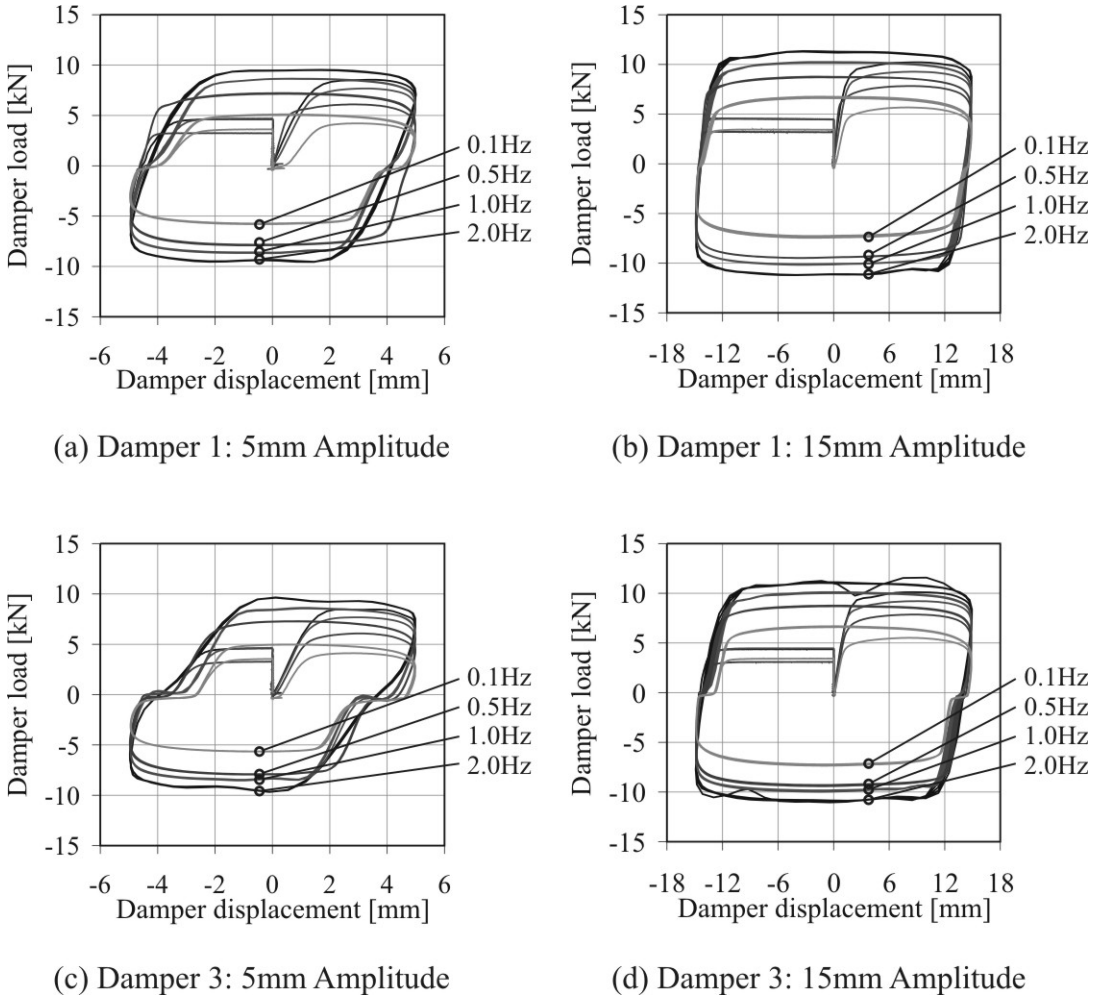

Figure 5.16 Experimental force-displacement response of the fluid viscous dampers

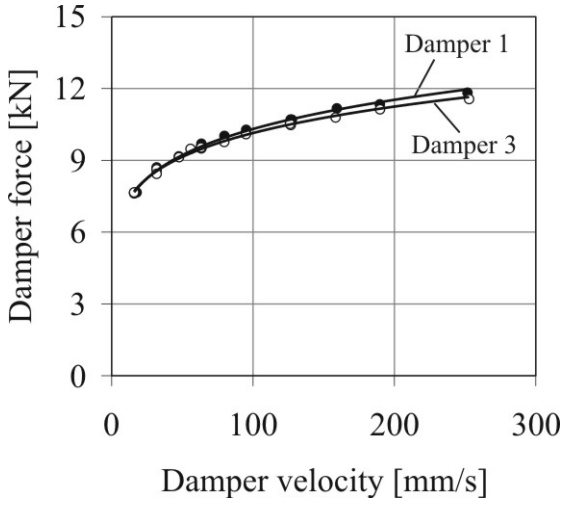

Figure 5.17 Experimental damper force-velocity relationship

The damping coefficient c_{vd} and the velocity exponent α for each FVD are summarised in Table 5.9.

Table 5.9 FVD damping coefficient c_{vd} and velocity exponent α

	Damper 1	Damper 2	Damper 3	Damper 4	Average
c_{vd} [kNs$^{\alpha}$/mm$^{\alpha}$]	4.912	4.923	5.102	4.841	4.945
α	0.161	0.160	0.149	0.141	0.153

5.8. EXPERIMENTAL RESULTS

The lateral load-displacement response of Wall 1 to Wall 5 is presented in the following sections. To aid in the interpretation of the results, three graphs are shown for each wall test (with the exception of Wall 1): each graph plots the lateral response under an excitation frequency of 0.5, 1.0 and 2.0Hz. The response under the three frequencies is compared to the response under an excitation frequency of 0.1Hz, which represents the response under quasi-static loading. The 0.5Hz excitation response is not shown for Wall 1 as the velocity dependency on the lateral response of this test is negligible.

5.8.1. Wall 1: Post-Tensioned Only

The high-speed cyclic response of Wall 1 was very stable during each excitation frequency in Figure 5.18. The response is completely non-linear-elastic with no strength or stiffness degradation of any kind. Furthermore, there is no velocity dependency observed throughout the test. The capacity of the post-tensioned wall is largely dictated by the initial post-tensioning load, the total number of tendons and the unbonded tendon length. Testing under the three frequencies suggested that the tendons experienced negligible strain-rate effects (with regards to the elastic modulus of the material) up to an excitation frequency of 2.0Hz.

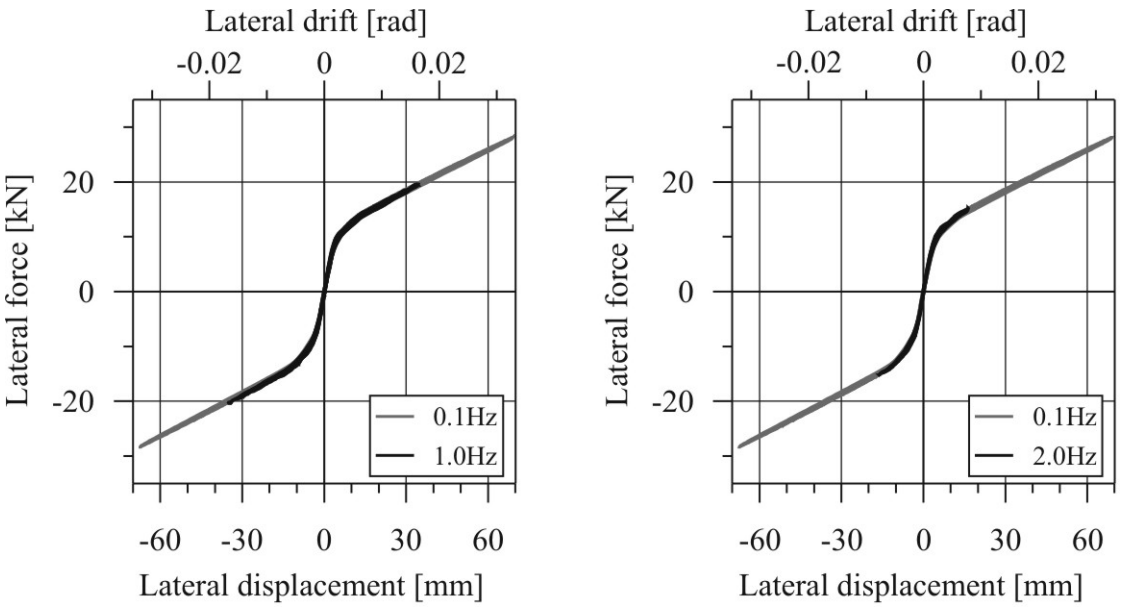

(a) 0.1 Hz versus 1.0Hz (b) 0.1 Hz versus 2.0Hz

Figure 5.18 High speed cyclic response, Wall 1

5.8.2. Wall 2: Post-Tensioned with Fluid Viscous Dampers

While the lateral response of Wall 2 was very stable, the velocity dependency was minimal and is explained as follows. First, the proportion of lateral capacity provided by the FVDs was small when compared to the proportion provided by the tendons. In fact, the lateral capacity provided by the tendons was in the order of 3-5 times greater than that provided by the FVDs. Therefore, any strength enhancement of the FVDs would be difficult to detect as the actual strength enhancement to the system was minimal. Second, the velocity dependency of the dampers themselves was very minimal. The dampers have a velocity exponent of $\alpha = 0.153$. In Figure 5.19 (a) the dampers experience roughly a 500% increase in velocity going from an excitation frequency of 0.1Hz to 0.5Hz; however, this equates to a mere 28% increase in damper force. Furthermore, considering that the viscous forces are out of phase with the elastic forces (less so for nonlinear dampers), any increase in damper force is most noticeable when the base rotation is quite small as this coincides with the maximum system velocity. Therefore, the strength enhancement of the system (if any) will be most noticeable when the initial stiffness of the system reduces to the bilinear stiffness of the system (this corresponds to small base rotations with high angular velocities). Even with these points in mind, it is still difficult to observe any strength enhancement in Figure 5.19, which was primarily due to the low proportion of lateral capacity provided by the FVDs and the high non-linearity ($\alpha = 0.153$) of the viscous dampers.

Some pinching was observed within the lateral response during unloading in Figure 5.19. This pinching was associated with the mechanical clearances within ball-joint connections located at each end of the viscous damper. This pinching reduced the effectiveness of the dampers when the lateral drift ratio of the system was less than 1.0%. During testing at 2.0Hz, the maximum drift ratio was limited to 0.90%, governed by the velocity limitation of the shake-table. However, the increase in damper force associated with the larger velocities was not evident as the damper response was dominated by the pinched behaviour of the ball-joint connection.

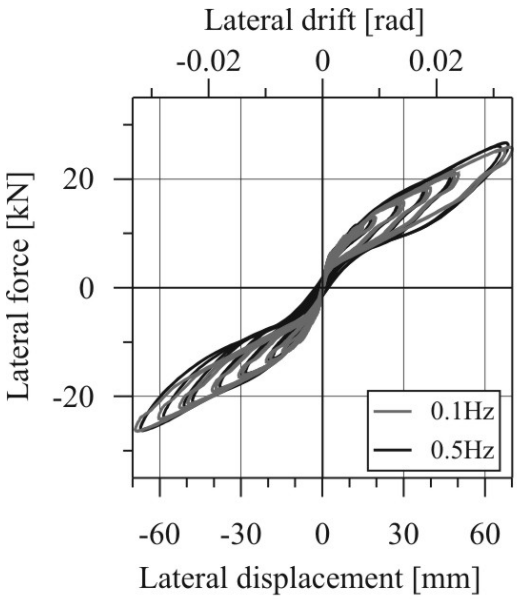

(a) 0.1 Hz versus 0.5Hz

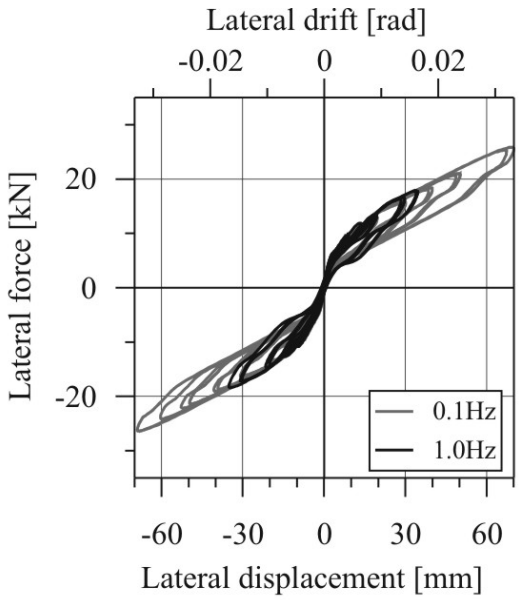

(b) 0.1 Hz versus 1.0Hz

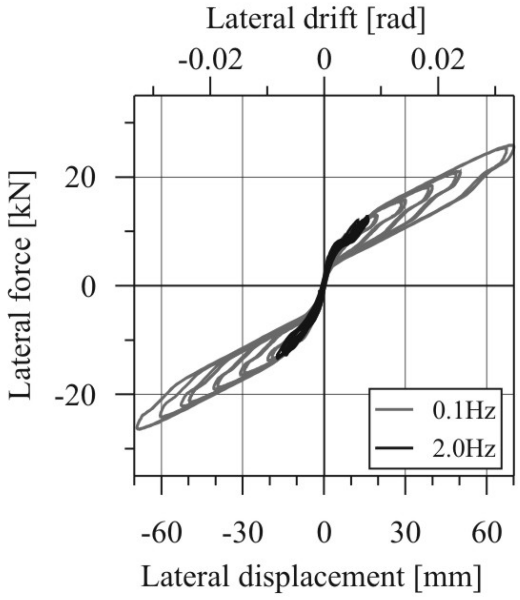

(c) 0.1 Hz versus 2.0Hz

Figure 5.19 High speed cyclic response, Wall 2

5.8.3. Wall 3: Post-Tensioned with Fluid Viscous Dampers and Mild Steel Dampers

Again, minimal velocity dependency was observed for Wall 3. In this case the proportion of lateral capacity provided by the FVDs was even less than the proportion in Wall 2. Therefore, the FVDs had even less of an influence on the lateral response of the section. The lateral response was extremely stable and the amount of energy dissipation was large.

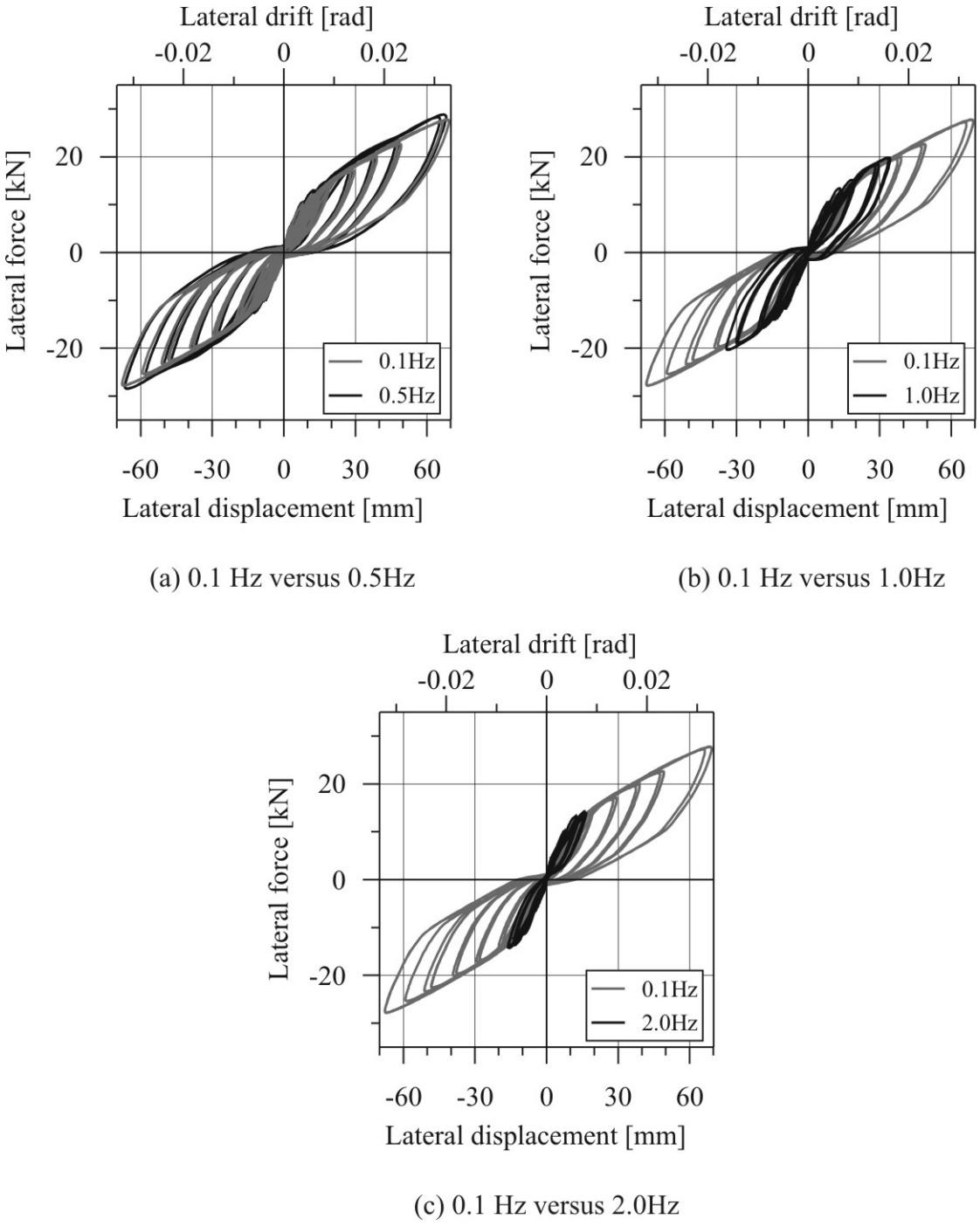

Figure 5.20 High speed cyclic response, Wall 3

It is also interesting to note that the static residual deformations were negligible. As the velocity approached zero, the force within the FVDs also approached zero; hence, the re-centring ratio of the system increased. It was also difficult to gauge any strength enhancement due to strain-rate effects of the mild steel TCY dampers.

5.8.4. Wall 4: Post-Tensioned with Mild Steel Dampers (High Mild Steel Reinforcement Content)

The only velocity dependency in Wall 4 was associated with strength enhancement due to strain-rate effects of the mild steel (TCY dampers) and the post-tensioned tendons. If there any increase in strength was observed, the increase was very minimal. In fact, it was difficult to associate any strength enhancement with strain rate effects of the dampers as small differences could be equally associated with variations in the material properties between each batch of mild steel used in the fabrication of the TCY dampers.

All the inelastic behaviour was confined entirely to the TCY damper elements. The damage to the TCY dampers is apparent in Figure 5.21 (b) when the outer confining tube was removed after testing. Buckling is clearly evident, but is of a very higher order. It was concluded that the yielding region was sufficiently restrained by the epoxy-injected anti-buckling steel tube: this allowed efficient yielding in both tension and compression.

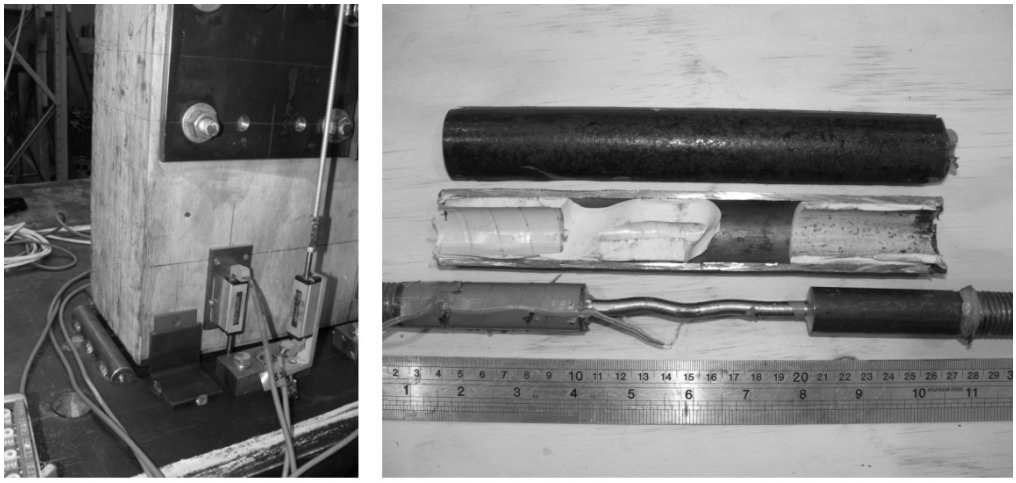

(a) Uplift of wall during testing

(b) State of the TCY dampers following cyclic testing to a drift ratio of 3.5%

Figure 5.21 Photos taken during and after testing of Wall 4

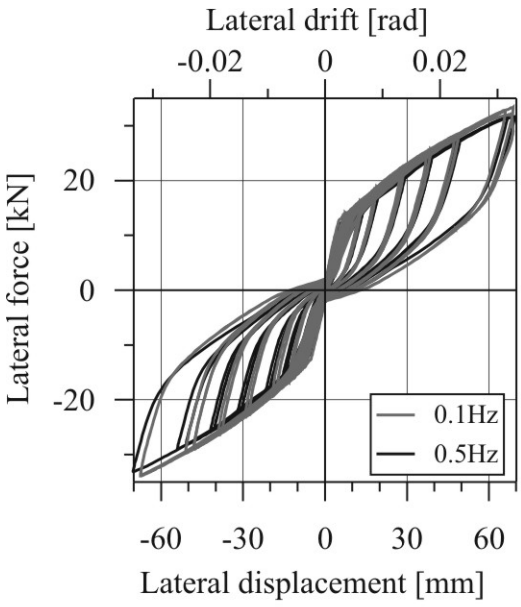

(a) 0.1 Hz versus 0.5Hz

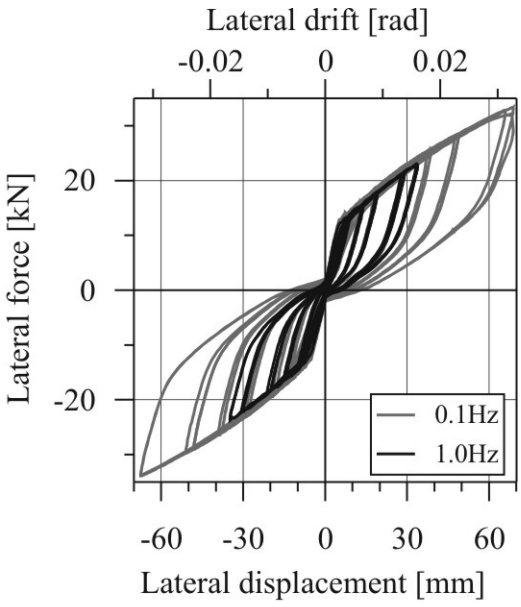

(b) 0.1 Hz versus 1.0Hz

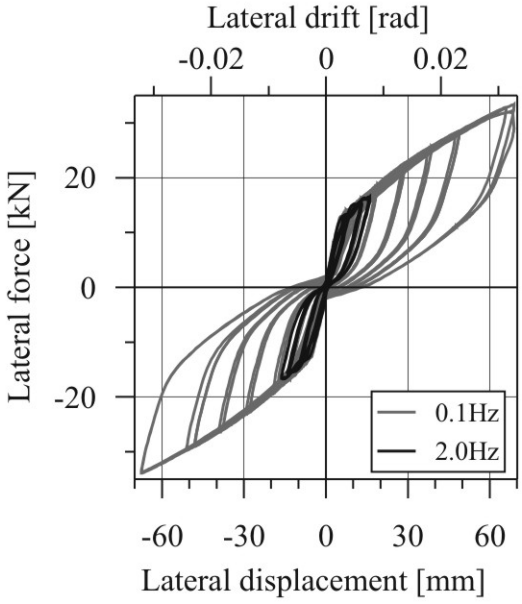

(c) 0.1 Hz versus 2.0Hz

Figure 5.22 High speed cyclic response, Wall 4

5.8.5. Wall 5: Post-Tensioned with Mild Steel Dampers (Low Mild Steel Reinforcement Content)

Similar to Wall 4, the same trends were apparent for Wall 5. If strain-rate effects were present, their influence was even more negligible as the proportion of lateral resistance provided by the mild steel was significantly less than Wall 4. The response was extremely stable; stiffness degradation was minimal. The proportion of mild steel reinforcement to the prestressed reinforcement was so low that residual static displacements were negligible.

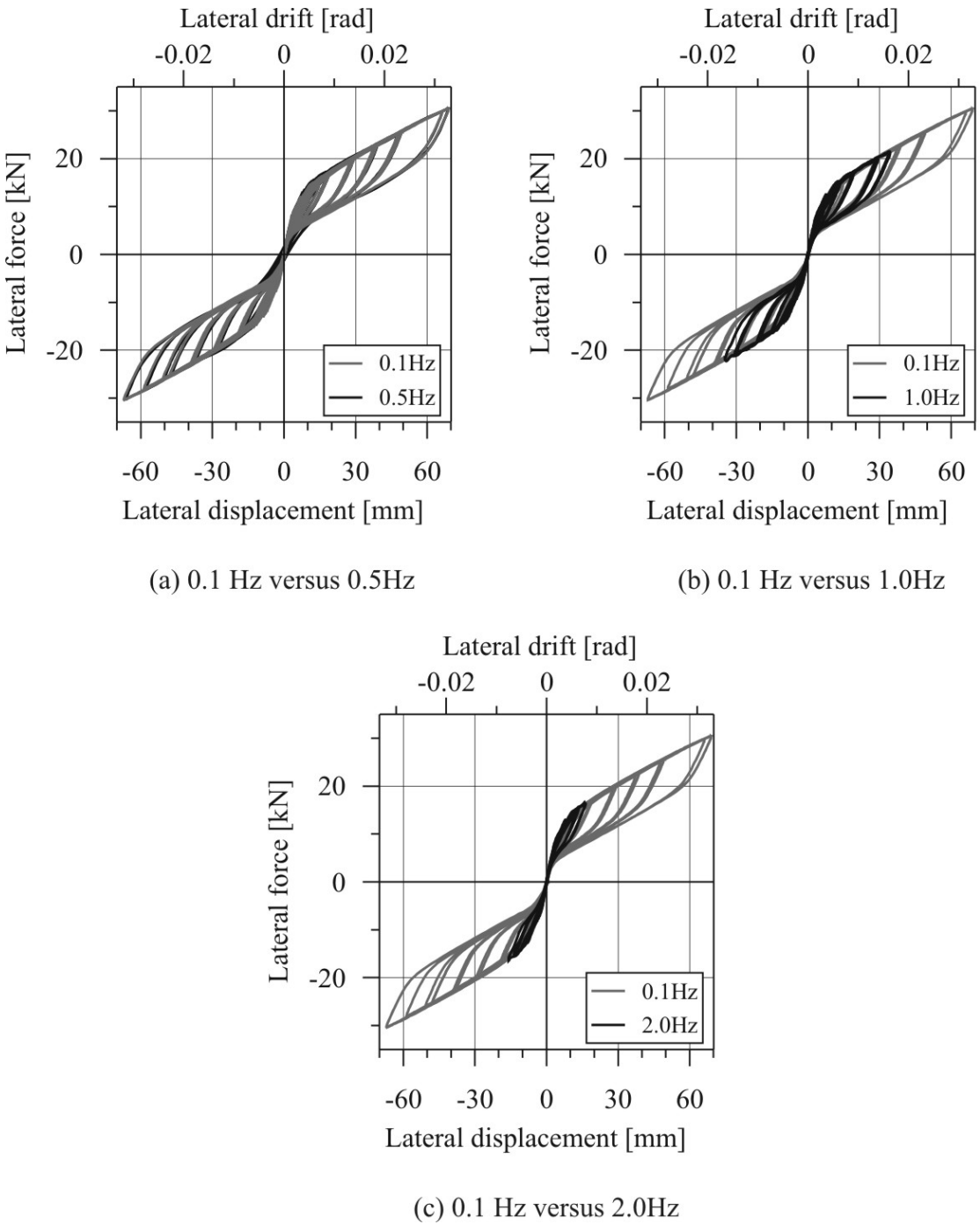

Figure 5.23 High speed cyclic response, Wall 5

5.9. DISCUSSIONS

5.9.1. Equivalent Viscous Damping

The area-based equivalent viscous damping (area-based EVD) was computed for each of the five post-tensioned walls test and is graphed in Figure 5.24. The computation was carried out during the 2nd steady-state cycle at each of the specified drift ratios in Table 5.8. The results in Figure 5.24 are plotted at an excitation frequency of 0.5Hz. The response of Wall 2 and Wall 3 had no noticeable velocity dependency and, hence, the difference in EVD was negligible between each excitation frequency. As expected, Wall 4 had the highest proportion of energy dissipation followed closely by Wall 3. Both Wall 2 and Wall 5 were very comparable in terms of EVD, while Wall 1 was essentially non-linear elastic.

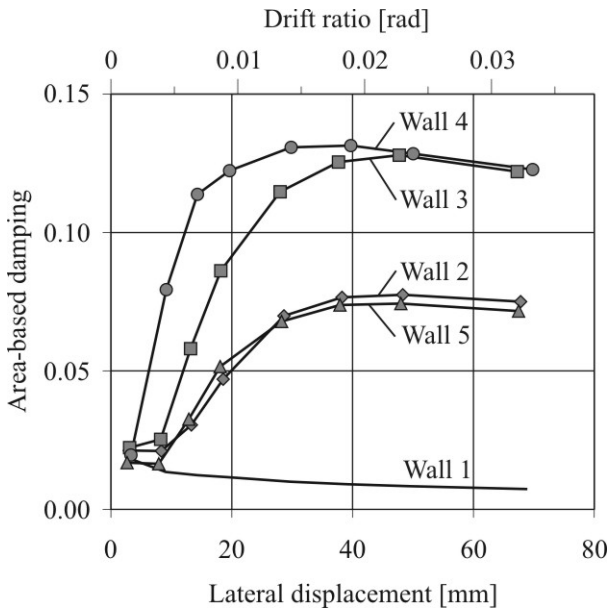

Figure 5.24 Area-based equivalent viscous damping on cycling at a excitation frequency of 0.5Hz (2nd cycle)

5.9.2. Effectiveness of the Fluid Viscous Dampers

The fluid viscous dampers FVDs had little dependency on excitation frequency for a number of reasons

- The velocity exponent of the damper was very low at $\alpha = 0.153$. For a five fold increase in velocity, the force in the damper increases by only 28%.
- The moment contribution provided by the FVDs was minimal when compared to the total moment contribution (for Wall 2, the proportion of lateral resistance provided by the FVDs was in the order of 15%-25% of the total lateral resistance). Therefore, if the force in the damper was to increase by 30%, for example, the capacity of the system would increase by only 5-8%.
- Finally, the contribution of the FVDs to lateral resistance is greatest when the velocity of the damper and internal lever arm is large. When the wall reaches its maximum velocity at the origin (zero displacement), the velocity in the

damper at the rocking interface is theoretically zero. For small lateral displacements either side of the origin the wall deforms in pure flexure (no rocking of the base), hence, the angular velocity of the base is zero. As the displacement of the wall exceeds the decompression limit and the base of the wall begins to uplift, the FVDs are subjected to a non-zero velocity. Very soon after the initial uplift, the FVDs experience their maximum velocity demand. It is during the time of maximum velocity and maximum internal lever arm that the FVD moment contribution is the greatest. That is, the largest FVD moment contribution occurs at low drift levels, where the damper velocity is large and the lever arm is modest in size.

5.9.3. Strain-Rate Effects

The maximum measured strain rates for Wall 4 and Wall 5, under each excitation frequency, are listed in Table 5.10 for the TCY dampers (left column) and the post-tensioned tendons (right column). The displacement elongation of the TCY dampers were recorded via a potentiometer, hence, the strain rate could be determined by computing the gradient of the displacement time-history (with respect to time) divided by the length of the yielding (fused) region. The fuse length of the TCY damper was 136mm and 90mm for Wall 4 and Wall 5 respectively.

Table 5.10 Maximum measured strain rates for the TCY dampers (left column) and post-tensioned tendons (right column) recorded during high-speed cyclic testing of Wall 4 and Wall 5

Excitation frequency	Wall 4		Wall 5	
0.1Hz v_{max} = *46.2mm/s* Δ_{max} = *73.5mm*	0.096 s^{-1}	0.004 s^{-1}	0.100 s^{-1}	0.004 s^{-1}
0.5Hz v_{max} = *230.9mm/s* Δ_{max} = *73.5mm*	0.383 s^{-1}	0.015 s^{-1}	0.311 s^{-1}	0.012 s^{-1}
1.0Hz v_{max} = *230.9mm/s* Δ_{max} = *36.8mm*	0.168 s^{-1}	0.007 s^{-1}	0.164 s^{-1}	0.007 s^{-1}
2.0Hz v_{max} = *237.5mm/s* Δ_{max} = *18.9mm*	0.144 s^{-1}	0.006 s^{-1}	0.117 s^{-1}	0.005 s^{-1}

Research carried out by Manjoine [1944] on steel strain-rate effects is graphed in Figure 5.25. The graph shows the effects of strain rates on the strength and strain behaviour of mild steel. In general, as the strain rate increases the yield strength and ultimate strength increases, while the ratio between the ultimate and yield stress decreases. From Figure 5.25 it can be seen that for a strain rate of $0.35s^{-1}$, the yield strength is increased by approximately 35%. Similarly, for a strain rate of $0.1s^{-1}$ a strength increase of approximately 30% can be expected.

Mander et al. [1984] summarised a series of tests carried out by the ACI Committee 439, ACI [1968]. The test results are listed in Table 5.11 below comparing the increase in yield strength with the test strain rate. The factors in Table 5.11 are slightly lower than those of Manjoine [1944]. Moreover, the data in Table

5.11 suggests that the strength enhancement due to strain-rates reduces for high strength steel: this trend was also observed by Restrepo et al. [1994].

Table 5.11 Yield strength enhancement of mild steel due to varying strain rate effects, ACI [1968]

Strain rate [s^{-1}]	f_y = 310 MPa	f_y = 352 MPa	f_y = 393 MPa	f_y = 558 MPa
0.001	1.05	1.07	1.02	1.03
0.01	1.11	1.14	1.07	1.05
0.1	1.19	1.21	1.16	1.08
1.0	1.28	1.28	1.25	1.10

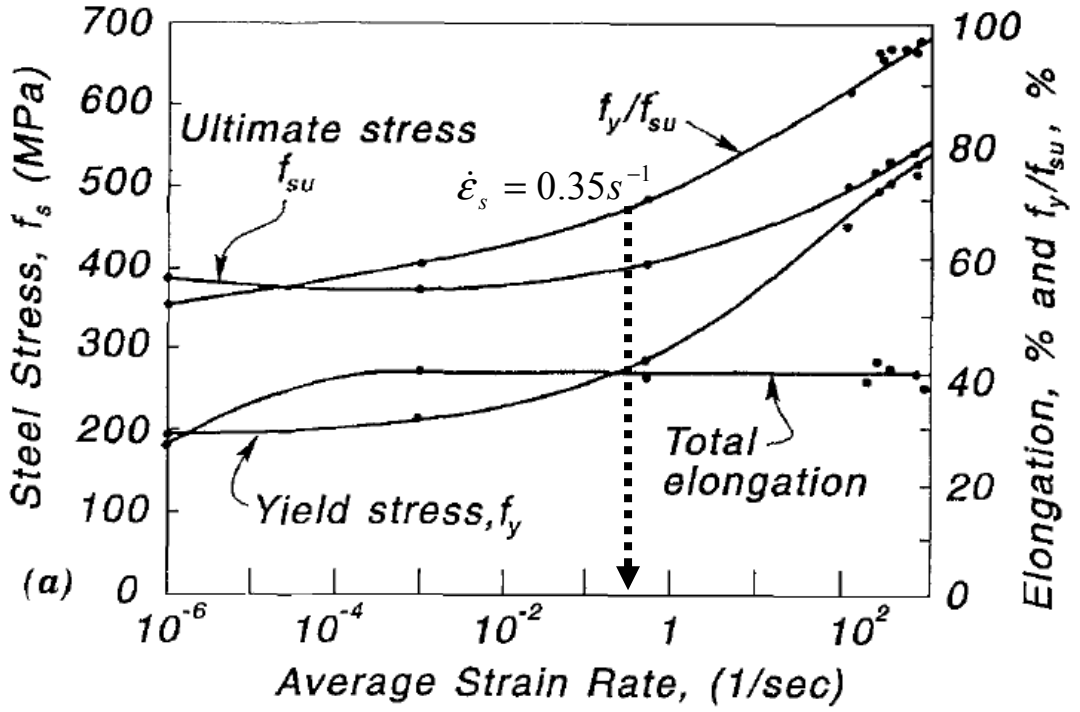

Figure 5.25 Test results of Manjoine [1944] presenting the effects of strain rate on the behaviour of mild steel tensile properties. A strain rate of 0.35s^{-1} is indicated in the graph with a dashed arrow.

With this in mind, any strength enhancement following the high-speed testing of the post-tensioned systems tested herein was difficult to detect for the following reasons:

- The maximum strain rates of the dampers are roughly in phase with the peak velocity of the system. As the maximum system velocity is out-of-phase with the maximum displacement the strain rate effects will have the greatest influence on the section capacity when the velocities (hence, strain rates) are high, i.e. when the displacement of the system is small. That is, the strength enhancement is greatest as the system travels through the origin, and is a minimum as the system approaches the peak displacement response.
- As mentioned above, the proportion of lateral capacity provided by the TCY dampers was small for Wall 4 and Wall 5: 30-40% and 20-25% of the total

lateral capacity respectively. Therefore, the strength enhancement of the total system due to the mild steel alone was further reduced.

- The measured strain-rates of the post-tensioned tendons were minimal. The large unbonded length (in the order of 25 times the fuse length of the TCY dampers in this case) reduces strain rates to very low levels. Furthermore, the strain-rate based strength enhancement reduces for high strength steel, further reducing any strength enhancement of the post-tensioned tendons.

5.10. CONCLUSIONS

The high-speed cyclic response of five post-tensioned rocking wall systems was presented. Each post-tensioned wall had a combination of viscous and hysteretic dampers.

The cyclic behaviour of all the post-tensioned walls with dampers was found to be very stable. Damage was entirely confined to the external dampers; in the case of the post-tensioned viscous wall no damage was observed. Full static re-centring was achieved in all five wall systems. In fact, a combined hysteretic-viscous system can utilise a larger proportion of total mechanical damping (hysteretic plus viscous) because the force in the viscous dampers reduce to zero at the end of the response. Hence, the re-centring capacity of the system only needs to consider the proportion of the hysteretic and the post-tensioning moment contribution.

There was very little difference in response observed for any of the post-tensioned walls with viscous dampers as the excitation frequency increased. This was partly due to the high non-linearity of the viscous dampers ($\alpha = 0.153$) where a 400% increase in damper velocity resulted in an increase to the damper force of only 24%. Furthermore, the slop in the connections at each end of the viscous dampers (due to manufacturing clearances) reduced the ability of the damper to provide large damping forces under larger velocities during low amplitude cycles. That is, for an excitation frequency of 2.0Hz where the maximum input displacement was limited to 18.9mm (due to the limiting table velocity of 235mm/s) the slop in the damper connections prevented large velocities from entering the viscous damper.

Strain rate effects appeared to have little influence on the lateral response of any of the post-tensioned walls with hysteretic dampers. The maximum strain rate occurs during periods of maximum system velocity (or thereabouts). Therefore, any strength enhancement occurs when the system passes through the origin. Furthermore, for the purely hysteretic systems (Wall 4 & 5), the proportion of lateral capacity provided by the hysteretic dampers was in the range of 30-40% for Wall 4, and 20-25% for Wall 5. Considering Wall 5 for example, if strain-rates suggested a strength enhancement of the hysteretic dampers of 20%, the strength enhancement to the entire system would be in the range of 4-5%.

Strain rate effects were found to be negligible for the post-tensioned tendons. The large unbonded length of the tendon reduced the strain rates by roughly a factor of 25 when compared to that of the TCY dampers. This conclusion was further supported in that strain-rates are known to have less of an effect on high strength steel

5.11. REFERENCES

ACI. (1968). "Effect of steel strength and reinforcement ratio on the mode of failure and strain energy capacity of reinforced concrete beams." *ACI Structural Journal*, 66(3), 165-173.

Chase, J. G., Hudson, N. H., Lin, J., Elliot, R. and Sim, A. (2005). "Nonlinear Shake Table Identification and Control for near-Field Earthquake Testing." *Journal of Earthquake Engineering. Vol. 9, no. 4, pp. 461-482. July 2005*.

Ghee, A. B. (1985). "Seismic Shear Strenght of Circular Bridge Piers." University of Canterbury Research Report, University of Canterbury, Christchurch.

Mander, J. B., Priestley, M. J. N. and Park, R. (1984). "Seismic design of bridge piers." Report 84-02, University of Canterbury, Christchurch.

Manjoine, M. J. (1944). "Influence of rate of strain and temperature on yield stress of mild steel." *Journal of Applied Mechanics*(11), 211-218.

Marriott, D., Pampanin, S. and Bull, D. (2007). "Improving the Seismic Performance of Existing Reinforced Concrete Buildings using Advanced Rocking Wall Solutions." *NZSEE*, Palmerston North, New Zealand.

Restrepo, J. I., Dodd, L. L., Park, R. and Cooke, N. (1994). "Variables affecting cyclic behavior of reinforcing steel." *ASCE Journal of Structural Engineering*, 120(11), 3178-3196.

6. Dynamic Testing of Post-Tensioned Precast Concrete Walls with Viscous and Hysteretic Dissipation

6.1. INTRODUCTION

The quasi-static cyclic response of post-tensioned (PT) bridge piers was presented in Chapter 4, while the high-speed cyclic testing of PT walls with fluid viscous dampers (FVD) and tension-compression-yielding (TCY) dampers was presented in Chapter 5. This chapter complements these two earlier chapters by presenting the results from a series of dynamic tests on PT walls carried out on the shake-table. In particular, free-vibration release testing on five PT walls with various damper configurations is investigated to understand and quantify contact damping. Following this, the same five walls are subjected to two recorded strong ground motions representing the design basis event (500 year return period) and two ground motions representing the maximum considered event (2000 year return period).

6.2. DETAILS AND CONSTRUCTION OF THE PROTOTYPE POST-TENSIONED WALL

Five post-tensioned walls are tested under dynamic shake-table testing. The damper arrangement (number and type of dampers) fitted to each post-tensioned wall tested herein is identical to the post-tensioned walls tested in Chapter 5. While the PT walls tested in Chapter 5 were constructed of Laminated Veneer Lumber (LVL), for dynamic testing the PT wall and foundation were constructed from reinforced concrete (RC). The walls were constructed from reinforced concrete as information relating to the energy lost during rocking was studied (contact damping). The dynamic behaviour was likely to be dependant on the material of the rocking wall; therefore, a more common construction material was thought appropriate. The design of the prototype wall was discussed in Chapter 5, where a reference to further information was made to a publication in Appendix B, Marriott et al. [2007].

The precast RC wall in Figure 6.1 was detailed with a heavily confined rocking toe region comprising of boundary elements and fabricated steel channels at each end of the wall. Each boundary element comprised of 8-D10 longitudinal bars with R6 confining stirrups (6mm in diameter) placed at 60mm centres. The longitudinal bars were terminated 5-10mm from the end of the precast unit. The reinforcing cage is pictured in Figure 6.1 (a), while construction drawings can be found in Appendix C. Two PVC ducts ran the height of the precast wall to accommodate the unbonded post-tensioned tendons. Additional protection and confinement of the toe was provided by

a fabricated steel channel cast within the toe of the precast wall (Figure 6.1 (a) & (b)). As the wall rocked from toe to toe, this confining element would limit damage to the cover concrete.

The precast foundation was constructed with a large pocket on the underside to provide access to the PT anchorages. A recess was also cast into the top of the foundation to locate the precast wall when lowered into position (Figure 6.1 (c) & Figure 6.3 (a)).

Similar to the construction of the post-tensioned LVL wall in Chapter 5, the external dampers were connected to the precast wall by stiff steel brackets. These steel brackets were bolted to a steel plate attached to the side of the precast wall. The method in which the steel plate was attached to the precast wall is shown in Figure 6.2; the surface of the steel plate and the side of the concrete wall were roughened and a layer of high strength epoxy (Hilti RE 500) was applied to both surfaces. The steel plate was located in position and 8 high strength (880MPa) threaded rods were tightened to 65% of their proof load: this would enable the damper forces to be transferred to the wall via friction/mechanical interlock. Two plates were fixed to each side of the wall.

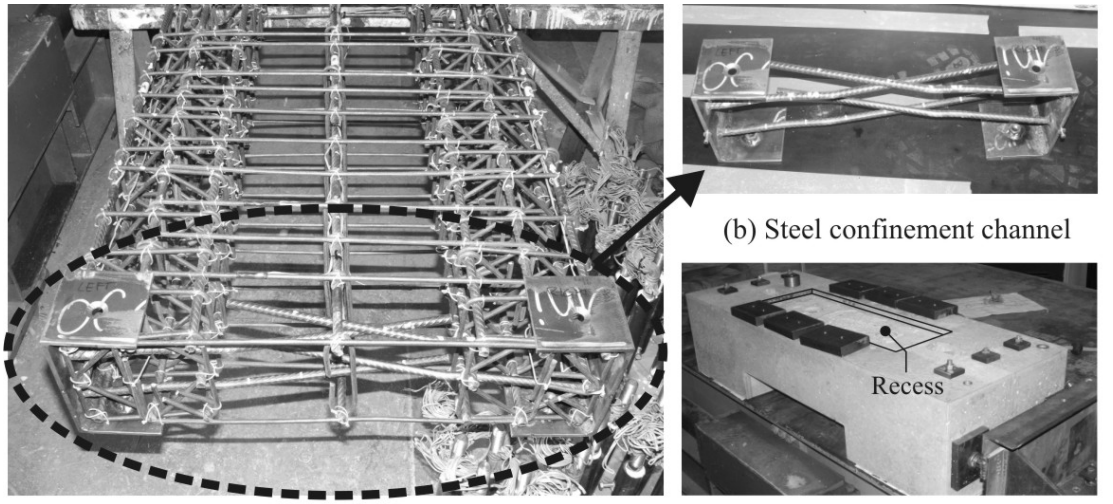

Figure 6.1 Reinforcement details of the precast wall and foundation

(a) Preparing the steel plate (b) Preparing the concrete surface (c) Fastened steel plate

Figure 6.2 Assembly of the steel plate to attach the steel damper brackets

After the precast wall was lowered into position, within the foundation recess, a high flow epoxy grout (Sikadur 42) was pumped under pressure beneath the rocking interface (Figure 6.3 (a) & (b)). The recess provided shear transfer between the wall and foundation whilst also preventing slip along the rocking interface. The completed wall is pictured in Figure 6.3 (c).

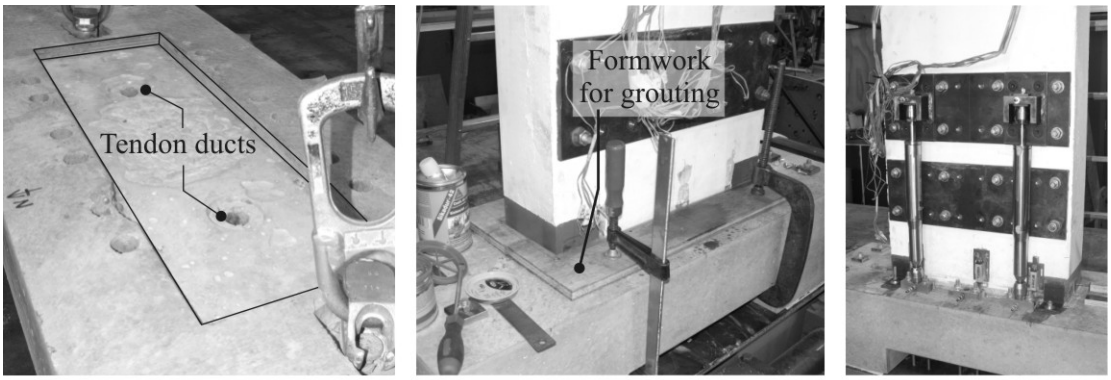

(a) Foundation recess to accommodate wall (b) Wall lowered in position, and ready for epoxy grout (c) Completed wall (Wall 2 shown)

Figure 6.3 Assembly of the wall-foundation and grouting of the rocking interface

Table 6.1 Post-tensioning and damper details of the five PT walls

Specimen	Initial Post-Tensioning	Dissipation
Wall 1	Two tendons stressed to 50kN each ($0.321f_{py}$)	None
Wall 2	Two tendons stressed to 30kN each ($0.192f_{py}$)	4 fluid viscous dampers
Wall 3	Two tendons stressed to 20kN each ($0.128f_{py}$)	4 fluid viscous dampers and 2-7mm diameter TCY dampers
Wall 4	Two tendons stressed to 30kN each ($0.192f_{py}$)	4-7mm diameter TCY dampers
Wall 5	Two tendons stressed to 40kN each ($0.256f_{py}$)	2-7mm diameter TCY dampers

The fluid viscous dampers (FVD) and the tension-compression-yielding (TCY) dampers that were tested in Chapter 4 had identical properties to those used for dynamic testing herein. A summary of the post-tensioning and the type and number of dampers installed on each PT wall is given in Table 6.1. Further details specific to the dampers can be found in Chapter 5.

6.3. LABORATORY TEST SET-UP AND INSTRUMENTATION

6.3.1. Experimental Test Set-Up

The general layout of the laboratory shake-table set-up is illustrated in Figure 6.4. The driving mass is a 3.84 tonne concrete block suspended from the laboratory crane. The steel bracing system supporting the concrete mass (details to follow) was designed to ensure that the mass did not twist about the vertical and out-of-plane axis.

The precast wall was located to one side of the shake table such that is was line with the laboratory strong floor bolt locations: this allowed a steel reaction frame to be located in line with the wall. One steel channel was located on each side of the post-tensioned (PT) wall to prevent out-of-plane movement (Figure 6.4 (c)). Frictionless roller bearings were located between the steel channels and the precast wall to prevent/minimise friction as the wall moved between the channels. The steel reaction frame at the end of the shake-table in Figure 6.4 (d) was also used to apply a lateral load to the top of the wall for free vibration release testing. A hydraulic jack was bolted to the reaction frame and pulled against the precast wall via a threaded rod and load-cell arrangement. When the wall reached a pre-defined release displacement, the threaded rod is cut to allow the wall to undergo free vibration.

6.3.2. Driving Mass

The driving mass in Figure 6.5 was attached to the precast wall by a Circular Hollow Section (CHS). A universal joint was located at both ends of the CHS brace to ensure bending was not transmitted into the brace, Figure 6.5 (c). Furthermore, expanding pins were located within the universal joints to prevent hammering during high speed due to the mechanical clearance between the pin and the universal bearing.

Two Square Hollow Section (SHS) braces formed an apex out the front of the concrete block (Figure 6.5 (a) & (c)). This brace prevented the mass from rotating about the vertical axis due to any horizontal eccentricity between the centre of mass and the connection of the CHS to the concrete block. These diagonal braces are denoted as Brace A in Figure 6.5 (a) & (c). A steel collar was welded at the apex of Brace A. A steel shaft passed through this collar and was attached to a load cell, which was in turn attached to the main CHS brace. The other end of the steel shaft was attached to the precast wall via a universal joint: refer to the enlargement in Figure 6.5 (c). The lubricated steel shaft passed through the collar without interference: this ensured the load cell did not return erroneous readings.

Four Equal Angle (EA) braces were welded to Brace A to prevent the mass from rotating about the out-of-plane axis due to any vertical eccentricity between the centre of mass and the connection of the CHS to the concrete block. These braces are denoted as Brace B in Figure 6.5 (a) & (c)). Brace A and Brace B confined the motion

of the mass to a single translation mode. Had these braces not been installed, additional modes would have interfered with the translation mode, complicating the rocking response significantly.

The translational mode shape of the post-tensioned wall is illustrated in Figure 6.6. As the wall pulls the concrete mass, a majority of the motion is horizontal translation; however, there is a small amount of out-of-plane rotation of the mass due to a downwards displacement of the connection at end **2** of the brace (refer Figure 6.6 (a)). Likewise, as the block travels in an arc, the block's centre of mass (and hence the connection at end **1**) will displace upwards by a small amount. The vertical displacement will case a small shear load will be transmitted through the universal joint to the wall at end **2** of the brace. This shear force is small in magnitude when compared to the lateral load and the tendon loads; therefore, will have little effect on the response.

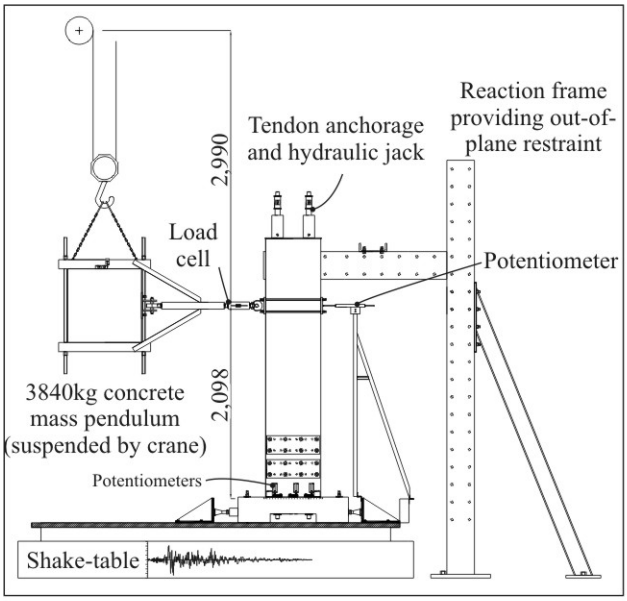

(a) Shake-table test set-up elevation

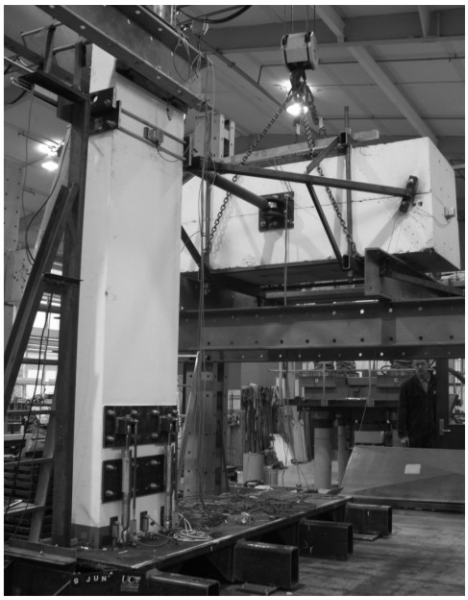

(b) Photo of test set-up

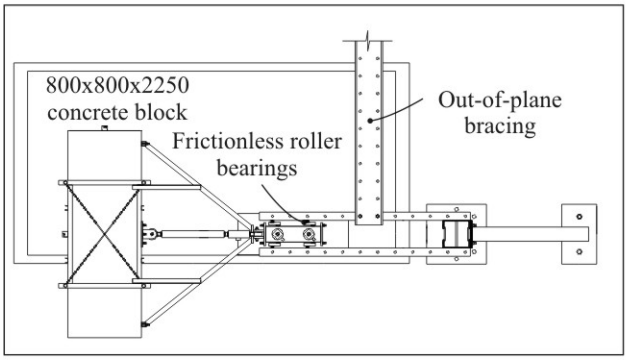

(c) Plan of shake-table test set-up

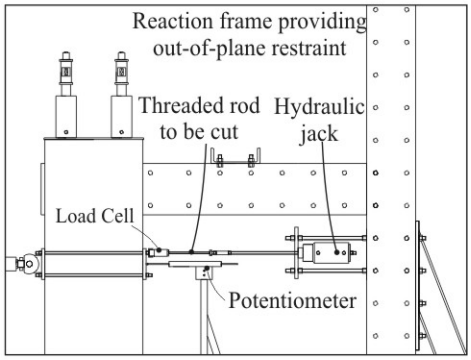

(d) Release testing apparatus

Figure 6.4 Shake-table laboratory set-up

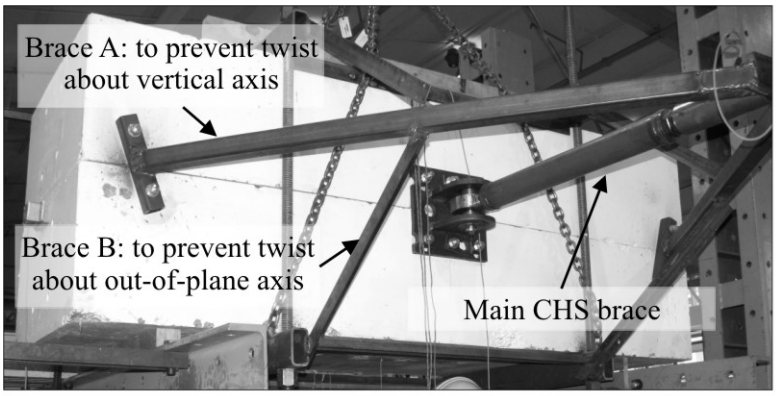

(a) Driving mass and bracing layout

(b) Laboratory crane

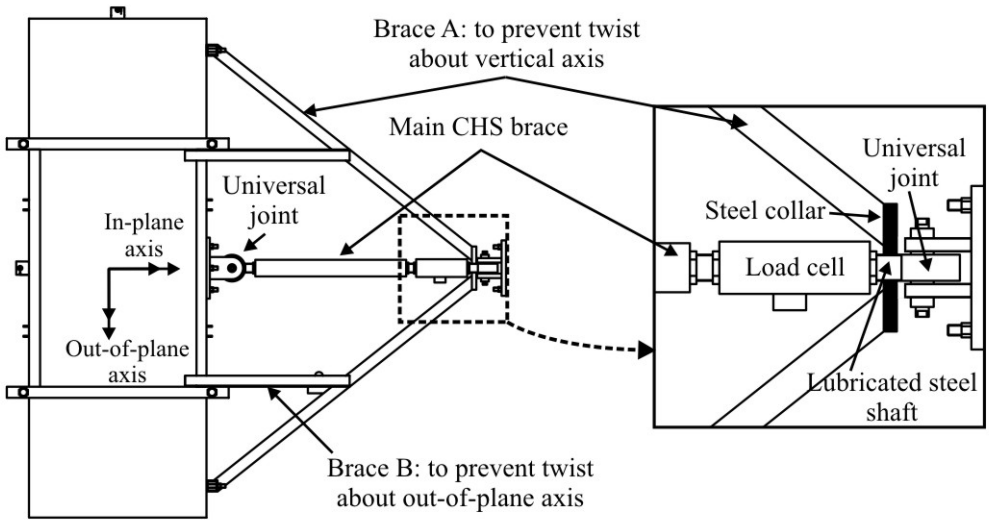

(c) Detailed brace formation and enlargement of lubricated collar connection

Figure 6.5 Steel brace configuration for controlling the driving mass

P-Δ loads were easily computed for the system. In this case, the P-Δ loads acted as a restoring force (as opposed to a de-stabilising force in the more conventional sense of a cantilever bridge pier). The restoring force $\boldsymbol{F_{P\Delta}}$ of the mass acting on the wall can be computed from Eq.(6.1) which is dependant on the total displacement of the mass $\boldsymbol{\Delta_{mass}}$ and the pendulum length (2990mm). This restoring force can be included within a macro model by placing an elastic spring at the height of the mass with stiffness equal to $\boldsymbol{K_{PD}} = 37.67kN/2.99m = 12.6kN/m$.

$$F_{P\Delta} = \frac{\Delta_{mass}}{2990mm} 37.67kN \qquad \textbf{6.1}$$

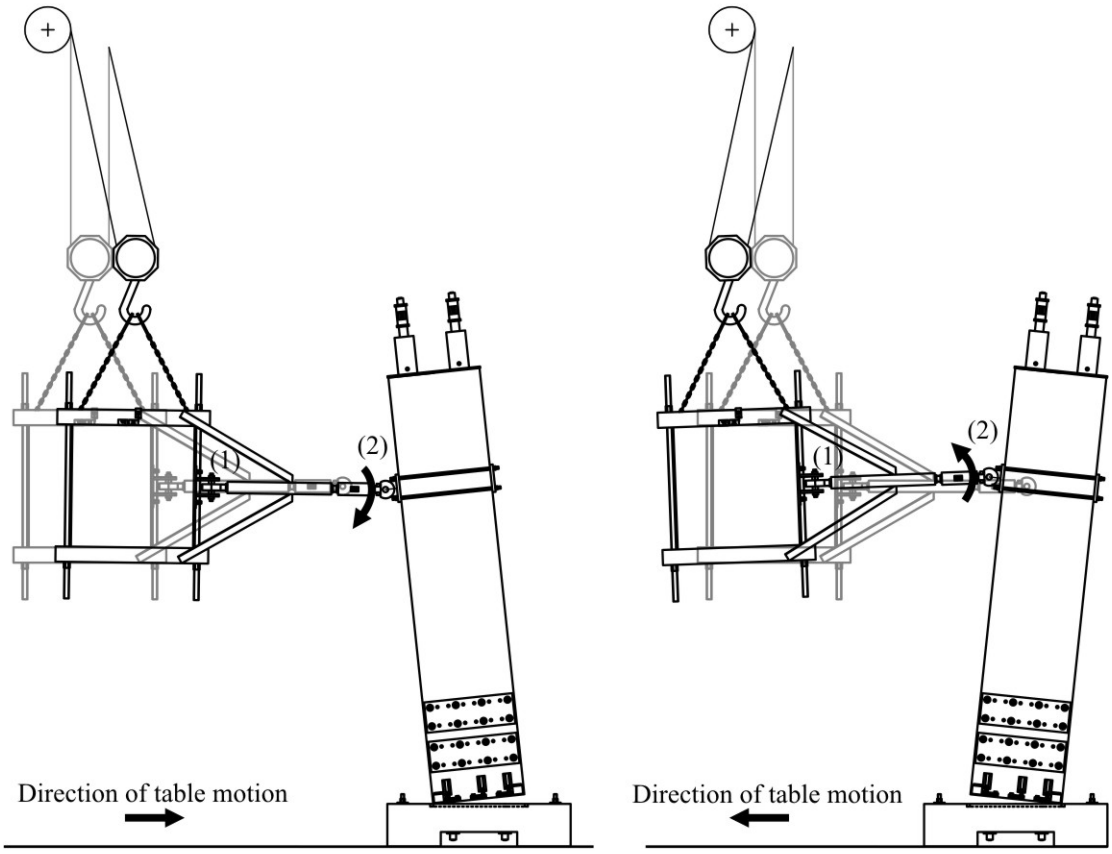

Figure 6.6 Translation mode shape of the rocking wall

6.3.3. Instrumentation

An extensive array of instrumentation was placed on the precast wall and the concrete mass. A majority of the instrumentation on the wall was identical to that used during the high-speed testing in Chapter 5, with the exception of accelerometers. The suspended concrete mass was heavily instrumented to monitor acceleration along the three axes in addition to angular velocity about the vertical axis and out-of-plane axis. Hence, five of the mass' six degrees of freedom were monitored. Two accelerometers were also placed on the precast wall at a height of 2100mm above the rocking interface (inline with the driving mass). This enabled horizontal and vertical accelerations to be measured at the effective height of the precast wall. A complete list of all instrumentation is summarised in Appendix B.

The same data acquisition system used during the high-speed testing in Chapter 5 was also used during dynamic testing. Data was sampled at 100Hz during loading to the release displacement prior to free vibration and 1000Hz after release and during earthquake excitation. While the full effect of sampling at 1000Hz was not be felt due to the analogue filter (passband of 200Hz), it was retained in order to have a sufficient sample size for filter options during post-processing.

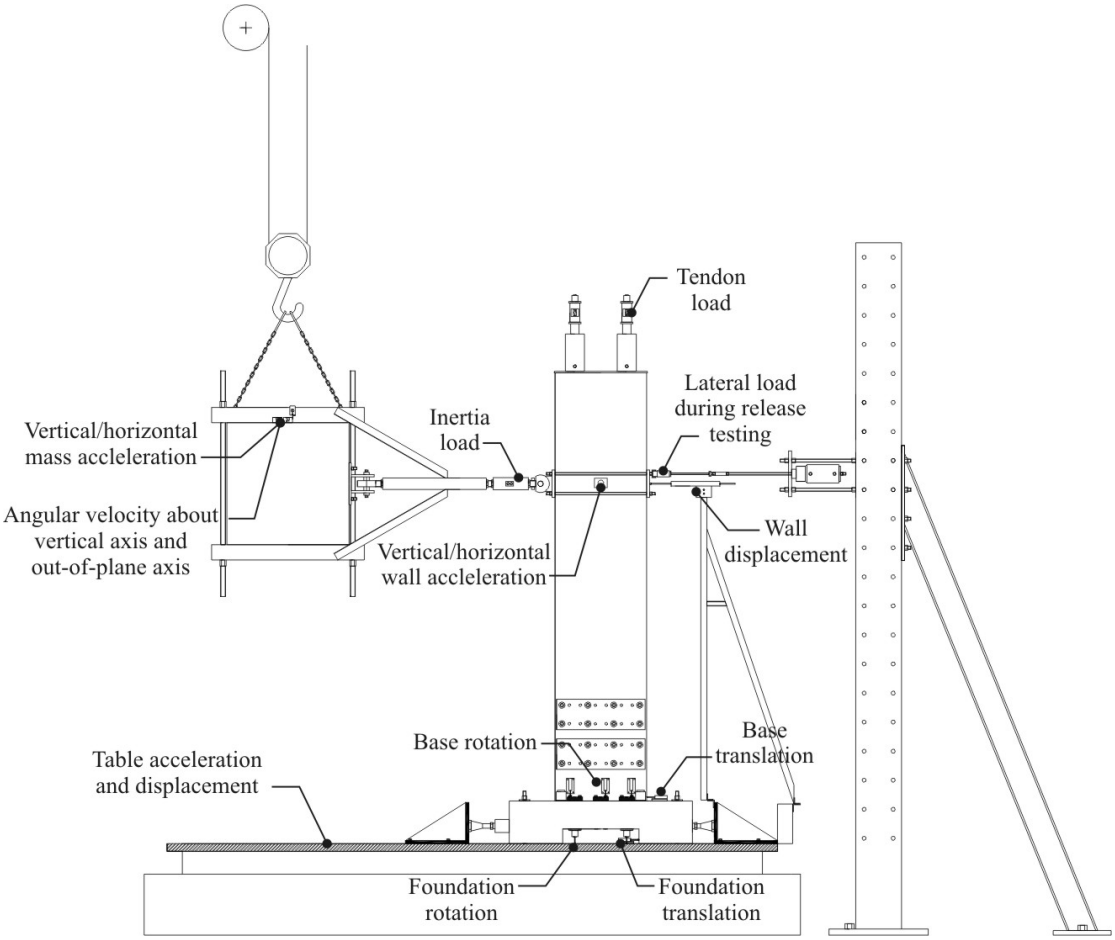

Figure 6.7 Shake table instrumentation

6.4. EXPERIMETNAL PROGRAM

The testing program consisted of free-vibration release testing followed by shake-dynamic testing using recorded earthquake ground motions. The earthquake records used for this study were based on two seismic hazard levels: the maximum considered event (MCE) and the design basis event (DBE, equivalent to 2/3MCE in FEMA [2003]). Two earthquake records were chosen for each hazard level; one near-field (NF) and one far-field (FF). As an example, the far-field maximum considered event is identified as MCE-FF.

The free-vibration testing was undertaken for release drift amplitudes of 1.5% and 2.5%. One additional free-vibration test was carried out for Wall 1 and Wall 2 at an amplitude of 0.5% lateral drift. At the DBE level, for each wall specimen, the free-vibration testing was first carried out, followed by one near-field ground motion and then one far-field ground motion. The TCY steel dampers were replaced and the testing sequence repeated for the MCE level. The testing program is outlined as follows and also summarised in Table 6.2

1. Free vibration test (1.5% drift amplitude)
2. Near-field ground motion (DBE)
3. Far-field ground motion (DBE)
4. TCY steel dampers replaced.
5. Free vibration test (2.5% drift amplitude)
6. Near-field ground motion (MCE)
7. Far-field ground motion (MCE)

Table 6.2 Free-vibration and shake-table testing program

	-	DBE			MCE		
	0.5% FV	1.5% FV	NF	FF	2.5% FV	NF	FF
Wall 1	✓	✓	✓	✓	✓	✓	✓
Wall 2	✓	✓	✓	✓	✓	✓	✓
Wall 3		✓	✓	✓	✓	✓	✓
Wall 4		✓	✓	✓	✓	✓	✓
Wall 5		✓	✓	✓	✓	✓	✓

6.4.1. Selection and Scaling of the Ground Motions

The earthquake records were scaled to the New Zealand seismic design spectrum for a zone factor of 0.4 located on soil category C, NZS1170.5 [2004]. Scaling is carried out for $\boldsymbol{R} = 1.0$ (equivalent to the DBE seismic intensity) and $\boldsymbol{R} = 1.5$ (representing the MCE seismic event). The records are scaled over a period range of 0.45s to 1.0s following a displacement-based retrofit procedure of the prototype structure (further details relating to this design procedure can be found in Marriott et al. [2007], Appendix B). The earthquake ground motions and the spectral scaling factors are summarised in Table 6.3.

The records that were selected required careful consideration as the laboratory shake table at the University of Canterbury has a maximum output velocity of approximately 242mm/s. When a similitude scale factor of 1/3 is considered, spectrum-scaled earthquake records could not exceed a velocity of 415mm/s. This velocity limitation proved to be extremely difficult in locating appropriate near-field records with dominant high velocity pulses associated with directivity effects. Recent studies carried out on the shake table by the Mechanical Engineering Department at the University of Canterbury developed two methods to modify the acceleration time-history when the velocity demand exceeded the shake table capacity, Chase et al. [2005] and Mulligan [2007]. Details of this record modification follow in a later section. Three of the ground motion records in Table 6.3 were modified as the ground velocity exceeded the limitation of the shake-table: Loma Prieta, Cape Mendocino and Northridge.

Table 6.3 Ground motion records selected for shake table testing and their corresponding spectrum-scaled PGA, PGV and spectral scale factor

	Earthquake record	Recording Station	Scaled PGA	Scaled PGV [mm/s]	Scale factor
DBE_FF	Kobe	Sakai	0.256	276	1.633
DBE_NF	Loma Prieta	Saratoga-W Valley	0.220	408	0.663
MCE_FF	Cape Mendocino	Rio Dell Overpass	0.382	434	0.992
MCE_NF	Northridge	La Dam	0.364	530	1.044

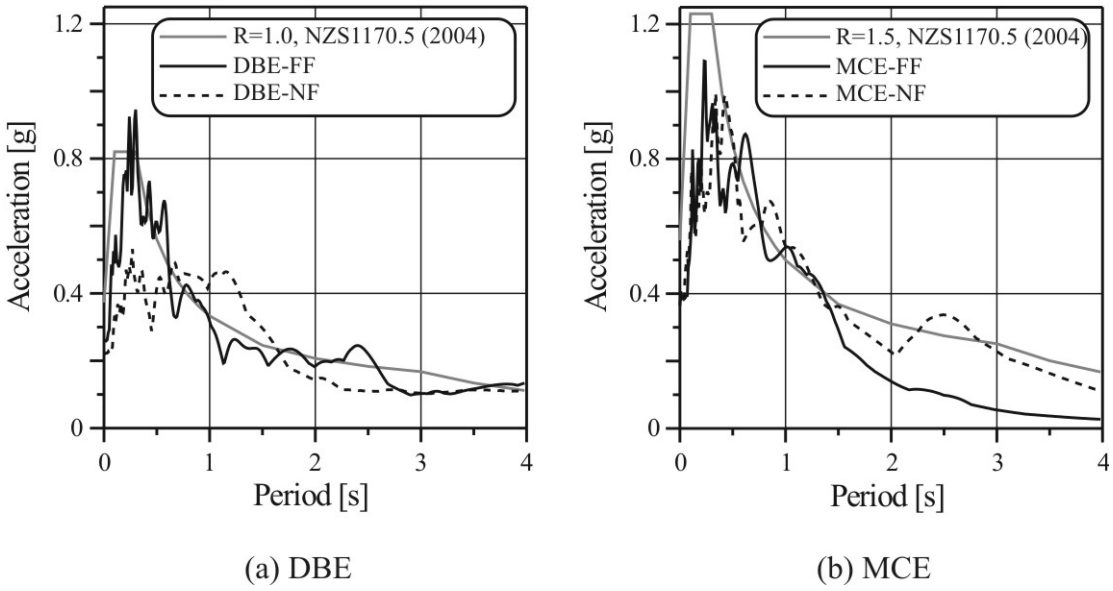

Figure 6.8 Record response spectra, scaled to the New Zealand elastic design spectrum (5% damped)

6.5. SHAKE TABLE CONTROL

6.5.1. Record Modification to Avoid Velocity Saturation

Two record modification techniques were used to adjust the acceleration time-history response for ground motions whose peak velocity exceeded the capacity of the table: the two methods are defined as Method A and Method B. While the table saturation velocity has a limit of approximately 242mm/s, a limiting velocity of $V_{max}=230mm/s$ was chosen to ensure sufficient protection against saturation during testing.

The premise behind Method A is illustrated in Figure 6.9, after Chase et al. [2005]. A generic acceleration time history command signal is indicated on the left. Integrating the area beneath the curve defines the velocity; in this case the area cannot physically exceed the velocity limit, i.e. $A \le A' = 230mm/s$. Two options exist to avoid saturation in this case. The first option is to retain the original duration of the acceleration pulse with reduced amplitude, while the second option is to retain the same acceleration amplitude with a reduced duration: these two options are shown schematically on the right of Figure 6.9. The second option is the preferred case as it

retains the forces associated with dynamic testing. The detailed procedure for Method A is outlined in Appendix C.

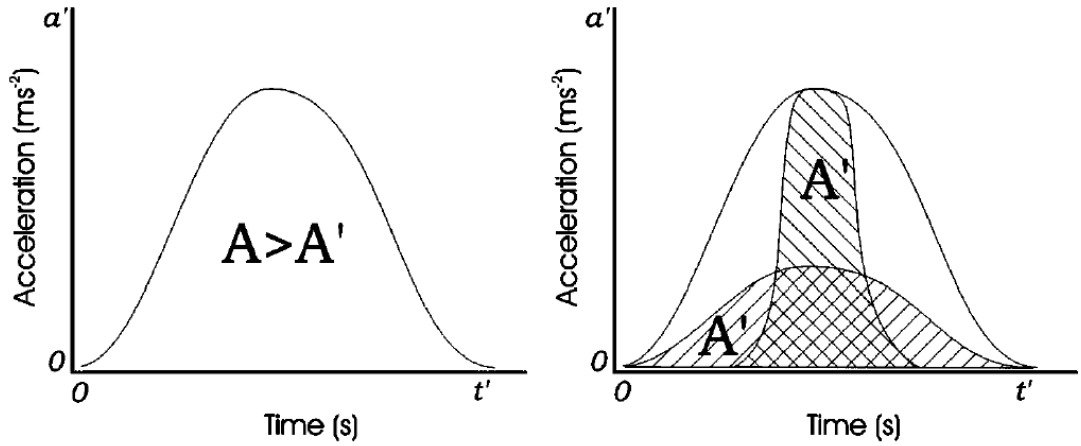

Figure 6.9: Modified acceleration profiles, Chase et al. [2005]

The second method, Method B, was developed within the Department of Mechanical Engineering at the University of Canterbury[1,2] (Mulligan [2007]). By truncating the velocity time history outlined in Method A, the intensity of the earthquake ground motion will be reduced. The idea behind Method B is that the velocity time history is still truncated; however, the lost energy is relocated to a region where the velocity is below saturation, thus retaining as much intensity as possible. This method is slightly more complicated to implement. Furthermore, Method B inherently requires a baseline adjustment to be made for both the velocity and displacement time history. The detailed procedure for Method B is outlined in detail in Appendix C.

(a) Comparison Between Record Modification Methods: Method A vs. Method B

For each earthquake record in Table 6.3 the modification method was determined on a case by case basis. In some cases Method A proved more effective than Method B and visa versa.

- Method B appears more attractive as it retains more of the earthquakes intensity when compared to Method A. However, for minor truncations in the velocity, Method A will suffice.
- Method A is computationally simpler than Method B.
- In some cases, for large truncations of the velocity, the baseline correction required of Method B can exceed the displacement capacity of the shake-table.

Table 6.4 summarises the modification method used for each record. Also shown in the same table is the peak velocity and acceleration before and after modification. The Northridge record underwent the largest reduction in peak velocity of 26%. It can be

[1] Dr. Kerry Mulligan, Department of Mechanical Engineering, University of Canterbury
[2] Geoffrey Rodgers, Department of Mechanical Engineering, University of Canterbury

seen that while the velocity was significantly reduced, the peak ground acceleration was only slightly reduced, thus retaining much of the original intensity.

Table 6.4: Record modification methods used showing the peak input velocity before and after modification

	Earthquake Event	Modification method	Max velocity before (mm/s)	Max velocity after (mm/s)	Max accel before (g)	Max accel after (g)
2/3MCE_FF	Kobe	-	159	159	0.256	0.256
2/3MCE_NF	Loma Prieta	B	236	230	0.220	0.217
MCE_FF	Cape Mendocino	A	251	232	0.382	0.375
MCE_NF	Northridge	B	306	226	0.364	0.359

A comparison between the acceleration response spectra, before and after modification, is presented in Figure 6.10 for the two MCE ground motions. For the Cape Mendocino record (far-field), the response of the original and modified record is very similar. This is because only a small amount of velocity is truncated within the modified record (251mm/s reduced to 232mm/s). The response spectrum of the Northridge record (near-field) is significantly modified (peak ground velocity is reduced from 306mm/s to 226mm/s). For the Northridge record, this resulted in an obvious difference in the response spectrum before and after modification. A large reduction in spectral acceleration occurs over a period range of 0.5sec to 1.0sec, coinciding with the operating period range of the prototype test system. A reduction in spectral acceleration can also be seen within the high frequency range of Figure 6.10 (less than 0.25sec). The Northridge record required a large reduction in peak velocity and for this reason Method B was preferred over Method A as it retained more of the earthquake's original intensity.

The displacement, velocity and acceleration time histories for the two MCE records are graphed in Figure 6.11 comparing the difference in time history before and after the record modification. As expected from the response spectrum analysis of Cape Mendocino in Figure 6.10 (a), it is difficult to detect any differences within the velocity or acceleration trace between the original and modified record. The velocity of the Cape Mendocino record was truncated from 251mm/s to 232 mm/s at a time of approximately 17sec.

The Northridge record shows an obvious difference within the displacement and velocity trace before and after modification. While it is difficult to detect any significant difference within the acceleration-time domain, it is not until a response spectrum analysis is carried out that the difference becomes more evident (refer Figure 6.10 (b)). The velocity of the Northridge record was truncated at approximately 17sec, while the lost ground intensity was relocated within the next velocity cycle between 17sec and 18sec (as per Method B).

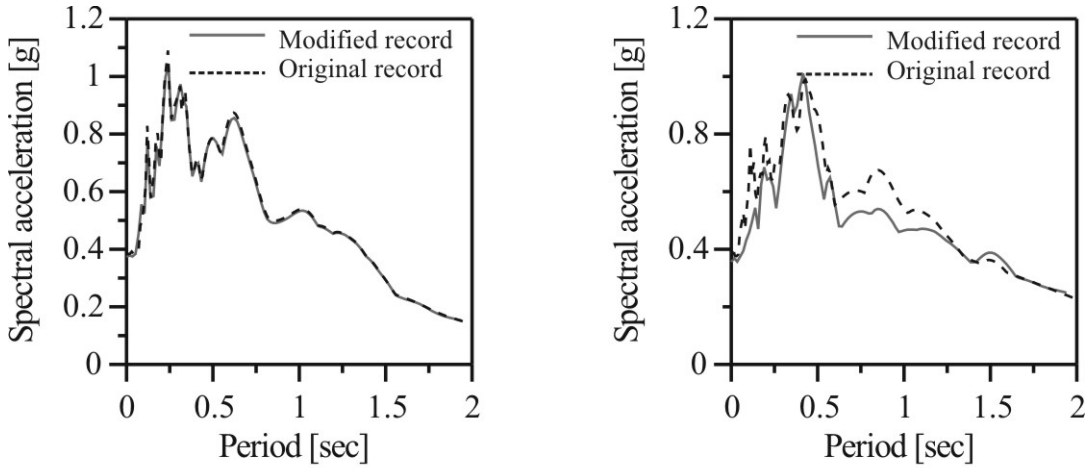

(a) Cape Mendocino (MCE-FF) (b) Northridge (MCE-NF)

Figure 6.10: Comparison of the response spectra between the original and modified record

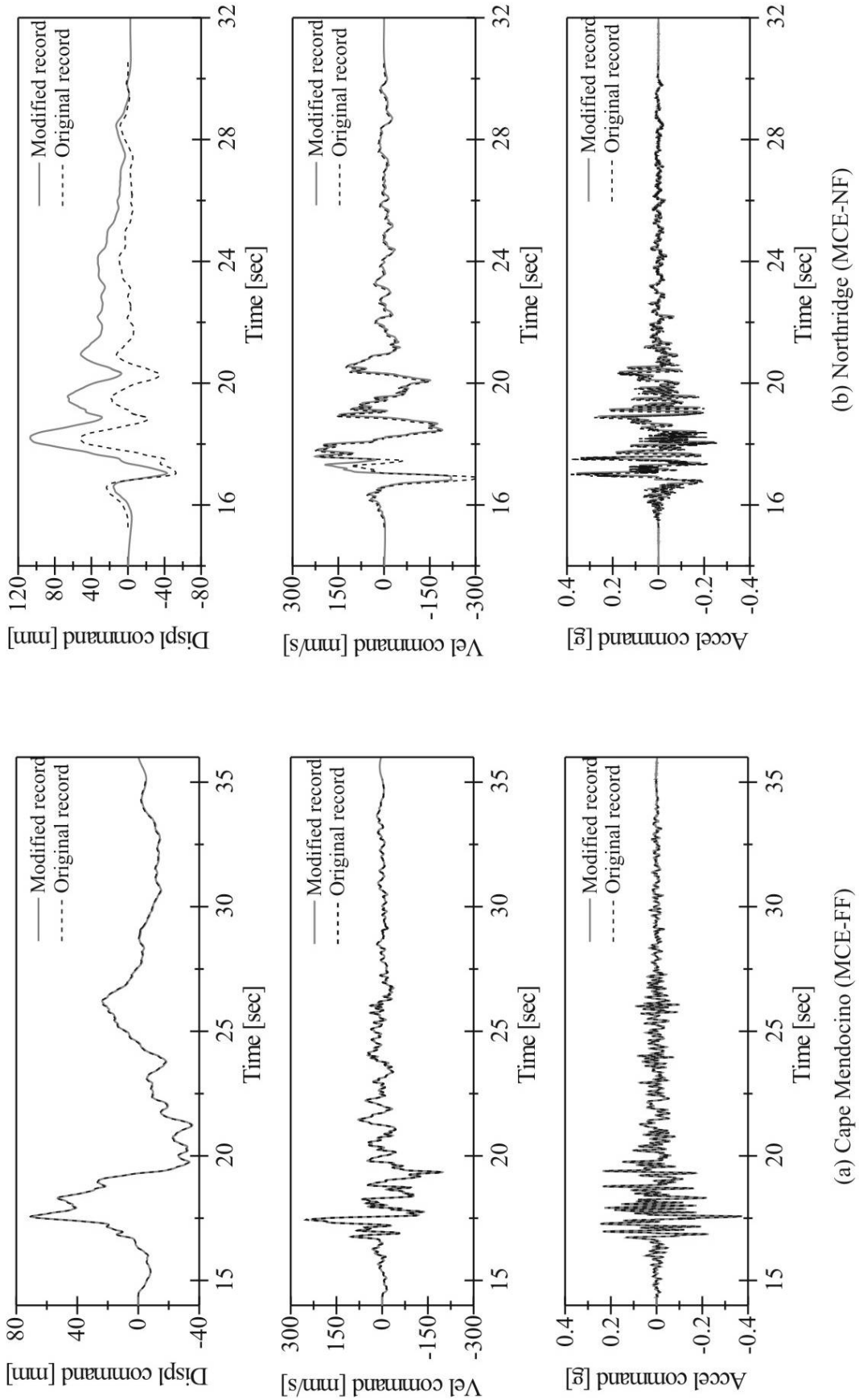

Figure 6.11 Comparison of the response spectra between the original and modified record

6.5.2. Similitude Scaling for Dynamic Testing

The velocity limitation of the shake table meant that similitude scaling had to conform to a constant stress, constant acceleration law. The scale factors for this law are summarised in Table 6.5. The subscript ***T*** refers to the laboratory test specimen, while the subscript ***P*** refers to the full scale prototype specimen. The length scale factor is defined as λ, in which all other scaled parameters can be related to.

Table 6.5 Similitude scaling factors for shake table testing

Parameter	Unit	Test-to-Prototype relationship	Test-to-prototype scale factor
Stress, σ	σ	$\sigma_T=\sigma_P$	1
Acceleration, α	a	$a_T=a_P$	1
Length, L	L	$L_T=\lambda L_P$	λ
Force, F	$F=\sigma L^2$	$\sigma_T L_T^2=\sigma_P \lambda^2 L_P^2$	λ^2
Moment, M	M=FL	$F_T L_T=\lambda^2 F_P \lambda L_P$	λ^3
Mass, m	m=F/a	$F_T/a_T=\lambda^2 F_P/a_P$	λ^2
Mass density, ρ	$\rho=m/L^3$	$m_T/L_T^3=\lambda^2 m_P/(\lambda^3 L_P^3)$	$1/\lambda$
Time, T	$T=(L/a)^{0.5}$	$(L_T/a_T)^{0.5}=(\lambda L_P/a_P)^{0.5}$	$\lambda^{0.5}$
Velocity, v	v=L/T	$L_T/T_T=\lambda L_P/(\lambda^{0.5} T_P)$	$\lambda^{0.5}$
Weight, W	W=F	-	λ^2

6.5.3. Performance and Tuning of the Shake Table

(a) Table Tuning and Tracking

Preliminary shake table testing indicated a number of abnormal behavioural characteristics of the table. The most significant abnormality was the table's inability to correctly track the displacement command during the rocking response of the wall. In particular, while the table was able to accurately track the displacement command when the table velocity was large, tracking became more of an issue when trying to command small displacements of the table during periods of low velocity. Table tracking was not an issue when the post-tensioned wall was removed from the table. The rocking impact of the wall appeared to significantly interact with the table response, making it difficult to control.

In an effort to improve table control, a sensitivity study was undertaken to investigate how the table would respond to varying table control parameters. In particular, the proportional ***P*** and integral ***I*** gain control within the shake table control software were explored. Previous studies investigating shake table control had found that the table could be controlled with reasonable accuracy with ***P*** = 10 and ***I*** = 1.0, Chase et al. [2005]. However, this study was carried out with no structure on the table. The study discussed in this section was carried out with the post-tensioned wall located on the table in order to include the effects of table-structure interaction. No damping devices were attached to the post-tensioned wall.

The results from the parametric study are presented in Figure 6.11 showing two excitation time interval windows. The response under the default values of

proportional and integral gain controls are shown in Figure 6.11 (a), where $\boldsymbol{P}$ = 1-0 and $\boldsymbol{I}$ = 1. The first time window is from 26sec to 27sec during a period of low velocity, while the second window is from 29sec to 37sec at the end of the record. When the velocity (displacement gradient) is low, it is possible to observe the rocking interaction: a secondary wave form appears to be superimposed on top of the desired displacement command in Figure 6.11 (a). What is more disturbing is the behaviour between 29sec and 37sec at the end of the earthquake record in Figure 6.11 (a). As the displacement and velocity approach zero the table begins to interact significantly with the post-tensioned wall. The displacement amplitude of the wall and the table increase as the system is put into resonance.

The table-structure interaction was reduced significantly when the integral grain was lowered to $\boldsymbol{I}$ = 0.4. Some interaction is still observed during both time windows in Figure 6.11 (b), but the response is significantly improved: the resonance has been almost completely removed at the end of the record, allowing the response of the wall to naturally decay to zero. Further reducing the integral gain to $\boldsymbol{I}$ = 0.3 in Figure 6.11 (c) resulted in better results than the original value of $\boldsymbol{I}$=1.0, but was less effective than $\boldsymbol{I}$ = 0.4.

Figure 6.11 (d) shows that increasing the proportional gain to $\boldsymbol{P}$ = 12 with $\boldsymbol{I}$ = 0.3 gave some improvement to tracking during the first time window. In addition to altering the gain parameters, a single low amplitude sine wave with a wave length of one second was added to the end of the record. This was to encourage the table to track a non-zero command displacement and prevent interaction. However, the added sine wave had little effect in controlling table interaction.

The investigation was further complicated in that the interaction was also dependant on the initial stiffness/strength of the post-tensioned wall. Reducing the initial post-tensioning from 100kN (50kN per tendon) to 60kN (30kN per tendon) resulted in chaotic resonance where wall displacement amplitudes approached almost 30mm. However, with this said, an intermediate level of post-tensioning equal to 80kN (40kN per tendon) resulted in almost zero interaction.

From this study, it was concluded that it would be very difficult, if not impossible, to determine a set of generic control parameters to satisfy any situation. It was to this end that the control parameters were fixed at $\boldsymbol{P}$ = 10 and $\boldsymbol{I}$ = 0.4 for the remainder of the shake table test program.

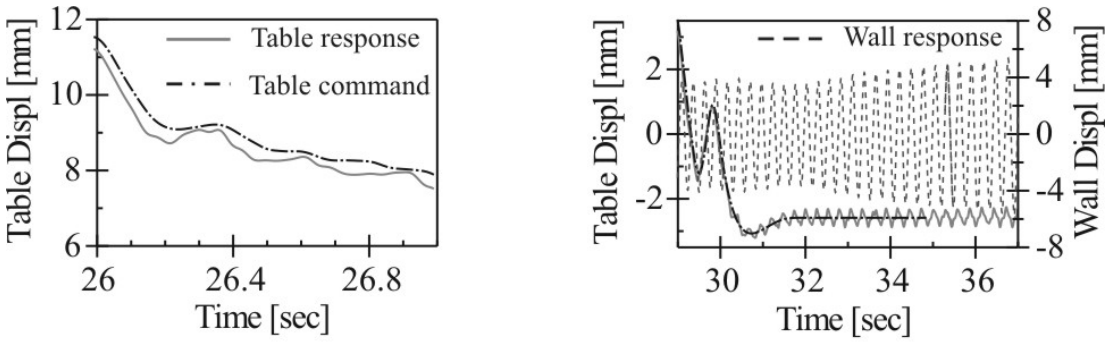

(a) P=10, I=1.0

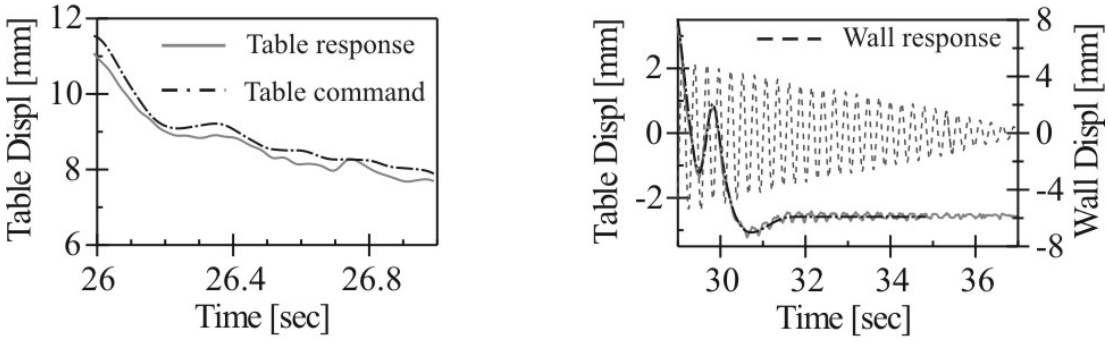

(b) P=10, I=0.4

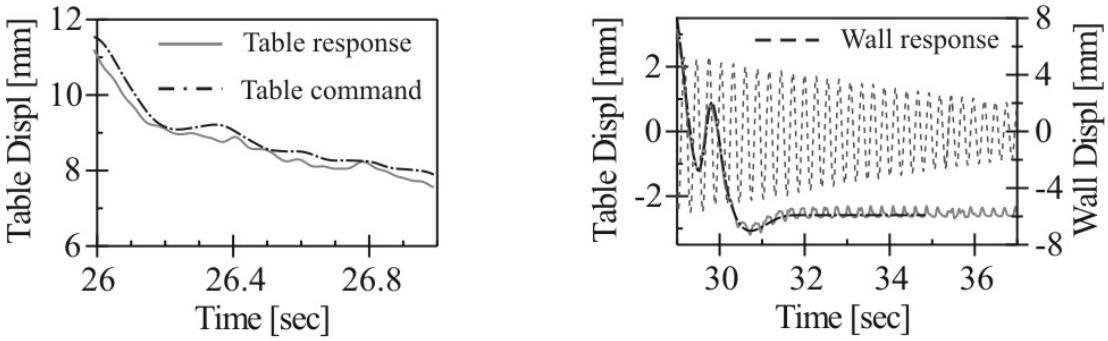

(c) P=10, I=0.3

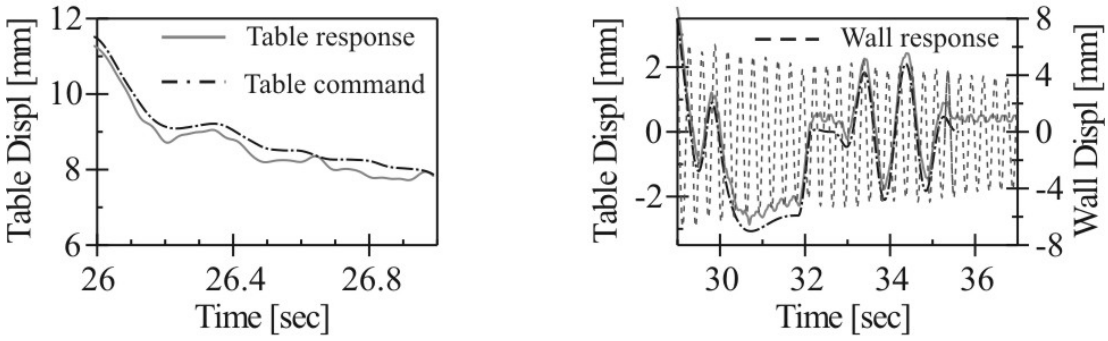

(d) P=12, I=0.3

Figure 6.12 Shake table tuning investigation with Wall 1

(b) Table Tracking of Small Displacements and Lead-In Period

A second investigation on the shake-table was carried out to determine how well the shake table could track small displacement amplitudes in the order of ±1mm (considering the bare table alone). From the previous investigation, it was felt that the table may have lacked the resolution to control the table-structure interaction.

A comparison between the table command and table response is presented in Figure 6.13 for a low amplitude sine wave varying in displacement amplitude from 0.25mm to 1.0mm and excitation frequency from 1Hz and 3.66Hz. Two important properties of the table were found. The first was that the table was able track the small displacements with reasonable accuracy. The second important point indicated that there was a long period of time at the beginning of the displacement command where the table was immobile: that is, no attempt was made by the table to track the displacement command. The solid black arrow in Figure 6.13 indicates the point in time at which the table suddenly began to track the displacement command. The implication being that large table accelerations were generated as the table suddenly began to track. This behaviour had actually been recognised in previous shake table studies[3]. The recorded acceleration response of Figure 6.13 (b) shows an acceleration spike at the instant the table begins to track. However, as the command sine wave was only 0.5mm in amplitude, the magnitude of the acceleration spike was low. From the information gathered in this study, in order to prevent large acceleration spikes at the beginning of the displacement command, a series of low amplitude, low frequency, sine waves were added to the beginning of every table command. This initiated table tracking and reduced the magnitude of the unavoidable acceleration spike.

Preliminary testing also revealed movements of the shake table bulkhead relative to the laboratory strong floor. During free-vibration testing bulkhead displacements in the order of 1.1mm were measured relative to the laboratory floor. The sliding of the table relative to the strong floor further complicated the ability of the table to track the displacement command. It was felt that little could be done to resolve each of the table issues discussed above due to the limited time and resources available. Given that every effort was undertaken to measure and control the table abnormalities, useful data could still be successfully obtained from the shake table testing of the post-tensioned walls.

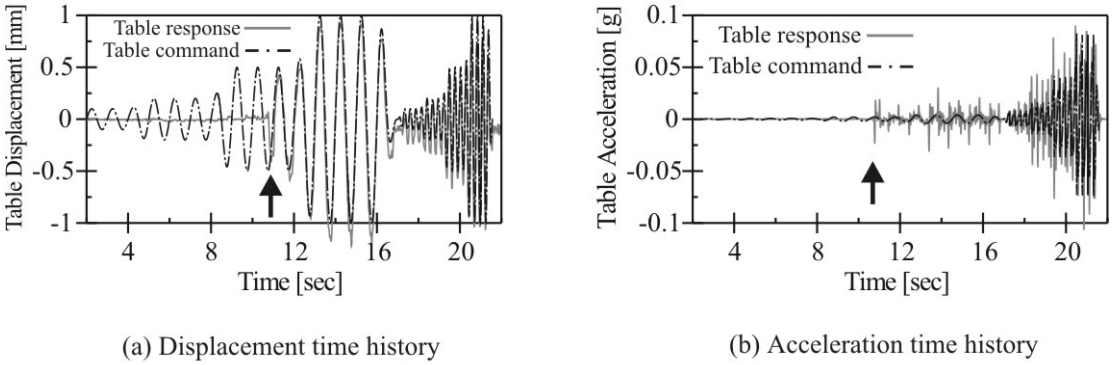

(a) Displacement time history

(b) Acceleration time history

Figure 6.13 Lead-in behaviour of the shake table

[3] Geoffrey Rodgers, Department of Mechanical Engineering, University of Canterbury

6.6. EXPERIMENTAL RESPONSE

6.6.1. Free Vibration Release Tests

The theoretical concept describing the conservation-of-energy under free vibration is illustrated in Figure 6.14 for a generic elastic (non-linear or linear) system with viscous damping. The initial input energy $E_{initial}$ is equal to the stain energy at the time of release $E_{SE}(t = 0)$ and remains constant for all time. During each cycle, the energy of the system interchanges between strain energy (related to the instantaneous displacement of the system) and kinetic energy (related to instantaneous velocity of the system). Concurrently, energy is lost from the system. This is defined as viscous energy dissipation and is proportional to the instantaneous velocity of the system. As the kinetic energy reduces, the rate at which energy is removed from the system also decreases. As all of the input energy is converted to viscous energy dissipation, the displacement and velocity approach zero (asymptotically).

In the following section conclusions are made on the behaviour of only two post-tensioned walls. The remaining test results are compared to an analytical model in Chapter 7. The free vibration response of Wall 1 and Wall 2, when released from two drift ratios (0.5% and 2.5%), is shown in Figure 6.15 and Figure 6.16 respectively. Within each figure, four relationships are plotted: the displacement decay of the wall with time, the lateral force-displacement response of the wall, the absolute input and kinetic energy of the wall and the table displacement response. During release of Wall 1 in Figure 6.15, the shake table reacted with a displacement of 1.0-1.5mm in amplitude. Thereafter, the table began to resonate as it struggled to control the energy being returned from the rocking wall: the amplitude of these table displacements are of approximately 0.5mm. This table movement modifies the input energy to the system. The kinetic and input energy is graphed in Figure 6.15 (a) & (b) indicating that the input energy is not constant over time, but fluctuates during the rocking response of the wall. Depending on whether the table oscillates in-phase or out-of-phase with the wall, input energy is added to, or removed from the system respectively. In particular, input energy in Figure 6.15 (a) is removed from the system; in this case, the table motion is out-of-phase with the wall response. This has the effect of over-damping the response and gives a false sense of energy dissipation. The energy plot of Figure 6.15 (b) indicates that the table interaction added input energy to the system; in fact, this was the case for most of the tests. Adding input energy to the free vibration decay has the effect of under-damping the system and lengthens the time for the response to decay.

Two of the free-vibration tests carried out on Wall 2 (combining post-tensioning with fluid viscous dampers (FVD)) are presented in Figure 6.16 for drift ratios of 0.5% and 2.5%. During each free vibration test the table still interacted with the post-tensioned wall. As the wall was released the table was subjected to an initial displacement pulse similar in magnitude to that measured immediately after the release of Wall 1 (1.0-2.0mm); however, the magnitude of the table displacements following initial pulse are smaller than those measured during testing of Wall 1. Consequently, table-structure interaction was reduced; that is, less input energy was added to (or removed from) the system during the testing of Wall 2. During each cycle a larger amount of energy was dissipated by the FVDs. This minimised the amount of potential energy that could be transmitted back into the shake table. As a result, the damped response was more regular for Wall 2 and decayed at a more natural rate with less table interaction.

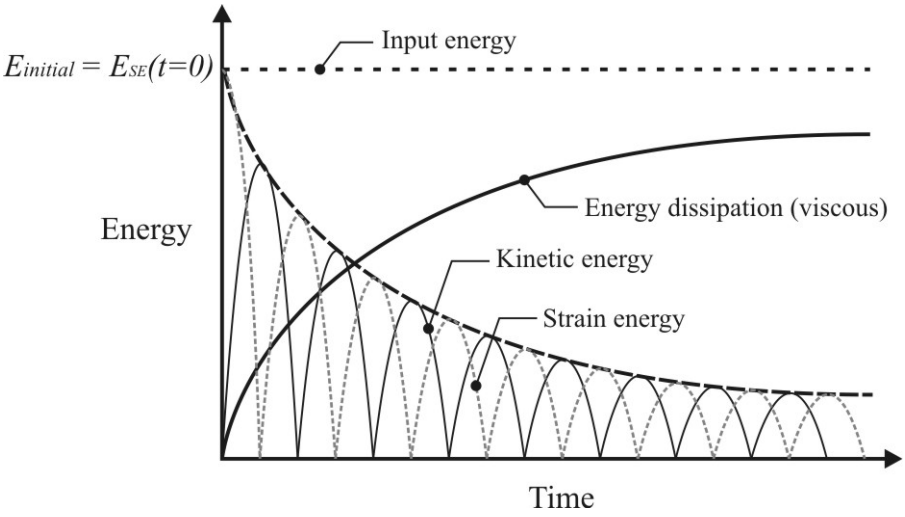

Figure 6.14 Conservation of energy (absolute) under free vibration for an elastic system

The hysteretic (force-displacement) behaviour of Wall 2 in Figure 6.16 indicates that only a modest amount energy is dissipated during each cycle owing to the sloppy behaviour of the fluid viscous dampers (FVDs). As discussed previously, excessive clearances within the ball-joint connections at each end of the viscous dampers resulted in a pinched hysteretic response. The pinched response was more evident during the smaller displacement cycles of Wall 2 in Figure 6.16 (a).

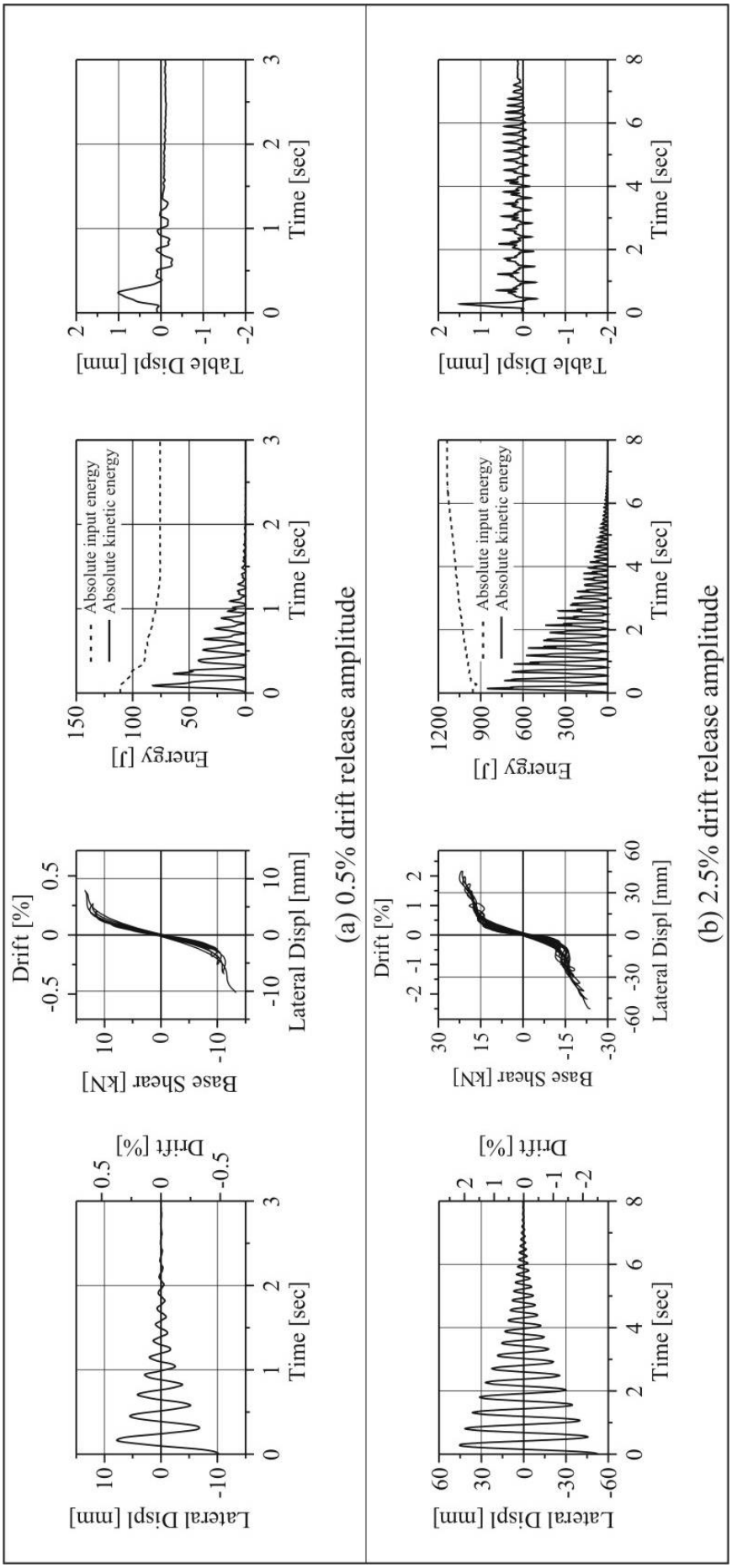

Figure 6.15 Free vibration response of Wall 1

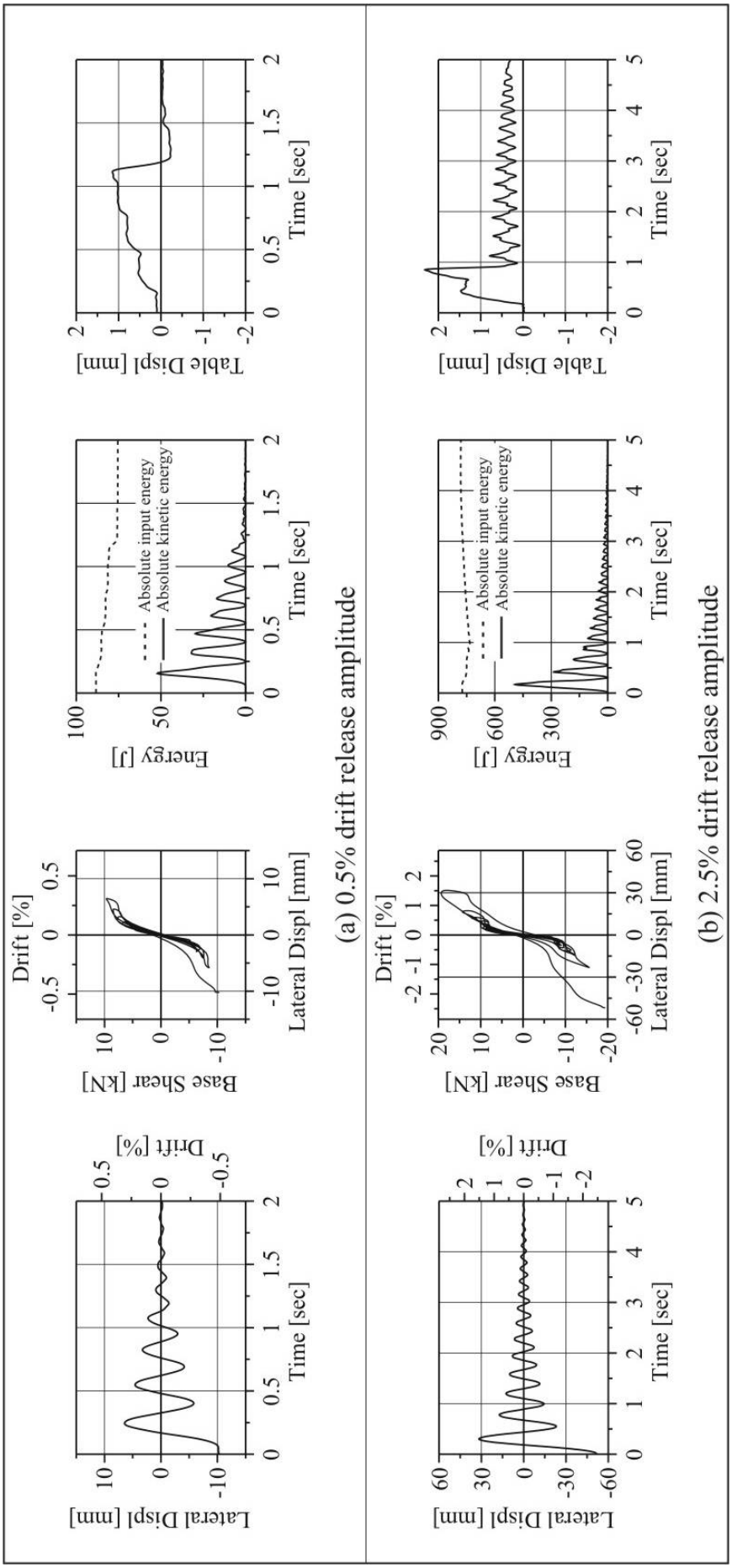

Figure 6.16 Free vibration response of Wall 2

6.6.2. Energy Balance Considerations

The illustration in Figure 6.17 summaries the energy balance of a generic hysteretic yielding system indicating that the total dissipated energy is a combination of irrecoverable strain energy (hysteretic energy dissipation) and viscous energy dissipation (non-hysteretic energy dissipation). The remaining energy is interchanged between recoverable strain energy and kinetic energy. It is possible to compute the experimental hysteretic energy dissipation by integrating the total strain energy throughout each cycle; however, the integral can be dependant on the noise of the data and the type of filter used during post-processing. Errors can accumulate during numerical integration of the strain energy over each cycle and the data can become meaningless. Nevertheless, the three components of energy are computed (strain energy, kinetic energy and input energy) for all five post-tensioned walls subjected to free-vibration testing at a drift of 1.5% and graphed in Figure 6.19. The energy balance of Wall 1 differs substantially from the other three walls. In Chapter 5 the high-speed cyclic testing of an identical post-tensioned-only wall was characterised by a near-perfect non-linear elastic response: that is, no hysteretic damping took place during cyclic loading. If the integration of strain-energy is correct, then Figure 6.19 indicates that a large amount of irrecoverable (hysteretic) strain energy developed. This is more likely a result of numerical integration error due to the violent nature of the test. In fact, in Section 6.8, data is presented showing high frequency horizontal acceleration spikes that were measured during rocking. These horizontal base shear spikes will add to the numerical integration error when evaluating the strain energy. The actual decay was more likely attributed to micro crushing of dislodged concrete and grout particles beneath the rocking interface. A dust plume was visible up the toe of the post-tensioned wall suggesting this was the case, pictured in Figure 6.18.

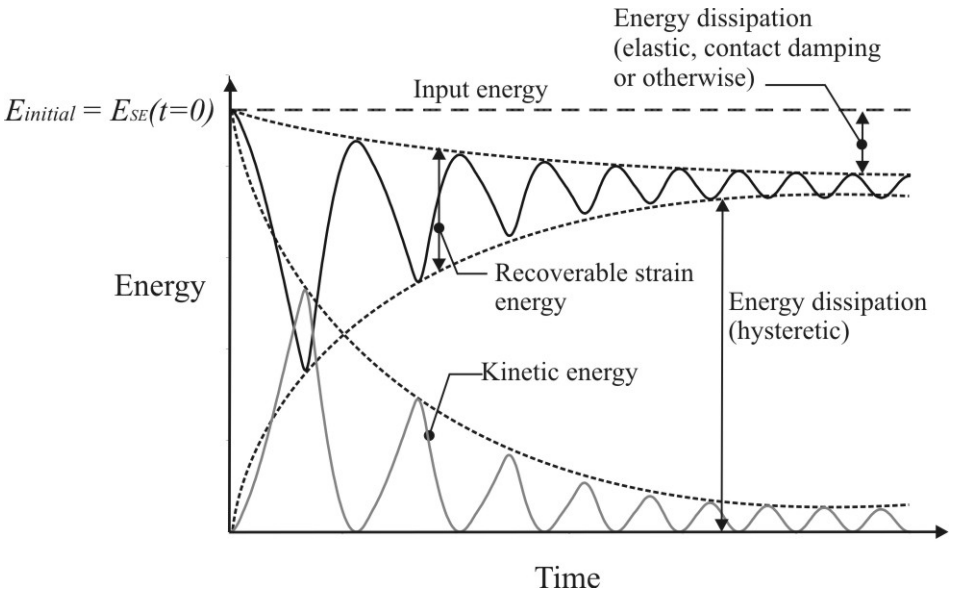

Figure 6.17 Energy balance concept for hysteretic yielding systems with elastic viscous damping

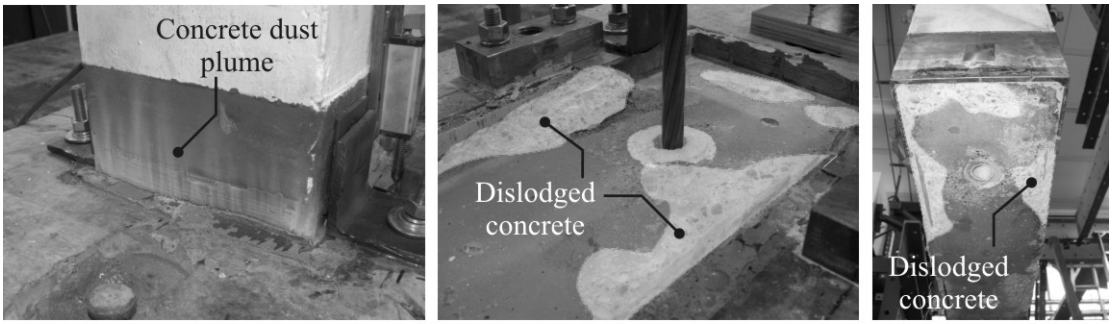

(a) Concrete plume at toe

(b) & (c) Crushing of the dislodged concrete beneath the post-tensioned wall (shaded)

Figure 6.18 Crushing of dislodged concrete beneath the rocking wall

Testing of the highly damped walls (Wall 2 and Wall 3) was less violent and more confidence could be placed on the numerical integration of the measured strain energy. In contrast to Wall 1, the free vibration tests of Wall 3 and Wall 4 illustrate that almost all of the damping results from irrecoverable hysteretic energy dissipation. The hysteretic damping was so dominant within Wall 3 and Wall 4, and the displacement decayed at such a great rate, there was less opportunity for contact damping to occur. The displacement response of Wall 2 decayed over a relatively long period of time due to the poorly performing FVD devices. It is likely that contact damping was a contributing factor to the total damping within Wall 2 as more rocking cycles developed over time. Similar conclusions are made with regards to Wall 5 in that the lower (mechanical) damping content allowed more rocking cycles to develop over time, thus contact damping was likely to be significant within Wall 5.

Due to the difficulty in being able to very accurately compute the strain energy for each post-tensioned wall, it was not possible to disaggregate the total dissipated energy into actual hysteretic (mechanical) dissipation and energy dissipation associated with non-hysteretic damping (contact damping or otherwise).

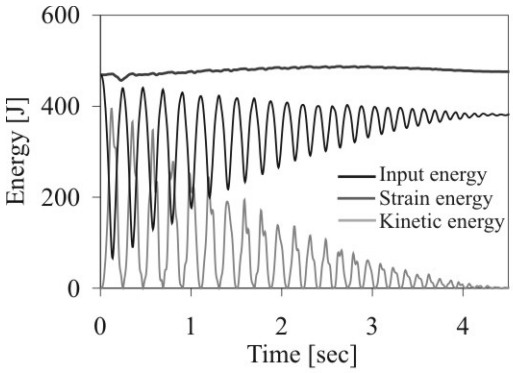

(a) Wall 1: No devices

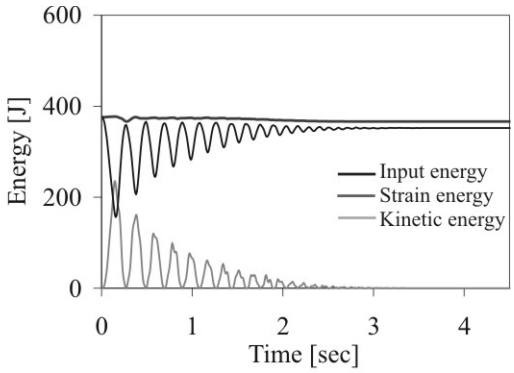

(b) Wall 2: FVD devices

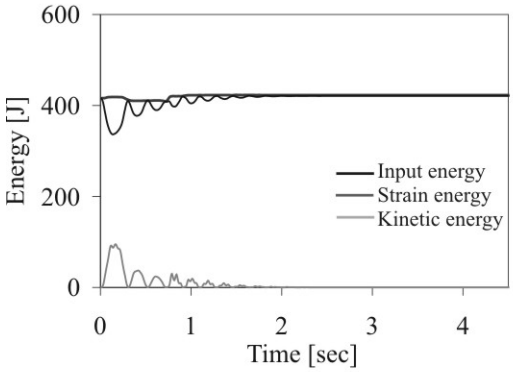

(c) Wall 3: FVD plus TCY devices

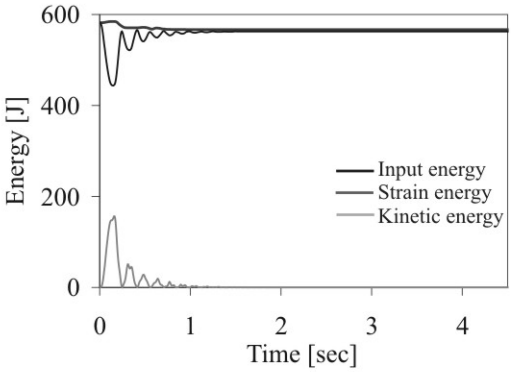

(d) Wall 4: TCY devices

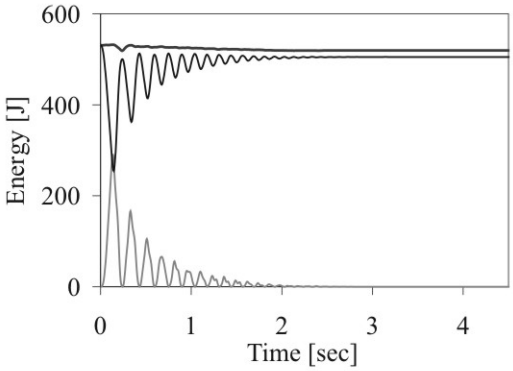

(e) Wall 5: TCY devices

Figure 6.19 Energy balance (absolute formulation) under free vibration at 1.5% drift

6.6.3. Earthquake Excitation

The maximum response parameters (base shear V_{max}, relative wall displacement Δ_{max} and drift ratio, relative wall velocity v_{max} and absolute wall acceleration a_{max}) are summarised in Table 6.6 for each post-tensioned wall under each of the four ground motions. The near-field records were significantly less demanding on each of the post-tensioned walls when compared to the far-field records of similar spectral intensity (i.e. DBE and MCE intensity). Reasons for this were discussed in Section 6.4.1 where table limitations prevented intense near-fault records (with strong directivity effects) from being used. The maximum base shear demand was similar for each of the five walls as each wall was designed to have similar lateral capacity at a drift ratio of 1.5%.

The velocity dependency of the FVDs was minimal ($\alpha = 0.15$) which meant the dynamic properties of the FVDs were more akin to a hysteretic device. It is for this reason that Wall 2, being purely viscous (highly non-linear viscous), had trends that were similar in nature to the hysteretic post-tensioned walls. Wall 3 and Wall 4 were the most effective post-tensioned wall systems: the peak displacement response was consistently low, and the high level of structural damping ensured peak accelerations were also low. Contrary to this, Wall 1 generally returned the largest peak displacement and acceleration; however, it still satisfied the target drift ratio of 1.5% when subjected to ground motions that were scaled to the MCE seismic intensity. Accelerations were higher for Wall 1 because the system had very little damping; hence, if slightly greater accelerations can be tolerated Wall 1 is a viable system.

Table 6.6 Maximum Base shear, displacement (drift ratio in brackets) and acceleration response of the five post-tensioned walls during the 2/3MCE and MCE scaled ground motions

		Wall 1	Wall 2	Wall 3	Wall 4	Wall 5
	Devices	-	4xFVD	4xFVD 2xTCY	4xTCY	2xTCY
DBE-NF	V_{max} [kN]	10.38	10.40	12.35	9.62	11.57
	Δ_{max} [mm]	2.89 (0.14%)	8.06 (0.38%)	9.09 (0.43%)	3.87 (0.18%)	4.71 (0.22%)
	v_{max} [mm/s]	68.2	162.2	155.4	81.0	103.2
	a_{max} [g]	0.518	0.324	0.372	0.295	0.306
DBE-FF	V_{max} [kN]	16.77	14.69	14.88	15.46	14.76
	Δ_{max} [mm]	22.35 (1.06%)	17.97 (0.86%)	12.91 (0.61%)	8.02 (0.38%)	8.48 (0.40%)
	v_{max} [mm/s]	389.7	271.8	239.2	161.1	198.9
	a_{max} [g]	0.468	0.409	0.413	0.431	0.404
MCE-NF	V_{max} [kN]	16.00	14.00	13.62	16.51	17.82
	Δ_{max} [mm]	20.39 (0.97%)	16.56 (0.79%)	12.45 (0.59%)	13.13 (0.63%)	15.96 (0.76%)
	v_{max} [mm/s]	378.0	282.7	251.5	229.9	295.2
	a_{max} [g]	0.473	0.372	0.389	0.446	0.499
MCE-FF	V_{max} [kN]	18.29	19.62	19.78	18.64	21.13
	Δ_{max} [mm]	27.56 (1.31%)	35.04 (1.67%)	27.63 (1.32%)	19.70 (0.94%)	28.71 (1.37%)
	v_{max} [mm/s]	422.7	416.8	317.6	249.7	371.4
	a_{max} [g]	0.518	0.591	0.575	0.537	0.617

The displacement time-history and the force-displacement response are only presented for Wall 1-4 under the two MCE level ground motions: Northridge in Figure 6.20 (near-field) and Cape Mendocino in Figure 6.21 (far-field). Sufficient information can be gathered by studying these 8 tests without graphing the remaining 12 tests. Under the MCE near-field ground motion, the response of each wall was not very demanding; the FVDs in Wall 2 were hardly activated, and while the TCY dampers in Wall 3 and Wall 4 did yield, their ductility demand was very low. The displacement demands were much greater for the Cape Mendocino ground motion in Figure 6.21. Under the Cape Mendocino record the FVDs in Wall 2 provided a good amount of damping, but the energy dissipation of Wall 3 and Wall 4 was even more significant. Even considering the large inelastic cycles developed in Wall 3 and Wall 4 during the Cape Mendocino record, the residual displacements were negligible. The benefit of using a combination of viscous and hysteretic dampers was evident at the end of the test: as the ground velocity diminished the force in the FVD approached zero. Because the force within the FVDs were zero the viscous-hysteretic wall was able to return to its original position as the capacity of the remaining TCY dampers was less than the clamping capacity provided by the post-tensioned tendons.

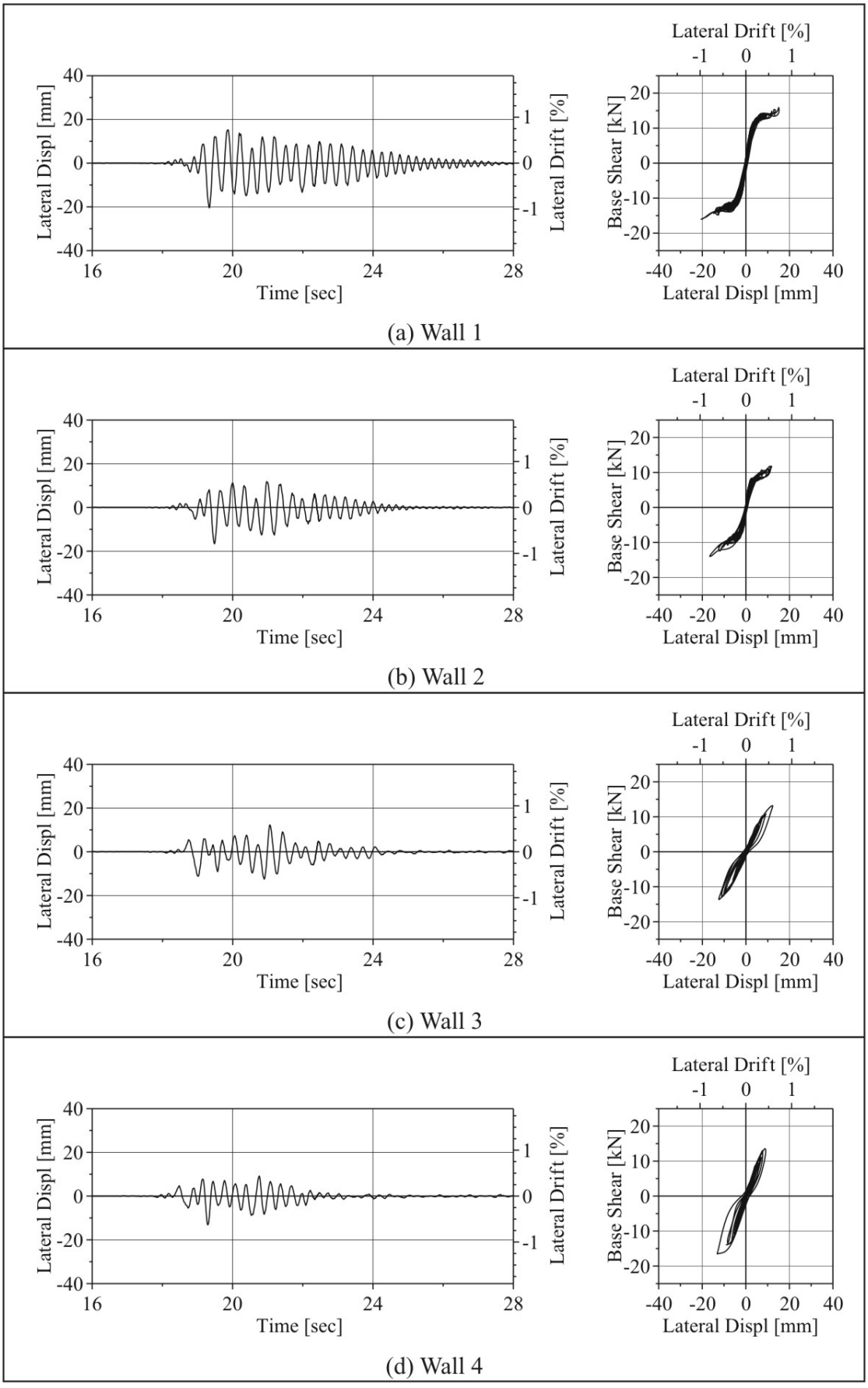

Figure 6.20 MCE response near-field (Northridge)

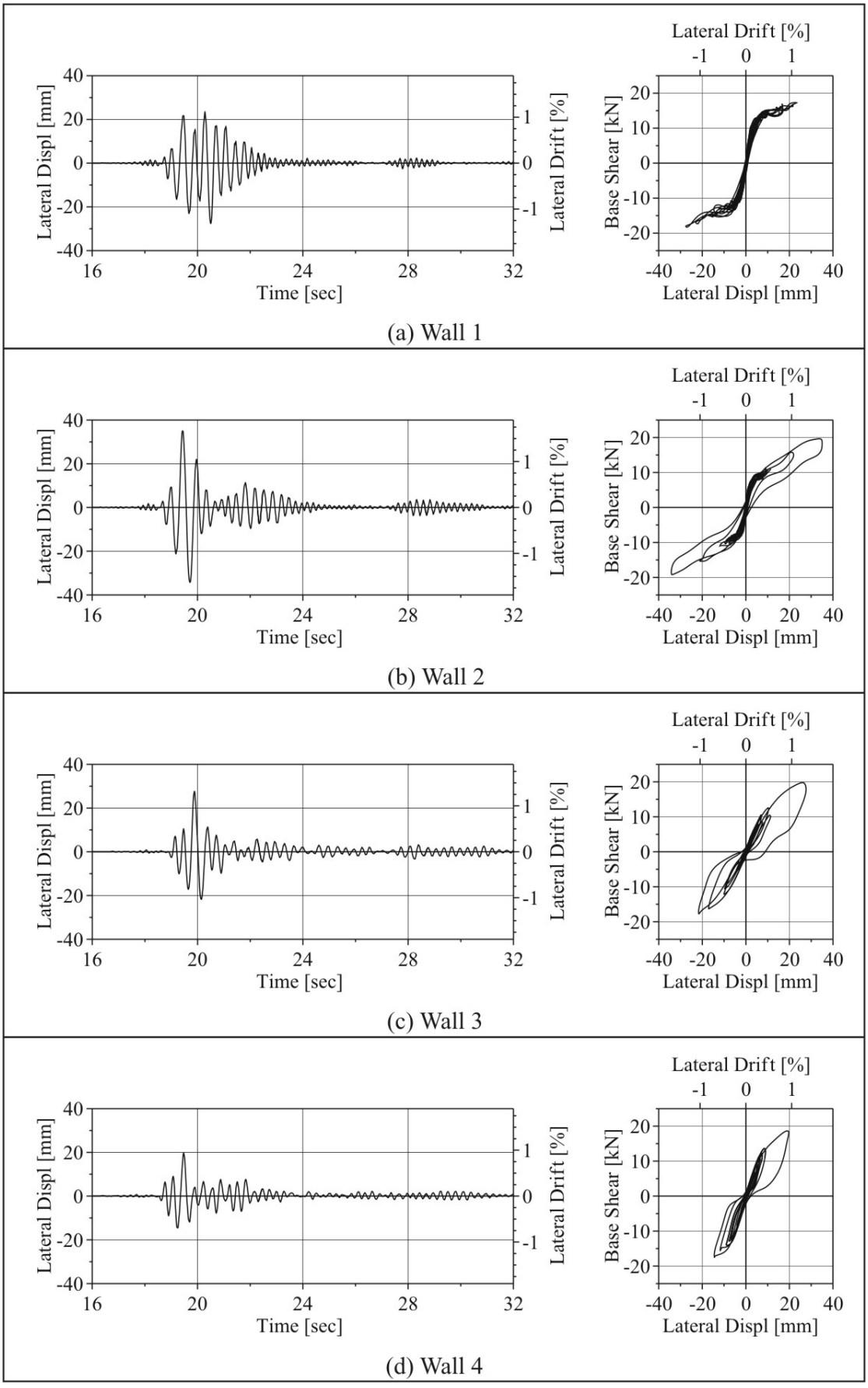

Figure 6.21 MCE response far-field (Cape Mendocino)

6.7. STRAIN-RATES

The maximum strain-rates for the hysteretic TCY dampers were recorded during free-vibration testing and during earthquake excitation and are shown for Wall 4 & Wall 5 in Table 6.7. The strain-rates are very high during free-vibration testing due to the large release displacement at a lateral drift of 2.5%. In contrast, the strain-rates measured during earthquake excitation are similar in magnitude to those recorded during the high-speed cyclic testing in Chapter 5.

Strain-rates were discussed following the high-speed cyclic testing in Chapter 5. The strain rates measured during the high-speed cyclic testing were similar in magnitude to those measured during dynamic testing herein (or only slightly larger), therefore no further discussion is justified.

Table 6.7 Maximum strain rates of the TCY dampers recorded during free-vibration testing (FV) and earthquake excitation (DBE, MCE) for Wall 4 and Wall 5

	Wall 4	Wall 5
FV 2.5%	0.586 s^{-1}	0.779 s^{-1}
FV 1.5%	0.393 s^{-1}	0.520 s^{-1}
DBE-NF	0.060 s^{-1}	0.063 s^{-1}
DBE-FF	0.165 s^{-1}	0.161 s^{-1}
MCE-NF	0.278 s^{-1}	0.348 s^{-1}
MCE-FF	0.336 s^{-1}	0.533 s^{-1}

6.8. HORIZONTAL ACCELERATIONS DURING ROCKING IMPACT

During free vibration of the post-tensioned walls high frequency horizontal accelerations develop within the wall due to the rocking impact. These acceleration spikes (hence, base shear spikes) are in the range of 50Hz-60Hz. The results presented thus far were post-processed using a 6^{th} order low-pass Butterworth filter with a cut-off frequency of 18Hz. All data was sampled at 1000Hz; however, an analogue filter was also incorporated within the computer software. This analogue filter had a passband frequency of 200Hz, corresponding to a normalised passband voltage of 0.707. It was possible to observe the horizontal acceleration spikes caused by rocking by increasing the cutoff frequency within the Butterworth filter to above 60Hz. Figure 6.22 compares the base shear versus lateral displacement of Wall 1 at three different cutoff frequencies: 25Hz, 50Hz and 100Hz. The horizontal base shear spikes become more evident as they pass through the digital filter. Similarly, when the free-vibration acceleration and displacement time-history are viewed within the first 0.6sec of release in Figure 6.23, the horizontal acceleration spikes during rocking impact are clear. A transient horizontal acceleration response appears to overlay the harmonic response in Figure 6.23. The energy associated with the high frequency acceleration spikes in Figure 6.23 (b) decays between successive rocking impacts due to material damping within the wall. At the point of release (time equal to zero), a high frequency, high amplitude acceleration signal is recorded as the load is suddenly transferred to the wall; this is not related to impact loads during rocking and should be

disregarded. When these high frequency horizontal accelerations are completely filtered with a cutoff frequency of 25Hz as in Figure 6.22 (a), the quasi-static push-over capacity of the post-tensioned wall can be observed in clarity.

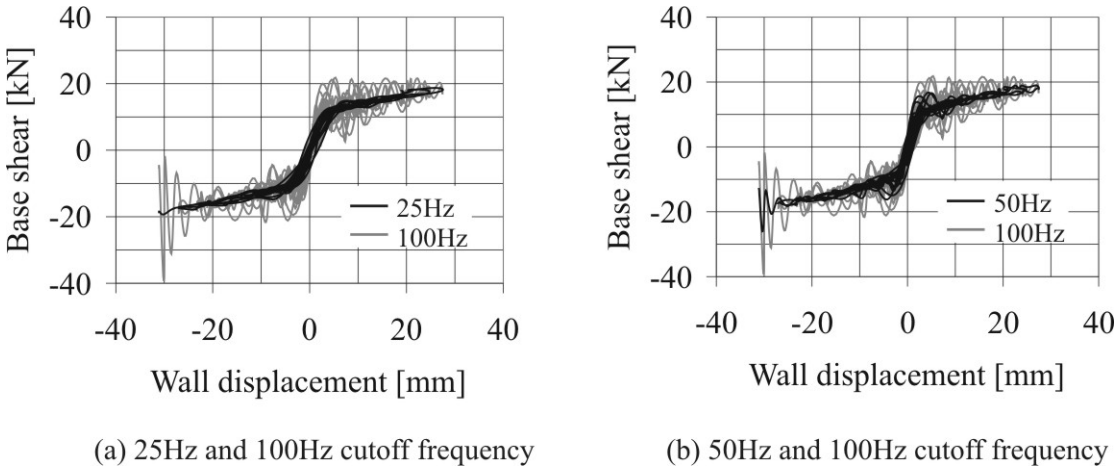

(a) 25Hz and 100Hz cutoff frequency (b) 50Hz and 100Hz cutoff frequency

Figure 6.22 Base shear spikes for Wall 1 during release testing from 1.5% drift ratio for two different Butterworth cutoff frequency filters

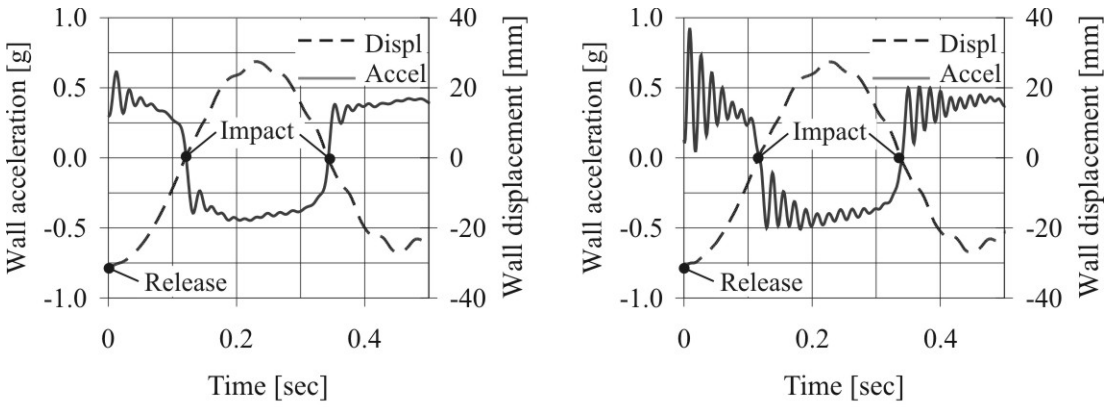

(a) 50Hz cutoff frequency (b) 100Hz cutoff frequency

Figure 6.23 Horizontal acceleration and displacement time history for Wall 1 during release testing from 1.5% drift ratio for two different Butterworth cutoff frequency filters

The horizontal acceleration spikes were significantly smaller for Wall 4 when compared to Wall 1 during free vibration (Wall 4 was the most heavily damped Wall). While some base shear spikes are still evident during impact in Figure 6.24 the magnitude and duration is significantly reduced in Figure 6.25 when compared to Wall 1 in Figure 6.23. In light of this, it would seem appropriate that the severity of these horizontal accelerations would be proportional to the magnitude of the vertical accelerations during impact (this is discussed in Section 6.9 to follow). With that noted, the vertical and horizontal acceleration spikes appear to be proportional to the mechanical damping within post-tensioned system: as the mechanical damping is

increased, the horizontal velocity demand reduces, decreasing the magnitude of the impact forces during rocking.

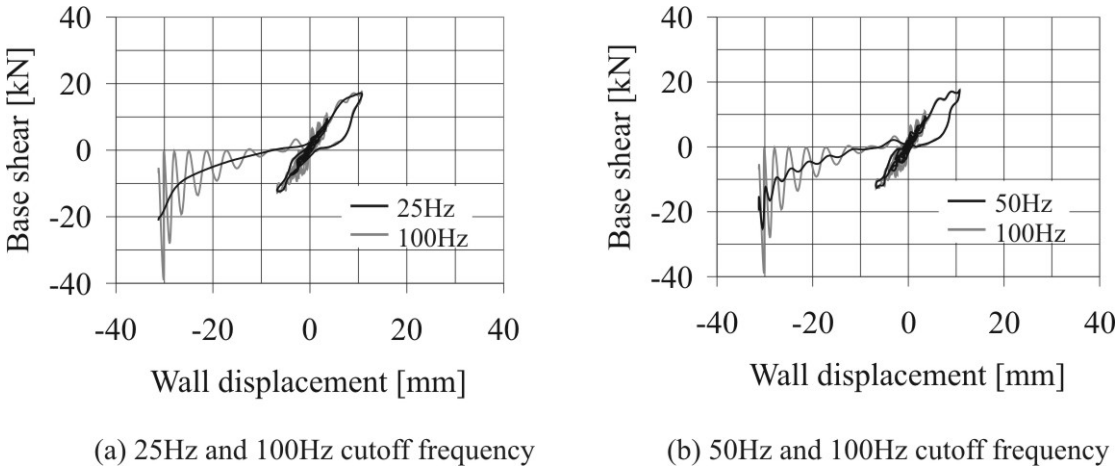

Figure 6.24 Base shear spikes for Wall 4 during release testing from 1.5% drift ratio for two different Butterworth cutoff frequency filters

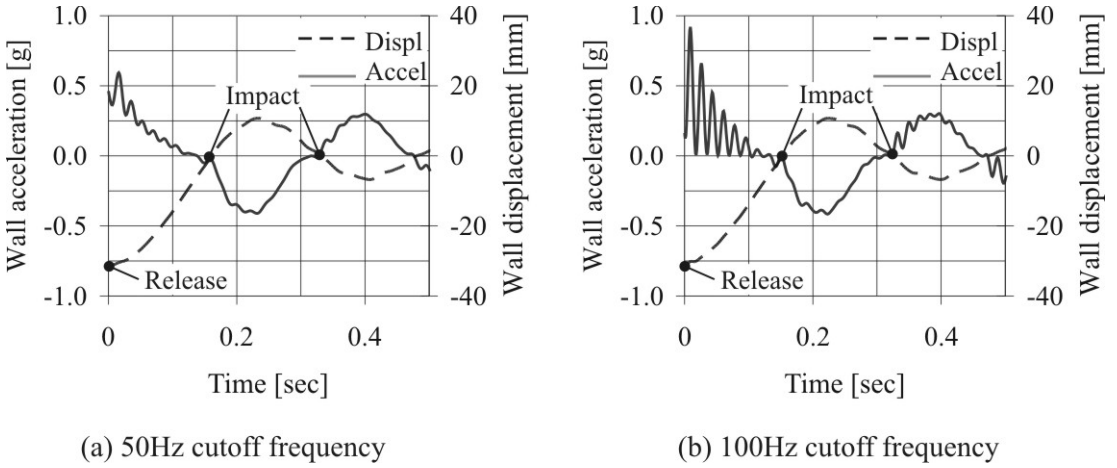

Figure 6.25 Horizontal acceleration and displacement time-history for Wall 4 during release testing from 1.5% drift ratio for two different Butterworth cutoff frequency filters

6.9. VERTICAL ACCELERATIONS DURING ROCKING IMPACT

Vertical accelerations were measured at the centre of the post-tensioned wall to capture the vertical impact loading during rocking. The vertical acceleration decay measured for each wall when released from a drift ratio of 1.5% is plotted in Figure 6.26. Positive accelerations correspond to the impact during rocking, while negative accelerations coincide with the peak vertical displacement of the wall during each cycle. The basic decay of the vertical acceleration decay takes on the same shape as the horizontal displacement and velocity decay: therefore, vertical acceleration is directly proportional to the displacement amplitude during the cycle. Furthermore, the magnitude of the vertical accelerations appears to be proportional to the level of

mechanical damping across the rocking interface. The area-based damping of each post-tensioned wall was computed in Chapter 5 which indicated that Wall 2 and Wall 3 had a similar level of damping content, while Wall 4 was more heavily damped by approximately 16% to that of Wall 3 at a drift ratio of 1.5%. As the mechanical damping increases a reduction in kinetic energy is expected as energy is removed from the system, hence the horizontal displacements and vertical accelerations during impact are expected to reduce also.

The maximum recorded vertical wall accelerations for the four ground motions are tabulated in Table 6.8. When rocking was initiated, peak vertical accelerations were in the range of 20%-60% of the horizontal acceleration. These vertical accelerations can have huge implications on the design of non-structural components in much the same way horizontal accelerations do. In general Wall 1 returns the largest peak vertical accelerations, with the exception of Wall 2 for the MCE-FF record. Specific to this ground motion the horizontal displacement demand was larger for Wall 2 than Wall 1 and so larger vertical accelerations were expected. There is a clear trend between an increased level of mechanical damping and reduced vertical accelerations.

Table 6.8 Maximum recorded vertical wall accelerations [g]

	Wall 1	**Wall 2**	**Wall 3**	**Wall 4**	**Wall 5**
Devices	-	4xFVD	4xFVD 2xTCY	4xTCY	2xTCY
DBE-NF	0.022	0.087	0.086	0.027	0.044
DBE-FF	0.271	0.196	0.160	0.080	0.110
MCE-NF	0.224	0.198	0.161	0.122	0.178
MCE-FF	0.303	0.353	0.209	0.132	0.262

The peak vertical acceleration is compared to the peak horizontal velocity in Figure 6.27. This relationship is plotted for the free vibration tests of Wall 1-5 in Figure 6.27 (a) and all four ground motions (DBE and MCE) in Figure 6.27 (b). From both of these graphs, the vertical acceleration is directly proportional to the horizontal velocity alone, and bears little relationship to the amount of damping within the wall. It can be concluded that the damped walls returned smaller vertical accelerations primarily because the peak horizontal velocity were reduced. That is, two walls with very different damping contents can experience similar peak vertical accelerations during rocking if both are subjected to similar peak horizontal velocity demands.

Based on these results it would seem logical for contact damping to be proportional to the vertical acceleration during impact. If contact damping is related to the vertical acceleration and hence, horizontal velocity as per Figure 6.27, then a pure viscous damping model would seem appropriate. However, given that velocity is also proportional to displacement, a contact damping model with damping forces proportional to both velocity (viscous) and displacement (friction) is proposed. What is uncertain is the level of viscous damping to be assigned to contact damping within the system: this is quantified in Section 6.10.

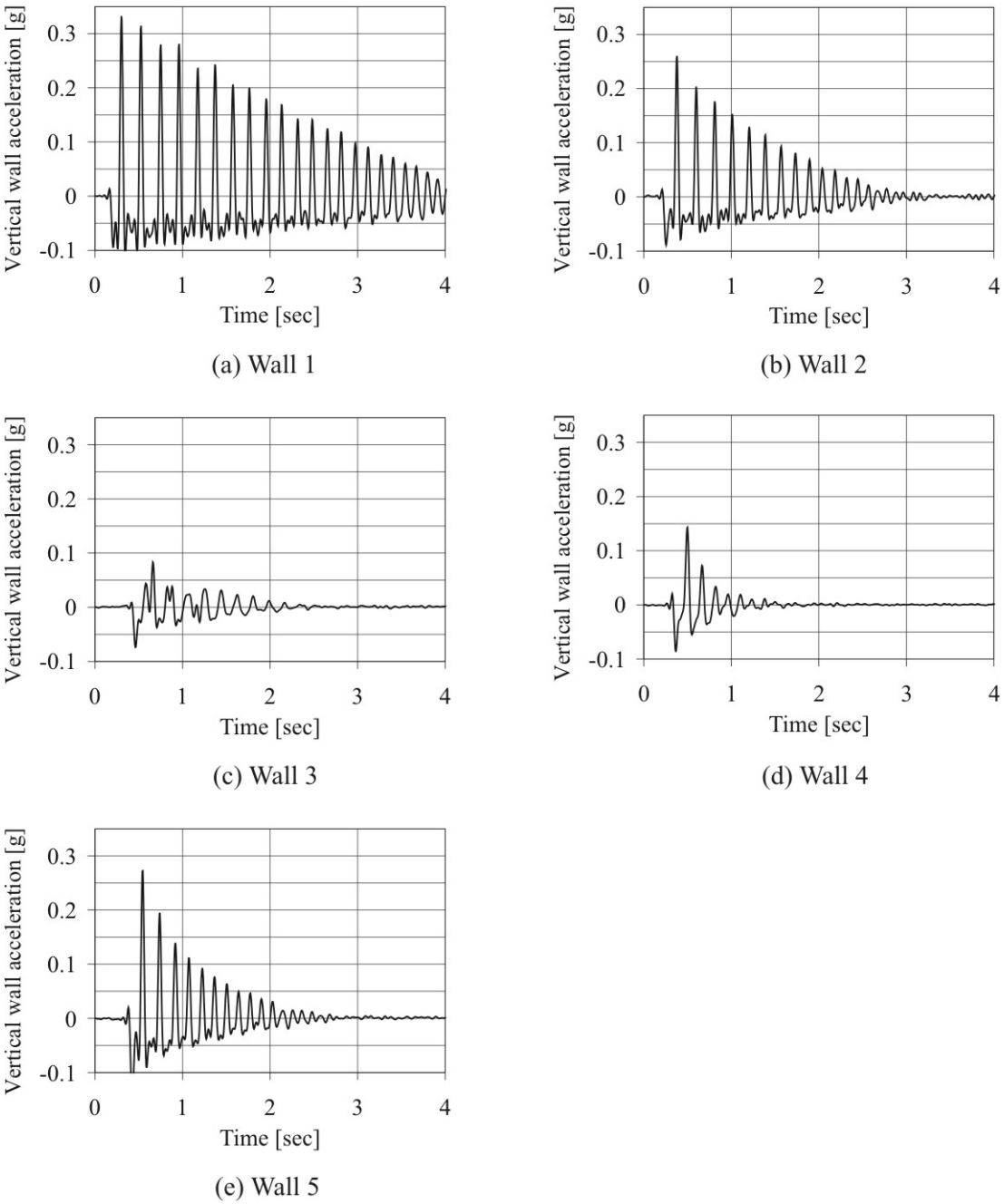

Figure 6.26 Vertical acceleration decay during free vibration, release drift ratio of 1.5%

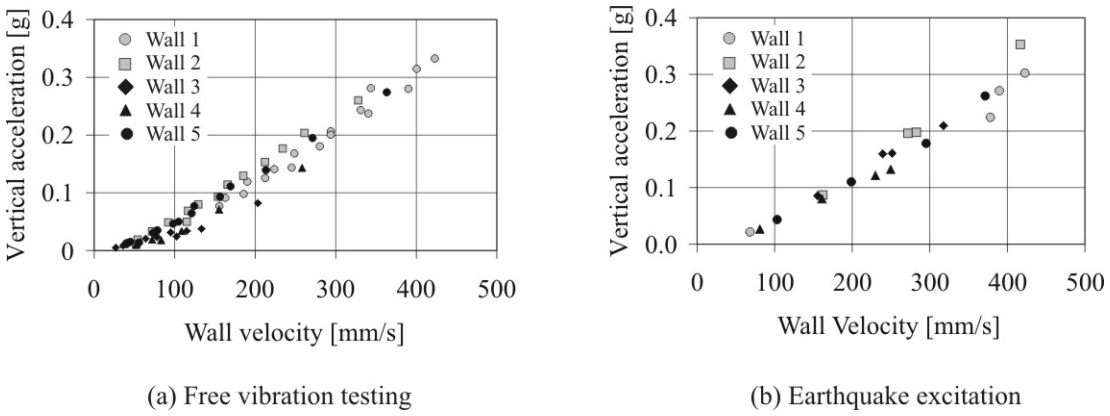

(a) Free vibration testing (b) Earthquake excitation

Figure 6.27 Relationship between horizontal velocity and vertical acceleration

6.10. ESTIMATING THE EQUIVALENT VISCOUS DAMPING ASSOCIATED WITH CONTACT DAMPING

6.10.1. Equivalent Viscous Damping Based on Pure Free-Vibration

Based on free vibration displacement decay it is possible to determine the equivalent viscous damping (elastic) of a system. For a post-tensioned only rocking system this damping is likely to be a combination of pure contact damping, material nonlinearity of the concrete at the rocking interface and intrinsic material damping of the precast element. To simply modelling these contributions are lumped together and equated as the total (elastic) equivalent viscous damping of the system. With reference to Figure 6.28, the equivalent viscous damping can be determined from Eq.(6.2) which relates the displacement ratio between ***n*** successive displacement peaks. ***T*** is the period of free vibration of the system.

$$\lambda = \frac{1}{2n\pi}\ln\left(\frac{x(t)}{x(t+nT)}\right) \qquad \textbf{6.2}$$

However, Eq.(6.2) is limited to linear elastic systems only: more specifically, elastic structures whose period remains constant with amplitude. Eq.(6.2) is only valid for non-linear elastic rocking systems when the displacement demand is within the (initial) elastic range. Furthermore, Eq.(6.2) is limited to free vibration alone. In the case where significant interaction exists between the ground (table) and the system, the input energy is not constant during free vibration and alternative methods are needed to define the equivalent viscous damping of the system.

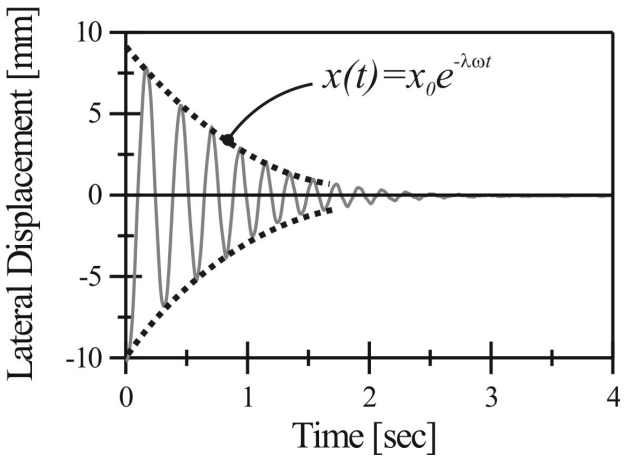

Figure 6.28 Free vibration decay

6.10.2. Equivalent Viscous Damping Considering an Energy Balance Approach

The conservation of energy for a SDOF system is given by the absolute formulation of Eq.(6.3).

$$E_{SE} + E_{VD} + E_k^{ab} = E_{input}^{ab} \qquad \textbf{6.3}$$

Where

$\boldsymbol{E_{SE}}$ = strain energy (recoverable for elastic systems)

$\boldsymbol{E_{VD}}$ = dissipated energy (energy lost from the system). For systems remaining elastic a viscous damping term is normally included to account for non-structural damping and some material non-linearity within the elastic range.

$\boldsymbol{E_k^{ab}}$ = kinetic energy of the system (in absolute terms)

E_{input}^{ab} = input energy of the system.

The system in Figure 6.29 plots the conservation of energy for a system under pure free vibration. In this case, the input energy E_{input}^{ab} is equal to the initial energy at release $\boldsymbol{E_{initial}}$. No energy is added to the system (in the form of ground excitation); therefore, the input energy remains constant with time. The incremental form of Eq.(6.3) can be written as Eq.(6.4).

$$\Delta E_{SE} + \Delta E_{VD} + \Delta E_k^{ab} = \Delta E_{input}^{ab} \qquad \textbf{6.4}$$

The mathematical formulations of each component are defined in Appendix C. The energy dissipated by equivalent viscous damping over time is given by Eq.(6.5).

$$E_{VD} = \int_0^t \{v_r(t)\}^T [c] \{v_r(t)\} dt \qquad \textbf{6.5}$$

Considering simple harmonic motion, the viscous decay curve $\boldsymbol{E_{VD}}$ in Figure 6.29 can be computed by the integration of Eq.(6.5), resulting in the following

$$E_{VD} = \frac{1}{2} X_0^2 \omega^2 m \left[1 - e^{-2t \cdot \lambda\omega}\right] \qquad \textbf{6.6}$$

Where

$\boldsymbol{X_0}$ = the release displacement
$\boldsymbol{\omega}$ = circular natural frequency of the system
$\boldsymbol{m}$ = mass of the system
$\boldsymbol{t}$ = time from release
$\boldsymbol{\lambda}$ = equivalent viscous damping, expressed as a ratio of critical damping, i.e. $\lambda = \frac{c}{c_c} = \frac{c}{2m\omega}$.

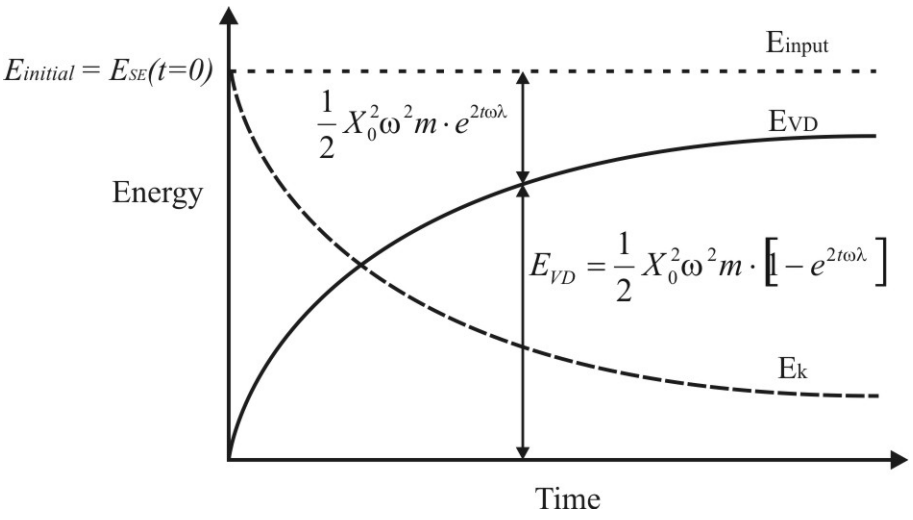

Figure 6.29 Conservation of energy during free vibration

The initial input energy can be calculated from the strain energy prior to release of the system (area beneath the force-displacement push-over) $\boldsymbol{E_{SE}(t=0)}$. From the equations in Figure 6.29, the initial input energy $\boldsymbol{E_0}$ can also be defined by Eq.(6.7).

$$E_0 = E_{SE}(t=0) = \frac{1}{2} X_0^2 \omega^2 m \qquad \textbf{6.7}$$

Recognising the conservation of energy between kinetic energy $\boldsymbol{E_k}$ and viscous energy dissipation $\boldsymbol{E_{VD}}$ the equivalent viscous damping ratio can be computed between successive velocity peaks from Eq.(6.8).

$$\lambda = \frac{1}{2t \cdot \omega} \ln\left[\frac{E_0}{E_k(t)}\right] \qquad \textbf{6.8}$$

Where;

- λ = equivalent viscous damping expressed as a ratio of the critical damping of the system.
- E_0 = initial input energy to the system, equal to the strain energy at release, $E_{SE}(t = 0)$.
- $E_k(t)$ = kinetic energy of the system at time t
- ω = circular natural frequency of the system. In order to account for the elongated period of a non-linear system, ω should be equal to the cumulative average circular natural frequency up until time t. It should be recognised that Eq.(6.8) is still an approximation for non-linear elastic systems even if the cumulative average value of ω is used.

The formulation of Eq.(6.8) can be modified to account (approximately) for input energy added to the system during free vibration. Consider the system in Figure 6.30 below where the free vibration is amplified due to additional input energy ΔE_{input}. The additional input energy is assumed to be equally divided between the kinetic energy and the dissipated energy, i.e. $0.5\Delta E_{input}$. Again, following the principle of conservation of energy, the equivalent viscous damping can be computed from Eq.(6.9).

$$\lambda = \frac{1}{2t \cdot \omega} \ln\left[\frac{E_0}{E_k(t) + 0.5\left[E_0 - E_{input}(t)\right]}\right] \qquad \textbf{6.9}$$

In Eq.(6.9) the input energy at time t is defined by $E_{input}(t)$. Eq.(6.9) reduces to Eq.(6.8) when no input energy is added to the system , i.e., $\Delta E_{input}(t) = E_{input}(t) - E_0 = 0$.

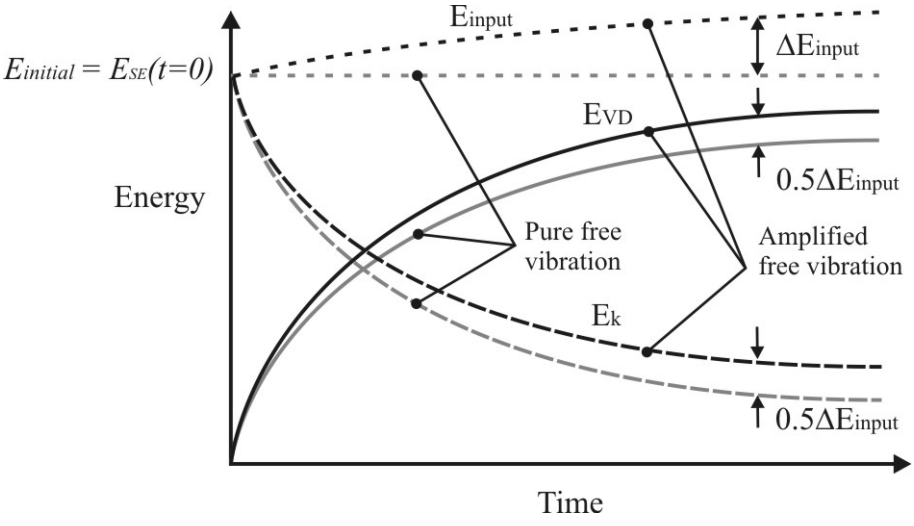

Figure 6.30 Conservation of energy during free vibration with added input energy

(a) Evaluation of the Equivalent Viscous Damping from Experimental Free Vibration Testing

The modified damping equation of Eq.(6.9) was used to estimate the equivalent viscous damping (EVD) associated with contact damping during the free vibration testing of Wall 1. The equivalent viscous damping (EVD) was estimated from the release tests at a drift ratio of 1.5% and 2.5% (0.5% was not included as limited rocking occurred during this test). Eq.(6.9) was used to compute the EVD during each cycle of free-vibration. Each data point is graphed in Figure 6.31 for the two free-vibration tests (1.5% and 2.5% lateral drift ratio). The first cycle was omitted from the data set due to the violent nature of the system immediately following release. The EVD was computed for every other cycle until the kinetic energy fell below 25% of the strain-energy at release, or until rocking of the base was no longer evident, which ever occurred first. From the data points in Figure 6.31, the following conclusions were made

- The EVD was found to be approximately proportional to the secant stiffness at release for both free-vibration tests. That is, as the release displacement was increased, the damping coefficient decreased: as the release amplitude was increased the velocity of the system also increased, resulting in larger damping forces.
- The scatter within each test in Figure 6.31 was minimal suggesting that the viscous damping coefficient was approximately constant during free-vibration; however, it is proposed that the magnitude of the damping coefficient depends on the secant stiffness of the system at the release displacement.

From this analysis, a damping ratio of 2.4% was computed and was estimated to be proportional to the secant stiffness at release. By applying an error of ±25% to the calibrated damping, all of the experimental data falls within these limits (Figure 6.31).

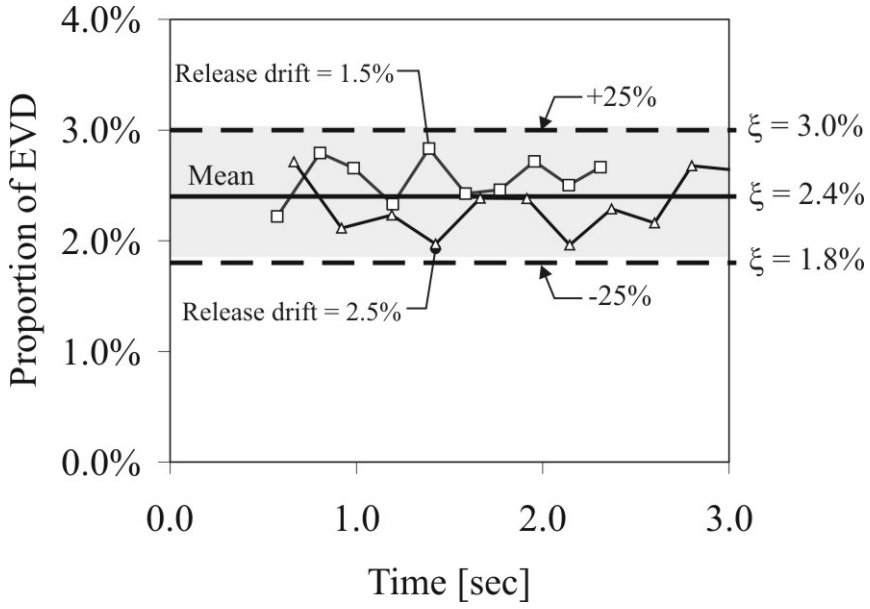

Figure 6.31 EVD (proportional to secant stiffness at release) evaluation of Wall 1 based on the modified approach to account for input energy added to the system

6.11. CONCLUSIONS

This chapter presented the experimental response of five post-tensioned precast concrete walls under free-vibration and four earthquake ground motions. Each post-tensioned wall was fitted with a combination of viscous fluid dampers (FVD) and mild steel hysteretic dampers (TCY). The shake-table was found to be incapable of reproducing the characteristics of near-field records with large velocity pulses with strong forward-directivity. Hence, the near-field records that were selected were less intense than the equivalent far-field records corresponding to the same theoretical seismic hazard.

Dynamic testing confirmed the conclusions derived from Chapter 5 in that the efficiency of the viscous dampers were compromised due to tolerances within the connections at each end of the damper; thus, some slipping/pinching was observed. As a result, the dampers were not properly activated until drift demands exceeded approximately 1.0%. Considering all four earthquake records Wall 3 (hysteretic plus viscous) and Wall 4 (hysteretic) offered the best performance in terms of low peak floor-accelerations and peak displacements. While, this was largely attributed to the larger damping offered by these two systems, Wall 3 could also guarantee full dynamic (and static) re-centring when the velocity within the FVDs approached zero. Furthermore, if higher floor-accelerations can be tolerated, a solution with minimal damping (or zero, as in the case of Wall 1) provided an equally viable option, although from a design perspective the peak system response will be computed with less uncertainty.

The vertical accelerations during rocking were found to be significant for lightly damped post-tensioned walls. In such systems, vertical accelerations of 0.35g were recorded. The peak vertical acceleration was found to be directly proportional to the peak horizontal velocity regardless of the level of mechanical damping within the system: damping acted to reduce the velocity, displacements and vertical acceleration demand during impact. From this trend, a contact damping model proportional to the peak velocity and displacement of the system was proposed.

The contact damping of a post-tensioned only wall (Wall 1) was calibrated from free-vibration testing. An equivalent viscous damping (EVD) ratio of 2.4% was determined. For simplicity, the proposed contact damping model incorporated three fundamental properties

- Based on the time-history decay, the damping coefficient (computed from the calibrated EVD) was assumed to be constant during free-vibration.
- From the two release amplitudes, the magnitude of the damping coefficient was estimated to be proportional to the secant stiffness at the maximum displacement, i.e. the secant stiffness of the system at the release displacement. Hence, the calibrated 2.4% EVD ratio was constant and independent of the displacement amplitude during free vibration.
- The damping forces are proportional to both velocity and displacement.

6.12. REFERENCES

Chase, J. G., Hudson, N. H., Lin, J., Elliot, R. and Sim, A. (2005). "Nonlinear Shake Table Identification and Control for near-Field Earthquake Testing." *Journal of Earthquake Engineering. Vol. 9, no. 4, pp. 461-482. July 2005*.

FEMA. (2003). *NEHRP Recommended Provisions for Seismic Regulations for New Buildings and Other Structures: FEMA 450*, Washington, D.C.

Marriott, D., Pampanin, S. and Bull, D. (2007) "Improving the Seismic Performance of Existing Reinforced Concrete Buildings using Advanced Rocking Wall Solutions." *NZSEE*, Palmerston North, New Zealand.

Mulligan, K. (2007). "Experimental and analytical studies of semi-active and passive structural control of buildings," University of Canterbury, Christchurch.

NZS1170.5. (2004). "Structural Design Actions, *Part 5: Earthquake actions*." Standards New Zealand, Wellington.

7. Modelling the Monotonic, Cyclic and Dynamic Response of Post-Tensioned Rocking Systems

7.1. INTRODUCTION

In this chapter modelling techniques are developed for post-tensioned rocking systems. In particular, the monotonic, cyclic and dynamic modelling of post-tensioned cantilever elements is presented in detail. The ability of a model to accurately capture the global response of a post-tensioned rocking system is dictated by the ability of the model to capture the local rocking behaviour. Monotonic backbone models are first presented that utilise an existing global member compatibility requirement to define the internal actions at the rocking interface within a section analysis. Suggestions to account for the cyclic response of steel, confinement due to armouring of the cover concrete, alternative stress-strain relationships within the compression zone of the rocking body and the inclusion of external, velocity dependant (viscous) or hysteretic dampers are all addressed in detail. The section analysis is further extended to bi-axial loading, where various bi-axial interaction surfaces are developed and intended to be used in design and modelling. Macro modelling techniques are then presented to model the cyclic behaviour of post-tensioned rocking connections. In particular, focus is given to a multi-axial spring model introduced in Chapter 3. A method is developed to calibrate the axial stiffness of the multi-spring unit. The macro-model is further extended to 3-demensions to capture the global and local bi-axial response of rocking systems. Suggestions on how to calibrate the axial stiffness of the 3-dimensional multi-spring unit is also discussed. In the final section, a technique to account for the energy lost during rocking impact is proposed (contact damping). The proposed damping model is a simple extension of the macro-model to include a velocity proportional and displacement proportional damper at the effective height of the system: the properties of damping model are calibrated from experimental testing in Chapter 6.

7.2. MODELING THE MONOTONIC RESPONSE OF POST-TENSIONED ROCKING SYSTEMS

This first section deals with constructing the monotonic loading envelope of post-tensioned rocking systems. In this context, a post-tensioned rocking system includes any rocking system with or without dissipation, either internal or external to the section. A number of issues are discussed in this section. In particular, an existing analogy that was developed to compute the section response of a hybrid system is simplified for post-tensioned only systems and systems with externally mounted

devices. Furthermore, issues relating to alternative stress-strain models within the compression zone of the rocking body, accounting for the cyclic behaviour of steel and a method to assess the response of post-tensioned systems with non-linear viscous dampers are also discussed. Procedures are also developed to assess the bi-axial response of any post-tensioned rocking system. A series of design charts are subsequently developed for post-tensioned rocking systems considering bi-directional earthquake loading.

It can be difficult to capture the cyclic backbone response of an experimental monotonic model. More often than not, the envelope encompassing the cyclic response of a system will be quite different to the monotonic response; generally, for well detailed elements the capacity of a cyclic test will appear greater than an equivalent monotonic test. Furthermore, under cyclic loading low-cycle fatigue will initiate early rupture, reducing the apparent displacement capacity of the system. This section will aim to accurately define the capacity envelope of a post-tensioned rocking system considering either cyclic or monotonic loading.

7.2.1. The Revised Monolithic Beam Analogy for Post-Tensioned Rocking Systems with Internally Grouted Mild Steel, Palermo [2004]

The revised Monolithic Beam Analogy (rMBA), which was described in detail in Chapter 3, was developed specifically for post-tensioned precast concrete rocking systems with internally grouted mild steel reinforcement; these elements are referred to as post-tensioned hybrid systems (or simply "hybrid" systems). The analogy computes a theoretical curvature at the rocking interface by relating member displacements of the rocking element to those of an equivalently reinforced monolithic (EM) system. This section discusses a number of modelling issues which have not yet been addressed.

(a) Monotonic Backbone Model of Reinforcing Steel, Accounting for Cyclic Loading

Two constitutive relationships describing the stress-strain behaviour of reinforcing steel are used in this research. When experimental test data is available, the relationship originally proposed by Mander et al. [1984] and later revisited by Dodd and Restrepo-Posada [1995] is adopted as it makes use of the test data to better describe the non-linear strain-hardening branch of the stress-strain curve (a coordinate along the strain-hardening portion of the stress-strain curve is used). For analyses where experimental stress-strain data is not present, the relationship used by King et al. [1986] is more appropriate. The mathematic equations describing the monotonic stress-strain envelope used by Dodd and Restrepo-Posada [1995] is summarised below. Reference to the nomenclature is also illustrated in Figure 7.1.

For $\varepsilon_{ms} \leq \varepsilon_{y,ms}$

$$f_{ms} = E_{ms}\varepsilon_{ms} \qquad \textbf{7.1}$$

For $\varepsilon_{y.ms} < \varepsilon_{ms} \leq \varepsilon_{sh}$

$$f_{ms} = f_{y.ms} \tag{7.2}$$

For $\varepsilon_{sh} < \varepsilon_{ms} \leq \varepsilon_{u,ms}$

$$f_{ms} = f_{u.ms} + \left(f_{y.ms} - f_{u.ms}\right)\left[\frac{\varepsilon_{su,ms} - \varepsilon_{ms}}{\varepsilon_{su,ms} - \varepsilon_{sh}}\right]^{P} \tag{7.3}$$

In Eq.(7.3) ***P*** is a parameter describing the non-linear power relationship to capture the strain-hardening curve.

$$P = \frac{\log_{10}\left(\frac{f_{su.ms} - f_{x,ms}}{f_{su.ms} - f_{y,ms}}\right)}{\log_{10}\left(\frac{\varepsilon_{su.ms} - \varepsilon_{s,x}}{\varepsilon_{su.ms} - \varepsilon_{s,sh}}\right)} \tag{7.4}$$

Where,

- ε_{ms} = generic steel strain (the subscript ***ms*** denotes mild steel)
- $\varepsilon_{y,ms}$ = yield strain of the mild steel
- $\varepsilon_{sh,ms}$ = strain hardening of the mild steel
- $\varepsilon_{x,ms}$ = strain coordinate on the strain hardening curve from experimental data
- $\varepsilon_{su,ms}$ = ultimate strain of the mild steel defined by the maximum obtained stress
- f_{ms} = generic mild steel stress, i.e. $f_{ms}(\varepsilon_{ms})$
- $f_{y,ms}$ = yield stress of the mild steel
- $f_{x,ms}$ = stress coordinate on the strain hardening curve from experimental data
- $f_{su,ms}$ = maximum obtained stress of the mild steel

The cyclic stress-strain behaviour of mild steel is illustrated in Figure 7.1. When steel is unloaded from the monotonic loading envelope it softens and departs from the idealised elasto-plastic response: this is known as the Bauschinger [1887] effect. When the steel is unloaded back to the origin (ε_s approaching zero), the strength exceeds the idealised elasto-plastic capacity in compression. With respect to post-tensioned hybrid connections, the compression strains within the grouted longitudinal reinforcement (located inside the neutral axis) can be quite small ($>-\varepsilon_{sh}$) due to the unbonded length provided to the longitudinal reinforcement. The magnitude of the compression strains will primarily depend on the level of post-tensioning, the amount of prestressed reinforcement and the unbonded length of the mild-steel reinforcement. When re-loading from the unloading branch the stress-strain curve can intersect the yield plateau along the monotonic envelope. This gives an apparent reduction to the onset of strain hardening ε_{sh} as shown in Figure 7.1. Hence, the monotonic stress-

strain envelope can differ significantly from the cyclic stress-strain envelope. The cyclic stress-strain envelope is dependant on the magnitude of the compression strain when re-loaded from the unloading branch.

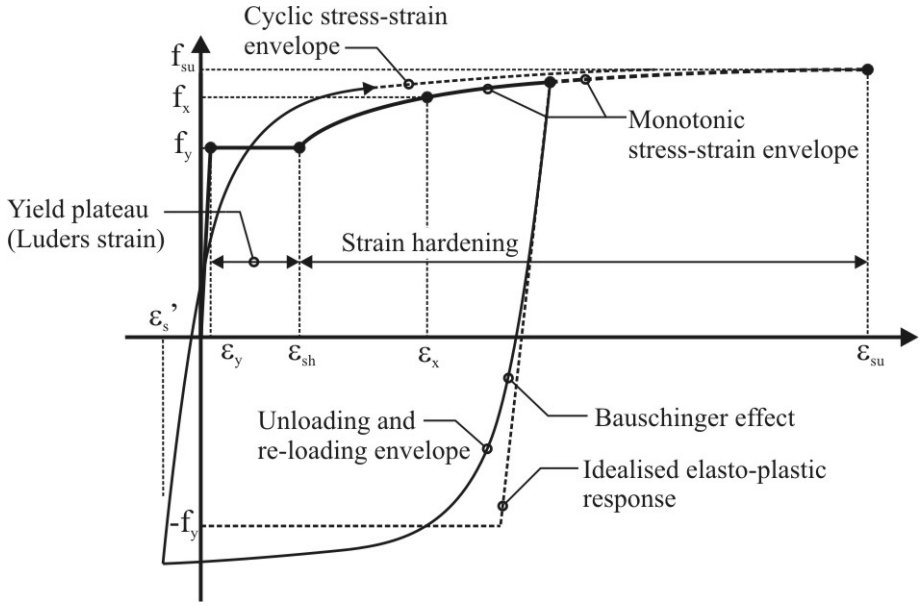

Figure 7.1 Stress-strain behaviour of mild steel, unloading from the strain-hardening region and reloading from an unloading branch. Note the difference between the monotonic and cyclic stress-strain envelope.

Figure 7.2 compares two steel tests. One test is a monotonic tension test, while the other test is a cyclic tension test on an identical steel specimen (Grade 300MPa reinforcement). The steel used in these tests was of the same material used in the fabrication of the tension-compression-yielding (TCY) dampers discussed in Chapter 4. While the material tested in Figure 7.2 was Grade 300MPa round bar, it had identical properties to conventional (deformed) longitudinal reinforcement (of the same grade). Three properties are noted with regards to Figure 7.2:

- The strain coordinates describing the cyclic envelope have been shifted closer to the origin when compared to the monotonic envelope.
- The ultimate strain of the steel is significantly reduced when subjected to cyclic loading due to low-cycle fatigue and will be heavily dependant on the loading history.
- The strength of the steel in compression is substantially greater than an elastic-plastic idealisation in compression.

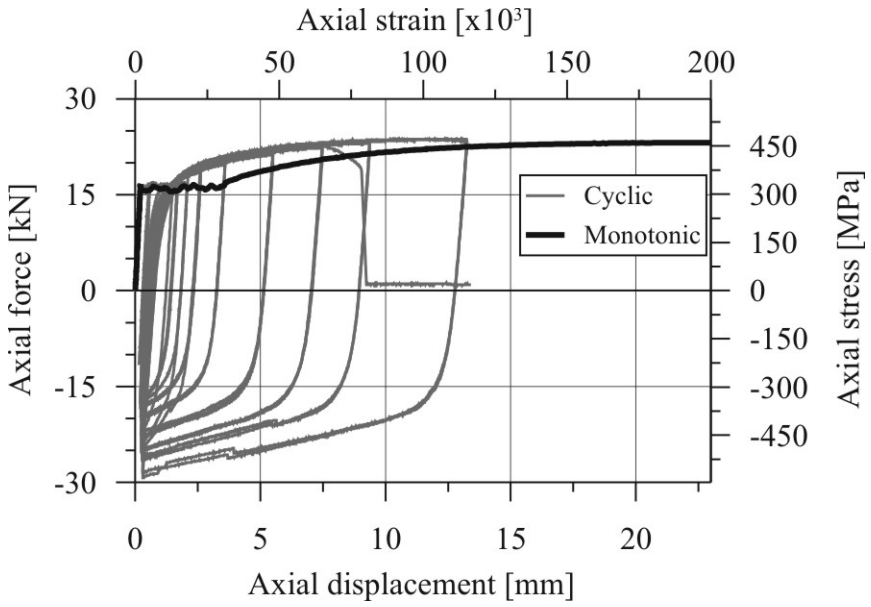

Figure 7.2 Comparison between a monotonic and a cyclic test of a mild steel TCY damper representative of grade 300MPa mild-steel.

While some researches have proposed "origin-shifting" methods to account for cyclic behaviour, Presland [1999], these methods were not found to correctly model the observed behaviour shown in Figure 7.2. A method was developed to define an equivalent stress-strain envelope to account for cyclic loading of steel. The premise behind the proposed cyclic back-bone envelope is illustrated in Figure 7.3. The onset of the apparent strain hardening $\varepsilon_{sh,app}$ is defined in Eq.(7.5) as the peak compression strain ε_s' plus 50% of the strain at strain-hardening ε_{sh}.

$$\varepsilon_{sh,app} = \varepsilon_s' + 0.5\varepsilon_{sh} \qquad \textbf{7.5}$$

The ultimate strain of the steel under cyclic loading was more difficult to define as the ultimate strain was highly dependant on the cumulative strain ductility demand during loading. Specific to the loading protocol adopted during the material tests in Chapter 4, the strain at rupture due to cyclic loading was equal to approximately 50% of the rupture strain corresponding to a monotonic test, i.e. for grade 300MPa mild steel, the rupture strain could be estimated as $100\text{x}10^{-3}$ mm/mm under cyclic loading. The cyclic testing protocol that was imposed on the steel TCY dampers was similar to the displacement demand that was expected during in-situ testing. This was quite a demanding protocol comprising of many ductility cycles (3 cycles at each displacement, followed a single cycle at an intermediate displacement). As mentioned, steel compression strains within a post-tensioned hybrid system are likely to be small for steel layers located inside the perimeter of the section. It is for this reason that an approximate form of Eq.(7.5) can be used: $\varepsilon_{sh,app} = 0.5\varepsilon_{sh}$. Eq.(7.5) can not be used for steel layers that are subjected to very large compression strains, which is the case for steel layers located outside of the section. For large compression strains, the apparent strain hardening $\varepsilon_{sh,app}$ can be less than the yield strain ε_y of the material, i.e. truncating the elastic loading region. This procedure to shift the strain coordinates is

simple and the reduced strain values ($\varepsilon_{sh,app}$ and ε_{su}) can be used within Eqs.(7.1) to (7.4). Alternatively, the entire stress-strain curve can be constructed by fitting Eqs.(7.1) to (7.4) directly to experimental test data.

As mentioned, the apparent stress-strain envelope will be loading dependant. If a near-fault earthquake event is considered comprising of a single large velocity pulse, then the stress-strain envelope will be better represented by a monotonic envelope. On the other-hand the stress-strain envelope of a system subjected to a far-field ground motion, having a number of smaller cycles before the larger excursions, may be better captured considering a cyclic stress-strain envelope. For a structural analysis/assessment where the ground hazard is not known with any great certainty, it would be prudent to determine the significance of the two stress-strain envelopes on the global response of the system and define a range of possible solutions to be used during design.

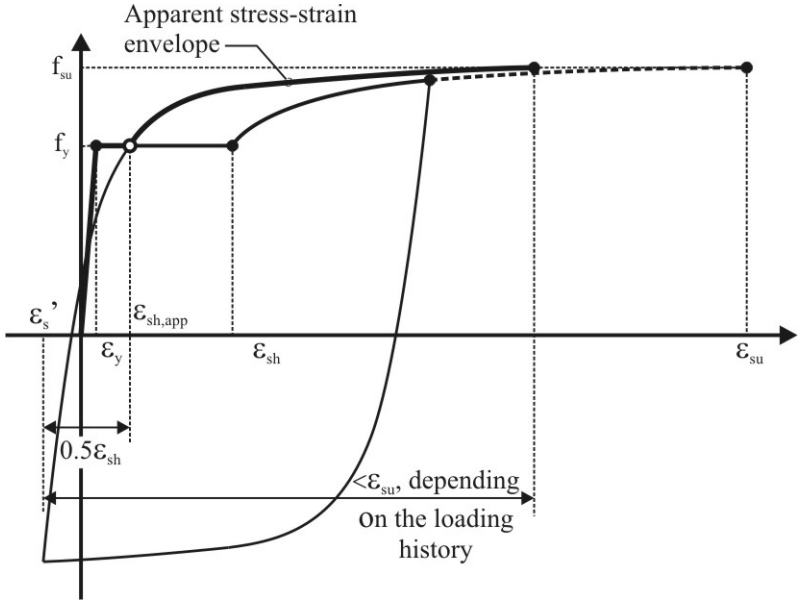

Figure 7.3 Method to construct a stress-strain envelope that accounts for cyclic loading

(b) Monotonic Backbone Model for Prestressed Reinforcing Steel

All of the experimental test specimens discussed in this research were designed to avoid yielding of the prestressed reinforcement. This was opted to allow multiple tests to be carried out on each specimen. It is for this reason that an elastic stress-strain relationship is later used to model the post-tensioned reinforcement within each test. In the event that yielding is plausible, Eqs.(7.1) through to Eq.(7.4) above are used; however, the yield plateau is removed from the piecewise equations. That is, the onset of strain hardening $\varepsilon_{sh,pt}$ is equal to the yield strain $\varepsilon_{y,pt}$ below.

For $\varepsilon_{pt} \leq \varepsilon_{y,pt}$

$$f_{pt} = E_{pt}\varepsilon_{pt} \qquad \textbf{7.6}$$

For $\varepsilon_{y.pt} < \varepsilon_{pt} \leq \varepsilon_{u,pt}$

$$f_{pt} = f_{u.pt} + \left(f_{y.pt} - f_{u.pt}\right)\left[\frac{\varepsilon_{su,pt} - \varepsilon_{pt}}{\varepsilon_{su,pt} - \varepsilon_{y,pt}}\right]^{P} \quad \textbf{7.7}$$

Where,

$$P = \frac{\log_{10}\left(\frac{f_{su.pt} - f_{x,pt}}{f_{su.pt} - f_{y,pt}}\right)}{\log_{10}\left(\frac{\varepsilon_{su.pt} - \varepsilon_{x,pt}}{\varepsilon_{su.pt} - \varepsilon_{y,pt}}\right)} \quad \textbf{7.8}$$

The subscripts ***pt*** in Eq.(7.6) to (7.8) refer to the post-tensioned reinforcement. Tension testing of the post-tensioned reinforcement was found to agree well with this model (testing of the post-tensioned reinforcement was discussed in Chapter 4).

(c) Strength and Strain Enhancement of Confined Concrete

The effect of concrete confinement has been heavily researched in literature by many authors, with various expressions proposed to estimate the enhanced concrete strength and ultimate concrete strain as early as 1928: Richart et al. [1928]; Kent and Park [1971]; Mander et al. [1988]; Dodd and Cooke [1992]. The expression developed by Mander et al. [1988] to determine the confined compressive strength and ultimate strain has been widely accepted in literature as it has been developed based on theoretical understanding and calibrated against experimental tests on axially loaded column members with unconfined concrete strengths less than 50MPa. Mander et al. [1988] computes the strength enhancement of a symmetrical square section, considering equal lateral confining stresses in both transverse directions from Eq.7.9.

$$\frac{f_{cc}^{'}}{f_{c}^{'}} = \left(-1.254 + 2.254\sqrt{1 + \frac{7.94 f_{l}}{f_{c}^{'}}} - 2\frac{f_{l}}{f_{c}^{'}}\right) \quad \textbf{7.9}$$

In this equation $\boldsymbol{f_{cc}'}$ is the maximum confined concrete stress, $\boldsymbol{f_{c}'}$ is the maximum unconfined concrete stress and $\boldsymbol{f_{l}}$ is the lateral confining stress. Consider Figure 7.4, the effective lateral confinement area is not uniform within the confined core; rather unconfined parabolas are located between each lateral restraint (anchored transverse reinforcing bars). The effective confinement within the confined core of a square section is computed from Eq.(7.10) which assumes that the transverse reinforcement is yielding $\boldsymbol{f_{yh}}$. This is the maximum theoretical lateral confining stress that can be obtained from the transverse reinforcement (neglecting strain hardening).

$$f_{l,e} = \rho_{v} f_{yh} \quad \textbf{7.10}$$

A confinement effectiveness factor C_e relates the area of effectively confined concrete A_e to the total confined core area A_{cc} (the area bounded by the centreline of the peripheral hoops, i.e. $A_{cc} = h_{cx} \cdot h_{cy}$ in Figure 7.4). The effectively confined area A_e accounts for the confinement arching effects between the longitudinal reinforcement (in plan) and the stirrup sets (in elevation), i.e. $A_e = b_{ex} \cdot b_{ey}$ in Figure 7.4. This confinement model is known as a smeared model, whereby the effective lateral confining stress f_{le} within the effective core A_e is averaged (smeared) over the area bounded by the centreline of the peripheral hoops A_{cc} such that the average lateral confining stress is given by

$$f_l = C_e f_{l,e} = C_e \rho_v f_{yh} \qquad \textbf{7.11}$$

Where the confinement effectiveness factor C_e is given by

$$C_e = \frac{A_e}{A_{cc}} \qquad \textbf{7.12}$$

Priestley et al. [2007] has found that C_e is generally in the order of 0.75-0.85 for well-designed square sections. For a symmetrical square section, the transverse reinforcement ρ_v ratio in Eq.(7.11) is summed in the two directions.

$$\rho_v = \rho_{ax} + \rho_{ay} = \frac{A_{shx}}{h_{cy} s} + \frac{A_{shy}}{h_{cx} s} \qquad \textbf{7.13}$$

Where A_{shx} is the total area of transverse reinforcement providing confinement in the x-direction, h_{cy} is the width of the confined core in the y-direction (measured to the centre-line of the peripheral hoops) and s is the spacing of the transverse reinforcement sets. Further explanation of these terms is illustrated in Figure 7.4.

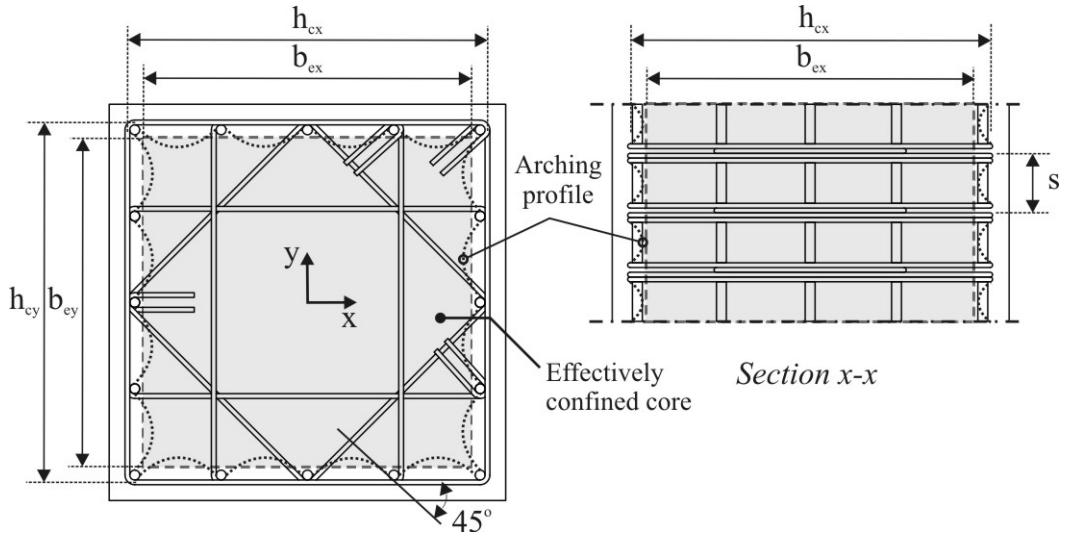

Figure 7.4 Nomenclature of a confined column/pier section

Wang and Restrepo [2001] incorporated a Poisson dilation effect within the Mander et al. [1988] confinement model to account for the actual lateral strain within the transverse reinforcement during axial loading of the element. Hence, the lateral confining pressure acting within the section is dependant on the axial strain within the section. This extension provides greater accuracy during initial loading; however, the added computation can be unnecessary if the primary goal is to evaluate the confinement effects at high ductility demands where the strain in the transverse reinforcement is likely to be greater than yield in any case. Considering a poisons ratio of $\nu = 0.2$ and grade 300MPa transverse reinforcement, the strain in the transverse reinforcement will approach yield at an axial strain of 0.0075; depending on the level of confinement reinforcement, confined concrete can experience axial strains exceeding 0.1, Allington [2003]. This method to incorporate the Poisson effect is really only appropriate for axially loaded elements, and would be difficult to accurately implement into an analysis considering combined bending and axial load.

Wang and Restrepo [2001] also developed an approximate closed form solution of the Mander et al. [1988] confinement model to allow the confinement of rectangular sections with unequal confining stresses to be rapidly computed without the use of the well-known confinement chart published in Mander et al. [1988]. When the section is not symmetrical, the lateral confining pressure (f_l in Eq.(7.11)) in each direction of the section (f_{lx} and f_{ly}) is computed from the corresponding reinforcement ratio ρ_{ax}, ρ_{ay}. The strength enhancement is then computed from the product of α_1 and α_2 below.

$$\frac{f_{cc}^{'}}{f_{c}^{'}} = \alpha_1 \alpha_2 \qquad \textbf{7.14}$$

Where α_1 and α_2 are given by Eq.(7.14) and (7.15).

$$\alpha_1 = 1.25\left(1.8\sqrt{1+7.94\frac{F_1}{f_c'}} - 1.6\frac{F_1}{f_c'} - 1\right) \qquad \textbf{7.15}$$

$$\alpha_2 = \left[1.4\frac{F_2}{F_1} - 0.6\left(\frac{F_2}{F_1}\right)^2 - 0.8\right]\sqrt{\frac{F_1}{f_c'}} + 1 \qquad \textbf{7.16}$$

In the above expressions F_1 is the larger of f_{lx} and f_{ly}, while F_2 is the smaller of the two lateral stresses. The closed form relationships of Eqs.(7.14) to (7.16) are well suited to a segmented concrete confinement model. A segmented method avoids averaging the effective confinement over the confined core; rather, it disaggregates the section into effectively confined concrete, ineffectively confined concrete and unconfined cover concrete and has been used by many researches: Presland [1999]; Wang and Restrepo [2001] and Allington [2003]. The disaggregated areas are computed as equivalent rectangular blocks defining discrete segments of each confined concrete component as illustrated in Figure 7.5. If a segmented model is used the lateral confining stress is computed using Eq.(7.11) with $C_e = 1.0$. Presland [1999] demonstrated that the strength of a bridge pier under combined bending and axial load is more conservatively estimated when using a segmented confinement model when compared to a smeared model. Intuition would suggest that the lateral

confining pressure within the ineffectively confined region will be less than the full confining pressure within the effectively confined core. Allington [2003] originally postulated a 50% reduction in lateral confining pressure within the ineffectively confined region; however, revised this value based on a regression analysis of experimental data and back calculation to form the following relationship

$$f_{l,i} = 0.4 f_{l,e} \frac{N}{A_g f_c'} \qquad \textbf{7.17}$$

Where, $f_{l,i}$ is the lateral confining stress within the ineffectively confined region, $f_{l,e}$ is the full confining pressure within the confined core and N is the applied axial load.

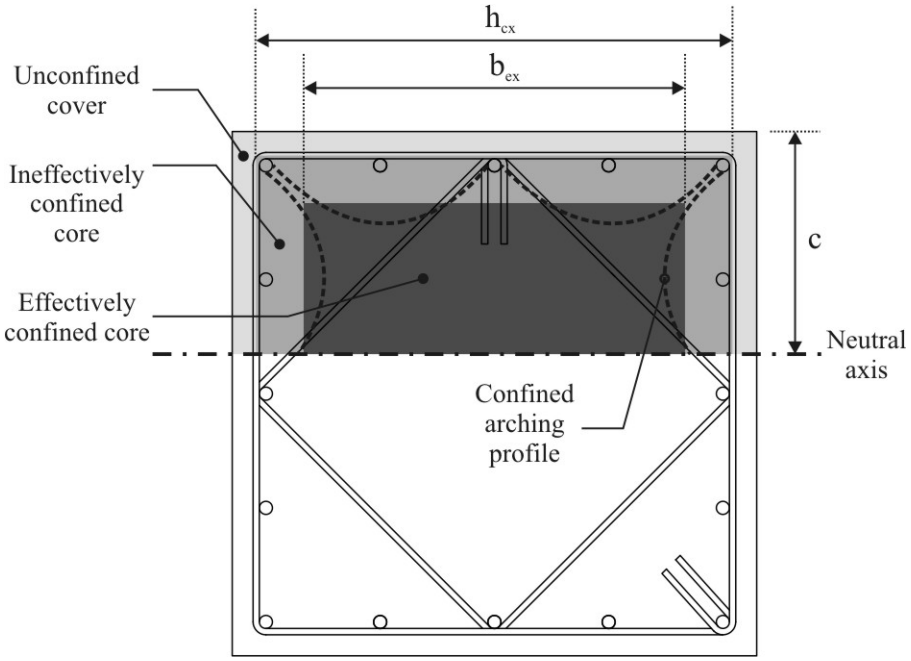

Figure 7.5 Segmented confined concrete model, reproduced from Allington [2003].

(d) Confinement of Post-Tensioned Rocking Systems with Concrete Cover Protection

If a post-tensioned rocking section has no cover concrete protection around the perimeter to prevent damage during rocking, then the traditional smeared or segmented approach discussed in Section 7.2.1 (c) can be implemented. If the section has some protection via cast in-situ steel angles or Fibre-Reinforced-Polymer (FRP) wrapping at the rocking base, then some additional confinement will be imposed on the concrete section. The level of additional confinement afforded by the concrete cover protection will depend on how it is anchored and detailed to the precast element and how much confinement material is supplied. The confinement of a post-tensioned system with protection around the perimeter is illustrated in Figure 7.6 (this protection is similar to the steel-angle assembly cast into base of the test specimen HBD1 and

HBD2 presented in Chapter 4). From Figure 7.6 the total confinement will be made up of three components:

- Confinement provided by the transverse reinforcement (stirrups) plus that provided by the concrete cover protection element
- Confinement provided by the concrete cover protection element only
- Unconfined concrete between the parabolic arches

Wang and Restrepo [1996] formulated a method to compute effective confining areas for concrete columns with external FRP confining jackets. While a similar method could be carried out, difficultly will arise when accounting for the effective arching in the orthogonal direction as the confinement is not uniformly applied over the length of the specimen, rather, it is provided at the rocking toe region only. Furthermore, if heavy steel protection is provided around the perimeter, it is unlikely to yield and will violate the theory behind Eq.(7.10). These two factors make it very difficult to estimate the amount of additional lateral confining stress provided to the section.

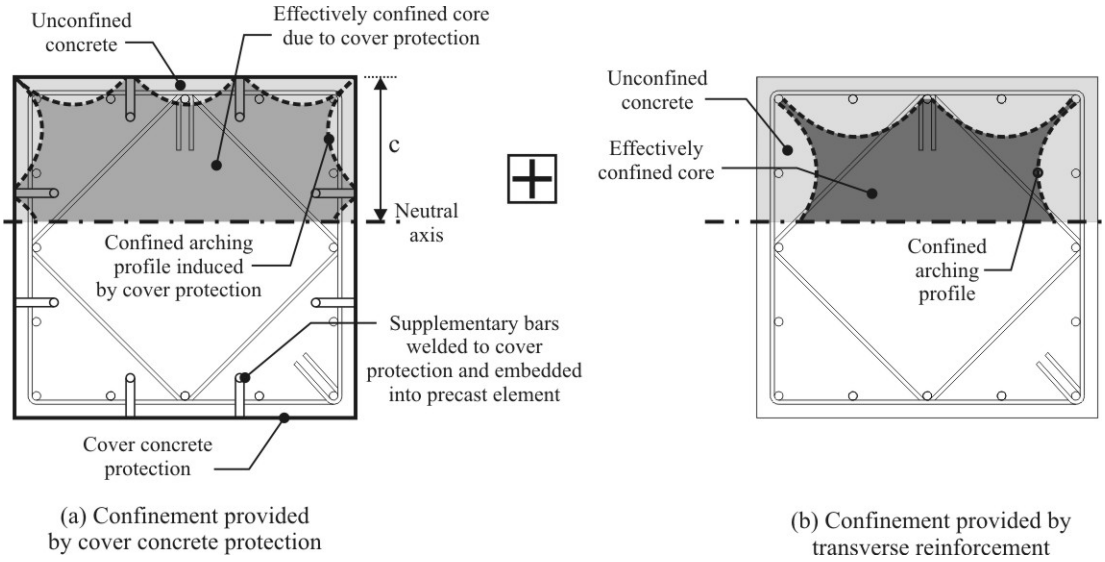

Figure 7.6 The addition of confinement provided by external concrete cover protection and transverse reinforcement

To simplify the computation of confinement three methods are presented. The first method simply ignores the additional confinement provided by the perimeter confining element, while the other two methods acknowledge some degree of confinement.

- *Hybrid Confinement Method A:* Ignore the confinement provided by the perimeter steel and consider only the confinement provided by the transverse reinforcement. In this case, the segmented confinement model of Figure 7.5 above would apply, while the smeared confinement model would use Eq.(7.12) to determine the effective confinement coefficient $\boldsymbol{C_e}$ (reproduced below) and applied over the confined core area $\boldsymbol{A_{cc}}$ only. An unconfined concrete model would be used for the concrete outside of the peripheral hoops.

$$C_e = \frac{A_e}{A_{cc}} \qquad \textbf{7.18}$$

- *Hybrid Confinement Method B:* Assumes the perimeter steel provides confinement to the cover concrete that is as effective as the ineffectively confined core concrete located between the effectively confined core and the peripheral hoops (Figure 7.7 (a)). There is no unconfined concrete in this model; therefore, a segmented model should only consider two confinement regions namely, the ineffectively confined region and the effectively confined region in Figure 7.7 (a). A smeared model should average the effectively confined core over the entire cross-section A_g. Considering a smeared model where the ineffectively confining stress is zero, the confinement effectiveness coefficient C_e is given by

$$C_e = \frac{A_e}{A_g} \qquad \textbf{7.19}$$

- *Hybrid Confinement Method C:* Assumes the perimeter element provides a moderate level of lateral confining stress to the concrete between the peripheral hoops and the effectively confined core (Figure 7.7 (b)). The level of confinement is defined as moderately confined $f_{l,m}$ and is computed from Eq.(7.20).

$$f_{l,m} = f_{l,e}\frac{\left[A_g / A_{cc} - 1\right]}{\left[A_{cc} / A_e - 1\right]} \qquad \textbf{7.20}$$

This lateral confining stress is derived based on an average level of lateral confining stress equal to $f_{l,e}A_e/A_{cc}$ acting over the entire gross area A_g. A segmented model should consider three levels of confinement: the effectively confined core with area A_e and confining stress $f_{l,e}$ (computed from Eq.(7.10)), the moderately confined core with area A_{cc}-A_e and confining stress $f_{l,m}$ (computed from Eq.(7.20)); and the ineffectively confined cover concrete with area A_g-A_{cc} and confining stress $f_{l,i}$. A smeared model computes the lateral confining stress from Eq.(7.11), ignoring the presence of the perimeter steel and applies it to the entire gross area A_g with the confinement coefficient C_e computed as

$$C_e = \frac{A_e}{A_{cc}} \qquad \textbf{7.21}$$

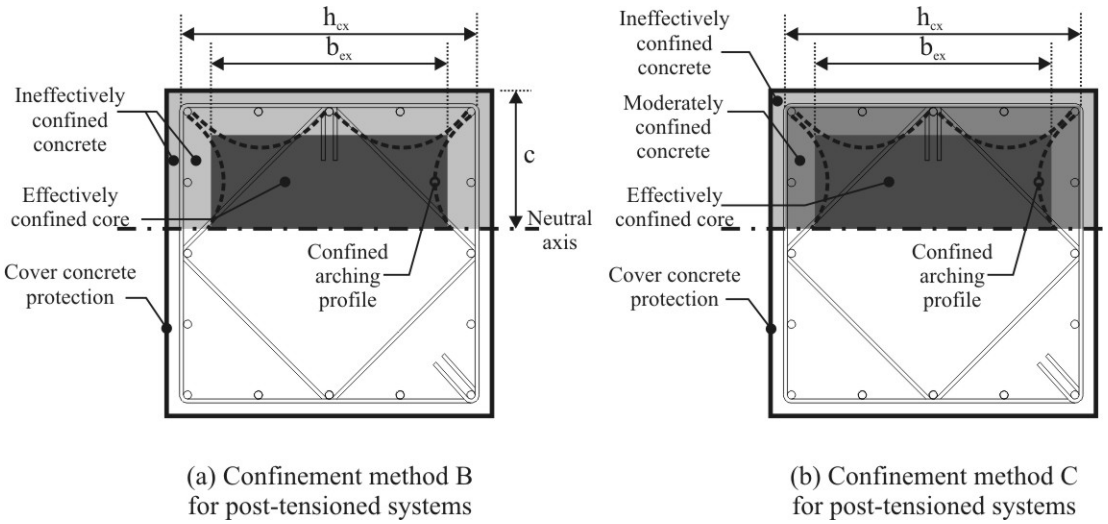

Figure 7.7 Confinement methods for post-tensioned systems to account for perimeter protection elements

Of the three methods presented, Method A would present a conservative (with respect to strength) lower bound, while Method C is a semi-upper bound solution. A true upper bound solution would assume the perimeter elements provide fully effective confinement, i.e., they are yielding. If the level of additional confinement provided by the perimeter element is difficult to compute, then a "solution window" should be computed to provide insight to the expected range of possible solutions. A summary of the three confinement models is listed in Table 7.1, indicating the lateral confining stress to be used within each confinement region of the section considering either a segmented or smeared confinement model.

Table 7.1 Summary of lateral confining stresses within post-tensioned systems for Methods A, B and C considering either a segmented or smeared confinement model

		Lateral confining stress	
	Regional areas	**Segmented model, $C_e = 1$**	**Smeared model**
Method A	$\mathbf{A_g\text{-}A_{cc}}$	0	0
	$\mathbf{A_{cc}\text{-}A_e}$	$f_{l,i}$ equal to 0.5fl,e or Eq.(7.17)	$f_l = C_e f_{l,e}$
	$\mathbf{A_e}$	$f_{l,e}$ from Eq.(7.10)	$C_e = A_e / A_{cc}$
Method B	$\mathbf{A_g\text{-}A_{cc}}$	$f_{l,i}$ equal to $0.5f_{l,e}$ or Eq.(7.17)	$f_l = C_e f_{l,e}$
	$\mathbf{A_{cc}\text{-}A_e}$		$C_e = A_e / A_g$
	$\mathbf{A_e}$	$f_{l,e}$ from Eq.(7.10)	
Method C	$\mathbf{A_g\text{-}A_{cc}}$	$f_{l,i}$ equal to $0.5f_{l,e}$ or Eq.(7.17)	$f_l = C_e f_{l,e}$
	$\mathbf{A_{cc}\text{-}A_e}$	$f_{l,m}$ from Eq.(7.20)	$C_e = A_e / A_{cc}$
	$\mathbf{A_e}$	$f_{l,e}$ from Eq.(7.10)	

(e) Modelling the Constitutive Stress-Strain Envelope of Unconfined and Confined Concrete

The non-linear loading envelope of an axially loaded confined concrete specimen in Figure 7.8 is based on the same mathematical expression that is used for unconfined concrete as suggested by Popovics [1973]. Mander et al. [1988] expressed the longitudinal concrete compressive strain by the following formula

$$f_c(x) = \frac{f_{cc}^{'} xr}{r - 1 + x^r} \qquad \textbf{7.22}$$

Where,

$$x = \frac{\varepsilon_c}{\varepsilon_{cc}} \qquad \textbf{7.23}$$

Where $\boldsymbol{\varepsilon_c}$ is the longitudinal strain in the concrete and $\boldsymbol{\varepsilon_{cc}}$ is the strain in the concrete corresponding to the peak confined concrete stress $\boldsymbol{f'_{cc}}$. The concrete strain corresponding to the maximum stress for confined concrete is given by the following expression

$$\varepsilon_{cc} = \varepsilon_{co}\left[1 + 5\left(\frac{f_{cc}^{'}}{f_c^{'}} - 1\right)\right] \qquad \textbf{7.24}$$

$\boldsymbol{\varepsilon_{co}}$ is the strain corresponding to the peak unconfined concrete stress $\boldsymbol{f'_c}$ and is normally assumed to equal 0.002. The term $\boldsymbol{r}$ is defined as

$$r = \frac{E_c}{E_c + E_{\text{sec}}} \qquad \textbf{7.25}$$

$\boldsymbol{E_c}$ is the elastic modulus of the confined (and unconfined) concrete and is computed from the following expression, where $\boldsymbol{f'_c}$ and $\boldsymbol{E_c}$ are in MPa.

$$E_c = 5000\sqrt{f_c'} \qquad \textbf{7.26}$$

The secant modulus $\boldsymbol{E_{sec}}$ is given by,

$$E_{\text{sec}} = \frac{f_{cc}^{'}}{\varepsilon_{cc}} \qquad \textbf{7.27}$$

Finally, the ultimate strain $\boldsymbol{\varepsilon_{cu}}$ attained by confined concrete is given by the following

$$\varepsilon_{cu} = 0.004 + \frac{1.4\rho_v \cdot f_{yh} \cdot \varepsilon_{su}}{f_{cc}^{'}} \qquad \textbf{7.28}$$

The definition of the ultimate confined concrete compression strain in Eq.(7.28) was developed by equating the strain energy in the concrete at rupture of the transverse reinforcement, Mander et al. [1988] and Priestley et al. [1996]. Typically, only concrete columns subjected to very high axial loads will fail due to rupture of the transverse reinforcement, while failure under combined axial-flexure loading is generally unrelated to rupture of the transverse reinforcement. Experimental tests have shown that Eq.(7.28) is conservative under combined axial-flexure loading in the order of 50%, Kowalsky and Priestley [2000]. In fact, a suggestion to multiply Equation by 1.4 has been adopted by Montejo and Kowalsky [2007] as a more realistic estimate of the concrete strain when the transverse reinforcement ruptures under combined axial-flexure loading.

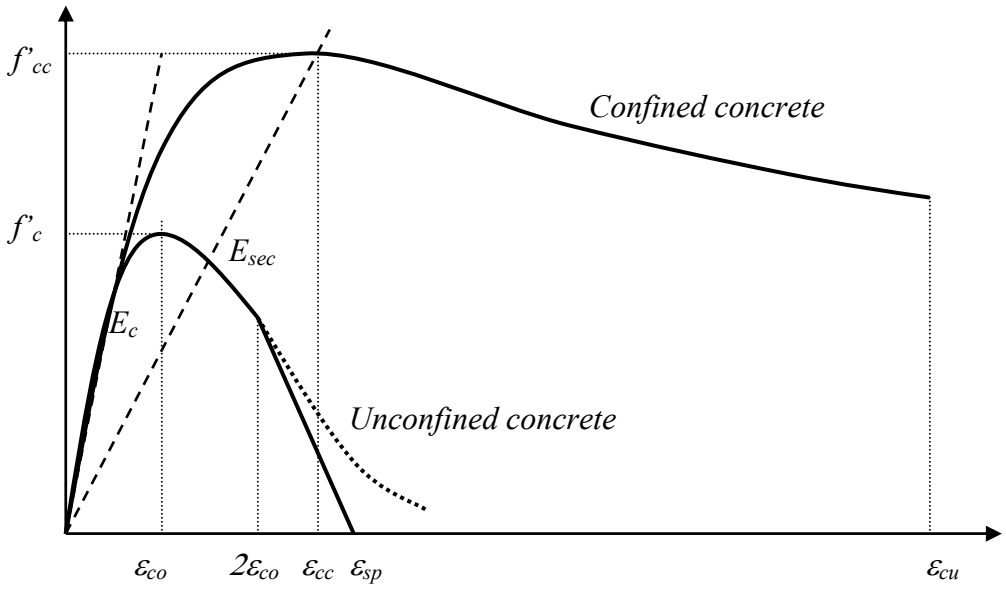

Figure 7.8: Confined and unconfined concrete model

For unconfined concrete, the stress-strain relationship can be modelled using Eqs.(7.22) to (7.28) by setting f'_{cc} equal to f'_c, i.e., a confinement ratio of 1.0. Alternatively, the unconfined concrete model of Popovics [1973] can be used; however, the former is used in this research. The spalling strain ε_{sp} of unconfined concrete is normally in the range of 0.004-0.0065.

(f) Equivalent Stress Block Factors for Confined Concrete

In some cases, integration of the complete stress-strain curve of concrete may not be warranted; especially when a rapid estimation of the moment capacity is required. Typically in design, equivalent stress-block factors are used to compute the resultant compression force within unconfined concrete. These factors are derived from integration of the entire unconfined stress-strain curve and typically depend on the unconfined compression strength f'_c. Two factors α and β define the magnitude and the location to the centroid to the resultant concrete compression force C_c. The resultant concrete compression force C_c is given by Eq.(7.29)

$$C_c = \alpha \cdot f_c' \cdot \beta \cdot c \cdot B \qquad \textbf{7.29}$$

Where

α	= stress block coefficient (magnitude)
f'_c	= unconfined concrete compression strength
β	= stress block coefficient (depth)
c	= neutral axis depth
B	= width of the section

The location to the centroid of the resultant compression force is given by Eq.(7.30) where a is the depth of the equivalent stress block.

$$a/2 = (\beta \cdot c)/2 \qquad \textbf{7.30}$$

Using Eq.(7.29) & (7.30) concrete stress block factors are derived for confined concrete with the intention of being used in the same way current unconfined concrete stress-block factors are. Through numerical integration of the confined concrete stress-strain constitutive relationship presented in Section 7.2.1(e) stress block factors are summarised in Appendix D as a function the unconfined concrete compression strength f'_c, the concrete confinement ratio f'_{cc}/f'_c and the maximum concrete compression strain at the extreme fibre ε_{cu}.

(g) Elastic Deformations of the precast element

After defining the moment-rotation response of a post-tensioned section, the elastic deformation Δ_e is computed by integration of the curvature along the precast element. For a cantilever element with a linear distribution of curvature, the elastic displacement is computed as follows

$$\Delta_e = \frac{F \cdot H_e^3}{3E \cdot I_e} \qquad \textbf{7.31}$$

Where,

F	= applied lateral load
H_e	= height to the applied load F
E	= elastic modulus of the cantilever element
I_e	= effective (cracked) second moment of area of the cantilever element

In fact, the total elastic deformation is a combination of the curvature induced by the lateral load plus the additional curvature caused by the post-tensioned moment differential at the top of the cantilever illustrated in Figure 7.9. This moment differential is caused by the variation of tendon force throughout the section at the top of the cantilever. When accounting for both components, the elastic displacement at H_e is given by Eq.(7.32), where clockwise bending moments are treated as being

positive causing tension on the left-hand side of the cantilever in Figure 7.9, i.e. $\sum T_{pt,i} d_{pt,i} = -T_{pt1} d_{pt1} + T_{pt2} d_{pt2} < 0$.

$$\Delta_e = \frac{F \cdot H_e^3}{3E \cdot I_e} + \frac{\left(\sum T_{pt,i} d_{pt,i}\right) \cdot H_e^2}{2E \cdot I_e} \qquad \textbf{7.32}$$

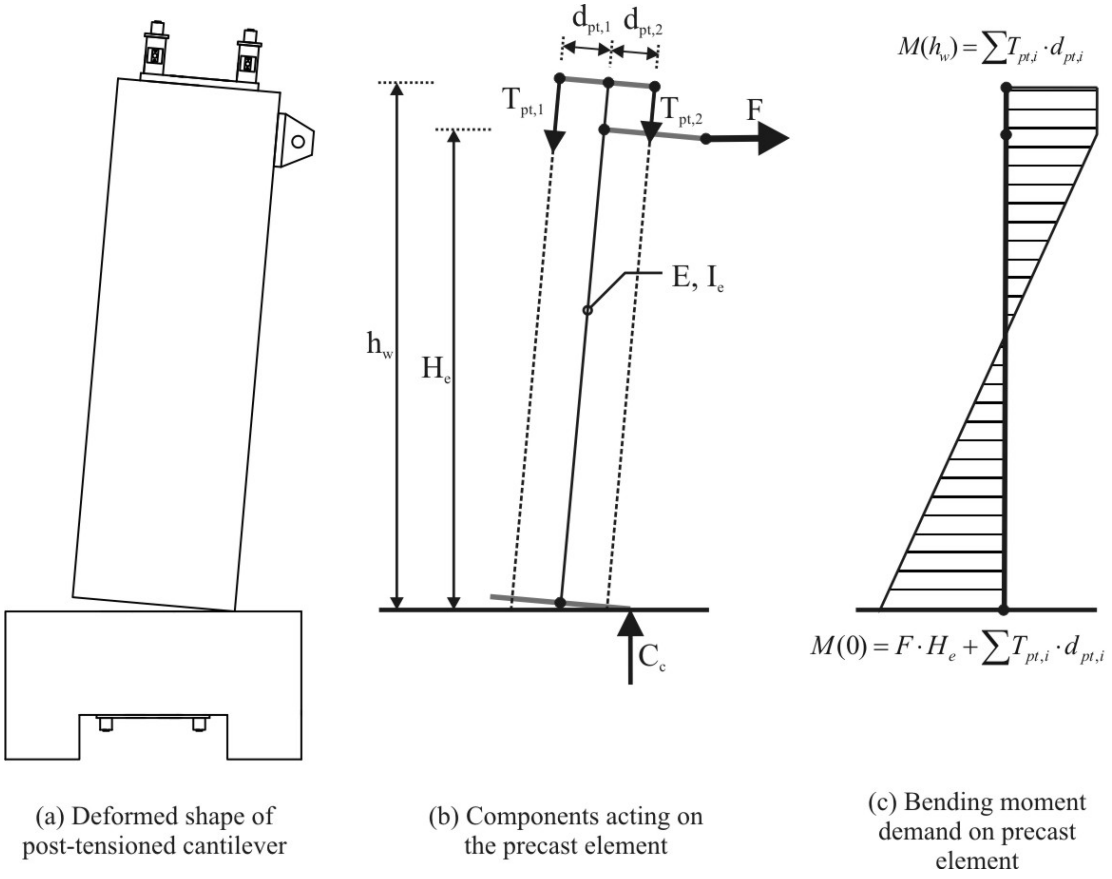

Figure 7.9 Components of elastic deformation for the precast cantilever element

The axial stiffness of the precast element will also effect the tendon elongation. As the tendon load is increased the precast element will shorten, reducing the effective axial stiffness of the post-tensioned tendons. By considering the axial stiffness of the tendons and the precast element in series (Figure 7.10), a stiffness reduction factor $\boldsymbol{K_{red}}$ is defined

$$K_{red} = \frac{1}{1 + \rho_{pt} \dfrac{E_{pt}}{E_e} \dfrac{h_w}{L_{ub,pt}}} \qquad \textbf{7.33}$$

As an example, if the unbonded length of the tendon $\boldsymbol{L_{ub,pt}}$ is equal to the height of the wall $\boldsymbol{h_w}$ and a post-tensioned reinforcement ratio $\boldsymbol{\rho_{pt}}$ of 0.5% is considered, $\boldsymbol{K_{red}}$ is equal to 0.968. The total axial stiffness of the tendon group is equal to the following

$$k_{pt} = K_{red} \frac{n_{pt} A_{pt} E_{pt}}{L_{ub,pt}} \qquad \textbf{7.34}$$

Where, $\boldsymbol{k_{pt}}$ is the total axial stiffness of all tendon elements in the section, $\boldsymbol{n_{pt}}$ is the total number of tendons in the section and $\boldsymbol{A_{pt}}$ is the cross sectional area of one tendon. It some situations the reduction factor $\boldsymbol{K_{red}}$ may be insignificant enough to ignore.

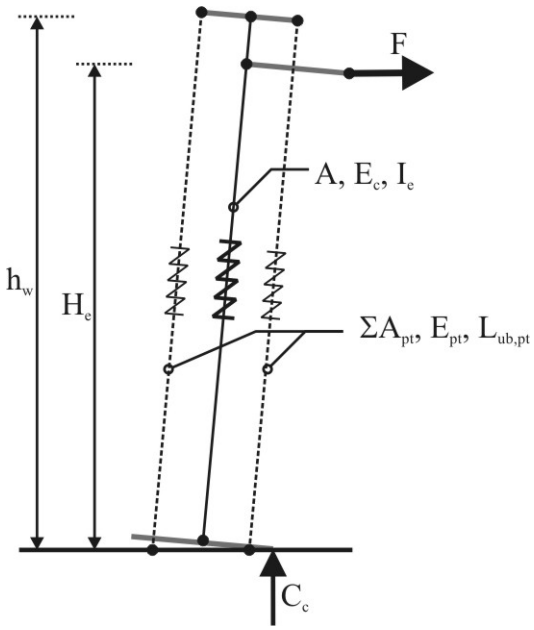

Figure 7.10 Axial stiffness of post-tensioned rocking system

It can be argued that additional tendon elongation can also be attributed to the fixed-end rotation at the top of the cantilever element as pictured in Figure 7.11. The fixed end rotation at the top of the cantilever is computed by integrating the curvature demand over the height of the precast element. The curvature demand is comprised of two contributions; curvature due to the applied lateral load and curvature due to the post-tensioned moment differential. The fixed end rotation due to the applied lateral load is given by

$$\theta_1 = \frac{F \cdot H_e^2}{2 E_c I_e} \qquad \textbf{7.35}$$

The fixed end rotation due to the post-tensioned moment differential is given by Eq.(7.36) where $\sum T_{pt,i} d_{pt,i} < 0$.

$$\theta_2 = \frac{\left(\sum T_{pt,i} d_{pt,i}\right) \cdot h_w}{E_c I_e} \qquad \textbf{7.36}$$

The net elongation of each tendon is a summation of the two fixed end rotations.

$$\Delta_{pt,i} = \pm\frac{F \cdot H_e^2}{2E_c I_e} d_{pt,i} \pm \frac{\left(\sum T_{pt,i} d_{pt,i}\right) \cdot h_w}{E_c I_e} d_{pt,i} \qquad \textbf{7.37}$$

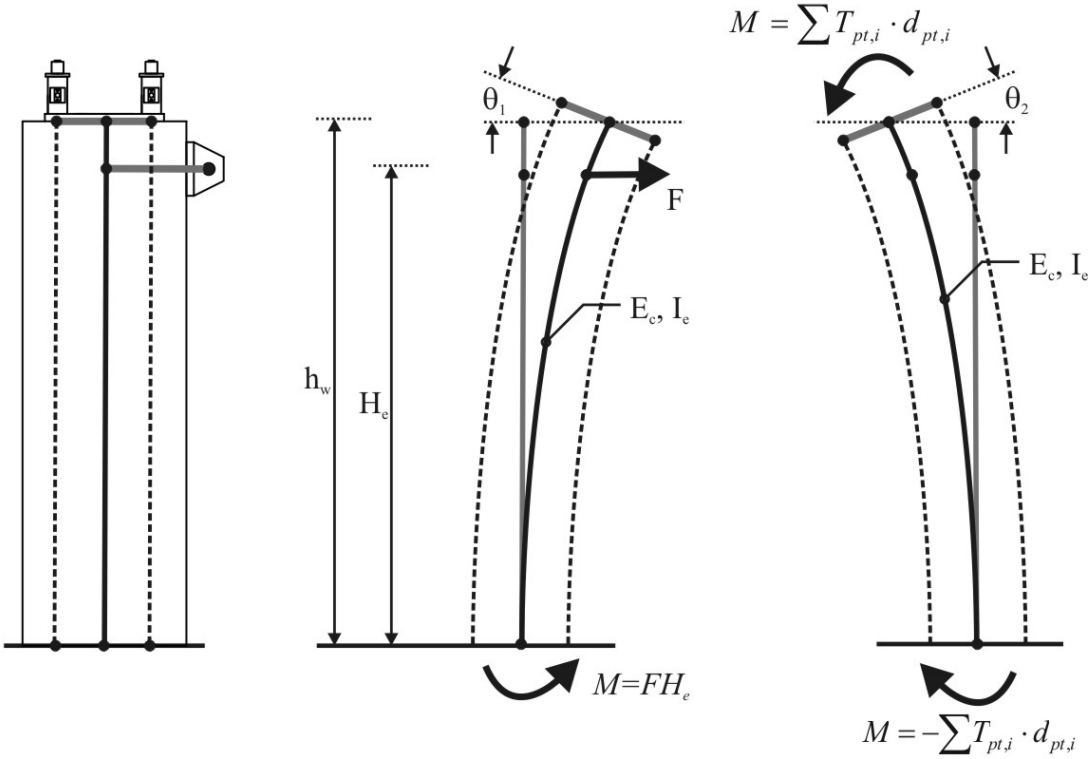

Figure 7.11 Tendon elongation due to elastic flexure

After deriving Eq.(7.37) it becomes obvious that tendon elongation due to the fixed-end rotation can be neglected as the end rotations oppose each other and are likely to be similar in magnitude. Furthermore, even if the second term in Eq.(7.37) is zero the computed elongation can be insignificant enough to ignore altogether.

7.2.2. Comparison of an Analytical Monotonic Backbone Model with Experimental Test Results

The ability to accurately model the local rocking response (at the base of the precast element) is of particular importance for post-tensioned rocking systems, i.e. the base rotation θ versus the over-turning moment M. The over-turning moment is related to the applied lateral force F by Eq.(7.38), while the base rotation is related to the total displacement Δ by Eq.(7.39).

$$M = F \cdot H_e \qquad \textbf{7.38}$$

Where, M is the over-turning moment at the base, F is the applied load at the effective height of the system and H_e is the effective height of the effective mass, defining the location of the resultant inertia force (applied lateral load).

$$\Delta = \theta \cdot H_e + \Delta_e \qquad \textbf{7.39}$$

In Eq.(7.39) Δ is the total displacement at the effective mass, θ is the rotation of the base due to the gap opening and Δ_e is the elastic flexural displacement of the precast element.

In this section, a number of analytical models are compared to experimental test results in terms of the global force and displacement/drift ratio. In doing so, the elastic flexural stiffness of the precast element within the analytical model was calibrated to the experimental response. That is, the rigid body displacement θH_e was deducted from the total displacement Δ, leaving the elastic component Δ_e (refer Eq.(7.39)). This method was opted for the primary reason that any differences between the experimental response and analytical model are associated with the response at the rocking base and not the elastic deformation of the precast element. This method essentially converts the rotation response at the base to a global response at the location of the applied load.

Each analytical model in this section is compared to a number of post-tensioned specimens whose experimental response was presented in Chapter 4, 5 & 6. For reference throughout this section, a brief summary of each test specimen is presented in Table 7.2. It should be recognised that while the five post-tensioned walls were referred to as Wall 1 to Wall 5 in Chapter 5 & 6, they are referred to as PC Wall or LVL Wall in this chapter to distinguish the difference between the precast concrete walls, tested in Chapter 6, and the LVL walls tested in Chapter 5.

Table 7.2 Summary of test specimens providing a comparison to the monotonic analytical model

	Brief description	Material at rocking interface	Dissipation
PT1	Precast concrete post-tensioned bridge pier.	Concrete	None
PT2	Precast concrete post-tensioned bridge pier.	Steel plate	None
HBD1	Precast concrete post-tensioned bridge pier.	Concrete	Traditional internally grouted mild steel
HBD2	Precast concrete post-tensioned bridge pier.	Concrete	Internally grouted mild steel with discrete yielding region
PC Wall 1	Precast concrete post-tensioned wall.	Concrete	None
PC Wall 4	Precast concrete post-tensioned wall.	Concrete	Externally mounted TCY dampers
PC Wall 5	Precast concrete post-tensioned wall.	Concrete	Externally mounted TCY dampers
LVL Wall 1	Post-tensioned LVL wall.	LVL	None
LVL Wall 4	Post-tensioned LVL wall.	LVL	Externally mounted TCY dampers

(a) An Analytical Model for Traditional Hybrid Post-Tensioned systems with Internally Grouted Reinforcement

The accuracy of the monolithic beam analogy (MBA) in capturing the response of a hybrid post-tensioned system will be tested against the experimental response of the hybrid bridge pier HBD1. HBD1 is a conventional post-tensioned bridge pier with internally grouted mild steel reinforcement. The experimental and analytical lateral force versus displacement of the bridge pier is compared in Figure 7.12 (a) while the response of the post-tensioned tendons is compared in Figure 7.12 (b). A comparison is also made at a local level in Figure 7.13, comparing the depth of the rocking contact along the rocking interface and the strain within the mild steel reinforcement layer (due to symmetry, only one mild steel layer is shown). This analytical model presented in Figure 7.12 and Figure 7.13 considers each modelling aspect discussed in Section 7.2.1. That is, the monotonic stress-strain envelope of the steel accounts for cyclic loading, while the confined concrete is modelled using Method C; this applies the smeared core confinement over the entire gross area of the section to recognise some confinement provided by the steel angle around the perimeter of the rocking surface. Furthermore, the elastic deformation of the precast element accounts for the PT moment differential, while the stiffness of the tendon is reduced to account for the axial flexibly of the precast element. A summary of the key model parameters is listed in Table 7.3. The analytical model compares well to the experimental response at a global and local level. The tendon force is over-estimated slightly, while the depth of contact during rocking is modelled with good accuracy. Furthermore, the growth of the strain within the mild steel reinforcement appears to be captured well, confirming the accuracy of the revised monolithic beam analogy (rMBA) and the improved modelling techniques discussed in Section 7.2.1.

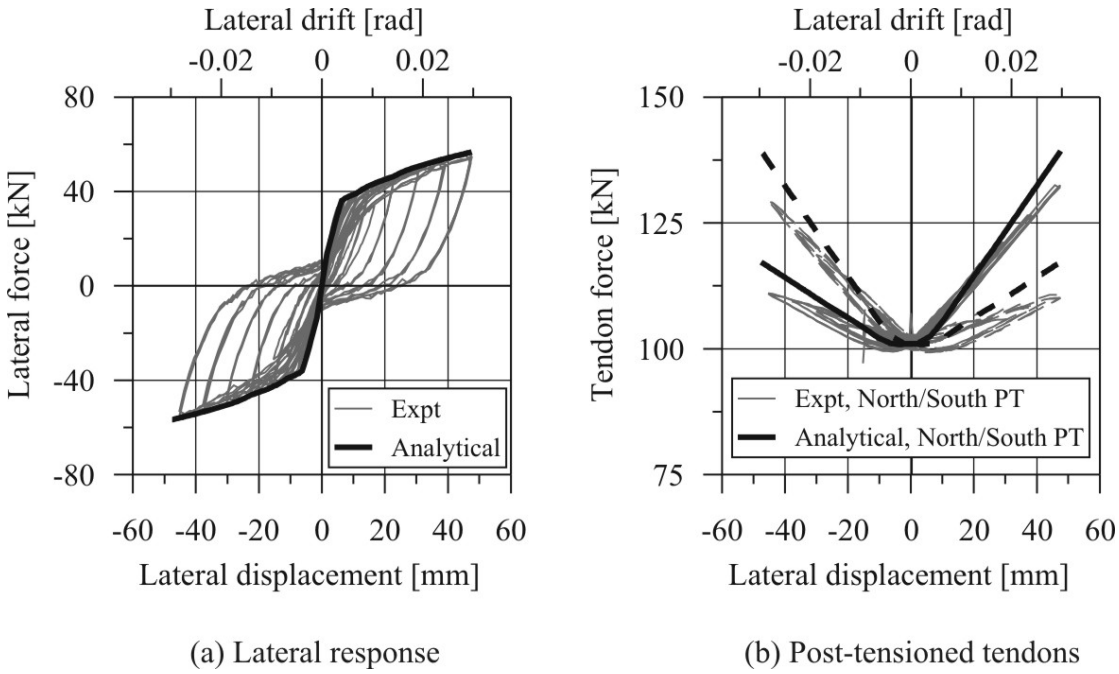

Figure 7.12 Comparison between the experimental response and the RMBA analytical model of HBD1

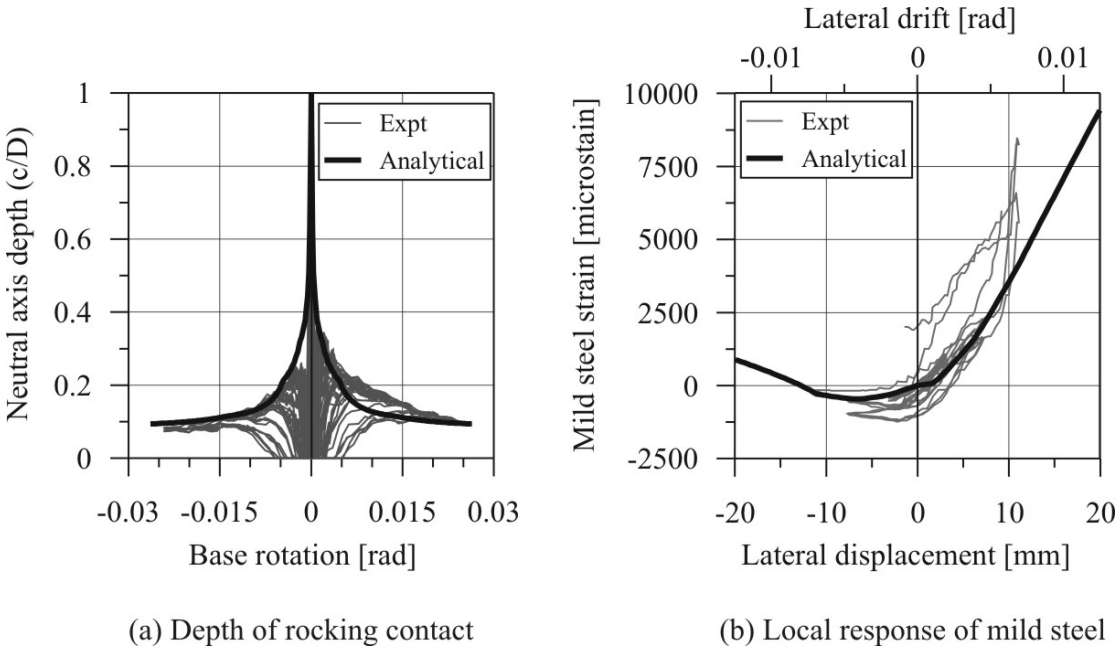

Figure 7.13 Comparison at a local level between the experimental response and the RMBA analytical model of HBD1

Table 7.3 Analysis properties of HBD1

Precast properties	
Calibrated flexural stiffness, E_cI_e	14473 kNm^2
Computed confinement ratio, f'_{cc}/f'_c	1.19
Measured Unconfined compression strength, f'_c	54MPa
Measured post-tensioning properties	
Initial post-tensioned force, $T_{pt,0}$	202kN (0.031f'$_c$A$_g$)
Unbonded length, $L_{ub,pt}$	2685mm
Young's modulus, E_{pt}	197100MPa
Area of tendon, A_{pt}	99mm^2
Measured mild steel properties	
Unbonded length, $l_{ub,ms}$	50mm
Diameter of mild steel, d_b	16mm
Young's modulus, E_{ms}	194000MPa
Yield strain, $\varepsilon_{y,ms}$	0.00157
Strain hardening, $\varepsilon_{sh,ms}$	0.011
Stain x, $\varepsilon_{x,ms}$	0.031
Strain at ultimate, $\varepsilon_{su,ms}$	0.11
Yield stress, $f_{y,ms}$	304MPa
Stress x, $f_{x,ms}$	395MPa
Ultimate stress, $f_{u,ms}$	450MPa

Considering each of the modelling issues discussed in Section 7.2.1 above, three alternative models (Model 2, 3 & 4) are compared to the analytical model above in Figure 7.14. The four models are described below.

Model 1 is the analysis discussed above and presented in Figure 7.12. This model compares well with the experimental envelope.

Model 2 is identical to (1), however, the monotonic steel constitutive relationship does not account for cyclic loading, rather, monotonic stress-strain parameters are used.

Model 3 is identical to (2), although, the steel angle around the perimeter of the rocking toe is ignored from the analysis and the cover concrete is modelled as unconfined concrete. In this analysis the spalling strain of concrete is set to $\boldsymbol{\varepsilon_{sp}} = 0.005$.

Model 4 is identical to (3), however, the tendon stiffness is not reduced to account for axial shortening of the precast element (that is, $\boldsymbol{K_{red}} = 1.0$ in Eq.(7.33)) and the elastic displacement of the precast element does not include the tendon moment differential: only the displacement due to the lateral load is included, i.e. the right-hand side of Eq.(7.36) is equal to zero.

With reference to each model in Figure 7.14, when cyclic loading is not accounted for within the steel constitutive model the lateral load accumulates an error of roughly 7%. This error escalades when the confinement provided by the perimeter steel angle is ignored. Model 3 in Figure 7.14 indicates that the cover concrete begins to spall at a lateral drift ratio of 3%; however, no signs of spalling were observed during testing of HDB1. This suggests that accounting for some confinement of the cover concrete seems very appropriate in this instance. The errors associated with the axial shortening of the precast element, and the tendon-induced elastic curvatures are

negligible. When the lateral displacement is less than 30mm, all four models return a similar response. At these low levels of displacement the steel strain is just entering the strain hardening region, while the stress in the cover concrete is just beginning to peak ($\varepsilon_c = 0.002$). The error associated with each of the three alternative models continues to grow as the lateral drift exceeds 3.5% in Figure 7.14.

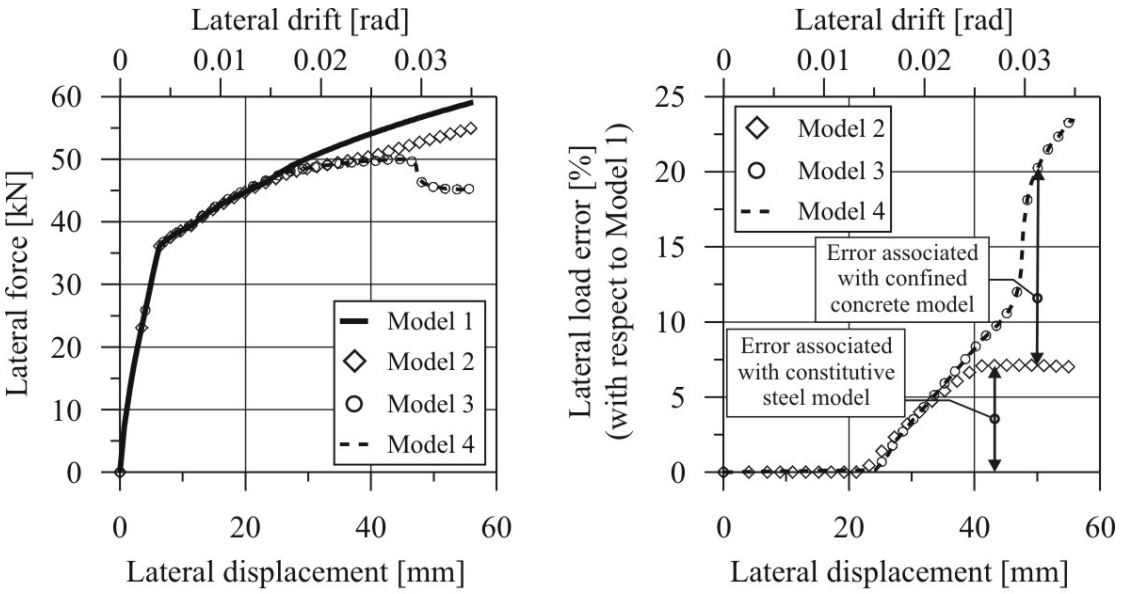

Figure 7.14 Comparison between four models considering variations in the constitutive relationships of the material

(b) An Analytical Model for a Variation of a Hybrid Post-Tensioned system with Internally Grouted Reinforcement

The second analytical-experimental comparison is undertaken on a variation of a traditional hybrid system with internally grouted reinforcement. The hybrid pier HBD2 differs from a traditional solution in that the internal mild steel has a discrete yielding region along a fused diameter. The mild steel bar is threaded into the foundation and grouted within the precast pier (see Chapter 4). The steel strain equations derived from the revised Monolithic Beam Analogy (rMBA) require modification in this analysis as the diameter of the bar varies along the length. The internally grouted mild steel bar has a discrete yielding region along the bar: in particular, the diameter of the unbonded portion of the bar d_s (with unbonded length l_{ub}) is less than the diameter of the bar d_b that is grouted within the precast pier (Figure 7.15). It should be appreciated that the strain penetration in this case is not as significant as bonded reinforcement with constant diameter. The strain profile of a bonded bar with a reduced diameter outside of the bonded area is illustrated in Figure 7.15. There is a sudden discontinuity in strain where the diameter of the bar increases. It will be shown that the average strain ε_b acting along the strain penetration length l_{sp} is reduced depending on the ratio of the fused bar diameter d_s to the diameter of the bonded bar d_b.

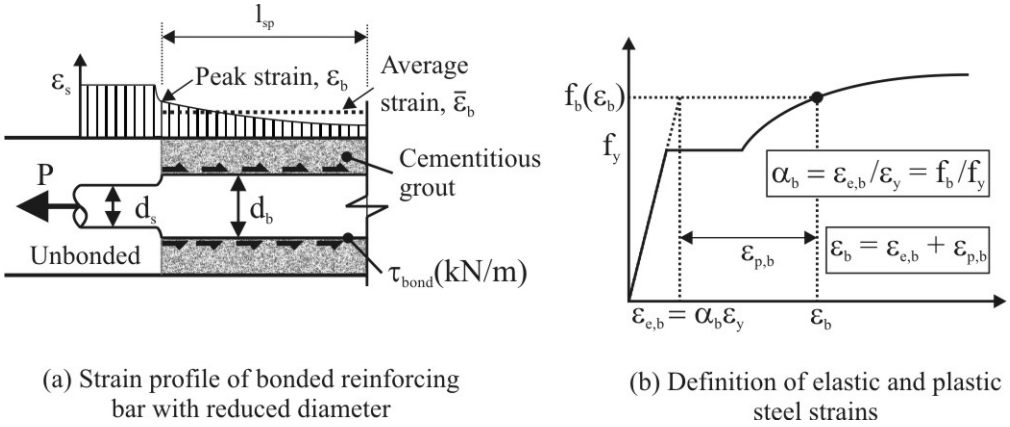

(a) Strain profile of bonded reinforcing bar with reduced diameter

(b) Definition of elastic and plastic steel strains

Figure 7.15 Strain distribution within bonded reinforcement

Referring to the strain relationships within the rMBA discussed in Chapter 3, the total elongation of the mild steel reinforcement Δ_{ms} is the integral of the strain along the unbonded length plus the integral of the strain along the strain penetration length.

$$\Delta_{ms} = \varepsilon_s \cdot l_{ub.ms} + 2\Delta_{sp} \qquad \textbf{7.40}$$

In Eq.(7.40) ε_s is the strain in the unbonded region of the reinforcing bar. The integral of the strain along the strain penetration depth l_{sp} is defined by Sritharan. [1998] as

$$\Delta_{sp} = \frac{2}{3} l_{sp} \varepsilon_{e,b} + l_{sp} \varepsilon_{p,b} = \frac{2}{3} l_{sp} \alpha_b \varepsilon_y + l_{sp} \left(\varepsilon_b - \alpha_b \varepsilon_y \right) \varepsilon_{p,b} \qquad \textbf{7.41}$$

Where

l_{sp} = strain penetration depth defined as $l_{sp} = 0.022 f_y d_b$

f_y = yield stress of the bonded reinforcement

d_b = diameter of the bonded reinforcement

ε_b = the peak strain within the bonded portion of the reinforcing bar, i.e. the strain at the unbonded-bonded interface: no load is yet transferred to the surrounding grout, $\varepsilon_b = \varepsilon_{e,b} + \varepsilon_{p,b}$

$\varepsilon_{e,b}$ = elastic strain within the bonded region of the reinforcing bar, corresponding to the peak strain ε_b (refer Figure 7.15 (b))

$\varepsilon_{p,b}$ = plastic strain within the bonded region of the reinforcing bar, corresponding to the peak strain ε_b (refer Figure 7.15 (b))

$\alpha_{i,b}$ = ratio of the steel stress in the bonded bar f_b to the yield stress f_y, $\alpha_b = f_b / f_y = \varepsilon_{e,b} / \varepsilon_y$

The subscript b refers to the portion of the bar that is bonded, while s refers to the portion of the bar that is unbonded. By substitution of Eq.(7.41) into Eq.(7.40) the strain in the unbonded region ε_s can be written as

$$\varepsilon_s = \frac{\Delta_{ms} - 2\left[\frac{2}{3} l_{sp}\alpha_b\varepsilon_y + l_{sp}\left(\varepsilon_b - \alpha_b\varepsilon_y\right)\right]}{l_{ub,ms}} \qquad \textbf{7.42}$$

If the bonded portion of the bar is yielding $\varepsilon_b > \varepsilon_y$, then Eq.(7.42) is written as

$$\varepsilon_s = \frac{\Delta_{ms} - 2l_{sp}\varepsilon_b + \frac{2}{3} l_{sp}\alpha_b\varepsilon_y}{l_{ub,ms}} \qquad \textbf{7.43}$$

Note, that Eq.(7.43) requires iteration as the strain in the unbonded region ε_s must be known to be able to compute the strain in the bonded region ε_b and α_b. The steel stress f_b within the bonded region can be computed from the steel stress f_s along the unbonded region using Eq.(7.44); however, the corresponding strain ε_b must be found from the inverse of the preferred stress-strain relationship, that is $\varepsilon_b = \mathbf{f}(f_b)$.

$$f_b\left(\varepsilon_b\right) = f_s\left(\frac{d_s}{d_b}\right)^2 \qquad \textbf{7.44}$$

However, if the bonded portion of the bar is not yielding $\varepsilon_b < \varepsilon_y$, then $\alpha_b\varepsilon_y = \varepsilon_b$ and Eq.(7.42) reduces to the following.

$$\varepsilon_s = \frac{\Delta_{ms}}{l_{ub,ms} + \frac{4}{3} l_{sp}\left(\frac{d_s}{d_b}\right)^2} \qquad \textbf{7.45}$$

When the strain in the bonded region is elastic ($\varepsilon_b < \varepsilon_y$), ε_b can be computed directly from the steel stress along the unbonded region f_s.

$$\varepsilon_b = \frac{f_s}{E_s}\left(\frac{d_s}{d_b}\right)^2 \qquad \textbf{7.46}$$

When the fused diameter d_s is equal to the bonded diameter d_b, Eq.(7.43) and (7.45) reduce back to the traditional rMBA formulation for bonded reinforcement with constant diameter. If the ratio of $d_b/d_s > \sqrt{f_u/f_y}$ then the bonded portion of the bar is guaranteed not to yield: this allows Eq.(7.45) can be used with confidence, knowing that yielding is confined entirely to the unbonded portion of the bar.

This revised steel strain model compares reasonably well at a global level to the experimental test data in Figure 7.16 (a). However, when the model is compared in detail at the local level in Figure 7.17 (a), the stiffness of the rocking interface appears to be over-estimated. In fact, permanent plastic concrete strains are likely to have occurred along the rocking interface due to the prior testing of HBD1. When the rocking interface has "softened" a greater compression depth is needed to balance the internal forces within the section; hence, the model will over-estimate the stiffness of

the rocking interface. It is for this reason that the analytical model will also over-estimate the tendon forces. This is seen in that the analytical model over-estimates the lateral stiffness for negative displacements less than 30mm in Figure 7.16 (a). The confined concrete model used in HBD1 is also used in this model for the analysis of HBD2. A summary of the parameters used in the analytical model are listed in Table 7.4.

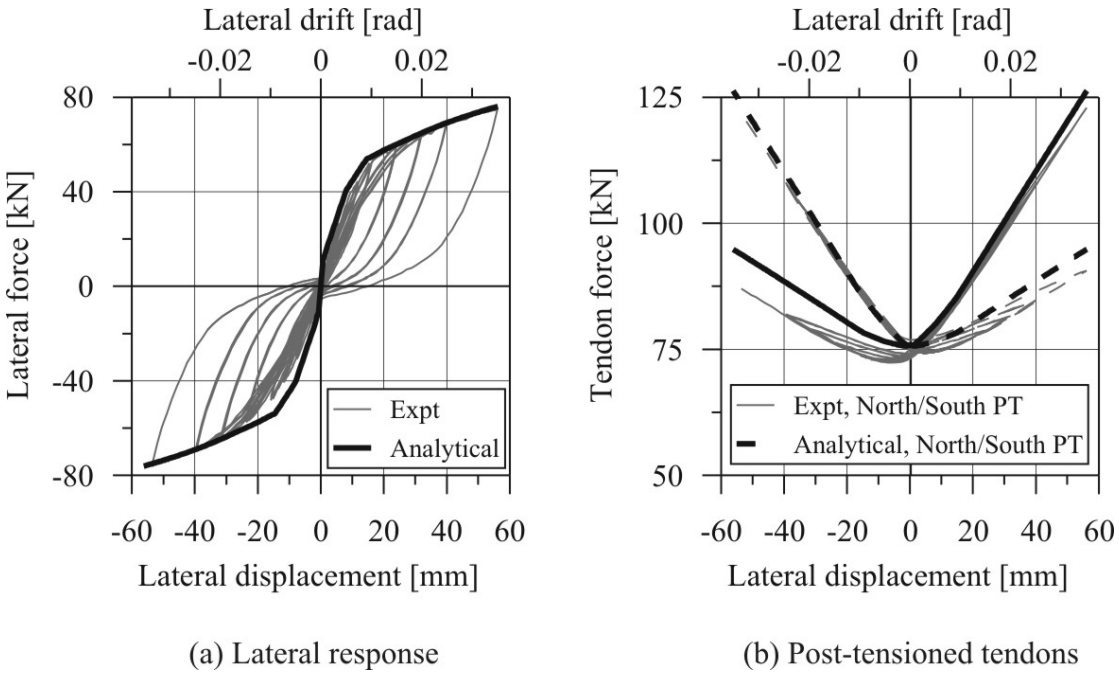

Figure 7.16 Comparison between the experimental response and the analytical model of HBD2

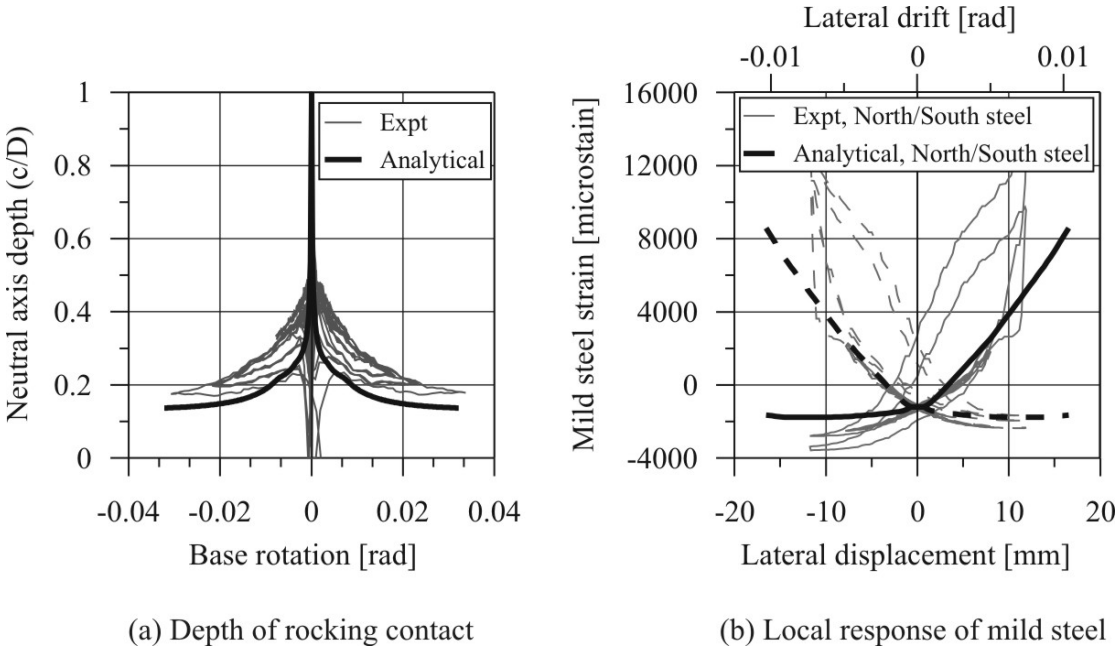

Figure 7.17 Comparison at a local level between the experimental response and the analytical model of HBD2

Table 7.4 HBD2 analytical model properties

Precast properties	
Calibrated flexural stiffness, E_cI_e	21733 kNm^2
Computed confinement ratio, f'_{cc}/f'_c	1.19
Measured Unconfined compression strength, f'_c	54MPa
Measured post-tensioning properties	
Initial post-tensioned force, $T_{pt,0}$	303.2kN ($0.046f'_cA_g$)
Unbonded length, $L_{ub,pt}$	2270mm
Young's modulus, E_{pt}	197100MPa
Area of tendon, A_{pt}	99mm^2
Measured mild steel properties	
Unbonded length, $l_{ub,ms}$	50mm
Diameter of unbonded region of the bar, d_s	12.5mm
Diameter of the bonded region of the bar, d_b	20mm
Young's modulus, E_{ms}	218460MPa
Yield strain, $\varepsilon_{y,ms}$	0.0026
Strain hardening, $\varepsilon_{sh,ms}$	0.008
Stain x, $\varepsilon_{x.ms}$	0.0153
Strain at ultimate, $\varepsilon_{su,ms}$	0.044
Yield stress, $f_{y,ms}$	568MPa
Stress x, $f_{x.ms}$	633MPa
Ultimate stress, $f_{u,ms}$	704MPa

(c) An Analytical Model for Post-Tensioned Systems with No Dissipation

For post-tensioned (PT) systems with no internally grouted reinforcement the monolithic beam analogy (rMBA) must be revisited further. In the explanations that follow MBA refers to the originally proposed analogy Pampanin et al. [2001], rMBA refers to the revised analogy put forward by Palermo [2004]. A new analogy is proposed for PT only systems with no dissipation, referred to as ptMBA. No yielding takes place in a PT only system; therefore, the equivalent monolithic (EM) element (equivalent in terms of reinforcement and geometry) should also remain elastic. The reinforcement within the EM connection must be consistent with the PT connection. The proposed analogy states that the EM connection contains no bonded mild steel reinforcement, only prestressed reinforcement; this is consistent with the reinforcement passing the rocking interface within the PT connection. According to this new analogy the EM element must respect two important aspects. First, the prestressed reinforcement within the EM element is bonded within the section to insure strain compatibility exists and cracking is distributed throughout the element. This will prevent the formation of a single crack occurring at the foundation interface. If a single crack were to occur, an infinite curvature develops at the base and Bernoulli's hypothesis "*plane sections remain plane"* would be violated. Second, the bonded reinforcement is unstressed. The axial load at the base of the EM element is a combination of an applied axial load $\boldsymbol{N_{mono}}$, plus the additional tendon load due to strain compatibility $\boldsymbol{\Delta T_{pt}}$ within the PT element. The total axial load history acting on the EM element ($\boldsymbol{N_{mono}}$+$\boldsymbol{\Delta T_{pt,mono}}$) should be consistent with the total tendon load acting within the rocking interface of the PT element $\boldsymbol{T_{pt}}$, i.e. $N_{mono} = T_{pt} - \Delta T_{pt,mono}$ If the unbonded tendons within the PT element are to remain elastic then the unstressed, grouted tendons within the EM element must also remain elastic. Recall from Chapter 3, the rMBA for traditional hybrid PT connections is divided into three distinct regions. The proposed ptMBA analogy is reduced to two regions and is illustrated in Figure 7.18 and discussed in further detail below.

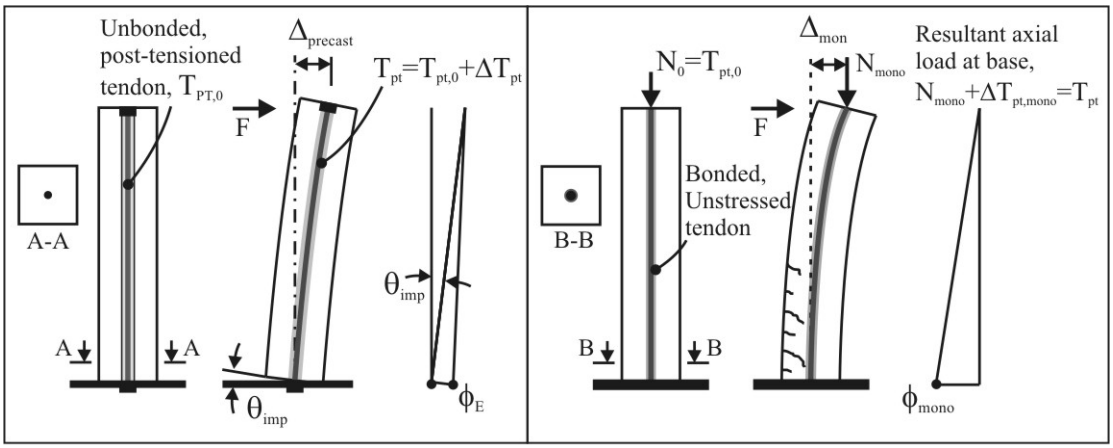

Figure 7.18 Monolithic beam analogy for post-tensioned only systems: no yielding elements, (ptMBA)

The first region relates concrete compression strains between the PT connection and the EM connection for displacements less than the decompression displacement Δ_{dec}. In this region, the maximum concrete compression strains within the EM and PT connection are equal and defined by

$$\varepsilon_{hybrid} = \varepsilon_{mono} = \varepsilon_0 + \phi_{mono} \cdot \frac{D}{2} \qquad \textbf{7.47}$$

Where

ε_0 = initial compression strain within the section due to the presence of axial load and/or initial post-tensioning.
D = depth of the section
ϕ_{mono} = curvature at the base of the cantilever due to the applied load F

The system is linear up until decompression, requiring only a single strain calculation at the onset of uplift of the base, $\theta_{imp} = 0$. The second region relates concrete compression strains within the PT element to those within the EM element for displacements between the decompression and the yield limit of the EM element. The displacement of the PT element $\Delta_{PT,sys}$ is given by a rigid base rotation plus the elastic displacement of the precast cantilever element $\Delta_{elastic}$.

$$\Delta_{PTsys} = \theta_{imp} \cdot L_{cant} + \Delta_{elastic} \qquad \textbf{7.48}$$

The displacement of the monolithic element Δ_{mono} is equal to the integration of the curvature demand ϕ_{mono} along the height of the cantilever.

$$\Delta_{mono} = \frac{\phi_{mono} \cdot L_{cant}^2}{3} \qquad \textbf{7.49}$$

Considering a lateral load F acting on the two systems, the displacement of a PT system will be greater than an EM system with identical geometry and reinforcement, i.e. $\Delta_{PTsys} > \Delta_{mono}$. Recalling from Chapter 3, the key statement behind the revised monolithic beam analogy (rMBA) is: *"the additional displacement beyond the decompression point of an EM element (Δ_{mono}-Δ_{dec}) is equal to the rigid rotation displacement of a PT element ($\theta_{imp}L_{cant}$)"*. This statement yields Eq.(7.50) below

$$\theta_{imp} \cdot L_{cant} = \Delta_{mono} - \Delta_{dec} = \frac{\phi_{mono} \cdot L_{cant}^2}{3} - \frac{\phi_{dec} \cdot L_{cant}^2}{3} \qquad \textbf{7.50}$$

Rearranging Eq.(7.50) and solving for the hypothetical concrete strain ε_c at the rocking interface of the PT element yields the following

$$\varepsilon_c = \left[\frac{3\theta_{imp}}{L_{cant}} + \phi_{dec} \right] c \qquad \textbf{7.51}$$

The rotation limits in which this strain relationship is valid to can be derived from Eq.(7.50) by setting the curvature demand ϕ_{mono} to equal to the yield curvature ϕ_y.

$$0 < \theta_{imp} < \left(\phi_y - \phi_{dec}\right)\frac{L_{cant}}{3} \qquad \textbf{7.52}$$

If the tendons remain elastic, then Eq.(7.51) will apply for all imposed rotations θ_{imp}.

To illustrate the difference between the ptMBA and the current rMBA, the theoretical curvature ε_c/c at the rocking interface is compared in Figure 7.19. The concrete strain relationship derived within the rMBA analogy is reproduced from Chapter 3 in Eq.(7.53) below. This strain relationship is used for a PT-yielding (hybrid) connection.

$$\varepsilon_c = \left[\frac{\dfrac{3\theta_{imp}}{L_{cant}} - \left(\phi_y - \phi_{dec}\right)}{\dfrac{3L_p}{L_{cant}}\left(1 - \dfrac{L_p}{2L_{cant}}\right)} + \phi_y\right] \cdot c \qquad \textbf{7.53}$$

Considering a cantilever with length L_{cant} = 10m and a plastic hinge length of $0.1L_{cant}$ the two strain relationships are plotted considering two different yield and decompression curvatures in Figure 7.19. The decompression curvature has negligible effect on both relationships, while reducing the yield curvature increases the theoretical curvature within the PT-yielding (hybrid) system. Figure 7.19 indicates that for the same imposed rotation the theoretical curvature (related to compression strains) within a PT only connection can be in the order of 1/3 that of a PT yielding (hybrid) connection.

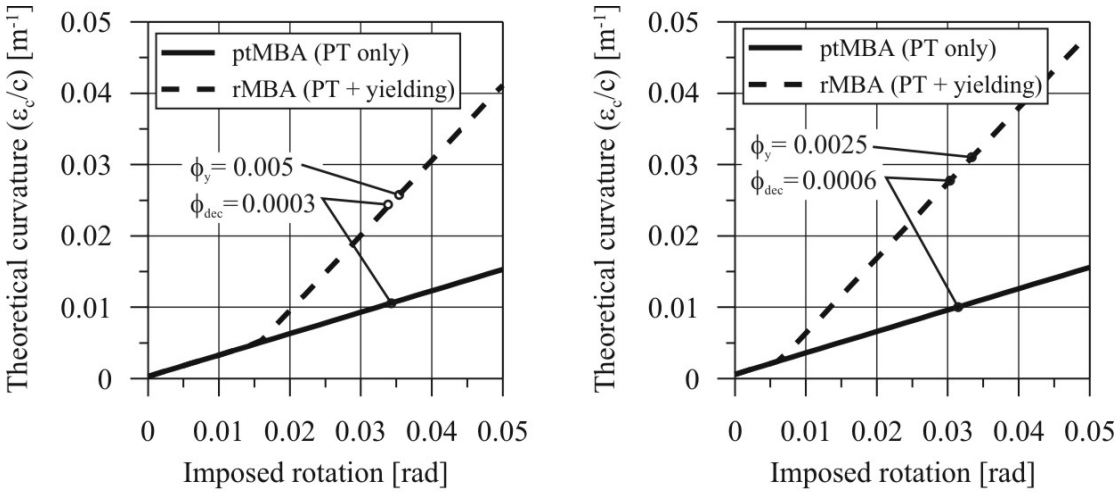

(a) Theoretical curvature comparison ϕ_y=0.005 and ϕ_{dec}=0.0003

(b) Theoretical curvature comparison ϕ_y=0.0025 and ϕ_{dec}=0.0006

Figure 7.19 The relationship between the theoretical curvature and imposed rotation, compared between the PT only analogy (ptMBA) and PT yielding analogy (rMBA)

The ptMBA is compared to the experimental response of one PT-only wall test that was presented in Chapter 6 and two PT-only bridge pier tests that were presented in Chapter 4. The PT-only wall test, PC Wall 1 (Chapter 6), is a monotonic push-over test recorded during loading to the release displacement prior to free-vibration testing. The analytical-experimental comparison in Figure 7.20 for PC Wall 1 agrees very well at a global and local level. The comparison of the tendons is not shown, for if the neutral axis depth is well modelled then the tendon elongation will be correctly captured too. The analytical model in Figure 7.20 uses a confined concrete model similar to that used in the previous analytical models. The parameters used in this analytical model are listed in Table 7.5.

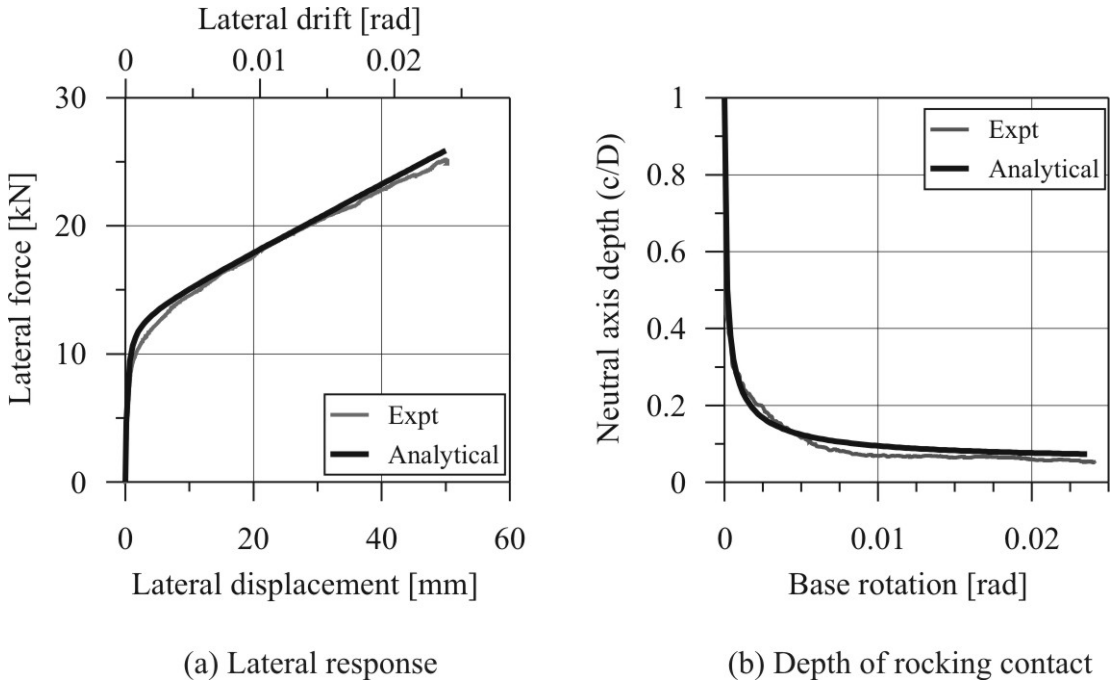

Figure 7.20 Comparison between the experimental push-over response (prior to release of free vibration) and the RMBA analytical model of the precast concrete post-tensioned wall, PC Wall 1

Table 7.5 Model properties of PC Wall 1

Precast properties	
Calibrated flexural stiffness, E_cI_e	103846 kNm^2
Computed confinement ratio, f'_{cc}/f'_c	1.91
Measured Unconfined compression strength, f'_c	45.1 MPa
Measured post-tensioning properties	
Initial post-tensioned force, $T_{pt,0}$	98.9kN ($0.021f'_cA_g$)
Unbonded length, $L_{ub,pt}$	3558mm
Young's modulus, E_{pt}	197100MPa
Area of tendon, A_{pt}	99mm^2

The ptMBA is next compared to the experimental response of the post-tensioned pier PT1. Details of this pier were discussed in Chapter 4 (and briefly summarised in

Table 7.2) where it was mentioned that testing was only carried out to a lateral drift ratio of 0.75% to prevent damage under subsequent testing. Again, Figure 7.21 indicates the local and global response parameters are matching well. The analytical model captures the initial loading stiffness well and the transition to the bilinear stiffness. A summary of the parameters used in the modelling of PT1 are listed in Table 7.6.

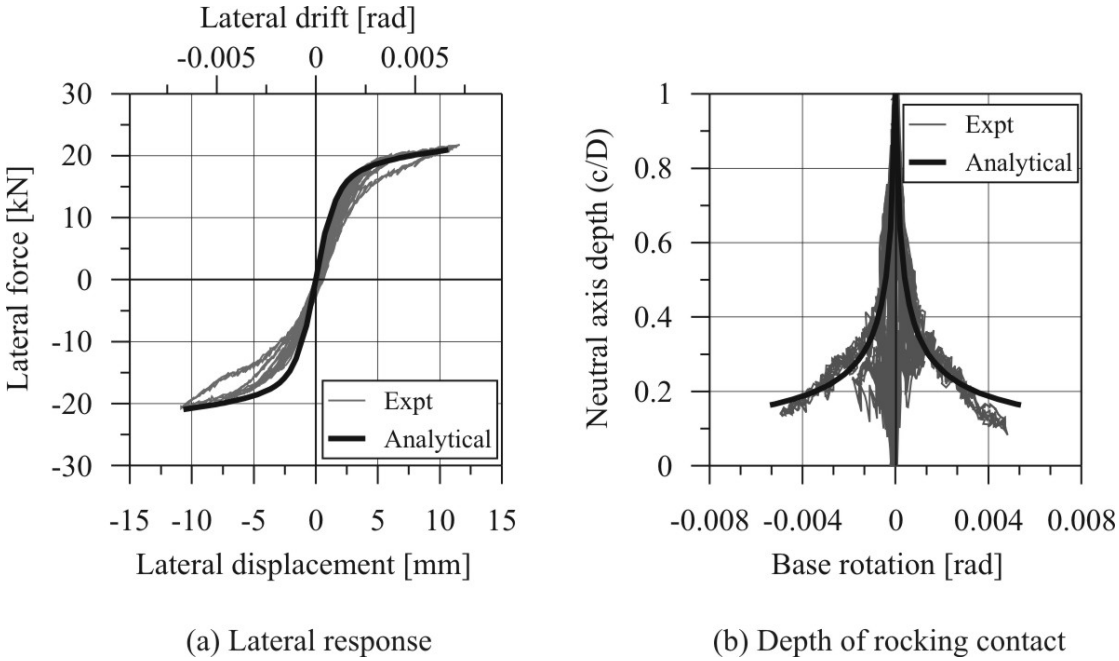

Figure 7.21 Comparison between the experimental cyclic response and the RMBA analytical model of the post-tensioned only pier PT1

Table 7.6 Model properties of PT1 (precast concrete)

Precast properties	
Calibrated flexural stiffness, E_cI_e	13784 kNm^2
Computed confinement ratio, f'_{cc}/f'_c	1.19
Measured Unconfined compression strength, f'_c	54MPa
Measured post-tensioning properties	
Initial post-tensioned force, $T_{pt,0}$	204kN ($0.031f'_cA_g$)
Unbonded length, $L_{ub,pt}$	2685mm
Young's modulus, E_{pt}	197100MPa
Area of tendon, A_{pt}	99mm^2

The final analytical-experimental comparison is carried out on the post-tensioned pier PT2. This precast concrete post-tensioned pier was detailed with a 25mm steel plate at the base of the pier. There is some uncertainty as to what constitutive material model to use within the rocking interface. Two extreme bounds exist: the first is to model the material as confined concrete as per the analysis of HBD1, HBD2 and PT1, while the other bound is to model the material as an elasto-plastic material representative of steel. In fact, these two analytical models are compared to the experimental test in

Figure 7.22. The model labelled *Analytical E = 200GPa* refers to an elasto-plastic steel constitutive rule, while *Analytical E = 36.7GPa* is a non-linear confined concrete model. While neither model accurately captures the entire response, a more correct solution lies somewhere within this window. It is quite a difficult task to precisely define the correct constitutive stress-strain relationship that should be adopted due to interaction between the steel plate and the surrounding concrete. A rather arbitrary linear stress-strain relationship with a Young's modulus of 100GPa is shown in Figure 7.23; the response lies somewhere in the middle of the two aforementioned solutions. A summary of the parameters used in this model are listed in Table 7.7.

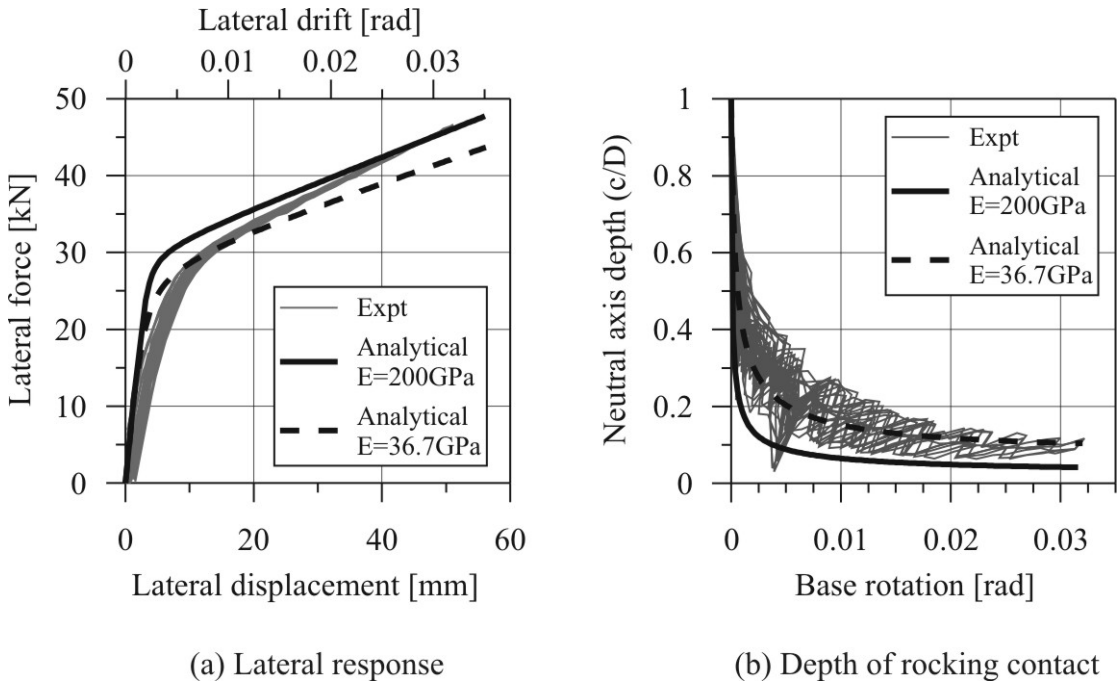

Figure 7.22 Comparison between the experimental cyclic response and two RMBA analytical models providing an upper and lower bound solution for the post-tensioned only pier PT2

Table 7.7 Model properties of PT2 (precast concrete with steel base plate)

Precast properties	
Calibrated flexural stiffness, E_cI_e	11487 kNm^2
Young's modulus at rocking interface	100,000MPa
Measured post-tensioning properties	
Initial post-tensioned force, $T_{pt,0}$	294kN (0.044f'$_c$A$_g$)
Unbonded length, $L_{ub,pt}$	2685mm
Young's modulus, E_{pt}	197100MPa
Area of tendon, A_{pt}	99mm^2

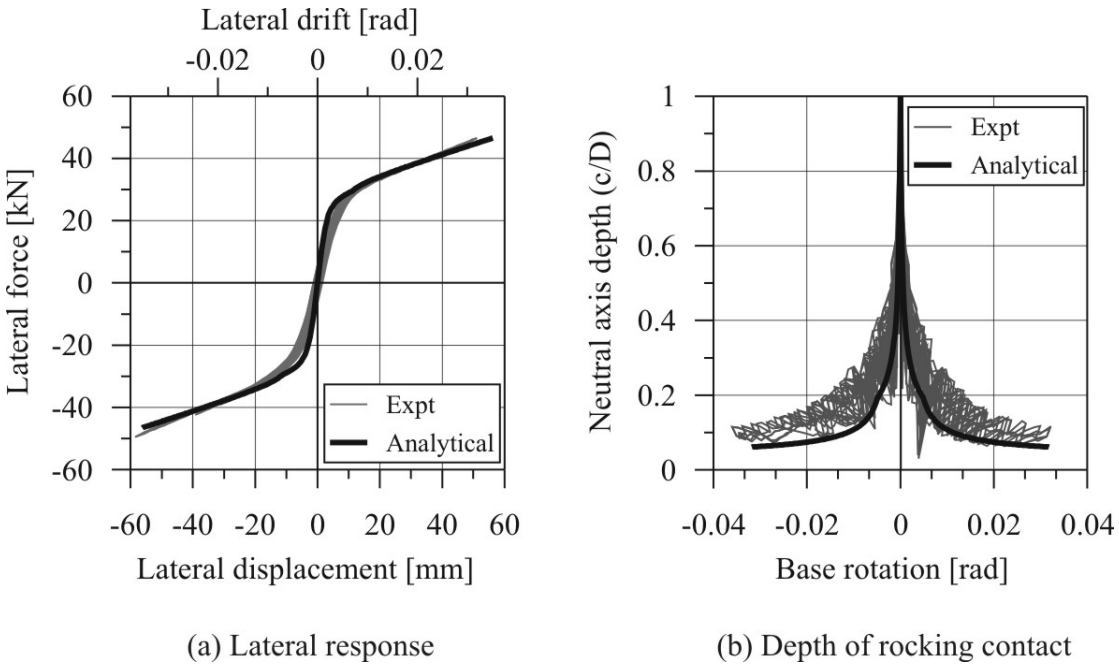

Figure 7.23 Comparison between the experimental cyclic response and the RMBA analytical model of the post-tensioned only pier PT2

(d) An Analytical Model for Post-Tensioned Only Systems with Alternative Material Constitutive Relationships

Following on from Section 7.2.2(c) which touched on the use of an elastic stress-strain material relationship at the rocking interface, this section studies the use of alternative non-linear constitutive relationships in detail. The PT-only Monolithic Beam Analogy (ptMBA) is suitable for post-tensioned systems with any material constitutive relationship. As no yielding taking place within the PT section, the PT-only analogy is valid in this case. If yielding steel elements are located internal to the PT section (bonded reinforcement) then an analogy is required to relate the compression strains within a PT connection to those within an equivalent yielding monolithic connection made of the same non-linear material– this can be difficult to develop for material other than concrete.

Laminated Veneer Lumber (LVL) is well suited for its application in rocking systems as the strength is comparable to that of concrete; however, the stiffness (parallel to the timber grain) is approximately 1/3 that of concrete. Furthermore, the stress-strain relationship is very similar in shape to unconfined concrete and can be modelled with existing mathematical relationships. The monotonic stress-strain relationship of three LVL test specimens (testing presented in Chapter 5) are compared with two non-linear stress-strain models in Figure 7.24. The first analytical model is a 5th order polynomial fitted to the test data using regression analysis. The stress of the LVL f_{LVL} is given by Eq.(7.54), where ε_{LVL} is the LVL strain and the five coefficients are listed below

$$f_{LVL}(\varepsilon_{LVL}) = A\varepsilon_{LVL}^{5} + B\varepsilon_{LVL}^{4} + D\varepsilon_{LVL}^{3} + D\varepsilon_{LVL}^{2} + E\varepsilon_{LVL} \qquad \textbf{7.54}$$

The coefficients of $f_{LVL}(\varepsilon_{LVL})$ are given below and are in units of ***MPa***.

$A = -21588\text{x}10^{7}$
$B = 22758\text{x}10^{6}$
$C = -46751\text{x}10^{4}$
$D = 25859\text{x}10^{2}$
$E = 5294$

This polynomial was chosen as it could accurately capture the initial softening observed during each test, Figure 7.24 (a). The polynomial was found to be only appropriate for strains less than $\varepsilon_{LVL} = 0.011$. For strains greater than 0.011, the polynomial deviates from the test data; rather a linear descending branch with stiffness equal to the derivative of the polynomial at $\varepsilon_{LVL} = 0.0085$ is more appropriate if stress-strain data is needed for strains greater than $\varepsilon_{LVL} = 0.011$. The second proposed non-linear model is used extensively for unconfined concrete, Popovics [1973], where the stress f_{LVL} is related to strain ε_{LVL} by the following

$$f_{LVL}(\varepsilon_{LVL}) = \frac{n \cdot (\varepsilon_{LVL}/\varepsilon_{LVL}')}{n - 1 + (\varepsilon_{LVL}/\varepsilon_{LVL}')^{nk}} f_{LVL}' \qquad \textbf{7.55}$$

Where,

f_{LVL}' = peak compressive stress, corresponding to a strain of ε_{LVL}'
k = curve fitting parameter effecting the post peak branch of the curve
n = curve fitting parameter equal to $n = E_{LVL}/(E_{LVL} - E_{LVL}')$
E_{LVL} = initial stiffness when ε_{LVL} is zero.
E_{LVL}' = secant stiffness to the peak compressive stress $E_{LVL}' = f_{LVL}'/\varepsilon_{LVL}'$

The Popovics [1973] curve could only be compared to the material testing if a strain offset was added to the curve to shift the curve to the right to account for the initial softening that was observed within the test data, Figure 7.24 (b). To do so, the Popovic curve was shifted along the positive x-axis by an amount equal to $\varepsilon_{offset} = 0.00067$. By ignoring the initial softening the modulus of elasticity for LVL was found to equal $E_{LVL} = 10{,}600$MPa. The remaining Popovics [1973] parameters are listed below

$\varepsilon'_{LVL} = 0.0063$
$f'_{LVL} = 54$MPa
$E_{LVL}' = 8571$MPa
$n = 5.22$
$k = 0.67$

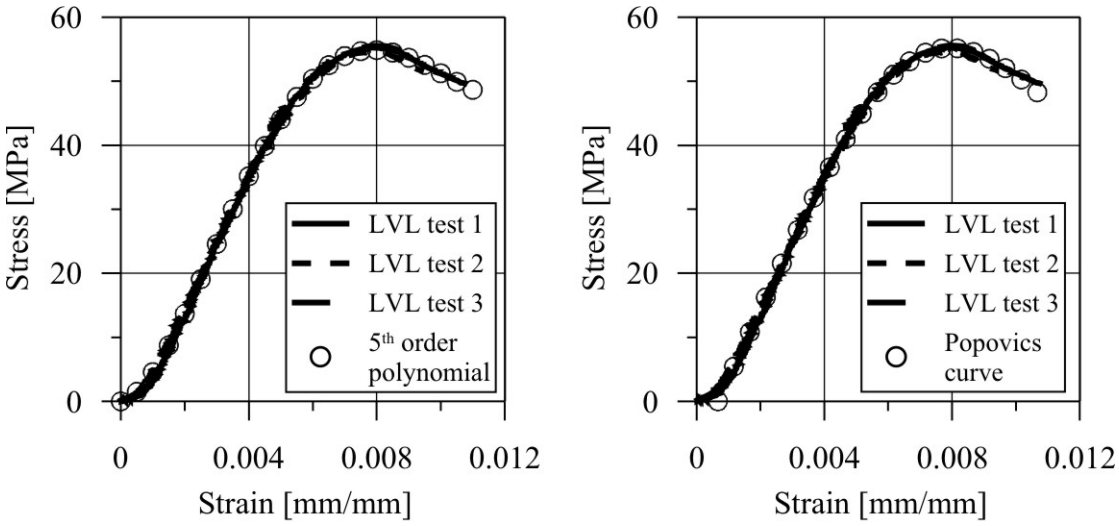

(a) 5th order polynomial to capture initial non-linear softening

(b) Popovics unconfined concrete curve with strain offset

Figure 7.24 Analytical models used for the stress-strain constitutive relationship of LVL

Both non-linear stress-strain curves are only shown up to a maximum strain of $\varepsilon_{LVL} = 0.011$; however, this is sufficient for the analyses herein. Referring to the strain relationships in Figure 7.19, the strains within a post-tensioned-only system are significantly lower than a traditional hybrid system with internal (bonded) yielding elements (in the order of 50% for a base rotation of 0.03). Many of the experimental tests presented in this document have relatively low axial load and prestressed reinforcement ratios. This allowed many tests to be carried out without comprising subsequent tests due to damage of the rocking connection. It is for this reason that the theoretical LVL compression strains are also low and tend to be well below the peak strain ε'_{LVL}. In Section 7.2.1(e) equivalent stress block factors were presented for confined concrete based on the integration of the confined stress-strain curve. A similar exercise was carried out for the non-linear stress-strain curve of LVL. The stress block factors (α and β) are summarised in Table 7.8 and Figure 7.25 where ε_{LVL} is the compression strain in LVL and ε'_{LVL} is the compression strain corresponding to the peak LVL stress f'_{LVL} (refer Figure 7.25).

Table 7.8 LVL stress block factors for design[1]

	$\varepsilon_{LVL}/\varepsilon'_{LVL}$[2]										
	0.4	**0.6**	**0.8**	**1.0**	**1.2**	**1.4**	**1.6**	**1.8**	**2.0**	**2.2**	**2.4**
α	0.352	0.565	0.761	0.927	1.056	1.152	1.224	1.277	1.318	1.347	1.369
β	0.689	0.683	0.671	0.656	0.638	0.620	0.603	0.587	0.573	0.560	0.548

[1] Descending branch is linear with a gradient equal to -1808MPa (Figure 7.25)

[2] $\varepsilon'_{LVL} = 0.0076$mm/mm

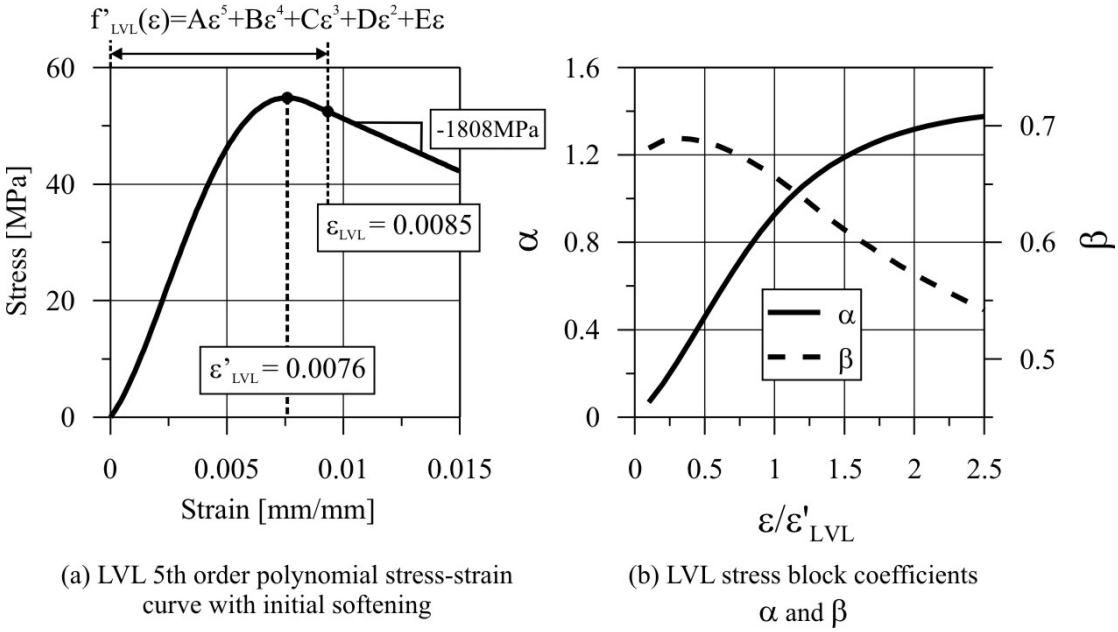

(a) LVL 5th order polynomial stress-strain curve with initial softening

(b) LVL stress block coefficients α and β

Figure 7.25 LVL stress block factors as a function of compression strain

The ptMBA analytical model, utilising an alternative stress-strain relationship, is compared to the experimental response of the post-tensioned wall LVL Wall 1 in Figure 7.26. The stress-strain at the rocking interface is modelled with a 5th order polynomial (with the coefficients listed above) to model the initial softening of the LVL material. This model compares extremely well to the test data at a local and global level; the model parameters are listed in Table 7.9.

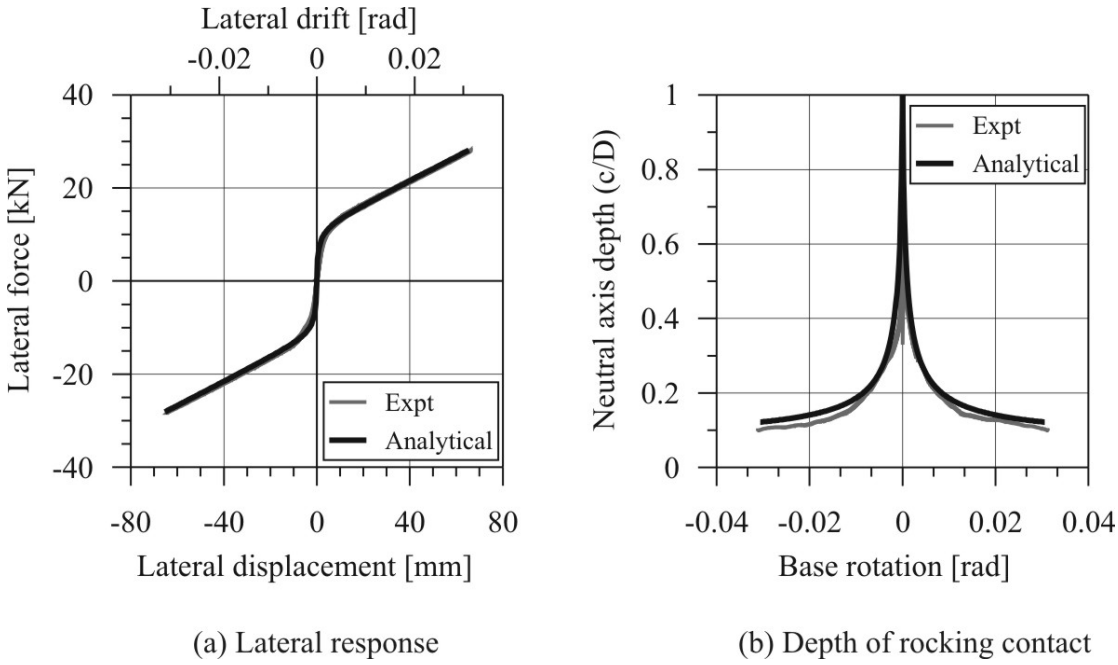

(a) Lateral response

(b) Depth of rocking contact

Figure 7.26 Comparison between the experimental cyclic response and the RMBA analytical model of the LVL post-tensioned only wall, LVL Wall 1

Table 7.9 Model properties of LVL Wall 1

Precast properties	
Calibrated flexural stiffness, E_cI_e	41664 kNm^2
LVL constitutive relationship	5th order polynomial
Measured post-tensioning properties	
Initial post-tensioned force, $T_{pt,0}$	98.96kN (0.0179f'$_{LVL}$A$_g$)
Unbonded length, $L_{ub,pt}$	3400mm
Young's modulus, E_{pt}	197100MPa
Area of tendon, A_{pt}	99mm^2

Figure 7.27 compares the global and local analytical response of two LVL stress-strain relationships: one includes the initial LVL softening shown in Figure 7.24 (a), the other ignores it. The 5th order polynomial, which accounts for the initial softening of the LVL material, is plotted as a solid black line while the Popovics [1973] curve (with no strain offset), which does not account for the initial softening, is plotted as a dashed black line. At a global level, the difference is relatively minor and it could be argued that either solution will agree reasonably well with the test data of Figure 7.26. The difference is more evident at the local level, where it can be appreciated that by accounting for the initial softening, the stiffness of the rocking interface better compares to the experimental data.

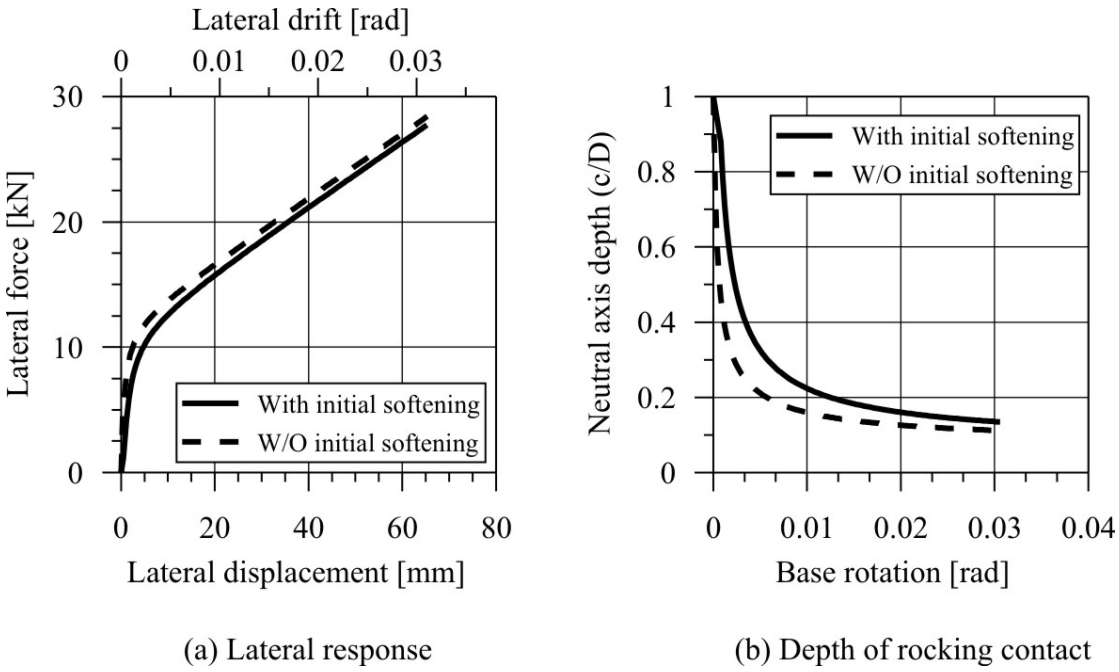

Figure 7.27 Comparison between two analytical models: one including the initial LVL softening, the other neglecting it. The analysis is carried out for the LVL post-tensioned wall, LVL Wall 1

It is important to understand that the above ptMBA analogy can be applied to any post-tensioned-only rocking system having any constitutive material relationship at the rocking interface only if (bonded) yielding elements are not present within the rocking connection. That is, there is no plastic hinge or strain penetration within the

equivalent monolithic connection. In fact, previous experimental and analytical studies have been carried out on post-tensioned LVL connections for use in seismic applications by Newcombe [2007]. As part of an extensive testing program, testing included post-tensioned LVL connections with internally bonded (with epoxy) reinforcement within the rocking connection. In this case expressions were developed to determine the plastic hinge length (related to the strain penetration of the epoxied reinforcement) and yield curvature of an equivalently reinforced LVL monolithic connection. Newcombe [2007] presents a number of recommendations to estimate the strain penetration and plastic hinge lengths for such connections.

(e) An Analytical Model for Post-Tensioned Systems with External Damping Elements

The extension of the MBA analogy to include post-tensioned systems with external yielding elements is relatively minimal. While yielding is taking place, it is external to the section and no plastic strain develops (or strain penetration) within the section; therefore, no plastic hinge develops. Figure 7.28 illustrates the analogy between a post-tensioned (PT) system with external yielding elements and an equivalently reinforced monolithic (EM) system. In the analogy, the EM section has identical external reinforcement to the PT system in addition to bonded, unstressed tendons, which are required as part of the PT-only analogy (ptMBA) discussed in Section 7.2.2 (c). Apart from the external elements, no yielding takes place within the EM element; therefore, the curvature of the cantilever is linear with height (and remains elastic). In fact, the external elements are analogous to an additional axial load acting on the section. It is possible that some curvature demand is deducted from the monolithic element if the forces in the yielding elements are not of equal magnitude or sign (Figure 7.28 (b)). This is denoted as $\Delta\phi$ in Figure 7.28 (b); however, for all practical purposes, the forces in the yielding elements are assumed to be similar in magnitude and of the same sign (i.e. both in tension); therefore, $\Delta\phi$ is assumed to be small enough that it can be neglected.

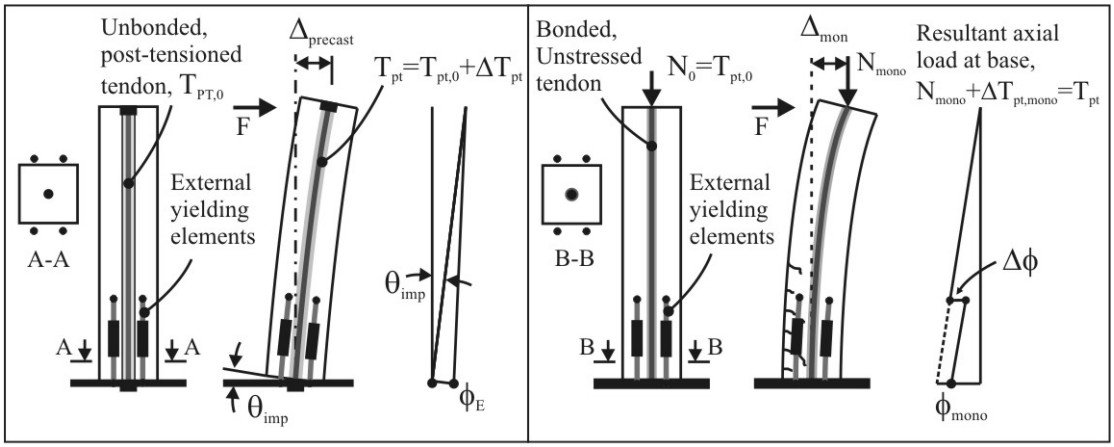

(a) Displacement components of a post-tensioned connection with external yielding elements

(b) Displacement components of an equivalently reinforced monolithic connection

Figure 7.28 Monolithic beam analogy for post-tensioned only systems with external damping elements

With this analogy in mind, the compression strains at the rocking interface of the PT element are computed from Eq.(7.56). In fact, this relationship can be used for any post-tensioned connection which does not have internally grouted reinforcement. This relationship is referred as the Post-Tensioned Monolithic Beam Analogy (ptMBA) and is appropriate for any post-tensioned connection with or without external dissipation (viscous or hysteretic).

$$\varepsilon_c = \left[\frac{3\theta_{imp}}{L_{cant}} + \phi_{dec} \right] c \qquad \textbf{7.56}$$

The ptMBA analogy for PT systems with external yielding dampers is compared with two experimental tests. The first comparison is made to the monotonic push-over response of a precast concrete post-tensioned wall with external tension-compression-yielding (TCY) steel dampers, PC Wall 5. The push-over response was recorded prior to release of the free-vibration testing (Chapter 6). The analytical model compares well at a global level in Figure 7.29 and at the local level in Figure 7.30. Being a monotonic push-over test, the mild steel stress-strain envelope does not account for cyclic loading within the analytical model; this issue was discussed in Section 7.2.1 (a). The confined concrete model is identical for each of the PC Wall analytical models in that the confinement is smeared over the entire cross section to account for confinement provided by the steel channel at the rocking toe.

The second analytical-experimental comparison is carried out for the cyclic response of an LVL post-tensioned wall: LVL Wall 4 in Figure 7.31. The stress-strain model of LVL follows a 5^{th} order stress-strain polynomial (Section 7.2.2(e)), while the stress-strain backbone curve of the mild steel dissipaters accounts for the effects of cyclic loading (Section 7.2.1(a)). Again, the comparison is excellent at the global and local level. A summary of the model parameters for both wall models are listed in Table 7.10.

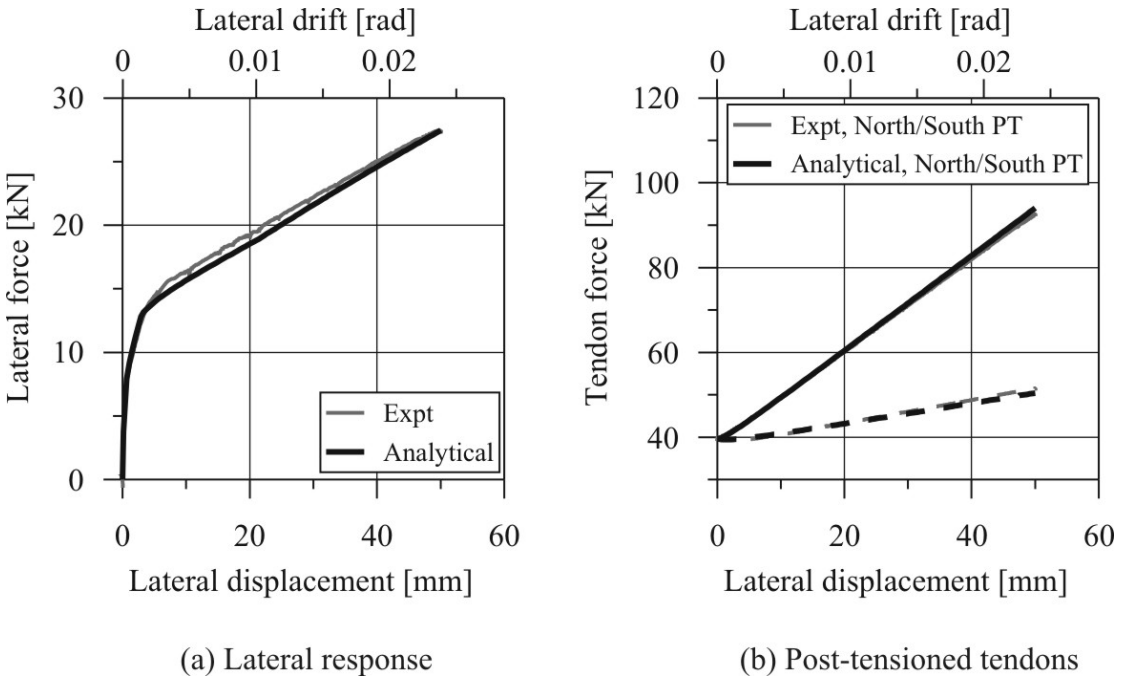

Figure 7.29 Comparison between the experimental push-over response (prior to release of free vibration) and the RMBA analytical model of the precast concrete post-tensioned wall, PC Wall 5

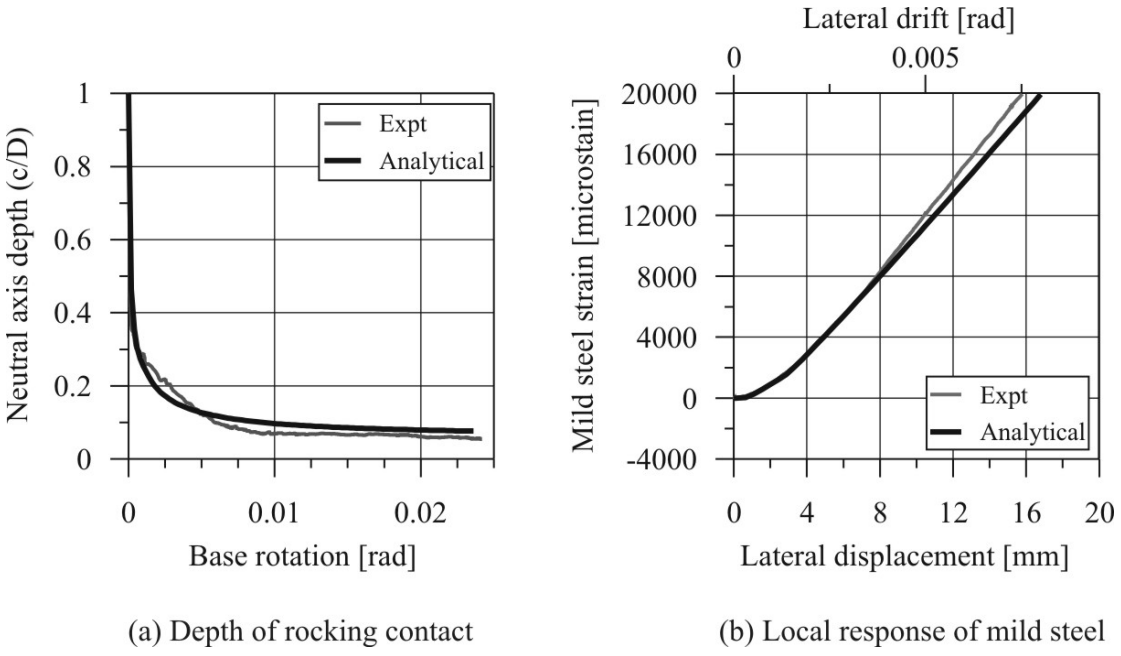

Figure 7.30 Comparison at a local level between the experimental push-over response (prior to release of free vibration) and the PT-MBA analytical model of the precast concrete post-tensioned wall, PC Wall 5

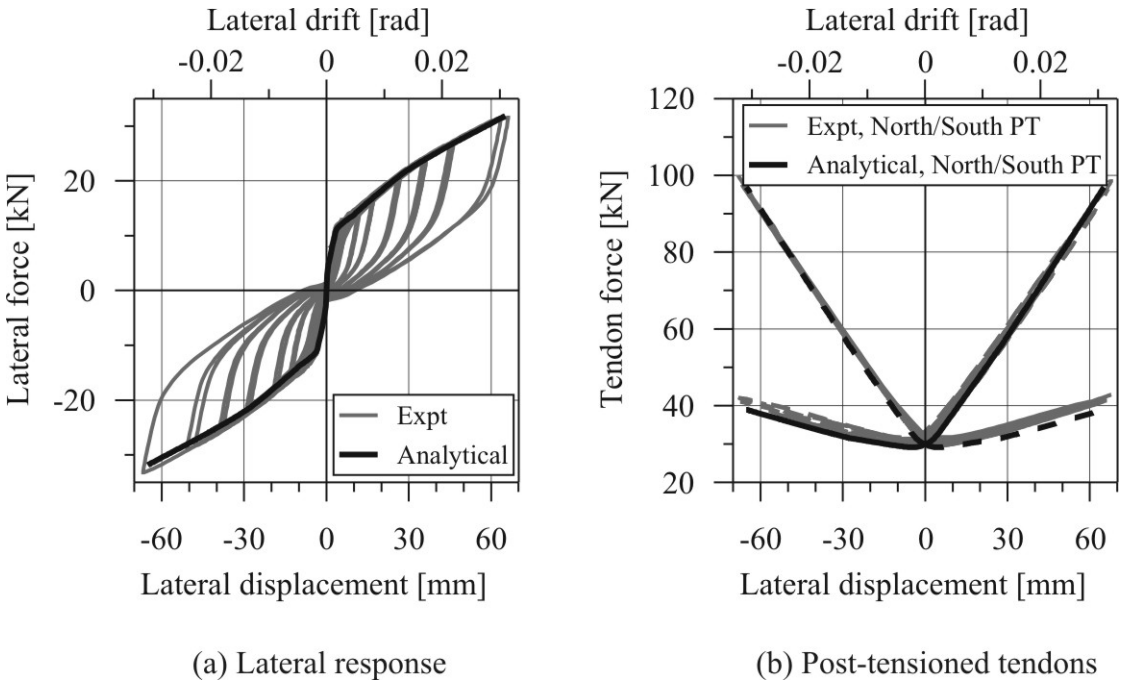

Figure 7.31 Comparison between the experimental cyclic response and the PT-MBA analytical model of the LVL post-tensioned wall, LVL Wall 4

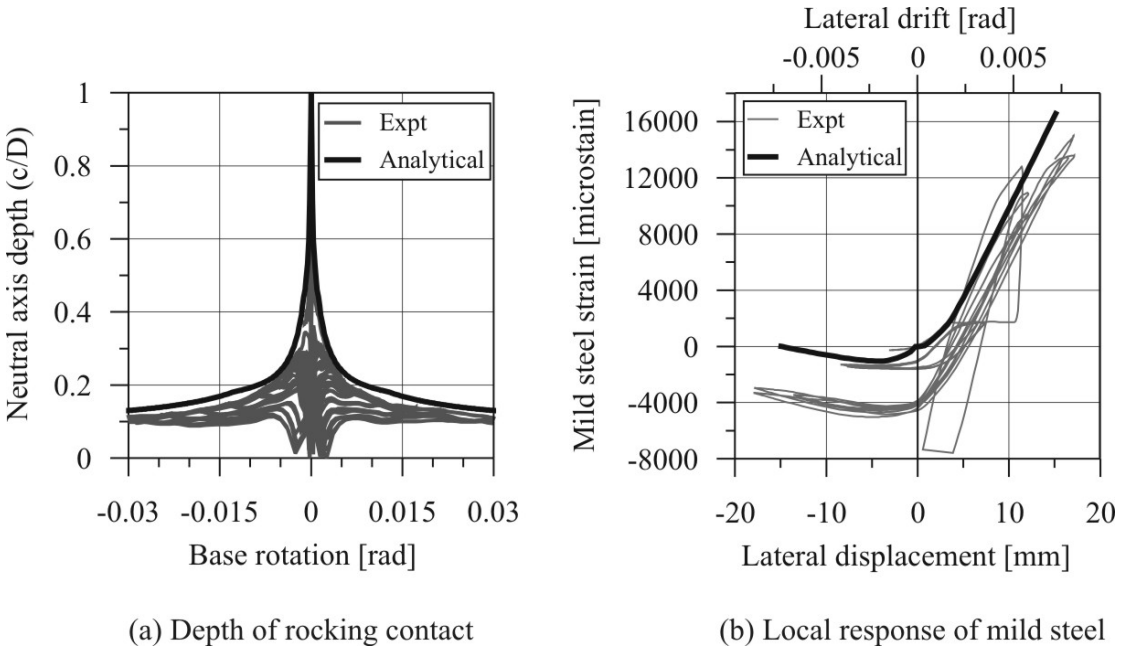

Figure 7.32 Comparison at a local level between the experimental cyclic response and the PT-MBA analytical model of the LVL post-tensioned wall, LVL Wall 4

Table 7.10 Model properties of LVL Wall 4 (cyclic envelope) and PC Wall 5 (push-over envelope)

Precast properties	LVL Wall 4 (Cyclic envelope)	PC Wall 5 (Monotonic envelope)
Calibrated flexural stiffness, E_cI_e	41664 kNm^2	113092 kNm^2
Constitutive stress-strain relationship	LVL 5th order polynomial	Confined concrete
Computed confinement ratio, f'_{cc}/f'_c	-	1.91
Measured Unconfined compression strength, f'_c	-	45.1MPa
Measured post-tensioning properties		
Initial post-tensioned force, $T_{pt,0}$	60.2 kN (0.011 $f'_{LVL}A_g$)	79.3 kN (0.017 f'_cA_g)
Unbonded length, $L_{ub,pt}$	3400 mm	3558 mm
Young's modulus, E_{pt}	197100 MPa	197100 MPa
Area of tendon, A_{pt}	99 mm^2	99 mm^2
Measured mild steel properties		
TCY damper fuse length, l_{fuse}	136 mm	90 mm
Diameter of fuse, d_s	7 mm	7 mm
Diameter of the bar outside fuse, d_b	20 mm	20 mm
Total length of the dissipater, l_{diss}	337.5 mm	337.5mm
Young's modulus, E_{ms}	202500 MPa	201250 MPa
Yield strain, $\varepsilon_{y,ms}$	0.00167	0.0016
Strain hardening, $\varepsilon_{sh,ms}$	0.0094	0.0264
Stain x, $\varepsilon_{x.ms}$	0.024	0.055
Strain at ultimate, $\varepsilon_{su,ms}$	0.100	0.2
Yield stress, $f_{y,ms}$	336 MPa	322 MPa
Stress x, $f_{x.ms}$	416 MPa	400 MPa
Ultimate stress, $f_{u.ms}$	485 MPa	457 MPa

(f) An Analytical Model for Post-Tensioned Systems with External Viscous Damper Elements

The section analysis procedure for post-tensioned (PT) connections with external viscous damper elements is identical to that of a PT connection with external hysteretic damper elements; the difference is how the damper forces are computed within the section and how the section is assessed. To perform a moment-rotation section analysis of a PT-viscous system two parameters must be defined

- The first is the target displacement $\boldsymbol{\Delta_d}$ to which the analysis will run to.
- The second is the excitation period $\boldsymbol{T_e}$, or the time taken to reach the target displacement; this will define the velocity time-history of the analysis.

Generally, the response of a structure during its excursion to the maximum displacement is assumed to be of steady-state harmonic motion. Thus, the displacement time-history can be represented by sinusoidal motion to the peak displacement $\boldsymbol{\Delta_d}$; that is, the displacement $\boldsymbol{\Delta(t)}$, velocity $\boldsymbol{v(t)}$ and acceleration $\boldsymbol{a(t)}$ time-history are given by the following relationships

$$\Delta(t) = \Delta_d \sin\left(2\pi \frac{t}{T_e}\right) \qquad \textbf{7.57}$$

$$v(t) = \Delta_d \frac{2\pi}{T_e} \cos\left(2\pi \frac{t}{T_e}\right) \qquad \textbf{7.58}$$

$$a(t) = -\Delta_d \frac{4\pi^2}{T_e^2} \sin\left(2\pi \frac{t}{T_e}\right) \quad \textbf{7.59}$$

Alternatively, if the excitation period $\boldsymbol{T_e}$ is not specified, then the maximum system velocity $\boldsymbol{v_d}$ can be specified. In doing so, the excitation period is computed from below

$$T_e = \frac{\Delta_d}{v_d} 2\pi \quad \textbf{7.60}$$

Initially, the analysis should assume the precast element is rigid such that the base rotation time-history $\boldsymbol{\theta(t)}$ is defined by

$$\theta(t) = \frac{\Delta(t)}{H_e} = \frac{\Delta_d}{H_e} \sin\left(2\pi \frac{t}{T_e}\right) \quad \textbf{7.61}$$

Therefore, the angular velocity at the base $\dot{\theta}(t)$ is given by

$$\dot{\theta}(t) = \frac{v(t)}{H_e} = \frac{\Delta_d}{H_e} \frac{2\pi}{T_e} \cos\left(2\pi \frac{t}{T_e}\right) \quad \textbf{7.62}$$

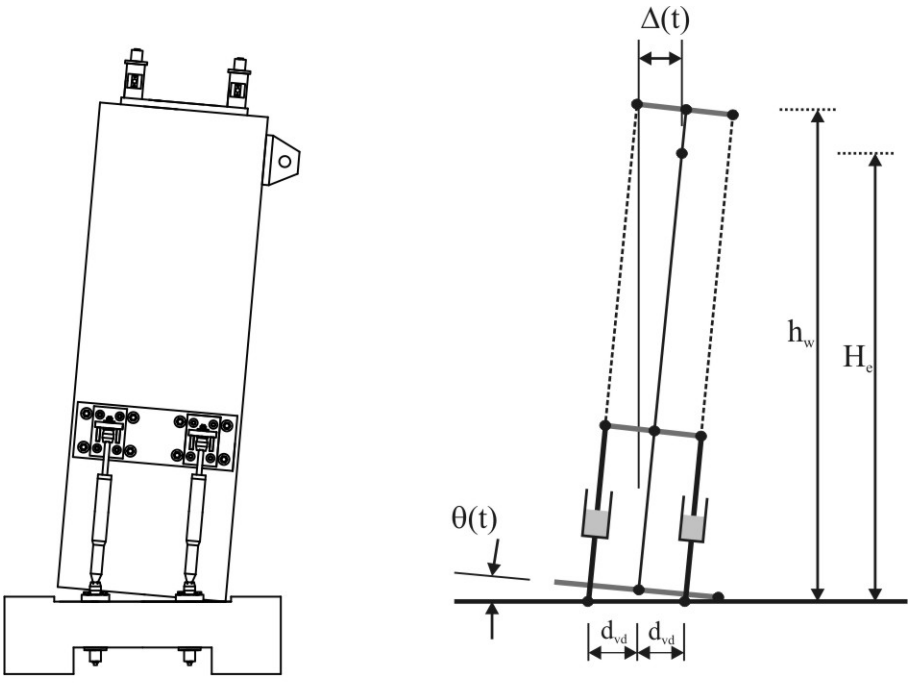

(a) Deformed shape of post-tensioned viscous wall

(b) Centerline geometry of the post-tensioned viscous wall

Figure 7.33 Mechanics of a post-tensioned system with viscous dampers

From geometry, the velocity of each damper layer $v_{vd,i}(t)$ is given by the following expression

$$v_{vd,i}(t) = \dot{\theta}(t) \cdot \left[D(0.5 - \chi) \pm d_{vd} \right] \quad \textbf{7.63}$$

Where

D = the depth of the section
χ = the dimensionless neutral axis depth $\chi = c/D$
d_{vd} = the distance from the centreline of the section to the damper layer. The sign of d_{vd} will depend on the which damper layer is being considered.

The force in each damper layer $F_{vd,i}(t)$ is computed from

$$F_{vd,i}(t) = n_{vd,i} c_{vd} \left(v_{vd,i}(t) \right)^{\alpha} \cdot sign\left(v_{vd,i}(t) \right) \quad \textbf{7.64}$$

Where

$n_{vd,i}$ = the number of damper elements at layer i
c_{vd} = the damper coefficient
α = the non-linear viscous damper exponent
$sign\left(v_{vd,i}(t) \right)$ = the sign of the velocity (+ or –). This is necessary to define the entire force-displacement time-history of the damper

If the elastic (flexural) displacement of the cantilever element is included in the analysis, the analysis increases in complexity. The total displacement $\Delta(t)$ at the effective height will be equal to the rigid-body rotation displacement $\theta(t)H_e$ plus the elastic displacement of the cantilever element $\Delta_e(t)$ in Eq.(7.65). However, the elastic displacement is a function of the lateral load, which in itself is a function of time; therefore, the elastic displacement will also be a function of time.

$$\Delta(t) = \theta(t) H_e + \Delta_e(t) \quad \textbf{7.65}$$

The angular velocity at the base $\dot{\theta}(t)$, accounting for the flexibility of the precast element, can be re-derived to account for the proportion of velocity associated with the elastic deformation ($d\Delta_e(t)/dt$) of the cantilever as follows

$$\dot{\theta}(t) = \frac{1}{H_e} \left[\Delta_d \frac{2\pi}{T_e} \cos\left(2\pi \frac{t}{T_e} \right) - \frac{d\Delta_e(t)}{dt} \right] \quad \textbf{7.66}$$

Furthermore, the elastic component of velocity is not unique as the lateral force (hence displacement, and velocity) varies with time and must be defined at each time increment Δt

$$\frac{d\Delta_e(t)}{dt} = \frac{\Delta_e(t) - \Delta_e(t-\Delta t)}{\Delta t} \qquad \textbf{7.67}$$

The velocity and force in the damper layer is then computed from Eq.(7.63) and Eq.(7.64), respectively, where $\dot{\theta}(t)$ was defined in Eq.(7.66) to account for the column/wall flexibility. It follows that iteration on $\theta(t)$ is required at each time step in order to converge on the target displacement $\Delta(t)$ at time t; however, this is computationally time consuming. In some cases the elastic displacement can be ignored. For example, in Section 7.2.1 (g) it is shown that the elastic displacement of a cantilever element may be negligible if the tendon groups are located to either side of the centreline of the precast section. However, in the event that they cannot be ignored, a simplified section analysis technique is developed to target any displacement Δ_d.

1. First, carry out a section analysis including elastic displacements. However, instead of imposing a displacement time-history $\Delta(t)$ (which requires iteration at each time step), re-write the analysis to impose a base-rotation time history $\theta(t)$ (no iteration required) according to Eq.(7.68) below. The elastic displacement $\Delta_e(t)$, and hence the total displacement $\Delta(t)$, will be a bi-product of the analysis.

$$\theta(t) = \theta_d \sin\left(2\pi \frac{t}{T_e}\right) \qquad \textbf{7.68}$$

2. Determine the ratio between the target displacement Δ_d and the maximum total displacement $\Delta(T_e/4)$ resulting from the analysis in Step 1, i.e. $\Delta_d / \Delta(T_e/4)$. Reduce the target base rotation θ_d in Step 1 by this same ratio and repeat the section analysis. Depending on the accuracy required, only a single iteration may be needed for an acceptable convergence of $\Delta_d / \Delta(T_e/4) \approx 1$.

The cyclic force-displacement time-history of a viscous damper can be uniquely defined by the single equation of Eq.(7.64). Unlike steel, which requires complex mathematical equations to be able to describe the loading, unloading and reloading branches, the simplicity in describing the hysteretic response of a non-linear viscous damper is well suited to a pseudo-cyclic analysis. That is, because the damper force can be described by a single closed form solution, a cyclic section-analysis can be computed for a PT-viscous connection from $0 < T < T_e/2$. The analysis is termed pseudo-cyclic if only a backbone stress-strain curve is used to model the material at the rocking interface (concrete, LVL etc), as opposed to a conventional cyclic analysis which adopts the full loading, unloading and re-loading branches.

The response of the PT-viscous analytical model is compared to the global experimental response of LVL Wall 2 under an excitation frequency of 0.5Hz in Figure 7.34. Each drift cycle represents a single analysis (a total of seven analyses are required to complete the monotonic backbone curve). Only the loading cycle is shown: the unloading response is ignored for clarity. Each analysis cycle reveals a

sudden drop in lateral load at the end of the loading cycle as the damper velocity approaches zero. The lateral load and tendon response compare very well in Figure 7.34. The analytical model is able to capture the local behaviour of the neutral axis depth in Figure 7.35 (a) and the damper velocity in Figure 7.35 (b) reasonably well. A positive damper velocity in Figure 7.35 (b) represents the damper layer furthermost from the rocking toe, while a negative velocity represents the damper layer closest to the rocking toe. More error is associated with the damper layer located closest to the rocking toe, in fact this damper layer was located very close to the neutral axis: the damper layer was located at a depth of 0.217***D*** (where ***D*** is the depth of the wall element). It is for this reason that some error can be expected in capturing the velocity of this damper layer.

The PT-viscous model is next compared to the test specimen LVL Wall 3 under an excitation frequency of 0.5Hz, which has both viscous and hysteretic dampers. Again, a total of seven analyses are undertaken to generate the entire monotonic backbone response. The global response in Figure 7.36 compares very well. Again, both the neutral axis depth and the damper velocity are both well captured in Figure 7.37. A summary of the model properties for LVL Wall 2 and LVL Wall 3 is listed in Table 7.11.

Table 7.11 Model properties of LVL Wall 2 and LVL Wall 3

Precast properties	**LVL Wall 2**	**LVL Wall 3**
Calibrated flexural stiffness, E_cI_e	41664 kNm^2	41664 kNm^2
Constitutive stress-strain relationship	5th order polynomial	5th order polynomial
Computed confinement ratio, f'_{cc}/f'_c	-	-
Measured Unconfined compression strength, f'_c	-	-
Measured post-tensioning properties		
Initial post-tensioned force, $T_{pt,0}$	29.7 kN (0.011 f'$_{LVL}$A$_g$)	20.0 kN (0.0072 f'$_c$A$_g$)
Unbonded length, $L_{ub,pt}$	3400 mm	3400 mm
Young's modulus, E_{pt}	197100 MPa	197100 MPa
Area of tendon, A_{pt}	99 mm^2	99 mm^2
Measured mild steel properties		
TCY damper fuse length, l_{fuse}	-	90 mm
Diameter of fuse, d_s	-	7 mm
Diameter of the bar outside fuse, d_b	-	20 mm
Total length of the dissipater, l_{diss}	-	337.5mm
Young's modulus, E_{ms}	-	185250 MPa
Yield strain, $\varepsilon_{y,ms}$	-	0.00183
Strain hardening, $\varepsilon_{sh,ms}$	-	0.0108
Stain x, $\varepsilon_{x.ms}$	-	0.024
Strain at ultimate, $\varepsilon_{su,ms}$	-	0.1033
Yield stress, $f_{y,ms}$	-	339 MPa
Stress x, $f_{x.ms}$	-	404 MPa
Ultimate stress, $f_{u.ms}$	-	484 MPa
Measured FVD properties		
Damping coefficient, c_{vd}	4.945 kNs$^\alpha$/mm$^\alpha$	4.945 kNs$^\alpha$/mm$^\alpha$
Velocity power coefficient, α	0.153	0.153

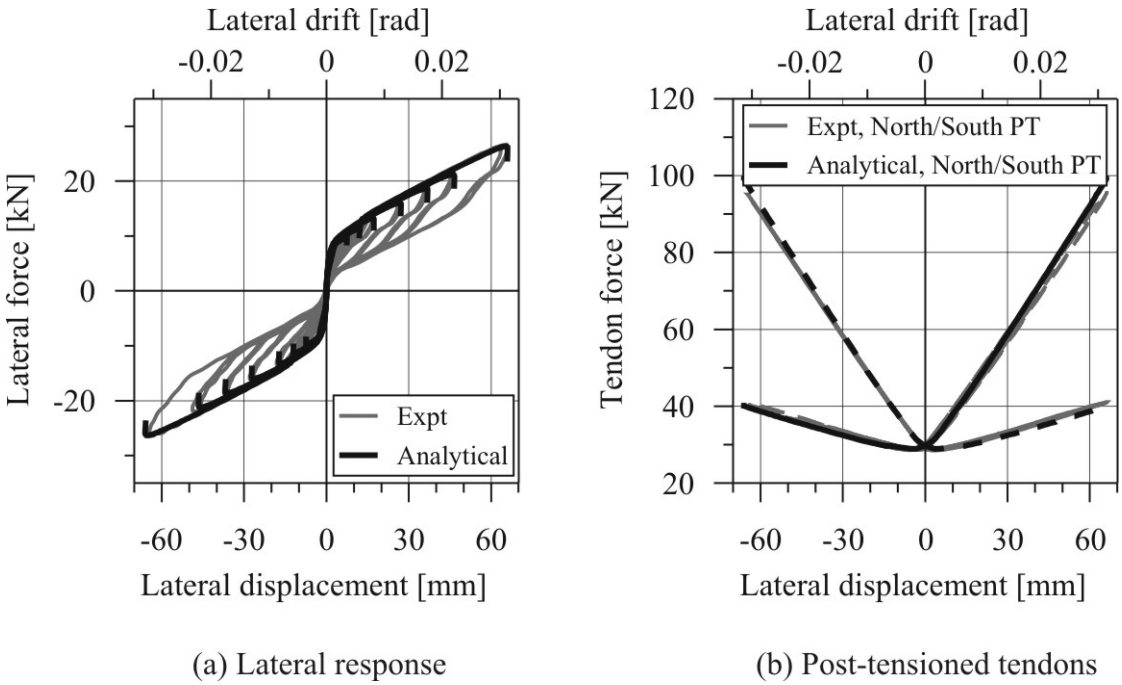

Figure 7.34 Comparison between the experimental cyclic response and the PT-MBA analytical model of the LVL post-tensioned wall, LVL Wall 2 under an excitation frequency of 0.5Hz

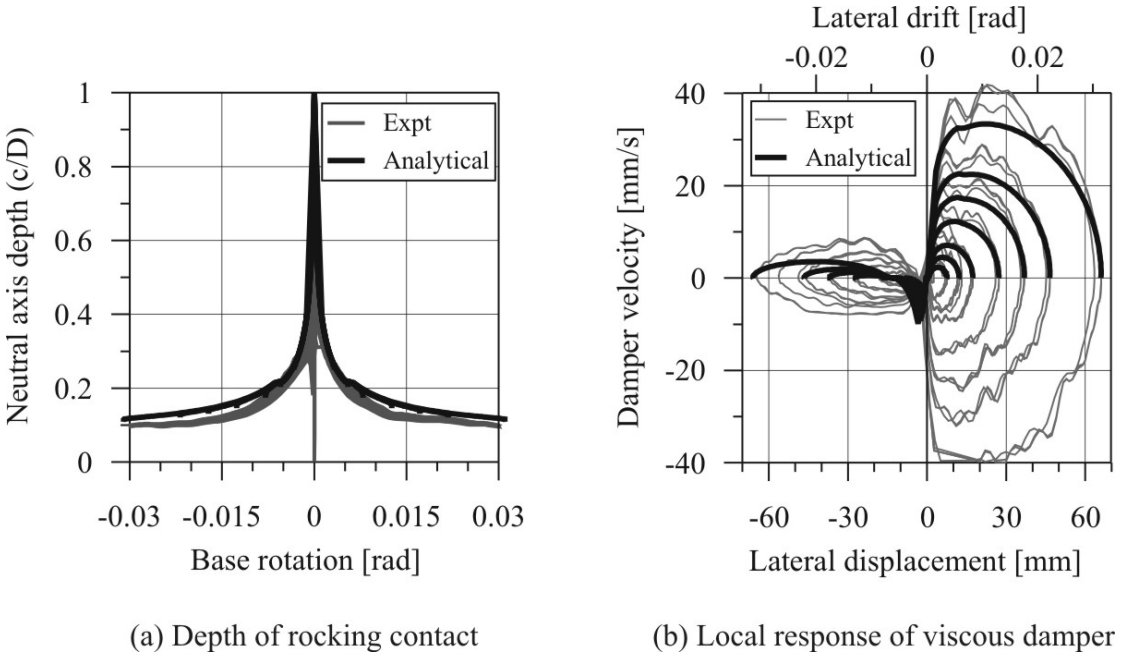

Figure 7.35 Comparison at a local level between the experimental cyclic response and the PT-MBA analytical model of the LVL post-tensioned wall, LVL Wall 2 under an excitation frequency of 0.5Hz

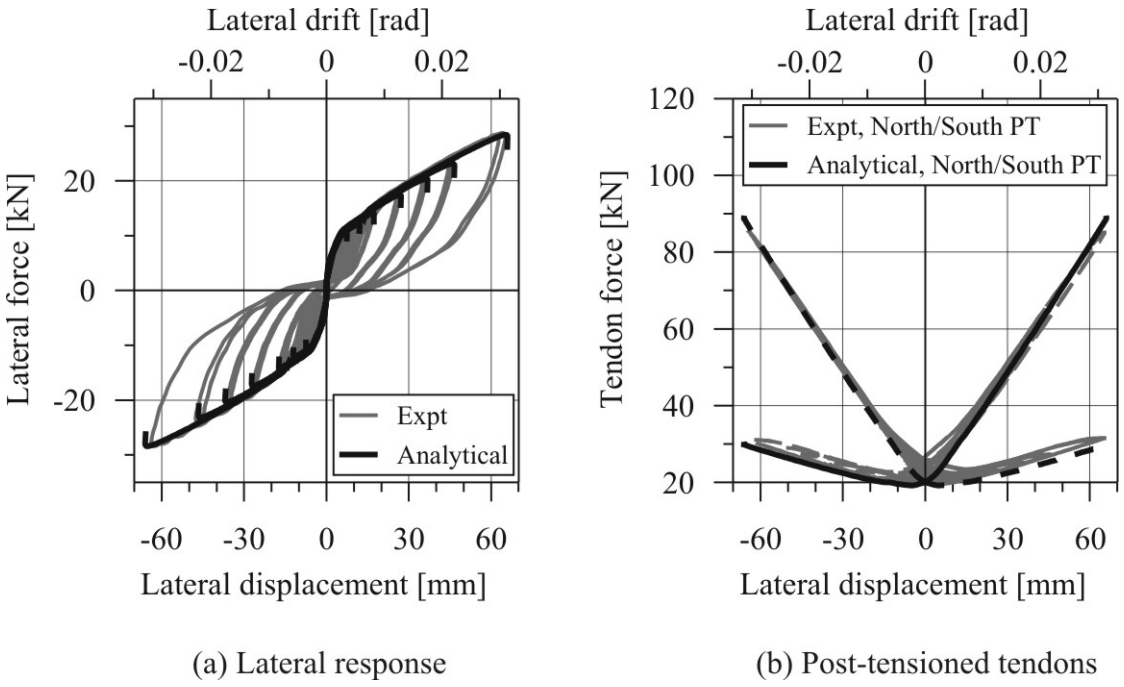

Figure 7.36 Comparison between the experimental cyclic response and the PT-MBA analytical model of the LVL post-tensioned wall, LVL Wall 3 under an excitation frequency of 0.5Hz

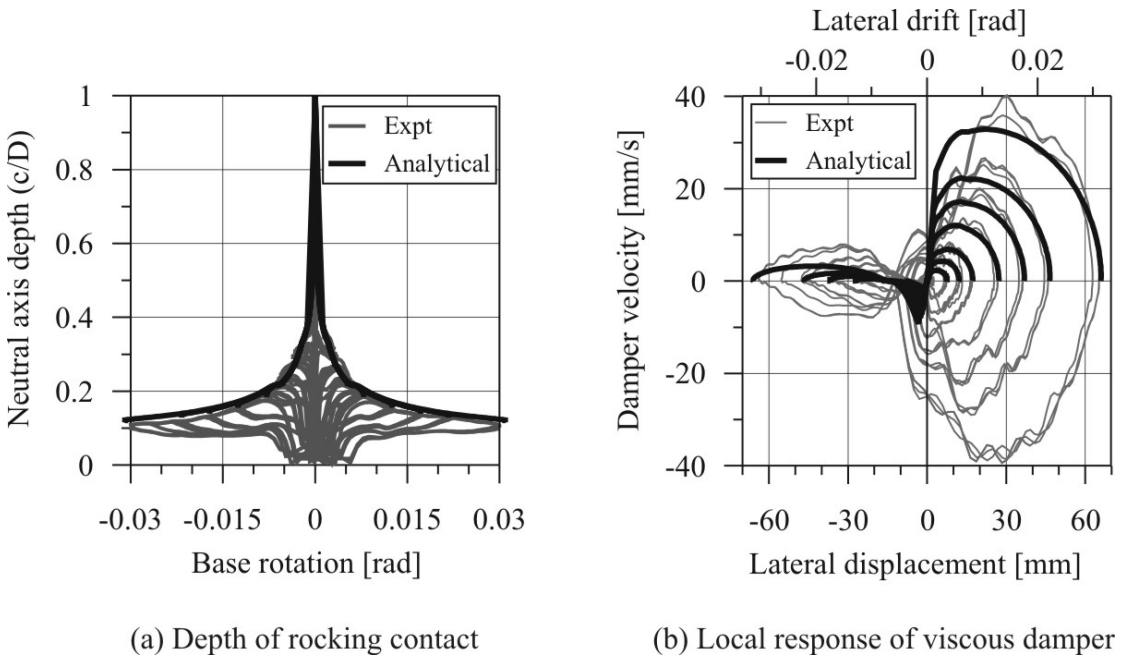

Figure 7.37 Comparison at a local level between the experimental cyclic response and the PT-MBA analytical model of the LVL post-tensioned wall, LVL Wall 3 under an excitation frequency of 0.5Hz

Based on the confirmation of the analytical PT-viscous model, a parametric analysis was undertaken to study the influence of input velocity and damper properties on the lateral response of a PT-viscous system. The parametric study considers a PT-concrete wall of identical geometry and properties to PC Wall 2 (for simplicity elastic deformations are ignored). Three parameters are varied: the velocity exponent α, the damper coefficient c_{vd} and the period of excitation T defining the input velocity. The results of the parametric analyses are presented in Figure 7.38 for three levels of α (0.15, 0.5 and 1.0) in terms of the lateral load versus base rotation. Also plotted in Figure 7.38 is the normalised proportion of overturning moment provided by the viscous dampers ($\mathbf{M_{vd}/M_{total}}$). For each level of α two excitation periods (T = 0.5 and 1.0 seconds) and two damping coefficients c_{vd} are studied. To simplify the comparisons between each wall, c_{vd} reduces as α increases to ensure the damper forces are not excessively different for each analysis (this can dictate the compression depth at the rocking interface).

By comparing the two solid lines and the two dashed lines (i.e. black versus grey), it is obvious that as α decreases, the influence of input velocity on the lateral load reduces: that is, the lateral load becomes increasingly dependant on the damping coefficient c_{vd} alone.

By comparing the two black lines and the two grey lines (i.e. solid versus dashed), as the damping coefficient c_{vd} is increased the increase in the proportion of damper moment remains almost constant for all values of α. That is, by doubling the damper coefficient c_{vd}, under each excitation period, the increase in the damper moment ratio M_{vd}/M_{total} is relatively constant for each level of α.

If the neutral axis depth remains relatively constant between each of the parametric analyses, then the normalised damper force and damper moment is primarily dependant on the velocity exponent α. Figure 7.39 (a) indicates that as α decreases, the damper force approaches a constant value while travelling to the peak response. As α increases the response becomes increasingly non-linear and the maximum damper force occurs at a base rotation of approximately 33% of the peak base rotation. A similar trend is observed with respect to the damper moment of Figure 7.39 (b) where the peak damper moment may or may not occur at the point in time as the peak damper force. The damper moment is a product of the damper force and the distance to the centroid of the compression region, therefore, the peak damper moment will also depend on the location of the neutral axis and the position of the centroid of the concrete compression force. Depending on α, the peak damper moment occurs between 33% and 50% of the peak base rotation. It is interesting to observe the phase difference between the system velocity and the peak damper force and damper moment. In the following chapter, the design of PT-viscous systems adopts a second design displacement (in addition to the target displacement Δ_d). This intermediate design displacement Δ_r is equal to $\Delta_d / \sqrt{2}$, which is defined by the intersection of the system velocity and system displacement curves in Figure 7.39 (intersection of the grey curves). At this intermediate displacement Figure 7.39 illustrates that the damper force and damper moment is equal to at least 80% of the peak value, depending on the velocity exponent α of the damper.

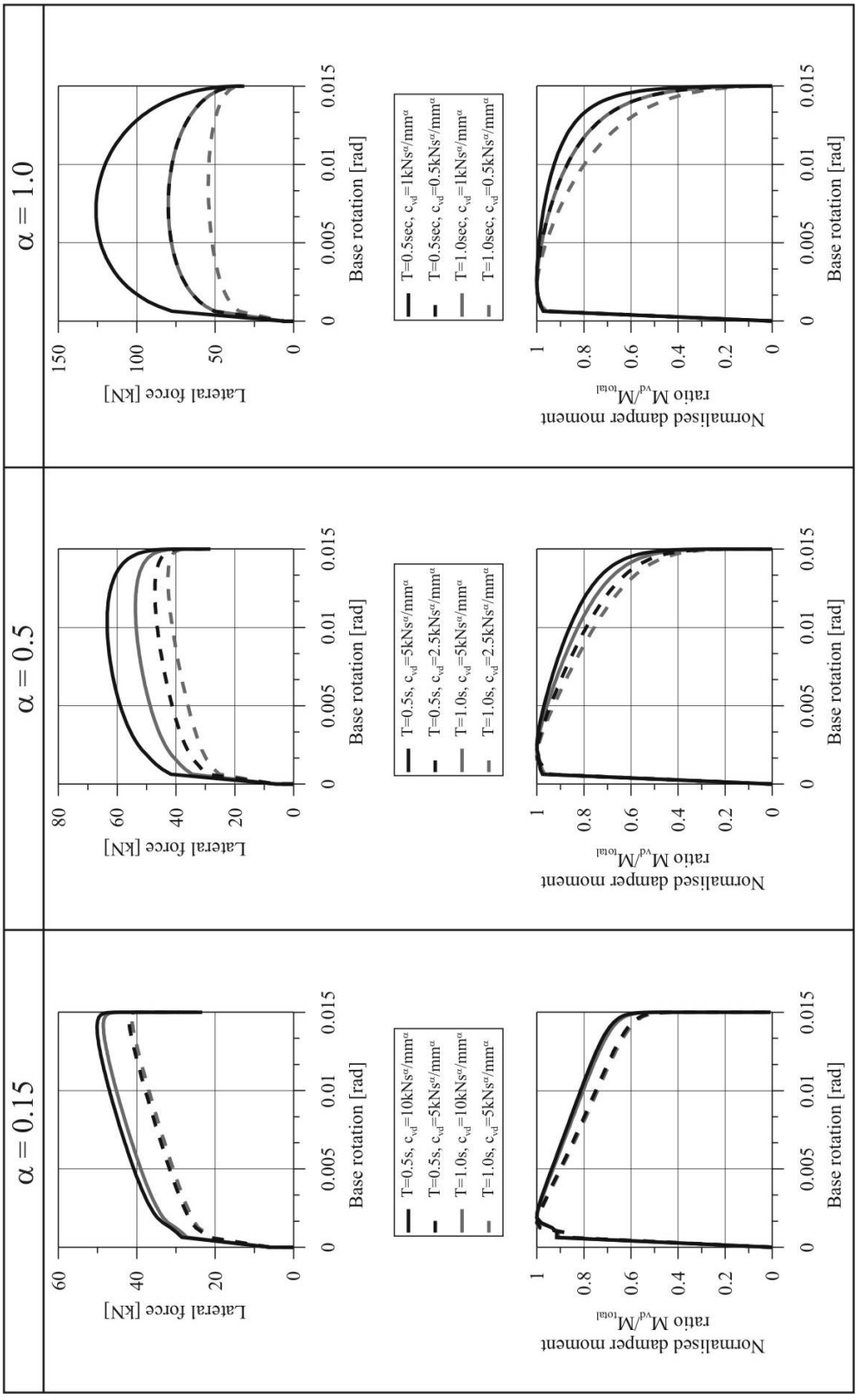

Figure 7.38 Lateral response and moment contribution of a PT viscous wall following a parametric analysis

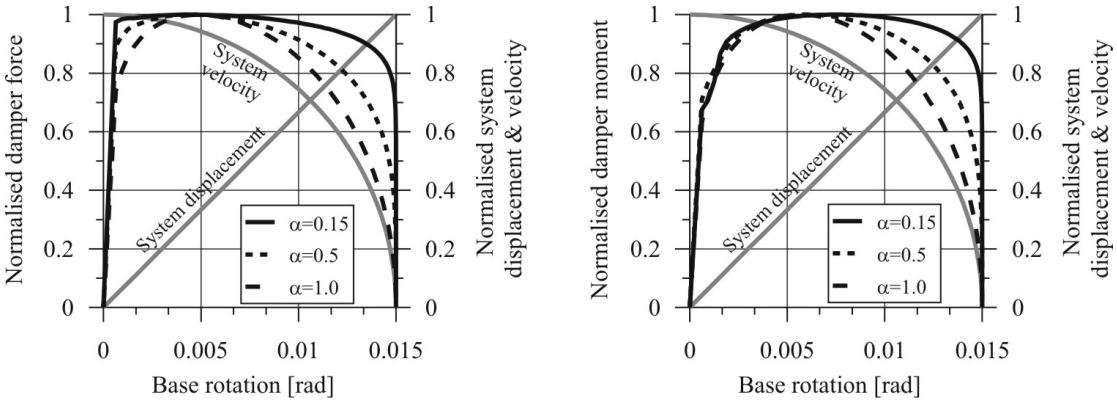

(a) Damper force relationship (b) Damper moment relationship

Figure 7.39 Normalised viscous damper, force and moment relationship following a parametric analysis of a PT viscous wall

7.2.3. An Analytical Model for Post-Tensioned Systems Subjected to Biaxial Bending

The general failure surface of a symmetric column section under biaxial bending is illustrated in Figure 7.40. Generally, for a given axial load ***P***, the failure surface is expressed by an elliptical formulation proposed by Bresler [1960]

$$\left[\frac{M_{nx}}{M_{x0}}\right]^{\alpha} + \left[\frac{M_{ny}}{M_{y0}}\right]^{\alpha} = 1 \qquad \textbf{7.69}$$

Where

M_{nx} = x-axis component of the biaxial applied moment
M_{ny} = y-axis component of the biaxial applied moment
M_{x0} = capacity of the section about the principle x-axis
M_{y0} = capacity of the section about the principle y-axis
Θ = skew angle defining the orientation of the applied moment.

Many analytical studies have been carried out to quantify (or qualify) the exponent α describing the interaction surface in Figure 7.40. Such studies vary significantly in complexity ranging from simplified section analyses to detailed fibre and finite-element models, Sakai and Mahin [2004]. Generally, the exponent α is in the range of 1.5-2 and is a function of the reinforcement ratio, axial load, concrete strength, reinforcement yield strength and the ratio between the long dimension and short dimension of a column section, Furlong [1960]; Parme et al. [1966].

With reference to Figure 7.40, the influence of axial load is generally assumed to vary linearly from the pure compression load P_c to the balanced point of the section P_b. It is also assumed to vary linearly from the pure tension P_t capacity to pure flexure P_0. Between pure flexure and the balanced point a parabolic relationship is commonly adopted as this is typically where the section will be designed to operate about.

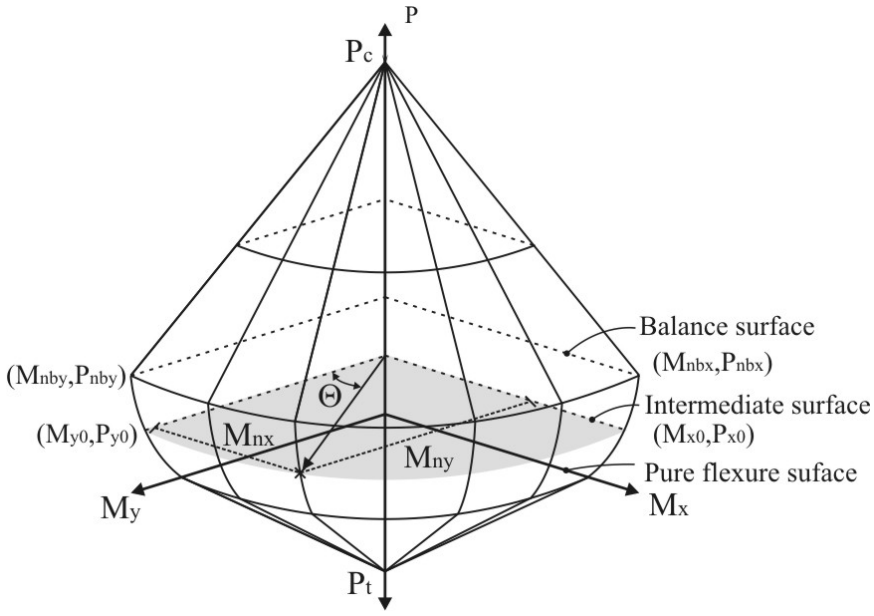

Figure 7.40 3-Dimensional biaxial limit-state surface of a (symmetric) column

To construct an accurate biaxial failure surface a 3-dimensional section analysis must be carried out in which the skew angle Θ and axial load N act as global variables. The moment-curvature and moment-rotation methods discussed in Section 7.2 are extended in this section to perform a biaxial section analysis about any skew angle Θ. With respect to a monolithic section, the biaxial analysis is performed following the illustration in Figure 7.41 (a). The following variables are defined

c	= neutral axis depth
c_x	= neutral axis depth in the x-direction along the centreline of the section
c_y	= neutral axis depth in the y-direction along the centreline of the section
ϕ_i	= imposed curvature
$\overline{Y}$	= location from the extreme edge of the section to the centroid of the concrete compression region
C_c	= resultant concrete compression force
C_s	= resultant steel compression force
N	= Axial load acting on the section
T_s	= resultant steel tension force
x, y	= original coordinate system parallel to the geometry of the section
x', y'	= skewed coordinate system parallel to the imposed curvature

Further accuracy is incorporated into the program by accounting for unconfined cover concrete and confined core concrete as shown in Figure 7.41 (b).

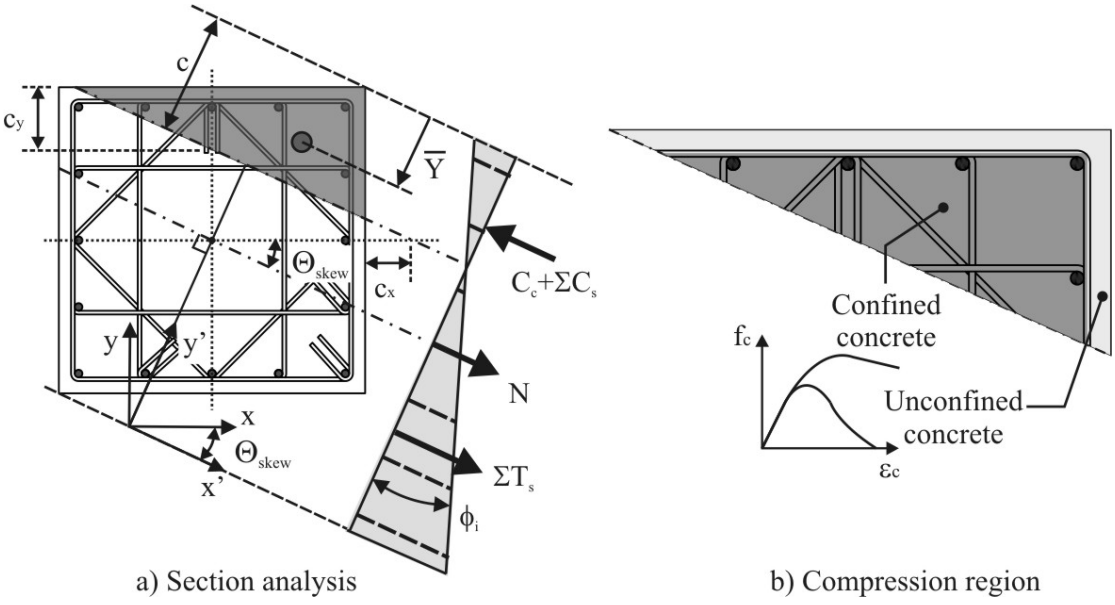

Figure 7.41 Generic 3-Dimensional section analysis technique

It should be appreciated that the 3-dimensional lateral response of a column section is dependant on the displacement path. That is, a displacement path following a clover-shape will result in a different lateral response than, for example, a square or diagonal displacement path. The unique clover-shaped displacement protocol adopted during the experimental testing in Chapter 4 requires the program to step through curvature increments ϕ_i as well as skew angle increments Θ_i. This ensures that the resulting displacement path from the section analysis approximates that of the displacement demand imposed during testing. The incremental moment-curvature analysis in Figure 7.42 (a) is shown as a solid grey circle which traces the imposed curvature demand (black dashed line). The results of each analysis increment can be viewed in Cartesian coordinates ($\phi_{X,i}$, $\phi_{Y,i}$) & ($M_{X,i}$, $M_{Y,i}$) as in Figure 7.42 (b), or in polar coordinates (Θ_i, ϕ_i & M_i).

The displacement of the section is computed by integration of the curvature over the length of the element in each Cartesian direction. For a cantilever element, where the curvature demand $\phi_{X/Y,i}$ is less that the yield curvature ϕ_y, the displacement is computed from Eq.(7.70), otherwise Eq.(7.71) is used (refer Figure 7.43). Where, $\Delta_{X/Y,y}$ is the uniaxial yield displacement in the ***x*** or ***y*** direction. In Eq.(7.71) the plastic hinge length is computed from expressions developed for uniaxial flexure (see Chapter 3).

$$\Delta_{X/Y,i} = \phi_{X/Y,i} \frac{H_e^2}{3} \qquad \textbf{7.70}$$

$$\Delta_{X/Y,i} = \Delta_{X/Y,y} + \left(\phi_{X/Y,i} - \phi_y\right) L_p \left(H_e - 0.5L_p\right) \qquad \textbf{7.71}$$

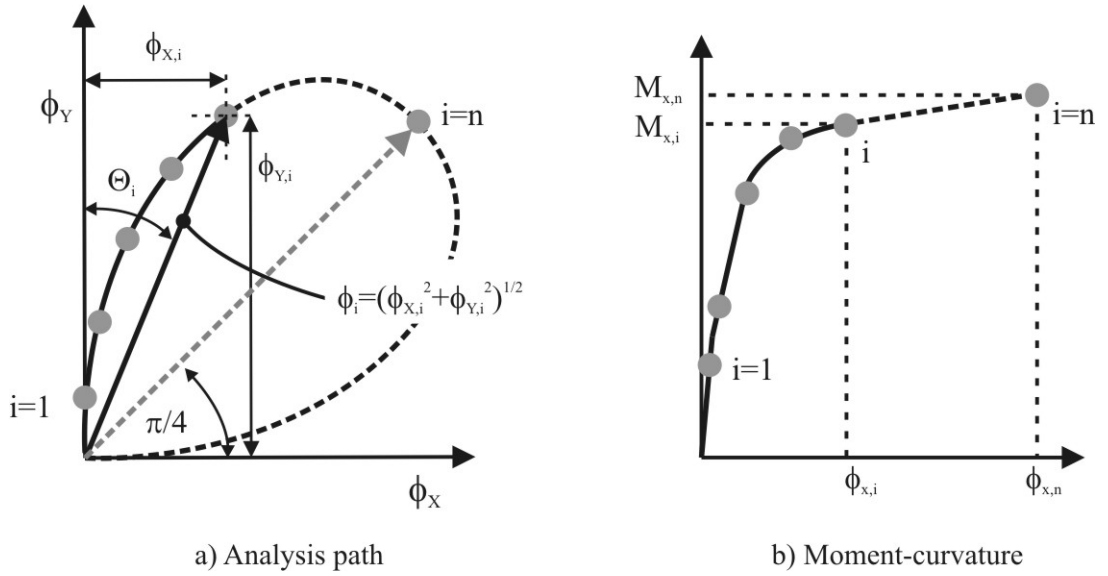

Figure 7.42 3-Dimensional section analysis considering a clover-shape displacement path

At the end of the analysis, the resulting displacement path computed using Eq.(7.70) and Eq.(7.71) should agree with the imposed experimental displacement path: this ensures a proper comparison exists between the analytical model and the experimental test. For this to occur, at each analysis step (skew angle increment Θ_i) the curvature ϕ_i should be adjusted until there is agreement between the computed and known displacement. However, to avoid this computationally demanding iteration at each skew angle, the clover-shape relationship can be enforced at the curvature level, as opposed to the displacement level. The curvature coordinates are then computed from the following expressions

$$\phi_{X,i} = \phi_n \cdot \sin(2\Theta_i) \cdot \cos(\Theta_i) \qquad \textbf{7.72}$$

$$\phi_{Y,i} = \phi_n \cdot \sin(2\Theta_i) \cdot \sin(\Theta_i) \qquad \textbf{7.73}$$

Where ϕ_n is the magnitude of curvature at $\Theta = 45°$. ϕ_n is adjusted until the computed displacement at $\Theta = 45°$ agrees with the imposed experimental displacement, i.e. $\Delta_n = \Delta_{expt}$. In fact, the adjusted curvature ϕ_n can be computed by rearranging Eq.(7.71) for $\phi_n = \phi_{X,Y,i}$. Hence, instead of satisfying the displacement at all skew angles during the incremental analysis, only the final displacement at $\Theta = 45°$ will compare to the experimental displacement demand.

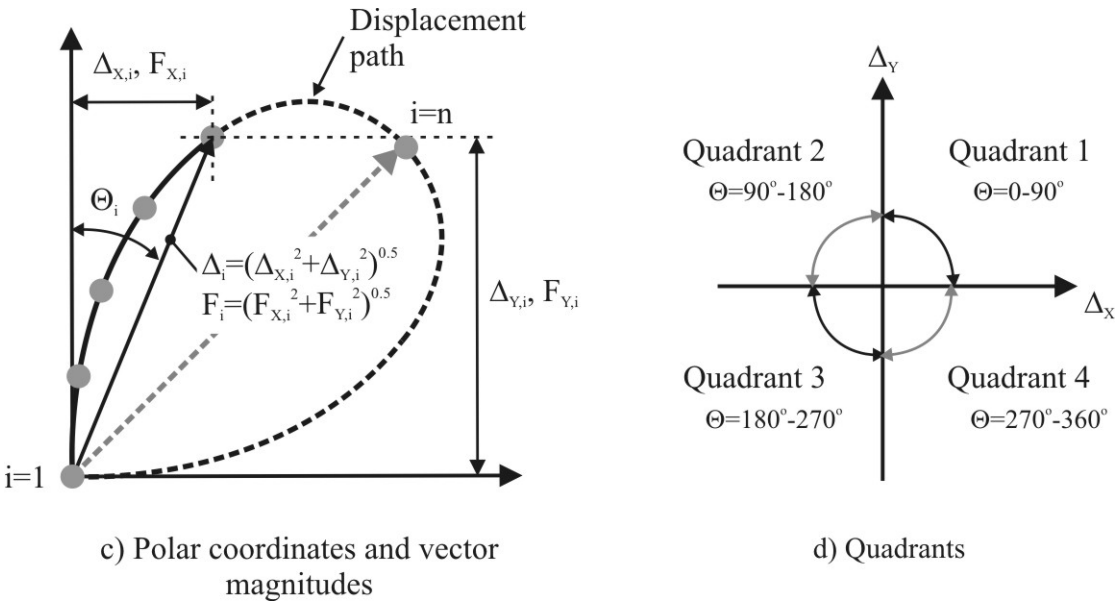

c) Polar coordinates and vector magnitudes

d) Quadrants

Figure 7.43 Polar coordinates, vector magnitudes and quadrants following a biaxial analysis

With respect to the analysis path of a PT system, the imposed curvature is replaced with an imposed base-rotation θ_i,

$$\theta_{X,i} = \theta_n \cdot \sin(2\Theta_i) \cdot \cos(\Theta_i) \qquad \textbf{7.74}$$

$$\theta_{Y,i} = \theta_n \cdot \sin(2\Theta_i) \cdot \sin(\Theta_i) \qquad \textbf{7.75}$$

Where θ_n is the base rotation at $\Theta = 45°$. Again, θ_n is adjusted until the computed displacement at $\Theta = 45°$ agrees with the experimental displacement, i.e. $\Delta_n = \Delta_{expt}$. For a PT system the displacement at the effective height is computed from Eq.(7.76)

$$\Delta_{X/Y,i} = \theta_{X/Y,i} \cdot H_e + \Delta_{X/Y,e} \qquad \textbf{7.76}$$

Where $\Delta_{X/Y,e}$ is the elastic displacement in the ***x*** and ***y*** direction. The elastic displacement is computed from Eq.(7.77) below, ignoring the prestressed induced elastic deformations (refer Section 7.2.1 (g)). $I_{X/Y,e}$ represents the effective second moment of area to be used when calculating the displacements in the ***x*** and ***y*** direction respectively.

$$\Delta_{X/Y,e} = \frac{F_{X/Y,i} \cdot H_e^3}{3E \cdot I_{X/Y,e}} \qquad \textbf{7.77}$$

Again, to avoid iterating at each rotation increment in order to satisfy the actual experimental displacement path, the clover-shape can be imposed at the base rotation

level (as opposed to the global displacement level). The resulting displacement profile at the effective height will not exactly match the experimental displacement profile; however, the difference is minimal in the case of a PT system.

Table 7.12 Summary of test specimens providing a comparison to the biaxial analytical model

	Brief description	Material at rocking interface	Dissipation
MON	Precast concrete monolithic bridge pier.	Cast in-situ concrete	16-D10 cast-in longitudinal reinforcing bars
HBD5	Precast concrete post-tensioned bridge pier.	Steel plate	8-8mm externally mounted TCY dampers

(a) Biaxial Section Analysis: Comparison with the Experimental Response of a Monolithic Bridge Pier (MON)

The biaxial section analysis is first compared to the experimental response of a traditional reinforced concrete section i.e. a moment-curvature analysis. The biaxial moment-curvature analysis is compared to the experimental response of MON in Figure 7.44. The graph plots two sets of data: one for each set of quadrants. Furthermore, only the loading cycle is shown. With reference to Figure 7.43 (a) above, instead of plotting the response in Cartesian coordinates ([$\mathbf{F_{Xi}}$, $\mathbf{\Delta_{Xi}}$] & [$\mathbf{F_{Yi}}$, $\mathbf{\Delta_{Yi}}$]), the data points are plotted using vector magnitudes ($\mathbf{F_i}$, $\mathbf{\Delta_i}$) for the two quadrant sets (Quadrant 1&3 and Quadrant 2&4) as shown in Figure 7.43 (b). By displaying the results in this way the loading envelope is independent of the path; however, it is only appropriate to plot the loading data as the unloading portion will give erroneous results when the load becomes negative in either the ***x*** or ***y*** direction. As mentioned, two plots are shown on the same graph in Figure 7.44: Quadrant 1&3 and Quadrant 2&4. The analytical (biaxial) model compares very well to the experimental response. The initial stiffness, yield displacement and post-yield stiffness are all captured well. As the displacement ductility increases the model does not capture the strength degradation associated with bond degradation and rupture of the longitudinal reinforcement. It should be recognised that the program only produces a monotonic backbone curve; therefore, stiffness degradation is obviously not included in the analysis.

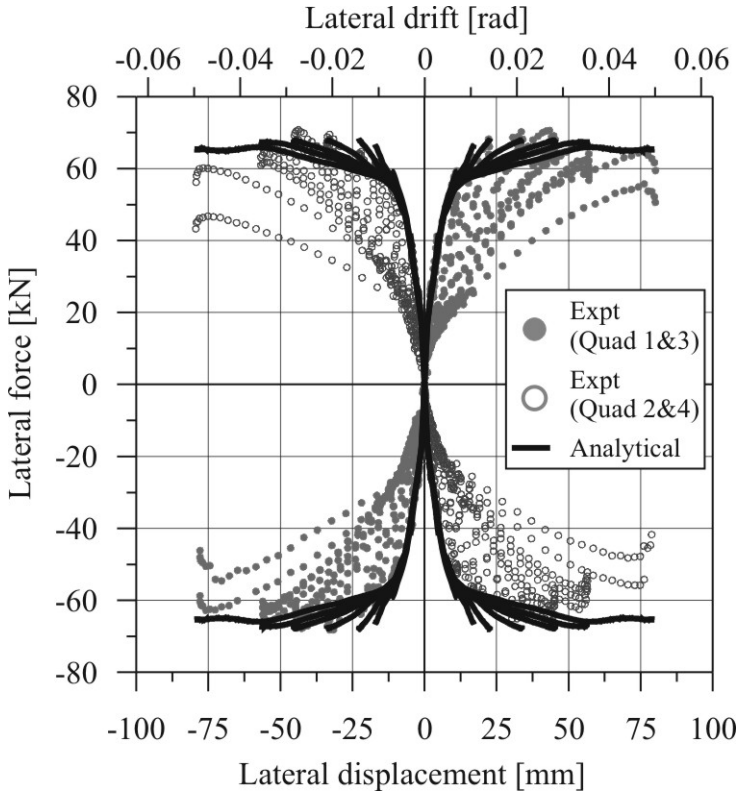

Figure 7.44 Biaxial global comparison between the analytical model and the experimental response of the monolithic bridge pier MON.

Table 7.13 Model properties of MON

Precast properties	
Computed confinement ratio, f'_{cc}/f'_c	1.19
Measured Unconfined compression strength, f'_c	54 MPa
Axial load, N	200 kN (0.030 f'_cA_g)
Measured mild steel properties	
Diameter of reinforcement, d_b	10 mm
Young's modulus, E_{ms}	187000 MPa
Yield strain, $\varepsilon_{y,ms}$	0.00170
Strain hardening, $\varepsilon_{sh,ms}$	0.03
Stain x, $\varepsilon_{x.ms}$	0.078
Strain at ultimate, $\varepsilon_{su,ms}$	0.2
Yield stress, $f_{y,ms}$	317 MPa
Stress x, $f_{x.ms}$	400 MPa
Ultimate stress, $f_{u.ms}$	433 MPa

(b) Biaxial Section Analysis: Comparison with the Experimental Response of a Hybrid Post-Tensioned Bridge Pier (HBD5)

The biaxial moment-rotation analysis of HBD5 (Hybrid PT bridge pier with external hysteretic dampers, refer Table 7.12) is compared to the biaxial experimental response in Figure 7.45 below. The global response presented in Figure 7.45 (a) shows good agreement between the model and the experiment. As discussed in Section 7.2.2 (c) the flexibility of the rocking interface of HBD5 is not trivial, but rather difficult to quantify. The steel plate at the base of the precast concrete adds a degree of complexity to the problem: the actual stiffness and strength of the composite system will lie somewhere between the two different materials (concrete and steel). The uniaxial analysis of PT2 in Section 7.2.2 (c) indicated that an effective elastic stiffness of 100,000MPa for the material at the rocking interface appeared to return reasonable results. These same material properties were used with the biaxial analysis of HBD5. The model parameters of HBD5 are summarised in Table 7.14 below.

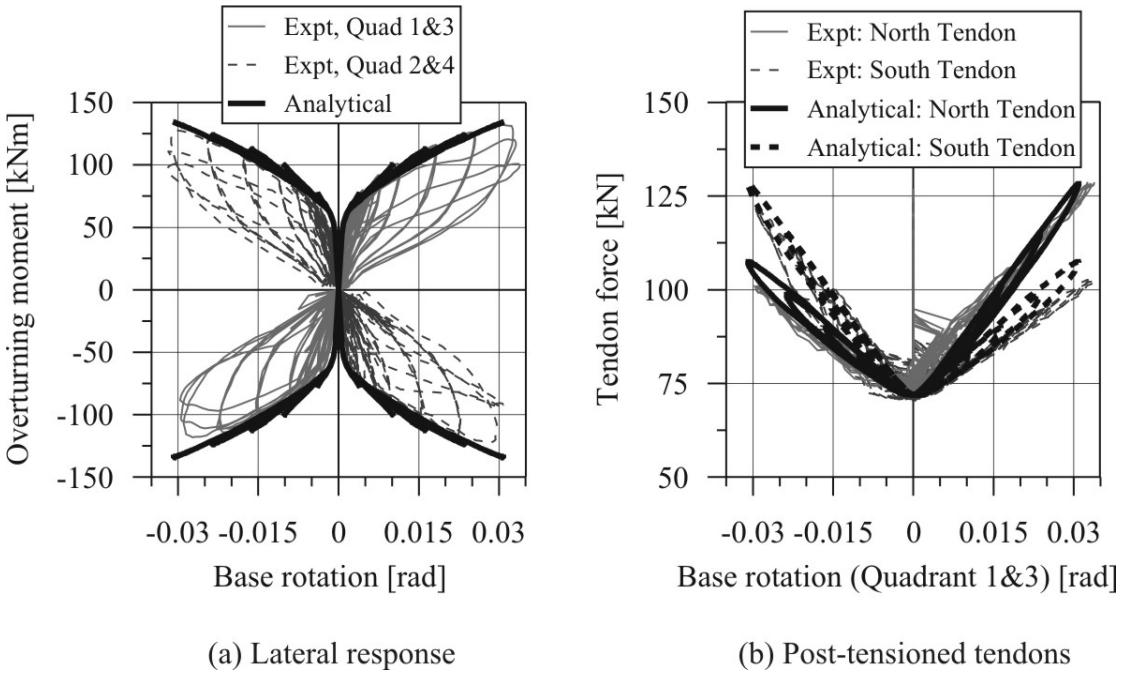

Figure 7.45 Comparison between the experimental cyclic response and the biaxial analytical model of a post-tensioned pier, HBD5

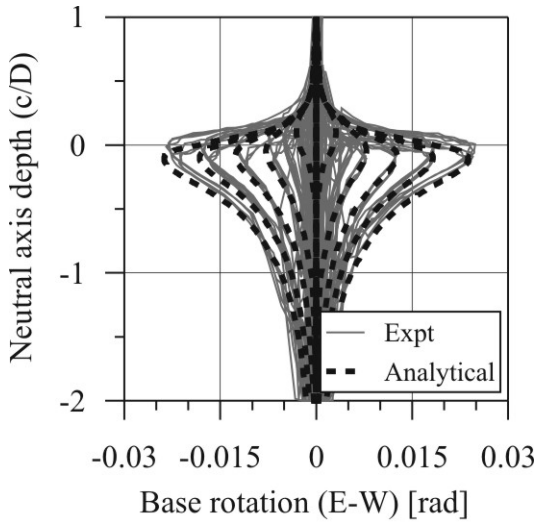

(a) Depth of rocking contact

Figure 7.46 Comparison at a local level between the experimental cyclic response and the biaxial analytical model of a post-tensioned pier, HBD5

Table 7.14 Model properties of HBD5

Precast properties	
Calibrated flexural stiffness, E_cI_e	11027 kNm^2
Constitutive stress-strain relationship	Linear elastic
Flexibility of the rocking interface, E	100,000MPa
Measured post-tensioning properties	
Total initial post-tensioned force, $T_{pt,0}$	288.0 kN (0.044 f'$_c$A$_g$)
Unbonded length, $L_{ub,pt}$	2340 mm
Young's modulus, E_{pt}	197100 MPa
Area of tendon, A_{pt}	99 mm^2
Measured mild steel properties	
TCY damper fuse length, l_{fuse}	115 mm
Diameter of fuse, d_s	8 mm
Diameter of the bar outside fuse, d_b	20 mm
Total length of the dissipater (short/long), l_{diss}	250mm/300mm
Young's modulus, E_{ms}	193,900 MPa
Yield strain, $\varepsilon_{y,ms}$	0.00165
Strain hardening, $\varepsilon_{sh,ms}$	0.011
Stain x, $\varepsilon_{x.ms}$	0.030
Strain at ultimate, $\varepsilon_{su,ms}$	0.111
Yield stress, $f_{y,ms}$	320 MPa
Stress x, $f_{x.ms}$	400 MPa
Ultimate stress, $f_{u.ms}$	461 MPa

(c) Biaxial Moment-Interaction Parametric Analysis: Design Charts for Monolithic and Post-Tensioned Rocking Connections

Following on from the experimental confirmation of the biaxial section analysis in the previous section, a parametric analysis was undertaken to develop a series of biaxial moment-interaction design charts. The parametric study was undertaken considering two connection typologies: a monolithic ductile pier and a Hybrid PT pier with internally grouted mild steel reinforcement. It should be noted that the moment capacity of a PT pier considering either external or internal reinforcement is comparable: the design charts are, therefore, expected to be applicable to any hybrid post-tensioned connection (internal or external hysteretic dissipaters). The two symmetrical pier sections used to undertake the parametric analyses are illustrated in Figure 7.47. Each connection has a total of 16 longitudinal reinforcing bars uniformly distributed around the perimeter of the section. The monolithic pier was modelled considering confined core concrete within the peripheral hoops and unconfined cover concrete. The PT pier was assumed to have cover concrete protection around the perimeter; therefore, the core confinement was extended to the perimeter of the section (Confinement Model C, refer Section 7.2.1 (d)).

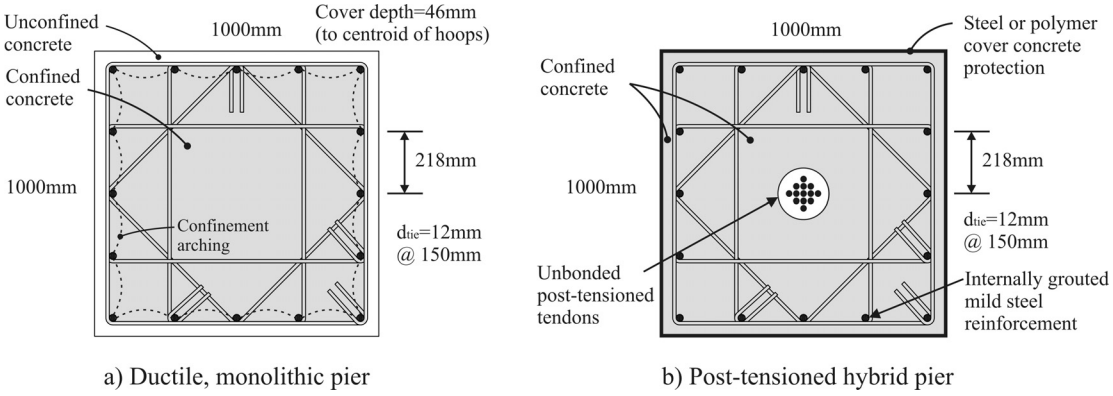

Figure 7.47 Details of the pier sections used in the biaxial parametric analysis

For both the monolithic and PT bridge piers the mild steel mechanical reinforcement ratio ω_{ms} was varied from 0.1, 0.2 to 0.3. This covers a significant portion of the practical range of reinforcement contents within design, where $\omega_{ms} = f_y A_s / f'_c BD$ and A_s is the total area of steel reinforcement. The axial load ratio $\nu = N/f'_c BD$ was varied from 0.05, 0.15, 0.25 to 0.35. For the post-tensioned pier, the axial load ratio included the initial post-tensioning load such that $\nu = (N+T_{pt0})/f'_c BD$. The prestressed mechanical reinforcement ratio ω_{pt} was varied from 0.15 to 0.45, where $\omega_{pt} = f_{y,pt} A_{pt} / f'_c BD$ and A_{pt} is the total area of post-tensioned reinforcement. Finally, the confinement ratio f'_{cc}/f'_c was varied from 1.1 to 1.4 to encompass an upper and lower bound of possible solutions.

Two limit states were considered when defining the interaction surfaces: the nominal-yield interaction-surface and the design-capacity interaction-surface. The nominal yield surface is useful for macro-models utilising lumped plasticity modelling

techniques that adopt a user-defined biaxial yield surface. The nominal yield moment was defined by either a concrete strain of $\varepsilon_c = 0.004$ or a mild steel strain of $\varepsilon_s = 0.015$. The design capacity surface is a useful tool for satisfying strength requirements during design accounting for orthogonal earthquake loading. The design capacity was defined by either a mild steel strain of $\varepsilon_s = 0.6\varepsilon_{su}$, where $\varepsilon_{su} = 0.1$ for mild steel with a characteristic yield stress of 500MPa, or a tendon strain of $\varepsilon_{pt} = 0.9\varepsilon_{pt,y}$ where $\varepsilon_{pty} = 0.0078$, or a concrete strain of $\varepsilon_c = \varepsilon_{cu}$. The concrete strain limit ε_{cu} is defined by Eq.(7.78), where all terms have been defined in Section 7.2.1 (e).

$$\varepsilon_{cu} = 0.004 + \frac{1.4\rho_v \cdot f_{yh} \cdot \varepsilon_{su}}{f'_{cc}} \qquad \textbf{7.78}$$

First, the results of the parametric analyses are presented to show the nominal-yield interaction-surface. The normalised and dimensionless moment-interaction charts corresponding to the nominal yield strength of a monolithic square pier (or column) is presented in Figure 7.48 as a function of the mild steel mechanical reinforcement ratio ω_{ms} and the axial load ratio ν. The dimensionless moment capacity μ is defined by the equation $\mu = M/f'_cBD^2$, where M is the moment capacity of the section (the yield moment in this case). By definition, at nominal yield the concrete strain will be less than or equal to 0.004, hence, the concrete confinement will have negligible effect on the nominal moment capacity of the section or on the shape of the biaxial interaction surface (the confinement ratio of $f'_{cc}/f'_c = 1.1$ is presented in Figure 7.48). As ω_{ms} and ν is increased, Figure 7.48 confirms that the nominal moment capacity increases and the biaxial interaction becomes more linear (α reduces). As intuition would suggest, as the axial load ratio increases, the shape of the yield surface has less dependency on ω_{ms}.

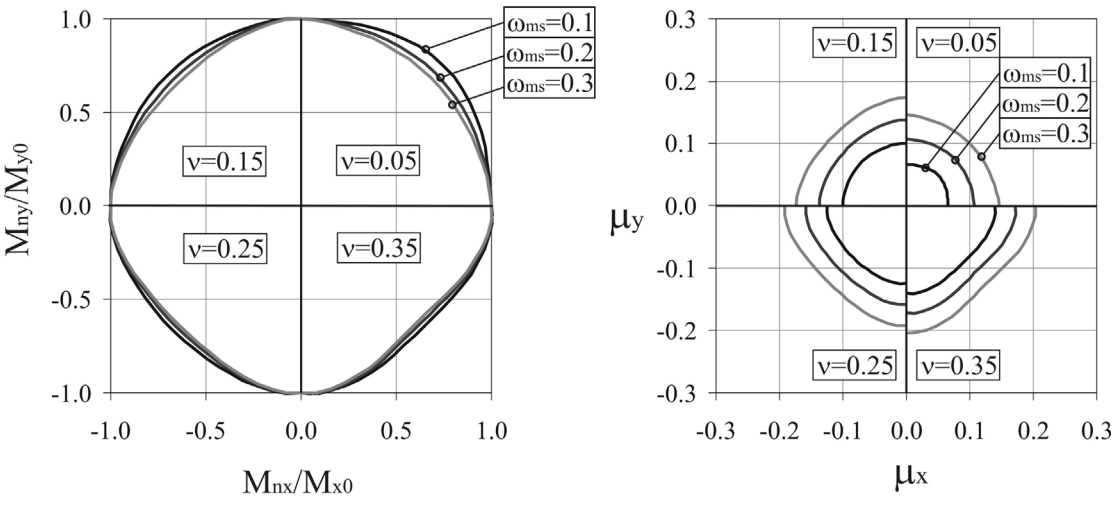

Figure 7.48 Nominal yield surface for monolithic ductile square piers/columns.

The normalised and dimensionless nominal yield moment-interaction charts are shown in Figure 7.49 for a square post-tensioned hybrid pier (or column) as a function of the mild steel mechanical reinforcement ratio ω_{ms} and the axial load (plus initial post-tensioning T_{pt0}) ratio ν. The PT steel mechanical reinforcement ratio in Figure 7.49 is equal to $\omega_{pt} = 0.15$; in fact, ω_{pt} has very little influence on the response of the section at nominal yield as the tendon elongation is minimal. The dependency on ω_{pt} further reduces as the axial load and initial post-tensioning increase. The shape of the yield surface in Figure 7.49 (a) is almost independent of the mild steel mechanical reinforcement ratio ω_{ms} for all levels of axial load and initial post-tensioning ν within the section.

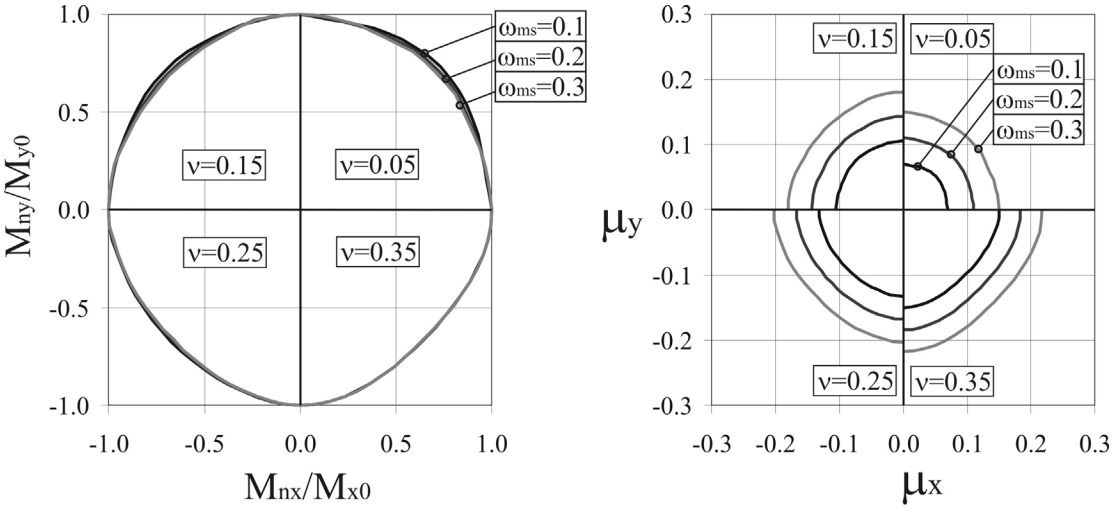

Figure 7.49 Nominal yield surface for post-tensioned, hybrid square piers/columns.

Following a least-squares regression analysis, the yield surfaces of Figure 7.48 (Monolithic connection) and Figure 7.49 (PT connection) were fitted to the biaxial interaction surface of Eq.(7.69). The exponent α for a monolithic square section is equal to the following linear equation with an average coefficient of variation of 8.3% for the range of variables considered in this parametric study.

$$\alpha = 2.04 - 1.54\nu \qquad \textbf{7.79}$$

The exponent α for a hybrid PT square section is equal to the following linear equation with an average coefficient of variation of 2.6% for the range of variables considered in this parametric study.

$$\alpha = 2.03 - 1.17\nu \qquad \textbf{7.80}$$

The dimensionless design moment capacity for a monolithic square pier or column is shown in Figure 7.50 as a function of ω_{ms}, ν and the level of concrete confinement within the section f'_c/f'_{cc}. Recalling that the design capacity corresponds to one of three strain limit states, the concrete strains are likely to be in the range of 0.01 to 0.02. For concrete strains in this range, the level of concrete confinement can have a significant influence on the capacity of the section and can be seen by the comparison of Figure 7.50 (a) with (b).

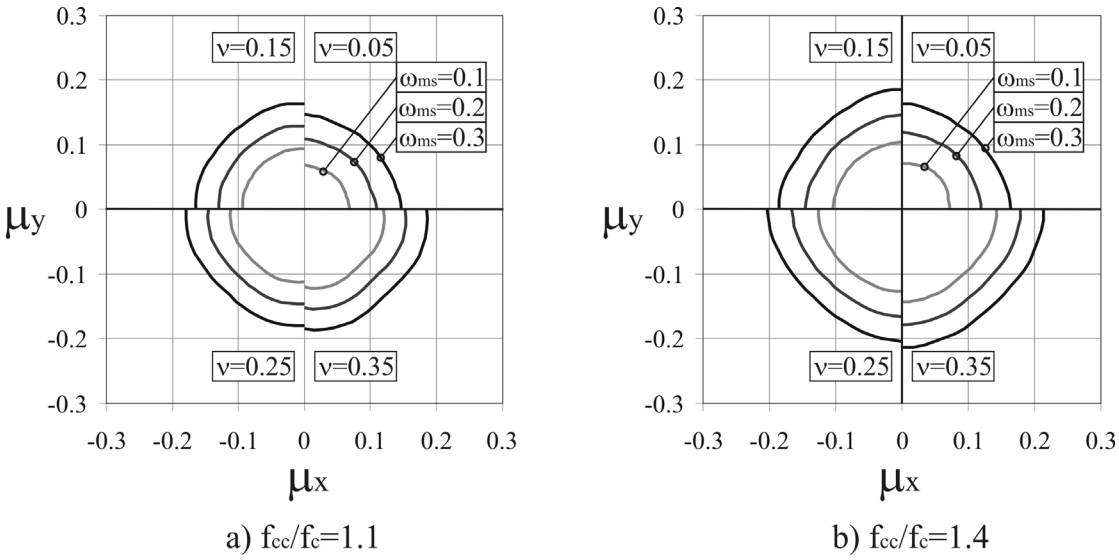

Figure 7.50 Design capacity moment interaction-surface for monolithic square pier/columns

The same design charts are produced for a hybrid post-tensioned square section in Figure 7.51 as a function of ω_{ms}, ω_{pt}, ν and the level of concrete confinement within the section f'_c/f'_{cc}. The design charts confirm that the confinement of the section has a great effect on the capacity: confinement has a significant effect on the strength of the section as the axial load (plus initial post-tensioning load) increases.

A least-squares regression analysis was carried out on the deign-level interaction-surfaces. The exponent α for a monolithic connection is defined by the following linear relationship having a coefficient of variation of 4.4% for the range of parameters considered in this parametric study.

$$\alpha = 1.83 + 0.47\nu \qquad \textbf{7.81}$$

For a post-tensioned hybrid system the exponent α has a coefficient of variation of 5.4% and is defined by the following expression

$$\alpha = 1.65 + 0.67\nu \qquad \textbf{7.82}$$

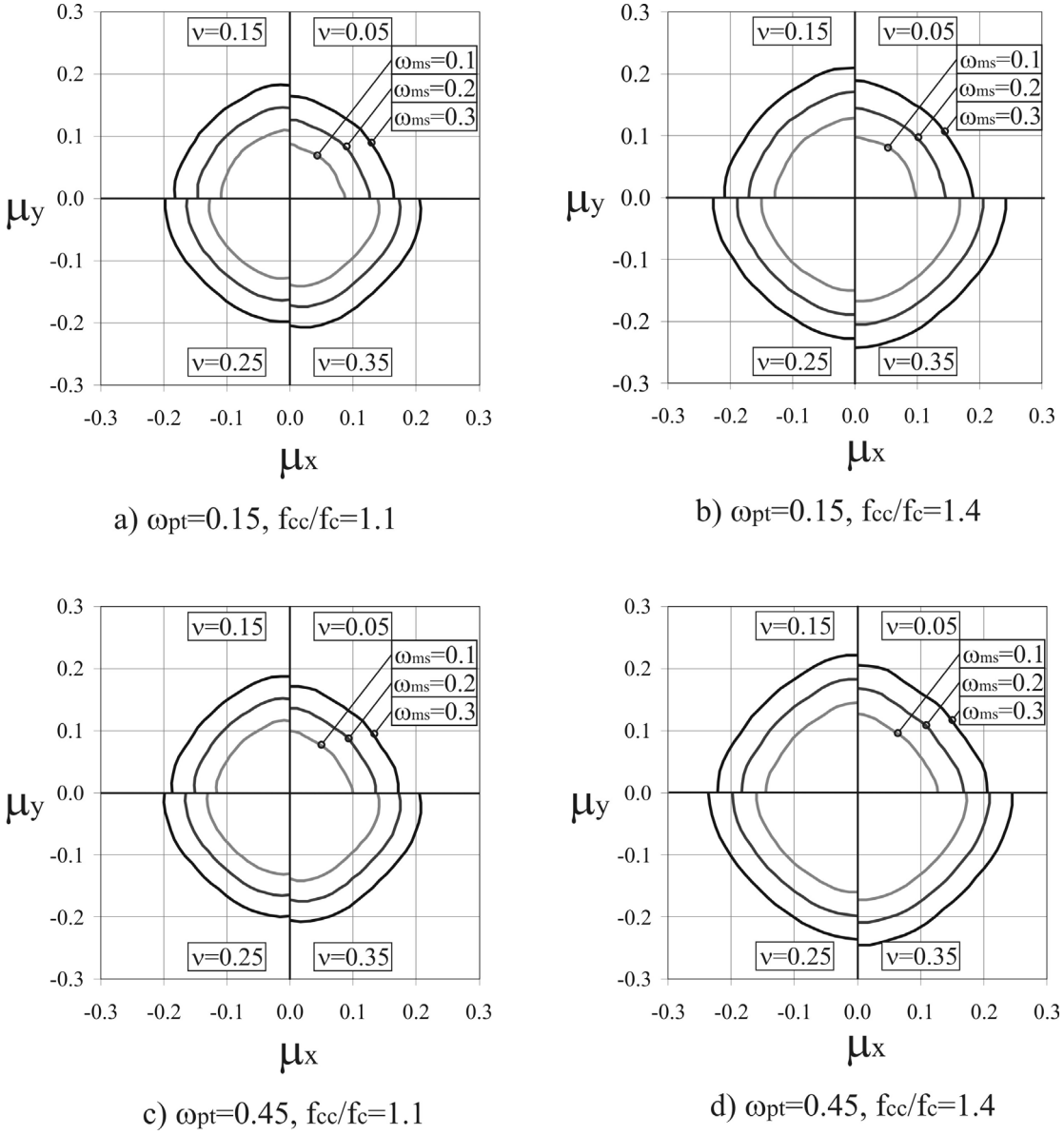

Figure 7.51 Design capacity moment interaction-surface for post-tensioned hybrid square pier/columns

It can be seen that PT systems are more linear (lower α) than an equivalent monolithic connection at the design level. In fact, at the design level, the PT connection has a total axial load that includes the tendon elongation of the post-tensioned tendons. Therefore, for a given initial axial load ratio ν, in reality, the axial load acting on a PT connection is greater than that acting on the monolithic connection due to the axial load within the tendons.

7.3. A CYCLIC MACRO-MODEL FOR POST-TENSIONED ROCKING SYSTEMS

Two macro-models were presented in Chapter 3 to model the cyclic response of PT rocking connections. The first was a lumped plasticity model to represent the rocking response via a set of rotational springs at the location of the rocking interface. The second model was a variation of a lumped plasticity model with multiple axial springs (multi-spring model) distributed along the rocking interface to directly capture the rocking characteristics of a PT system. Both models currently exist in literature; the multi-spring model has the greatest potential in terms of accuracy versus computational effort. In this section, a method is developed to accurately implement a multi-spring model within a PT macro model. In particular, this section presents a systematic method to define the axial stiffness of the multi-spring element: this parameter is the most difficult to quantify and can greatly affect the accuracy of the model.

The implementation of a macro-model incorporating a multi-axial spring model is illustrated in Figure 7.52. The damper springs (dissipaters) are non-linear inelastic, while the multi-spring contact element is a linear-elastic element. If the tendons can be guaranteed to remain elastic throughout the analysis, then these can also be modelled as a linear elastic spring, otherwise an appropriate non-linear relationship should be adopted. The precast element is modelled as an elastic Giberson element with effective section properties corresponding to the expected limit state. This macro-model is implemented into the computer program Ruaumoko, Carr [2005]. Details of the material models are discussed in greater detail in the following section.

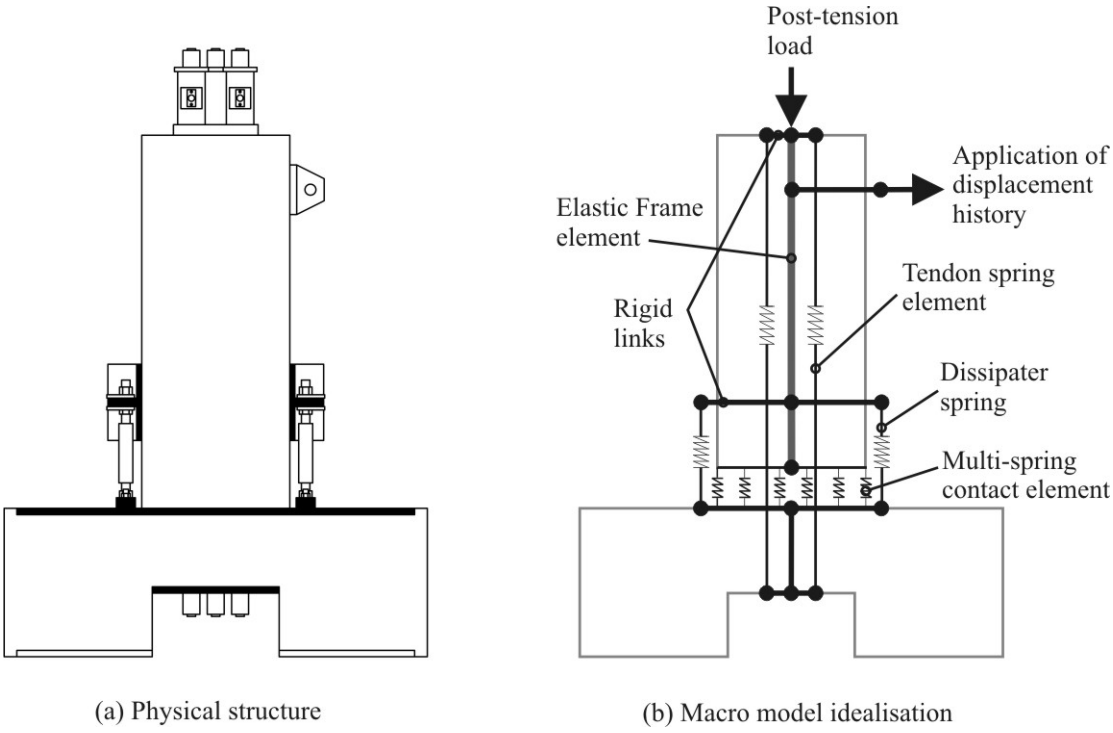

Figure 7.52 Multi-spring macro model for a PT system with external replaceable mild-steel dampers

7.3.1. Cyclic Material Models for Use within a Multi-Spring Macro Model

(a) Non-linear Inelastic Steel Model

The cyclic response of a PT system with any form of damper is essentially dictated by the behaviour of the damper. It is for this reason that the ability of the macro-model to accurately capture the cyclic response will depend on how accurately the damper element is modelled at the rocking interface.

The cyclic steel model of Dodd and Restrepo-Posada [1995] was the preferred option to accurately describe the non-linear behaviour of the mild steel dampers. This model has the ability to accurately capture the entire loading and unloading cycle as shown in Figure 7.53. The model does have some difficulty in capturing the measured load in compression when unloaded from large displacement ductility; however, this error is small. The experimental test in Figure 7.53 is the behaviour of a tension-compression-yielding (TCY) damper presented in Chapter 4.

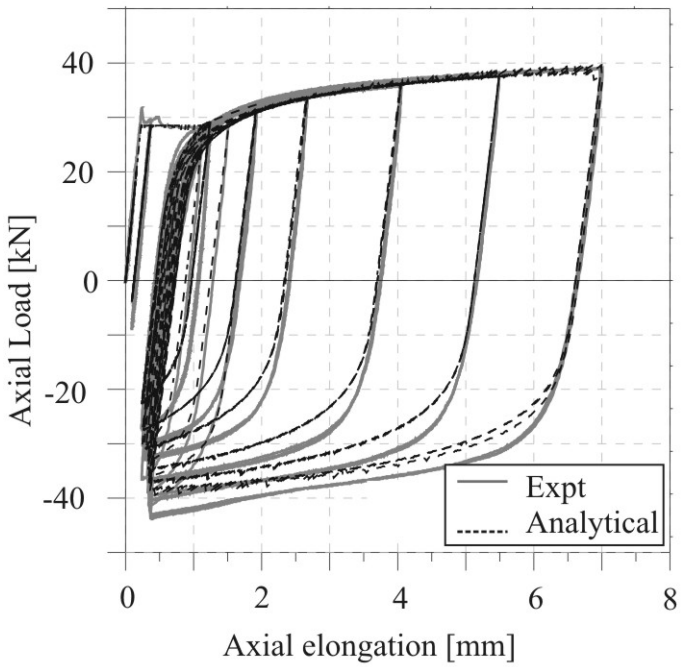

Figure 7.53

(b) Linear Elastic Compression-Only Axial Springs Along the Rocking Interface

A series of linear-elastic axial springs model the contact/uplift at the rocking interface. The springs act in compression only, allowing uplift to occur when subjected to tensile strain. A linear-elastic spring is preferred over a more complicated non-linear inelastic relationship for two reasons:

- In most cases the amount of energy dissipation associated with the non-linear behaviour of the concrete (or other non-linear material) is relatively small in

comparison to the total energy dissipation within the connection. Therefore, ignoring this contribution will not affect the accuracy of the model to any serious degree.

- Using a non-linear inelastic relationship will actually complicate the calibration of the axial spring stiffness as a larger number of parameters must be defined. The axial springs have units of force and displacement; therefore, any material stress-strain parameters must consider some equivalent spring length by which to convert to the correct spring units. An equivalent spring length adds yet another parameter to determine.

The main difficulty in the implementation of a multi-spring macro model is the calibration of the axial spring stiffness. A method to accurately determine the axial stiffness is discussed in the following section.

7.3.2. Calibration of the Axial Stiffness of a Multi-Spring Element via a Moment-Rotation Section Analysis

In order to accurately determine the total stiffness of the multi-spring unit k_{multi}, a moment-rotation section analysis is first carried out. In fact, specific to calibration of the multi-spring stiffness, the section analysis does not include the mild steel (or viscous) dampers. Rather the additional axial load that would be induced by the dampers (at the rocking interface) is added to the axial load (or initial post-tensioning force). If all the damper elements are expected to be in tension, then the additional axial load to be added to the section is equal to $\Delta N = \rho_s A_g f_y$, where ρ_s is the mild steel reinforcement ratio passing through the rocking interface. If the section is heavily reinforced and some of the dampers are expected to be in compression, then one needs to apply some judgement in determining the net value of axial load to be applied to the section. In carrying out this step, any error associated with calibration is isolated with the multi-spring element at the rocking interface, as opposed to errors associated with the damper elements. Replacing the damper forces with an equivalent axial load ensures that the concrete compression strain is similar in magnitude to that expected within the section with dampers: this improves the accuracy of the calibration when the dampers are later added to the model.

The properties of the macro model that is generated for calibration of the axial stiffness are identical to those used to carry out the section analysis, including the total axial load acting on the section (including the additional axial load from removal of the damper elements) and the axial stiffness of each post-tensioned tendon group k_{PT}. For calibration, the macro-model can be simplified by ignoring the cantilever element and by locating the tendon springs directly over the rocking interface as shown in Figure 7.54. Ruaumoko has four distribution options describing the location and stiffness of the individual axial springs within the multi-spring element. The four distribution options are: Lobatto Distribution, Gaussian Distribution, Trapezoidal Distribution and a Uniform Distribution. Typically, a uniform distribution is sufficient, but the actual distribution is situation dependant (offering yet another parameter to consider). Details of the stiffness weighting and location factors for a Lobatto and Gaussian distribution can be found elsewhere, Spieth et al. [2004b].

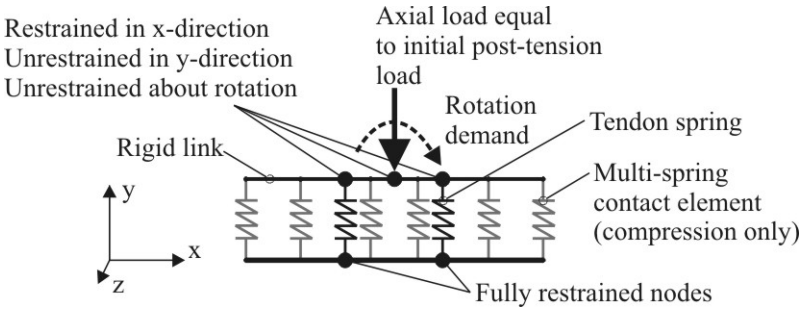

Figure 7.54 Simplified macro model of a multi-spring element to be used in the calibration of a section analysis

If the displacement of the spring located at the compression edge of the section is defined as Δ_A and by Δ_B at the uplifted edge of the section, then the dimensionless neutral axis depth χ is computed from

$$c/D = \chi = \frac{\Delta_A}{\Delta_B - \Delta_A} \qquad \textbf{7.83}$$

During calibration, both the section analysis and the macro-model are subjected to the same monotonically increasing rotation demand. Calibration concerns three key section parameters (as a function of rotation): the moment capacity, the neutral axis position and the position to the centroid of the contact compression force. The centroid of the compression region can be computed by considering moment equilibrium of the section in Eq.(7.84), where a is the length of the equivalent rectangular compression block, $a/2$ is the depth to the centroid (from the compression edge of the section), $jd_{PT,i}$ is the distance from the compression edge of the section to each tendon layer i, $T_{PT,i}$ is the total force in each tendon layer and M is the total base moment.

$$a/2 = \frac{\sum_{i=1}^{n_{PT}} T_{PT,i} jd_{PT,i} - M}{\sum_{i=1}^{n_{PT}} T_{PT,i}} \qquad \textbf{7.84}$$

The axial stiffness of the multi-spring unit k_{multi} is updated until agreement is met between the section analysis and the multi-spring macro model. The agreement can be by visual observation or by computing a goodness of fit such as the Coefficient of Determination R^2. If the agreement is not satisfactory, then the axial stiffness is updated; hence, the procedure is iterative but will converge rapidly if the initial "guess" of k_{multi} is of an appropriate order of magnitude. Based on limited calibration, the empirical equation of Eq.(7.85) can be used as an initial estimate to compute the axial stiffness k_{multi} (in kN/m); where, L_{cant} is the cantilever length of the element (in meters); B is the width/depth of the cross-section (in meters); and E is the elastic modulus of the material at the rocking interface (in GPa).

$$k_{multi} = 18.75 \times 10^6 B^2 \left(\frac{E}{200}\right)^{0.5} \left(\frac{10}{L_{cant}}\right)^{1.1} kN/m \qquad \textbf{7.85}$$

As an example, Figure 7.55 shows the calibration of the axial spring stiffness for LVL Wall 1. The dashed line is the response of the macro model (with multi-axial spring), while the solid line is the response of the section analysis. The total axial stiffness of the multi-spring unit is $\boldsymbol{k_{multi}} = 1.2\text{x}10^6$ kN/m and has a Lobatto spring distribution. The moment-rotation and tendon load agree very well. The local response of the neutral axis depth in Figure 7.56 is also very well captured, while there is only a small error with regards to locating the centroid to the resultant compression force. It is unlikely that an exact agreement will exist between the macro-model and the section analysis for all parameters. As the compression strains increase in non-linearity both the neutral axis and the location of the centroid are unlikely to agree. This is because an effective elastic multi-spring is being used to capture the response of a non-linear material; if this is the case then some error must be accepted within both the neutral axis and force centroid. Alternatively, a bilinear-elastic multi-spring could be introduced in such situations to account for the large non-linearity of the rocking interface. A bilinear spring option was not investigated due to instability issues within the analysis; furthermore, the accuracy achieved when using a linear-elastic multi-spring was more than acceptable.

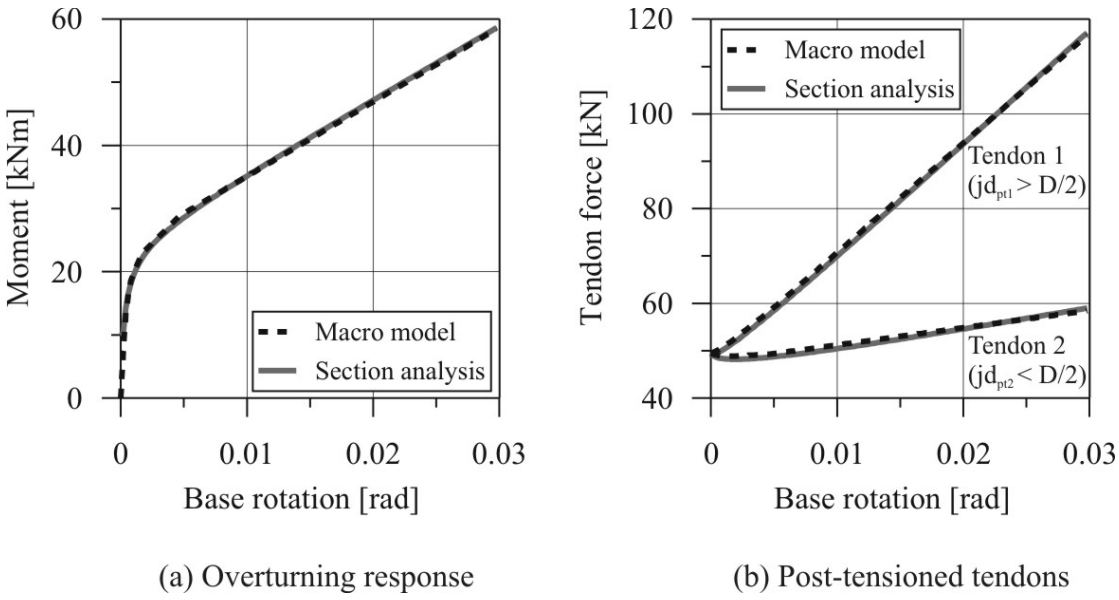

Figure 7.55 Comparison between a calibrated multi-spring macro model and a section analysis of the LVL post-tensioned wall, LVL Wall 1

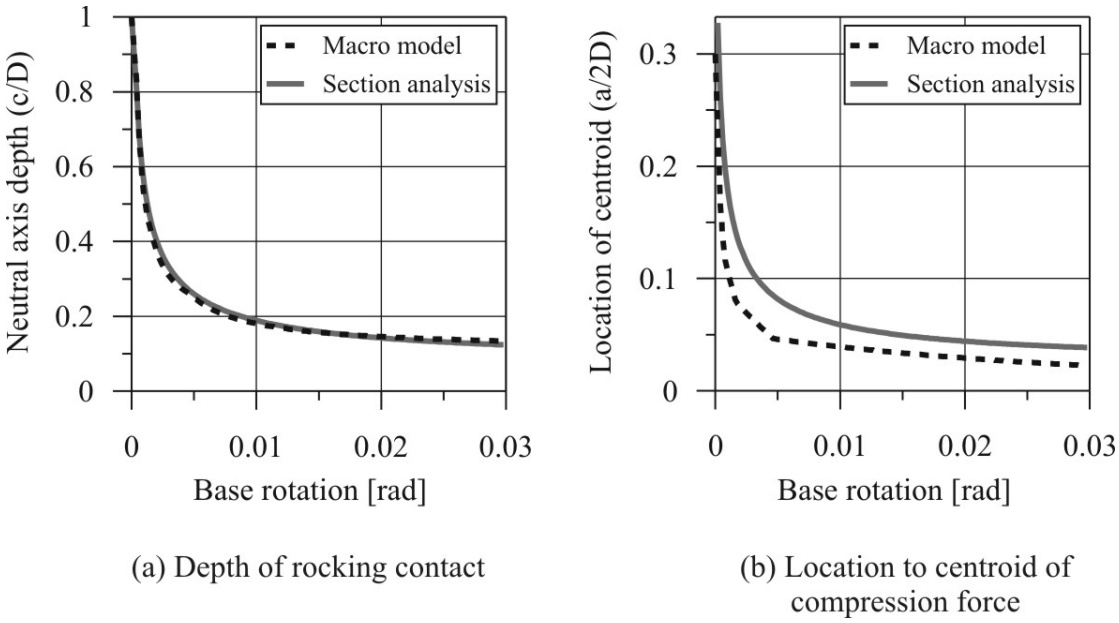

(a) Depth of rocking contact

(b) Location to centroid of compression force

Figure 7.56 Comparison at a local level between a calibrated multi-spring macro model and a section analysis of the LVL post-tensioned wall, LVL Wall 1

7.3.3. Additional Modelling Issues to be Considered when Dealing with a Multi-Spring Macro-Model

(a) Modification to the Axial Stiffness of the Precast Frame Element

By placing a multi-spring at the base of a frame element to represent the precast column/wall section, the axial flexibility of the system is inherently increased (refer Figure 7.57). While this is unlikely to result in significant errors in the analysis, a simple method to increase the area of the precast element to compensate for the reduction in stiffness is presented. In fact, this added axial flexibility has also been noted by Spieth et al. [2004a]

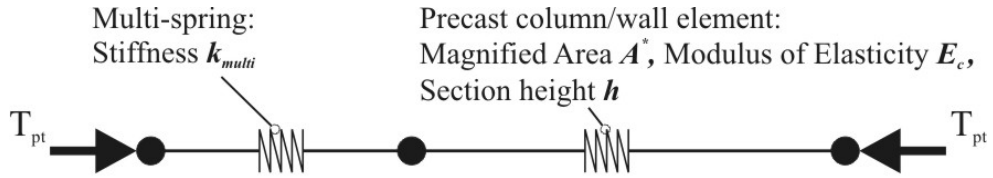

Figure 7.57 Two springs in series to represent the multi-spring axial stiffness (rocking surface) and the frame axial stiffness (precast element)

With reference to Figure 7.57, the total axial stiffness of the system is given by Eq.(7.86), where A^* is the magnified cross-section area of the section to account for the increased flexibility of the multi-spring element. Note that increasing the actual cross-sectional area A will only effect the axial stiffness of the element (ignoring shear stiffness): the flexural stiffness is not effected.

$$k = \frac{A \cdot E_c}{h} = 1 \Big/ \left(\frac{1}{k_{multi}} + \frac{A^* E_c}{h} \right) \qquad \textbf{7.86}$$

Thus the increased cross-section area $\boldsymbol{A^*}$ is computed as

$$A^* = A \left[\frac{1}{1 - (A \cdot E_c)/(h \cdot k_{multi})} \right] \qquad \textbf{7.87}$$

(b) Elastic Shortening Due to the Application of the Initial Post-Tensioning Force

When the initial post-tensioning force is applied to the macro-model, either by internal prestressing of the tendon springs or via an axial load at the top of the frame element, elastic shortening and load transfer reduces the apparent axial load within the frame element. To overcome this, the following equation is derived which increases the initial post-tensioning force to ensure the target post-tensioning force $\boldsymbol{T_{PT,0}}$ is achieved within the frame element.

$$T^*_{PT,0} = \frac{T_{PT,0}}{1 - \left(h \cdot \sum k_{PT,i}\right)/(A \cdot E_c)} \qquad \textbf{7.88}$$

Where

$T^*_{PT,0}$ = is the increased (total) initial post-tensioned force applied to the section, either by internal prestressing of the tendon springs or via an axial load.

$\boldsymbol{T_{PT,0}}$ = is the target (total) initial post-tensioned force required.

$\boldsymbol{\Sigma k_{PT,i}}$ = is the sum of the axial stiffness of all tendons within the section, where $\sum k_{PT,i} = \sum A_{PT} E_{PT} / l_{ub,pt}$.

(c) Application of the Initial Post-Tensioning Force to Prevent Excessive Pre-Load within the Hysteretic Dampers

When the initial post-tensioning force is applied to a post-tensioned rocking system with external dampers, the dampers are normally installed after post-tensioning. This is also the case for internally grouted systems: the mild steel is grouted after the post-tensioning load is applied. In doing so, the initial load in the dampers is zero, while the surrounding precast element resists the entire post-tensioned load. That is, no post-tensioning force is transferred to the damper elements. Consider the macro model in Figure 7.52 presented at the beginning of Section 7.3 above; it is impossible to ensure that the load within the external damper elements are zero by lumping the initial post-tensioning load at the top of the section (or by internally prestressing the tendon springs) as illustrated. In fact, it is possible for the damper springs to yield under the post-tensioning load alone (prior to any lateral load). A method of load application, by means to two post-tensioning forces, is described below to ensure the load in the each damper layer is zero after the application of the (total) initial post-tensioning load.

Consider the macro-model and nomenclature in Figure 7.58. First, the stiffness of a few sub-elements are determined. k_1 is the axial stiffness of the frame element (accounting for the multi-spring) up to the height of the dampers.

$$k_1 = \frac{1}{h_{diss} / \left(A^* \cdot E_c\right) + 1/k_{multi}} \quad \textbf{7.89}$$

k_2 includes the total stiffness of all dampers

$$k_2 = k_1 + \sum k_{diss} \quad \textbf{7.90}$$

k_3 is the axial stiffness of the frame element above h_{diss}

$$k_3 = \left(A^* \cdot E_c\right) / \left(h - h_{diss}\right) \quad \textbf{7.91}$$

k_{total} is the total (net) axial stiffness of the macro model

$$k_{total} = \frac{1}{1/k_3 + 1/k_2} + \sum k_{PT,i} \quad \textbf{7.92}$$

The three step procedure is described as follows, with reference to Figure 7.58.

Step 1

Apply an initial post-tensioning force $T_{pt,0}^{*1}$ to the top of the frame section equal to the following, where $T_{PT,0}$ is the target (total) initial post-tensioning force.

$$T_{pt,0}^{*1} = \frac{T_{PT,0}}{1 - \sum k_{PT,i} / k_{total}} \quad \textbf{7.93}$$

Step 2

Apply an additional force $T_{pt,0}^{*2}$ at height h_{diss} equal to the following

$$T_{pt,0}^{*2} = \frac{T_{PT,0}}{\left(1 - \sum k_{PT,i} / k_{total}\right)} \left[\frac{k_2}{k_1} - 1\right] \quad \textbf{7.94}$$

Step 3

An internal prestressing force F_{diss} is applied to each damper, acting internally within the spring element (the sign of this internal force acts to put the damper spring into tension). This internal prestressing force must not affect the surrounding nodal forces or adjoining elements (Ruaumoko has the option to ensure that the internal prestressing force is internal to the element only). In Eq.(7.95) ΣF_{diss} is the total internal prestressing force across all damper layers and should be divided equally into each damper layer within the section.

$$\sum F_{diss} = \frac{\sum k_{diss}}{k_2}\left[T^{*2}_{pt,0} + T_{PT,0}\right] \qquad \textbf{7.95}$$

When viscous dampers (with no hysteretic dampers) are implemented within the macro-model this three-step procedure is not necessary, rather the initial post-tensioning force can be computed from Eq.(7.88) above and applied to the top of the cantilever (or via internal prestressing of the tendon springs) as per a post-tensioned only model.

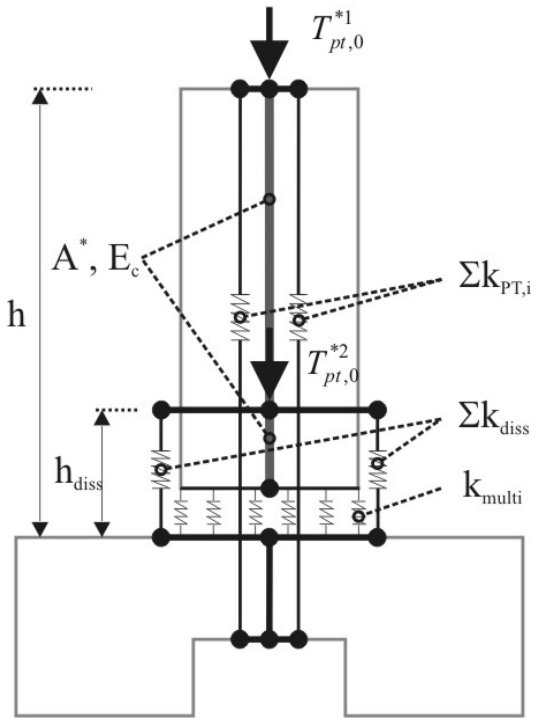

Figure 7.58 Stiffness properties of the macro-model and the implementation of a set of applied loads (or internal prestressing) to prevent induced damper forces immediately following post-tensioning.

(d) Multi-Spring Model versus a Simple Two Spring Model

In Chapter 3 an early version of a multi-spring model that was proposed by Conley et al. [1999] was discussed. This model incorporated only two axial compression-only springs within the connection. A single spring was located at each end of the rocking interface positioned at the centroid of the resultant compression force. It was mentioned that this over-simplified method could lead to a non-conservative overestimation of the moment capacity of the connection. This model assumes that the uplift at the base of the wall is generated by pivoting about the centroid of the resultant compression force, which is also assumed to be fixed in a given position. However, in reality the "pivot" point is located at the neutral axis within the section and is varying during rocking. Given that the uplift of the wall dictates the elongation of the tendon and damper elements, if only a few axial springs are located along the

rocking interface (two in this case) the tendon elongation and internal moment can be significantly overestimated. It can be shown that the error between a two spring model and multi-spring model with an infinite number of springs can be related by Eq.(7.96).

$$error = 100 \cdot \left(\left[\frac{0.5 - \beta\chi}{0.5 - \chi} \right] - 1 \right)\% \qquad \textbf{7.96}$$

Where,

β = equivalent stress block depth parameter

χ = dimensionless neutral axis depth, $\chi = c/L_w$

As an example, if $\beta = 0.85$ a 4% error occurs if $\chi = 0.1$ while a 15% occurs if $\chi = 0.25$. That is, if the strains within the compression region is high, or the depth of the compression region is large, then greater accuracy will be achieved by increasing the number of axial springs along the rocking interface.

7.3.4. An Analytical Macro-Model for LVL Wall 4 with Hysteretic Dampers

In this section the multi-spring macro model is first compared to the experimental response of LVL Wall 4. At a global level (Figure 7.59) and at a local level (Figure 7.60) the ability of the model to capture the entire cyclic response is very good.

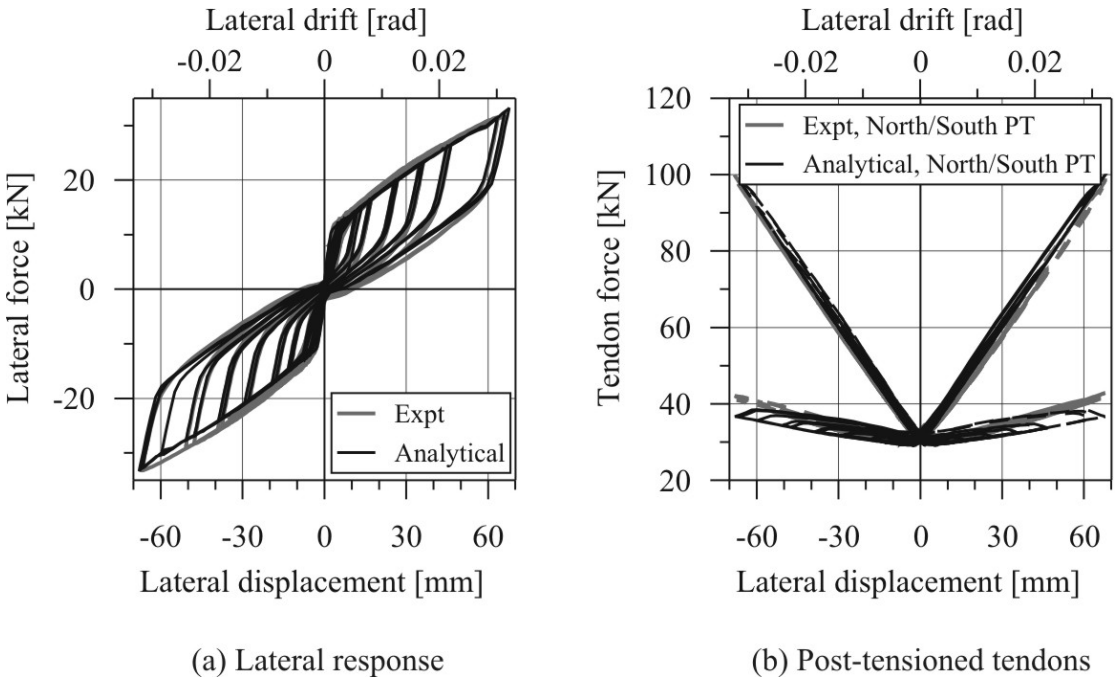

Figure 7.59 Comparison between the experimental cyclic response and the analytical macro model of the LVL post-tensioned wall, LVL Wall 4

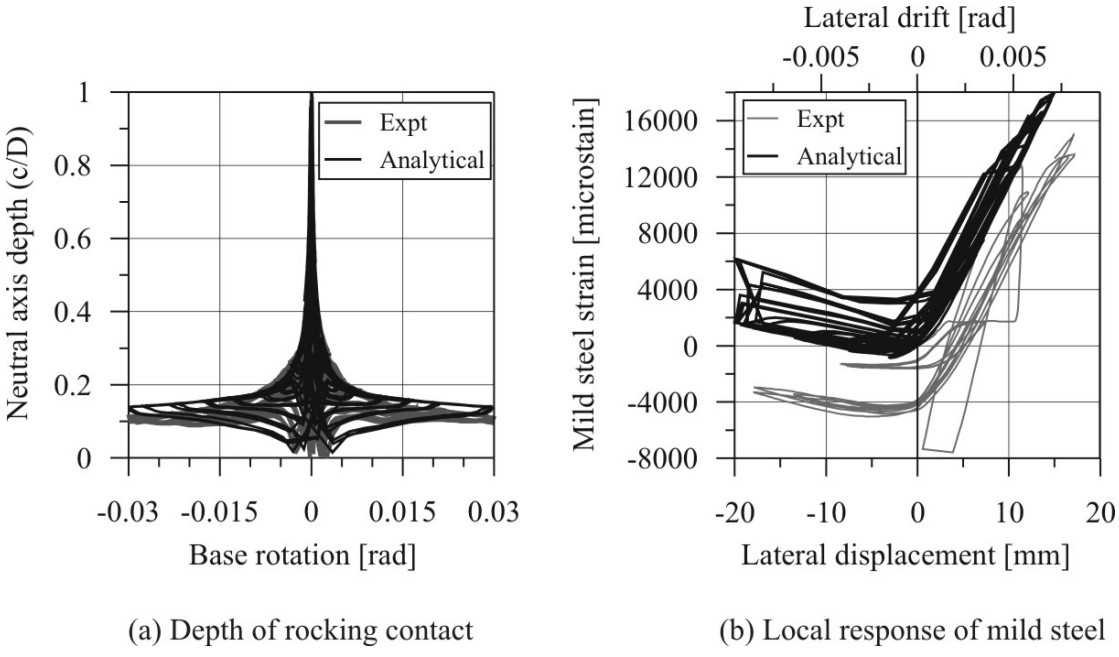

Figure 7.60 Local comparison between the experimental cyclic response and the analytical macro model of the LVL post-tensioned wall, LVL Wall 4

7.3.5. An Analytical Macro-Model for LVL Wall 2 with Non-Linear Viscous Dampers

A non-linear viscous damper element is available within the element library of Ruaumoko (Carr [2005]). Component testing of the viscous dampers in Chapter 5 revealed slackness within the connections at each end of the viscous dampers due to the mechanical tolerances within the spherical connections. This slackness totalled to approximately Δ_{slack} = 1.5mm. To account for this in the macro-model a linear elastic gap element was implemented in series with the non-linear viscous damper spring as illustrated in Figure 7.61. The elastic stiffness of the gap spring was sufficiently high to confine any elongation greater ±0.75mm to the viscous damper, in this case a stiffness of k_{gap} = 7500kN/m was used.

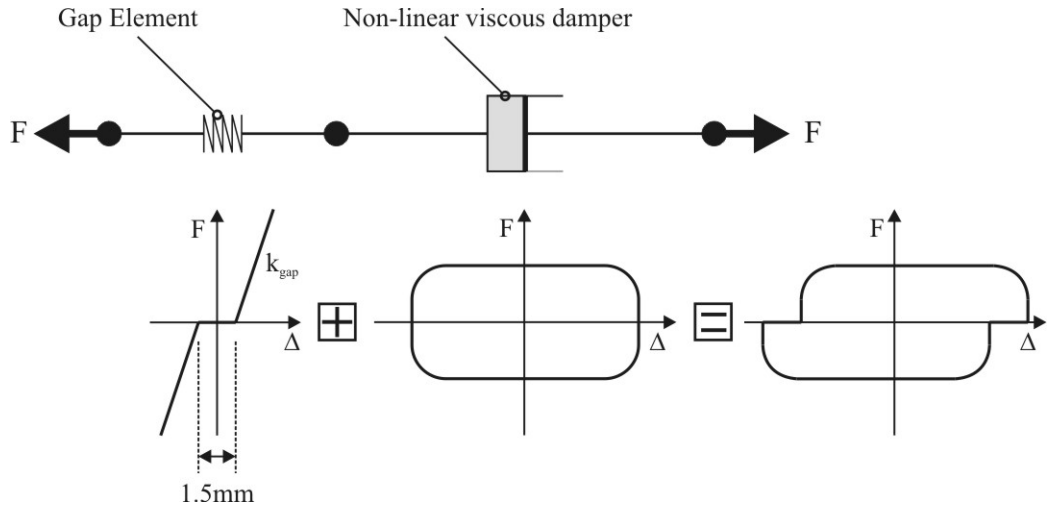

Figure 7.61 Modelling the slackness within the non-linear viscous dampers

By accounting for the slackness within the damper the lateral response of the macro model compares well with the experimental response in Figure 7.62 and Figure 7.63. In fact, the importance of including the gap spring becomes more obvious when comparing the response of the model at higher excitation frequencies in Figure 7.64. During high frequency testing, the maximum wall displacement that could be achieved was reduced, which was limited by the velocity capacity of the shake-table. Figure 7.64 indicates that the slackness of the damper begins to dominate the response of the wall when the displacements of the dampers are small. The local response of the neutral axis position and the velocity of the damper elements are well represented in Figure 7.63. Some instability is observed in Figure 7.63 (b) when the velocity is small. This instability can be an issue for highly non-linear dampers (α<<1), which essentially have a very large axial stiffness.

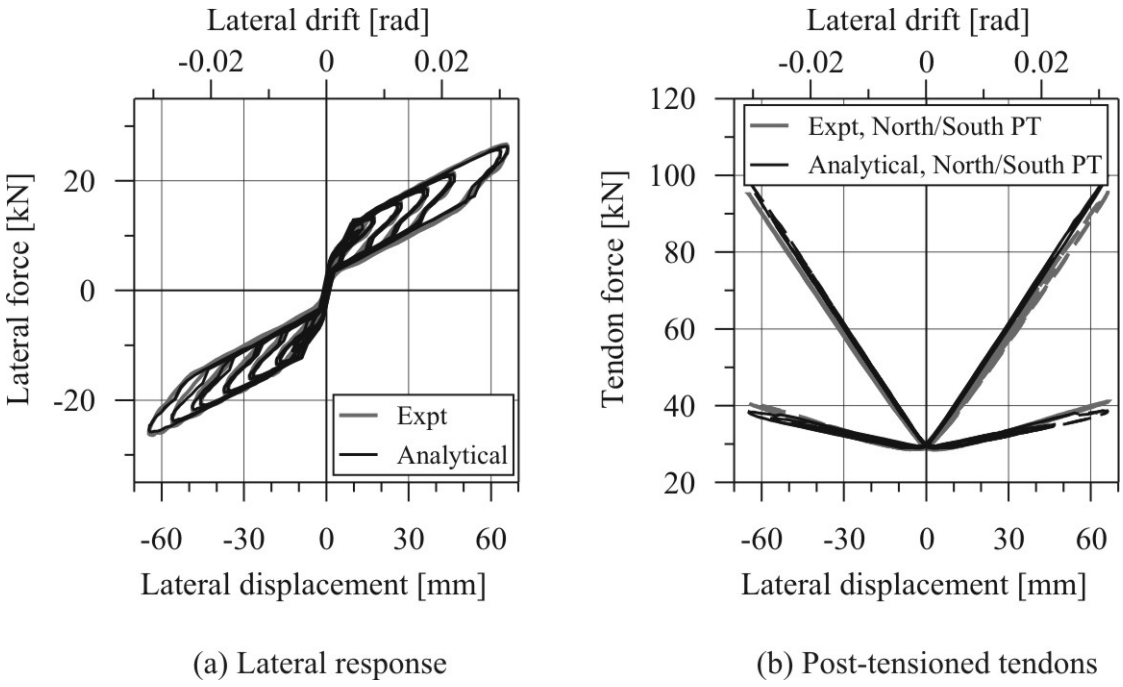

Figure 7.62 Comparison between the experimental cyclic response and the analytical macro model of the LVL post-tensioned wall, LVL Wall 2

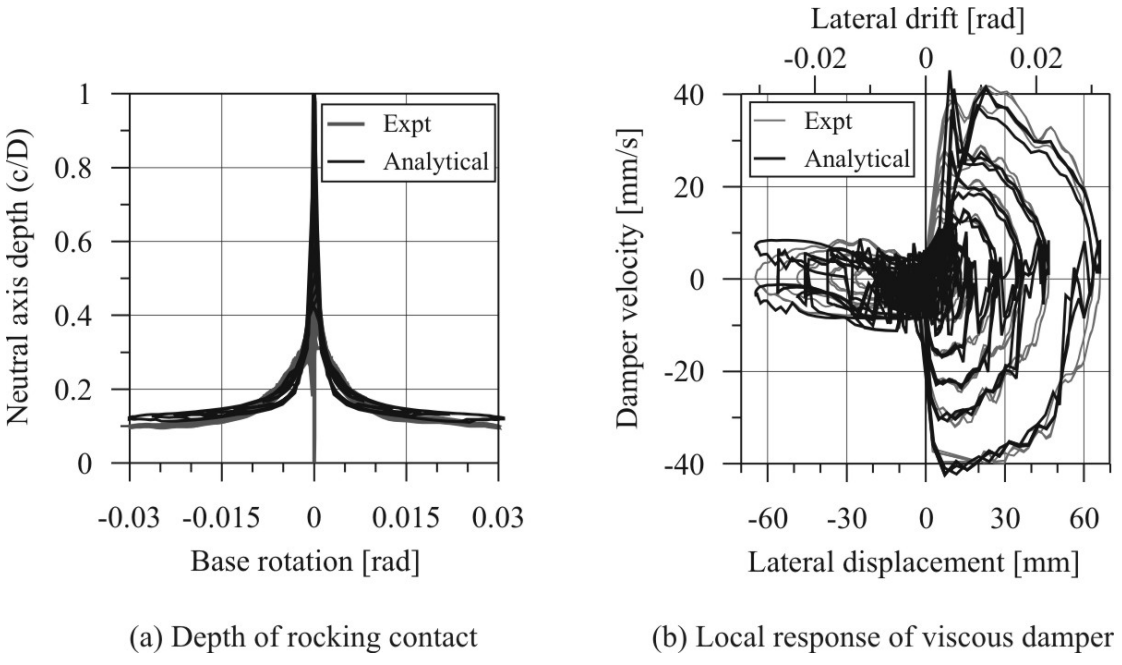

Figure 7.63 Local comparison between the experimental cyclic response and the analytical macro model of the LVL post-tensioned wall, LVL Wall 2

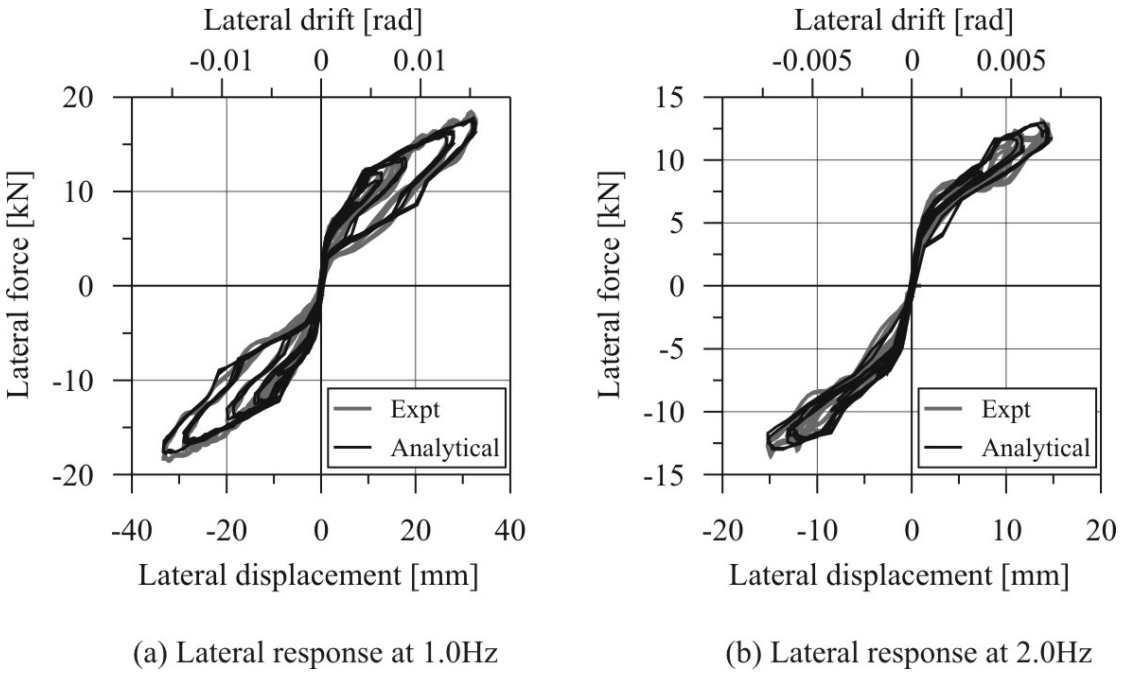

Figure 7.64 Comparison between the experimental cyclic response and the analytical macro model of the LVL post-tensioned wall, LVL Wall 2 for excitation frequencies of 1.0Hz and 2.0Hz

7.3.6. A 3-Dimensional Macro-Model for Post-Tensioned Rocking Systems

In this section the 2-dimensional multi-spring macro model is extended to 3-dimensions using Ruaumoko3D (Carr [2005]). The macro model of the PT bridge pier HBD5 is illustrated in Figure 7.65, which comprises of 10 sets of multi-spring elements at the rocking interface. Each multi-spring has 10 individual springs resulting in a total of 100 axial springs. Calibration of a 3D model requires two section analyses to be carried out: one about the principle axis and the other 45 degrees to the principle axis. Calibration of the axial stiffness is undertaken for both section analyses and is likely to result in two different values for the multi-spring stiffness k_m. Three methods of calibration are suggested below.

1) Adopt an average value of k_m for the calibration along the principal axis and that 45 degrees to the principal axis

2) Adjust the axial stiffness of all individual springs located around the perimeter of the section such that the principle and 45 degree response compare well with the two section analyses

3) Adjust the axial stiffness of the individual springs located in the corner toe of the pier section. This option achieves good accuracy whilst minimising the work involved in calibration. The response along the principle axis is little affected by altering the stiffness of a few of the corner springs.

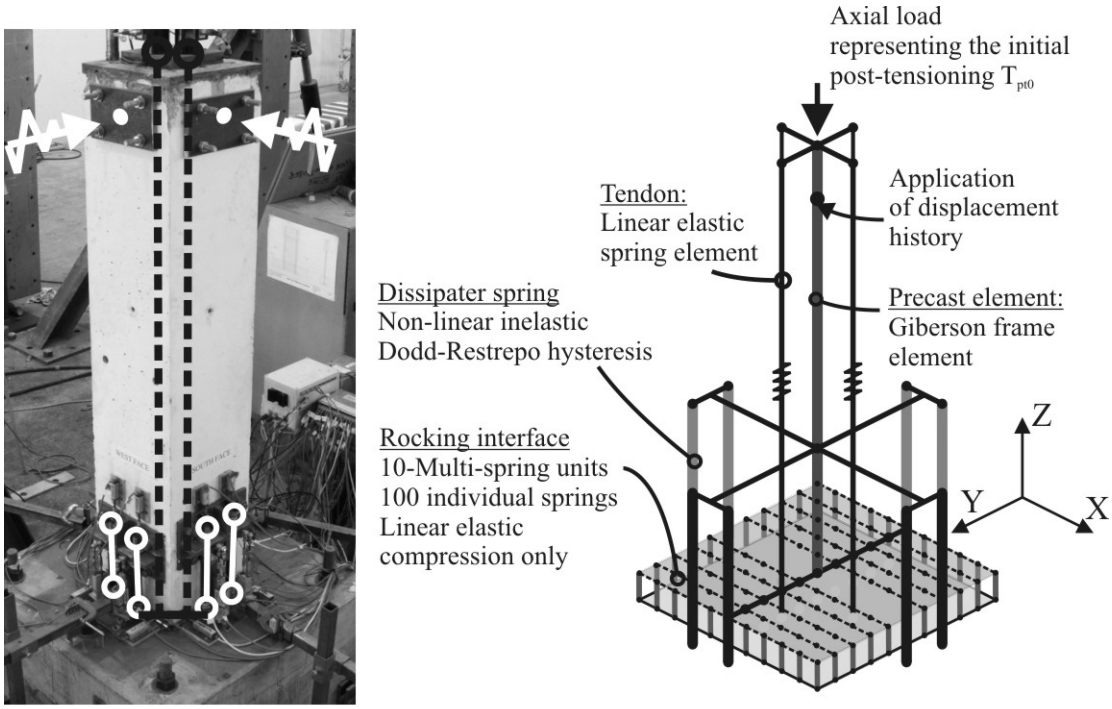

(a) As-built structure (dampers and tendons highlighted)

(b) 3-Dimensional post-tensioned rocking pier, macro model (multi-spring)

Figure 7.65 3-Dimensional macro model utilising a multi-spring rocking interface for the post-tensioned pier HBD5

The comparison of the 3-dimensional macro-model with the biaxial experimental response of HBD5 is graphed in Figure 7.66 and Figure 7.67. The global response compares well within Figure 7.66 in that the initial stiffness, lateral strength and tendon force are well captured. In fact, for this 3-Dimensional model calibration of the multi-spring stiffness about the two orientations (the principle axis and 45 degrees to the principle axis) resulted in the same axial stiffness for both analyses. A value of $\boldsymbol{k_m} = 3.5\text{x}10^6$ kN/m, being equal to the total axial stiffness of the multi-spring unit, was used. The lantern shape describing the neutral axis behaviour in Figure 7.67 appears to be accurately modelling the flexibility of the rocking interface, suggesting that the calibrated multi-spring properties were of the correct magnitude.

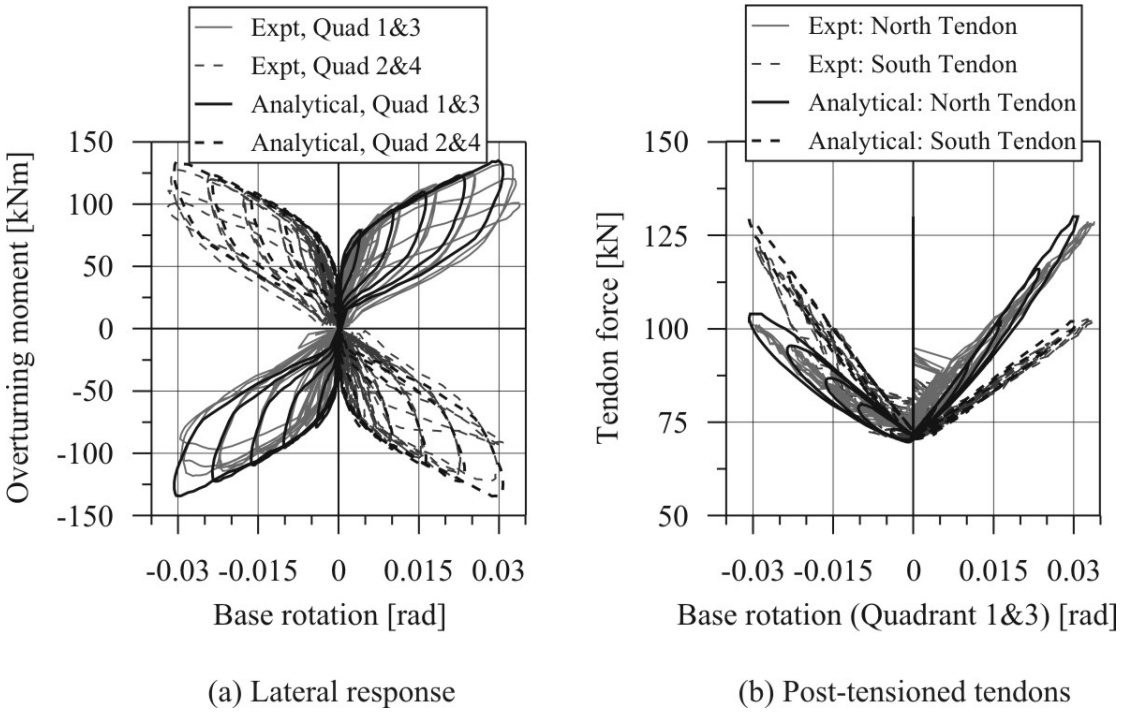

Figure 7.66 Biaxial comparison between the experimental cyclic response and the analytical macro model of the post-tensioned pier, HBD5

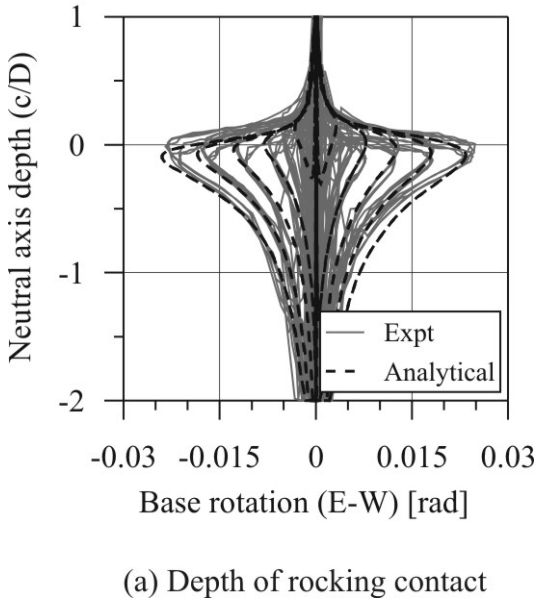

Figure 7.67 Biaxial comparison at a local level between the experimental cyclic response and the analytical macro model of the post-tensioned pier, HBD5

7.4. MODELLING THE DYNAMIC RESPONSE OF POST-TENSIONED ROCKING SYSTEMS

7.4.1. Modelling the Contact Damping in Post-Tensioned Rocking Systems

(a) Existing Contact Damping Models in Literature

During impact of a colliding body some portion of energy is lost: this energy loss is referred to as contact damping. The energy loss was first included within an equation of motion by Housner [1963]. Housner expresses the energy lost during impact by a reduction in kinetic energy. Eq.(7.97) defines the coefficient-of-restitution as the ratio of angular velocity immediately before $\dot{\theta}_1$ and immediately after $\dot{\theta}_2$ impact.

$$e = \frac{\dot{\theta}_2}{\dot{\theta}_1} \qquad \textbf{7.97}$$

Jankowski [2005] describes the problem of impact as being a complex phenomenon involving inelastic deformations, cracking, crushing and friction energy. A majority of the literature pertaining to contact damping models focus on the impact during structural pounding of buildings in series or along bridge decks. The most commonly adopted model is the classical linear visco-elastic model comprising of a linear-elastic spring (representing the stiffness of the two elements in contact) located in parallel with a linear viscous damper (representing the energy lost during contact): these elements are only activated when the two systems come into contact. A common method of quantifying the energy dissipated during impact is to relate the damping coefficient of the linear dashpot to the coefficient-of-restitution $\boldsymbol{e}$: Anagnostopoulos [1988]; Maison and Kasai [1992]; Jankowski et al. [1998]; Jankowski [2006]. A second commonly adopted model is a non-linear elastic spring model, Chau and Wei [2001]. In Eq.(7.98) the force within a non-linear elastic spring $\boldsymbol{F}$ is given by a coefficient $\boldsymbol{\beta}$ multiplied by the contact displacement $\boldsymbol{X}$ raised to the power $\boldsymbol{\chi}$. The Hertz spring is a special case of the non-linear elastic spring with $\boldsymbol{\chi}$ = 1.5 originally developed to model the contact of a sphere on an adjacent body, Davis [1992].

$$F = \overline{\beta}(X)^{\chi} \qquad \textbf{7.98}$$

Because the non-linear spring of Eq.(7.98) is elastic, energy dissipation must be accounted for by other means, either by including a coefficient-of-restitution or a calibrated linear/non-linear viscous damper in parallel to the non-linear spring, Jankowski [2005]. What ever modelling option is selected most research conclude that the displacement response has little effect on the amount of damping associated with impact and a slightly conservative response can be expected if energy dissipation is neglected altogether. Some research indicate that the accelerations, and to a lesser extent velocities, can be sensitive to the model parameters (Anagnostopoulos [1988]); however, the actual energy lost during impact is only a small percentage of the total energy dissipated by the entire structure, Maison and Kasai [1992].

(b) Proposed Contact Damping Model for Post-Tensioned Rocking Systems

In this section a physical contact damping model for PT rocking systems is incorporated within the macro-model presented in Section 7.3 above. The existing contact damping models discussed above, consisting of a spring and dashpot in parallel, form the basis of the contact damping model adopted within the macro-model herein. With reference to the classical linear visco-elastic model, the spring element representing the impact region already exists within the macro-model as a multi-spring element (the multi-spring models the rocking response at the interface). The axial stiffness of the multi-spring element is determined (calibrated) from a detailed section analysis (see Section 7.3.2). The only missing piece of the model is an allowance for energy dissipation during (rocking) impact. As various researchers have concluded that the response can be quite insensitive to the amount of energy dissipation included within the model, the proposed model should be as simple as possible: anything more complicated is simply not justified. It is for this reason that the contact energy is accounted for by means of an additional damper element at the effective height of the system.

In Chapter 6 the contact damping was quantified from free-vibration testing, where an equivalent viscous damping (EVD) ratio of 2.4% was found. This EVD ratio was found to be proportional to the secant stiffness of the system at the maximum displacement. The secant stiffness $\boldsymbol{K_e}$ is defined as the lateral load at the maximum displacement $\boldsymbol{F_m}$ divided by the maximum system displacement $\boldsymbol{\Delta_m}$. The maximum displacement is defined as the peak displacement response from earthquake excitation, or in the case of free-vibration, the release displacement of the system.

Chapter 6 mentioned that the energy lost during contact should be proportional to the vertical acceleration during rocking impact. Chapter 6 also showed that the maximum vertical acceleration during impact was directly proportional to the maximum system velocity, regardless of the amount of mechanical damping within the system. It was concluded in Chapter 6 that as the peak velocity is proportional to the peak displacement, the forces within the damping model should be proportional to both velocity and displacement. However, the actual proportion of contact energy dissipation attributed to both velocity and displacement was not quantified. From analytical comparisons with experimental free-vibration decay it was found that a 50/50 split captured the response decay well. That is, a damping model utilising a velocity proportional damper element and a displacement proportional damper element, each dissipating an equal portion of the total energy lost due to contact damping. The velocity component was be modelled as a linear viscous dashpot, while the displacement component was modelled as a friction, or elasto-plastic spring. These two damping components (viscous and friction) are conceptually disaggregated in Figure 7.68. The linear viscous damper has a damping coefficient $\boldsymbol{C_e}$ equated from Eq.(7.99). This equation includes the calibrated damping ratio of $\boldsymbol{\xi} = 2.4\%$ and the 50% proportion of total EVD attributed to the viscous element. The secant stiffness $\boldsymbol{K_e}$ is computed from the maximum system displacement $\boldsymbol{\Delta_m}$. In the case of design, $\boldsymbol{\Delta_m}$ is equal to the target design displacement $\boldsymbol{\Delta_d}$. For an assessment (or time-history analysis) of an existing system, iteration may be required as the maximum displacement $\boldsymbol{\Delta_m}$ will not be known prior to carrying out the analysis.

$$C_e = 0.5\left(2 \cdot \xi \cdot \omega \cdot m_e\right) = 0.024\omega \cdot m_e = 0.024\sqrt{K_e m_e} \qquad \textbf{7.99}$$

A constant damping model was used to represent the level of contact damping within the system. That is, the damping coefficient and the friction force do not change during the analysis. Details of the macro-model incorporating the proposed damping elemens is illustrated in Figure 7.69, showing the contact damper elements located at the effective height of the system.

The friction damper yield force $\boldsymbol{F_D}$ is calculated by relating the hysteretic area of the damper to equivalent viscous damping (EVD). The area-based EVD formulation is presented in Eq.(7.100), which includes the proposed 50% proportion of total EVD.

$$0.5\xi = \frac{1}{4\pi}\frac{E_D}{E_{so}} = \frac{1}{4\pi}\frac{4F_D\Delta_m}{0.5F_m\Delta_m} \qquad \textbf{7.100}$$

By rearranging Eq.(7.100) and substituting in an EVD of $\boldsymbol{\xi}$ = 2.4% the friction damper yield force $\boldsymbol{F_D}$ is computed as follows

$$F_D = \frac{K_e\Delta_m\pi}{4}\xi = 0.006 \cdot K_e\Delta_m\pi \qquad \textbf{7.101}$$

Also included within the macro-model of Figure 7.69 is an allowance for rotational flexibility of the foundation. The average spring stiffness was calibrated directly from the experimental data: this was calculated during the loading phase of the free-vibration tests. The rotational stiffness of the foundation was equal to 48.82MNm/rad.

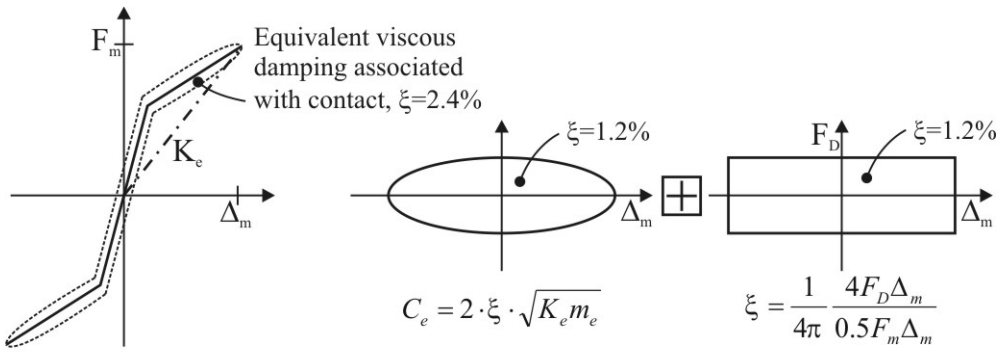

(a) Lateral response of a PT system (b) Components of EVD associated with contact

Figure 7.68 The proposed components of equivalent viscous damping (EVD) for the macro model

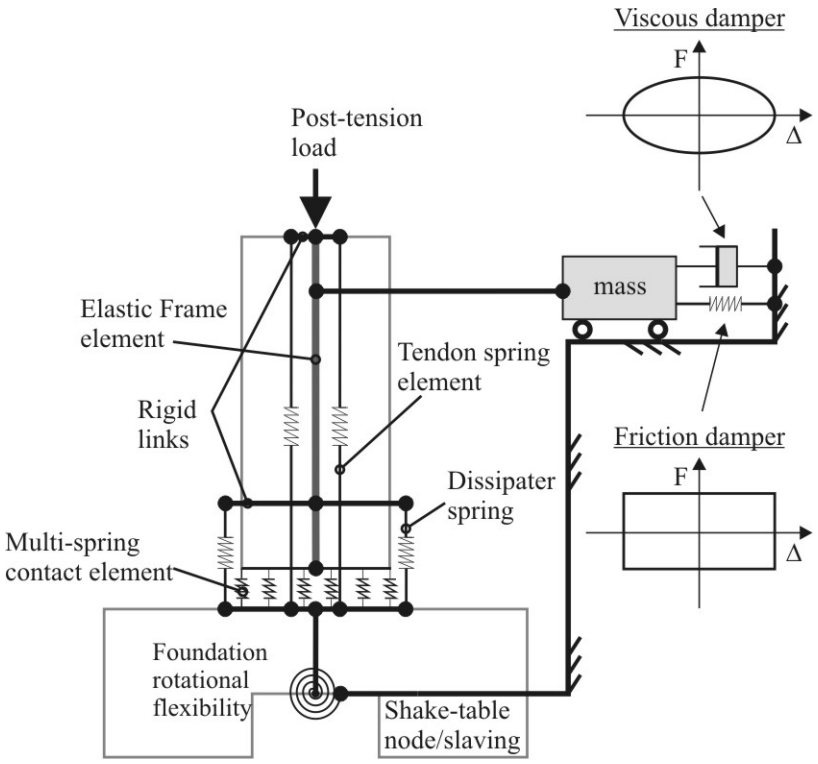

Figure 7.69 Macro model incorporating system dynamic properties

The global response of the macro-model is compared to a number of experimental shake-table tests in Appendix D. Each macro-model analysis incorporates the calibrated level of EVD of 2.4%, equal to a constant value and proportional to the secant stiffness of the system at the maximum displacement response. The macro-model is compared to the experimental free-vibration testing of the PT concrete walls when released from a lateral drift ratio of 1.5% in Figure (D.1) to Figure (D.5). The comparison at 2.5% of drift is not included as similar conclusions were drawn. The analytical-experimental free-vibration comparison shows the displacement time-history in addition to the various energy components of the system (input and kinetic). For each PT wall test the macro model is also compared to the experimental response under each MCE earthquake ground motion in Figure (D.6) to Figure (D.25). A comparison at the DBE intensity is not presented as sufficient evidence is given by the MCE comparison. The analytical-experimental comparison of each of the MCE time-history responses in Figure (D.6) to Figure (D.25) is presented for the calibrated level of contact damping of $\xi = 2.4\%$, but also includes a ±25% variation of contact damping to illustrate the sensitivity of the analysis to additional damping.

It is worth mentioning that when the macro-model is analysed under free-vibration decay, the shake-table nodes are not fixed. Recalling from the experimental results presented in Chapter 6, table-interaction significantly modified the response of the wall. It is for this reason that the table displacement time-history recording during the experimental tests were used as a displacement input to the table nodes within the analytical model.

Under free vibration, the analytical models with low levels of mechanical damping show some variation from the experimental response, which can be expected for

systems with low levels damping. In fact, the response of these systems (in particular, the PT-only system) is very sensitive to the level of damping adopted. The sensitivity to damping is illustrated in the time-history response of Figure (D.6), where a variation in contact damping of ±25% results in an entirely different displacement response. Two conclusions are made with regards to the response of the PT-only wall (PT Wall 1) under both MCE earthquake ground motions,

- The peak ground displacement and displacement decay is captured when considering a damping window of ±25% of the calibrated value, $\xi = 2.4\%$.
- Neither of the damping ratio bounds has the capability of capturing both the peak displacement response and the actual displacement time-history decay.

With respect to the PT walls with larger levels of mechanical damping (Wall 3, 4 & 5), the contact damping represents only a small portion of the overall system damping. Therefore, the ability of the model to capture the free-vibration and earthquake excitation response is largely dictated the by how well the hysteretic damping is modelled along the rocking interface.

Some instability was present within the models that had only non-linear viscous dampers (PC Wall 2 in Figure (D.10) to Figure (D.13)). These non-linear elements have a very high axial stiffness when the damper velocity is small. Furthermore, additional modelling complexity was included within the non-linear dampers by including a gap element to account for the slipping within the spherical connections at each of the viscous dampers (Section 7.3.5). While all effort was undertaken to minimise the instability, the current results were the best that could be achieved with the current version of Ruaumoko. The instability was related to the small out-of-balance forces associated with high modes of the system. The chaotic response was not observed within the displacement time-history analyses. The response became less chaotic when hysteretic damping was combined with the viscous dampers, as seen in the comparison of PC Wall 3: Figure (D.15) to Figure (D.17).

Table 7.15 summarises the maximum displacement and velocity obtained from the analytical model and compares this to the peak experiment response parameters measured during each PT wall test. The table also summarises the peak response of each analytical model considering a contact damping window of ±25%. With the exception of the PT-only system, the peak displacement and velocity response compares well with the peak experimental response given the calibrated level of contact damping equal to $\xi = 2.4\%$. Furthermore, in most cases the displacement time-history decay was also captured reasonably well. In the event that the peak displacement or displacement time-history did not compare, the experimental response appeared to lie within the ±25% error window. For the heavily damped walls of PC Wall 3 and PC Wall 4, the response was only slightly affected by varying the level of contact damping. In this case, the energy dissipation was dominated by the hysteretic and viscous dampers. On the contrary as the level of mechanical damping reduced, as in PC Wall 2 and PC Wall 5, a slightly larger variation in response was observed considering a contact damping variation of ±25%.

The peak absolute acceleration is compared between the model and the experiment in Table 7.16. There is some significant discrepancy here, which can largely be attributed to the digital filter that was applied during post-processing of the

experimental data: acceleration is particularly sensitive to the Butterworth cut-off frequency. However, with this said the comparison is not too conflicting.

In summary, two main conclusions are made, based on whether contact damping should be included within a model:

- For all practical levels of mechanical damping, the option to ignore contact damping will have little effect on the maximum response of the system: from a performance-based design philosophy this is justified and, in fact, slightly conservative
- For PT systems with zero (or very low levels of) mechanical damping, the peak response is largely affected by small levels of damping. In this case, it is worth accounting for contact damping, as well as a possible variation (error window). This will determine how sensitive the response is under different levels of contact damping, as the actual amount of contact damping is difficult to accurately quantify from experimental testing.

Table 7.15 Analytical-experimental comparison of the maximum displacement and velocity of each post-tensioned wall (PC Wall 1 to PC Wall 5) under the NF & FF MCE ground motions. The maximum response of the analytical model considers a damping window of ±25% (0.75ξ and 1.25ξ).

		Peak displacement Δ_{max} [mm]				Peak velocity v_{max} [mm/s]			
		Expt	Model			Expt	Model		
			0.75ξ	ξ	1.25ξ		0.75ξ	ξ	1.25ξ
Wall 1	NF	**20.4**	*19.8*	***20.1***	*19.4*	**378**	*364*	***376***	*350*
	FF	**27.6**	*26.8*	***13.9***	*7.4*	**423**	*434*	***298***	*188*
Wall 2	NF	**16.6**	*13.8*	***14.3***	*14.1*	**283**	*272*	***262***	*248*
	FF	**35.0**	*38.7*	***36.6***	*33.5*	**417**	*436*	***412***	*370*
Wall 3	NF	**12.5**	*12.8*	***12.1***	*11.7*	**252**	*230*	***218***	*206*
	FF	**27.6**	*30.4*	***28.8***	*27.2*	**318**	*320*	***300***	*284*
Wall 4	NF	**13.1**	*12.9*	***12.3***	*11.8*	**230**	*208*	***206***	*202*
	FF	**19.7**	*21.4*	***19.4***	*17.5*	**250**	*222*	***212***	*204*
Wall 5	NF	**16.0**	*16.2*	***15.4***	*14.8*	**295**	*268*	***262***	*256*
	FF	**28.7**	*35.6*	***31.2***	*26.6*	**371**	*430*	***360***	*290*

Table 7.16 Analytical-experimental comparison of the maximum absolute acceleration of each post-tensioned wall (PC Wall 1 to PC Wall 5) under the NF & FF MCE ground motions. The maximum response of the analytical model considers a damping window of ±25% (0.75ξ and 1.25ξ).

		Peak acceleration a_{max} [g]			
		Expt	Model		
			0.75ξ	ξ	1.25ξ
Wall 1	NF	**0.473**	*0.412*	***0.410***	*0.408*
	FF	**0.518**	*0.455*	***0.365***	*0.316*
Wall 2	NF	**0.372**	*0.332*	***0.332***	*0.328*
	FF	**0.591**	*0.483*	***0.471***	*0.452*
Wall 3	NF	**0.389**	*0.335*	***0.325***	*0.321*
	FF	**0.575**	*0.471*	***0.460***	*0.450*
Wall 4	NF	**0.446**	*0.375*	***0.370***	*0.363*
	FF	**0.537**	*0.462*	***0.445***	*0.422*
Wall 5	NF	**0.499**	*0.405*	***0.398***	*0.394*
	FF	**0.617**	*0.551*	***0.523***	*0.490*

7.5. CONCLUSIONS

This chapter has presented an exhaustive description relating to the monotonic, cyclic and dynamic modelling of systems with post-tensioned rocking connections. Furthermore, attention has also been given to modelling the biaxial response of post-tensioned rocking connections.

A number of refinements to an existing global-member-compatibility condition for post-tensioned rocking systems were proposed. In particular, the most recent revision by Palermo [2004] considers three compatibility regions: it was shown that this analogy reduces to only two regions for post-tensioned systems with external devices (or no devices at all, PT-only). It was also shown that this two-region member-compatibility-analogy could be applied to any post-tensioned connection with any stress-strain constitutive relationship.

Simple methods were developed to account for the cyclic loading of steel within a monotonic section analysis. Furthermore, three options to account for the confinement effects of a post-tensioned section with protective elements located around the perimeter of the section were proposed. While the additional confinement provided to the section was not explicitly computed, an allowance was made. In cases where the response was sensitive to confinement, it was suggested that the upper and lower bound response should be considered.

Further refinements include a modification to existing strain-displacement relationships for hybrid systems with "fused" internally grouted reinforcement. It was shown that the mild-steel elongation associated with strain penetration is significantly reduced in such hybrid connections. What's more, stress-block factors were developed for confined concrete and LVL, derived by direct numerical integration of the Mander et al. [1988] stress-strain relationship for confined concrete and the proposed non-linear polynomial for LVL.

A method to assess the monotonic response of post-tensioned systems with fluid viscous dampers was developed, using an effective period of excitation and a target displacement to define the forces within the non-linear viscous dampers. The monotonic modelling concluded with an extension to biaxial bending of post-tensioned connections. An accurate section analysis was presented to compute the biaxial response of a PT connection and was shown to compare very well to experimental testing. A number of biaxial-moment interaction design charts were developed to define the biaxial moment capacity of a post-tensioned section at the *equivalent yield* and at the *Damage Control* limit state.

An existing macro-model utilising multi(axial)-spring elements to replicate the rocking characteristics of a post-tensioned connection was developed further. In particular, a method was outlined to calibrate the stiffness of the multi(axial)-spring from a section analysis. Some minor refinements were discussed with regards to the application of the initial post-tensioned force to avoid pre-loading the external devices. A method to calibrate a 3-Dimensional multi(axial)-spring macro-model from a biaxial section analysis was also discussed and found to compare very well to experimental testing.

Finally, a damping model was presented to account for energy lost due to the rocking impact of post-tensioned connection under dynamic loading (contact damping). The key properties of the model are listed

- The damping forces within the contact damping model are proportional to velocity and displacement, where the total energy dissipated by both components is equal.
- The velocity dependency is modelled as a linear viscous damper, while the displacement dependency is modelled as a friction, or elasto-plastic spring
- The magnitude of the damping coefficient and the friction force is proportional to the secant stiffness, which is defined by the maximum displacement response of the system. An equivalent viscous damping ratio of $\xi = 2.4\%$ is implemented. This was calibrated from experimental testing in Chapter 6.
- The viscous damping coefficient and friction force are constant throughout the analysis.

The response of the lightly damped post-tensioned walls was found to be sensitive to the level of contact damping used. However, by including a ±25% contact-damping window the model was able to capture both the peak displacement and the displacement time-history decay reasonably well. The analytical model compared well with the more heavily damped walls as the performance of the model was governed by how well the mechanical dampers were modelled. While peak response parameters compared reasonably well, peak horizontal accelerations did not compare as well as acceleration data was sensitive to the choice of the digital filter used during post-processing.

Finally, it was concluded that for all practical levels of mechanical damping, the option to ignore contact damping will have little effect on the maximum response of the system. For PT systems with zero (or very low levels of) mechanical damping, the peak response is largely affected by small levels of damping. In this case, it is worth accounting for contact damping and to also include some variation of contact damping within the analysis. This will determine how sensitive the response is under different levels of contact damping as it has been shown that the actual contact damping is difficult to accurately quantify from experimental testing.

7.6. REFERENCES

Allington, C. (2003). "Seismic performance of moment resisting frame members produced from lightweight aggregate concrete," University of Canterbury, Christchurch.

Anagnostopoulos, S. A. (1988). "Pounding of buildings in series during earthquakes." *Earthquake Engineering & Structural Dynamics*, 16(3), 443-456.

Bauschinger, J. (1887). "Variations in the elastic limit of iron and steel [summarized translation from "Mittheilungen aus dem Mechanischen Technischen Laboratorium der k. Hochschule in Munchen"]." *Journal of Iron and Steel*, 1, 442-444.

Bresler, B. (1960). "Design criteria for reinforced concrete columns under axial load and biaxial bending." *ACI Journal*, 57(11), 481-490.

Carr, A. (2005). "RUAUMOKO." Christchurch, Inelastic Dynamic Analysis.

Chau, K. T. and Wei, X. X. (2001). "Pounding of structures modelled as non-linear impacts of two oscillators." *Earthquake Engineering & Structural Dynamics*, 30(5), 633-651.

Conley, J., Sritharan, S. and Priestley, M. J. N. (1999). "Precast Seismic Structural Systems PRESSS-3: The Five Story Precast Test Building Vol. 3-1: Wall Direction Response." Report No. SSRP-99/19, Department of Structural Engineering, University of California, San Diego.

Davis, R. O. (1992). "Pounding of Buildings Modelled by an Impact Oscillator." *Earthquake Engineering & Structural Dynamics*, 21, 253-274.

Dodd, L. L. and Cooke, N. (1992). "The dynamic behaviour of reinforced concrete bridge piers subjected to New Zealand seismicity." Research report 92-4, University of Canterbury, Christchurch.

Dodd, L. L. and Restrepo-Posada, J. I. (1995). "Model for predicting cyclic behavior of reinforcing steel." *Journal of Structural Engineering*, 121(3), 433-444.

Furlong, R. W. (1960) "Ultimate Strength of Square Columns Under Biaxially Eccentric Loads." *ACI 56th annual convention*, New York.

Housner, G. (1963). "The Behaviour of Inverted Pendulum Structures During Earthquakes." *Bulletin of the Seismoligical Society of America*, 53(2), 403-417.

Jankowski, R. (2005). "Non-linear viscoelastic modelling of earthquake-induced structural pounding." *Earthquake Engineering & Structural Dynamics*, 34(6), 595-611.

Jankowski, R. (2006). "Analytical expression between the impact damping ratio and the coefficient of restitution in the non-linear viscoelastic model of structural pounding." *Earthquake Engineering & Structural Dynamics*, 35(4), 517-524.

Jankowski, R., Wilde, K. and Fujino, Y. (1998). "Pounding of superstructure segments in isolated elevated bridge during earthquakes." *Earthquake Engineering & Structural Dynamics*, 27(5), 487-502.

Kent, D. and Park, R. (1971). "Flexural members with confined concrete." *ASCE Journal of Structural Engineering*, 97.

King, D., Priestley, M. J. N. and Park, R. (1986). "Computer programs for concrete column design," University of Canterbury, Christchurch.

Kowalsky, M. J. and Priestley, M. J. N. (2000). "Improved analytical model for shear strength of circular reinforced concrete columns in seismic regions." *ACI Structural Journal*, 97(3), 388-396.

Maison, B. F. and Kasai, K. (1992). "Dynamics of pounding when two buildings collide." *Earthquake Engineering & Structural Dynamics*, 21(9), 771-786.

Mander, J. B., Priestley, M. J. N. and Park, R. (1984). "Seismic design of bridge piers." Report 84-02, University of Canterbury, Christchurch.

Mander, J. B., Priestley, M. J. N. and Park, R. (1988). "Theoretical Stress-Strain Model for Confined Concrete." *Journal of Structural Engineering*, 114(8), 1804-1826.

Montejo, L. A. and Kowalsky, M. J. (2007). "CUMBIA: Set of codes for the analysis of reinforced concrete members."

Newcombe, M. (2007). "Seismic design of multistorey post-tensioned timber buildings," University of Pavia, Pavia.

Palermo, A. (2004). "The Use of Controlled Rocking in the Seismic Design of Bridges," PhD.Thesis, Technical University of Milan, Milan.

Pampanin, S., Priestley, M. J. N. and Sritharan, S. (2001). "Analytical Modelling of the Seismic Behaviour of Precast Concrete Frames Designed with Ductile Connections." *Journal of Earthquake Engineering*, 5(3), 329-367.

Parme, A., Nieves, J. M. and Gouwens, A. (1966). "Capacity of reinforced rectangular columns subjected to biaxial bending." *ACI Journal*, 62(3), 327-342.

Popovics, S. (1973). "A numerical approach to the complete stress-strain curves for concrete." *Cement and Concrete Reseach*, 3(5), 583-599.

Presland, R. (1999). "The seismic performance of retrofitted RC bridge piers."

Priestley, M. J. N., Calvi, G. M. and Kowalsky, M. J. (2007). *Displacement-Based Seismic Design of Structures*, IUSS, Pavia.

Priestley, M. J. N., Seible, F. and Calvi, G. M. (1996). *Seismic design and retrofit of bridges*, John Wiley & Sons inc, New York.

Richart, F. E., Brandtzaeg, A. and Brown, R. L. (1928). "A study of the failure of concrete under combined concrete compressive stresses." Bulletin No 185, University of Illinios Engineering Experimental Station.

Sakai, J. and Mahin, S. A. (2004). "Mitigation of Residual Displacements of Circular Reinforced Concrete Bridge Columns." *13 WCEE: 13th World Conference on Earthquake Engineering Conference Proceedings*.

Spieth, H. A., Carr, A. J., Murahidy, A. G., Arnolds, D., Davies, M. and Mander, J. B. (2004a) "Modelling of post-tensioned precast reinforced concrete frame structures with rocking beam-column connections." *2004 NZSEE Conference*, Rotarua.

Spieth, H. A., Carr, A. J., Pampanin, S., Murahidy, A. G. and Mander, J. B. (2004b). "Modelling of Precast Prestressed Concrete Frame Structures with Rocking Beam-Column Connections." University of Canterbury Research Report 2004-01, N. t. c. o. r. n. o. p. r. thesis, ed., University of Canterbury, Christchurch.

Sritharan., S. (1998). "Analysis of concrete bridge joints subjected to seismic actions," University of California, San Diego.

Wang, Y. and Restrepo, J. (1996). "Strength enhancement of concentrically loaded reinforced concrete columns using TYFO S fibrewrap jackets." Research report 96/12, University of Canterbury, Christchurch.

Wang, Y. C. and Restrepo, J. I. (2001). "Investigation of concentrically loaded reinforced concrete columns confined with glass fibre-reinforced polymer jackets." *ACI Structural Journal*, 98(3).

8. Direct Displacement-Based Design of Post-Tensioned Rocking Systems, Part I: SDOF Rocking Systems with Viscous Dampers

8.1. INTRODUCTION

This chapter outlines a design procedure for single degree of freedom (SDOF) post-tensioned (PT) rocking systems incorporating external supplementary viscous damper devices. Following from the introduction of DDBD given in Chapter 3, an extension is proposed for the design of post-tensioned rocking systems with viscous dampers. The damped response of SDOF systems with non-linear viscous damping is investigated. A series of damped response spectra are presented to quantify the reduction in displacement and velocity response of a SDOF system with supplementary non-linear viscous damping. After relating the system damping to the maximum displacement and velocity response, the mechanics of post-tensioned rocking systems are investigated in detail to relate the local damping properties (of the devices) at the rocking interface to the global damping properties of the SDOF system (at the effective height of the system). Finally, the (mechanical) local-to-global damping relationship is uses the calibrated SDOF damped response to complete the design procedure. The chapter concludes by verifying the design procedure on six prototype post-tensioned walls. The error between the target displacement and the mean of the maximum displacements agreed well; with the exception of one prototype, each system achieved a displacement that was less than 5% of the target.

8.1.1. Design Issues for Post-Tensioned Rocking Systems with Viscous Dampers

Two fundamental issues arise when considering the displacement-based design (DBD) of a system with viscous dampers. First, as there is no defined yield point of a viscous damper, ductility is not an appropriate design parameter. Figure 8.1 compares the components of a PT-Hysteretic and a PT-Viscous system. The PT-Hysteretic system has a defined yield point corresponding to yield of the hysteretic (EP) element. The PT-Viscous has no defined yield point corresponding to yield of the damper. While there is a transition from an initial elastic stiffness to a bilinear stiffness, this does not define the energy dissipated by the non-linear damper. Figure 8.1 also indicates the high non-linearity of a PT-viscous system in that the viscous force is 90 degrees out-of-phase with the system displacement. In this chapter a DBD procedure is developed for PT-viscous systems in which the design displacement spectra is not reduced according to damping-ductility equations, but reduced according to equivalent viscous damping properties of a SDOF system that have been calibrated to

time-history-analysis (THA). The second issue specific to a PT-viscous system is that the capacity of the system is dependant on the excitation velocity. Traditional displacement-based design procedures consider the response of the SDOF system at the peak displacement. The procedure developed herein adopts an intermediate system displacement with non-zero velocity. The procedure uses the displacement spectrum in addition to a velocity spectrum: the two spectra have independent reduction factors to recognise the out-of-phase response between spectral velocity and spectral displacement. While design procedures for systems with viscous dampers are in literature (Pekcan et al. [1999], Whittaker et al. [2003]) these methods are unable to be incorporated within a displacement-based design framework, which is the key concept behind the design procedure developed as part of this research.

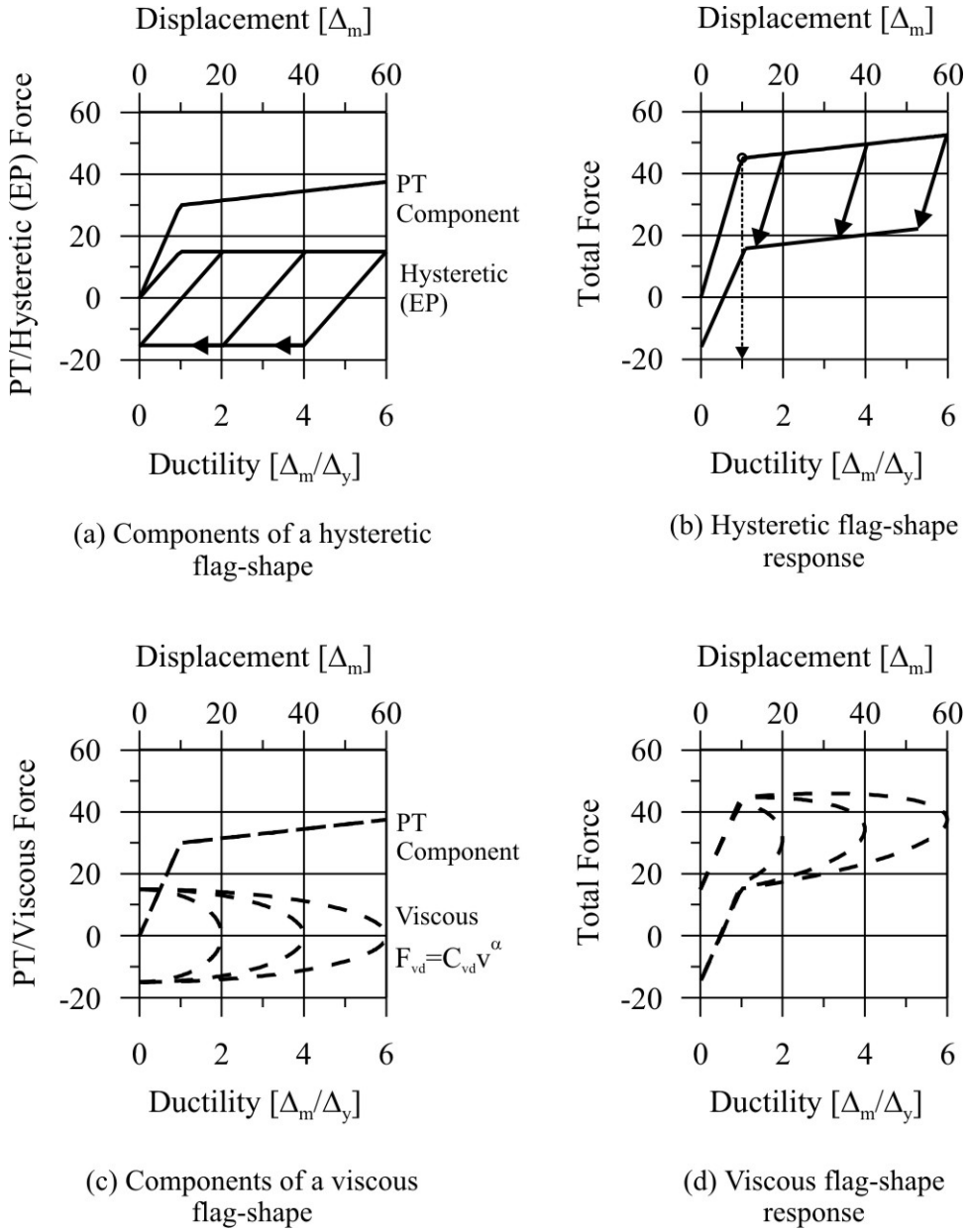

(a) Components of a hysteretic flag-shape

(b) Hysteretic flag-shape response

(c) Components of a viscous flag-shape

(d) Viscous flag-shape response

Figure 8.1 Comparison between a traditional hybrid system (a)-(b) and a hybrid viscous system (c)-(d)

To further illustrate the independency of ductility-damping of a PT-viscous system a series of area-based damping curves are graphed in Figure 8.2. The area-based equivalent viscous damping of a non-linear inelastic system is given by Eq.(8.2).

$$\xi_{eq,area-based} = \frac{1}{2\pi}\frac{E_d}{F_m \Delta_m} \qquad \textbf{8.1}$$

Where

E_d = Energy dissipated in one complete cycle

F_m = Lateral force of the system at the peak displacement Δ_m.

For a PT-hysteretic system with elasto-plastic (EP) damping this equation can be written as

$$\xi_{eq,area-based} = \frac{1}{2\pi}\frac{4F_{y,ms}\left(\Delta_m - \Delta_{y,ms}\right)}{\left[F_{y,PT} + \left(\Delta_m - \Delta_{y,PT}\right)rK\right]\Delta_m} \qquad \textbf{8.2}$$

Where

$F_{y,ms}$ = EP yield force

$\Delta_{y,ms}$ = EP yield displacement

$F_{y,PT}$ = Force at the transition from the initial K to the bilinear stiffness rK of the PT component (apparent PT "yield" force)

$\Delta_{y,PT}$ = Displacement at the transition from the initial K to the bilinear stiffness rK of the PT component (apparent PT "yield" displacement)

Δ_m = Peak system displacement

For a PT-viscous system (linear viscous) this equation can be written as

$$\xi_{eq,area-based} = \frac{1}{2}\frac{F_{vd}(v_{\max})}{\left[F_{y,PT} + \left(\Delta_m - \Delta_{y,PT}\right)rK\right]} \qquad \textbf{8.3}$$

Where

$F_{vd}(v_{max})$ = Maximum viscous damper force (at maximum velocity)

The two systems in Figure 8.1 above are used as examples to plot the area-based damping curves in Figure 8.2 using Eq.(8.1) and (8.2) above. Three peak damper force magnitudes are shown, $F_{vd} = F_{y,ms} = 15$, 20 and 25 units. Figure 8.2 indicates that the PT-hysteretic damping curve is very dependant on the system ductility (in addition to the EP yield force), though the dependency reduces as the ductility increases. On the contrary, the PT-viscous damping relationship has minimal dependency on system ductility. In fact, this dependency is entirely related to the bilinear stiffness of the PT component. In the case where the bilinear stiffness of the PT component is zero (which is typically the case for a bridge system with P-Δ induced loads) the dependency on ductility is zero, Figure 8.2 (b). This example clearly illustrates why ductility can not be used as a design parameter for a PT-viscous system, instead the actual properties of the viscous damper give a better indication of the level of equivalent damping within the system.

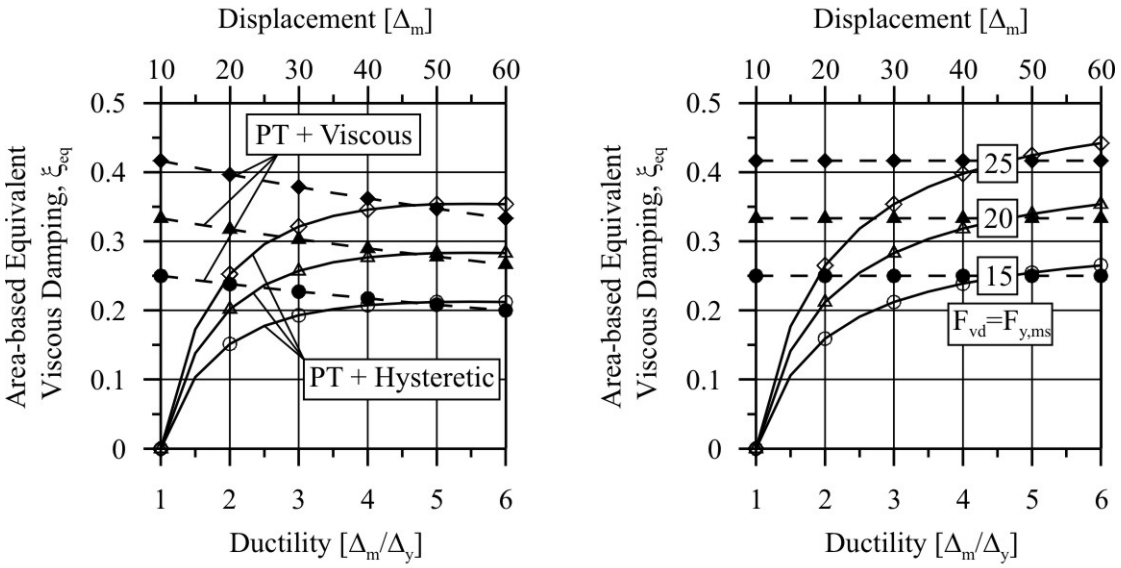

(a) Damping-ductility curves for r = 0.05 (b) Damping-ductility curves for r = 0.0

Figure 8.2 Damping-ductility relationship of a PT-Viscous and PT-Hysteretic (EP) system

8.2. DEVELOPMENT OF A DAMPED DESIGN SPECTRA FOR SYSTEMS WITH NON-LINEAR VISCOUS DAMPING

An extensive series of time history analyses (THA) were undertaken to develop a set of damped response spectra for the design of post-tensioned (PT) rocking systems incorporating supplementary viscous damping. The push-over envelope of a generic post-tensioned system with viscous damping is presented in Figure 8.3 (a), achieving a target design displacement Δ_d. The non-linear elastic PT component is shown as a black dashed line. Besides the input signal, there are five major parameters defining the push-over response of a viscous flag-shape

1. The initial stiffness, K_{PT}
2. The bilinear stiffness rK_{PT}
3. The force defining the transition from the initial to the bilinear stiffness of the PT spring, $F_{y,PT}$
4. The supplementary viscous damper coefficient, C_{VD}
5. The velocity exponent of the supplementary damper, α

In order to reduce the number of variables above from five to three, the system was simplified by representing the non-linear elastic PT spring as an effective elastic spring with *secant* stiffness to the target displacement Δ_d. This is illustrated in Figure 8.3 (b), where K_e is the effective elastic stiffness of the PT spring. The non-linear elastic PT spring has been replaced with an equivalent elastic spring of stiffness K_e: the response of the viscous damper is not affected by the linearisation of the PT spring. The premise of linearising the PT spring defines the SDOF model used to develop the design response spectra. In a later section, consideration is given to modification factors to account for the actual bilinear loading envelope.

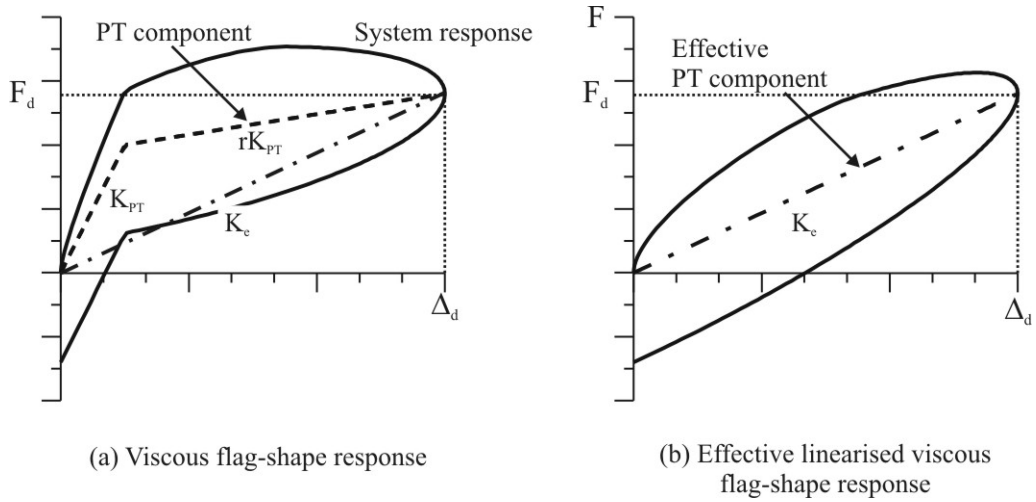

(a) Viscous flag-shape response

(b) Effective linearised viscous flag-shape response

Figure 8.3: Linearisation of a viscous hybrid system

8.2.1. Description of the SDOF System and THA Model Parameters

A SDOF model was created for the development of a set of damped response spectra. An effective linear model with non-linear viscous damper properties was used in to undertake the analysis. This linearization of the model was discussed above and illustrated in Figure 8.3. A schematic of the elastic SDOF model is pictured in Figure 8.4 consisting of an equivalent linear elastic PT spring and two dashpot elements: one representing the supplementary viscous damper (linear or non-linear) and one representing the elastic (intrinsic) system damping. The elastic spring was kept constant and equal to a value of k_e=1000kN/m, while the mass M was varied in order to achieve the desired structural (secant) period. The analysis stepped in period increments of 0.5sec, beginning at T=0.5sec and ending at T=4sec. The elastic damping was equal to 5% of critical damping. Because the SDOF model is an effective elastic system, a 5% initial, tangent or secant stiffness proportional damping model are identical in this case. For each structural period T, the supplementary damper properties were varied as follows,

1. The damping coefficient C_{VD} was normalised with respect to critical damping C_c, defining the parameter $\Omega = C_{VD}/C_c$. This parameter is referred to as the Supplementary Damping Ratio (SDR). Five SDR ratios were considered, Ω: 0.05, 0.10, 0.15, 0.20 and 0.30. For each analysis the damping coefficient C_{VD} is defined by the following expression

$$C_{VD} = \Omega \cdot C_c = \frac{\Omega \cdot 2K_e T}{\pi} \qquad \textbf{8.4}$$

2. Five velocity exponents were also studied, α : 0.15, 0.30, 0.50, 0.75 and 1.00.

This resulted in 200 SDOF structural models and a total of 6000 individual time-history analyses. The model matrix is illustrated in Figure 8.5.

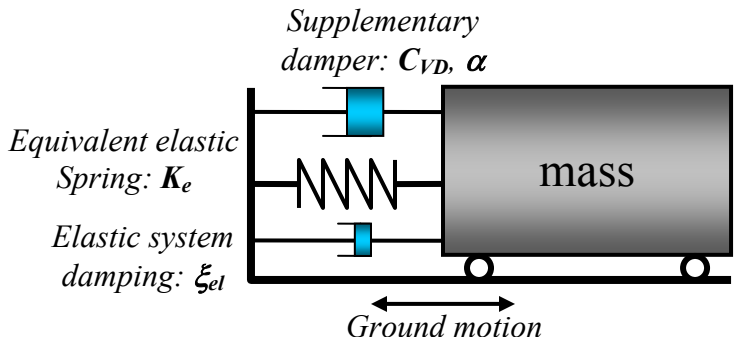

Figure 8.4 Equivalent elastic SDOF model

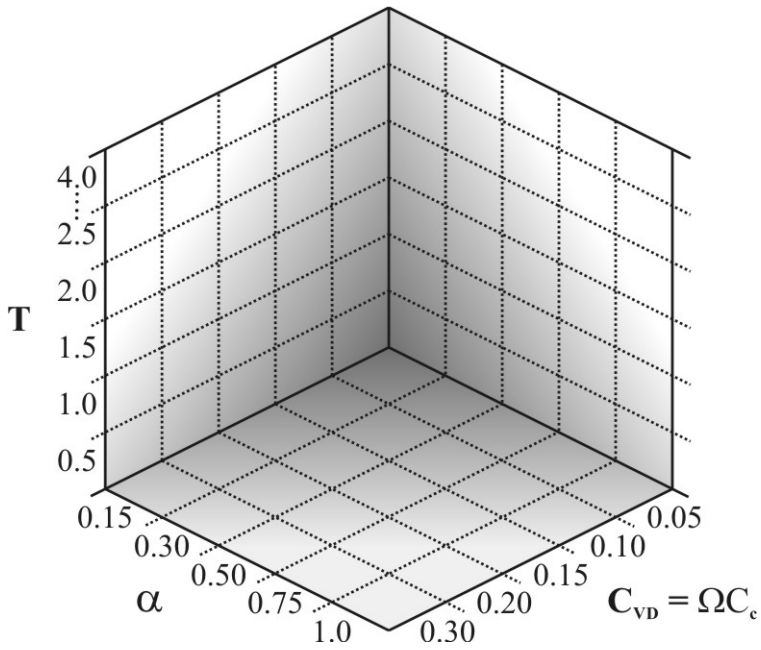

Figure 8.5 SDOF model matrix

8.2.2. Selection and Scaling of the Earthquake Ground Motions

Two strong ground motion data sets were compiled: a far-field suite and a near-field suite. The far-field records comprised of 10 historical records and 5 spectrum compatible artificial records. The 10 historical far-field records were those of previous studies specifically concerning the development of DDBD, Pettinga and Priestley [2005] and Sullivan et al. [2006]. The artificial records were assembled using the Ruaumoko package, SIMQKE (Carr [2005]). The near-field records comprised of 15 historical ground motions recorded within 15km of the rupture source. In many cases it proved difficult to scale near-field ground motions to the design acceleration or displacement spectrum because of the directivity characteristics of near-field acceleration records. It is for this reason that the ground motions were scaled to the New Zealand (pseudo) design velocity spectrum over a period range of 0-4sec,

NZS1170.5 [2004]. The records were scaled to a ground motion hazard having a zone factor $z = 0.28$, soil class C, return period of 500years $R_u = 1.0$ and a structural performance factor $S_p = 1.0$. The far-field ground hazard had a distance of 20km to the fault, while the near-field ground hazard had a distance of 2km to the fault. Following the scaling procedure, the mean of the 5% damped acceleration, velocity and displacement response spectra are compared to the corresponding New Zealand design spectra in Figure 8.7. The method of scaling to the velocity spectrum proved to be an appropriate method as the mean spectral response compares well with the target design spectra. The agreement is less accurate for periods greater than 3sec, where for larger periods the New Zealand design displacement spectrum is truncated, making it difficult to fit records over the entire period range.

Table 8.1 Selected far-field earthquake ground motions

EQ evetnt	Year	Station	Mw	R[1] [km]	Rupture Mech	Orientation	Soil type[2]	PGA [g]	PGV [m/s]	k[3]
El Centro	1940	Imperial Valley	6..95	6.09	Strike-Slip	270	D	0.215	0.298	1.089
Chi Chi	1999	CWB TCU047	7.62	35	Reverse-Oblique	N-S	C	0.413	0.402	1.114
Tabas	1978	70 Boshrooyeh	7.35	28.8	Reverse	L1	D	0.107	0.137	2.339
Cape Men	1992	Fortuna Blvd	7.01	20.0	Reverse	0	D	0.116	0.300	1.597
Loma Prieta	1989	Hollister Diff Array	6.93	24.8	Reverse-Oblique	165	D	0.269	0.439	0.883
Erzican	1992	95 Erzican	6.69	4.4	Strike-Slip	E-W	D	0.496	0.643	0.572
Northridge	1994	LA-Baldwin Hills	6.69	29.9	Reverse	90	D	0.239	0.148	1.656
Kobe	1995	Amagasaki	6.9	11.3	Strike-Slip	90	D	0.363	0.462	0.701
Kobe	1995	Sakai	6.9	28.1	Strike-Slip	90	E	0.122	0.146	1.923
Landers	1992	Yermo Fire Station	7.28	23.6	Strike-Slip	270	D	0.245	0.514	1.030
Artificial	-	-	-	-	-	-	-	0.385	0.524	1.000
Artificial	-	-	-	-	-	-	-	0.385	0.291	1.000
Artificial	-	-	-	-	-	-	-	0.385	0.396	1.000
Artificial	-	-	-	-	-	-	-	0.385	0.427	1.000
Artificial	-	-	-	-	-	-	-	0.385	0.370	1.000

[1] Closest distance from the site to the rupture area
[2] Soil classifications, equivalent NZS 1170.5 classification
[3] Scale factor for 10% probability of exceedance in 50 years i.e. R_u=1.0

Table 8.2 Selected near-field earthquake ground motions

EQ evetnt	Year	Station	Mw	R[1] [km]	Rupture Mech	Orientation	Soil type[2]	PGA [g]	PGV [m/s]	k[4]
Northridge	1994	Sylmar Olive View	6.69	5.3	Reverse	360	D	0.843	1.29	0.404
Northridge	1994	LA Dam	6.69	5.92	Reverse	334	B	0.349	0.51	0.766
Northridge	1994	Jensen filter plant	6.69	5.43	Reverse	22	C	0.571	0.76	0.511
Imp. Valley	1979	El Centro Array #5	6.53	3.95	Strike-Slip	230	D	0.377	0.91	0.603
Imp. Valley	1979	El Centro Array #7	6.53	0.56	Strike-Slip	230	D	0.463	1.09	0.556
Loma Prieta	1989	Saratoga W Valley	6.93	13.7	Reverse-Oblique	270	D	0.332	0.62	0.815
Loma Prieta	1989	Los Gatos Pres	6.93	0.92	Reverse-Oblique	0	B	0.931	1.09	0.327
Chi Chi	1999	TCU068	7.62	0.32	Reverse-Oblique	270	B	0.566	1.77	0.410
Chi Chi	1999	CHY101	7.62	9.96	Reverse-Oblique	0	D	0.440	1.15	0.594
Turkey	1999	Gebze	7.51	10.92	Strike-Slip	0	B	0.244	0.50	1.584
Iran	1978	Tabas	7.35	2.05	Reverse	TR	B	0.852	1.21	0.453
Pacoima Dam	1971	Dam abutment	6.61	1.81	Reverse	164	B	1.230	1.13	0.436
Landers	1992	Lucerne	7.3	1.1	Strike-Slip	260	B	0.727	1.47	0.640
Landers	1992	Joshua Tree	7.3	11.6	Strike-Slip	90	D	0.284	0.43	1.008
Turkey	1999	Duzce	7.1	8.2	Strike-Slip	270	D	0.535	0.84	0.592

[1] Closest distance from the site to the rupture area [km]
[2] Soil classifications , equivalent NZS 1170.5 classification
[3] Scale factor for 10% probability of exceedance in 50 years i.e. R_u=1.0

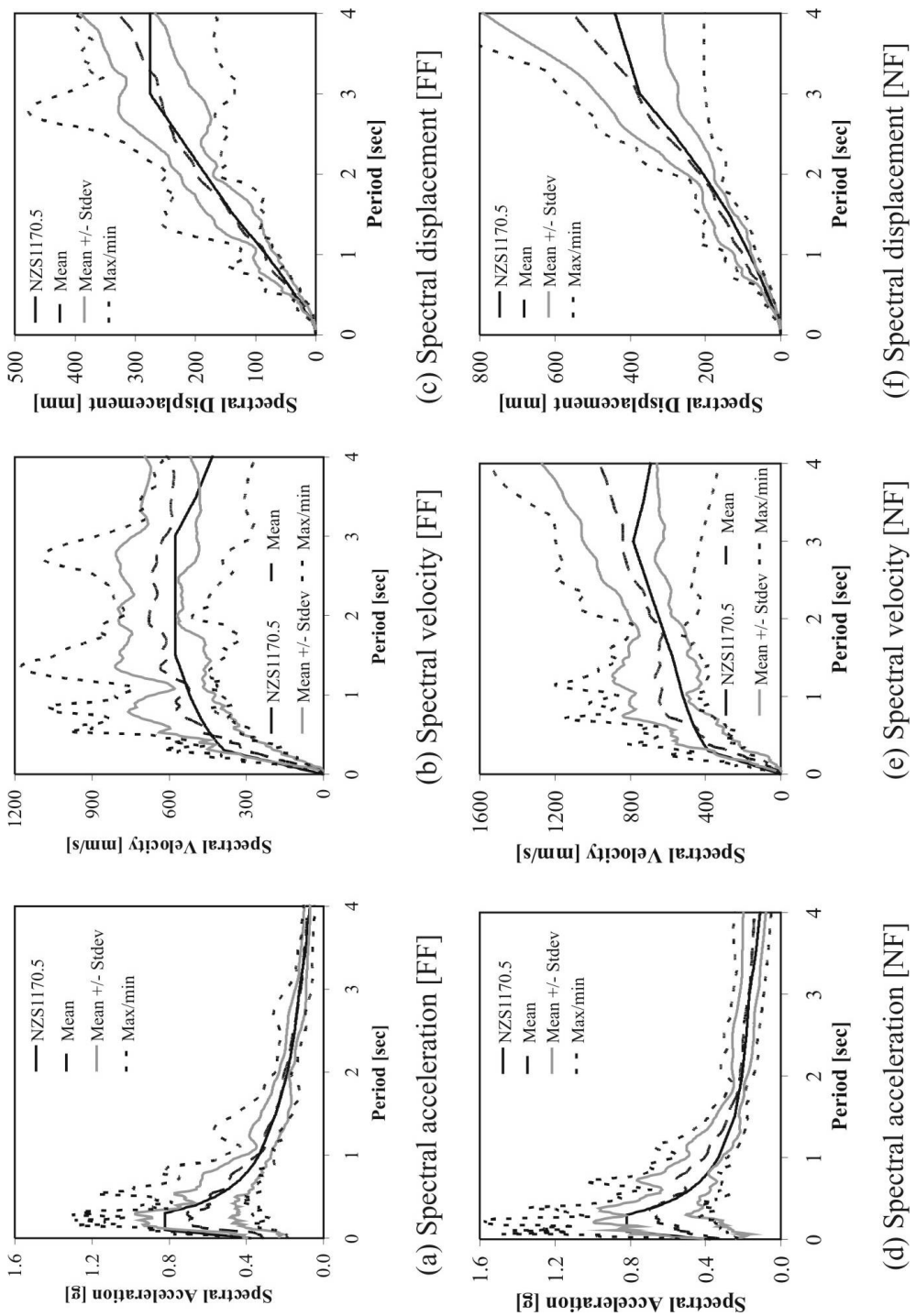

Figure 8.6 Response spectra for 15 far-field records (a)-(c) and 15 near-field records (d)-(f)

8.2.3. Spectral Reduction Factors for Linear Viscous Dampers

In developing a set of damped response spectra, attention was first be given to the pure viscous case i.e. linear viscous dampers with $\alpha = 1.0$. The mean displacement, velocity and acceleration response spectra are presented in Figure 8.7 for far-field (a)-(c) and near-field (d)-(f) ground motions. Each response spectrum is presented for the six supplementary damping ratios (SDR) discussed previously, $\Omega = 0\text{-}0.30$. In this case, because the supplementary damping is linear ($\alpha = 1.0$), Ω is exactly equal to EVD, i.e. $\Omega = \xi_{eq}$. Also shown in the same figure are six corresponding NZ design spectra (grey dashed lines): the first being the 5% damped spectra, while the other five correspond to increasing levels of damping. These five damped spectra levels are reduced from the elastic spectrum according to a calibrated level of equivalent viscous damping (EVD), calibrated to each SDR Ω (0.05 to 0.30). The damping reduction factor η adopted for DDBD is rewritten below in Eq.8.5. This factor represents the ratio of the x% damped response to the 5% damped response. In this equation S represents the maximum response, being displacement, velocity or acceleration. While some publications impose a lower limit for η (the now superseded European code enforced a lower limit of $\eta > 0.7$, Eurocode:8 [1998]), no lower limit is used in Eq.8.5 as the reduction is computed directly from calibrated time-history analysis (THA)

$$\eta = \sqrt{\frac{0.07}{0.02 + \xi_{eq}}} = \frac{S_{\xi\%}}{S_{5\%}} \qquad \textbf{8.5}$$

The maximum response from THA $S_{\xi\%}$ (being acceleration, velocity or displacement), is divided by the 5% damped response $S_{5\%}$ at each period (0.5s to 4.0s). This defines the spectral reduction η as a function of period, i.e. $\eta(T)$. This reduction is then averaged over the entire period range to define a single reduction factor $\eta = \eta_{ave}$. This is repeated for each SDR Ω defining the spectral reduction η as a function of Ω. The reduction in spectral displacement, velocity and acceleration is graphed in Figure 8.8 as a function of the supplementary damping ratio Ω. It is immediate evident that as Ω increases, the spectral reduction η significantly differs between displacement, velocity and acceleration. As the level of damping is increased, the traditionally adopted in-phase response of acceleration and 90 degrees out-of-phase response of velocity is no longer valid (considering steady-state harmonic motion). It is also important to illustrate the variation of η over the entire period range to confirm the viability of an average value. Figure 8.9 plots the error between the spectral reduction at each period $\eta(T)$ and the average spectral reduction η_{ave} over the entire period range. For design purposes, the variation is relatively minor and reduces as the amount of supplementary damping increases. Furthermore, for near-field ground motions [Figure 8.9(b)], the difference is found to be less than 5% over the entire period range for all damping ratios.

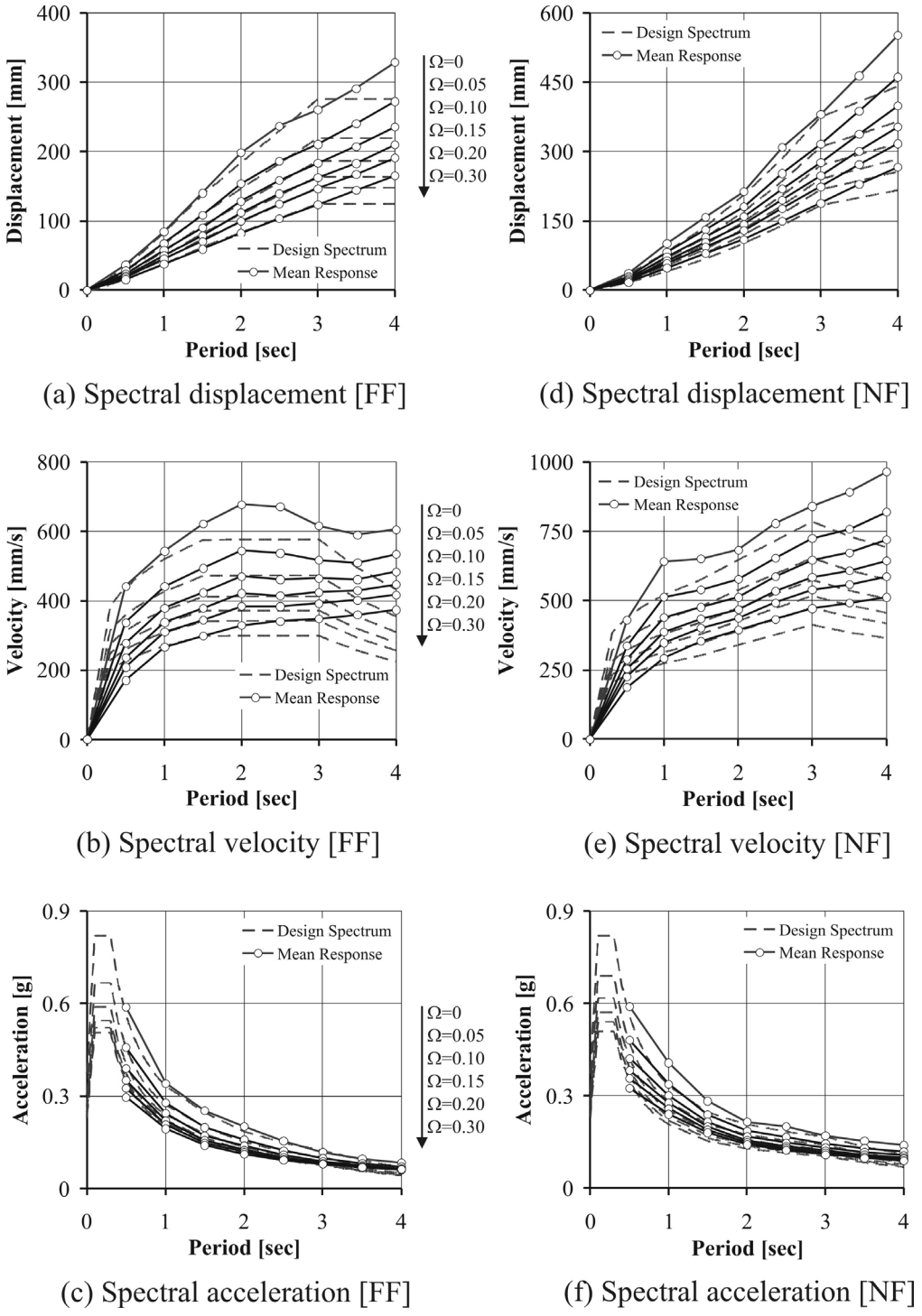

Figure 8.7 Damped response spectra (α=1.0) for far-field records (a)-(c) and near-field records (d)-(f)

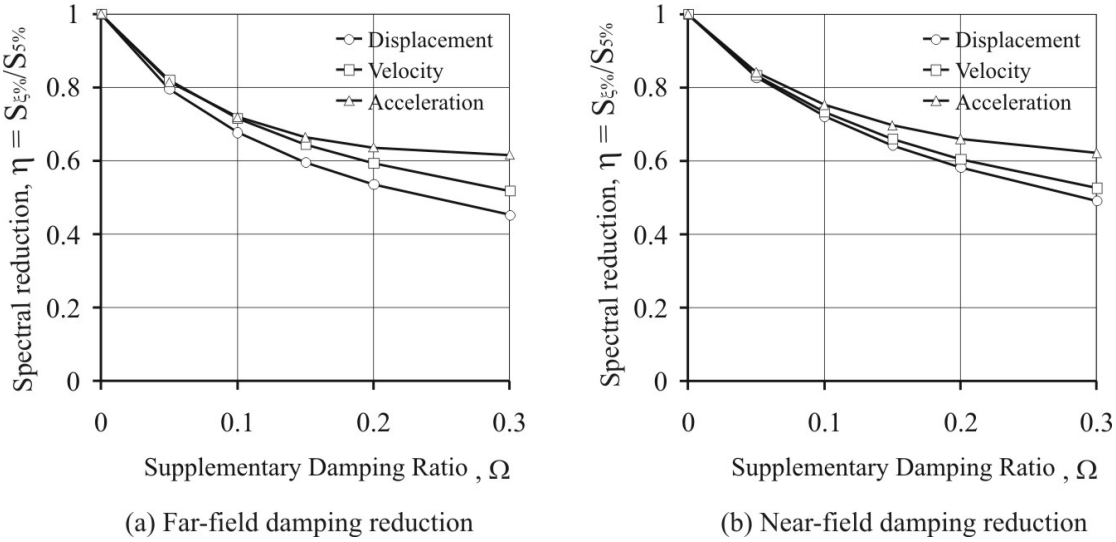

Figure 8.8 Spectral reduction-supplementary damping relationship (□=1.0)

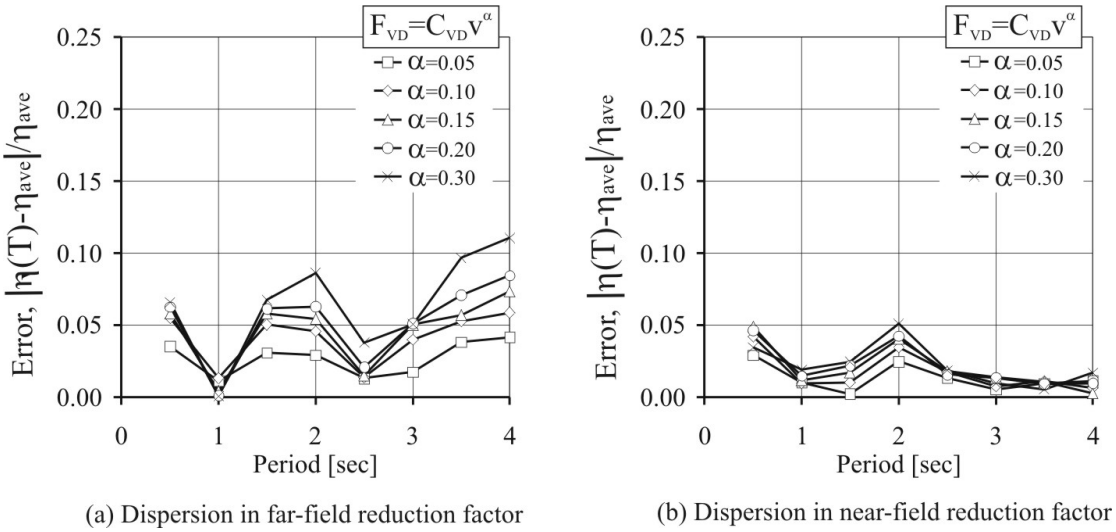

Figure 8.9 Variation in spectral displacement reduction with period

It is also important to recognise the difference in spectral reduction between the far-field ground motions in Figure 8.8(a) and the near-field ground motions in Figure 8.8(b). This figure would suggest that, for design, the damping reduction relationships will depend on the ground motion hazard of the site. In fact, work by Bommer and Mendis [2005] has shown that the spectral reduction is dependant on a number of ground motion properties; the reduction decreases as magnitude increases, decreases as site-to-source distance decreases, increases for softer soils and decreases as duration of shaking increases. This work also supported the suggestion by Priestley [2003] to adopt the spectral reduction relationship of Eq.(8.6) for near-field ground motions having a forward directivity velocity pulse (in Eq.(8.6) an exponent of 0.25 is used as opposed to 0.5 used in Eq.(8.5) for far-field ground motions). The ***0.25***

exponent essentially recognises (hysteretic) damping is less effective for systems subjected to velocity pulse type ground motions.

$$\eta = \left(\frac{0.07}{0.02 + \xi_{eq}} \right)^{0.25} \quad \textbf{8.6}$$

For the proposed design procedure it is not desirable to have two different equations describing the spectral reduction (one for far-field and one for near-field). The proposed design procedure uses the spectral reduction of Eq.8.5 (adopting the 0.5 exponent) to describe the reduction of both near-field and far-field ground motions. In fact, the spectral reduction shape of Eq.(8.6) did not agree with the observed time-history reduction for either the far-field or near-field ground motions. Using the relationship of Eq.(8.5) above the EVD $\boldsymbol{\xi_{eq}}$ is calibrated to the observed spectral reduction from THA, $S_{5\%}/S_{\xi\%}$ in Figure 8.8. Calibration of Eq.(8.5) is carried out by rearranging and solving for $\boldsymbol{\xi_{eq}}$. In this particular case, the EVD is made up of two components: the elastic damping $\boldsymbol{\xi_{el}}$ (5% of critical herein) and the supplementary damping component $\boldsymbol{\xi_{vd}}$. By substitution of $\xi_{eq} = \xi_{vd} + \xi_{el}$ into Eq.(8.5), the EVD associated with the supplementary damper $\boldsymbol{\xi_{vd}}$ is computed from Eq.(8.7).

$$\xi_{vd} = \frac{0.07}{\eta^2} - 0.02 - \xi_{el} = 0.07\left[\left(\frac{S_{5\%}}{S_{\xi\%}} \right)^2 - 1 \right] \quad \textbf{8.7}$$

As a final step, $\boldsymbol{\xi_{vd}}$ can be expressed as a function of the supplementary damping ratio $\boldsymbol{\Omega}$. This relationship is graphed in Figure 8.10 (a) & (b) for spectral displacement and spectral velocity respectively, considering far-field and near-field ground motions. The EVD relationship is expressed as a linear equation for displacement [Eq.(8.8)] and velocity [Eq.(8.9)]. The coefficients of the linear regression analysis are summarised in Table 8.3. Note that for the linear case, one would expect the coefficient $\boldsymbol{a_1}$ to be approximately equal to 1.0; this difference results from the specific ground motions used and the spectral reduction formula to which calibration was performed to (Eq.(8.5) herein).

$$\xi_{eq}^{disp} = a_1 \Omega + \xi_{el} \quad \textbf{8.8}$$

$$\xi_{eq}^{vel} = b_1 \Omega + \xi_{el} \quad \textbf{8.9}$$

Hence, using Eq.(8.8) and Eq.(8.9) the displacement and velocity spectral reduction are computed from the following expressions

$$\eta_{disp} = \sqrt{\frac{0.07}{0.02 + \xi_{eq}^{disp}}} \quad \textbf{8.10}$$

$$\eta_{vel} = \sqrt{\frac{0.07}{0.02 + \xi_{eq}^{vel}}} \qquad \textbf{8.11}$$

Table 8.3 EVD, spectral reduction coefficients (α=1.0)

	Far-field	Near-field
a_1	0.884	0.707
b_1	0.645	0.609

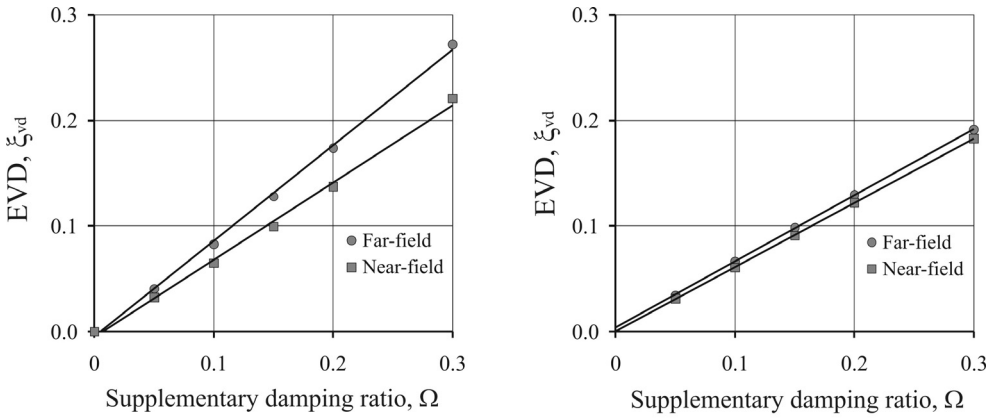

Figure 8.10 Relationship between EVD and the supplementary damping ratio for linear viscous dampers (α=1.0)

8.2.4. Spectral Reduction Factors for Non-Linear Viscous Dampers

The procedure outlined in Section 8.2.3 for linear dampers was repeated for non-linear dampers having velocity exponents of $\alpha = 0.15$, 0.30, 0.50 and 0.75. The response spectra are shown in Appendix E for displacement and velocity. Acceleration is not actually necessary for the proposed design procedure and is, therefore not presented. The mean spectral displacement reduction η versus the SDR Ω is graphed in Figure 8.11 for α ranging from 0.15 to 1.0. Figure 8.11(a) plots the spectral reduction for far-field ground records, while Figure 8.11(b) plots the spectral reduction for near-field ground records. For each supplementary damping ratio Ω the spectral reduction increases as the linearity of the supplementary damper increases i.e. η increases as α approaches 1.0. This relationship is not linearly proportional: the spectral reduction η becomes independent of the velocity exponent α as it approaches 0.75.

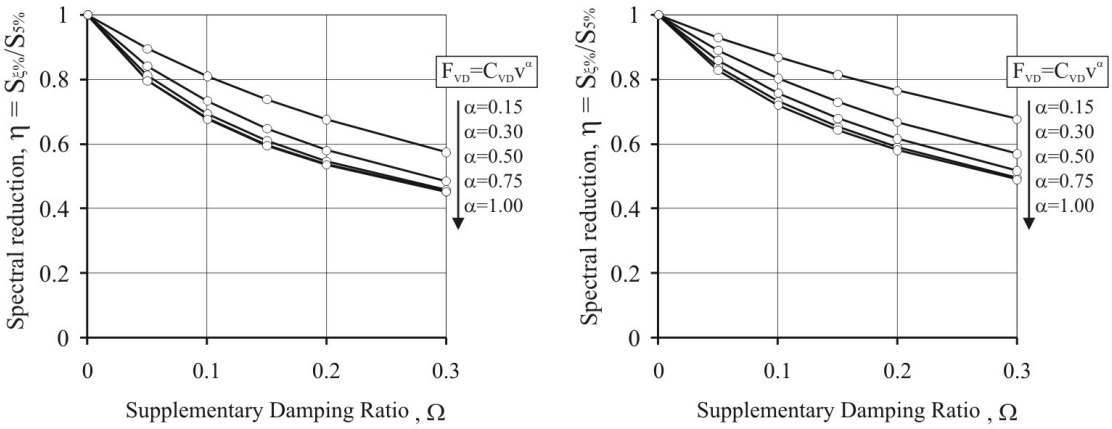

Figure 8.11 Spectral reduction factors (α=0.15 to 1.0)

It is interesting to note that the variation in spectral reduction across the period range is larger for the far-field ground motions [Figure 8.12(a)]. Considering effective periods in the range of T_{eff}=1.0-4.0s, which is appropriate to buildings and bridges, the variation in spectral reduction is likely to be less than 10% for far-field ground motion and 5% for near-field ground motion.

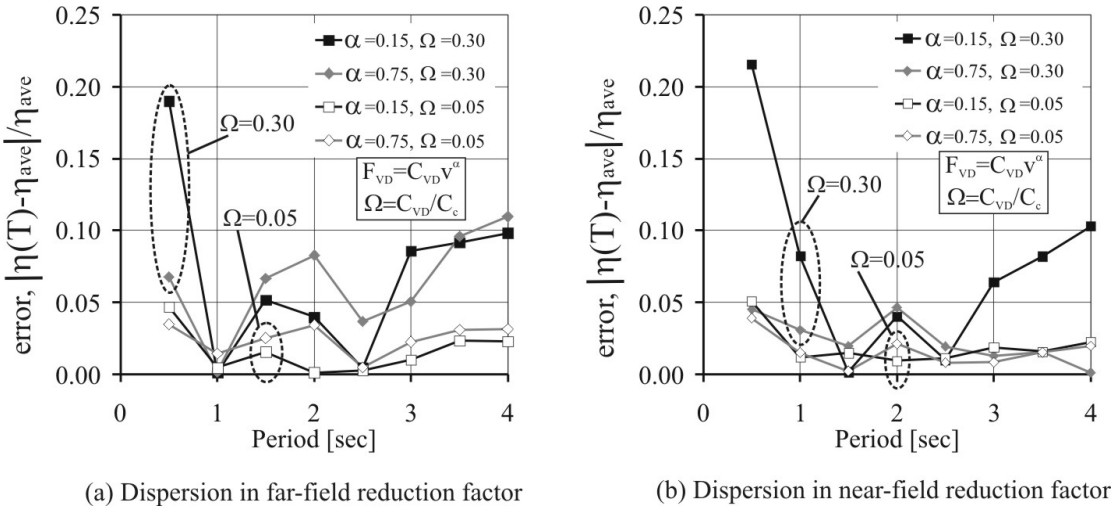

Figure 8.12 Variation of spectral displacement reduction with period for α=0.15 & 0.75 and Ω=0.05 & 0.30

The spectral reduction relationships are summarised in Figure 8.13 by relating the EVD (viscous damper component ξ_{vd}) to the SDR Ω as a function of the velocity exponent α. For α = 0.75 & 1.0 the difference in spectral reduction is negligible, thus, an average is used.

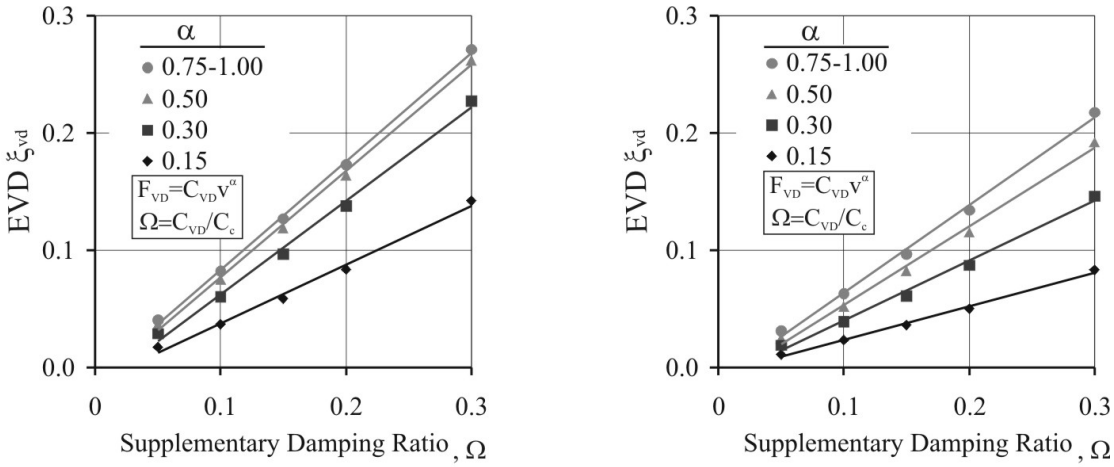

(a) EVD ratio for Far-field motions (b) EVD for Near-field motions

Figure 8.13 Relationship between EVD and the supplementary damping ratio for non-linear viscous dampers (α=0.15 to 1.0)

Recalling from Eq.(8.8) & (8.9) the EVD ξ_{eq} is related to the supplementary damping ratio (SDR) Ω by a linear relationship with coefficients a_1 (for spectral displacement) and b_1 (for spectral velocity) in the following form

$$\xi_{eq}^{disp} = a_1\Omega + \xi_{el} \qquad \textbf{8.12}$$

$$\xi_{eq}^{vel} = b_1\Omega + \xi_{el} \qquad \textbf{8.13}$$

Following the linear regression of Figure 8.13 the coefficients a_1 and b_1 are summarised below in Table 8.4 for any non-linear damper in the range of $0.15 < \alpha < 1.0$ and considering either a far-field or near-field seismic hazard.

Table 8.4 EVD coefficients

	Velocity exponent, α							
	1.0-0.75[1]		0.50[1]		0.30[1]		0.15[1]	
a_1	0.880	0.693	0.839	0.602	0.714	0.456	0.440	0.262
b_1	0.642	0.598	0.608	0.526	0.521	0.412	0.341	0.243

[1]Values in the left column relate to far-field seismicity, values in the right column refer to near-field seismicity

8.2.5. Modification of the Spectral Reduction Factors to Account for a Bilinear Backbone Envelope

The spectral reduction factors determined in Section 8.2.3 and 8.2.4 were performed on a linear elastic system. The results of this calibration were found to be less accurate for systems with a bilinear-elastic loading envelope representative of a post-tensioned system. Figure 8.14 illustrates the common trend in that the peak maximum displacement of a bilinear system was consistently less than the maximum displacement of an equivalent linear system targeting the same displacement Δ_d. As there is no unique bilinear stiffness for post-tensioned systems an additional study was undertaken to address this issue.

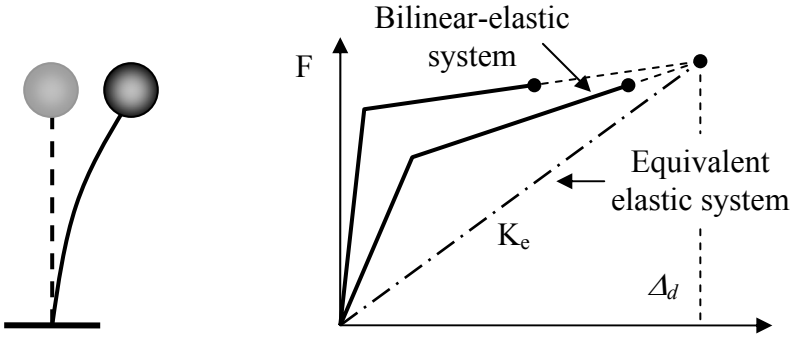

Figure 8.14 The effect of having a bilinear loading envelope represented by a secant stiffness

To reduce the number of structural models to a manageable number the study considers only a few system parameters. With respect to Figure 8.15, two damper velocity exponents are considered: $\alpha = 0.30$ & 0.75, as well as two supplementary damping ratios (SDR): $\Omega = 0.05$ & 0.30. Finally, three effective periods are selected: $T = 1.0$, 2.25 & 3.0sec, resulting in four parametric models at each of the three periods, Figure 8.15(a). For each parametric model, four unique bilinear-elastic backbone curves are constructed, Figure 8.15(b). Each bilinear-elastic model targets the mean of the maximum displacement response of the equivalent elastic system (determined from the THA output in Section 8.2). The four bilinear-elastic models are constructed considering two bilinear stiffness ratios ($0.02k_i$ and $0.05k_i$) and two 'yield' force ratios ($0.6V_b$ and $0.8V_b$). These four bilinear-elastic models are defined as Model A through to Model D. This study was undertaken for far-field and near-field seismicity, which equated to an additional 96 structural models, or 1440 individual time history analyses. An analysis matrix is illustrated in Figure 8.16 to further explain the parameters of the individual models: one matrix each for far-field and near-field seismicity.

In this bilinear study the elastic damping was again set equal to 5% of critical damping. In this case a constant damping was implemented and was computed considering the secant stiffness to the target displacement Δ_d. Hence, the elastic damping model was constant throughout the time history, but proportional in magnitude to the secant stiffness defining the target displacement.

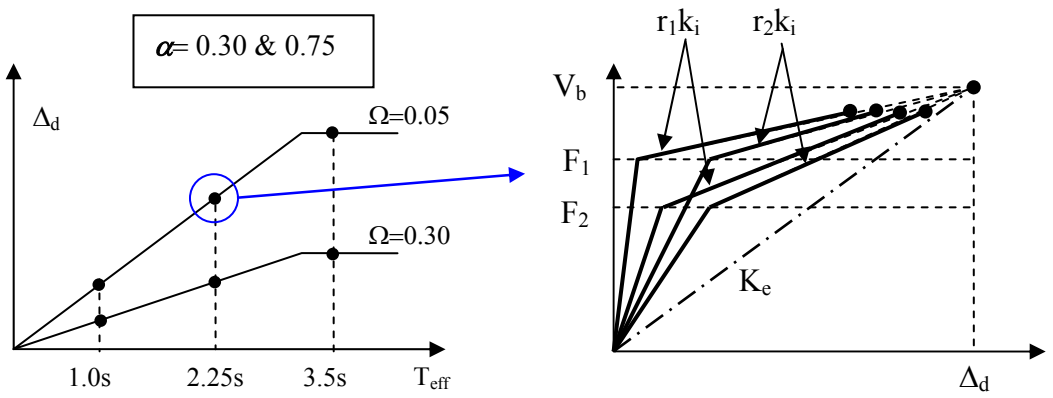

(a) Displacement spectrum

(b) Loading envelope, Model A-D

Figure 8.15 Bilinear study and the system parameters investigated

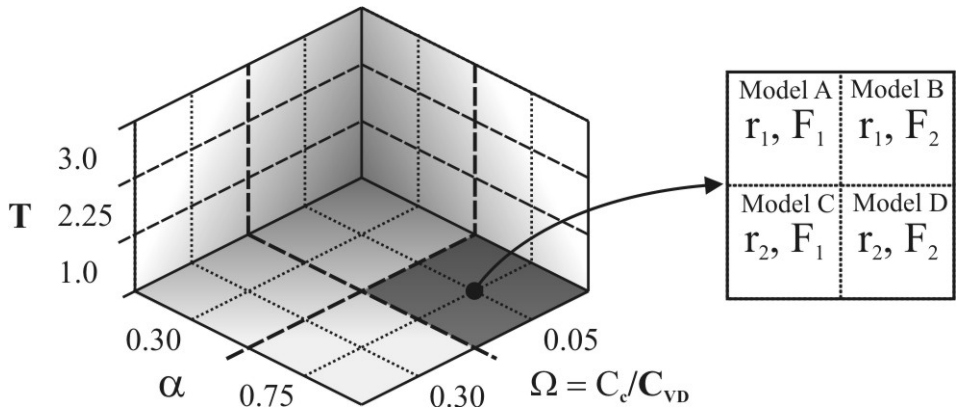

Figure 8.16 Bilinear study, model matrix

The ratio of the mean peak response of the bilinear system to the mean peak response of the equivalent elastic system is shown in Figure 8.18 (for far-field seismicity) and Figure 8.19 (for near-field seismicity). The graphs at the top of each figure present the displacement ratio, while the graphs on the bottom present the velocity ratio. Each graph has four divisions along the x-axis representing the four bilinear backbone models described previously (Model A to Model D). As the effective period increases, the dependency on each model appears to reduce, i.e. the slope of the lines approaches zero. From these results it can be assumed that the displacement (and velocity) ratio is independent of the backbone model and entirely dependant on the velocity exponent α and the supplementary damping ratio Ω. While there is some dependency on each model for effective periods equal to T = 1.0sec, this represents a lower bound solution and will be outside the range of typical effective periods. Furthermore, the response appears to be stable enough to allow interpolation to be carried out for intermediate values of α, Ω and T.

It is of particular importance to note that the displacement is significantly more effected than the velocity. In fact, the ratio of the mean peak bilinear velocity to the mean peak elastic velocity is relatively close to 1.0. It was to this end that no velocity modification is considered for the proposed design procedure.

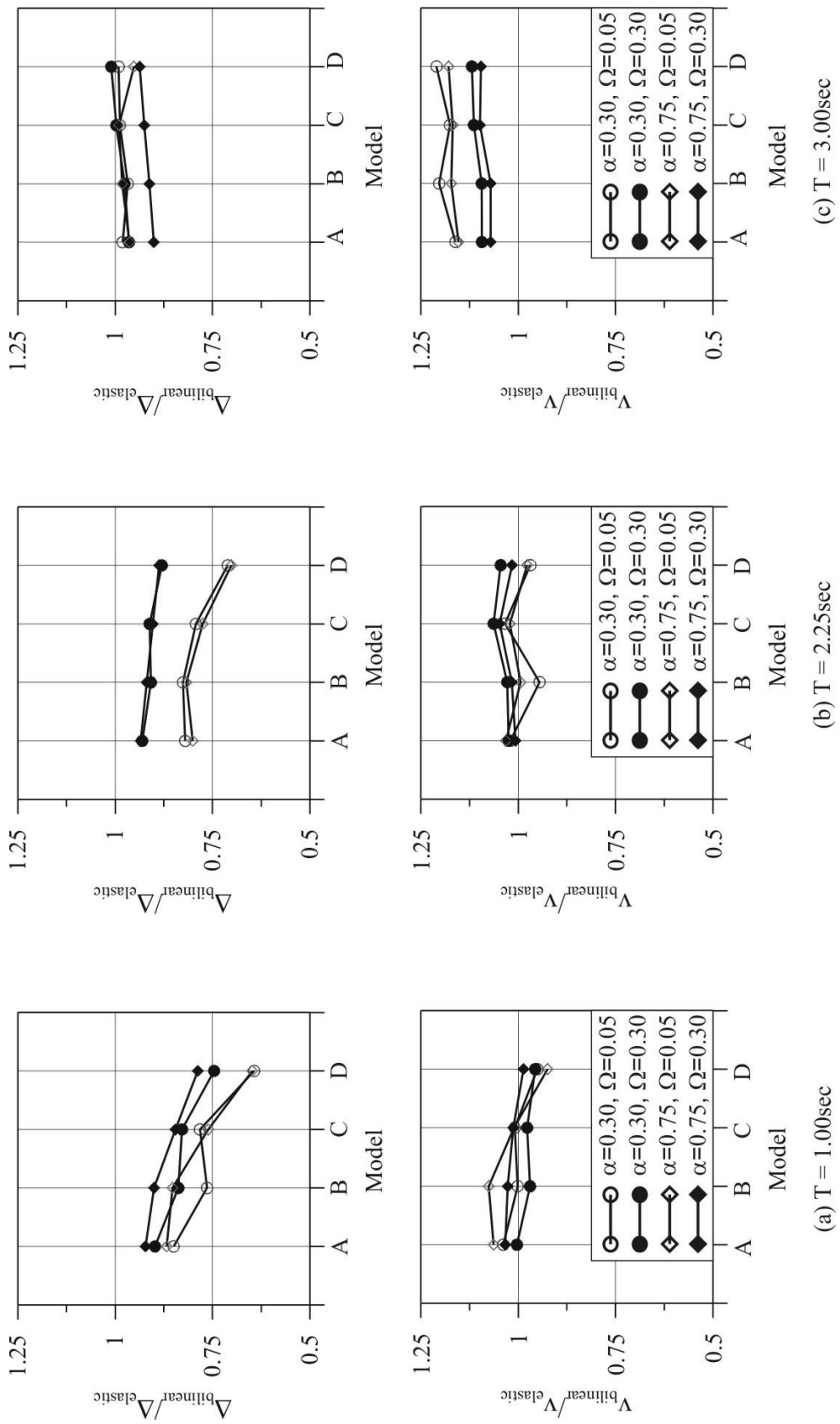

Figure 8.17 Ratio of peak bilinear response to the peak elastic response for displacement (Top) and velocity (bottom) when subjected to Far-Field ground motions

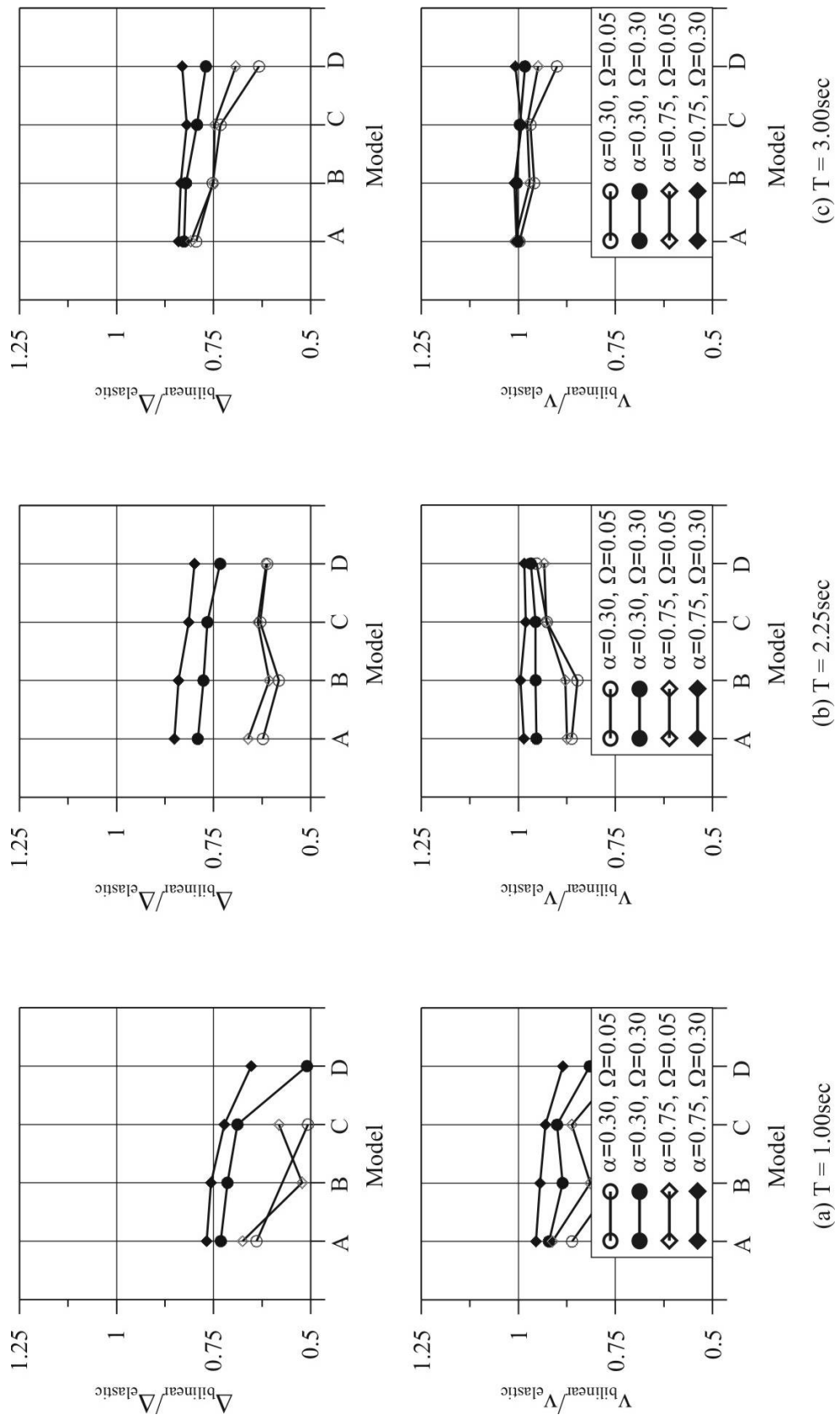

Figure 8.18 Ratio of peak bilinear response to the peak elastic response for displacement (Top) and velocity (bottom) when subjected to Near-Field ground motions.

In order to implement this displacement modification within design, an equivalent strain-energy approach was used. The PT loading component (ignoring the viscous contribution) in Figure 8.19 illustrates the original bilinear-elastic loading envelope (denoted as system (**1**)), having an elastic stiffness k_1 and bilinear stiffness rk_1 and based on a design strength of V^* at a displacement of Δ_d. In Figure 8.19 the strength of system (**2**) is reduced to a value of V_b by multiplying the design base shear V^* by a base shear reduction factor ϕ_{BL}, defined by Eq.(8.14). The bilinear reduction factor ϕ_{BL} is determined by equating the strain energy between the original bilinear system (**1**) and the reduced bilinear system (**2**), i.e. $E_1 = E_2$. From a strain energy point of view, the maximum bilinear displacement of the reduced system (**2**) will be similar in magnitude to the displacement of the equivalent elastic system Δ_d.

$$V_b = \phi_{BL} V^* \qquad \textbf{8.14}$$

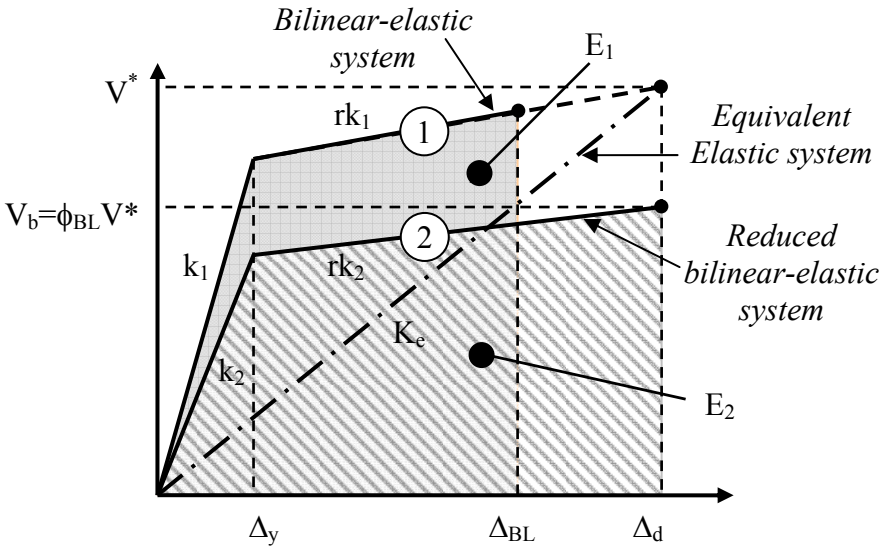

Figure 8.19 Equating strain energy between the bilinear backbone and the elastic backbone.

When Eq.(8.14) was used in the design of a system under near-field ground motions, this equal energy approximation was found to be violated. Under near-field ground motions the system achieved much larger displacements than expected from Figure 8.19. A further modification is proposed in Figure 8.20, which illustrates the original bilinear backbone denoted as (**1**) and the reduced bilinear system (**2**). Considering the near-field THA, the displacement response was better achieved with a base shear reduction defined by system (**3**). The reduction of system (**3**) is computed such that the base shear reduction is 50% of the base shear reduction considering far-field ground motions. The formulation of the bilinear base shear reduction factor ϕ_{BL} is outlined in Appendix E and summarised in Table 8.5 and Table 8.6 for far-field and near-field seismicity respectively.

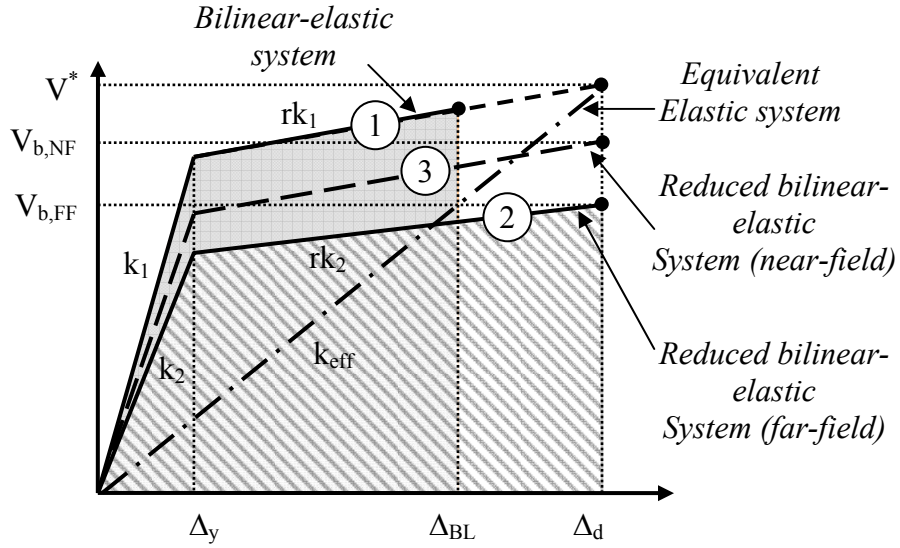

Figure 8.20 Bilinear reduction factor for near-field response

Table 8.5 Bilinear, base-shear reduction factors ϕ_{BL}: Far-field

ϕ_{BL}	α=0.30		α=0.75	
	Ω=0.05	**Ω=0.30**	**Ω=0.05**	**Ω=0.30**
Te=1.00s	0.717	0.794	0.744	0.837
Te=2.25s	0.755	0.888	0.731	0.892
Te=3.50s	0.978	0.983	0.966	0.900

Table 8.6 Bilinear, base-shear reduction factors ϕ_{BL}: Near-field

ϕ_{BL}	α=0.30		α=0.75	
	Ω=0.05	**Ω=0.30**	**Ω=0.05**	**Ω=0.30**
Te=1.00s	0.722	0.803	0.745	0.838
Te=2.25s	0.775	0.861	0.784	0.896
Te=3.50s	0.840	0.882	0.852	0.898

8.3. RELATING LOCAL SUPPLEMENTARY DAMPING PROPERTIES TO GLOBAL STRUCTURAL DAMPING PROPERTIES

The damper properties at the rocking interface (defined as *local* damper properties) must be converted to system damper properties at the effective height of structure (defined as *global* or *system* damper properties) to make use of the proposed design procedure. The focus of this chapter is on post-tensioned rocking wall or column systems with supplementary dampers located at the rocking interface. Consider the SDOF system in Figure 8.21; the forces within the viscous dampers $\boldsymbol{F_{vd}}$ can be expressed as an equivalent force at the effective height of the structure $\boldsymbol{F_{VD,sys}}$ by equating moment equilibrium of the section.

The following parameters in Figure 8.21 are defined below,

- $\boldsymbol{C_{VD}}$ = the global damping coefficient
- $\boldsymbol{v_r}$ = the system velocity at the effective height
- $\boldsymbol{n_{vd}}$ = the total number of supplementary damper devices at the rocking interface
- $\boldsymbol{c_{vd}}$ = the damper coefficient of the viscous damper devices at the rocking interface
- $\boldsymbol{v_{vd}}$ = the velocity of the damper
- $\boldsymbol{\alpha}$ = the damper velocity exponent

To begin with, the velocity of the dampers can be related to the velocity at the effective height by considering the geometry and the mechanics of the rocking system in Figure 8.21. These two considerations alone define a unique relationship relating the local damping properties to equivalent global (system) damping properties.

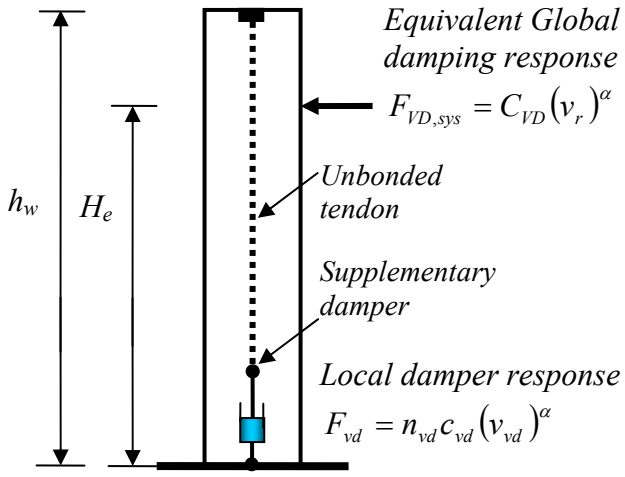

Figure 8.21 Relationship between system damping and local damping properties

Direct displacement-based design makes use of a target (or design) displacement at the peak response. The velocity is zero at the peak displacement response; therefore, it is impossible to relate any information about the viscous dampers using the current

design procedure. Therefore, in addition to the target displacement, it is necessary to define an intermediate design displacement such that the viscous damper forces will be non-zero. Assuming steady state harmonic motion during the excursion to the target displacement Δ_d, the intermediate displacement Δ_r is defined by the following equation

$$\Delta_r = \frac{\Delta_d}{\sqrt{2}} \qquad \textbf{8.15}$$

With reference to Figure 8.22, at the intermediate displacement Δ_r, the normalised velocity and displacement are equal; therefore, the influence of the velocity dependant components and the displacement dependant components on the capacity of the section will be similar in magnitude.

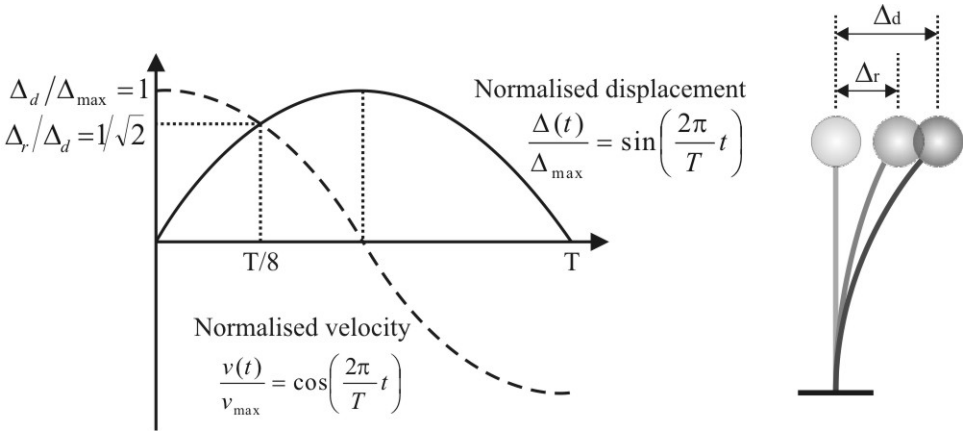

Figure 8.22 Normalised displacement and velocity time history describing sinusoidal harmonic motion

The spectral reduction factor η defined in Section 8.2.3 is explicitly expressed here as η_{disp} for the reduction in spectral displacement and η_{vel} for the reduction in spectral velocity. For low system damping the spectral velocity can be approximated by the pseudo-spectral velocity; however, as the supplementary damping increases, this relationship is increasingly violated. The damped spectral velocity $v(T,\xi)$ is related to the 5% damped spectral velocity $v(T,5\%)$ by

$$v(T,\xi) = v(T,5\%) \cdot \eta_{vel} \qquad \textbf{8.16}$$

Similarly for displacement

$$\Delta(T,\xi) = \Delta(T,5\%) \cdot \eta_{disp} \qquad \textbf{8.17}$$

Through substitution, the velocity v_r at the intermediate displacement Δ_r is defined as

$$v(T,\xi) = v_r = \Delta_d \frac{2\pi}{T_e}\left(\frac{\eta_{vel}}{\eta_{disp}}\right)\frac{1}{\sqrt{2}} \qquad \textbf{8.18}$$

Considering Figure 8.21, the system damper force $F_{VD,sys}$ is related to the system damping coefficient C_{VD} by the following

$$F_{VD,sys} = C_{VD}\left(v_r\right)^{\alpha} \qquad \textbf{8.19}$$

By equating moment equilibrium the system force is expressed in terms of the moment capacity at the rocking interface M_{vd}

$$F_{VD,sys} = \frac{M_{vd}}{H_e} = \frac{\sum_{i=1}^{n_{VIS}} n_{vd,i} c_{vd}\left(v_{vd,i}\right)^{\alpha} jd_{vd,i}}{H_e} = \frac{n_{vd} c_{vd}\left(\bar{v}_{vd}\right)^{\alpha} jD}{H_e} \qquad \textbf{8.20}$$

Where

- n_{vis} = the number of damper groups (or sets, or layers) within the rocking interface
- $n_{vd,i}$ = the number of supplementary damper devices within each group i at the rocking interface
- n_{vd} = the total number of supplementary damper devices at the rocking interface
- c_{vd} = the damper coefficient of the viscous damper devices at the rocking interface
- $v_{vd,i}$ = the velocity of the damper at i
- $jd_{vd,i}$ = the internal lever arm to damper group i
- $\bar{v}_{vd}$ = the average velocity considering all viscous devices
- jD = the internal lever arm to the centroid of the resultant damper force (sum of all damper forces)

Through Eqs.(8.19) and (8.20) a relationship is defined relating the global damping coefficient C_{VD} to the local damping coefficient c_{vd}. The ratio between the two is defined as β_{vd}.

$$\beta_{vd} = \frac{C_{VD}}{c_{vd}} = n_{vd}\left(\frac{jD}{H_e}\right)\cdot\gamma_{vd} \qquad \textbf{8.21}$$

A number of approximate methods can be employed to estimate the internal lever arm jD; however, accurate equations are derived in Appendix E. The term γ_{vd} in Eq.(8.21) is the ratio of the average damper velocity $\bar{v}_{vd}$ to the system velocity v_r (raised to the power of α), see Eq.(8.22). This velocity ratio can be approximated by Eq.(8.23); however, more accurate expressions are outlined in Appendix E if greater detail is required.

$$\gamma_{vd} = \left(\frac{\bar{v}_{vd}}{v_r} \right)^{\alpha} \qquad \textbf{8.22}$$

$$\frac{\bar{v}_{vd}}{v_r} \approx \frac{jD}{H_e} \qquad \textbf{8.23}$$

The ratio between the average velocity of the dampers and the system velocity is illustrated graphically in Figure 8.23. This ratio is largely a function of the aspect ratio A_r of the system (with respect to the effective height H_e) and, to a lesser extent, the depth of the concrete compression block $\beta\chi$. In Figure 8.23 β is the concrete stress block depth multiplier and χ is the dimensionless neutral axis depth (c/d). It is clear that the velocity of the damper is only a fraction of the velocity of the system.

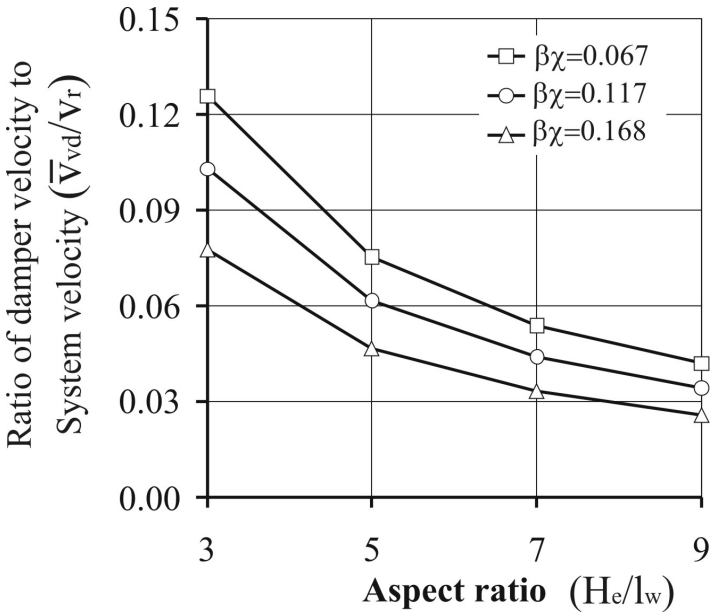

Figure 8.23 Ratio of damper velocity to system velocity versus aspect ratio

The ratio between the global damping coefficient and the local damping coefficient β_{vd} in Eq.(8.21) above is plotted in Figure 8.24. To do so, the concrete stress block depth $\beta\chi$ must be assumed. In Figure 8.24 an average value of $\beta\chi = 0.11$ is used.

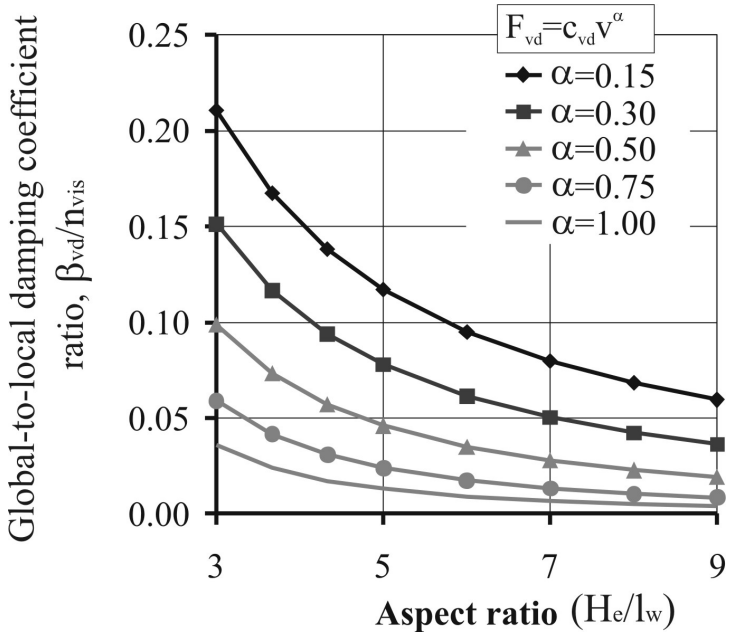

Figure 8.24 Ratio between the global to the local damping coefficient (assuming two dampers located at each damper layer)

The curves in Figure 8.24 are fitted to the closed form relationship of Eq.(8.24). In this closed form equation ***a*** is a constant and depends on the damper velocity exponent, given in Table 8.7.

$$\beta_{vd} = \frac{C_{VD}}{c_{vd}} = a \cdot n_{vis} \left(A_r\right)^{-(1+\alpha)} \qquad \textbf{8.24}$$

Table 8.7 Constant to be used in conjunction with Equation 8.24

α	***a***
0.15	0.746
0.30	0.632
0.50	0.514
0.75	0.405
1.00	0.324

The local-to-global damping relationship above is combined with the EVD formulations developed in Section 8.2.3 to directly relate the local damping properties to the equivalent viscous damping (EVD) of the SDOF system. The EVD associated with a reduction in spectral displacement is given by the following formula

$$\xi_{eq}^{disp} = a_1 \Omega + \xi_{el} = a_1 \frac{\beta_{vd} c_{vd}}{C_c} + \xi_{el} \qquad \textbf{8.25}$$

Here, C_c is the critical damping of the structure. Considering only the proportion of EVD attributed to the supplementary dampers, the formula reduces to

$$\xi_{vd} = a_1 \Omega = a_1 \frac{\beta_{vd} c_{vd}}{C_c} \qquad \textbf{8.26}$$

The EVD associated with the supplementary viscous dampers ξ_{vd} is graphed in Figure 8.26 against the dimensionless (local) damping coefficient $n_{vis} c_{vd} / C_c$ for far-field and near-field seismicity. This relationship is plotted as a function of the aspect ratio A_r. The variable $n_{vis} c_{vd} / C_c$ is a measure of the amount of damping provided at the rocking interface i.e. the damping supplied at a local level. As expected, as the amount of damping supplied increases (i.e. $n_{vis} c_{vd} / C_c$ increases) the amount of EVD ξ_{eq} also increases. It is interesting to note that as the non-linearity of the damper reduces (i.e. as α reduces) the EVD increases. It is difficult to comprehend this trend in Figure 8.26. The reason being that the damping coefficient must be related to the total (local) damping force F_{vd} to understand what is going on in the system; to do so, Eq.(8.20) & (8.21) above are rearranged for F_{vd} resulting in the following equation

$$F_{vd} = c_{vd} \left(v_r\right)^{\alpha} a \cdot n_{vis} \left(\frac{H_e}{jD}\right) \left(A_r\right)^{-(1+\alpha)} \qquad \textbf{8.27}$$

Where

- F_{vd} = the sum of the damper forces at the rocking interface
- c_{vd} = the local damper coefficient of a single damper
- v_r = the system velocity (demand) at the effective height H_e
- α = the damper non-linearity, or velocity exponent
- a = a coefficient used to relate the global-to-local damping coefficient in Table 8.7 above
- n_{vis} = the number of damper layers within the rocking interface
- jD = the internal lever arm to the centroid of the resultant damper force F_{vd}
- A_r = the aspect ratio of the system (to the effective height, H_e)

Consider two identical systems denoted as System 1 and System 2, both having a dimensionless damper coefficient of $n_{vis}c_{vd}/C_c = 4$. System 1 has a damper non-linearity of α_1=0.5 and the other $\alpha_2 = 0.75$, both are subjected to a velocity demand of $v_r = 0.5$m/s and each have an aspect ratio of $A_r = 5$. From Figure 8.26 (b), System 1 can expect to have an EVD 1.89 times that of System 2. It is not immediate obvious why the highly non-linear damper is associated with a greater level of damping until the total damping force is computed from Eq.(8.27): in this example, the total (local) damping force of System 1 is 2.26 times greater than System 2. Therefore, the greater level of damping is attributed to the larger damper forces that are induced at the rocking interface, which is not immediately obvious from Figure 8.26. Naturally, as the aspect ratio increases the damper velocities reduce, hence the EVD also reduces. Furthermore, Figure 8.26 also illustrates the reduction in EVD for near-field seismicity when compared to far-field seismicity.

A second relationship is plotted in Figure 8.27 to grasp a better understanding of the (local) damper forces F_{vd} and the EVD ξ_{eq}. The series of graphs in Figure 8.27 graph the relationship of EVD against the total damping force (divided by the critical damping of the system) as a function of the velocity exponent α, aspect ratio A_r and at two levels of peak velocity demand v_r for far-field seismicity (near-field seismicity is graphed in Figure 8.28). As intuition suggests, as the peak damper force increases the EVD increases in proportion. Furthermore, as the damper exponent decreases, or the aspect ratio increases, the EVD reduces.

Interestingly, as the velocity demand increases (considering a fixed damper force F_{vd}) the EVD reduces. As the velocity demand increases, the damper coefficient c_{vd} reduces (given that F_{vd} remains constant), hence the level of EVD reduces in proportion to the ratio of c_{vd}/C_c in Eq(8.26). As the velocity demand exceeds 1.0m/s Figure 8.27 indicates that more efficiency (in terms of greater EVD) can be achieved considering non-linear dampers. In fact, this last trend is investigated in greater detail in Figure 8.29. This figure plots the relationship between the (local) damper force (divided by the critical damping ratio) and the damper exponent α for five specified levels of EVD. Figure 8.29 can be used to determine the optimal damper properties (in terms of damper exponent and coefficient) appropriate for a PT viscous system. The cost of a fluid viscous damper (FVD) is directly proportional to the load capacity of the damper; therefore, the most efficient solution (in targeting some desired level of EVD) is the solution requiring the lowest damper forces F_{vd}. Figure 8.29 indicates that for velocity demands less than 1.0m/s, a linear damper is the optimal solution for all levels of EVD. For velocity demands equal to 1.0m/s a damper non-linearity in the range of $0.75 < \alpha < 1.0$ is the most efficient. For a velocity demand of 1.5m/s the most efficient solution is one requiring a damper exponent of $\alpha = 0.5$ for far-field seismicity and $\alpha = 0.75$ for near-field seismicity; this trend becomes more pronounced as the velocity demand increases. The optimal solution is indicated in each graph by a black dashed line. While Figure 8.29 is only presented for an aspect ratio of $A_r = 5$, the shape of each curve is unaffected, thus the optimal solution is primarily dependant on the velocity demand and not the geometry of the system. As a rough rule, a damper exponent of $\alpha = 0.75$ provides the most efficient system considering the entire velocity range and ground motion characteristics investigated.

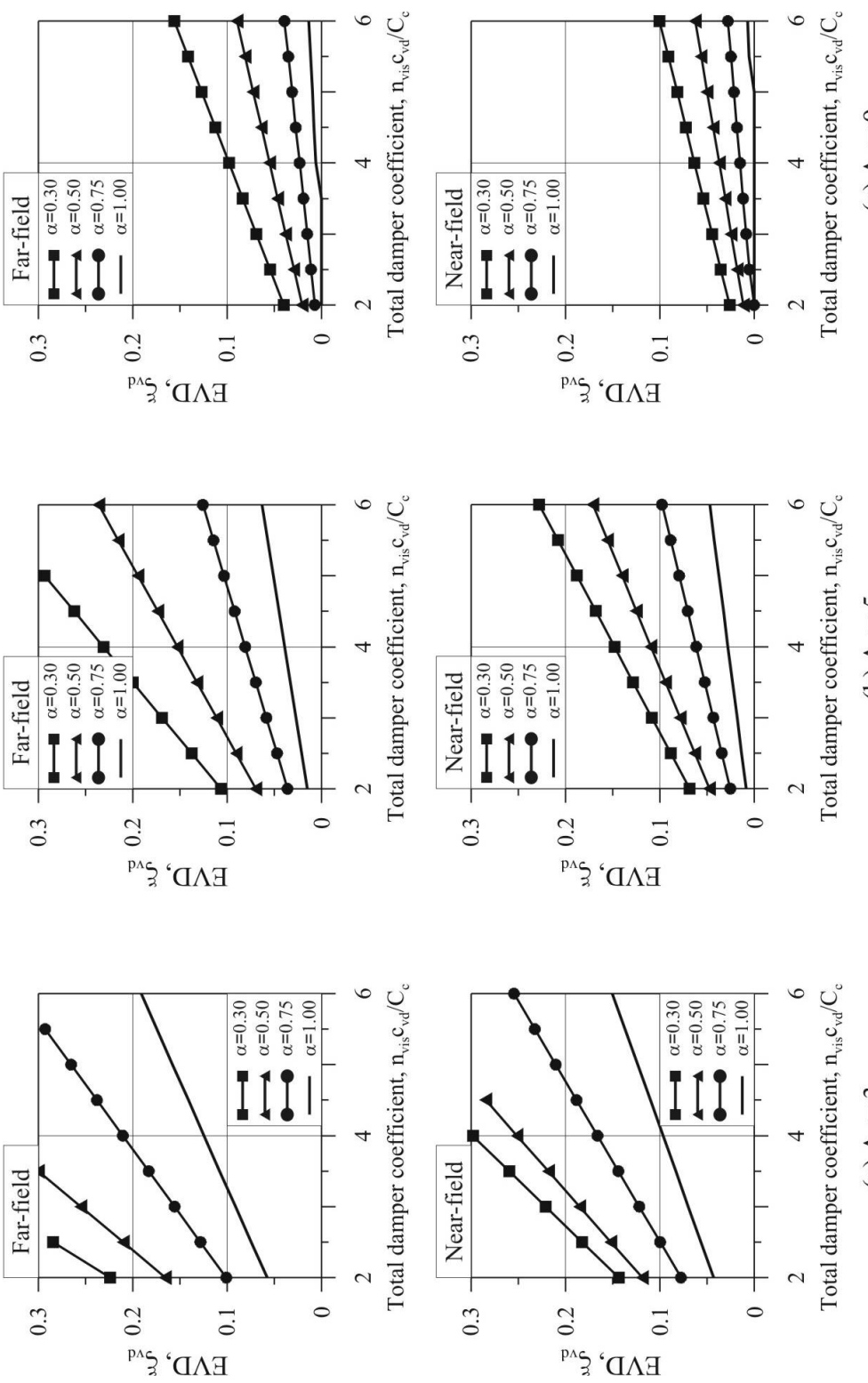

(a) $A_r = 3$ (b) $A_r = 5$ (c) $A_r = 9$

Figure 8.25 Relationship between EVD and the total damping coefficient for far-field (top) and near-field (bottom) seismicity as a function of the Aspect ratio ,A_r

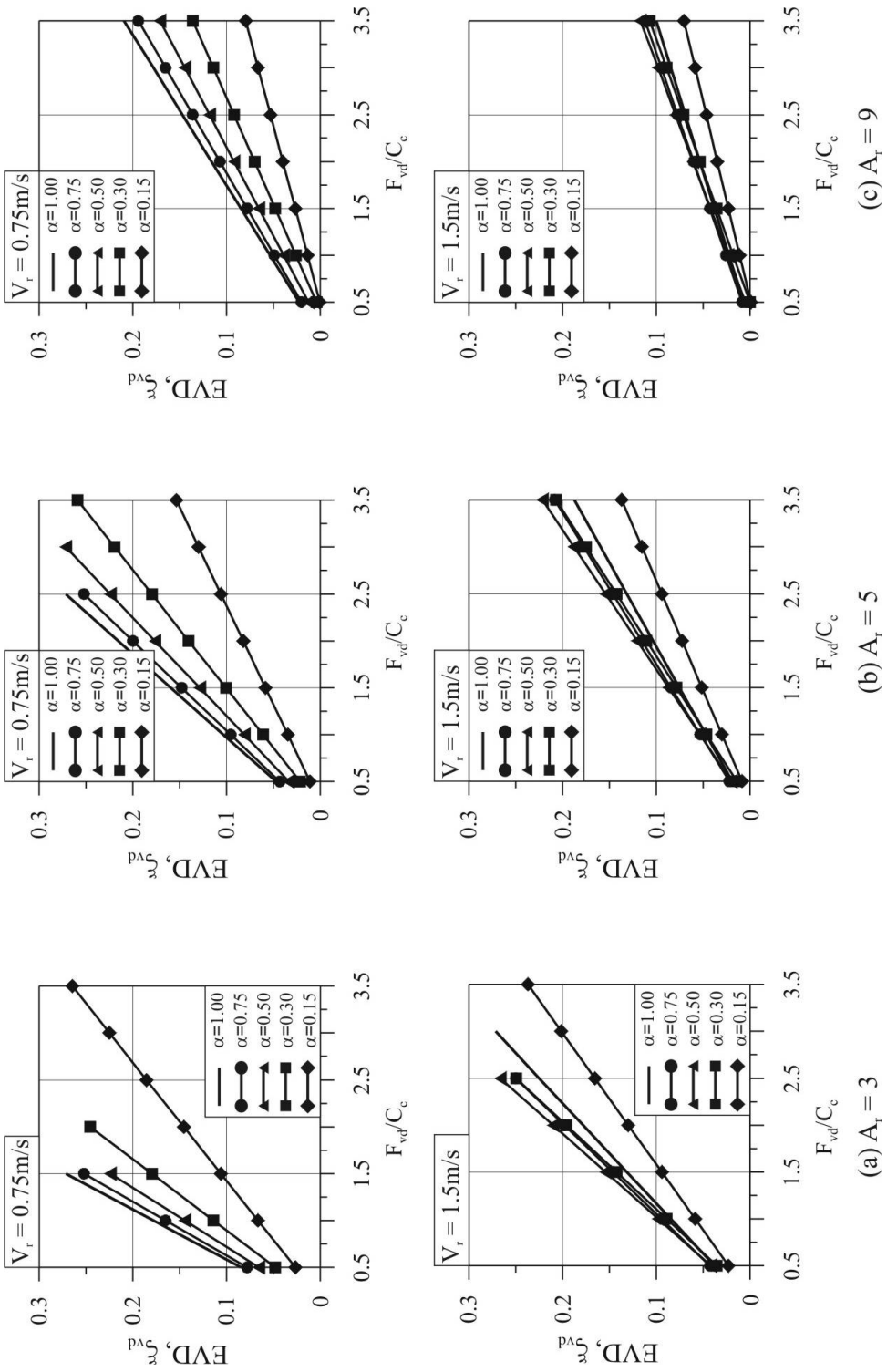

Figure 8.26 Relationship between EVD and the total (local) damping force for *far-field* seismicity as a function of the aspect ratio, A_r

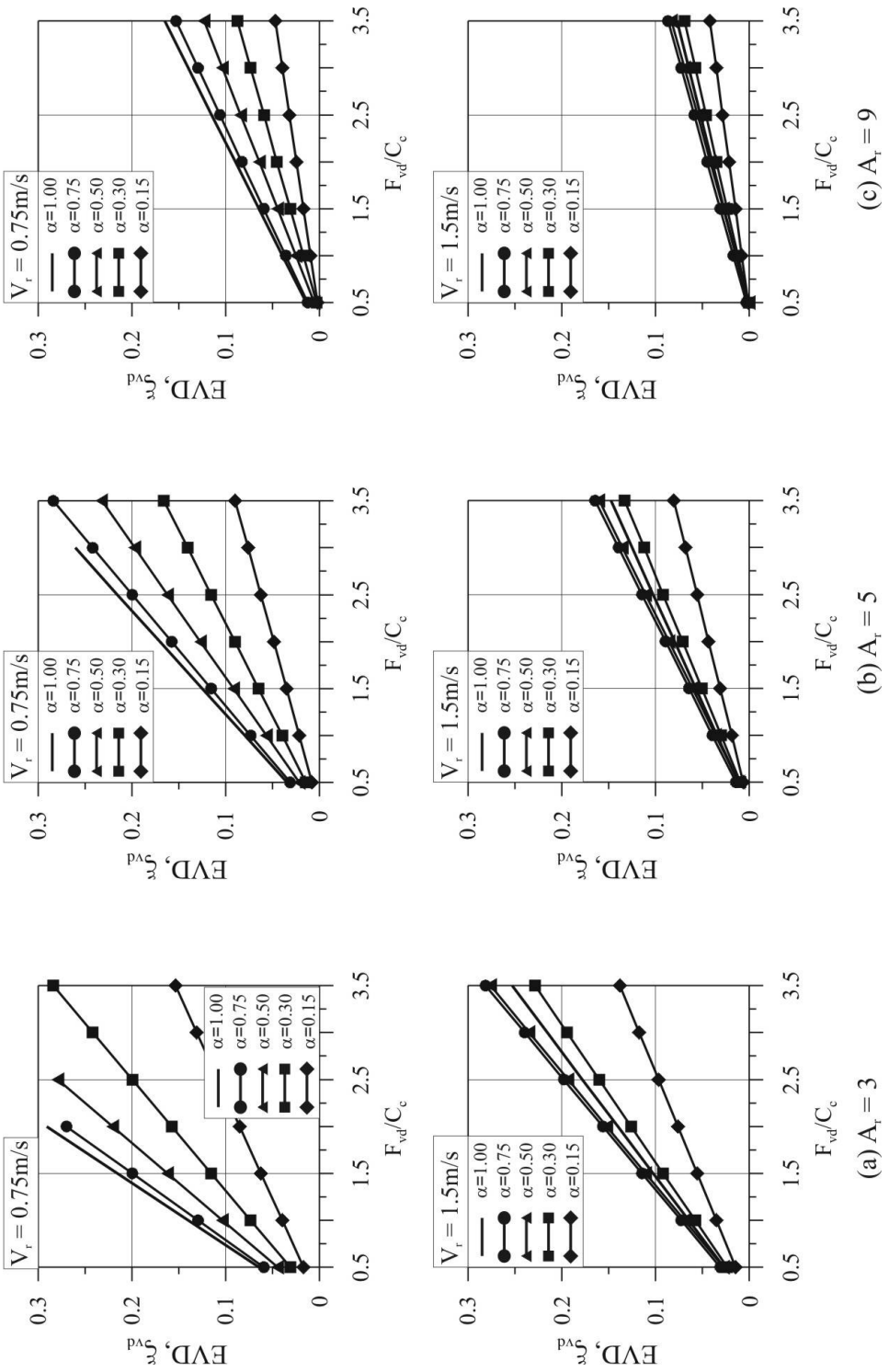

Figure 8.27 Relationship between EVD and the total (local) damping force for *near-field* seismicity as a function of the aspect ratio, A_r

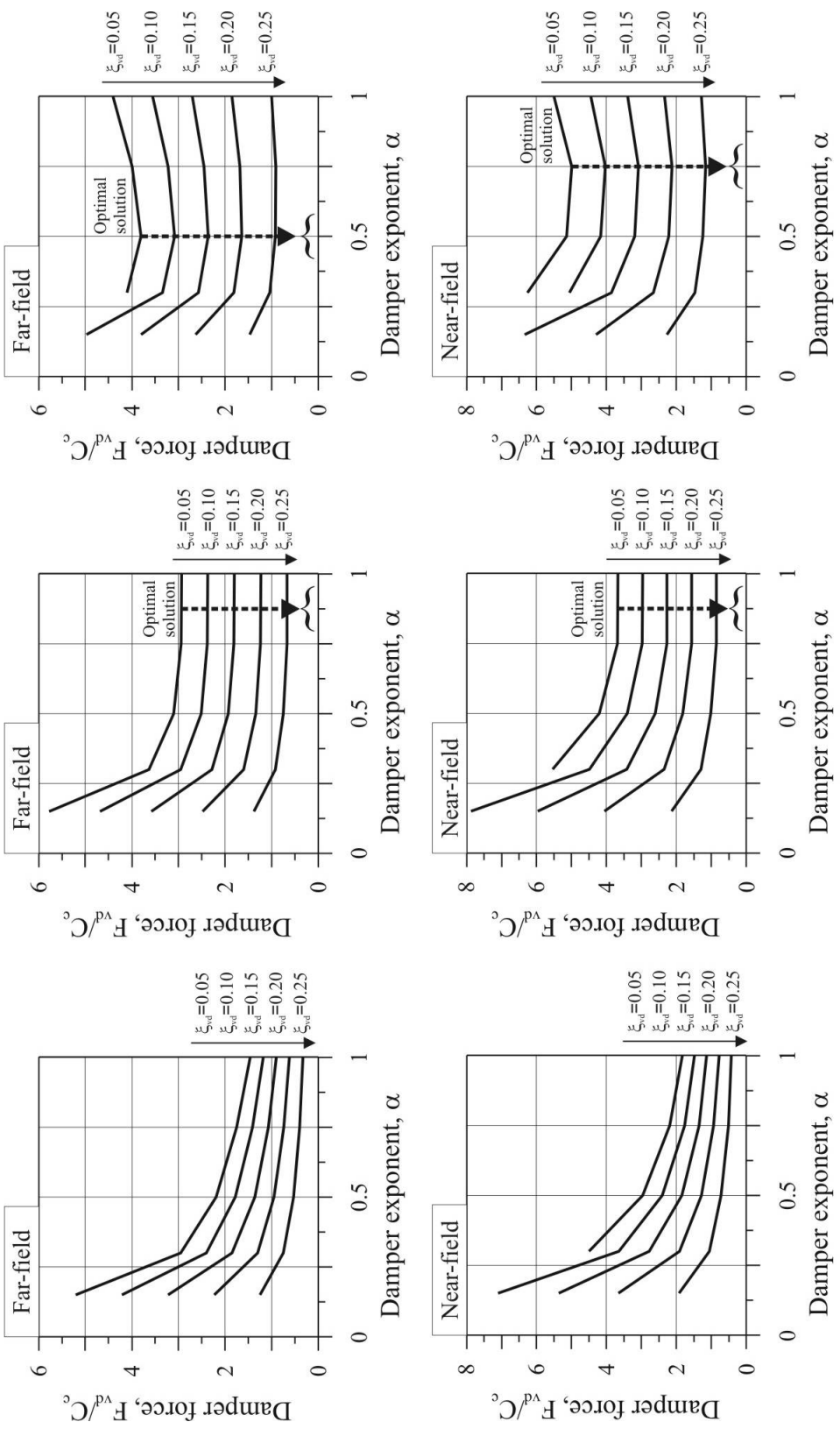

Figure 8.28 Relating damper force to damper exponent as a function of velocity demand to determine the most optimal solution (aspect ratio equal to Ar=5)

8.4. A VISCOUS DIRECT DISPLACEMENT-BASED DESIGN (VISCOUS-DDBD) PROCEDURE

In this section, a Direct Displacement-Based Design (DDBD) procedure is described with reference to a precast rocking wall structure having unbonded post-tensioned tendons and non-linear viscous damper devices located at the foundation level. The general procedure is termed Viscous-DDBD. Details of the precast wall, the mechanics of the rocking interface and the details of the viscous damper assembly are illustrated in Figure 8.29.

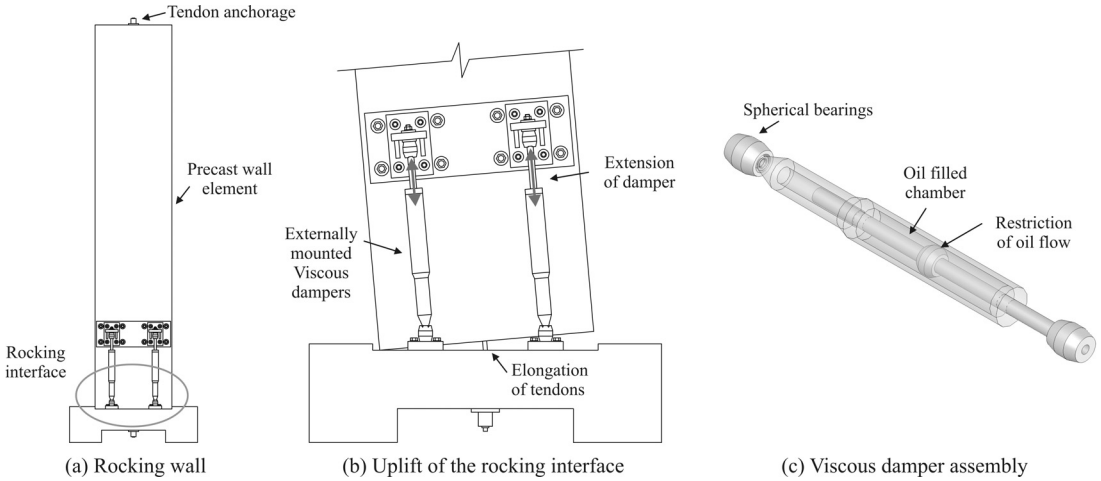

Figure 8.29 Schematic of a hybrid rocking system with viscous dampers located at the rocking interface

An overview of the design procedure is discussed below. Two design methods are presented in flowcharts within Figure 8.32 and Figure 8.33, while a worked example is presented in Appendix E.

Step 1. Defining the SDOF system.

As per Figure 8.30 the MDOF system is converted to an equivalent SDOF based on the elastic first mode-shape at the target displacement. Eq.(8.28), (8.29) and (8.30) are used to determine the effective mass, effective height and displacement of the effective mass respectively.

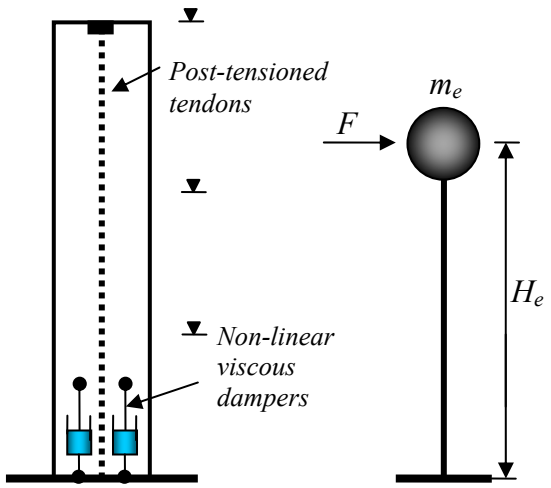

(a) MDOF structure (b) SDOF substitute

$$m_e = \frac{\sum_{i=1}^{n} m_i H_i}{\Delta_d} \qquad \textbf{8.28}$$

$$H_e = \frac{\sum_{i=1}^{n} m_i \Delta_i H_i}{\sum_{i=1}^{n} m_i \Delta_i} \qquad \textbf{8.29}$$

$$\Delta_d = \frac{\sum_{i=1}^{n} m_i \Delta_i^2}{\sum_{i=1}^{n} m_i \Delta_i} \qquad \textbf{8.30}$$

(c) SDOF effective properties

Figure 8.30: Conversion of the MDOF system to a SDOF system

Step 2. Local-to-Global Damper Properties

The parameter β_{vd}, defining the ratio between the global (system) damper coefficient C_{VD} and the local damper coefficient c_{vd}, is computed from the detailed expression of Eq.(8.31) or the approximate relationship of Eq.(8.32) and Figure 8.24. The ratio of c_{vd} and C_{VD} is a function of the aspect ratio A_r of the section, the non-linearity of the viscous damper α and the number of dampers within the section n_{vd}. The system damping coefficient C_{VD} is computed from Eq.(8.33).

$$\beta_{vd} = \frac{C_{VD}}{c_{vd}} = n_{vd}\left(\frac{jD}{H_e}\right)\cdot\gamma_{vd} \qquad \textbf{8.31}$$

$$\beta_{vd} = \frac{C_{VD}}{c_{vd}} = a\cdot n_{vis}\left(A_r\right)^{-(1+\alpha)} \qquad \textbf{8.32}$$

$$C_{VD} = \beta_{vd} c_{vd} \qquad \textbf{8.33}$$

Step 3. Defining the Equivalent Viscous Damping ξ_{eq} and the Effective Period T_e

The system damping C_{VD} is normalised with respect to critical damping C_c of the system, defining the supplementary damping ratio (SDR) Ω in Eq.(8.34). The elastic damping ξ_{el} is added to the proportion of EVD associated with the supplementary dampers ξ_{vd} to evaluate Ω considering spectral displacement and spectral velocity in

Eq.(8.35) & Eq.(8.36) respectively. The coefficients a_1 and a_2 are summarised in Table 8.4.

$$\Omega = C_{VD} / C_c \qquad \textbf{8.34}$$

$$\xi_{eq}^{disp} = a_1 \Omega + \xi_{el} \qquad \textbf{8.35}$$

$$\xi_{eq}^{vel} = b_1 \Omega + \xi_{el} \qquad \textbf{8.36}$$

Step 4. Damped Design Spectrum

The spectral reduction factor η_{disp} and η_{vel} is computed in order to reduce the 5% design displacement spectrum $\Delta(T,5\%)$ from (Eq.(8.37)) and the design pseudo-velocity spectrum $v(T,5\%)$ from (Eq.(8.38)). The target displacement Δ_d is located along the damped design spectrum and the effective period T_e is determined (refer Figure 8.31).

$$\eta_{disp} = \sqrt{\frac{0.07}{0.02 + \xi_{eq}^{disp}}} \qquad \textbf{8.37}$$

$$\eta_{vel} = \sqrt{\frac{0.07}{0.02 + \xi_{eq}^{vel}}} \qquad \textbf{8.38}$$

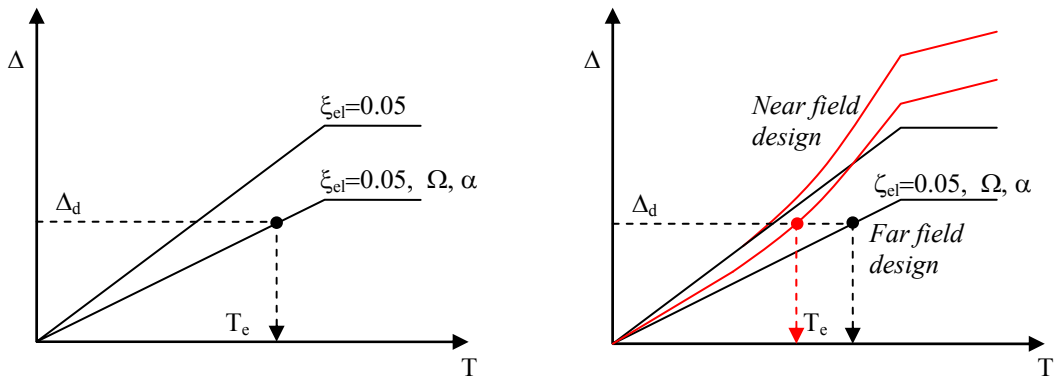

(a) Design Displacement Spectra

(b) Near-field and Far-Field Design Displacement Spectra

Figure 8.31: Design displacement spectra for viscously damped systems

Step 5. Base Shear Calculation

The effective (secant) stiffness K_e is determined from the effective period T_e in Eq.(8.39). The secant stiffness K_e is multiplied by the design displacement Δ_d of the

SDOF system, which equates to the base shear V^*. A base shear reduction factor ϕ_{BL} is applied to define the design base shear V_b in Eq.(8.40). This base shear reduction factor recognises the reduction in displacement of a bilinear-elastic system when compared to an equivalent elastic system to which the damped design equations were calibrated to. The base shear reduction factor ϕ_{BL} is summarised in Table 8.5 and Table 8.6.

$$K_e = 4\pi^2 m_e / T_e^2 \quad \textbf{8.39}$$

$$V_b = \phi_{BL} K_e \Delta_d \quad \textbf{8.40}$$

Following the above design procedure, two detailed approaches are developed; both methods are based on a target inter-storey drift θ_d defining a design displacement Δ_d.

Design Method A targets a specific level of EVD ξ_{eq} and then designs the properties of the damper (c_{vd}, α) and the post-tensioning to satisfy this level of damping. This design method is illustrated via the flowchart in Figure 8.32.

Design Method B is based on pre-defined damper properties (c_{vd}, α). The selected damper properties define the level of EVD ξ_{eq}. This method is presented in Figure 8.33.

Design Method A

Input design parameters: Target rotation θ_d and the target equivalent viscous damping (EVD), ξ_{eq}

Step 1

Determine the SDOF parameters: $m_e = \dfrac{\sum_{i=1}^{n} m_i H_i}{\Delta_d}$ $H_e = \dfrac{\sum_{i=1}^{n} m_i \Delta_i H_i}{\sum_{i=1}^{n} m_i \Delta_i}$ $\Delta_d = \dfrac{\sum_{i=1}^{n} m_i \Delta_i^2}{\sum_{i=1}^{n} m_i \Delta_i}$

Step 2

Determine the spectral reduction factor: $\eta = \sqrt{\dfrac{0.07}{0.02+\xi_{eq}}}$

Step 3

Reduce the elastic design displacement spectrum by η and compute the effective period $\mathbf{T}_e$ from Δ_d

Step 4

Determine the effective stiffness ($K_e = 4\pi^2 m_e T_e$), the base shear reduction factor ϕ_{BL} (Table 8.5 and 8.6) and compute the design base shear, $V_b = \phi_{BL} K_e \Delta_d$

Step 5

Compute the system critical damping C_c, followed by the system supplementary damping coefficient C_{VD} from the specified level of EVD ξ_{eq} using Eq.(8.7), note that a decision must be made on the velocity exponent of the damper in order to define the coefficient $\boldsymbol{a_1}$ below.

$$C_c = 2\sqrt{m_e K_e} \qquad C_{VD} = \left(\xi_{eq} - \xi_{el}\right)\frac{C_c}{a_1}$$

Step 6

Determine the parameter β_{vd} defining the ratio between the global-to-local damping coefficient estimated from Figure 8.23 (right) or from Eq.(8.19) below, where $\boldsymbol{a}$ is a constant from Table 8.7. Compute the local damping coefficient of the supplementary dampers $\mathbf{c_{vd}}$.

$$\beta_{vd} = a \cdot n_{vis} \left(A_r\right)^{(1+\alpha)} = C_{VD}/c_{vd}$$

$$c_{vd} = C_{VD}/\beta_{vd}$$

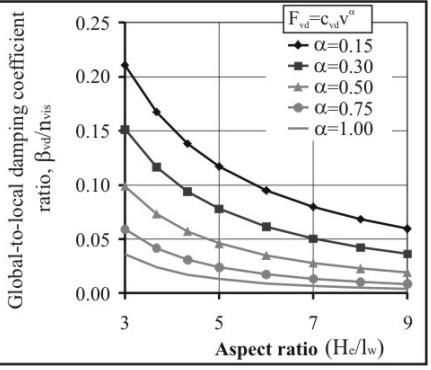

Step 7

The EVD associated spectral displacement and spectral velocity is computed from Eq.(8.5) & (8.6) respectively. Compute the corresponding spectral reduction factors η_{disp} and η_{vel}. Determine the design velocity v_r at the intermediate displacement Δ_r.

$$\xi_{eq}^{disp} = a_1 \frac{C_{VD}}{C_c} + \xi_{el} \qquad \eta_{disp} = \sqrt{\frac{0.07}{0.02+\xi_{eq}^{disp}}}$$

$$\xi_{eq}^{vel} = b_1 \frac{C_{VD}}{C_c} + \xi_{el} \qquad \eta_{vel} = \sqrt{\frac{0.07}{0.02+\xi_{eq}^{vel}}}$$

$$v_r = \Delta_d \frac{2\pi}{T_e}\left(\frac{\eta_{vel}}{\eta_{disp}}\right)\frac{1}{\sqrt{2}}$$

Step 8

Determine the average velocity of the supplementary dampers from Figure 8.22 or in detail from Appendix E. Alternatively, by estimating the internal lever arm to the centroid of the resultant damper force **jD** an approximate formula can be used to determine the average velocity. Determine the total resultant damper force $\mathbf{F_{vd}}$ (and hence approximate the individual damper force) to be sized and priced.

$$\bar{v}_{vd} \approx \frac{jD}{H_e} v_r \qquad F_{vd} = n_{vd} c_{vd} \bar{v}_{vd}$$

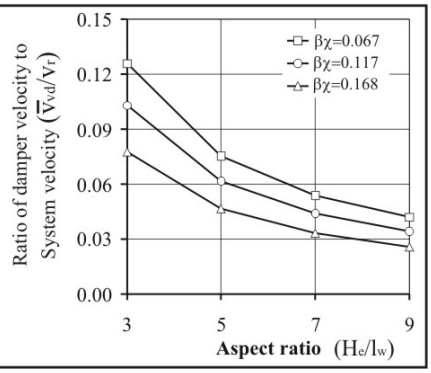

Figure 8.32 Design Method A for post-tensioned viscous systems

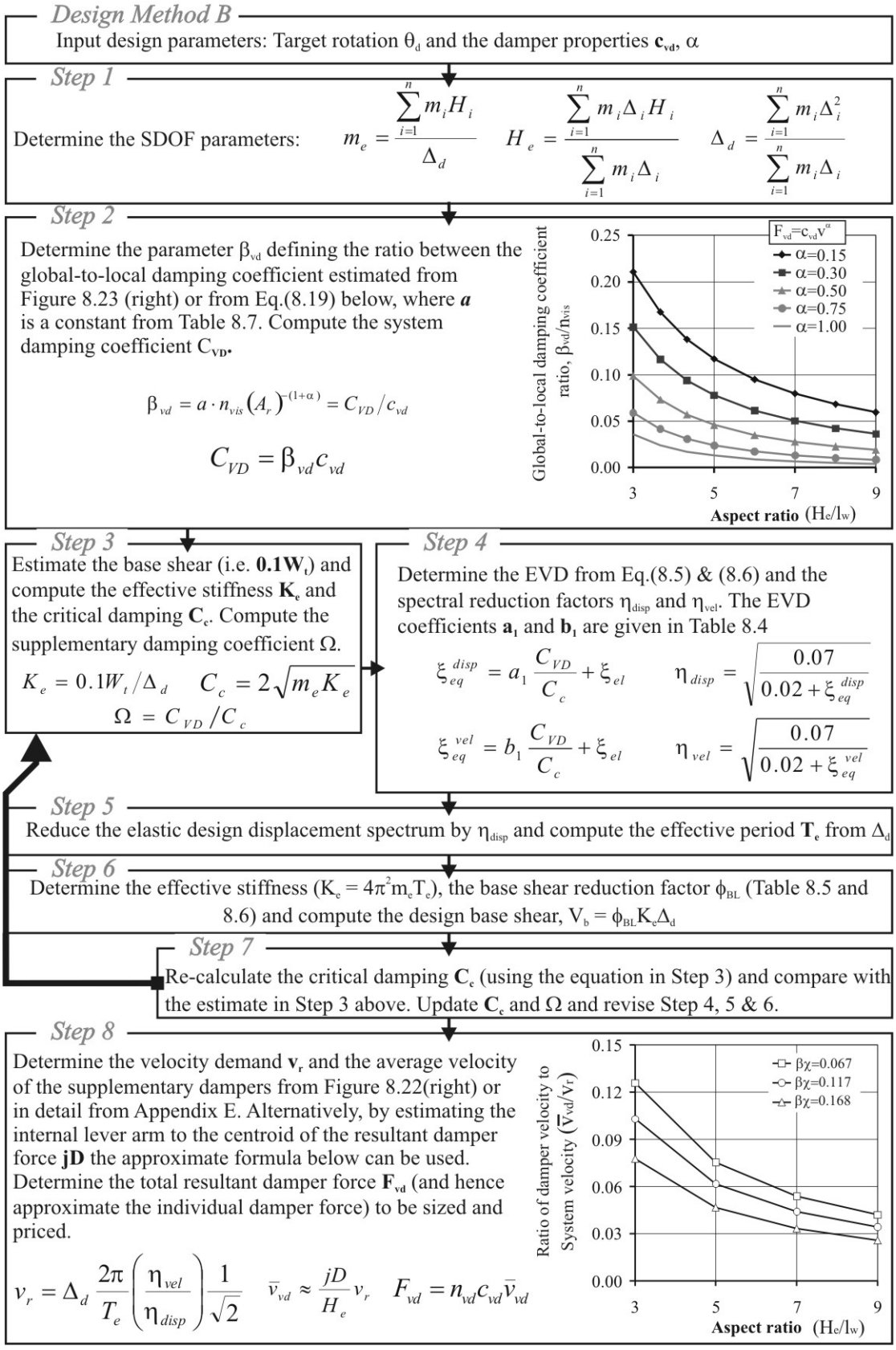

Figure 8.33 Design Method B for post-tensioned viscous systems

8.5. TIME HISTORY DESIGN VERIFICATION

Three prototype post-tensioned viscous wall systems were designed for far-field and near-field seismicity, resulting in a total of six prototype walls. A target rotation of 1% was chosen for design; although, specific to prototype 3, this was reduced to 0.725% as the target displacement was controlled by the corner period of the displacement spectrum. For simplicity the precast wall unit was assumed to be rigid, i.e. elastic flexural displacements were ignored, essentially reducing the MDOF system to a SDOF system. A summary of the properties of each wall unit is given in Table 8.8.

Table 8.8 Details of the prototype walls to verify the design procedure

	 **Prototype 1 (3 levels @ 3m)**	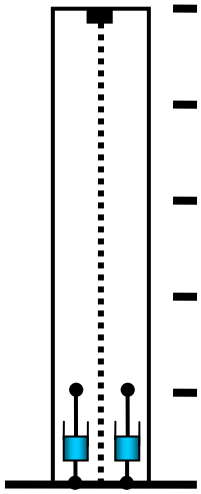 **Prototype 2 (5 levels @ 3m)**	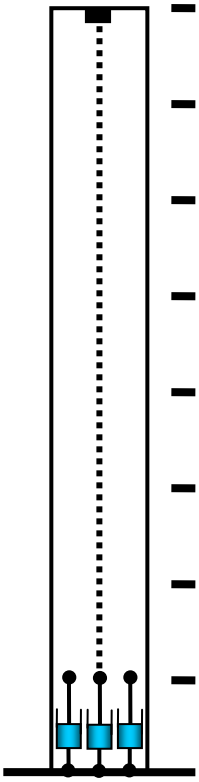 **Prototype 3 (8 levels @ 3m)**
H_n [m]	9	15	24
l_w [m]	1.8	2.5	3.5
t_w [m]	0.25	0.25	0.25
m_i	15 tonne	20 tonne	25 tonne
n_{vis}	1	2	3
n_{vd}	2	4	6
α	0.30	0.50	0.75
Ω	0.05	0.15	0.30

A summary of the design output, following the proposed design procedure above, is tabulated in Table 8.9. Furthermore, a worked design example of Prototype 2 under near-field seismicity (P2NF) is provided in Appendix E. A detailed section analysis was carried out for each post-tensioned wall based on modelling techniques discussed

in Chapter 7 to accurately determine the damping and spring properties to be implemented within the non-linear time history program Ruaumoko, Carr [2005]. In doing so, the amount of prestressing steel, initial prestress and the damping coefficient were determined for each post-tensioned wall. The two lateral load resisting components (post-tensioning and viscous) were calibrated to an appropriate hysteretic model. A bilinear-elastic spring was used to model the post-tensioning component and a viscous dashpot element was used to model the non-linear viscous damper component. Each prototype was subjected to the same 15 far-field and 15 near-field records used in the THA calibration of Section 8.2.

From the THA, the mean of the maximum displacement response $\Delta_{eq,ave}$ is reported in Table 8.10 and compared to the target design displacement Δ_d. The error between the target and recorded displacements are acceptable and are conservative in this case. The displacement error is made up of two components: the first is the error associated with the design procedure itself such as calibration and modelling simplifications. The second error is due to the difference between the design displacement spectrum (defining the target displacement) and the mean earthquake displacement spectrum of the scaled records (defining the demand). A larger displacement error exists for Prototype 1 under near-field ground excitation; being only lightly damped, more scatter was observed in the displacement response leading to a larger error.

Table 8.9 Design summary of the prototypes

	$T_{pt,0}$ [kN]	n_{duc}	$n_{pt\ (total)}$	C_{VD} [kNs$^{\alpha}$/m$^{\alpha}$]	c_{vd} [kNs$^{\alpha}$/mm$^{\alpha}$]	Δ_d [mm]	T_e [sec]	V_b [kN]
P1-FF	539	2	6	24.85	27.33	70	0.975	80.4
P2-FF	578	2	6	77.76	19.26	110	1.983	71.7
P3-FF	775	2	6	202.80	16.45	123.3	2.952	79.5
P1-NF	594	2	6	25.70	28.51	70	0.943	86.6
P2-NF	809	2	8	90.81	23.45	110	1.698	98.0
P3-NF	1374	2	10	264.15	19.46	123.3	2.267	134.8

[1]P1 refers to Prototype 1, ***FF*** & ***NR*** refer to the design according to far-field and near field seismicity respectively

Table 8.10 THA summary

	$\Delta_{eq,ave}$ [mm]	Δ_d [mm]	Error [%]
P1-FF	69.9	70	0.2%
P2-FF	104.6	110	4.9%
P3-FF	119.6	123.3	3.0%
P1-NF	63.0	70	10.1%
P2-NF	106.6	110	3.1%
P3-NF	120.0	123.3	2.7%

8.6. ACCOUNTING FOR ELASTIC DEFORMATIONS IN THE DESIGN OF POST-TENSIONED VISCOUS SYSTEMS

Depending on the structural application (walls, columns, bridge piers etc), elastic displacements may or may not need to be considered. If for example a wall system is to be used as a retrofit intervention for an existing reinforced concrete (RC) frame structure then the interaction between the cantilever displaced shape of the wall and the shear displaced shape of the frame will reduce the elastic deformation of the precast wall unit. However if elastic (flexural) displacements are important, as may be the case in a bridge pier system, then the following section outlines a method to account for elastic displacements within the design procedure above.

Figure 8.34 illustrates the displacement contribution of a post-tensioned (PT) rocking system. It is evident that the angular velocity of the base is directly related to the rigid body displacement Δ_θ at the top of the system h_w. The elastic deformation Δ_e due to flexure (and shear) does not induce any fixed-end rotation at the base. With this said, for a given displacement demand (and hence velocity demand), the elastic proportion should be deducted from the total displacement in order to determine the angular displacements and velocities at the rocking base.

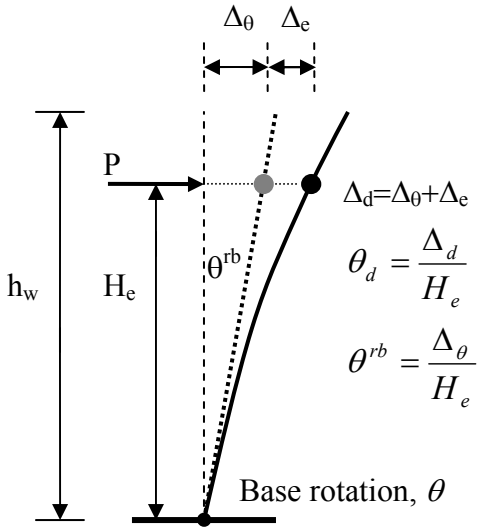

Figure 8.34: Displacement contributions of a rocking system

Using simple mechanics a relationship between the rigid body displacement Δ_θ and the total displacement Δ_d can be derived. The total displacement can be written as follows

$$\Delta_d = \Delta_\theta + \Delta_e = \theta H_e + \frac{PH_e^3}{3E_c I_e} \qquad \textbf{8.41}$$

Rearranging for the ratio between the rigid body displacement and the total displacement,

$$\frac{\Delta_\theta}{\Delta_d} = \frac{\theta h_w}{\theta h_w + \frac{M_i H_e^2}{3E_c I_e}} \qquad \textbf{8.42}$$

Here, M_i is the moment demand at the base of the precast element (which is equal to the moment capacity at the rocking interface) due to the applied load P. The precast element would be designed to satisfy capacity design and will, therefore, consider an over-strength moment at the rocking section. Considering a lower-bound case, the nominal flexural strength of the precast element $M_{n,pc}$ can be assumed to equal the moment at the base M_i multiplied by an over-strength factor ϕ_o as follows

$$M_{n,pc} = \phi_o M_i \qquad \textbf{8.43}$$

That is, ϕ_o represents the ratio of the nominal flexural capacity of the precast element $M_{n,pc}$ to the moment at the rocking base M_i. Considering a design moment equal to M_i, the moment demand acting on the precast element can be expressed as a proportion of its nominal flexural capacity. Recognising that the yield curvature ϕ_y is independent of strength and can be estimated from simple formulas (Priestley et al. [2007]), the moment demand acting on the precast element can be expressed as follows

$$M_i = M_{n,pc}/\phi_o \approx \phi_y E_c I_e/\phi_o \approx \frac{2\varepsilon_y}{\phi_o l_w} E_c I_e \qquad \textbf{8.44}$$

Substitution of Eq.(8.44) into Eq.(8.42) defines the rigid body displacement ratio Γ_Δ.

$$\Gamma_\Delta = \frac{\Delta_\theta}{\Delta_d} = \frac{1}{1 + \frac{2\varepsilon_y A_r}{\phi_o 3\theta}} \qquad \textbf{8.45}$$

In this equation ε_y is the yield strain of the longitudinal reinforcement within the precast element and A_r is the loaded aspect ratio (H_e/l_w). The over-strength ratio ϕ_o can be estimated considering a capacity design philosophy. Capacity design will ensure that yielding is confined to flexural yielding at the rocking interface and avoid flexural yielding of the precast element (a shear mechanism will also be avoided). Therefore, considering the nominal moment capacity of the rocking section M_n, the over-strength can be determined based on capacity design principals. The New Zealand concrete standard (NZS3101 [2006]) stipulates that the over-strength moment of a section should consider material over-strength of both the concrete and reinforcement. A concrete over-strength of (f'_c+15)MPa is suggested, while a reinforcement over-strength of $1.25f_y$ for grade 300MPa, $1.35f_y$ for grade 500MPa, and $1.10f_{pt,y}$ for prestressed reinforcement is recommended. With respect to rocking systems, the following comments are made

For hybrid systems having external viscous devices, the device over-strength should consider the uncertainty associated with spectral velocity as this will give rise to larger damper forces. This aleatory over-strength will be more significant for devices with velocity exponents close to $\alpha = 1.0$. In fact, damper over-strength actions resulting from incremental dynamic analysis is studied in further detail in Chapter 11. The conclusion from this study indicates that the over-strength from viscous dampers is no more significant than that of mild steel reinforcement.

For hybrid systems having mild steel TCY devices, the material over-strength will depend on whether grade 300MPa or Grade 500MPa is adopted. Grade 300MPa has more strain ductility than grade 500MPa which may influence the decision to use grade 300MPa. Furthermore, if the characteristic yield strength is adopted and the effect of strain hardening is included within the section analysis to define the characteristic moment capacity then the material over-strength may be relaxed from the suggestions above.

The over-strength resulting from an increase of the concrete compressive strength of 15MPa will depend on the type of analysis undertaken. If the characteristic compressive strength is adopted within the analysis and the effect of confinement is also included, then this consideration may also be relaxed. Furthermore, a concrete strength enhancement of 15MPa may have only a minor effect on the strength enhancement of the section.

For sections comprising of prestressing reinforcement, non-prestressed reinforcement and axial load, then the effective section over-strength factor can be weighted based on the contribution of each component to the total section capacity.

In light of these points, an effective section over-strength action of $\phi_o = 1.25$ would appear a conservative design choice for hybrid systems incorporating non-linear viscous devices with velocity power coefficients less than 1.0 i.e. $\alpha < 1.0$. The nominal moment capacity of the precast element could be estimated from the following

$$M_{n,pc} = \phi_o M_n = 1.25 M_n \qquad \textbf{8.46}$$

Therefore, at the design displacement where $M_i = M_n$

$$\frac{M_i}{M_{n,pc}} = \frac{1}{\phi_o} \qquad \textbf{8.47}$$

The ratio Γ_Δ defined in Eq.(8.45) is plotted in Figure 8.36 as a function of the aspect ratio A_r, mild steel yield strain ε_y, and over-strength ratio ϕ_o. As the strength (and hence stiffness) of the precast element increases, or the base rotation increases, a larger proportion of deformation is attributed to the rigid body rotation at the base.

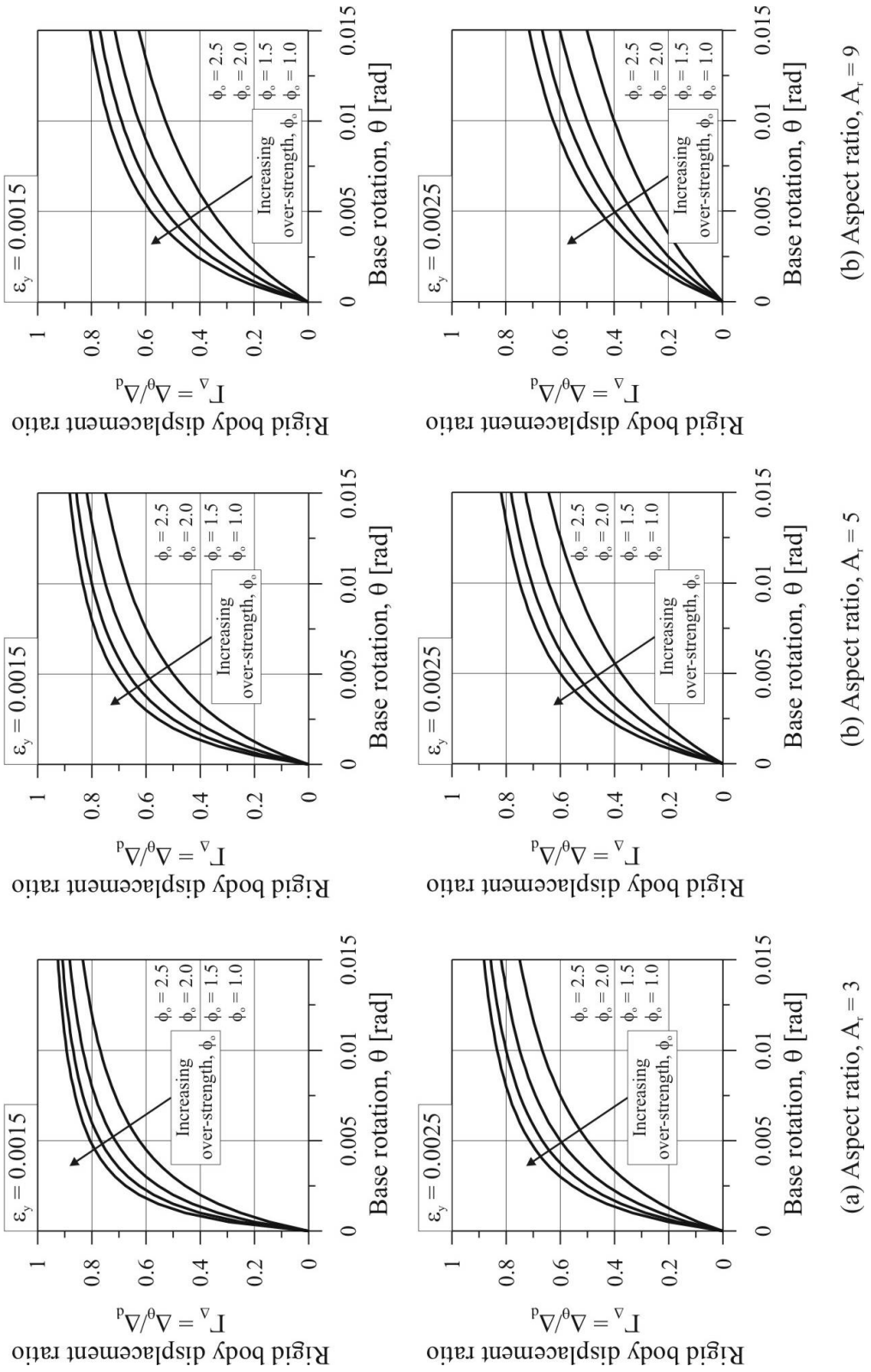

Figure 8.35: Rigid body displacement ratio shown for three aspect ratios and two grades of mild steel reinforcement

8.6.1. Design Parameters to be used Considering Elastic Deformations

To include the effects of elastic deformations, a displacement reduction factor is applied during design. With respect to Figure 8.34, the base rotation θ is equal to the rigid body rotation θ^{rb} . The design base rotation θ can be computed by reducing the system drift ratio $\theta_d = \Delta_d/H_e$ by the rigid body displacement factor Γ_Δ to account for the elastic deformation of the precast element.

$$\theta = \Gamma_\Delta \theta_d = \Gamma_\Delta \frac{\Delta_d}{H_e} \qquad 8.48$$

Similarly, the angular velocity of the rocking base is reduced as follows

$$\omega = \Gamma_\Delta \frac{\Delta_d}{H_e} \frac{2\pi}{T_e} \qquad \textbf{8.49}$$

The geometric constant that relates the average velocity of the damper group to the system velocity, discussed in Section 8.3, is repeated below

$$\gamma_{vd} = \left(\frac{\bar{v}_{vd}}{v_r} \right)^\alpha \qquad \textbf{8.50}$$

To account for flexural deformations the constant γ_{vd} is reduced by Eq.(8.51) to recognise a reduction in damper velocity $\bar{v}_{vd}$. The superscript e indicates that elastic flexural deformations are accounted for.

$$\gamma_{vd}^e = \gamma_{vd} \cdot \left(\Gamma_\Delta \right)^\alpha \qquad \textbf{8.51}$$

The parameter β_{vd} that relates the global system damping coefficient C_{VD} to the local damping coefficient c_{vd} is repeated below

$$\beta_{vd} = \frac{C_{VD}}{c_{vd}} \qquad \textbf{8.52}$$

Due to elastic deformations, β_{vd} is reduced according to Eq.(8.53) to recognise that the dampers have become less effective, resulting in a reduction to the equivalent system damping coefficient C_{VD}.

$$\beta_{vd}^e = \beta_{vd} \cdot \left(\Gamma_\Delta \right)^\alpha \qquad \textbf{8.53}$$

8.6.2. Design Considerations for Equivalent Viscous Damping of a System with Elastic Deformations

If the elastic deformations of the precast element are accounted for, then the damping associated with the rocking connection and the damping associated with the elastic displacements should be weighted based on the proportion of strain energy associated with each component. In this case, the system is essentially comprised of two springs in series: one spring representing the rigid rocking body, the other representing the precast element. This concept is analogous to that used in DDBD to account for damping associated with foundation flexibility, Priestley et al. [2007]. Hence, the total EVD ξ_{eq} of the system can be computed from the following equation

$$\xi_{eq} = \frac{\xi_{vd}\Delta_\theta + \xi_{el}\left(\Delta_e + \Delta_\theta\right)}{\Delta_\theta + \Delta_e} \qquad \textbf{8.54}$$

Where,

ξ_{eq} = the total system EVD

ξ_{vd} = the total damping associated with the rocking connection (this could be attributed to both viscous and hysteretic dampers as in Chapter 9)

ξ_{el} = the elastic damping associated with the elastic deformation of the precast element

Δ_θ = the displacement associated with the rigid rotation of the base

Δ_e = the elastic displacement of the precast element. The total displacement of the system is a summation of Δ_θ and Δ_e.

8.7. CONCLUSIONS

A Direct-Displacement Based Design (DDBD) was developed for post-tensioned connections with viscous dampers, termed DDBD-viscous. Two single-degree-of-freedom (SDOF) design methods are presented: both procedures consider two fundamental steps

1. The properties of the dampers at the rocking connection (the damping coefficient c_{vd} and the velocity exponent α) are converted to an equivalent damping coefficient C_{VD} at the effective height of the SDOF system.
2. The design displacement and velocity spectrum are reduced according equivalent viscous damping (EVD) equations calibrated from time-history analysis and depend entirely on the equivalent damper coefficient C_{VD} (normalised to the critical damping of the system C_c) and the velocity exponent α.

The design procedure is iterative as the critical damping C_c must be defined prior to design. To start with C_c is estimated from a design base shear of $V_b = 0.1W_t$, where an updated value is computed from $C_c = 2\sqrt{m_e K_e}$.

The damping of a non-linear viscous system is less effective for near-field ground motions. Hence, the amount of equivalent viscous damping (EVD) associated with a non-linear viscous system reduces if considering near-field seismic hazards. Furthermore, separate spectral reduction factors are defined for velocity and displacement.

As calibration of the spectral reduction was performed on a linear elastic system with non-linear dampers, a base shear reduction factor ϕ_{BL} was introduced (based on calibration) to account for the expected reduction in response of an equivalent bilinear system. Moreover, an intermediate design displacement is introduced Δ_r to enable the design of the system to be carried out considering a non-zero velocity. This is necessary to design the non-linear dampers within the section.

By considering the mechanics of a rocking post-tensioned system, the local damping coefficient of the dampers was related to an equivalent system damping coefficient: this ratio was primarily dependant on the aspect ratio of the section and the velocity exponent α of the non-linear dampers. Furthermore, the damper velocity was found to be only a fraction of the system velocity (5-15%), being roughly inversely proportional to the aspect ratio of the section.

Through parametric analyses it was revealed that, in general, a non-linear damper with a velocity exponent of $\alpha = 0.75$ is the optimal choice in terms of requiring the smallest damper force that is required to achieve a given level of EVD. Through time-history analyses of six prototype post-tensioned viscous systems, the design procedure was found to be very accurate, with the largest displacement error being 10%.

8.8. REFERENCES

Bommer, J. and Mendis, R. (2005). "Scaling of Spectral Displacement Ordinates with Damping Ratios." *Earthquake Engineering and Structural Dynamics*, 34, 145-165.

Carr, A. (2005). "RUAUMOKO." Christchurch, Inelastic Dynamic Analysis.

Eurocode:8. (1998). "Design Provisions for Earthquake Resistance of Structures - Part 1: General rules, seismic actions and general requirements for structures." CEN/TC 250, Brussels.

NZS1170.5. (2004). "Structural Design Actions, *Part 5: Earthquake actions*." Standards New Zealand, Wellington.

NZS3101. (2006). "Concrete Structures Standard: Part 1-The Design of Concrete Structures." Standards New Zealand, Wellington.

Pekcan, G., Mander, J. B. and Chen, S. S. (1999). "Fundamental considerations for the design of non-linear viscous dampers." *Earthquake Engineering & Structural Dynamics*, 28(11), 1405-1425.

Pettinga, J. and Priestley, M. J. N. (2005). "Dynamic behaviour of reinforced concrete frames designed with direct displacement-based design." ROSE Research Report No 2005/02, ROSE school, Pavia.

Priestley, M. J. N. (2003). *Myths and Fallacies in Earthquake Engineering, Revisited*.

Priestley, M. J. N., Calvi, G. M. and Kowalsky, M. J. (2007). *Displacement-Based Seismic Design of Structures*, IUSS, Pavia.

Sullivan, T. J., Priestley, M. J. N. and Calvi, G. M. (2006). "Seismic Design of Frame-Wall Structures." Research Report ROSE-2006/02, European School for Advanced Studies in Reduction of Seismic Risk, Pavia.

Whittaker, A. S., Constantinou, M. C., Ramirez, O. M., Johnson, M. W. and Chrysostomou, C. Z. (2003). "Equivilent Lateral Force and Modal Analysis Procedures of the 2000 NEHRP Provisions for Buildings with Damping Systems." *Earthquake Spectra*, 19, 959-980.

9. Direct Displacement-Based Design of Post-Tensioned Rocking Systems, Part II: SDOF Systems with Viscous and Hysteretic Dampers

9.1. INTRODUCTION

In Chapter 8 a Direct Displacement-Based Design (DDBD) procedure was developed for post-tensioned rocking systems with non-linear viscous dampers (termed Viscous-DDBD). This chapter extends the design procedure to include SDOF systems having a combination of non-linear viscous dampers and hysteretic dampers. The procedure focuses on applications to SDOF systems (MDOF systems are dealt within in the following Chapter), where the design procedure is verified using six prototype post-tensioned wall structures.

9.2. DIRECT DISPLACEMENT-BASED DESIGN OF POST-TENSIONED ROCKING SYSTEMS WITH HYSTERETIC DAMPING

An overview of DDBD specific to hysteretic systems was discussed in Chapter 3. However, what was not discussed in detail was the calculation of equivalent viscous damping (EVD). For traditional reinforced concrete (RC) or structural steel structures, the equivalent viscous damping is related to the displacement ductility μ_Δ of the system through a number of equations calibrated from non-linear time-history (NLTH) analyses; Blandon and Priestley [2005] and Priestley et al. [2007]. For MDOF systems, the displacement ductility is defined as the target displacement (at the effective height of the structure) divided by the equivalent yield displacement (also determined at the effective height of the structure)

$$\mu_\Delta = \frac{\Delta_d}{\Delta_y} \tag{9.1}$$

For RC frame structures the EVD is based on a "Fat" Takeda (TF) hysteresis rule, defined by

$$\xi_{eq} = 0.05 + 0.565\left(\frac{\mu_\Delta - 1}{\mu_\Delta \pi}\right) \tag{9.2}$$

For RC wall structures or bridges, the EVD is based on a 'Thin' Takeda (TT) hysteresis rule to account for a proportion of axial load acting on the section.

$$\xi_{eq} = 0.05 + 0.444\left(\frac{\mu_\Delta - 1}{\mu_\Delta \pi}\right) \quad \textbf{9.3}$$

Finally, for steel framed structures, the EVD is based on a Ramberg Osgood (RO) hysteresis rule, defined by

$$\xi_{eq} = 0.05 + 0.577\left(\frac{\mu_\Delta - 1}{\mu_\Delta \pi}\right) \quad \textbf{9.4}$$

The extension of the DDBD procedure to include post-tensioned hybrid systems is relatively minor. The refinement relates to the calculation of the equivalent yield displacement and the EVD, Palermo et al. [2005]. The yield rotation θ_y of a hybrid post-tensioned section can be estimated from

$$\theta_y = K_{\theta,yield}\frac{\varepsilon_y H_e}{D} \quad \textbf{9.5}$$

Where:

- $K_{\theta,yield}$ = a constant depending on the section geometry (square, rectangular etc)
- ε_y = the yield strain of the internally grouted mild steel crossing the rocking interface
- H_e = the effective height of the structure
- D = the cross-section length of the rocking section

Ignoring elastic displacements the ductility can be estimated from the lateral drift ratio of the structure $\theta_d = \Delta_d / H_e$.

$$\mu_\Delta \approx \frac{\theta_d D}{K_{\theta,yield}\varepsilon_y H} \quad \textbf{9.6}$$

Palermo et al. [2005] found that $K_{\theta,yield} \approx 0.5$ for square sections and 0.48 for rectangular sections. It should be recognised that if $K_{\theta,yield}$ is calibrated to the yield drift of the structure to include elastic deformations (as opposed to the yield rotation of the connection), then the validity of Eq.(9.6) will improve.

The EVD of a post-tensioned hybrid system is related to the displacement ductility μ_Δ of the system and the moment ratio λ. The moment ratio (also termed the re-centring ratio) is defined as the post-tensioned and axial load moment contribution divided by the hysteretic moment contribution (see Eq.(9.7)).The λ ratio can be expressed as a moment ratio of the rocking section (i.e. at a connection level) as in Eq.(9.7) or at a global ratio defined by the over-turning moment contributions of the system.

$$\lambda = \frac{M_{pt} + M_N}{M_{ms}} \qquad \textbf{9.7}$$

The moment ratio λ is used as a weighting factor to estimate the proportion of EVD associated with the hysteretic moment contribution M_{ms} and the non-linear elastic moment contribution M_{pt}+M_N. With reference to Eqs.(9.2) to (9.4), the EVD of a post-tensioned system is summarised in the following form (which adopts 5% damping for the PT component)

$$\xi_{eq} = \frac{\lambda}{1+\lambda}0.05 + \frac{1}{1+\lambda}\left(0.05 + R_\xi\left(\frac{\mu_\Delta - 1}{\mu_\Delta \pi}\right)\right) \qquad \textbf{9.8}$$

Where R_ξ depends on the type of hysteretic dissipation located at the rocking interface

R_ξ = 0.565 for internally grouted mild steel dissipation (TF)
R_ξ = 0.577 for externally mounted mild steel yielding devices (RO)
R_ξ = 0.670 for externally mounted friction devices (EPP)

9.3. DDBD OF POST-TENSIONED ROCKING SYSTEMS WITH VISCOUS AND HYSTERETIC DAMPING

The extension of the procedure to include both hysteretic damping and viscous damping involves the summation of two EVD contributions. The lateral response of a generic post-tensioned viscous-hysteretic system is presented in Figure 9.1(a). The three components providing lateral resistance are shown in Figure 9.1(b): the non-linear elastic post-tensioned component; the non-linear inelastic hysteretic steel component and the linear or non-linear viscous component. The hysteretic and viscous elements act in parallel to one another; therefore, the total absorbed energy (the area beneath the force-displacement response) is a straight summation of the two components (see Figure 9.1(c)).

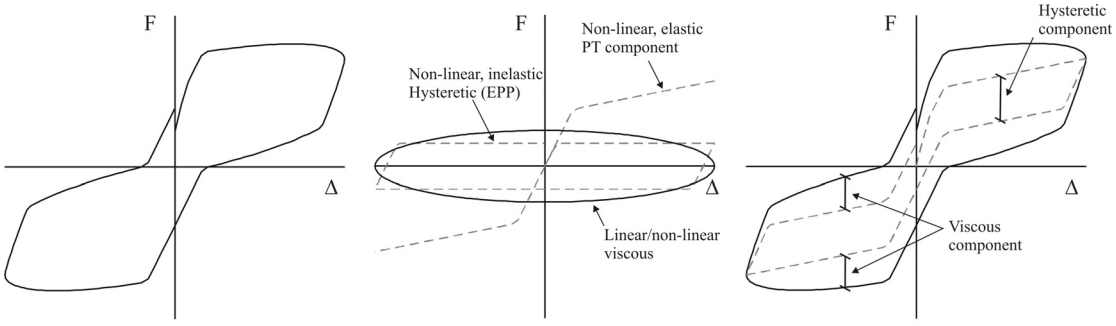

Figure 9.1 Disaggregated response of a post-tensioned system with viscous and hysteretic energy dissipation

9.3.1. Elastic Damping Component of EVD, ξ_{el}

For hysteretic systems, the EVD formulations in Eqs.(9.2) to (9.4) include both the elastic damping ξ_{el} and hysteretic damping ξ_{hyst} within a single equation. If the hysteretic component of EVD is defined separately (discussed in Section 9.3.3), then the elastic damping component must also be treated separately. Blandon and Priestley [2005] relate the secant damping of the equivalent elastic system to a tangent stiffness damping model. If an elastic damping ratio of 0.05 is assumed then the elastic component of EVD ξ_{el} is given by

$$\xi_{el} = 0.05\mu^{\lambda} \qquad \textbf{9.9}$$

Where λ, in this case, is a parameter relating tangent stiffness damping to secant stiffness damping and μ is the ductility of the system. For flag-shape hysteresis behaviour λ=-0.430.

9.3.2. Viscous Damper Component of EVD, ξ_{vd}

Recalling from Chapter 8 the viscous damper component of EVD associated with a reduction in displacement is given by

$$\xi_{vd} = a_1\Omega \qquad \textbf{9.10}$$

When the viscous damper component of EVD is to be associated with a reduction in velocity, the coefficient a_1 is replaced with b_1. The coefficients a_1 and b_1 are listed below in Table 9.1. This velocity/displacement aspect is discussed further in Section 9.3.5.

Table 9.1 EVD coefficients

	Velocity exponent, α							
	1.0-0.75[1]		0.50[1]		0.30[1]		0.15[1]	
a_1	0.880	0.693	0.839	0.602	0.714	0.456	0.440	0.262
b_1	0.642	0.598	0.608	0.526	0.521	0.412	0.341	0.243

[1]Values in the left column relate to far-field seismicity, values in the right column refer to near-field seismicity

The supplementary damping ratio (SDR) Ω is defined as

$$\Omega = \frac{C_{VD}}{C_c} = \frac{\beta_{vd} c_{vd}}{C_c} \qquad \textbf{9.11}$$

C_c is the critical damping of the equivalent elastic system and β_{vd} is a parameter relating the global damper coefficient C_{VD} to the local damper coefficient c_{vd}. An

approximate solution for β_{vd} is given by the following relationship (developed in Chapter 8)

$$\beta_{vd} = \frac{C_{VD}}{c_{vd}} = a \cdot n_{vis} \left(A_r\right)^{-(1+\alpha)} \qquad \textbf{9.12}$$

Where

a = a constant, listed in Table 9.2
n_{vis} = the number of viscous damper layers
A_r = the aspect ratio of the section H_e/D
α = the velocity exponent of the viscous damper

Table 9.2 Constant to be used in conjunction with Equation 9.12

α	a
0.15	0.746
0.30	0.632
0.50	0.514
0.75	0.405
1.00	0.324

The critical damping of the system is computed from

$$C_c = 2\sqrt{m_e K_e} \qquad \textbf{9.13}$$

The effective stiffness K_e is defined by the peak displacement of the system (where the viscous contribution to the lateral resistance is zero). The disaggregated system is illustrated in Figure 9.2 being the summation of a post-tensioned hysteretic system (a) and a viscous system (b).

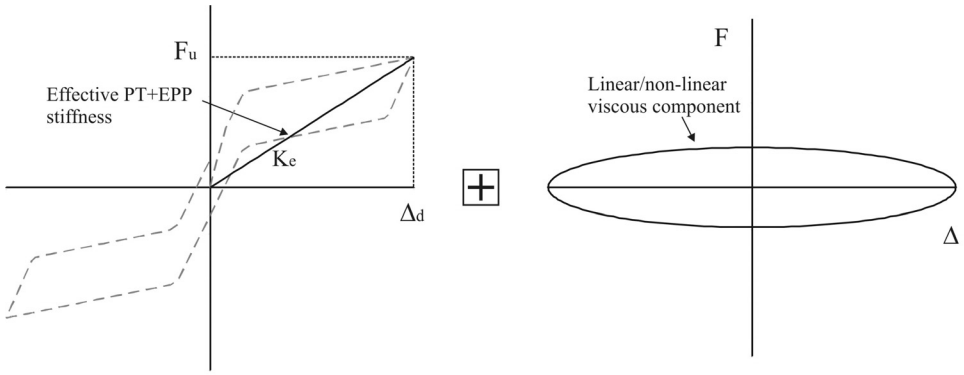

Figure 9.2 Post-tensioned hysteretic system combined with a viscous component

9.3.3. Hysteretic Component of EVD, ξ_{hyst}

Blandon and Priestley [2005] provide more detailed formulations for the hysteretic component of EVD ξ_{hyst} which have both period and ductility dependency. By also combining the post-tensioned moment ratio λ, the hysteretic EVD formulation can be written as

$$\xi_{hyst} = \frac{1}{1+\lambda}\left[a\left(1-\frac{1}{\mu^b}\right)\left(1+\frac{1}{(T_e+c)^d}\right)\right] \qquad \textbf{9.14}$$

Where:

a,b,c,d = constants depending on the hysteresis rule
μ = the system ductility
T_e = the effective period

The EVD coefficients a-d are summarised in Table 9.3.

Table 9.3 Coefficients to determine the hysteretic component of EVD

	a	*b*	*c*	*d*
Internally grouted steel (TF)	0.305	0.492	0.790	4.463
Externally mounted steel (RO)	0.289	0.622	0.856	6.460
Externally mounted friction (EPP)	0.224	0.336	-0.002	0.250

9.3.4. Modifying the Hysteretic Component of EVD for Near-Field Seismicity

In Chapter 8 it was discussed how the spectral reduction factor η in traditional DDBD takes on two forms. With reference to Eq.(9.15) the exponent α is equal to 0.5 for far-field seismicity and 0.25 for near-field seismicity. The procedure developed in Chapter 8 adopts only a single equation with $\alpha = 0.5$. Therefore, to ensure the two procedures (traditional DDBD and Viscous-DDBD) are compatible, a minor modification to the calculation of the hysteretic component of EVD ξ_{hyst} is required when considering design for near-field seismicity.

$$\eta = \left(\frac{0.07}{0.02+\xi_{eq}}\right)^{\alpha} \qquad \textbf{9.15}$$

By manipulating the spectral reduction factor of Eq.(9.15), the two DDBD procedures can become compatible if they adopt the common exponent of $\alpha = 0.5$ in Eq.(9.16), regardless of the seismicity. The manipulation of Eq.(9.15) is outlined in Appendix F with the results summarised below.

$$\eta = \sqrt{\frac{0.07}{0.02 + \xi_{eq}}} \qquad \textbf{9.16}$$

For the design of a post-tensioned viscous-hysteretic system under near-field seismicity, the hysteretic component of EVD ξ_{hyst} is computed in the following way

$$\xi_{hyst} = \left[0.07\left(0.07 + \xi_{hyst,DDBD}\right)\right]^{0.5} - 0.07 \qquad \textbf{9.17}$$

Where

$\xi_{hyst,DDBD}$ = the hysteretic component of EVD computed from Eq.(9.14)
ξ_{hyst} = the modified hysteretic damping component specific to near-field seismicity. For far-field seismicity $\xi_{hyst,DDBD} = \xi_{hyst}$.

9.3.5. Combining the Components of EVD

The total EVD associated with a reduction in displacement is a summation of the three components below: elastic damping ξ_{el}, hysteretic damping ξ_{hyst} and viscous damping $\xi_{vd} = a_1\Omega$.

$$\xi_{eq}^{disp} = \xi_{el} + \xi_{hyst} + a_1\Omega \qquad \textbf{9.18}$$

The total EVD associated with a reduction in spectral velocity is given by Eq.(9.19) below; the difference between Eq.(9.18) & (9.19) being the coefficients a_1 and b_1.

$$\xi_{eq}^{vel} = \xi_{el} + \xi_{hyst} + b_1\Omega \qquad \textbf{9.19}$$

The coefficients a_1 and b_1 are listed in Table 9.1 above as a function of the damper velocity exponent α. Hence, the spectral reduction factor for displacement is given by Eq.(9.20), while the spectral reduction factor for velocity is given by Eq.(9.21).

$$\eta_{disp} = \sqrt{\frac{0.07}{0.02 + \xi_{eq}^{disp}}} \qquad \textbf{9.20}$$

$$\eta_{vel} = \sqrt{\frac{0.07}{0.02 + \xi_{eq}^{vel}}} \qquad \textbf{9.21}$$

9.3.6. Design Displacement for Post-Tensioned Viscous-Hysteretic systems

An intermediate design displacement Δ_r was incorporated into the design of a post-tensioned viscous system in Chapter 8. Similarly, it is incorporated into the design of a post-tensioned viscous-hysteretic system. At the target displacement Δ_d the velocity is zero, hence, the viscous component of lateral resistance is also zero. The

intermediate displacement in Eq.(9.22) allow the viscous dampers to be assessed/designed for some non-zero velocity.

$$\Delta_r = \frac{\Delta_d}{\sqrt{2}} \qquad \textbf{9.22}$$

The system velocity demand v_r at the intermediate displacement Δ_r was derived in Chapter 8 and is reproduced below

$$v_r = \Delta_d \frac{2\pi}{T_e}\left(\frac{\eta_{vel}}{\eta_{disp}}\right)\frac{1}{\sqrt{2}} \qquad \textbf{9.23}$$

All parameters in Eq.(9.23) have been previously defined. In aid of more detailed calculations outlined in Chapter 8, the average damper velocity $\bar{v}_{vd}$ at the rocking interface can be approximated from Eq.(9.24), which requires an estimation of the internal lever arm jD to the centroid of the resultant damper force $\Sigma F_{vd,i}$.

$$\bar{v}_{vd} \approx \frac{jD}{H_e} v_r \qquad \textbf{9.24}$$

9.3.7. Bilinear Base Shear Reduction Factor, $\phi_{BL,sys}$

Recalling from Chapter 8 a base shear reduction factor ϕ_{BL} was incorporated to recognise the reduction in displacement response between a bilinear-elastic system and an equivalent elastic system. For systems with viscous and hysteretic energy dissipation the system base-shear reduction factor $\phi_{BL,sys}$ is determined from a weighted proportion of viscous and hysteretic energy dissipation as follows

$$\phi_{BL,sys} = \phi_{BL} + (1-\phi_{BL})\frac{\xi_{hyst}}{\xi_{hyst}+\xi_{vd}} \qquad \textbf{9.25}$$

The un-weighted base-shear factor ϕ_{BL} is listed in Table 9.4 for far-field seismicity and in Table 9.5 for near-field seismicity (reproduced from Chapter 8) and is a function of the effective period T_e, the damper velocity exponent α and the supplementary viscous damping ratio Ω. It follows that the design base shear V_b is defined by Eq.(9.26) below.

$$V_b = \phi_{BL,sys} K_e \Delta_d \qquad \textbf{9.26}$$

Table 9.4 Bilinear, base-shear reduction factors ϕ_{BL}: Far-field

	α=0.30		α=0.75	
	Ω=0.05	**Ω=0.30**	**Ω=0.05**	**Ω=0.30**
Te=1.00s	0.717	0.794	0.744	0.837
Te=2.25s	0.755	0.888	0.731	0.892
Te=3.50s	0.978	0.983	0.966	0.900

Table 9.5 Bilinear, base-shear reduction factors ϕ_{BL}: Near-field

	α=0.30		α=0.75	
	Ω=0.05	**Ω=0.30**	**Ω=0.05**	**Ω=0.30**
Te=1.00s	0.722	0.803	0.745	0.838
Te=2.25s	0.775	0.861	0.784	0.896
Te=3.50s	0.840	0.882	0.852	0.898

From Eq.(9.25), when the viscous damper component of EVD ξ_{vd} approaches zero, the base-shear reduction $\phi_{BL,sys}$ approaches 1.0 and the design reverts to a traditional DDBD procedure. Conversely, when the hysteretic damping component of EVD ξ_{hyst} approaches zero, the base-shear reduction $\phi_{BL,sys}$ approaches the un-weighted reduction factor ϕ_{BL} listed in Table 9.4 and Table 9.5 and the design reverts to the pure Viscous-DDBD procedure developed in Chapter 8.

9.4. TIME HISTORY DESIGN VERIFICATION

Three prototype wall systems are designed for far-field and near-field seismicity: resulting in a total of six prototypes. Each post-tensioned wall has a combination of hysteretic and viscous supplementary dampers located at the rocking interface. For simplicity, each precast wall unit is assumed to be rigid, i.e. elastic flexural displacements are ignored. A summary of each prototype is given in Table 9.6.

Table 9.6 Prototype summary

	 **Prototype 1 (3 levels @ 3m)**		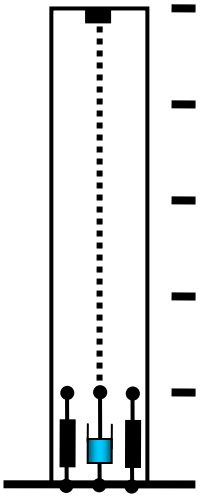 **Prototype 2 (5 levels @ 3m)**		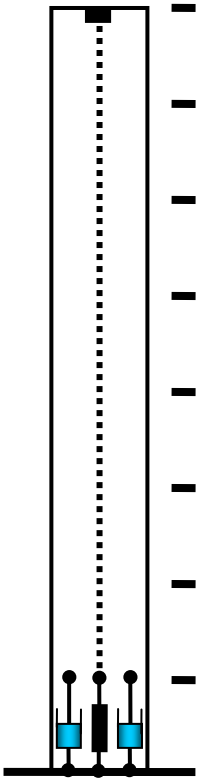 **Prototype 3 (8 levels @ 3m)**	
H_n [m]	9		15		24	
l_w [m]	1.8		2.5		3.5	
t_w [m]	0.25		0.25		0.25	
m_i	15 tonne		20 tonne		25 tonne	
n_{vis}	1		1		2	
n_{vd}	2		2		4	
α	0.30		0.50		0.75	
c_{vd} [kNs$^{\alpha}$/m$^{\alpha}$]	250	250	400	450	1000	1000
n_{ms}	2	2	2	2	1	1
λ	1.5	1.25	1.0	1.0	2.0	2.0

[1] The sub-divided columns on the bottom-left refer to far-field, while columns on the bottom-right refer to near-field

The design of each post-tensioned hysteretic-viscous wall is summarised in Table 9.7. A worked example of Prototype 2 designed for near-field seismicity (P2NF) is outlined in Appendix F. A section analysis was carried out on each post-tensioned

wall to accurately determine the damping and spring properties to be implemented into the non-linear time-history program Ruaumoko, Carr [2005]. In doing so, the post-tensioned steel content, initial post-tensioned force and the area of mild steel (hysteretic dampers) was determined. The over-turning moment capacity was disaggregated into the three components and calibrated to an appropriate hysteresis rule. The post-tensioned component was calibrated to a bilinear-elastic spring while a bilinear-inelastic spring was calibrated to the hsyteretic component. Finally, a dashpot element was used to model the non-linear viscous damper contribution. Elastic damping of the system was included within the model using a simple elastic dashpot, hence equivalent to a constant damping model. The magnitude of the elastic damping coefficient was equal to 5% of critical damping computed from the secant stiffness, defined by the design displacement of the system. The 15 far-field and 15 near-field ground motions used in Chapter 8 are used as the ground motions for this time-history validation.

Table 9.7 Design summary of each prototype

	Prototype 1 (P1)		**Prototype 2 (P2)**		**Prototype 3 (P3)**	
	FF	**NF**	**FF**	**NF**	**FF**	**NF**
θ_d [mm]	1.0%	1.75%	1.4%	1.5%	1.0%	1.4%
Δ_d [mm]	70	123	154	165	170	238
ξ_{el}	0.050	0.050	0.050	0.050	0.050	0.050
ξ_{hyst}	0.061	0.034	0.078	0.034	0.039	0.021
ξ_{vd}	0.042	0.048	0.050	0.023	0.077	0.054
ξ_{eq}	0.153	0.132	0.178	0.107	0.165	0.125
η	0.637	0.678	0.594	0.742	0.614	0.695
T_e [sec]	1.25	1.82	2.82	2.10	2.98	2.82
V_b [kN]	60.87	49.24	58.92	109.24	108.69	164.23
$\phi_{BL,sys}$	0.891	0.871	0.943	0.908	0.916	0.876
c_{vd} [kNs$^\alpha$/m$^\alpha$]	250	250	400	450	1000	1000
C_{VD} [kNs$^\alpha$/m$^\alpha$]	29218	30840	25738	27270	61861	61273
n_{pt} (total)	4	2	2	4	6	10
T_{pt0} [kN]	216	138	226	420	676	962
A_{st} [1] [mm]	586	515	792	1497	1091	1655

[1] Total area of steel (hysteretic) yielding dampers (tension-compression-yielding dampers-TCY)

The mean of the maximum displacement response $\Delta_{eq,ave}$ (THA results) is reported in Table 9.8 and compared with the target design displacement Δ_d. First, the mean error associated with the far-field design decreases as the proportion of hysteretic damping reduces. The error associated with the near-field design is consistently in the range of 18-20%. The reason this error is greater considering near-field seismicity is due to the hysteretic damping spectral reduction factor η_{disp}. In Eq.(9.5), $\alpha = 0.25$ is used for the hysteretic spectral reduction for near-field ground conditions. This factor is based on relatively limited analytical work and is likely to be significantly conservative. With this in mind, at the very least, the procedure appears to result in a conservative design while adopting logical reasoning behind each of the key design steps.

Table 9.8 Summary of the mean displacement response from THA

	$\Delta_{eq,ave}$ [mm]	Δ_d [mm]	Error [%]
P1-FF	62.1	70	11.3%
P2-FF	139.0	154	9.7%
P3-FF	167.1	170	1.7%
P1-NF	99.8	123	18.5%
P2-NF	133.2	165	19.3%
P3-NF	189.3	238	20.5%

9.5. DESIGN METHODS

Two Viscous-DDBD design methods are developed and illustrated in the form of a flow chart. Both methods are based on a target inter-storey drift θ_d defining the design displacement Δ_d.

Design Method A targets a specific supplementary damping ratio (SDR) Ω and then designs the properties of the damper (c_{vd}, α), mild steel and the post-tensioning to satisfy this level of damping. This design method is illustrated in the flowchart of Figure 9.3.

Design Method B is based on pre-defined damper properties (c_{vd}, α). The selected damper properties define the viscous component of EVD ξ_{vd}. This method is presented in Figure 9.4.

Design Method A

Input design parameters: Target rotation θ_d and the target supplementary damping ratio (SDR), Ω

Step 1

Determine the SDOF parameters: $m_e = \dfrac{\sum_{i=1}^{n} m_i H_i}{\Delta_d}$ $H_e = \dfrac{\sum_{i=1}^{n} m_i \Delta_i H_i}{\sum_{i=1}^{n} m_i \Delta_i}$ $\Delta_d = \dfrac{\sum_{i=1}^{n} m_i \Delta_i^2}{\sum_{i=1}^{n} m_i \Delta_i}$

Step 2

Compute the viscous damper component of EVD ξ_{vd} from Eq.(9.10) where the coefficient a_1 is listed in Table 9.1.

$$\xi_{vd} = a_1 \cdot \Omega$$

Step 3

Compute the hysteretic component of EVD ξ_{hyst} from the displacement ductility of the section μ_Δ from Eq.(9.6)

$$\mu_\Delta = \frac{\theta_d D}{K_{\theta,yield}\varepsilon_y H_e}$$

For far-field seismicity, Eq.(9.14)

$$\xi_{hyst} = \frac{1}{1+\lambda}\left[a\left(1-\frac{1}{\mu^b}\right)\left(1+\frac{1}{(T_e+c)^d}\right)\right]$$

For near-field seismicity, Eq.(11.14) & (11.17)

$$\xi_{hyst,DDBD} = \frac{1}{1+\lambda}\left[a\left(1-\frac{1}{\mu^b}\right)\left(1+\frac{1}{(T_e+c)^d}\right)\right]$$

$$\xi_{hyst} = \sqrt{0.07(0.07+\xi_{hyst,DDBD})} - 0.07$$

Step 4

Sum the EVD ξ_{eq} following Eq.(9.18) and determine the spectral reduction factor in Eq.(9.20)

$$\xi_{eq} = \xi_{hyst} + \xi_{vd} + \xi_{el} \qquad \eta = \sqrt{\frac{0.07}{0.02+\xi_{eq}}}$$

Step 5

Reduce the elastic design displacement spectrum by η and compute the effective period $\mathbf{T_e}$ from Δ_d

Step 6

Determine the effective stiffness ($K_e = 4\pi^2 m_e T_e$), the base shear reduction factor $\phi_{BL,sys}$ from Eq.(9.25) and compute the design base shear, $V_b = \phi_{BL,sys} K_e \Delta_d$

$$\phi_{BL,sys} = \phi_{BL} + (1-\phi_{BL})\frac{\xi_{hyst}}{\xi_{hyst}+\xi_{vd}}$$

Step 7

Compute the system critical damping C_c (Eq.(9.13), followed by the supplementary damping coefficient C_{VD} from the specified supplementary damping ratio (SDR) Ω in Eq.(9.11).

$$C_c = 2\sqrt{m_e K_e} \qquad C_{VD} = C_c \cdot \Omega$$

Step 8

Determine the parameter β_{vd} defining the ratio between the global-to-local damping coefficient estimated from the Figure on the right or from Eq.(9.12) below, where ***a*** is a constant listed in Table 9.2. Compute the local damper coefficient $\mathbf{c_{vd}}$ from Eq.(9.12).

$$\beta_{vd} = a \cdot n_{vis} (A_r)^{-(1+\alpha)} = C_{VD}/c_{vd}$$

$$c_{vd} = C_{VD}/\beta_{vd}$$

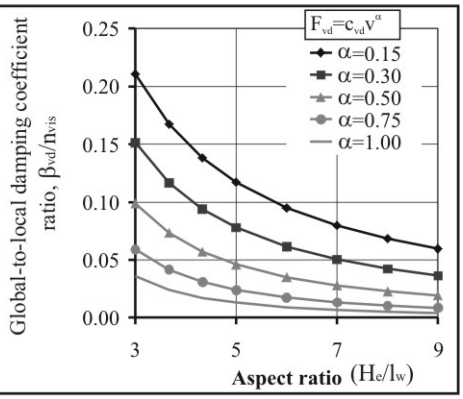

Step 9

Compute the EVD associated with spectral velocity following Eq.(9.19). Compute the corresponding spectral reduction factor η_{vel}, Eq.(9.21). Determine the design velocity v_r at the intermediate displacement Δ_r from Eq.(9.23).

$$\xi_{eq}^{vel} = \xi_{hyst} + b_1 \cdot \Omega + \xi_{el} \qquad \eta_{vel} = \sqrt{\frac{0.07}{0.02 + \xi_{eq}^{vel}}} \qquad v_r = \Delta_d \frac{2\pi}{T_e}\left(\frac{\eta_{vel}}{\eta_{disp}}\right)\frac{1}{\sqrt{2}}$$

Step 10

Determine the average velocity of the supplementary dampers. First, estimate the internal lever arm **jD** to the centroid of the resultant local damper force $\Sigma\mathbf{F}_{vd,i}$. The average damper velocity can be estimated from the geometric ratio in Eq.(9.24) or using the figure on the right. The resultant viscous damper force $\Sigma\mathbf{F}_{vd,i}$ can be computed and hence the individual dampers can be sized and priced.

$$\bar{v}_{vd} \approx \frac{jD}{H_e} v_r \qquad F_{vd} = n_{vd} c_{vd} \bar{v}_{vd}$$

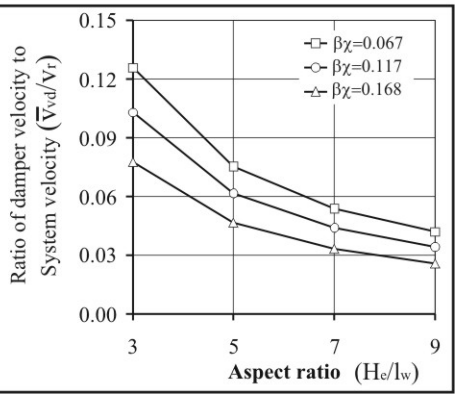

Figure 9.3 Design method A for post-tensioned viscous-hysteretic systems

Design Method B

Input design parameters: Target rotation θ_d and assumed damper properties $\mathbf{c_{vd}}$, α

Step 1

Determine the SDOF parameters: $m_e = \dfrac{\sum_{i=1}^{n} m_i H_i}{\Delta_d}$ $H_e = \dfrac{\sum_{i=1}^{n} m_i \Delta_i H_i}{\sum_{i=1}^{n} m_i \Delta_i}$ $\Delta_d = \dfrac{\sum_{i=1}^{n} m_i \Delta_i^2}{\sum_{i=1}^{n} m_i \Delta_i}$

Step 2

Determine the parameter β_{vd} defining the ratio between the global-to-local damping coefficient estimated from the Figure on the right or from Eq.(9.12) below, where ***a*** is a constant listed in Table 9.2. Compute the local damper coefficient $\mathbf{c_{vd}}$ from Eq.(9.12).

$$\beta_{vd} = a \cdot n_{vis} (A_r)^{-(1+\alpha)} = C_{VD}/c_{vd}$$

$$c_{vd} = C_{VD}/\beta_{vd}$$

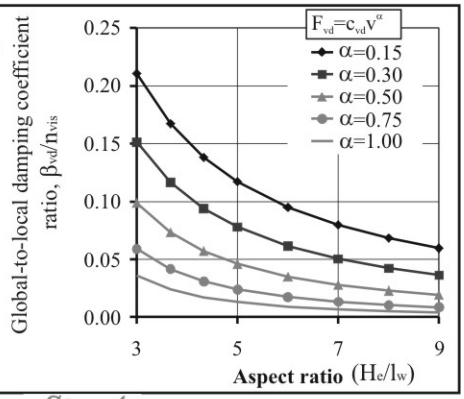

Step 3

Estimate the base shear (i.e. $\mathbf{0.1W_t}$) and compute the effective stiffness $\mathbf{K_e}$ and the critical damping $\mathbf{C_c}$. Compute the supplementary damping coefficient Ω.

$$K_e = 0.1W_t/\Delta_d \qquad C_c = 2\sqrt{m_e K_e}$$

$$\Omega = C_{VD}/C_c$$

Step 4

Compute the viscous damper component of EVD ξ_{vd} from Eq.(9.10) where the coefficient a_1 is listed in Table 11.1.

$$\xi_{vd} = a_1 \cdot \Omega$$

Step 5

Compute the hysteretic component of EVD ξ_{hyst} from the displacement ductility of the section μ_Δ from Eq.(9.6)

$$\mu_\Delta = \frac{\theta_d D}{K_{\theta,yield}\varepsilon_y H_e}$$

For far-field seismicity, Eq.(9.14)

$$\xi_{hyst} = \frac{1}{1+\lambda}\left[a\left(1-\frac{1}{\mu^b}\right)\left(1+\frac{1}{(T_e+c)^d}\right)\right]$$

For near-field seismicity, Eq.(9.14) & (9.17)

$$\xi_{hyst,DDBD} = \frac{1}{1+\lambda}\left[a\left(1-\frac{1}{\mu^b}\right)\left(1+\frac{1}{(T_e+c)^d}\right)\right]$$

$$\xi_{hyst} = \sqrt{0.07(0.07+\xi_{hyst,DDBD})} - 0.07$$

Step 6

Sum the EVD ξ_{eq} following Eq.(9.18) and determine the spectral reduction factor in Eq.(9.20)

$$\xi_{eq} = \xi_{hyst} + \xi_{vd} + \xi_{el} \qquad \eta = \sqrt{\frac{0.07}{0.02+\xi_{eq}}}$$

Step 7

Reduce the elastic design displacement spectrum by η and compute the effective period $\mathbf{T_e}$ from Δ_d

Step 8

Determine the effective stiffness ($K_e = 4\pi^2 m_e T_e$), the base shear reduction factor $\phi_{BL,sys}$ from Eq.(9.25) and compute the design base shear, $V_b = \phi_{BL,sys} K_e \Delta_d$

$$\phi_{BL,sys} = \phi_{BL} + (1-\phi_{BL})\frac{\xi_{hyst}}{\xi_{hyst}+\xi_{vd}}$$

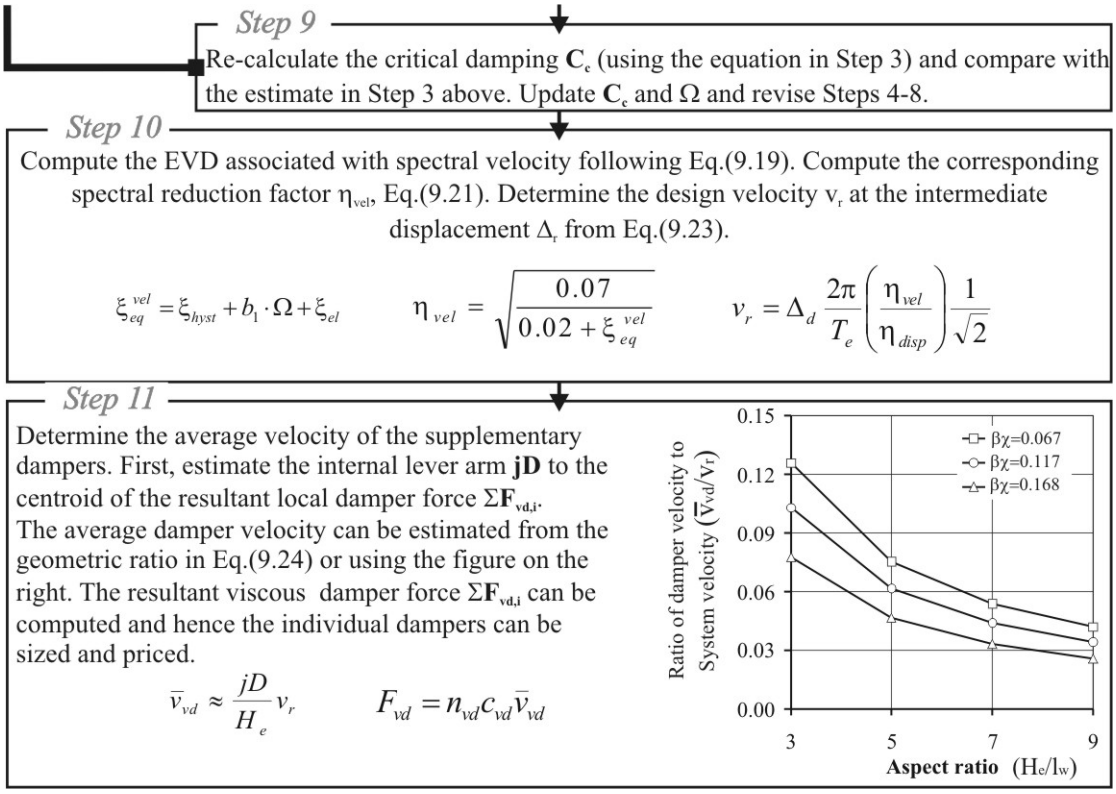

Figure 9.4 Design method B for post-tensioned viscous-hysteretic systems

9.6. CONCLUSIONS

A Direct-Displacement Based Design (DDBD) has been presented for single-degree-of-freedom (SDOF) post-tensioned systems with viscous and hysteretic dampers. The design procedure combines the traditional DDBD of hysteretic yielding systems with the DDBD-viscous procedure presented in Chapter 8. The design procedure was validated on six prototype SDOF systems subjected to time-history analysis. The largest displacement error for the systems designed for far-field seismicity was 11%, whereas an error of 21% was associated with systems designed for near-field seismicity. In both cases the designs were conservative. Additional conservatism was thought to exist within the hysteretic component of equivalent-viscous-damping (EVD). In particular, traditional DDBD heavily penalises hysteretic systems designed for near-field seismicity, which was found to be over-conservative in this case.

The procedure explicitly separates the three contributions of EVD: Viscous (supplementary), hysteretic and elastic. The individual viscous and hysteretic components of EVD must be defined as their ratio is used as a weighting factor within a base-shear reduction factor. As per Chapter 8, this reduction factor recognises the expected reduction in response of a bilinear system when compared to an equivalent elastic system.

It was discussed that traditional DDBD uses two different spectral reduction factors depending on whether near-field or far-field seismicity is considered, while a common EVD is used specific to the hysteretic system alone. In hind site, DDBD-viscous uses a common spectral reduction factor, but alters the level of EVD depending on whether far-field or near-field seismicity is considered. It was shown that the two procedures become compatible when a damping modification factor is incorporated for the hysteretic component of EVD when dealing with near-field seismicity. With these modifications in mind, it was shown that the DDBD-viscous procedure is 100% compatible with existing DDBD in all aspects.

9.7. REFERENCES

Blandon, C. A. and Priestley, M. N. (2005). "Equivalent Viscous Damping Equations for Direct Displacement Based Design." *Journal of Earthquake Engineering. Vol. 9, no. Special Issue 2, pp. 257-278. 2005*.

Carr, A. (2005). "RUAUMOKO." Christchurch, Inelastic Dynamic Analysis.

Palermo, A., Pampanin, S. and Calvi, G. M. (2005). "Concept and Development of Hybrid Solutions for Seismic Resistant Bridge Systems." *Journal of Earthquake Engineering. Vol. 9, no. 6, pp. 899-921. Nov. 2005*.

Priestley, M. J. N., Calvi, G. M. and Kowalsky, M. J. (2007). *Displacement-Based Seismic Design of Structures*, IUSS, Pavia.

10. Direct Displacement-Based Design of Post-Tensioned Rocking Systems, Part III: MDOF Systems with Viscous and Hysteretic Dampers

10.1. INTRODUCTION

In Chapter 8 a Direct Displacement-Based Design (DDBD) procedure was developed for SDOF post-tensioned rocking systems with viscous dampers (termed Viscous-DDBD). This procedure was extended to include SDOF post-tensioned rocking systems with viscous and hysteretic dampers in Chapter 9. This chapter extends the procedure to MDOF systems, with a specific emphasis on post-tensioned, rocking, continuous bridge systems. The fundamental concepts of DDBD are first discussed with respect to traditional reinforced concrete (RC) bridge systems; the procedure is then extended to include post-tensioned rocking bridge systems with viscous and hysteretic dampers. The design procedure is verified on six prototype bridge systems subjected to a suite of far-field and near-field ground motions.

10.2. AN OVERVIEW OF DDBD FOR CONVENTIONAL MDOF RC CONTINUOUS BRIDGE SYSTEMS

The DDBD procedure is somewhat more cumbersome for MDOF bridge systems when compared to MDOF buildings. This is because bridge systems will generally have two load paths to consider: the first being the bridge bents (piers) and the second being the superstructure (bridge deck) and abutments. The bridge bents will respond in the inelastic range, while the prestressed superstructure will, in general, be designed to remain elastic. It is for this reason that the design procedure is iterative (in fact, a double iteration is required); an initial estimate is required for the proportion of base shear resisted by the superstructure $\boldsymbol{x}$ as well as an estimate of the deformed shape of the bridge system $\boldsymbol{\phi}$. An initial estimate should adopt a parabolic displaced profile, while 50% of the base shear can initially be assumed to be resisted by the superstructure (via the abutments), i.e. $\boldsymbol{x} = 0.5$. The displacement capacity of the most critical pier can be estimated from the applied axial load (plus initial post-tensioned force) and the post-tensioned reinforcement content within the section; this will define the design displacement of the bridge system to which the design can target. In its most recent state, DDBD is discussed in great detail in Priestley et al. [2007]. This procedure is similar to the earlier approach of Kowalsky [2002], but with refined weighted damping equations and calibrated equivalent viscous damping (EVD) formulations, Grant et al. [2005] & Blandon and Priestley [2005]. A summary of DDBD for continuous bridge systems is presented below to provide an extension to post-tensioned rocking viscous-hysteretic bridge systems. With reference to Figure

10.1 below, the trial parabolic displaced shape ϕ for a continuous bridge, symmetrical about mid-span of the superstructure, is given by Eq.(10.1). The displaced shape ϕ should be written such that the value of ϕ_i at the location of the critical pier is equal to 1.0. The critical pier is defined as being the pier that achieves its governing limit-state displacement first (material or geometric). This requires the limit-state displacement to be computed for each pier based on allowable material strain limits following a performance-based design philosophy. This performance-based design philosophy was introduced in Chapter 3 and is applied and discussed in detail via a feasibility study in Chapter 11. In Eq.(10.1), ϕ is written such that the critical pier is located at the middle of the super-structure, i.e. $\phi_i(0.5L_{SS}) = 1.0$.

$$\phi_i = \frac{1-(0.5L_{SS}-u_i)^2}{(0.5L_{SS})^2} \qquad \textbf{10.1}$$

When $\phi_i = 1.0$ for the critical pier, the displacement profile of the superstructure is given by Eq.(10.2) where Δ_{crit} is the displacement of the critical pier. In some cases it is not obvious which pier is critical until the analysis is complete (or, at least the first iteration is carried out).

$$\Delta_i = \phi_i \Delta_{crit} \qquad \textbf{10.2}$$

Given the displacement profile of the bridge Δ_i, the displacement Δ_d of the effective mass m_e can be determined.

$$\Delta_d = \frac{\sum_{i=1}^{n} m_i \Delta_i^2}{\sum_{i=1}^{n} m_i \Delta_i} \qquad \textbf{10.3}$$

$$m_e = \frac{\sum_{i=1}^{n} m_i \Delta_i}{\Delta_d} \qquad \textbf{10.4}$$

After calculating the yield displacement of each pier $\Delta_{y,i}$ the ductility demand at each pier μ_i is defined by

$$\mu_i = \frac{\Delta_i}{\Delta_{y,i}} \qquad \textbf{10.5}$$

The equivalent viscous damping (EVD) ξ_i of each pier is calculated from Eq.(10.6), specific to a reinforced concrete bridge pier. This formulation of EVD includes a proportion of elastic EVD.

$$\xi_i = 0.05 + 0.444\left(\frac{\mu_i - 1}{\mu_i \pi}\right) \qquad \textbf{10.6}$$

The damping of each pier ξ_i is weighted to the equivalent work (shear force of the pier V_i multiplied by the pier displacement Δ_i) undertaken by each pier and summed over all piers n to define the total EVD ξ_{eq} of the system.

$$\xi_{eq} = \frac{\sum_{i=1}^{n} V_i \Delta_i \xi_i}{\sum_{i=1}^{n} V_i \Delta_i} \qquad \textbf{10.7}$$

Given that the superstructure will be responding elastically, a superstructure elastic damping ratio of ξ_{ss}=0.05 can generally be adopted and weighted within the total system damping as follows:

$$\xi_{eq} = \frac{\Delta_d(xV_b)\xi_{ss} + \sum_{i=1}^{n} V_i \Delta_i \xi_i}{\Delta_d(xV_b) + \sum_{i=1}^{n} V_i \Delta_i} \qquad \textbf{10.8}$$

As a further extension, damping associated with the abutments ξ_a (hysteretic or otherwise) can also be included and weighted in the following way:

$$\xi_{eq} = \frac{\Delta_a(xV_b)\xi_a + (\Delta_d - \Delta_a)(xV_b)\xi_{ss} + \sum_{i=1}^{n} V_i \Delta_i \xi_i}{(\Delta_d - \Delta_a)(xV_b) + \Delta_d(xV_b) + \sum_{i=1}^{n} V_i \Delta_i} \qquad \textbf{10.9}$$

Here, Δ_a is the average displacement of each abutment. Following the computation of the EVD, the effective period T_e, effective stiffness K_e and system base shear V_b are determined from the damped design displacement spectrum $\Delta(T_e, \xi_{eq})$. The base shear is then distributed along the bridge as discrete lateral loads P_i, proportioned according to the mass and displacement at each degree-of-freedom (DOF).

$$P_i = K_e \Delta_d \frac{m_i \Delta_i}{\sum m_i \Delta_i} = V_b \frac{m_i \Delta_i}{\sum m_i \Delta_i} \qquad \textbf{10.10}$$

Generally, each pier would be designed to have the same reinforcement content as this results in similar moment capacities for each pier (in reality, however, the height of each pier will differ, altering the axial load and the P-Δ induced moment demand acting on each pier). The lateral capacity of each pier element is related by the following

$$V_i = \frac{M_i}{H_i} \qquad \textbf{10.11}$$

Where, M_i is the moment demand and H_i is the height of each pier. The total pier shear $(1-x)V_b$ is distributed to each pier according to its strength. As each pier has the same/similar moment capacity, the total pier shear is proportioned according to $1/H_i$.

$$V_i = (1-x)V_b\left(\frac{1/H_i}{\sum_{i=1}^{n}1/H_i}\right) \qquad \textbf{10.12}$$

Using the applied loads P_i calculated in Eq.(10.10) and the pier shear V_i calculated in Eq.(10.12) a static analysis is carried out to update a) the proportion of base shear resisted by the superstructure x and b) the deformed shape of the bridge ϕ. With reference to Figure 10.1, a structural model of the bridge is constructed where the superstructure is modelled as an elastic beam element with section properties representative of the transverse response i.e. I_{yy}. Elastic springs are located at each DOF representing the effective stiffness of the piers (and abutments, if unrestrained) and defined as follows:

$$K_i = \frac{V_i}{\Delta_i} = (1-x)\frac{K_e\Delta_d}{\Delta_i}\left(\frac{1/H_i}{\sum_{i=1}^{n}1/H_i}\right) \qquad \textbf{10.13}$$

The design is revised using the updated deformed shape ϕ and the revised proportion of abutment shear x.

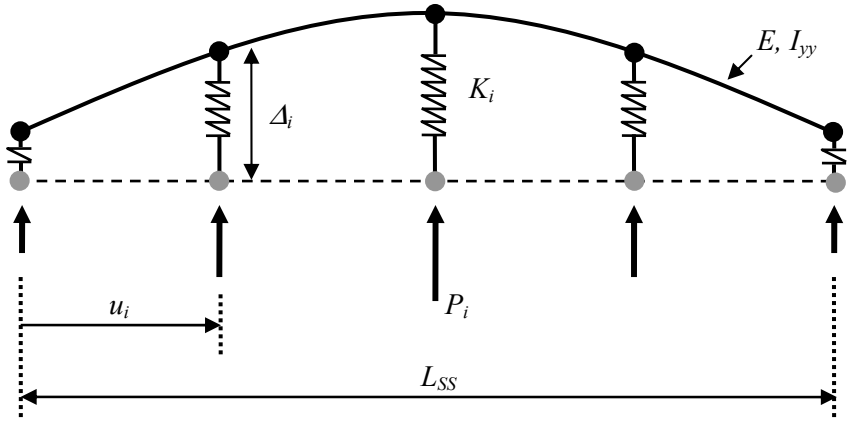

Figure 10.1 Structural analysis model of bridge to update the displaced shape (ϕ) and the proportion of base shear resisted by the abutments (x)

10.3. DDBD OF POST-TENSIONED HYBRID CONTINUOUS BRIDGE SYSTEMS

The extension of the traditional DDBD procedure to include hybrid post-tensioned systems was discussed in Chapter 9 for SDOF systems. The same extensions are also

applicable for MDOF systems. Specifically, for a post-tensioned system, the difference relates to the calculation of the yield displacement and the EVD. The equations are reproduced below from Chapter 9. The ductility of each pier is estimated from the yield rotation, or lateral drift of each pier θ_i.

$$\mu_i \approx \frac{\theta_i}{\theta_{y,i}} = \frac{\theta_i D_i}{K_{\theta,yield}\varepsilon_y H_i} \qquad \textbf{10.14}$$

Where, $K_{\theta yield}$ is approximately equal to 0.50 for square pier sections. The EVD of each pier is computed from the following relationship

$$\xi_i = \xi_{PT,i} + \xi_{ms,i} = \frac{\lambda_i}{1+\lambda_i}0.05 + \frac{1}{1+\lambda_i}\left(0.05 + 0.565\left[\frac{\mu_i - 1}{\mu_i \pi}\right]\right) \qquad \textbf{10.15}$$

Where, λ_i is the moment ratio of each pier. The remainder of the procedure follows the traditional procedure for RC systems discussed above in Section 10.2.

10.4. DDBD OF POST-TENSIONED ROCKING CONTINUOUS BRIDGE SYSTEMS WITH VISCOUS AND HYSTERETIC DAMPERS

The proposed Viscous-DDBD for viscous-hysteretic bridges is similar to that for SDOF systems, with the addition of a few important steps that are addressed below. Unlike traditional DDBD, it is necessary to divide the total proportion of EVD into the elastic ξ_{el}, the hysteretic damper ξ_{hyst} and viscous damper ξ_{vd} components. This has the advantage of being able to understand the contribution of each damping component, but is also necessary to compute the base-shear reduction factor ϕ_{BL}.

10.4.1. Elastic Damping Component, ξ_{el}

The global response of a post-tensioned bridge with viscous dampers is illustrated in Figure 10.2 showing the lateral contribution from the bridge piers (a) and the contribution from the superstructure via the abutments (b). Both the superstructure and bridge piers have a component of elastic damping ξ_{el} which is indicated by the grey line. The actual structural response is shown by a solid black line in each graph.

Recalling from Chapter 9, work carried out by Grant et al. [2005] defined the following relationship that converts the elastic damping of a substitute structure (with damping proportional to the secant stiffness) to damping that is proportional to the tangent stiffness of a non-linear system below

$$\xi_{el,i} = 0.05(\mu_i)^{\lambda} \qquad \textbf{10.16}$$

Where:

$\xi_{el,i}$ is the elastic damping of the pier at DOF i
μ_i is the displacement ductility of the pier at DOF i

λ is a factor depending on the hysteresis rule. For flag-shape systems λ=-0.430

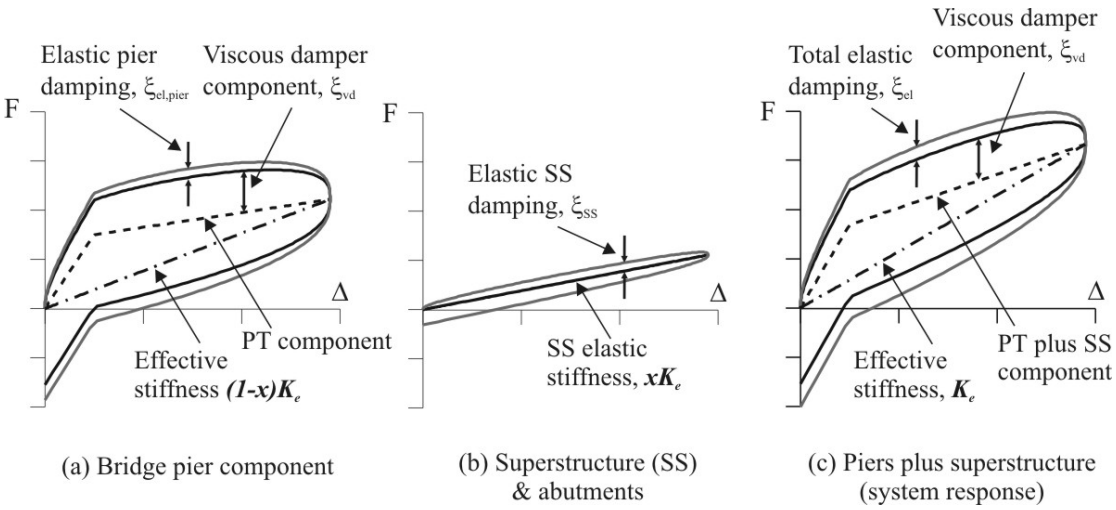

Figure 10.2 Decomposition of the transverse response of a post-tensioned bridge system with supplementary viscous and hysteretic dampers

The total elastic damping of the bridge system ξ_{el} will comprise of three elements; the elastic damping of all the pier elements $\xi_{el,i}$, the elastic damping of the superstructure ξ_{ss}, and the elastic damping of the abutments $\xi_{el,abut}$. Following from Eq.(10.9) and recognising that the shear is proportioned between each pier according to $1/H_i$ as in Eq.(10.12), the total elastic damping ξ_{el} can be expressed as:

$$\xi_{el} = \frac{x\Delta_a\xi_{el,abut} + x(\Delta_d - \Delta_a)\xi_{ss} + \dfrac{(1-x)}{\sum(1/H_i)}\sum_{i=1}^{n}(1/H_i)\Delta_i\xi_{el,i}}{x\Delta_a + x(\Delta_d - \Delta_a) + \dfrac{(1-x)}{\sum(1/H_i)}\sum_{i=1}^{n}(1/H_i)\Delta_i} \qquad \textbf{10.17}$$

All terms in Eq.(10.17) have been previously defined. Often the displacement of the abutments will be small such that their contribution to the total elastic damping in Eq.(10.17) can be neglected. When this is the case, Eq.(10.17) will reduce to the following:

$$\xi_{el} = \frac{x\Delta_d\xi_{ss} + \dfrac{(1-x)}{\sum(1/H_i)}\sum_{i=1}^{n}(1/H_i)\Delta_i\xi_{el,i}}{x\Delta_d + \dfrac{(1-x)}{\sum(1/H_i)}\sum_{i=1}^{n}(1/H_i)\Delta_i} \qquad \textbf{10.18}$$

In the event that the elastic damping across all piers is equal, then Eq.(10.17) further reduces to the following

$$\xi_{el} = x\xi_{ss} + (1-x)\xi_{el,i} \qquad \textbf{10.19}$$

10.4.2. Viscous (supplementary) Damper Component of EVD, ξ_{vd}

Following on from the design procedure for SDOF viscous-hysteretic systems presented in Chapter 8, the EVD of the system is directly related to the damping coefficient $C_{VD,i}$ of each pier at the height of the effective mass (height of the superstructure). The local damping properties at the rocking interface (c_{vd}, α) of each pier are converted to an equivalent damper coefficient $C_{VD,i}$ at the top of each pier (in line with the effective mass). It should be recognised that in this chapter $C_{VD,i}$ refers to the damper coefficient at the top of each pier, while C_{VD} refers to the glocal (weighted) system damper coefficient representative of the entire bridge system. Chapter 8 presented the following relationship between the damping coefficient $C_{VD,i}$ (at the location of the effective mass) and the local damping coefficient at the rocking interface c_{vd}.

$$\beta_{vd,i} = \frac{C_{VD,i}}{c_{vd,i}} \qquad \textbf{10.20}$$

In Chapter 8 it was shown that $\beta_{vd,i}$ is a function of the aspect ratio $A_{r,i}$ and the damper linearity α and an approximate relationship was derived as follows

$$\beta_{vd,i} = a \cdot n_{vis} \left(A_{r,i}\right)^{-(1+\alpha)} \qquad \textbf{10.21}$$

Where

a = a constant given in Table 10.1
n_{vis} = the number of damper layers
α = the damper velocity exponent

Table 10.1 Constant to be used in conjunction with 10.21

α	a
0.15	0.746
0.30	0.632
0.50	0.514
0.75	0.405
1.00	0.324

The relationship describing the parameter β_{vd} in Eq.(10.21) is graphically presented in Figure 10.3. As discussed in Chapter 8 β_{vd} is somewhat dependant on the depth of the compression zone $\chi = c/D$. Therefore, following the design and section analysis of each pier section, the estimate of β_{vd} used in design, should be updated (or verified), i.e. an additional iteration may be required.

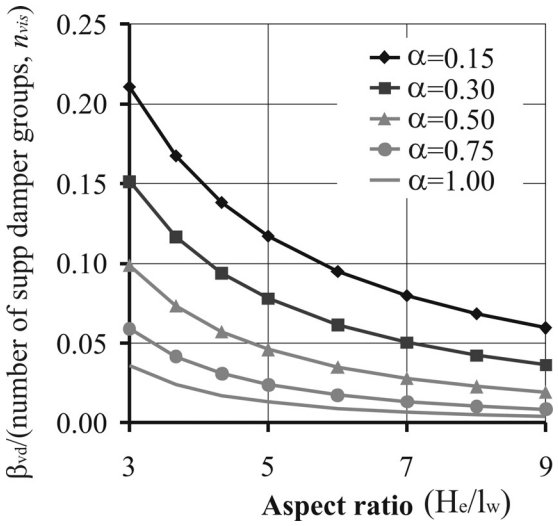

Figure 10.3 Ratio between the damping coefficient at the effective mass $C_{VD,i}$ to the local damping coefficient at the rocking interface c_{vd}.

For a bridge system having unequal pier heights H_e, β_{vd} will vary along the bridge as the aspect ratio A_r varies. It is recommended that in order to keep the design procedure simple, the viscous damper velocity exponent α should be kept constant from pier to pier; however, the damping coefficient c_{vd} and the number of dampers/layers located at the rocking interface can vary. The global (system) bridge damping coefficient C_{VD} is computed from a weighted distribution given by Eq.(10.22). The derivation of this weighting function is presented in Appendix G.

$$C_{VD} = \frac{\sum_{i=1}^{n_{piers}} C_{VD,i}\left(\Delta_i\right)^{\alpha+1}}{\left(\Delta_d\right)^{\alpha+1}} \qquad \textbf{10.22}$$

The viscous (supplementary) damper component of EVD ξ_{vd} associated with a reduction in displacement is computed from the supplementary damper ratio (SDR) $\Omega = C_{VD}/C_c$ as follows

$$\xi_{vd} = a_1 \cdot \Omega = a_1 \cdot \left(\frac{C_{VD}}{C_c}\right) \qquad \textbf{10.23}$$

When the viscous damper component of EVD is to be associated with a reduction in velocity, the coefficient a_1 is replaced with b_1. The coefficients a_1 and b_1 are listed below in Table 10.2.

The critical damping of the system in Eq.(10.23) above is computed from the effective stiffness K_e of the system.

$$C_c = 2\sqrt{m_e K_e} \qquad \textbf{10.24}$$

Table 10.2 EVD coefficients

	Velocity exponent, α							
	1.0-0.75[1]		0.50[1]		0.30[1]		0.15[1]	
a_1	0.880	0.693	0.839	0.602	0.714	0.456	0.440	0.262
b_1	0.642	0.598	0.608	0.526	0.521	0.412	0.341	0.243

[1]Values in the left column relate to far-field seismicity, values in the right column refer to near-field seismicity

10.4.3. Hysteretic Component of EVD, ξ_{hyst}

The formulation to compute the hysteretic component of EVD for each pier $\xi_{hyst,i}$ is identical to that outlined in Chapter 9 and reproduced below. The only difference is the EVD is calculated for each pier (and abutment if necessary) and appropriately weighted to determine the hysteretic damping contribution to the entire system ξ_{hyst}. The hysteretic damping of each individual pier is computed from the following relationship

$$\xi_{hyst,i} = \frac{1}{1+\lambda_i}\left[a\left(1-\frac{1}{\mu_i^b}\right)\left(1+\frac{1}{(T_e+c)^d}\right)\right] \qquad \textbf{10.25}$$

Where:

a,b,c,d = are constants depending on the hysteresis rule listed in Table 10.3 below

μ = is the system ductility

T_e = is the effective period

Table 10.3 Coefficients to determine the hysteretic component of EVD

	a	*b*	*c*	*d*
Internally grouted steel (TF)	0.305	0.492	0.790	4.463
Externally mounted steel (RO)	0.289	0.622	0.856	6.460
Externally mounted friction (EPP)	0.224	0.336	-0.002	0.250

From Chapter 9 it was discussed that the hysteretic EVD computed in Eq.(10.25) must be reduced when considering near-field seismicity from the following

$$\xi_{hyst,i} = \left[0.07\left(0.07+\xi_{hyst,DDBD}\right)\right]^{0.5} - 0.07 \qquad \textbf{10.26}$$

Where

$\xi_{hyst,DDBD}$ = the hysteretic component of EVD computed from Eq.(10.25)

$\xi_{hyst,i}$ = the reduced hysteretic damping component of EVD for near-field seismicity

The hysteretic damping computed for each pier $\xi_{hyst,i}$ is weighted according to the proportion of work (strain energy) achieved by each pier. The total pier shear is proportioned according to ***1/H***; therefore, the weighted hysteretic component of EVD is given by the following

$$\xi_{hyst} = \frac{\dfrac{(1-x)}{\sum(1/H_i)}\sum_{i=1}^{n}(1/H_i)\Delta_i\xi_{hyst,i}}{\dfrac{(1-x)}{\sum(1/H_i)}\sum_{i=1}^{n}(1/H_i)\Delta_i} \qquad \textbf{10.27}$$

Furthermore, if the abutments are also contributing to the hysteretic energy dissipation, as in the case of friction bearings or high damping rubber bearings, then the following extension is appropriate

$$\xi_{hyst} = \frac{x\Delta_a\xi_{hyst,abut} + \dfrac{(1-x)}{\sum(1/H_i)}\sum_{i=1}^{n}(1/H_i)\Delta_i\xi_{hyst,i}}{x\Delta_a + \dfrac{(1-x)}{\sum(1/H_i)}\sum_{i=1}^{n}(1/H_i)\Delta_i} \qquad \textbf{10.28}$$

In Eq.(10.28) $\xi_{hyst,abut}$ is the proportion of hysteretic damping associated with the abutments, calculated in a similar manner to that of the bridge piers.

10.4.4. Combining the Components of EVD

The total EVD ξ_{eq} is a summation of the elastic damping ξ_{el}, the viscous damper component ξ_{vd} and the hysteretic damper component ξ_{hyst}. The EVD associated with a reduction in displacement is given by Eq.(10.29), while the EVD associated with a reduction in velocity is given by Eq.(10.30) below. The coefficients a_1 and b_1 are listed in Table 10.2 above.

$$\xi_{eq}^{disp} = \xi_{el} + \xi_{hyst} + \xi_{vd}^{disp} = \xi_{el} + \xi_{hyst} + a_1 \cdot \Omega \qquad \textbf{10.29}$$

$$\xi_{eq}^{vel} = \xi_{el} + \xi_{hyst} + \xi_{vd}^{vel} = \xi_{el} + \xi_{hyst} + b_1 \cdot \Omega \qquad \textbf{10.30}$$

The spectral reduction factor for displacement η_{disp} and velocity η_{vel} is given by Eq.(10.31) and Eq.(10.32) respectively.

$$\eta_{disp} = \sqrt{\frac{0.07}{0.02 + \xi_{eq}^{disp}}} \qquad \textbf{10.31}$$

$$\eta_{vel} = \sqrt{\frac{0.07}{0.02 + \xi_{eq}^{vel}}} \qquad \textbf{10.32}$$

10.4.5. Design Displacement for Post-Tensioned Viscous-Hysteretic systems

For SDOF systems an intermediate design displacement Δ_r (defined in Eq.(10.33)) was incorporated into the design of post-tensioned rocking viscous-hysteretic systems to allow the viscous dampers to be designed/assessed at some non-zero velocity.

$$\Delta_r = \frac{\Delta_d}{\sqrt{2}} \qquad \textbf{10.33}$$

The velocity demand v_r of the SDOF system at the intermediate design displacement was derived in Chapter 8 and is reproduced below.

$$v_r = \Delta_d \frac{2\pi}{T_e}\left(\frac{\eta_{vel}}{\eta_{disp}}\right)\frac{1}{\sqrt{2}} \qquad \textbf{10.34}$$

It follows that the design velocity v_i of each pier is related to the design displacement Δ_i at each pier in the same way.

$$v_i = \Delta_i \frac{2\pi}{T_e}\left(\frac{\eta_{vel}}{\eta_{disp}}\right)\frac{1}{\sqrt{2}} \qquad \textbf{10.35}$$

This allows the damper velocity and damper forces at the rocking interface of each individual pier to be determined from geometric formulations presented in Chapter 8.

10.4.6. Bilinear Base-Shear Reduction Factor, $\phi_{BL,sys}$

A bilinear base-shear reduction factor ϕ_{BL} was introduced in Chapter 8 & 9 and was weighted according to the proportion of hysteretic to viscous damping (ξ_{hyst} versus ξ_{vd}). For MDOF continuous bridge systems the reduction factor is further weighted to the proportion of base-shear resisted by the superstructure x. The total (system) weighted base-shear reduction factor $\phi_{BL,sys}$ is given by Eq.(10.36), where the term in the square brackets [ ] is identical to that presented in Chapter 9 for SDOF systems weighted according to the proportion of viscous and hysteretic damping. The modification outside the square brackets accounts for the dual load path of a continuous bridge system; that is, the combination of the linear elastic superstructure and the non-linear bridge piers.

$$\phi_{BL,sys} = \left[\phi_{BL} + (1-\phi_{BL})\frac{\xi_{hyst}}{\xi_{hyst} + \xi_{vd}}\right](1-x) + x \qquad \textbf{10.36}$$

The un-weighted base-shear factor ϕ_{BL} is tabulated in Chapters 8&9. Following this reduction, the design base shear V_b is defined by Eq.(10.37) below

$$V_b = \phi_{BL,sys} K_e \Delta_d \qquad \textbf{10.37}$$

It can be seen from Eq.(10.36) that as the superstructure's proportion of base-shear approaches one, i.e. as $\boldsymbol{x} \approx 1.0$, the response of the system is dictated by the linear elastic behaviour of the superstructure; hence, the reduction factor $\boldsymbol{\phi_{BL,sys}}$ approaches 1.0. Conversely, as the superstructure's proportion of base-shear $\boldsymbol{x}$ approaches zero, i.e. as $\boldsymbol{x} \approx 0.0$, the reduction factor $\boldsymbol{\phi_{BL,sys}}$ is entirely weighted to the piers' proportion of hysteretic $\boldsymbol{\xi_{hyst}}$ and (supplementary) viscous $\boldsymbol{\xi_{vd}}$ EVD.

10.5. DESIGN PROCEDURE FOR MDOF CONTINUOUS BRIDGE SYSTEMS WITH VISCOUS AND HYSTERETIC DAMPERS

The displacement-based design of a traditional (monolithic) MDOF continuous bridge system in itself can be a drawn out process unless it is automated in some way such as in a spread sheet or computer algorithm. The extension of the design procedure to include viscous and hysteretic dampers adds another level of complexity to the procedure. The full procedure is outlined in the design chart of Figure 10.4 via a flow chart with references to equations published in this chapter. While the SDOF design procedure in the previous two chapters contained two design methods, the MDOF design procedure is really limited to one method. The known parameters are the target rotation θ_d of the critical pier, and the damper properties at the rocking interface c_{vd}, α. Following the design of the bridge, the pier elements themselves will be designed to satisfy the parameters used in the design i.e, the amount of post-tensioned reinforcement, initial post-tensioning force, mild steel reinforcement etc. After the design and assessment of the piers (via a detailed section analysis for example) it is necessary to check the critical parameters that were used during design; in particular the global-to-local damping parameter β_{vd} and the hysteretic re-centring ratio λ (at the design displacement Δ_i) should be validated and updated if necessary.

Design Method

Input design parameters: Target rotation θ_d, assumed viscous damper properties ($\mathbf{c_{vd}}$, α) and target hysteretic re-centring ratio (λ)

Step 1

Estimate the displaced shape of the bridge system and the proportion of base shear resisted by the abutments. As a first iteration, a parabolic displaced shape should be assumed from Eq.(10.1) and the displacement profile is given by Eq.(10.2). Within the same iteration, 50% of the base shear can be proportioned to the abutments.

$$\phi_i = \frac{1-(0.5L_{SS}-u_i)^2}{(0.5L_{SS})^2} \qquad \Delta_i = \phi_i \Delta_{crit} \qquad \sum V_{abut} = 0.5V_b = 0.5K_e\Delta_d$$

Step 2

Determine the SDOF parameters: $m_e = \dfrac{\sum_{i=1}^{n} m_i H_i}{\Delta_d}$ $\Delta_d = \dfrac{\sum_{i=1}^{n} m_i \Delta_i^2}{\sum_{i=1}^{n} m_i \Delta_i}$

Step 3

Determine the parameter β_{vd} defining the ratio between the global-to-local damping coefficient for each bridge pier. This is estimated from the Figure on the right or from Eq.(10.21) below, where ***a*** is a constant listed in Table 10.1. Compute the damper coefficient $C_{VD,i}$ for each pier from Eq.(10.20).

$$\beta_{vd,i} = a \cdot n_{vis} (A_{r,i})^{(1+\alpha)}$$

$$\beta_{vd,i} = \frac{C_{VD,i}}{c_{vd,i}}$$

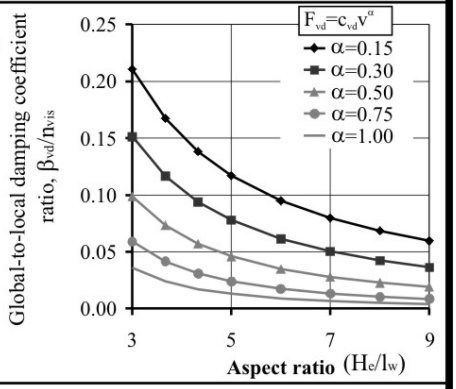

Step 4

Weight the damping coefficient $C_{VD,i}$ at each pier from Eq.(10.22) to define the system damping coefficient C_{VD}.

$$C_{VD} = \frac{\sum_{i=1}^{n_{piers}} C_{VD,i}(\Delta_i)^{\alpha+1}}{(\Delta_d)^{\alpha+1}}$$

Step 5

Estimate the base shear (i.e. $\mathbf{0.1W_t}$) and compute the effective stiffness $\mathbf{K_e}$ and the critical damping $\mathbf{C_c}$. Compute the supplementary damping coefficient Ω.

$$K_e = 0.1W_t/\Delta_d \qquad C_c = 2\sqrt{m_e K_e}$$

$$\Omega = C_{VD}/C_c$$

Step 6

Compute the viscous damper component of EVD ξ_{vd} from Eq.(10.23) where the coefficient $\boldsymbol{a_1}$ is listed in Table 10.2.

$$\xi_{vd} = a_1 \cdot \Omega = a_1 \cdot \left(\frac{C_{VD}}{C_c}\right)$$

Step 7

Compute the displacement ductility of each pier section μ_i from Eq.(10.14)

$$\mu_i \approx \frac{\theta_i}{\theta_{y,i}} = \frac{\theta_i D_i}{K_{\theta,yield}\varepsilon_y H_i}$$

Step 8

Compute the hysteretic component of EVD for each pier from Eq.(10.25)

$$\xi_{hyst,i} = \frac{1}{1+\lambda_i}\left[a\left(1-\frac{1}{\mu_i^b}\right)\left(1+\frac{1}{(T_e+c)^d}\right)\right]$$

Step 9

Weight the hysteretic damping at each pier from Eq.(10.27)

$$\xi_{hyst} = \frac{\dfrac{(1-x)}{\sum(1/H_i)}\sum_{i=1}^{n}(1/H_i)\Delta_i\xi_{hyst,i}}{\dfrac{(1-x)}{\sum(1/H_i)}\sum_{i=1}^{n}(1/H_i)\Delta_i}$$

Step 10

For near-field seismicity, reduce the weighted hysteretic system damping according to Eq.(10.26)

$$\xi_{hyst} = \sqrt{0.07(0.07+\xi_{hyst,DDBD})} - 0.07$$

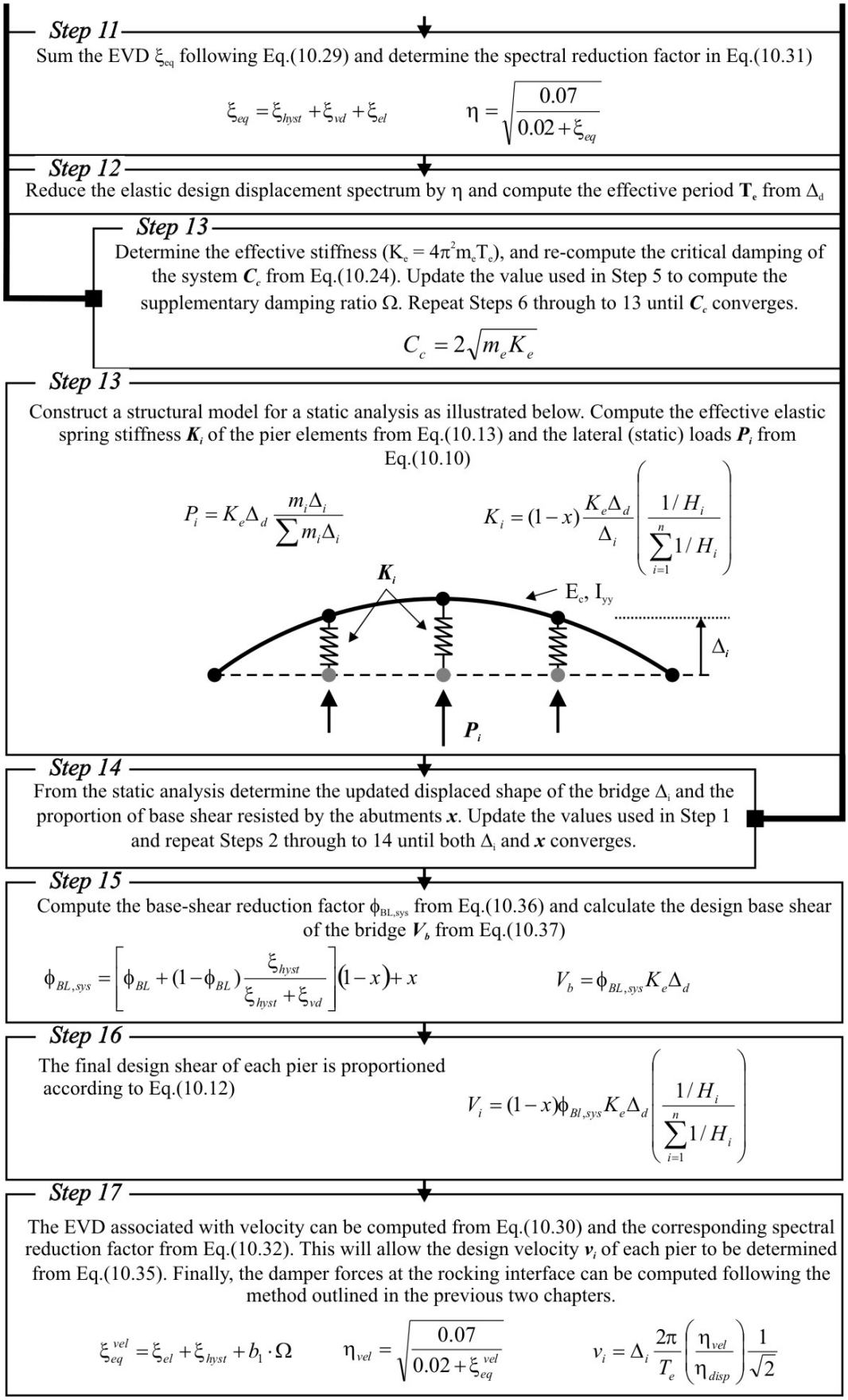

Figure 10.4 Design procedure for post-tensioned MDOF continuous viscous-hysteretic bridge systems

10.6. VERIFICATION OF THE MDOF VISCOUS-DDBD PROCEDURE USING THA

10.6.1. Description of the Prototype Bridges

The design verification was divided into two stages 1) verification of the design procedure for MDOF continuous bridges with viscous dampers only and 2) verification of the procedure for bridges with viscous and hysteretic dampers. For (1) and (2) above, three prototype bridges were created with geometric details indicated in Figure 10.5. Each bridge was designed for far-field and near-field seismicity. The abutments at each end were laterally restrained but free to rotate about the vertical axis. For consistency, the seismic intensity (representing the hazard within this study) was equivalent to that used in the development of the design procedures in Chapter 8 and Chapter 9. This seismic hazard corresponds to a 10% probability of exceedance in 50 years (i.e. a return period of 500 years within a 50 year working life). Depending on the bridge importance level, bridge design in New Zealand is typically carried out for a 4% probability of exceedance in 100 years (return period of 2500 years within a 100 year working life). With this in mind the seismic intensity used for the THA verification is 71% of the design intensity of a typical bridge design in New Zealand. Further details relating to the seismic hazard used in New Zealand bridge design is discussed in a feasibility study in Chapter 11.

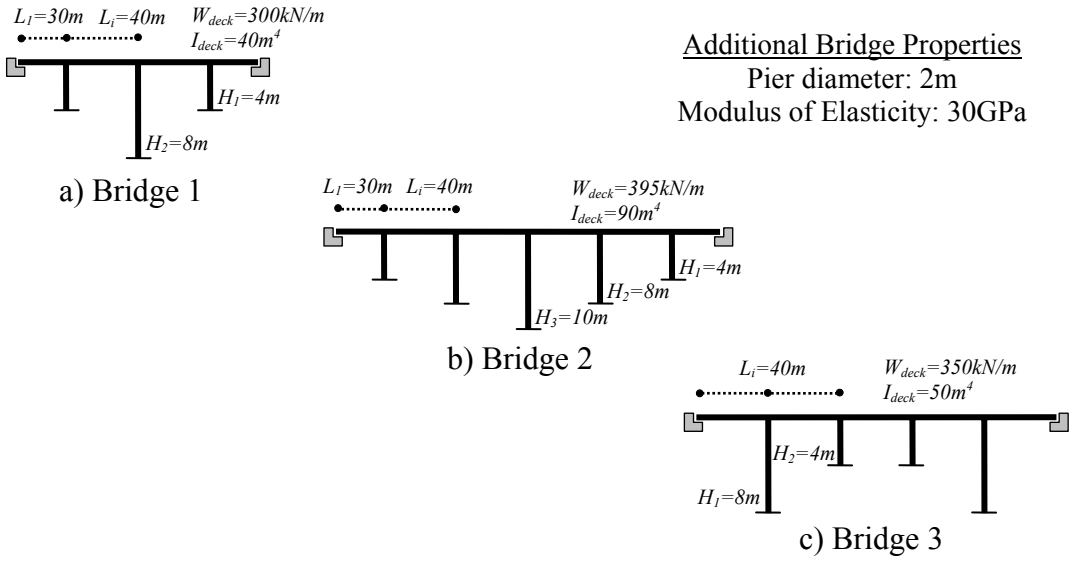

Figure 10.5 Prototype MDOF bridge systems

10.6.2. Bridge Modelling Issues

The bridge systems were modelled as a 2-dimensional model, where the piers were modelled as a combination of bilinear-elastic and bilinear-inelastic (EPP) translation springs and non-linear dashpots. The superstructure was modelled as an elastic frame element. A number of modelling techniques were adopted to minimise the uncertainty in response and to allow reasonable comparisons to be made with the target design (namely, the displacement and shears).

1. P-Δ actions were not included in the design of the piers or THA of the bridge. While P-Δ actions can be readily incorporated within the design procedure, the decision to ignore these limited the number of variables/uncertainties associated with the bridge response. P-Δ actions are accounted for in a feasibility study presented in Chapter 11.
2. The elastic damping of the structure was modelled using discrete dashpot elements at each DOF along the bridge system. While a tangent stiffness damping model is possible within Ruaumoko (Carr [2005]), individual dashpot members were used to better represent the equivalent elastic damping of the SDOF substitute structure. A description of the elastic damping dashpot model is discussed in Appendix G.
3. The abutments were laterally restrained to confine all of the damping (hysteretic and elastic) to the piers and to the elastic damping of the superstructure.
4. The mass of the piers was ignored, while the mass of the superstructure was lumped at each DOF.
5. The mass of the superstructure, and the target displacement of each bridge, are rather arbitrarily chosen. As discussed, the seismic intensity was relatively low requiring the superstructure mass, transverse stiffness and target displacement to be massaged so that the design objectives between the far-field and near-field seismic hazard are similar. With respect to a validation of the design procedure, the specified parameters will suffice; consideration is given to more realistic properties specific to a case study bridge in Chapter 11.

10.6.3. Design Verification 1: Continuous Bridge Systems with Supplementary Viscous Dampers

Each of the three prototype bridge systems above had a different arrangement of viscous dampers within the rocking section. However, the damper arrangement of each pier was identical for each bridge system. The damper properties for each bridge are listed in Table 10.4.

Table 10.4 Damper properties of each post-tensioned rocking viscous bridge

	Bridge 1	**Bridge 2**	**Bridge 3**
Damper coefficient, $c_{vd,i}$	$5500kN^{\alpha}s/m^{\alpha}$	$7500kN^{\alpha}s/m^{\alpha}$	$10000kN^{\alpha}s/m^{\alpha}$
Non-linearity, α	0.3	0.5	0.75
Total number of dampers, n_{vd}	2	4	6
Number of damper layers, n_{vis}	1	2	3

A summary of the DDBD analysis of each bridge is given in Table 10.5. Due to the low seismic demand it was difficult to establish a group of bridge systems having an effective period encompassing a larger range; however, the damping ratios vary significantly to provide a proper validate to the design procedure.

Table 10.5 DDBD summary of each post-tensioned rocking viscous bridge

	Bridge 1		Bridge 2		Bridge 3	
	FF	**NF**	**FF**	**NF**	**FF**	**NF**
Design displacement, Δ_{eq} [mm]	101.9	101.6	125.9	141.0	68.6	68.6
Equiv viscous damp, ξ_{eq} [%]	9.53	7.64	14.59	10.81	25.85	19.71
Spectral reduction, η	0.779	0.852	0.650	0.739	0.501	0.568
Effective period, T_{eq} [sec]	1.44	1.33	2.11	1.89	1.49	1.35
System base shear, V_b [kN]	6369	7225	6090	8306	5630	6832

The mean of the maximum displacement and moment demand are compared to the design profiles in Figure 10.6, Figure 10.7 and Figure 10.8 for each of three bridges: the response to the 15 far-field ground motions is shown on the left, while the response to the 15 near-field ground motions is shown on the right of each figure. The mean bridge response is shown, plus and minus one standard deviation. There is good agreement between the design and the mean response, with larger scatter evident within the near-field response. Naturally, there is a good agreement for the shear envelope as there are no higher modes within the pier elements themselves. The near-field response of Bridge 3 returned the largest error of 15.8% with respect to the displacement of the central piers.

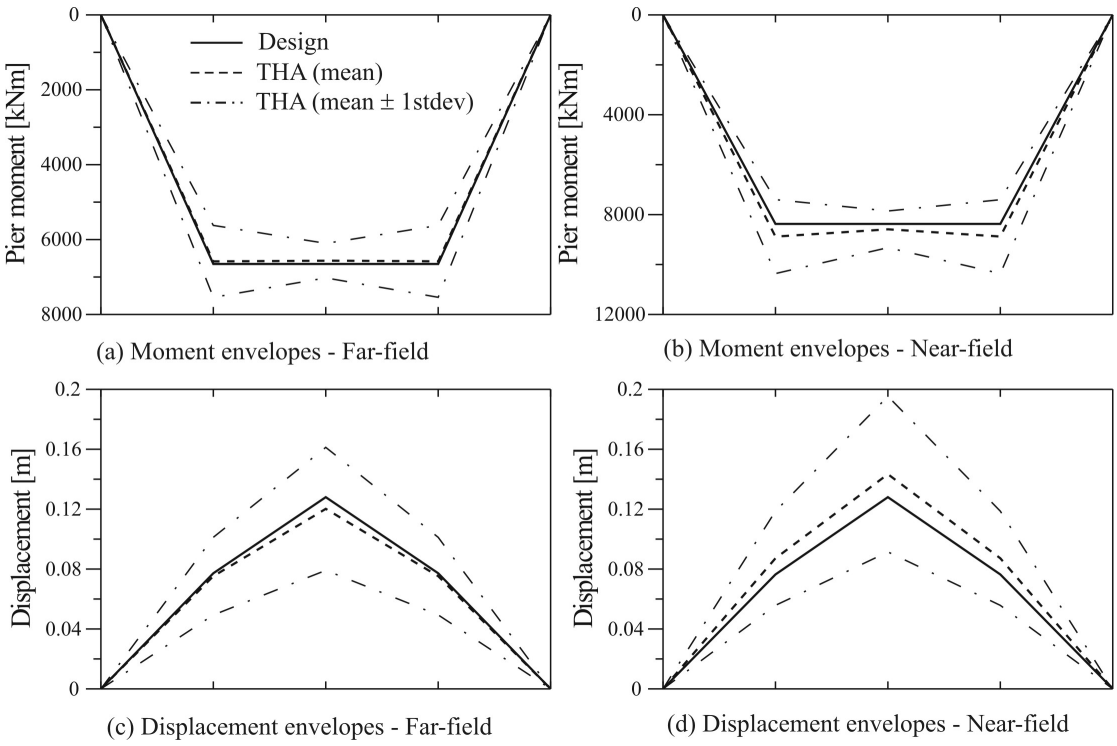

Figure 10.6 Bridge 1: displacement and moment envelopes for far-field (a)&(c) and near-field (b)&(d) seismicity

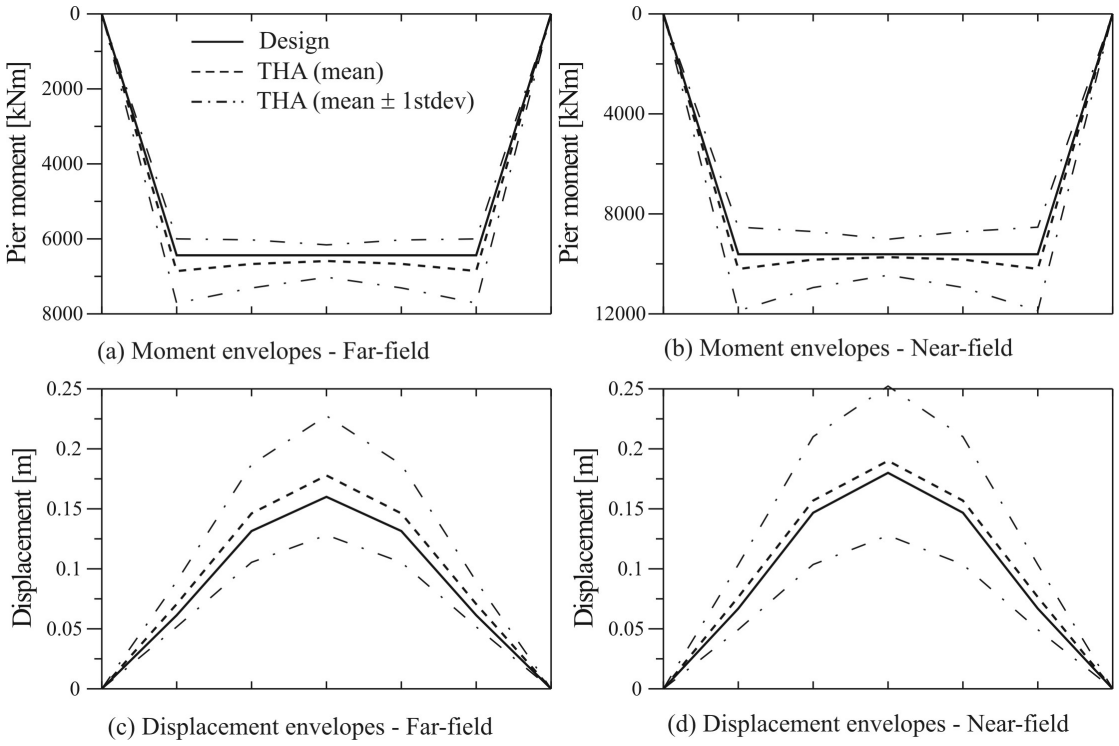

Figure 10.7 Bridge 2: displacement and moment envelopes for far-field (a)&(c) and near-field (b)&(d) seismicity

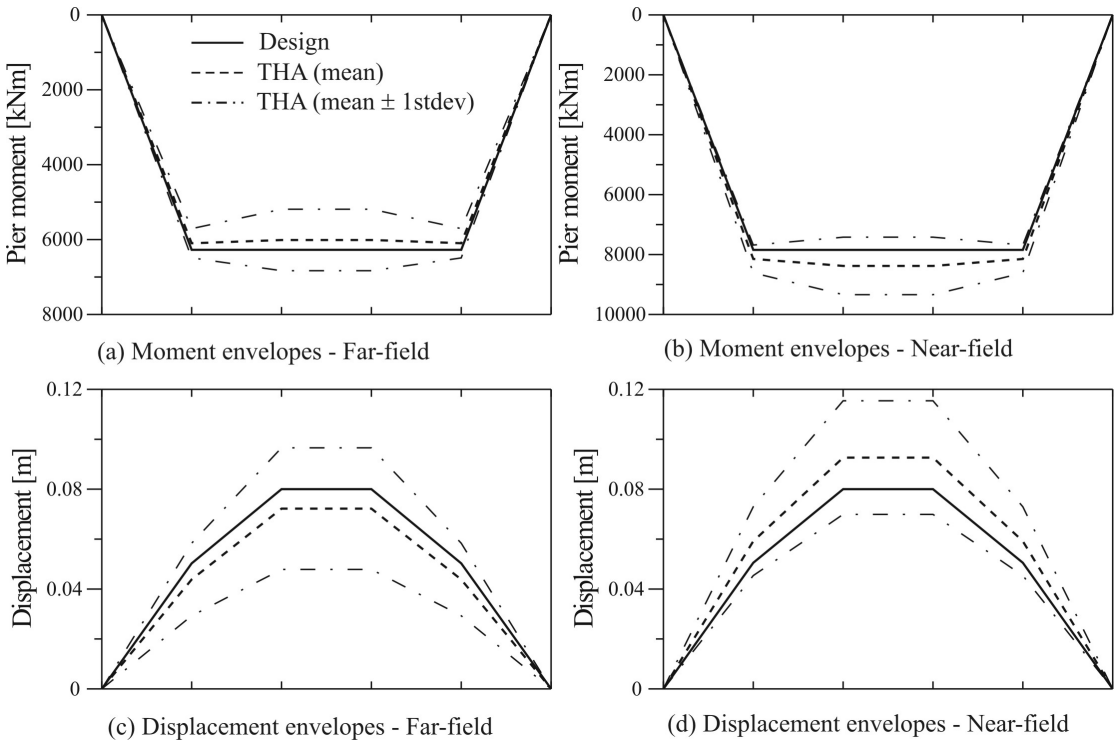

Figure 10.8 Bridge 3: displacement and moment envelopes for far-field (a)&(c) and near-field (b)&(d) seismicity

10.6.4. Design Verification 2: Continuous Bridge Systems with Supplementary Viscous and hysteretic Dampers

A second design verification was carried out on the same three bridge prototypes above (now termed Bridge 4, 5 and 6), which now incorporate viscous and hysteretic dampers at the rocking section. Again, the three bridges were designed for far-field and near-field seismicity. The break-down of the damper properties is summarised in Table 10.6, including the target design moment ratio λ.

Table 10.6 Damper properties of each post-tensioned rocking viscous-hysteretic bridge

	Bridge 4	Bridge 5	Bridge 6
Damper coefficient, $c_{vd,i}$	$5500kN^{\alpha}s/m^{\alpha}$	$7500kN^{\alpha}s/m^{\alpha}$	$7500kN^{\alpha}s/m^{\alpha}$
Non-linearity, α	0.3	0.5	0.75
Total number of FV dampers, n_{vd}	2	4	6
Number of FV damper layers, n_{vis}	1	2	3
$\lambda=(M_{pt}+M_n)/M_{ms}$	1.0	1.0	1.5

A summary of the DDBD output is given in Table 10.7. Presented within the table is the proportion of damping associated with the non-linear viscous dampers and the hysteretic dampers. It is worth noting that, as Eq.(10.36) suggests, the base shear reduction factor ϕ_{BL} has less influence on a MDOF structure due to the weighting attributed to the superstructure.

Table 10.7 DDBD summary of each post-tensioned rocking viscous-hysteretic bridge

	Bridge 4		Bridge 5		Bridge 6	
	FF	NF	FF	NF	FF	NF
Design displacement, Δ_{eq} [mm]	112.1	102.0	126.7	141.6	68.5	68.6
Hysteretic contribution to equiv viscous damp, ξ_{hyst} [%]	3.07	2.50	5.73	3.41	6.97	2.95
FV damping contribution to equiv viscous damp, ξ_{vd} [%]	6.55	3.12	12.40	6.67	16.00	10.46
Total equiv viscous damp, ξ_{eq} [%]	14.62	10.62	23.12	15.08	27.98	18.42
Spectral reduction, η	0.649	0.744	0.528	0.640	0.483	0.586
Effective period, T_{eq} [sec]	1.88	1.50	2.61	2.10	1.55	1.32
Bilinear base shear reduction ϕ_{BL}	0.95	0.92	0.93	0.88	0.89	0.86
System base shear, V_b [kN]	4737	6516	4664	7586	5434	7334
Lateral design coefficient [g]	0.090	0.124	0.054	0.087	0.078	0.105

The mean of the maximum displacement and moment profiles are compared to the design profiles in Figure 10.9, Figure 10.10 and Figure 10.11: the response of each bridge to the far-field ground motions is shown on the left, while the response to the near-field ground motions is shown on the right of each figure. The mean bridge response is shown, plus and minus one standard deviation. The agreement between the design and the mean response is very satisfactory. The far-field response of Bridge 6 returned the largest error of 14.8% with respect to the displacement of the central piers.

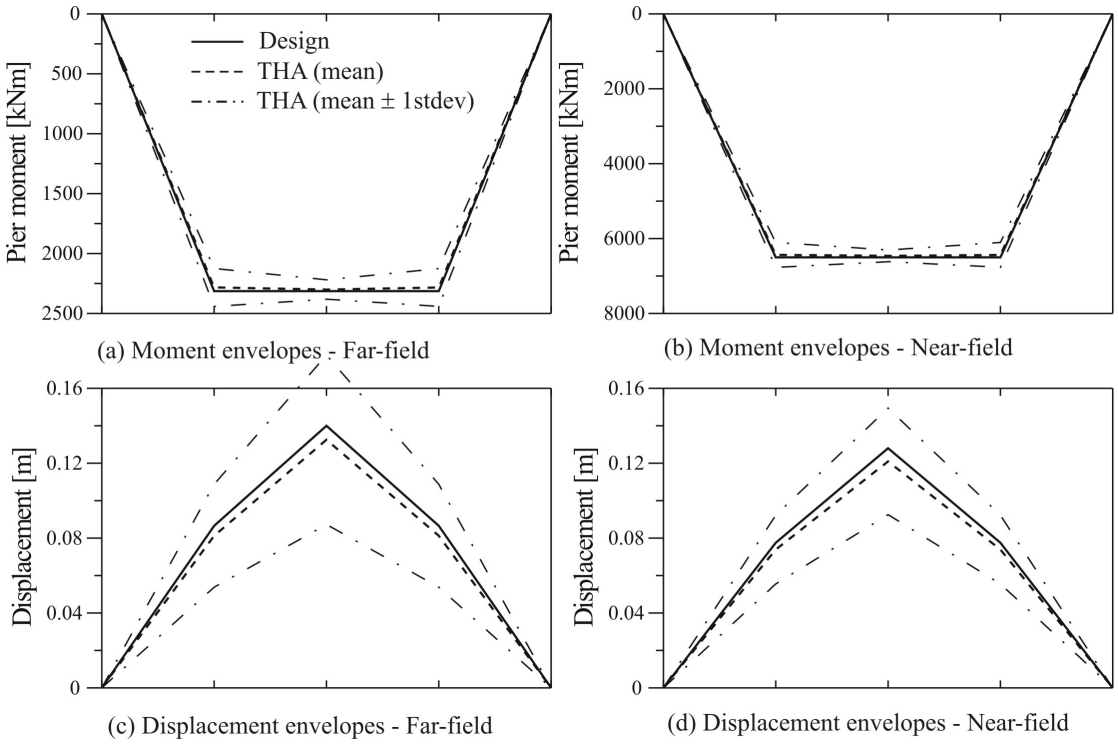

Figure 10.9 Bridge 4 displacement and moment envelopes for far-field (a)&(c) and near-field (b)&(d) seismicity

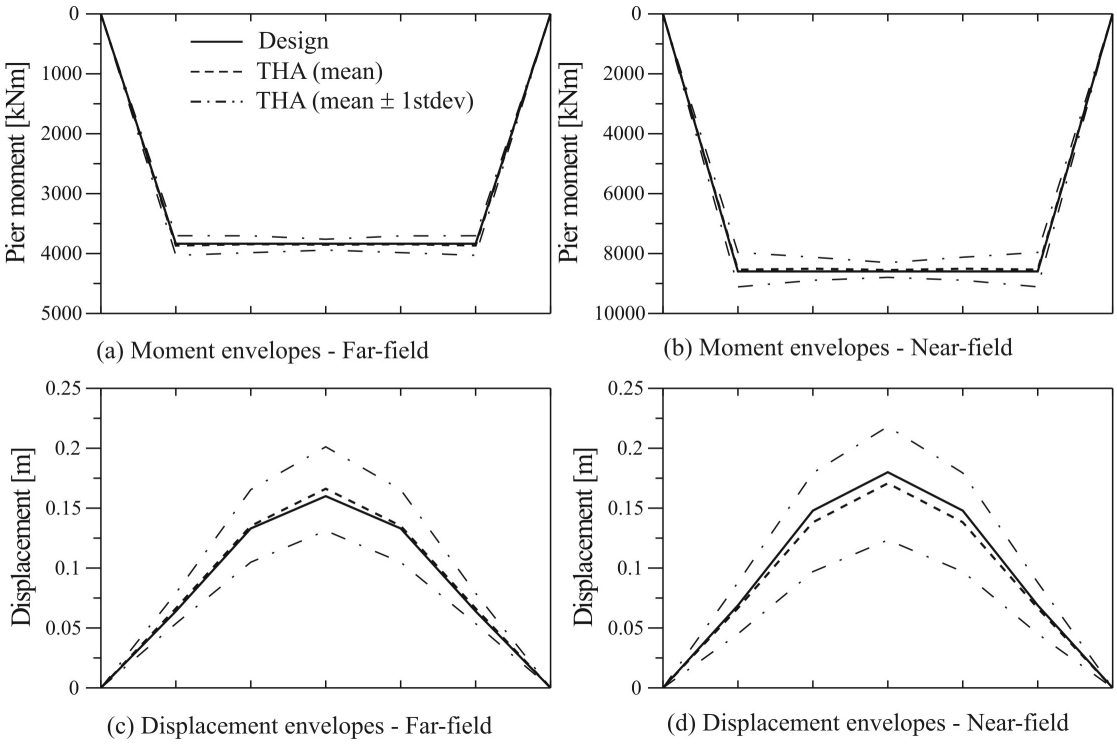

Figure 10.10 Bridge 5 displacement and moment envelopes for far-field (a)&(c) and near-field (b)&(d) seismicity

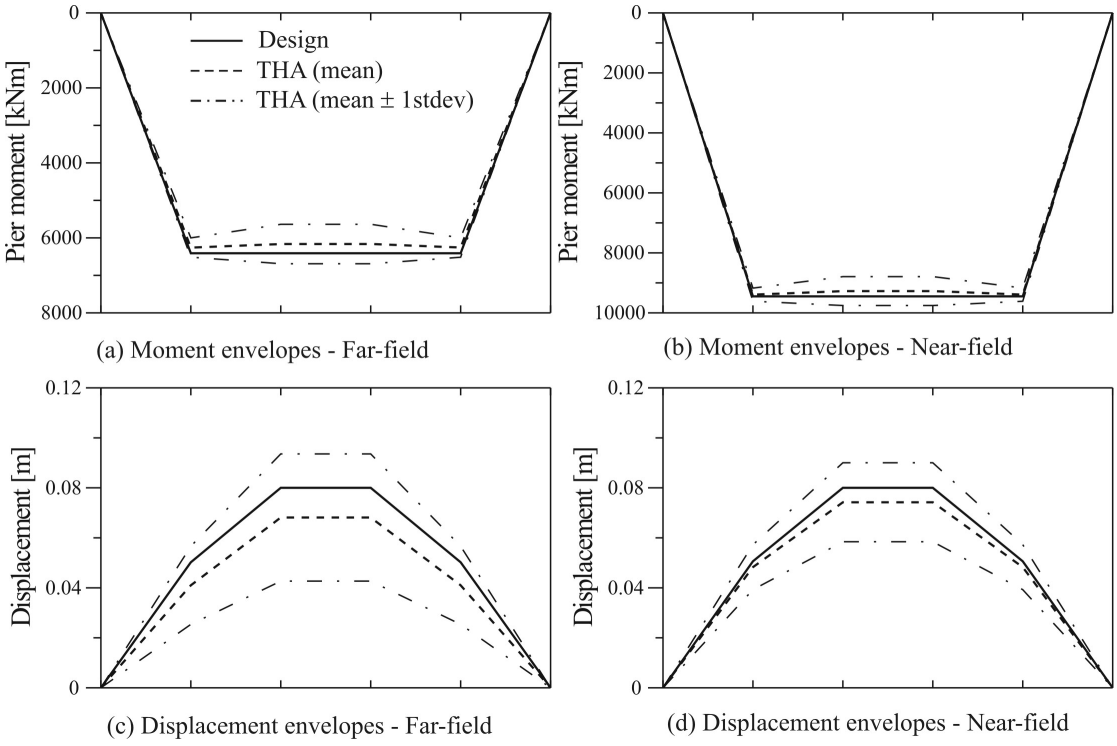

Figure 10.11 Bridge 6 displacement and moment envelopes for far-field (a)&(c) and near-field (b)&(d) seismicity

10.7. CONCLUSIONS

A brief overview of DDBD of multi-degree-of-freedom (MDOF) continuous bridge systems was presented. This was followed with the extension of the design procedure to include post-tensioned hybrid bridge systems. A detailed design procedure was presented for viscous-hysteretic MDOF post-tensioned bridge systems and summarised in a comprehensive flow-chart to aid in the iterative procedure. The procedure was extensively verified on 12 prototype bridge piers, where the peak displacement response was in very good agreement with the target design.

In Chapter 8 the local viscous damper coefficient at the rocking connection was related to an equivalent global viscous damping coefficient at the effective height of the system. This relationship was largely a function of the aspect ratio of the system. As bridge piers are likely to vary in length along the bridge, a weighting function was developed to compute the equivalent system viscous damping coefficient for the entire bridge system.

A base-shear reduction factor was introduced in Chapter 8 specific to the design of post-tensioned viscous systems. A weighting function was introduced in Chapter 9 to recognise the proportion of hysteretic and viscous (supplementary) damping. This base-shear reduction factor was further weighted for MDOF continuous bridge systems, where the additional weighting was based on the proportion of base shear resisted by the bridge abutments.

10.8. REFERENCES

Blandon, C. A. and Priestley, M. N. (2005). "Equivalent Viscous Damping Equations for Direct Displacement Based Design." *Journal of Earthquake Engineering. Vol. 9, no. Special Issue 2, pp. 257-278. 2005*.

Carr, A. (2005). "RUAUMOKO." Christchurch, Inelastic Dynamic Analysis.

Grant, D. N., Blandon, C. A. and Priestley, M. J. N. (2005). *Modelling Inelastic Response in Direct Displacement-Based Design*, IUSS, Pavia.

Kowalsky, M. J. (2002). "A displacement-based approach for the seismic design of continous concrete bridges." *Earthquake Engineering & Structural Dynamics*, 31, 719-747.

Priestley, M. J. N., Calvi, G. M. and Kowalsky, M. J. (2007). *Displacement-Based Seismic Design of Structures*, IUSS, Pavia.

11. The Feasibility of Advanced Post-Tensioned Bridge Systems Considering a Probabilistic Seismic Loss Assessment

11.1. INTRODUCTION

Performance-based earthquake engineering (PBEE) has been widely accepted as a means of quantifying the performance of a system over the working life of a structure. Traditional seismic design will typically consider two performance objectives 1) an ultimate limit state considering strength, and to a lesser extent, displacements and 2) serviceability limit state considering deflection, cracking and vibration etc. PBEE identifies multiple performance objectives (generally three or more) to encompass a set of anticipated hazards over the working life of the structure.

This chapter quantifies the performance of three post-tensioned (PT) reinforced concrete (RC) bridges and compares them to a conventional monolithic bridge. The four bridges are identical in terms of geometry and design objectives; however, they differ in terms of lateral capacity and mechanical damping. A seismic loss assessment is carried out for each bridge subjected to transverse earthquake response. The seismic loss assessment provides a means of directly comparing the performance of each system in terms of Expected Annual Loss (EAL) and the annual frequency of exceeding a specified level of loss (loss-hazard). This chapter first introduces the prototype bridge systems and then provides a brief overview of seismic loss assessment. A detailed description of the design, modelling, hazard model, damage measures and loss relationships are then introduced, followed by the results of the analysis. Finally, the loss assessment is extended to include an irregular bridge configuration to determine whether similar conclusions can be made.

11.2. GEOMETRY OF THE PROTOTYPE BRIDGE SYSTEMS

A symmetric, six-span, reinforced concrete prototype bridge is illustrated in Figure 11.1. The bridge is symmetric about pier 3 with internal spans of 50m and end spans of 40m (refer Figure 11.1). A segmented, precast concrete box girder deck system is seated on bearings located on top of the cap beam and abutments. Each pier and abutment is founded on shallow soil (NZS1170.5 [2004] soil category C) with piled foundations to the bedrock. Consultation with practising bridge engineers in Wellington[1] defined the dimensions of the box-girder deck, cap beam and piers. Dimensions of the bridge piers and box-girder deck are illustrated in Figure 11.2.

[1] Dr. R Presland, Holmes Consulting Group, Wellington Office.

While the actual dimensions of the box-girder deck were of little relevance, a reality check was considered important for a realistic estimate of the seismic mass and deck flexibility. The bridge is located on a Wellington site and therefore only near-fault rupture mechanisms are considered within the seismic hazard.

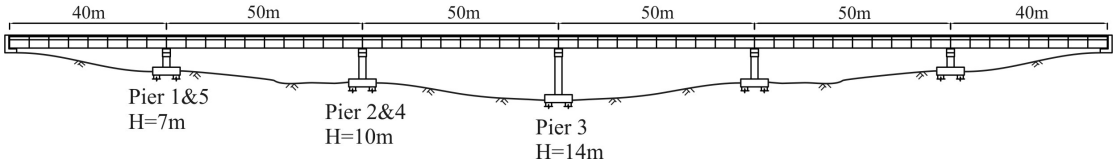

Figure 11.1 Longitudinal elevation of the prototype bridge –symmetric about pier 3.

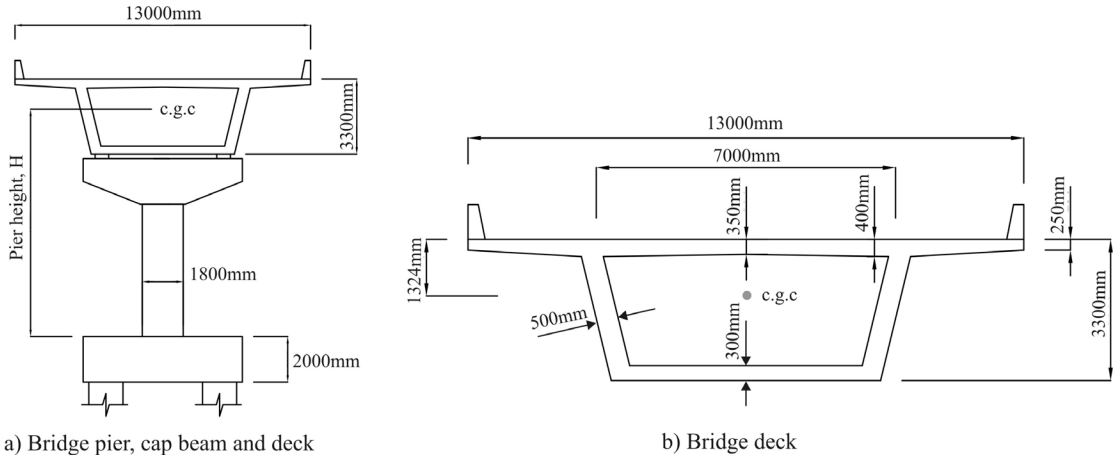

Figure 11.2 Geometry of the bridge piers and precast box girder bridge deck.

One ductile monolithic bridge and three post-tensioned hybrid equivalents are investigated. To aid in a direct comparison, each bridge is identical in geometry (pier heights and cross-section dimensions) and shown in Figure 11.1 and Figure 11.2. Three variations of post-tensioned, rocking bridge systems are considered. A brief description of each follows:

Bridge 1. A precast (or an emulation of cast in-situ) bridge with monolithic piers representing traditional ductile flexural hinging at the base of the piers, designed to satisfy the requirements of NZS3101 [2006]. This ductile system is termed *benchmark monolithic*.

Bridge 2. A precast bridge with post-tensioned rocking piers and internally grouted mild steel reinforcement. This system represents a traditional hybrid, post-tensioned solution. This system is termed *hybrid*.

Bridge 3. A precast bridge with post-tensioned rocking piers, internally grouted mild steel reinforcement and externally mounted non-linear fluid viscous dampers (FVD). This hybrid bridge is termed the Advanced Flag-Shape 1 Bridge (*AFS1*), after Kam et al. [2007].

Bridge 4. A precast bridge with post-tensioned rocking piers, externally mounted mild steel Tension-Compression-Yielding (TCY) dampers and externally mounted non-linear Fluid-Viscous Dampers (FVD). This hybrid bridge is termed the Advanced Flag-Shape 2 Bridge (*AFS2*).

Throughout this chapter the benchmark bridge is referred to as either the *benchmark*, *monolithic* or *ductile* bridge, while the post-tensioned bridges are simply referred to as *post-tensioned* or *PT* bridges.

Elasto-plastic abutments are located at each end of each bridge, representing either friction bearings or metallic (hysteretic) bearings.

11.3. DESIGN OF THE PROTOTYPE BRIDGES

Each bridge was designed to satisfy the requirements of the New Zealand Bridge Manual; TransitNZ [2003], the New Zealand Structural Design Standard for seismic loadings; NZS1170.5 [2004], and the Concrete Structures Standard; NZS3101 [2006]. The bridge was assigned an Importance Level 4 as the site is located along a primary arterial highway. "Importance Level 4" is a classification of a structure given by NZS1170.0 [2002] and TransitNZ [2003] as being of the highest importance and hence the highest seismic hazard.

A Direct Displacement-Based Design (DDBD) methodology was employed for the design of the benchmark bridge (Priestley et al. [2007]). The extension of the DDBD procedure by Palermo [2004] to include hybrid bridge systems was used for the design of the hybrid bridge. For the two advanced hybrid bridges (*AFS1* and *AFS2*), the procedure developed in Chapter 10 for multi-degree-of-freedom (MDOF) bridges was adopted.

11.3.1. Seismic Design Hazard

Bridges with Importance Level 3 and 4 require the design to be based on a seismic hazard with a return period of 2500 years within a 100 year working life (TransitNZ [2003]). Considering a Poisson probability model (Equation 11.1), an earthquake event having a return period of 2500 years is equivalent to a 3.9% probability of exceedance within a 100 year working life. In Equation 11.1, $\boldsymbol{P}$ is the probability of at least one occurrence of a specified level of ground motion, $\boldsymbol{\lambda}$ is the annual rate of exceedance (where $\boldsymbol{\lambda=1/T_r}$ and $\boldsymbol{T_r}$ is the return period) and $\boldsymbol{t}$ is the working life of the structure.

$$P = 1 - e^{-\lambda t} \qquad \textbf{11.1}$$

The New Zealand Uniform Hazard Spectra (UHS) was chosen as the design acceleration, design pseudo-velocity and displacement spectrum (NZS1170.5 [2004]). The structural performance factor $\boldsymbol{S_p}$ was ignored as previous discussions[2] on this reduction factor felt it to be inconsistent with other international seismic loadings codes and the subject of much debate (Priestley et al. [2007]). The return period

[2] Personal communication, Prof. M.J.N. Priestley

factors R_u tabulated in NZS1170.5 [2004] are based on a 50 year working life, requiring the probability of exceedance above to be converted to a return period based on a 50 year working life. From Equation 11.1 above, a 3.9% probability of exceedance in 100 years is equivalent to a return period of 1250 years within a 50 year working life. Based on the tabulated data within NZS1170.5 [2004], the return period factor at the design level was found to equal R_u=1.405. The corresponding design PGA was determined for the 1/3MCE, 2/3MCE and MCE seismic hazard and is summarised in Table 11.1 (where MCE is defined as the Maximum Considered Event). The 2/3MCE is equivalent to the Design-Basis Event (DBE); in this case, representing a 3.9% probability of exceedance in 100 years.

Table 11.1 Relationships between probability of exceedance and PGA for bridge design according to TransitNZ [2003]

	1/3 MCE	2/3MCE	MCE
Return period (100year working life)[1]	410 yrs	2500 yrs	7296 yrs
Probability of exceedance in 100 years	21.7%	3.9%	1.4%
Return period factor[2], R_u	0.703 (0.5)	1.405 (1.0)	2.108 (1.5)
PGA[3]	0.374g	0.747g	1.121g

[1] TransitNZ

[2] Equivalent return period factor associated with a working life of 50 years within NZS1170.5

[3] NZS1170.5 design spectral acceleration PGA.

11.3.2. Direct Displacement-Based Design (DDBD) Bridge Summary

The design of each bridge system followed a multi-level performance-based methodology. In particular, two design objectives were considered; damage control and collapse prevention. Details of the structural limit states and performance objectives are discussed in detail in Section 11.7. A summary of the DDBD output is presented in Table 11.2. The breakdown of the various contributions to Equivalent Viscous Damping (EVD) is also shown in the table. The total EVD ξ_{eq} is disaggregated into the pier's hysteretic EVD ξ_{hyst} (excluding the elastic damping), the pier's EVD associated with the fluid viscous dampers (FVD) ξ_{FVD} and the total elastic EVD ξ_{el} including the superstructure, abutments (both elastic and hysteretic) and the elastic pier damping. AFS1 was designed to have approximately a 1:1 ratio between the hysteretic EVD ξ_{hyst} and the viscous EVD ξ_{FVD}, while AFS2 was designed to have a ratio of approximately 1:2.

An allowable drift limit of 3.65% for piers 1&5 governed the design of the benchmark bridge. This drift limit corresponded to an allowable strain limit under the damage control performance objective: these performance objectives are discussed in detail in Section 11.7. For comparison purposes, this drift limit was used as the target drift limit for all four bridge systems. Therefore, all four bridges had the same (or similar) target displacement (i.e. displacement of the effective mass).

The summary table shows that the target displacement is similar between all four bridges: differing slightly for each system depending on the proportion of base shear resisted by the superstructure. Naturally, the base shear of the hybrid bridge is larger than the benchmark due to the lower EVD. However, it is interesting to note that

while the benchmark bridge has the largest EVD, it does not correspond to the lowest base shear; rather AFS1 and AFS2 record the lowest design base shears. It is important to recognise that the base shear for the AFS systems corresponds to the base shear at the target displacement i.e. when the velocity is zero. There will be some intermediate displacement (having a non-zero velocity) where the base shear, in particular the pier shear, can be larger than the design shear due to the velocity dependency of the FVD. It is vital that the precast pier element has sufficient over-strength to avoid unwanted flexural hinging, or at worst, brittle shear failure when the viscous damper forces are significant.

Table 11.2 DDBD summary of the bridge prototypes

	Benchmark	**Hybrid(traditional)**	**AFS1**	**AFS2**
Δ_{eq}	0.487m	0.494m	0.470m	0.474m
ξ_{eq}	14.70%	7.55%	10.96%	10.16%
ξ_{hyst}	11.61%	5.59%	4.74%	2.40%
ξ_{FVD}	-	-	3.96%	5.04%
ξ_{el}	3.09%	1.96%	2.25%	2.72%
T_{eff}	2.60s	2.39s	2.70s	2.65s
V_b	17226kN (0.226g)	20639kN (0.271g)	14578kN (0.191g)	14574kN (0.191g)

The velocity exponent α was selected considering over-strength damper forces under the MCE seismic hazard. Considering a multi-level performance-based design, the ratio between the displacement response of the bridge at the MCE level (collapse prevention) and at the 2/3MCE (damage control) was assumed to be similar in magnitude to the ratio of the design seismic hazard i.e. a ratio of $\boldsymbol{R} = 1.5$. Furthermore, the displacement ratio will be similar in magnitude to the ratio of the maximum velocity response at these two hazard levels. Finally, the ratio of the viscous forces between the MCE and 2/3MCE hazard can be related by

$$\frac{F_{viscous}^{MCE}}{F_{viscous}^{2/3MCE}} = \left(\frac{\Delta_{MCE}}{\Delta_{2/3MCE}} \right)^{\alpha} \qquad \textbf{11.2}$$

With respect to a FVD nonlinearity of $\alpha = 0.75$, this force ratio is equal to 1.36 and can be viewed as a device over-strength action. From experimental testing of mild steel reinforcement, the ratio between the ultimate strength and yield strength is in the order of $f_u / f_y \approx 1.45$ for Grade 300MPa (5^{th} percentile characteristic yield strength): for Grade 500MPa the ratio is in the order of $f_u / f_y \approx 1.25$. Therefore, considering $\alpha = 0.75$, an over-strength ratio of 1.36 is comparable to the material over-strength inherent in mild steel reinforcement and can be easily accommodated within design considering traditional capacity design principles. In fact, recognising that 1) the viscous forces are out-of-phase with the elastic forces and 2) the viscous contribution to the lateral capacity is unlikely to be greater than 50%, it is expected that the net viscous over-strength will be somewhat less than Equation 11.2.

11.4. DESIGN DETAILS OF THE BRIDGE SYSTEMS

11.4.1. Bridge 1: Monolithic Ductile Benchmark

The reinforcement detail for each bridge pier is presented in Figure 11.3 and tabulated in Table 11.3. A DDBD procedure would typically result in equal reinforcement contents for each pier; however, subtle variations can be seen for each. These variations come about because P-Δ actions are accounted for within the design and differ for each pier depending on the displacement demand, pier height and tributary deck load.

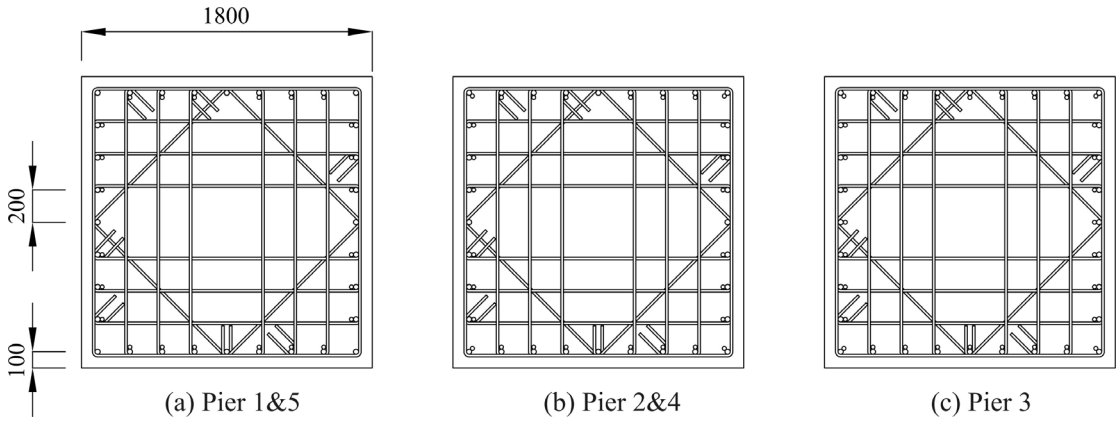

Figure 11.3 Reinforcement details of the ductile bridge piers (dimensions to the centroid of the longitudinal reinforcement)

Table 11.3 Reinforcement contents for the ductile bridge piers

	Longitudinal reinforcement[1]	Transverse reinforcement[1]
Piers 1&5	32-XD32 & 24 XD25 (1.16%)	XR16@ 200mm crs (1.16%)[2]
Piers 2&4	32-XD32 & 28 XD25 (1.22%)	
Pier 3	32-XD32 & 32 XD25 (1.28%)	

[1] XD refers to 500MPa deformed (ribbed) reinforcement, XR refers to 500MPa round (smooth) reinforcement.
[2] Reinforcement ratio calculated by area enclosed by the centreline of the peripheral hoops

11.4.2. Bridge 2: Traditional Post-Tensioned Hybrid Bridge

The traditional hybrid bridge adopts internally grouted mild steel reinforcement (having Grade 500MPa reinforcement) combined with unbonded post-tensioned tendons within each bridge pier. An elevation of the hybrid pier is shown in Figure 11.4 and has identical geometry to the benchmark bridge piers. The post-tensioned anchorages are located at the underside of the foundation and at the top of the pier cap beam. Details of the reinforcement at the rocking interface are illustrated in Figure 11.5 and summarised in Table 11.3.

The layout and quantity of the internally grouted reinforcement at the rocking interface (at the base of the pier) is the same for each pier. The grouted reinforcement consists of 28-XD40 longitudinal bars with an unbonded length of $6d_b$ (240mm):

Figure 11.5(a). These large diameter bars, while available, are not commonly used in practice. While XD-32 bars were originally considered, the capacity of the section was not sufficient unless a large number of bars were used. One benefit of using larger diameter bars is that the ductility of the section increases due to a larger strain penetration depth ($l_{sp} = 0.022 f_y d_b$): resulting in an increased plastic hinge length $\boldsymbol{L_p}$. This is quite significant for a jointed system, especially when using Grade 500MPa reinforcement which has relatively limited strain ductility when compared to the more ductile Grade 300MPa reinforcement. By using XD-40 bars the number of bars reduces, simplifying construction and grouting applications.

Four tendon ducts are located at the centre of each pier. The number of post-tensioned tendons (or the initial post-tensioning force) varies from pier to pier recognising the variation of moment demand throughout each pier. The reinforcement within the precast pier element (refer Figure 11.5 (b)) is identical with a total of 64-XD32 (evenly distributed in pairs) resulting in a reinforcement content of 1.59%. This reinforcement is terminated at the rocking interface and does not contribute to the moment capacity of the rocking section.

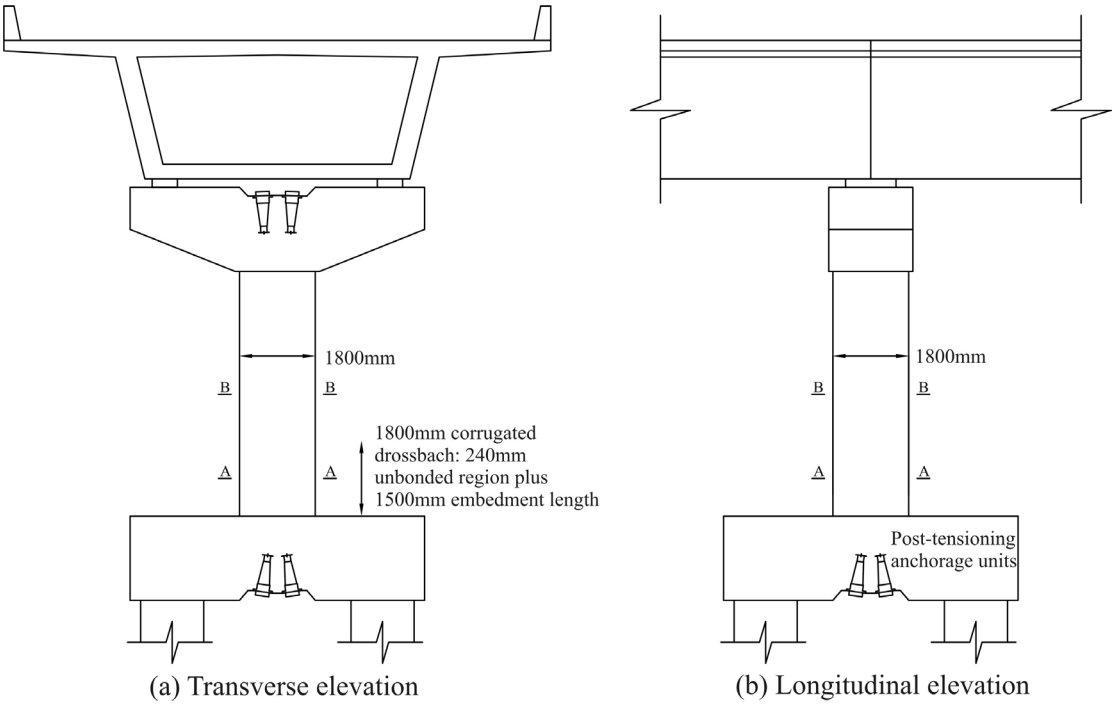

Figure 11.4 Elevation of the hybrid bridge pier

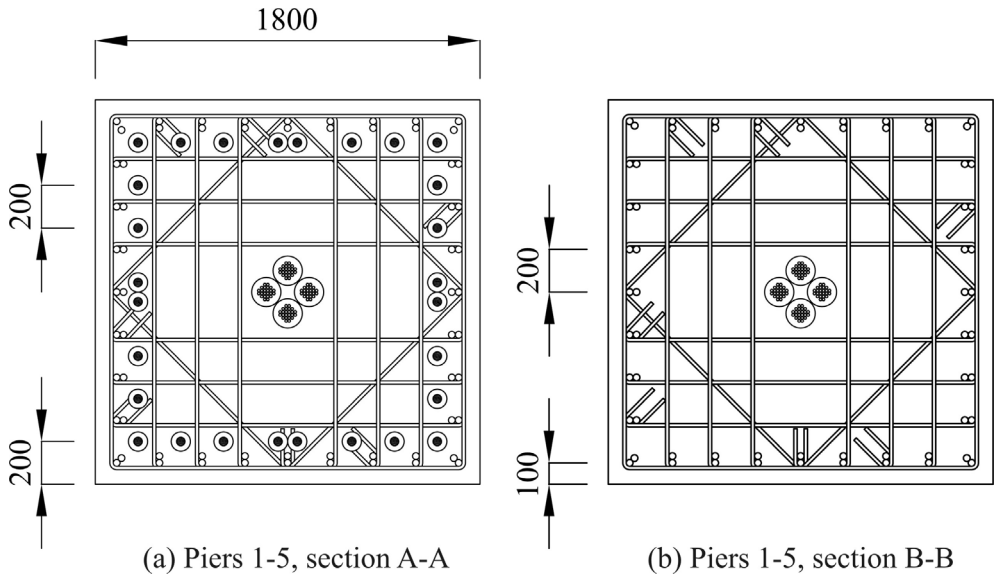

Figure 11.5 Section detail of the hybrid piers showing the reinforcement at the rocking interface (a) and the reinforcement of the precast element (b)

Table 11.4 Longitudinal and prestressed reinforcement details for the hybrid pier

	Prestressed reinforcement	**Internally grouted reinforcement**
Piers 1&5	124-12.7mm strands (ρ_{pt}=0.38%) with total initial prestressing force of 7,440kN. 4-#3105-31 BBR anchorage units.	28-XD40 grouted within 90mm diameter Drossbach duct. Provided with 240mm unbonded length. (ρ_s=1.09%)
Piers 2&4	124-12.7mm strands (ρ_{pt}=0.38%) with total initial prestressing force of 9,920kN. 4-#3105-31 BBR anchorage units.	
Pier 3	140-12.7mm strands (ρ_{pt}=0.43%) with total initial prestressing force of 13,300kN. 4-#3105-31 & 1-#1905-16 BBR anchorage units.	

11.4.3. Bridge 3: Advanced Hybrid Bridge AFS1.

The damper layout of the AFS1 bridge piers is illustrated in Figure 11.6, while the section details are illustrated in Figure 11.7. The external viscous dampers are mounted to the pier using fabricated steel brackets. For this application Taylor fluid viscous dampers (FVD) were used (www.taylordevices.com). The viscous devices were selected based on the required damping coefficient, non-linearity and maximum damper force required during the design process. In addition to the FVDs, a total of 20-XD40 internally grouted longitudinal bars and a single tendon group are located internal to the section (Figure 11.7(a)). The reinforcement content within the precast pier elements is the same as that used within the hybrid bridge above (Bridge 2).

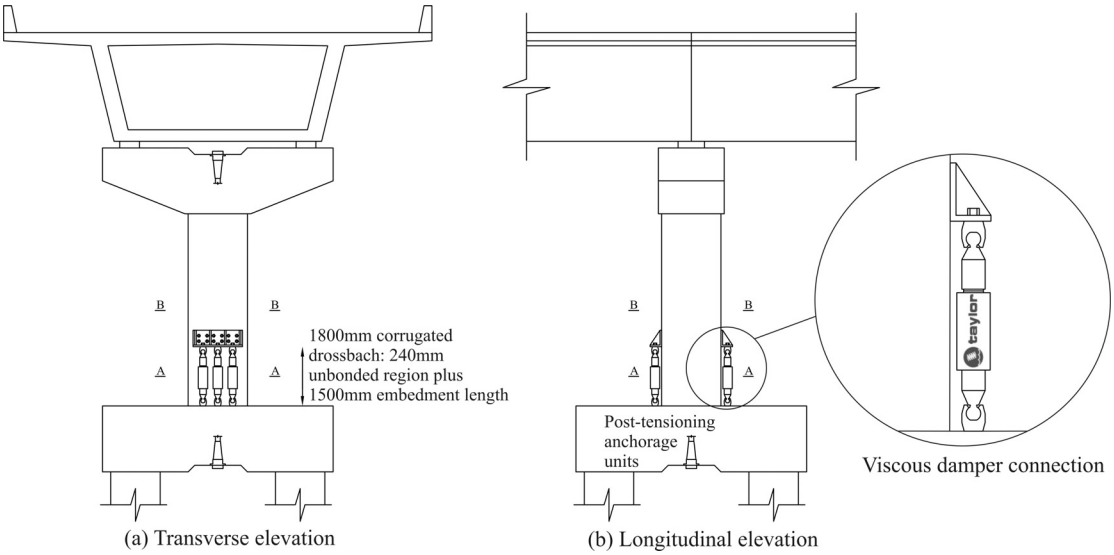

Figure 11.6 Elevation of the AFS1 hybrid bridge pier

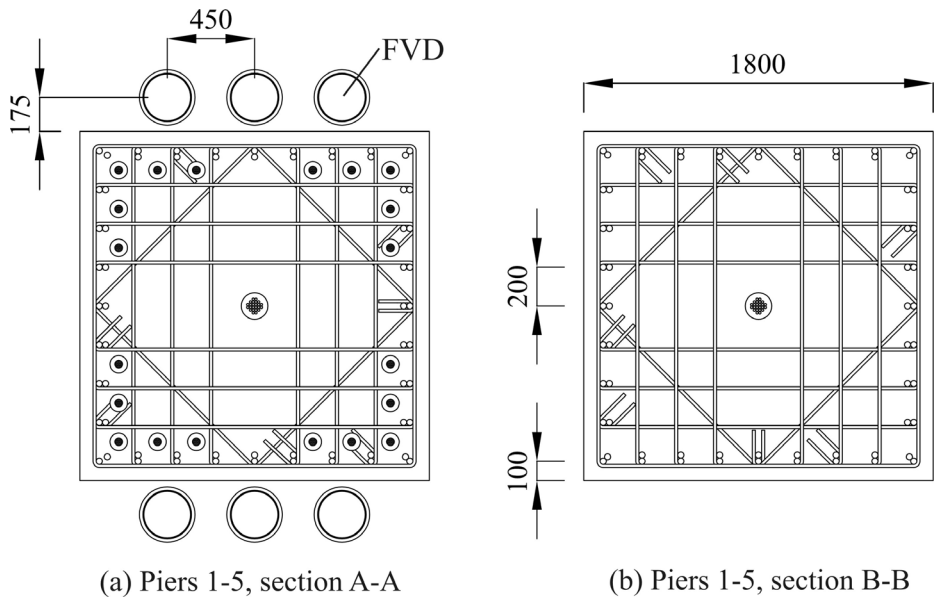

Figure 11.7 Section details of the AFS1 hybrid piers showing the reinforcement and external FVD devices at the rocking interface (a) and the reinforcement of the precast element (b)

Table 11.5 Longitudinal reinforcement, prestressing and dissipation details for the AFS1 hybrid pier

	Prestressed reinforcement	Internally grouted reinforcement	External viscous devices
Piers 1&5	44-12.7mm strands (ρ_{pt}=0.14%) with total initial prestressing force of 2,200kN. 2-#3105-22 BBR anchorage units.	20-XD40 grouted within 90mm diameter Drossbach duct. Provided with 240mm unbonded length. (ρ_s=0.78%)	6-Taylor fluid viscous dampers. 220Kip (979kN) device, ±100mm stroke. C_{vd}=6500kNs$^{\alpha}$/m$^{\alpha}$ Non-linearity, α=0.75
Piers 2&4	44-12.7mm strands (ρ_{pt}=0.14%) with total initial prestressing force of 3,080kN. 2-#3105-22 BBR anchorage units.		
Pier 3	60-12.7mm strands (ρ_{pt}=0.19%) with total initial prestressing force of 5,400kN. 2-#3105-30 BBR anchorage units.		

11.4.4. Bridge 4: Advanced Hybrid Bridge AFS2.

External dampers are mounted on all four sides of the AFS2 bridge piers. Each pier has six FVD Taylor devices and six TCY dampers (Figure 11.8 and Figure 11.9). Damper properties are given in Table 11.6 along with the prestressing content and initial post-tensioning. The FVDs are located along the extreme edges (considering transverse response), while the TCY dampers are located close to the middle of the section. Larger displacements (and hence velocities) occur at the extreme edge of the section and are more suited to the viscous devices.

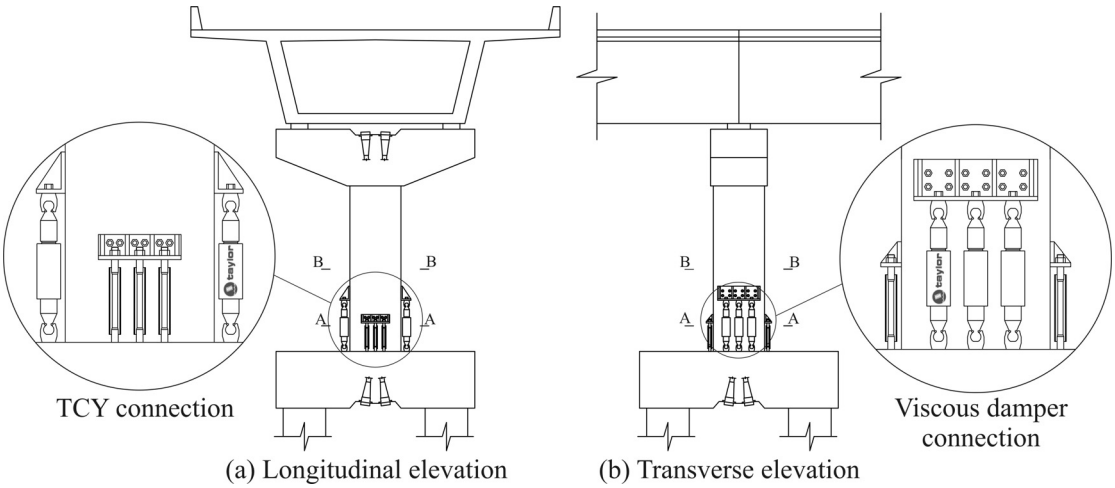

Figure 11.8 Elevation of the AFS2 hybrid bridge pier

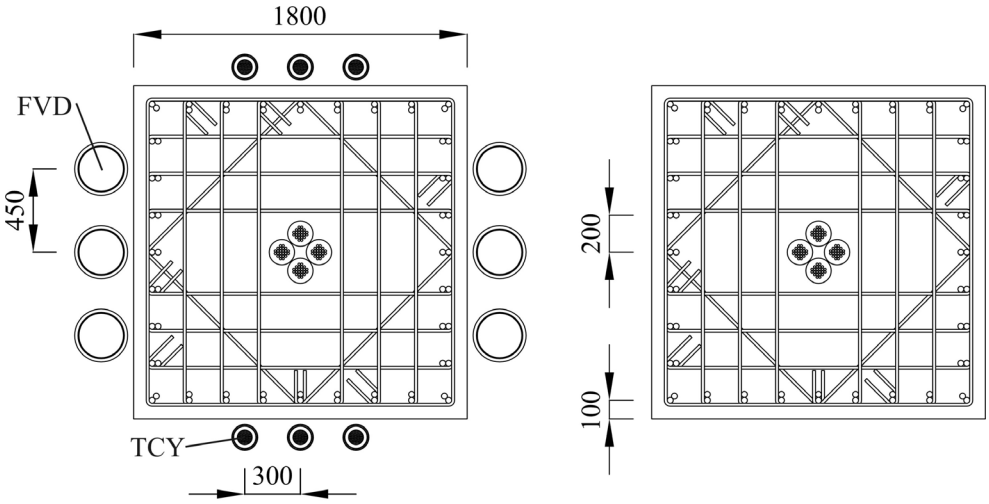

(a) Piers 1-5, section A-A (b) Piers 1-5, section B-B

Figure 11.9 Section details of the AFS2 hybrid piers showing the external devices at the rocking interface (a) and the reinforcement of the precast element (b)

Table 11.6 Prestressing and dissipation details for the AFS2 hybrid pier

	Prestressed reinforcement	External TCY devices	External viscous devices
Piers 1&5	64-12.7mm strands (ρ_{pt}=0.20%) with total initial prestressing force of 3,900kN. 4-#1905-16 BBR anchorage units.	6-65mm diameter, Grade 500MPa TCY dampers. Yielding fuse length of 650mm (ρ_s=0.61%)	6-Taylor fluid viscous dampers. 220Kip (979kN) device, ±100mm stroke. C_{vd}=4000kNs$^{\alpha}$/m$^{\alpha}$ Non-linearity, α=0.75
Piers 2&4	72-12.7mm strands (ρ_{pt}=0.22%) with total initial prestressing force of 5,950kN. 4-#1905-18 BBR anchorage units.		
Pier 3	95-12.7mm strands (ρ_{pt}=0.29%) with total initial prestressing force of 9,975kN. 5-#1905-19 BBR anchorage units.		

11.4.5. Cost Estimation

An initial estimation puts the cost of construction of the benchmark bridge at NZD12.74 million[3]. Without going into a detailed cost assessment, the actual cost is difficult to define as it will be extremely case specific and will depend on many factors including local soil conditions, geography and founding conditions (such as river bed or otherwise), the type of construction contract, the contractor involved, available resources etc. For the purpose of providing an initial feasibility study, the above figure will suffice.

[3] Assuming NZD3500 per m^2 of deck area in 2008.

(a) Post-Tensioning Cost Estimation

Construction details of the three post-tensioned bridges (Hybrid, AFS1 and AFS2) were sent to BBR Contect[4] to undertake a cost estimate for post-tensioning. The cost estimate included the following breakdown,

- Post-tensioning tendons; tendon anchorages; anchorage heads; special reinforcement.
- Stressing equipment, labour and on-site technical support
- Travel, freight, jack/gauge calibration etc

Good access and continuity of work was assumed during construction which would be carried out by local employees. Post-tensioning was estimated to cost NZD20,000 per tonne of post-tensioning. The difference in construction cost between the monolithic bridge and the post-tensioned bridge was assumed to be equal to the cost to undertake the post-tensioning of the hybrid bridge. This would seem appropriate given both systems are of precast construction. With that said, an additional 0.5% (cost of monolithic construction) was added to the cost of the post-tensioned systems to conservatively account for resources concerning the fabrication of the dissipater connection details as well as special reinforcement and detailing about the rocking interface. The cost-estimation is summarised in Table 11.7.

Table 11.7 Summary of the cost-estimation for the post-tensioned bridge systems

	Hybrid	AFS1	AFS2
PT content	4.597 tonne	1.740 tonne	2.731 tonne
PT cost	$91,933	$34,793	$54,619
Misc cost	$63,700	$63,700	$63,700
Total	$155,633	$98,493	$118,319
Total[1]	1.22%	0.77%	0.93%

[1] Based on a monolithic construction cost of 12.74 million

(b) Dissipater Cost Estimation

Each 220kip Taylor device costs approximately AUD11,240[5]. The AFS bridges required a total of 30 FVDs (six per bridge pier) equating to a total damper cost of NZD388,900[6] (for both AFS1 and AFS2). This is roughly 3.1% of the total cost of the benchmark bridge and must be appropriately assessed to gauge any benefit of the system. The cost to construct each of the AFS bridges includes the additional cost of post-tensioning as well as the cost of the external dampers. The fabrication cost of the TCY dampers, installed within the AFS2 Bridge, is not included. The cost to construct the TCY devices would be a small percentage of the total construction cost. Considering the method of cost estimation adopted, including the cost of the TCY devices would not add any accuracy to the cost estimation. The total construction cost of each of the four bridges is summarised in Table 11.8.

Table 11.8 Summary of bridge construction cost

	Monolithic	Hybrid	AFS1	AFS2
Cost	12.74M	12.90M	13.23M	13.25M

[4] Paul Blundell, Project Engineer, BBR Contech, Christchurch, New Zealand.
[5] Xavier Delattre, Granor Rubber & Engineering P/L for Taylor Devices, Australia and New Zealand
[6] Exchange rate based on 2008 1st quarter average of NZD/AUD=0.867 (Source: Reserve Bank of New Zealand)

11.5. LOSS ASSESSMENT WITHIN A PERFORMANCE-BASED SEISMIC ASSESSMENT FRAMEWORK

Seismic risk, quantified in the form of economic measures, is a conceptually simple way of expressing liability (financial) to a client (or stakeholder) based on the expected performance of a particular structural system throughout its operating life. Based on the anticipated seismic hazard (ground motion) and structural response, the structural performance (maximum displacements and/or accelerations) is related to damage and converted to monetary loss. This monetary loss is accumulated over the working life of the structure and converted to an expected annual loss, representing the average annual cost to the client.

The detailed theory pertaining to the development of expected annual loss is outside the scope of this research, this research adopts the ideas as a tool to quantify the comparative performance of three post-tensioned bridges.

The key tasks involved within a performance-based seismic assessment are illustrated in Figure 11.10 and discussed in detail below, while further details can be found in the following publications: Cornell and Krawinkler [2000]; Vamvatsikos and Cornell [2002]; Deierlein et al. [2003]; Aslani [2005]; Zareian and Krawinkler [2007].

1. The ground motion hazard represents the ground shaking intensity at a site. A seismic hazard analysis of the site is carried out to express the intensity measure (IM) as a function of annual frequency of exceedance (rate of exceedance λ). The intensity measure (IM) could be, for example, peak ground acceleration (PGA) or spectral acceleration, $S_a(T)$. Using empirically calibrated attenuation relationships a seismic hazard analysis predicts the level of shaking at a site based on earthquake magnitude, rupture mechanism, soil amplification, site-to-source distance and propagation path.

2. A structural response is carried out to determine the seismic response of the structure as a function of ground motion intensity (IM). The structural response is quantified by an engineering demand parameter (EDP). Typical EDPs include inter-storey drift, floor accelerations or material strains etc.

3. The structural response is related to structural damage of each component within the structure. Damage to components requiring repair is expressed as a damage measure (DM). Typical damage measures include buckling of the longitudinal reinforcement, spalling of cover concrete, flexural cracking etc. Fragility functions are generally employed, relating EDP to a specific damage measure (DM). That is, based on experimental testing, or otherwise, there exists a mean EDP (μ_{EDP}) and dispersion (β_{EDP}) associated with each DM. Furthermore, a damage state (DS) is a discrete state which loosely groups together a set of damage measures; that is, a specific damage state may consist of extensive cover spalling, longitudinal bar buckling and extensive flexural cracking.

4. The structural damage is related to loss in terms of repair costs, casualties and downtime (the time to reinstate the function of the structure). In particular,

damage states are related to loss (L) which are formulated, either from reconnaissance following major earthquake events, or engineering judgement.

5. Following the computed loss, a decision is made to determine whether the loss is acceptable, or how the loss of one structural system compares to the loss of another structural system.

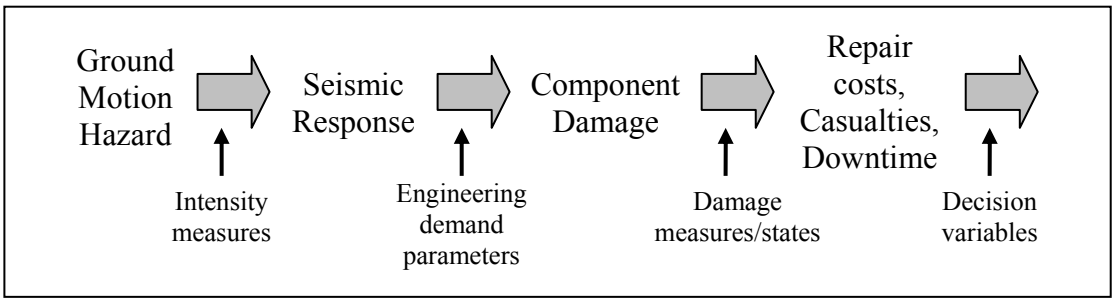

Figure 11.10 Schematic summarising the key steps within a performance-based assessment

The computed loss treats damage and loss as a continuous function, while, uncertainties associated with structural response, damage measures and loss are explicitly included within the loss algorithm.

11.5.1. Expected Annual Loss (EAL) Formulation

The Expected Annual Loss (EAL) is defined in Equation 11.3 in a continuous and a discrete formulation. EAL is the integral of the loss-hazard curve which relates loss to some probability of being exceeded in one year. In this equation, ***N*** is the number of discrete states resulting in loss. With reference to the discrete formulation, for each state the loss LR_i is multiplied by the probability of occurrence in one year ***P(LRi)***. The total loss is the summation of the expected loss over all states.

$$EAL = \int_0^{\infty} LR\left|dP(LR)\right| = \sum_{i=1}^{N} LR_i \cdot P(LR_i) \qquad \textbf{11.3}$$

The probability of exceeding a specific loss combines information from the structural response, seismic hazard and the fragility of the structural components.

11.6. SEISMIC HAZARD MODEL AND GROUND MOTIONS FOR THE LOSS ASSESSMENT

11.6.1. Loss Assessment Hazard Model

The NZS1170.5 [2004] seismic hazard curve was used to describe the relationship between seismic intensity (IM) and the annual rate of exceedance (λ) for the loss assessment. Referring to NZS1170.5 [2004], the seismic hazard is related to R_u while the annual rate of exceedance is related to $1/T$ (where T is the return period). This code-based IM-λ relationship was considered appropriate as the bridge systems were designed according to the New Zealand Uniform Hazard Spectrum (UHS). Additional seismic hazard analyses from Stirling et al. [2002] were required for annual rates of exceedance less than 2% in 50 years as data is not available in NZS1170.5 [2004]. In

this example, the design PGA was selected as the IM measure and was related to the return period factor R_u. This hazard relationship is illustrated in Figure 11.11.

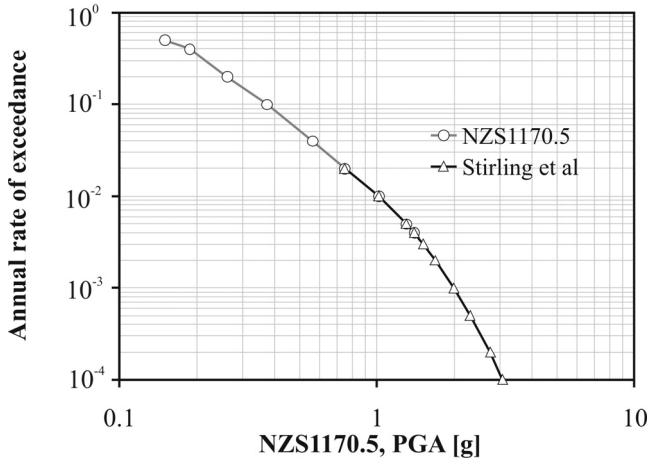

Figure 11.11 Seismic hazard curve based on NZS1170.5 [2004] and Stirling et al [2002]

An *efficient* IM measure is required for loss assessment as this will reduce the uncertainty associated with the expected annual loss. Typically, the spectral acceleration at the fundamental period of the structure with 5% equivalent viscous damping $S_a(T_1,5\%)$ is used as the IM measure (Shome and Cornell [1999]). This method scales the selected ground motions to a single spectral acceleration co-ordinate S_a. However, this method was not used in this example; instead, the ground motions were scaled to the UHS over a large period range as per NZS1170.5 [2004]: this scaling method has the advantage of being applicable to any system having a structural period (elastic or secant) within the scaled period range.

11.6.2. Scaling of the Selected Ground Motions

A suite of ground motions comprising of 22 earthquake records was used in this study. The ground motions all have strong directivity effects consistent with near-fault rupture mechanisms. A summary of the selected ground motions is given in Table 11.9. The ground motions were scaled to the velocity spectrum over a period of 0 to 4 seconds: similar to the method outlined in Chapter 8. The design acceleration, pseudo-velocity (design) and pseudo-displacement (design) spectra are compared to the relevant ground motion spectra in Figure 11.12. While some dispersion is evident, the mean displacement response spectrum compares well with the design displacement spectrum; refer Figure 11.12 (c). As mentioned previously, scaling the ground motions over a large period range returns scale factors that are not specific to a structure with a particular elastic, or secant period. This allows a single set of scaling factors to be used for all four bridge structures.

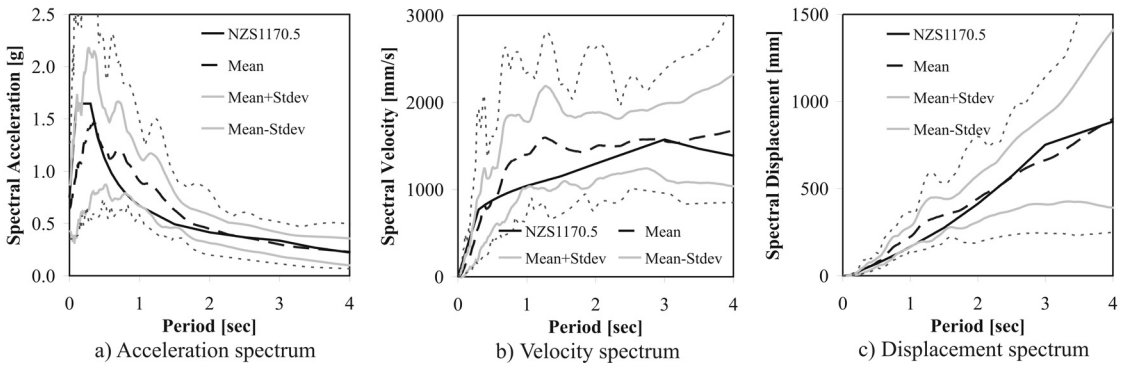

Figure 11.12 Scaled earthquake response spectra (5% damped) and comparison with the elastic design spectrum

Table 11.9 Selected earthquake ground motions

EQ evetnt	Year	Station	Mw	R[1]	Rupture Mech	Orientation	Soil type[2]	PGA[3]	PGV[3]	k[4]
Northridge	1994	Rinaldi receiving station	6.69	6.5	Reverse	228	B	0.825	1.60	0.690
Northridge	1994	Newhall fire station	6.69	5.92	Reverse	360	D	0.590	0.97	0.906
Northridge	1994	Sylmar-Olive View	6.69	5.3	Reverse	260	D	0.843	1.29	0.811
Northridge	1994	LA Dam	6.69	5.92	Reverse	334	A	0.349	0.51	1.537
Northridge	1994	Jensen filter plant	6.69	5.43	Reverse	22	B	0.571	0.76	1.026
Imp Valley	1979	El Centro Array #5	6.53	3.95	Strike-Slip	230	D	0.377	0.91	1.208
Imp Valley	1979	El Centro Array #7	6.53	0.56	Strike-Slip	230	D	0.463	1.09	1.116
Kobe	1995	KJMA	6.9	0.96	Strike-Slip	0	B	0.821	0.81	0.982
Kobe	1995	Takatori	6.9	1.47	Strike-Slip	0	E	0.611	1.27	0.695
Kobe	1995	Port Island	6.9	3.31	Strike-Slip	0	E	0.315	0.75	1.118
Kobe	1995	Kobe University	6.9	0.92	Strike-Slip	0	A	0.290	0.55	1.540
Loma Prieta	1989	Saratoga-W Valley	6.93	13.7	Reverse-Oblique	270	D	0.332	0.62	1.635
Loma Prieta	1989	Los Gratos Pres	6.93	0.92	Reverse-Oblique	0	A	0.931	1.09	0.656
Chi Chi	1999	TCU068	7.62	0.32	Reverse-Oblique	270	A	0.566	1.77	0.824
Chi Chi	1999	CHY101	7.62	9.96	Reverse-Oblique	0	D	0.440	1.15	1.193
Turkey	1999	Gebze	7.51	10.92	Reverse-Oblique	0	A	0.244	0.50	3.180
Iran	1978	Tabas	7.35	2.05	Reverse	TR	A	0.852	1.21	0.909
Morgan Hill	1984	Coyote Lake Dam	6.19	0.53	Strike-Slip	195	A	0.708	0.52	1.783
Pacoima Dam	1971	Dam abutment	6.61	1.81	Reverse	164	A	1.230	1.13	0.874
Landers	1992	Lucerne	7.3	1.1	Strike-Slip	260	A	0.727	1.47	1.285
Landers	1992	Joshua Tree	7.3	11.6	Strike-Slip	90	C	0.284	0.43	2.024
Turkey	1999	Duzce	7.1	8.2	Strike-Slip	270	D	0.535	0.84	1.188

[1] Closest distance from the site to the rupture area [km]
[2] Geomatrix soil classifications
[3] Values from response spectra analyses. PGA in units of g, PGV in units of m/s.
[4] Scale factor for 3.9% probability of exceedance in 100 years i.e. R_u=1.405

11.7. STRUCTURAL PERFORMANCE LIMITS, PERFORMANCE OBJECTIVES AND DESIGN CRITERIA

11.7.1. Material Limit States

The material strain limits below are specific to reinforced and unbonded post-tensioned concrete elements.

(a) Elastic Strain Limit

For design, the elastic strain limit corresponds to a concrete strain of $\varepsilon_c = 0.002$, and yield strain ε_y for mild steel reinforcement.

(b) Minor Distress

Minor distress is associated with low levels of strain ductility; for concrete this is defined as a strain of $\varepsilon_c = 0.004$, for mild steel reinforcement the strain limit is $\varepsilon_s = 0.015$.

(c) Moderate Distress

For concrete this corresponds to a strain equal to the concrete compression design strain limit $\varepsilon_{c,dc}$ in Eq.(11.4). This theoretical relationship is derived by equating the strain energy of the transverse reinforcement at rupture to the strain energy within the confined core of the section, discussed in Chapter 7.

$$\varepsilon_{c,dc} = 0.004 + 1.4\frac{\rho_v f_{yh} \varepsilon_{su}}{f'_{cc}} \qquad \textbf{11.4}$$

Where;

ρ_v is the sum of the transverse reinforcement ratio in the two directions of the section
f_{hy} is the yield stress of the transverse reinforcement
ε_{su} is the rupture strain of the transverse reinforcement
f'_{cc} is the confined concrete strength.

The strain in the longitudinal reinforcement is equal to 60% of the monotonic rupture strain $\varepsilon_s = 0.6\varepsilon_{su}$. The 0.6 factor accounts for the reduction in strain capacity due to reversed cyclic loading (into compression) and low-cycle fatigue associated with bar buckling.

According to the New Zealand concrete design standard (NZS3101 [2006]) the strain in the prestressed reinforcement is equal to 90% of the monotonic yield strain $\varepsilon_{pt} = 0.9\varepsilon_{pty}$.

(d) Extensive Distress

Extensive distress defines the onset of rupture. Extensive distress for concrete is associated with a compression strain equal to 150% of the design strain limit in Eq.(11.4), i.e. $\varepsilon_c = 1.5\varepsilon_{c,dc}$.

The strain in the longitudinal reinforcement is equal to 90% of the monotonic rupture strain $\varepsilon_s = 0.9\varepsilon_{su}$.

The strain in the prestressed reinforcement is equal to 90% of the monotonic rupture strain $\varepsilon_{pt} = 0.9\varepsilon_{ptu}$.

(e) Material Rupture

For concrete, this limit is $\varepsilon_c = 1.5\varepsilon_{c,dc}$ (being the same limit above). The strain in the longitudinal steel is equal to the monotonic rupture stain $\varepsilon_s = \varepsilon_{su}$, while the strain in the prestressed reinforcement is also equal to the monotonic rupture strain $\varepsilon_{pt} = \varepsilon_{ptu}$.

11.7.2. Structural Performance Levels

Six structural performance limits are identified below; each performance limit is governed by one of several material and/or geometric limit states. The governing material limit state is defined by the material which reaches the limit first. The performance limits below are further illustrated in Figure 11.13 which incorporates a number of performance objectives that are discussed in the following section.

(a) Elastic Limit State

The elastic limit state of the structure defines the onset of first yield. This is associated with the *Elastic Strain Limit* of the first material to yield.

(b) Nominal Yield State

This deformation limit state corresponds to the strength of the structure when it achieves nominal yield strength and is associated with a low level of ductility (nominally ductile). This limit state is defined by the *Minor Distress* material limit state.

(c) Design Limit State

The design limit state is governed by the *Moderate Distress* material limit state in addition to two geometric limit states. The first geometric limit state is a lateral drift corresponding to bar buckling based on a fragility function fitted to experimental test data determined by Berry and Eberhard [2005]. The second geometric limit state is a global limit state related to excessive second order effects: a limiting P-Δ stability index of θ_Δ=0.33 is used in Eq.(11.5), Priestley et al. [1996].

$$\theta_\Delta = \frac{P\Delta}{M} \qquad \textbf{11.5}$$

Where;

M is the moment capacity of the system
P is the vertical load acting at the effective height of the structure
Δ is the horizontal displacement of the vertical load

When θ_Δ=1.0 the lateral capacity of the system is equal to zero.

(d) Ultimate Limit State

The ultimate limit state is the onset of significant lateral strength degradation due to rupture and is defined by the *Extensive Distress* material limit state.

(e) Rupture Limit State

Rupture may not correspond to global collapse; however, the lateral load capacity is significantly compromised and can no longer be relied upon for lateral resistance. This corresponds to the *Material Rupture* limit state.

(f) Structural Collapse

No material limit states are associated with structural collapse, only geometric limit states. The collapse displacement is defined as the displacement corresponding to rupture plus one yield displacement. This allows for some residual displacement capacity of the system in the form of axial (gravity) restraint – provided the lateral resistance has not been reduced to zero due to P-Δ loads. In Eq.(11.6) Δ'_y refers to the nominal yield displacement. Alternatively, structural collapse can also correspond to a P-Δ stability limit of θ_Δ=1.0.

$$\Delta_{collapse} = \Delta_{rupture} + \Delta'_y \qquad \textbf{11.6}$$

The strain in the steel at rupture above refers to the monotonic rupture strain. Considering low-cycle fatigue, the actual strain at rupture is likely to be considerably lower, and is in fact accounted for at the design performance level by reducing the allowable strain to 0.6 of the monotonic rupture strain.

Each performance limit state has some level of aleatory uncertainty associated with both strength and deformation, essentially, due to variability in material properties (concrete, steel, bond etc), instrumentation and recording error and the variability in response of composite members. An uncertainty is associated with each structural performance limit defined as the dispersion β. The dispersion (also known as the lognormal standard deviation $\sigma_{ln(x)}$) is defined as,

$$\beta = \sigma_{\ln(x)} = \sqrt{\ln\left(\frac{\sigma_x^2}{\mu_x^2} + 1\right)} \qquad \textbf{11.7}$$

Where σ_x and μ_x are the standard deviation and mean of the raw data. For small dispersions (<0.3) β is approximately equal to the coefficient of variation,

$$\beta \approx \frac{\sigma_x}{\mu_x} = c.o.v \qquad \textbf{11.8}$$

The uncertainty associated with each structural performance limit (or material limit state) is generally found from an extensive library of experimental test data. Fragility curves are fitted to the experimental data (generally assumed to follow a lognormal distribution) defining the mean and dispersion for a specific limit state. For each of the structural limits above, a dispersion of β = 0.40 was selected for the monolithic

bridge piers. For the hybrid bridge systems, it is argued that the material strain limits can be estimated with greater accuracy as the deformation state is more predictable; that is, material strain limits are related to a lumped rotation at the rocking base as opposed to a ductile pier having some approximated plastic hinge length. Hence, a value of $\beta = 0.267$ was adopted for each of the post-tensioned bridge systems.

11.7.3. Performance Objectives

Three performance objectives were selected based on those presented in FEMA [2003]. The last two performance objectives were the primarily design goals for each of the bridge systems designed herein.

Immediate occupancy: Negligible damage to the structural system under a very frequent event. Specific to this bridge design, this corresponds to a 21.7% probability of exceedance within 100 years i.e. 1/3MCE. This seismic hazard is associated with the *nominal yield state* of the structure.

Damage control: Significant structural damage has occurred with some loss in strength and stiffness but the structure still retains significant margin against collapse. With respect to bridge design the seismic hazard has a 3.9% probability of exceedance within 100 years and is considered a rare event i.e. 2/3MCE. This seismic hazard is associated with the *design limit state*.

Collapse prevention: The gravity load carrying capacity of the structural system is maintained. Structural damage is significant and a majority of the stiffness is lost, combined with some loss in strength. For bridge design, the seismic hazard has a 1.4% probability of being exceeded within 100 years i.e. MCE. This seismic hazard is associated with the *ultimate limit state*.

Further explanation of the performance objectives and structural performance limits discussed previously are illustrated in Figure 11.13.

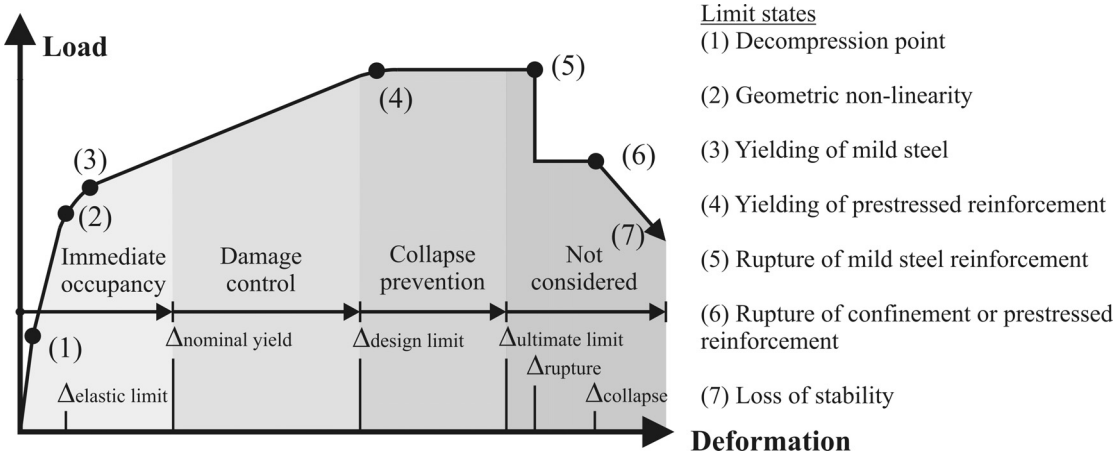

Figure 11.13 Structural performance limits and performance objectives for a post-tensioned pier

11.8. DAMAGE STATES AND LOSS RATIOS

The damage measures discussed herein are primarily related to damage of the pier elements. Any damage to the superstructure, abutments and bearings will be similar between each bridge as damage to these elements will be closely related to the maximum displacement response of the bridge in question. Therefore, only loss associated with pier damage was considered, restricting the study to a relative comparison between each bridge.

11.8.1. Damage States and Loss Ratios for Monolithic, Ductile Bridge Systems

The damage states for the monolithic bridge system were based on suggestions from previous research defined by *Hazus* (Basoz and Mander [1999]; Mander and Bosoz [1999]) and others (Mackie et al. [2007]; Solberg et al. [2008]). It is important to recognise that these loss ratios have some proportion of loss associated with the bridge superstructure, abutments and connections as discussed in Basoz and Mander [1999]. However, previous research investigating the loss comparison between two bridge systems, namely a ductile bridge system and a post-tensioned rocking system, associated these *Hazus* loss ratios (presented in Table 11.10) with pier structural damage alone, Solberg et al. [2008] and therefore it was felt appropriate to use these loss ratios in this study also.

The performance objectives discussed in detail above (immediate occupancy-collapse prevention) have been organised to correspond to specific levels of damage, in particular damage related to material strains (Priestley et al. [2007]). It was for this reason that each damage state (*DS*) is correlated to a discrete performance objective. Table 11.10 presents each damage state and the corresponding a) associated local damage, b) structural performance limit c) performance objective and d) the loss ratio.

Table 11.10 Damage states and loss ratios for the monolithic benchmark bridge system

	Local pier damage	Structural performance limit	Performance objective	Mean loss ratio (*LR*)[1]
DS1: None	Pre-yield	Elastic limit	-	-
DS2: Minor	Minor spalling and cracking of the section. Yielding of bars.	Nominal yield	Immediate occupancy	0.03 (0.01-0.03)
DS3: Moderate	Extensive spalling and cracking. Yielding and buckling of bars.	Design limit	Damage control	0.08 (0.02-0.15)
DS4: Extensive	Extensive elongation of the longitudinal and transverse reinforcement with degradation of the confined concrete core.	Ultimate limit	Collapse prevention	0.25 (0.10-0.40)
DS5: Collapse	Rupture of the longitudinal and/or transverse reinforcement and failure of core concrete (rupture plus one Δ_y)	Collapse	Not considered for design	1.0 (0.30-1.00)

[1] Values in brackets indicate the expected range of loss

Damage states and loss ratios are very subjective. However, the primary purpose of this study was not to accurately estimate the likely economic loss of any one bridge, but provide a comparison between four different bridge systems. Any ambiguity in the damage states, or loss ratios, would have little importance as the overall relative loss ratio will still be valid.
An uncertainty of $\beta = 0.2$ was associated with each loss ratio in Table 11.10. This uncertainty was constant for each damage state and each bridge and based on previous loss estimation studies and financial judgement (Bradley et al. [2008]).

11.8.2. Damage States and Loss Ratios for Hybrid, Post-Tensioned Bridge Systems

The loss ratios and damage states for the hybrid bridge piers are summarised in Table 11.11. For Damage State 2 (DS2: minor damage) the loss ratio was reduced to 67% of the ductile system. This is justified in that cracking will be significantly controlled due to the post-tensioned tendons, and residual crack widths are expected to be nonexistent. Spalling (if any) would be significantly localised at the very base of the pier.

Considering Damage State 3 (DS3: moderate damage), damage is almost entirely associated with concrete spalling. Two scenarios are considered; 1) the rocking toe is protected via a cast-in steel angle or similar, preventing expulsion and providing some confinement to the cover concrete, or 2) the rocking toe region is unprotected with significantly localised spalling at the base of the pier (as opposed to extensive spalling over the full length of the plastic hinge in a ductile pier). Buckling of the internally grouted mild steel reinforcement (dissipaters) does not occur as the bars are grouted within corrugated ducts and located some depth within the confined core of the pier section (and provided with appropriate anti-buckling ties). Furthermore, buckling of the longitudinal reinforcement within the precast element is not considered to be an issue as the strains are below yield (or at worst, nominally elastic). Bar buckling in this case would follow and elastic Euler buckling model but would require an effective length considerably longer than the spacing provided by the transverse reinforcement; therefore, it is assumed that the precast reinforcement within the pier element are not susceptible to buckling. Large tension strains would normally result in the development of larger flexure cracks and thus larger residual crack widths. However, provided an appropriate re-centring ratio λ is chosen, residual crack widths are likely to be minimal. Furthermore, residual pier displacements are expected to be minimal and therefore any costs associated with straightening of the piers would not be required in this instance.

The loss associated with Damage State 4 (DS4) is divided into two categories. If the structural limit state is governed by longitudinal steel strains then the damage to the section (in terms of concrete damage) will be minimal i.e. a slight increase in damage is expected over the previous damage state (DS3) with little to no damage to the confined concrete core. Given that the steel strains approach rupture (or have in fact ruptured), little physical damage is expected of the pier. The only economic loss would result from the cost associated to reinstate the strength of the pier (perhaps considering some form of external supplementary dissipation). Furthermore, given that post-tensioned tendons may have yielded, larger tension strains at the base of the pier may lead to significant residual crack widths.

If the structural limit state of DS4 is governed by the concrete compression strain, rupture of the transverse reinforcement is assumed to have occurred at a concrete strain equal to 150% of the theoretical confinement strain limit. Rupture of the transverse reinforcement is assumed to occur regardless of whether cover confinement (toe protection) is provided or not. This assumption could be challenged depending on the level of confinement (over and above the core confinement reinforcement) provided by the toe anchorage detail. In any case, it is assumed that this damage state is still lower than the equivalent damage state for the ductile pier based on a more localised region of confined core failure, reduced residual crack widths and reduced residual deformations.

Loss associated with downtime is not directly included within this study, primarily because there is minimal literature in this area and it is difficult to accurately quantify (Krawinkler and Miranda [2004]).

Table 11.11 Damage states and loss ratios for the hybrid bridge system

	Local pier damage	**Structural limit state**	**Performance objectives**	**Mean loss ratio (*LR*)[1]**
DS1: None	Pre-yield	Elastic limit	-	-
DS2: Minor	Spalling negligible with limited yielding of reinforcement. Crack control from prestressing.	Nominal yield	Immediate occupancy	0.01
DS3: Minor	Spalling minimal if cover concrete is protected and relatively localised if unprotected.	Design limit	Damage control	0.02 (protected) 0.03 (unprotected)
DS4: Moderate	Spalling minimal if cover concrete is protected and extensive localised spalling if unprotected. Extensive elongation of longitudinal and/or transverse reinforcement. Reduction in prestress force.	Ultimate limit	Collapse prevention	0.08 (governed by steel strain) 0.20 (governed by concrete strain)
DS5: Collapse	Rupture of transverse reinforcement, failure of core concrete, rupture of tendons (rupture plus one Δ_y)	Collapse	Not considered for design	1.0

[1] Protected refers to protection of the rocking toe region such as cast-in steel angles (or polymer confinement wrapping), fibre reinforced concrete etc.

The damage states and loss ratios for the two AFS systems are identical to the hybrid system above with the exception of Damage State 4 (DS4). At DS4 the loss ratio for the AFS1 bridge piers is set equal to 0.07 when governed by the strain limit of the internally grouted reinforcement. This slight reduction over the hybrid system of 0.08 was chosen as AFS1 has additional lateral redundancy being provided by the external viscous dampers when rupture of the grouted reinforcement has occurred. Therefore,

the costs associated to reinstate the pier to its original strength would be somewhat lower.

Table 11.12 Damage states and loss ratios (DS4 only) for the AFS1 bridge system

	Local pier damage	Structural limit state	Performance objectives	Mean loss ratio (*LR*)
DS4: Moderate	Spalling minimal if cover concrete is protected and extensive localised spalling if unprotected. Extensive elongation of longitudinal and/or transverse reinforcement. Reduction in prestress force.	Ultimate limit	Collapse prevention	0.07 (governed by steel strain) 0.20 (governed by concrete strain)

For the AFS2 bridge piers, the loss ratio associated with DS4 was further reduced below AFS1. If the damage state was governed by the strain of the externally mounted mild steel dissipaters, the loss ratio is equal to 0.05. This loss ratio was chosen as the cost to reinstate the strength of the pier is simply equal to the replacement cost of the external mild steel dampers in addition to any concrete repair. These mild steel dampers are of relatively low cost and only require the existing ruptured devices to be removed and replaced with new devices. Furthermore, the AFS2 bridge system has a greater redundancy over AFS1 which has a larger proportion of lateral resistance provided by the non-linear viscous dampers and post-tensioned tendons.

Table 11.13 Damage states and loss ratios (DS4 only) for the AFS2 bridge system

	Local pier damage	Structural limit state	Performance objectives	Mean loss ratio (*LR*)
DS4: Moderate	Spalling minimal if cover concrete is protected and extensive localised spalling if unprotected. Extensive elongation of the dissipaters and/or transverse reinforcement. Reduction in prestress force.	Ultimate limit	Collapse prevention	0.05 (governed by steel strain) 0.20 (governed by concrete strain)

For each Damage State (DS1 to DS4) the level of damage and loss ratio is compared between each bridge system in Table 11.14. It is interesting to note, that while each Damage State corresponds to a specific material strain limit, the level of physical damage is significantly lower for the post-tensioned bridge systems. As discussed previously, high material strains can be appropriately controlled and accommodated for in post-tensioned systems when compared to monolithic construction: resulting in less physical damage for the same Damage State.

Table 11.14 Comparison between damage states and loss ratios

	Monolithic	**Hybrid**	**AFS1**	**AFS2**
DS1	None -	None -	None -	None -
DS2	Minor 0.03	Minor 0.01	Minor 0.01	Minor 0.01
DS3	Moderate 0.08	Minor 0.02-0.03	Minor 0.02-0.03	Minor 0.02-0.03
DS4	Extensive 0.25	Moderate 0.08-0.20	Moderate 0.07-0.20	Moderate 0.05-0.20
DS5	Collapse 1.0	Collapse 1.0	Collapse 1.0	Collapse 1.0

11.9. MODELLING THE BRIDGE SYSTEMS

A lumped plasticity model was adopted for all bridge systems. The abutments were seated on elasto-plastic bearings considering transverse response. The elasto-plastic bearings had a yield force of 3450kN and an elastic stiffness of 690.5MN/m. No upper displacement limit was assigned to the abutment spring.

The prestressed superstructure (box-girder deck) was modelled as an elastic frame element with uncracked section properties. It was assumed that the lateral displacement of the deck required to cause extensive cracking, resulting in a significant loss in deck stiffness, would exceed the stability limit of the piers; therefore, collapse due to pier failure would occur before cracking of the superstructure occurred.

Each reinforced concrete pier section underwent a detailed moment-curvature analysis and moment-rotation analysis with respect to the post-tensioned piers. The section analysis was performed using the program created in Chapter 7. The force-displacement response was integrated from the section analysis, which included second order effects (P-Δ induced actions). This allowed the pier to be modelled as a single translation spring that included the rigid rotation of the plastic hinge, the elastic pier deformation and second-order effects. The elastic pier flexibility was computed based on the full pier height $\boldsymbol{H}$ (measured to the centroid of the bridge deck as in Figure 11.2). The 2-Dimensional structural bridge model is pictured in Figure 11.14: converting the model to 2-Dimensions would reduce the computation time needed to undertake the loss assessment.

Shear deformations were investigated but later ignored as they were minimal. Soil-structure interaction or foundation flexibility was not modelled. Including foundation flexibility within the structural model is likely to reduce the curvature demands within each of the reinforced concrete pier elements, but may increase the overall displacement demand on the superstructure. The decision to ignore foundation flexibility within each bridge was felt appropriate considering the piled nature of the bridge and the relative comparisons that would be made between each bridge system. Furthermore, non-synchronous motion was not included. Non-synchronous motion recognises the time for the rupture to travel along the length of the bridge, resulting in a phase difference to the acceleration time history between each pier: in this study all ground nodes were subject to the same acceleration time history.

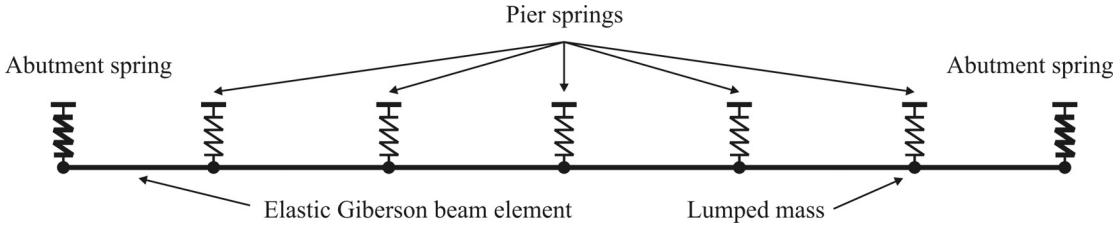

Figure 11.14 Structural bridge model

A Raleigh damping model proportional to the tangent stiffness was used for all analyses with a damping ratio of 0.05 in the first mode and 0.02 in the fourth mode (Priestley et al. [2007]). A 2-Dimensional non-linear, time-history programme (Ruaumoko) was used for the analysis (Carr [2005]).

11.9.1. Ductile, Benchmark Bridge

Each ductile pier was modelled with a Takeda spring (Otani [1974]) whose loading envelope was calibrated according to the pier's computed global force displacement response. The unloading and reloading stiffness parameters were chosen as $\alpha = 0.5$ (based on Emori and Schnobrich [1980]) and $\beta = 0.0$ respectively. Strength degradation starts at the rupture displacement $\Delta_{rupture}$ and ends at the collapse displacement $\Delta_{collapse}$; the collapse displacement $\Delta_{collapse}$ was defined as one displacement ductility beyond the rupture displacement $\Delta_{rupture}$. The residual strength capacity of the pier at $\Delta_{collapse}$ was equal to 33% of the yield force. Cyclic strength degradation was not modelled, where, depending on the level of ductile detailing, can be significant for structural elements that do not conform to the code. A summary of the spring properties and the structural limit states are given in Table 11.15, while Figure 11.15 illustrates the mechanics of the translation pier spring.

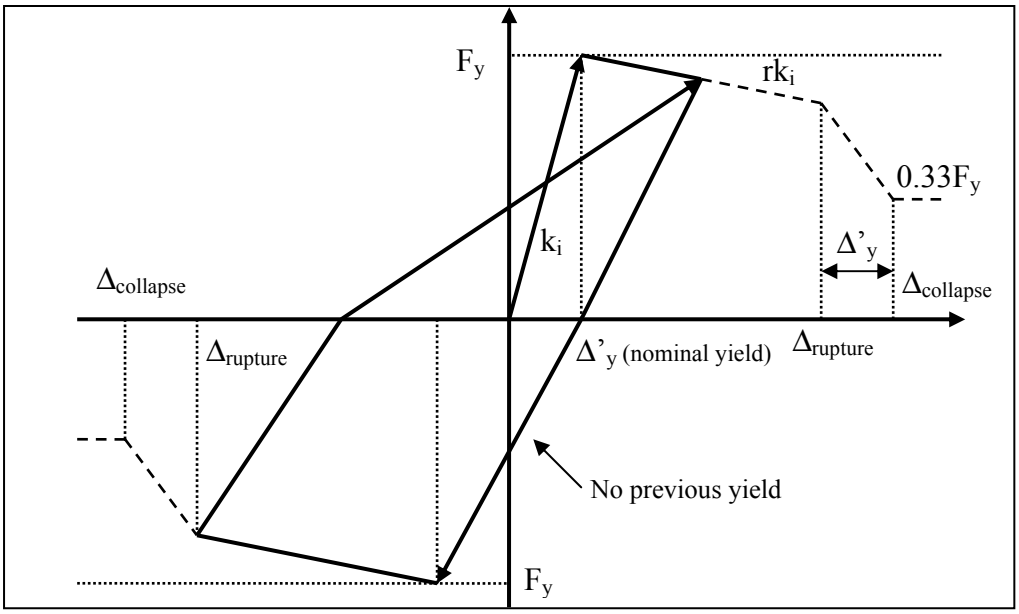

Figure 11.15 Takeda spring model used for the ductile bridge piers

Table 11.15 Spring properties for the ductile piers of the benchmark bridge

	Pier 1&5	Pier 2&4	Pier 3
F_y [kN]	3580	2617	1844
k_i [kN/m]	76220	28054	10199
r	-0.0036	-0.0252	-0.0684
$\Delta_{nominal}$ [m]	0.0907	0.1653	0.3038
Δ_{design} [m]	0.2588	0.4412	0.7462
$\Delta_{ultimate}$ [m]	0.3726	0.6292	1.0978
$\Delta_{collapse}$ [m]	0.4589	0.7866	1.3885

11.9.2. Post-Tensioned Hybrid Bridge

The hybrid pier was modelled with two translation springs in parallel. A bilinear elastic (BLE) spring modelled the post-tensioned and axial contribution (as well as the effects of the P-Δ induced moments) while a Takeda spring modelled the internally grouted mild steel. The Takeda unloading and reloading parameters were $\alpha = 0.3$ and $\beta = 0.6$ respectively. Strength degradation was accounted for within the Takeda spring as 50% of the yield force. The actual numerical value has little relevance as collapse is assumed to have occurred for any displacement greater than $\Delta_{collapse}$.
The spring properties and structural limit states are summarised in Table 11.16. The mechanics of the Takeda spring and the bilinear elastic spring are illustrated in Figure 11.16 to show the combined response.

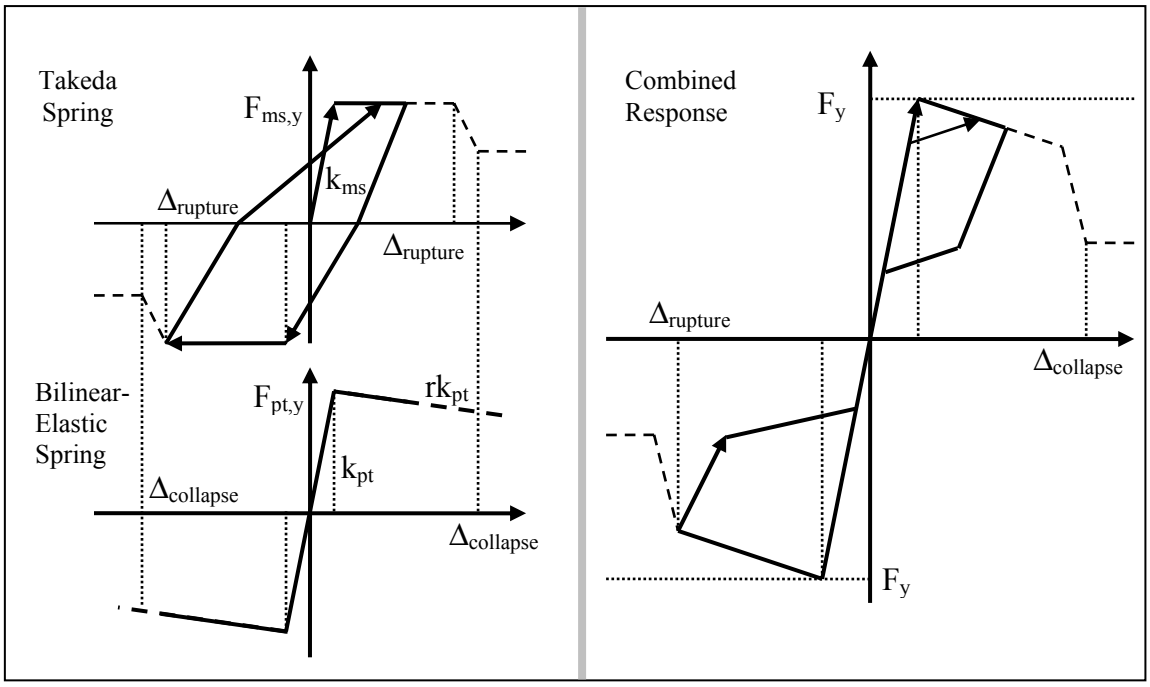

Figure 11.16 Two parallel spring hybrid pier model

Table 11.16 Spring properties and structural limit states for hybrid pier

	Pier 1&5[1]		**Pier 2&4[1]**		**Pier 3[1]**	
F_y [kN]	2523	1968	1748	1346	1282	906
k_i [kN/m]	40684	31239	15075	11309	5677	4149
r	-0.00479	0.02771	-0.04245	0.04278	-0.11280	0.07034
$\Delta_{nominal}$ [m]	0.1436		0.2395		0.4079	
Δ_{design} [m]	0.3922		0.6300		0.9850	
$\Delta_{ultimate}$ [m]	0.4990		0.7925		1.3454	
$\Delta_{collapse}$ [m]	0.5578		0.9065		1.5634	

[1] Values in left column refer to BLE spring, values in right column refer to Takeda spring

11.9.3. AFS1 Bridge

The AFS1 bridge piers were modelled with three translation springs in parallel (two translation springs and one non-linear dashpot). Similar to the hybrid pier, a BLE spring modelled the post-tensioned and axial contribution (as well as the effects of the P-Δ induced moments), a Takeda spring modelled the internally grouted mild steel while a dashpot element modelled the non-linear FVD contribution (Figure 11.17). A section analysis was computed for each pier section defining the spring properties of each contribution. The viscous damper moment-rotation response was converted to an equivalent translation dashpot at the deck level, i.e. an equivalent lateral dashpot at the effective mass. No structural limit states were assigned to the viscous dampers as the displacement and force capacity exceeded those corresponding to collapse. The spring and damper properties for AFS1 are summarised in Table 11.17.

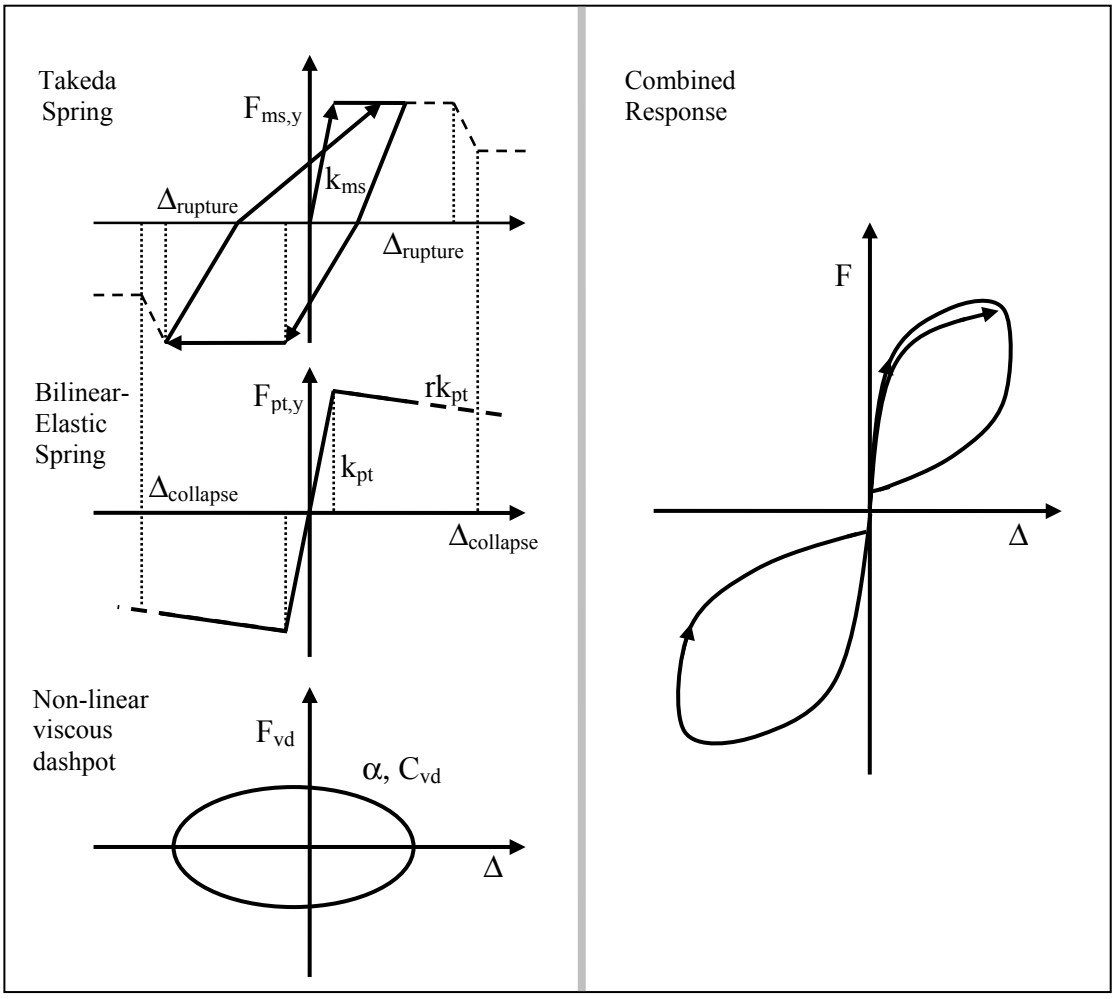

Figure 11.17 Two parallel spring plus dashpot AFS1 pier model

Table 11.17 Spring properties and structural limit states for AFS1 bridge piers

	Pier 1&5[1]		Pier 2&4[1]		Pier 3[1]	
F_y [kN]	1615	1383	1125	922	775	630
k_i [kN/m]	25750	22043	10105	8482	4103	3396
r	-0.02641	0.01972	-0.09214	0.03572	-0.17478	0.05585
C_{vd}	824		445		248	
α	0.75		0.75		0.75	
$\Delta_{nominal}$ [m]	0.1362		0.2250		0.3707	
Δ_{design} [m]	0.3798		0.6260		0.7475	
$\Delta_{ultimate}$ [m]	0.6574		0.9626		1.4132	
$\Delta_{collapse}$ [m]	0.7202		1.0714		1.5990	

[1] Values in left column refer to BLE spring, values in right column refer to Takeda spring

11.9.4. AFS2 Bridge

Similar to AFS1 above, the AFS2 piers were modelled as three translation springs in parallel (again, two translation springs and one non-linear dashpot). A BLE spring modelled the post-tensioned and axial contribution (as well as the effects of the P-Δ induced moments), a bilinear inelastic (BLI) spring modelled the externally mounted TCY dampers while a dashpot member modelled the non-linear viscous damper contribution (refer Figure 11.18). Similar to the procedure for the AFS1 system, a section analysis would determine the equivalent translation dashpot properties to be used in the model (properties summarised in Table 11.18).

Table 11.18 Spring properties and structural limit states for AFS2 bridge piers

	Pier 1&5[1]		Pier 2&4[1]		Pier 3[1]	
F_y [kN]	1722	1159	1220	754	894	482
k_i [kN/m]	28242	13200	10288	4670	4449	1641
r	-0.0005	0.02073	-0.05378	0.05615	-0.12605	0.11903
C_{vd}	1034		553		300	
α	0.75		0.75		0.75	
$\Delta_{nominal}$ [m]	0.1351		0.2292		0.3862	
Δ_{design} [m]	0.3611		0.5629		0.8834	
$\Delta_{ultimate}$ [m]	0.5148		0.7802		1.1952	
$\Delta_{collapse}$ [m]	0.6468		1.0013		1.5730	

[1] Values in left column refer to BLE spring, values in right column refer to BLI spring

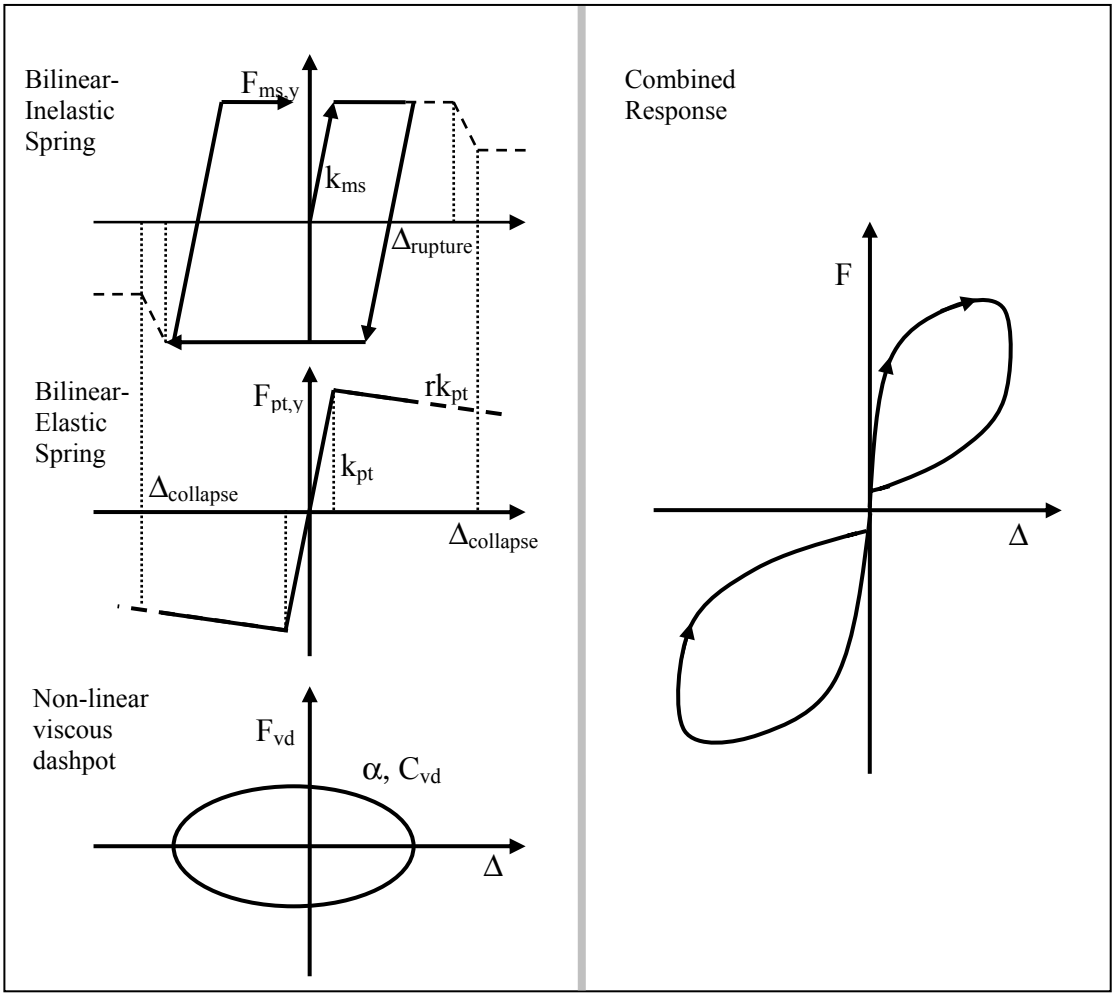

Figure 11.18 Two parallel spring plus dashpot AFS2 pier model

11.10. RESULTS OF THE PROBABALISTIC SEISMIC LOSS ASSESSMENT

11.10.1. Bridge Response Considering the 2/3MCE (Design level) and MCE (Ultimate level) Seismic Intensity

The maximum displacement, maximum shear force and residual displacements for each bridge system (mean envelope of the 22 ground motions) are illustrated in Figure 11.19. The graphs on the left of Figure 11.19, i.e. (a)-(c), presents the mean response when subjected to ground motions scaled to the 2/3MCE hazard level. The graphs on the right of Figure 11.19, i.e. (d)-(f), indicate the mean response when subjected to ground motions scaled to the MCE hazard level. The mean displacement response between all four bridges is comparable at the 2/3MCE level, while the two AFS bridge systems are almost coincident. The consistency between the mean displacement response of AFS1 and AFS2 gives further confidence to the proposed displacement-based design procedure developed in Chapter 10.

The mean response between all four bridge systems under the MCE hazard level is also similar. It is immediately obvious that the benchmark bridge suffers significant residual displacements (Figure 11.19(f)). The residual displacement of each post-tensioned bridge pier is dictated by the abutment residual displacement. In fact, the residual displacement of the abutments, combined with the post-tensioned restoring force, results in residual shears within the pier elements.

It is interesting to note that the maximum pier shear for AFS1 and AFS2 is no greater than the benchmark system (Figure 11.19 (b) and (e)). While the difference is only minimal, it dispels the idea that viscous systems may require additional protection against damper over-strength actions. There is, however, a significant increase in shear force for the hybrid bridge piers. With reference to DDBD, the reduced hysteretic damping of a re-centring system requires an increase in system strength to control the displacement response. A similar relationship is observed in Figure 11.20 showing the growth in shear demand (median shear) within each pier as a function of the PGA (IM) intensity. The shape of this relationship resembles the pier's push-over capacity. Very little over-strength shear demand is observed for the benchmark bridge as the moment capacity of the pier has minimal dependency on the displacement demand (and hence PGA intensity). Contrary to this, the hybrid bridge has significant over-strength demand due to the high bilinear stiffness associated with post-tensioned systems. The moment capacity at the rocking interface is significantly dependant on the displacement demand of the pier. For the post-tensioned AFS bridges with FVD, the over-strength shear demand is dependant on the displacement demand of the pier and the velocity demand; therefore, significant over-strength shear forces would be expected. It is interesting to find that the shear demand on the AFS bridges is lower for seismic intensities less than the MCE level, but increases for seismic intensities greater than the MCE level. The growth in shear over-strength (gradient) for the AFS bridges is comparable to that of the hybrid bridge. When the shear force within the AFS pier elements at the 2/3MCE and the MCE seismic hazard level are compared, the initial argument to use a velocity exponent of $\alpha = 0.75$ to minimise over-strength demand is supported. According to Equation 11.2 the over-strength demand associated entirely of the viscous force contribution was computed as 1.36. Considering that the viscous forces are out-of-phase with the hysteretic forces, a reduction in this over-strength can be expected: a further reduction will occur as the

proportion of FVDs reduces. The ratio between the median pier shear at the MCE level and the 2/3MCE level is presented in Table 11.19. Only a modest increase is observed for the post-tensioned systems; in particular the AFS systems. With this in mind, the over-strength shear demands that would result when using linear FVD (α = 1.0) are not likely to be significant greater than that of a post-tensioned hysteretic system.

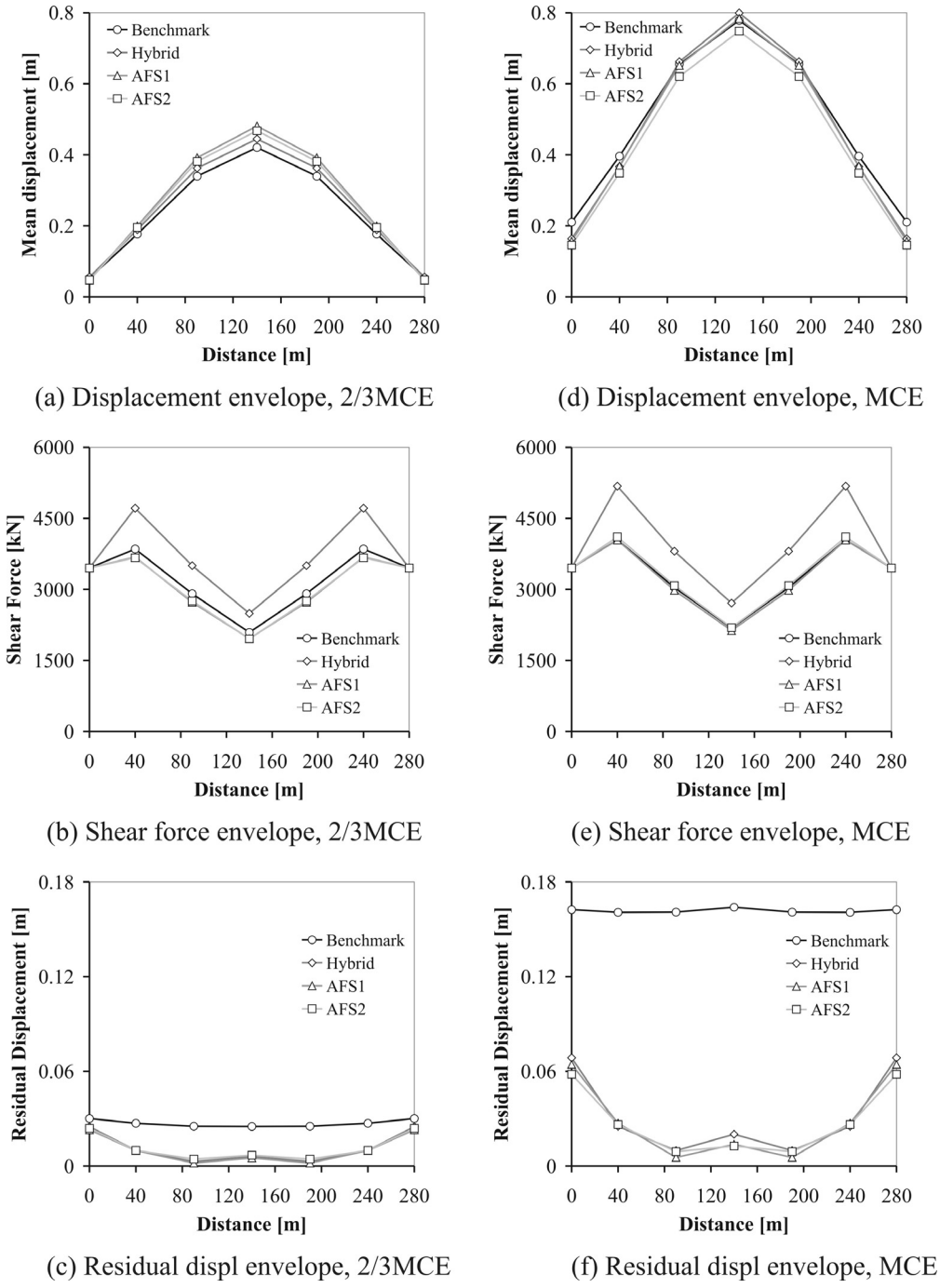

Figure 11.19 Mean displacements, shear force and residual envelopes for the 2/3MCE (a)-(c) and the MCE Seismic Intensity.

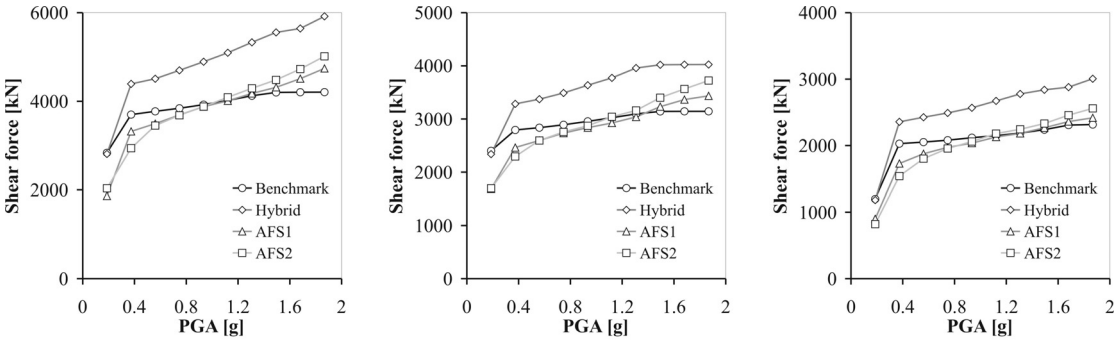

Figure 11.20 Median pier shear versus PGA intensity

Table 11.19 Ratio between median pier shear at MCE and 2/3MCE

	Benchmark	Hybrid	AFS1	AFS2
$V_{MCE}/V_{2/3MCE}$	1.05	1.08	1.09	1.11

11.10.2. Intensity-Drift (IM-EDP) Relationship

The seismic response of the bridges subjected to the suite of ground motions scaled to a range of IM levels is illustrated in the form of medium (and dispersion) displacement demands in Figure 11.21. The median PGA-Drift (IM-EDP) demand curve for each pier is presented in Figure 11.21 (a)-(c). This relationship indicates that as the intensity is increased, all four bridge systems yield a similar non-linear response. A larger non-linearity indicates larger demands; piers 1&5 have the largest non-linearity and are, therefore, subjected to larger displacement demands. There is very little difference between each system and, in fact, the monolithic system appears to return the lowest response. To compliment the IM-EDP relationships, the dispersion β (≈cov) for each pier is also presented in Figure 11.21 (d)-(f) and calculated neglecting the collapse cases. The AFS bridge systems indicate a reduced dispersion for PGA intensities below about 0.8g. For PGA intensities greater than 0.8g some earthquake records cause collapse of the bridges and the computed dispersion becomes invalid. The AFS bridges returned the lowest dispersion in displacement, followed by the monolithic and finally the hybrid bridge. In addition to reducing the median demand, a system which can minimise the dispersion associated with structural response is extremely beneficial in reducing loss.

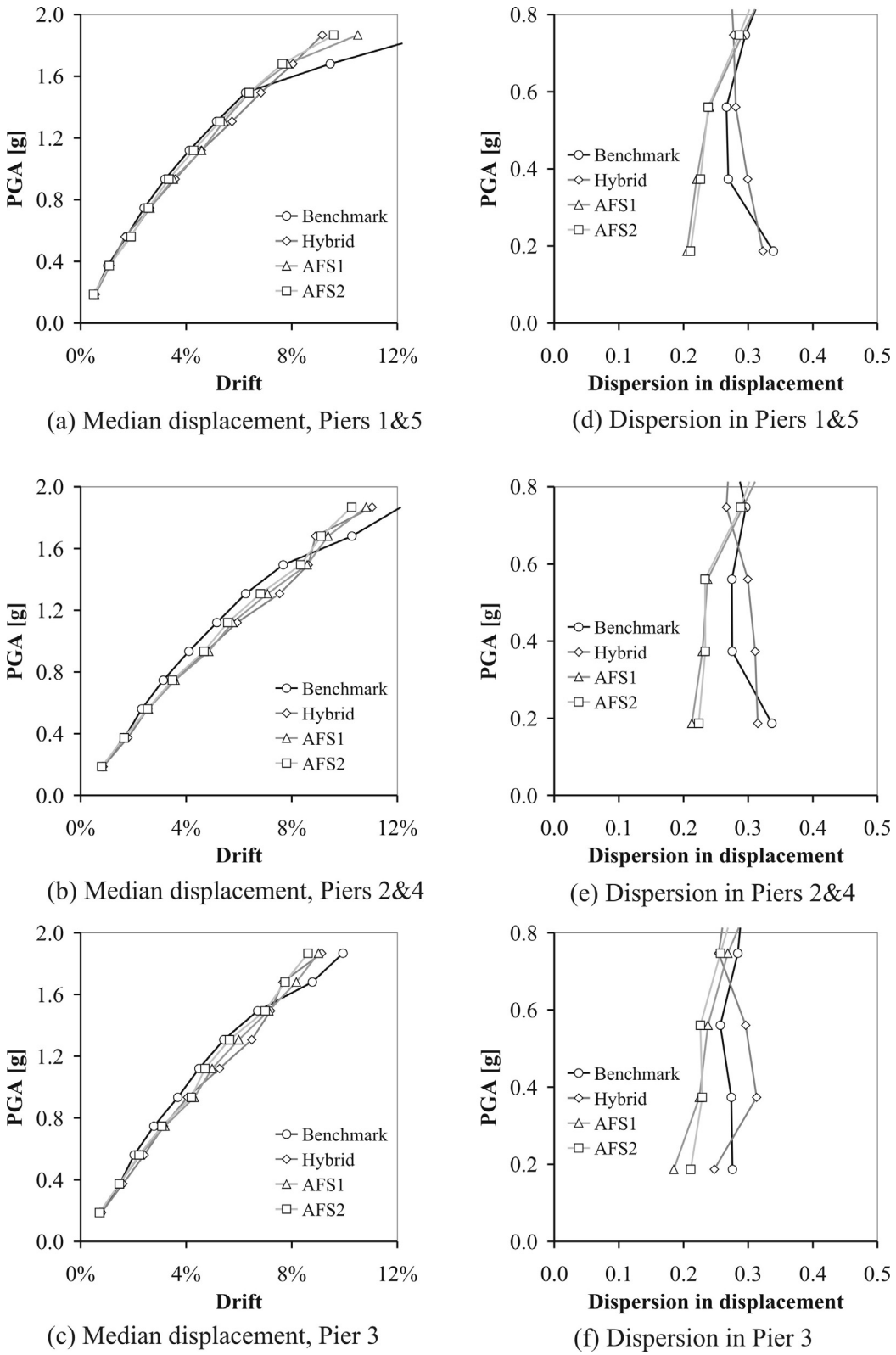

Figure 11.21 IM-EDP median demand curve (including collapse) (a)-(c) and the corresponding dispersion (without collapse) (d)-(f)

11.10.3. Annual Rate of Exceedance

The annual rate of exceeding a certain level of pier drift (EDP) is presented in Figure 11.22. This is obtained by integrating the IM-EDP and the IM-λ relationships. With respect to each drift level, there is no significant difference between each bridge system other than the annual rate of global collapse. Global collapse occurs when collapse of any one pier has occurred: indicated by a horizontal line in Figure 11.22. The annual rate and probability of global collapse (within a 100 year operating life) is summarised below in Table 11.20. The reduced annual rate of global collapse for the post-tensioned systems is attributed to the larger displacement capacity inherent of such systems. Table 11.20 indicates that the rate of global collapse for the AFS bridges is reduced by more than 50% with respect to the benchmark bridge.

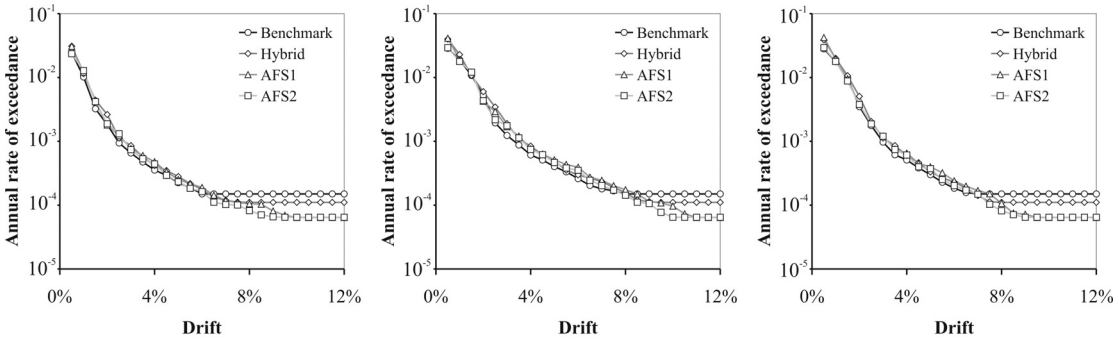

(a) Piers 1&5 (b) Piers 2&4 (c) Piers 3

Figure 11.22 Annual rate of exceedance

Table 11.20 Annual rate and probability of global collapse

	Benchmark	Hybrid	AFS1	AFS2
Annual rate of global collapse	1.50×10^{-4}	1.11×10^{-4}	0.64×10^{-4}	0.65×10^{-4}
Probability of global collpase[1]	1.49%	1.10%	0.64%	0.64%

[1] within a 100year operating life

11.10.4. Loss-Hazard Relationship

The loss associated with a given hazard (i.e. annual rate of exceedance) is illustrated in Figure 11.23. This calculation was performed using the software SLAT (Seismic Loss Assessment Tool, Bradley [2008]). The horizontal dashed lines in Figure 11.23 are the 1/3MCE, 2/3MCE and the MCE seismic hazard levels respectively. This loss-hazard relationship allows loss to be directly compared between each bridge system for a given annual rate of exceedance. However, for the loss comparison to be correctly compared, each of the post-tensioned systems must include the additional cost of construction (over and above the cost to construct the benchmark).

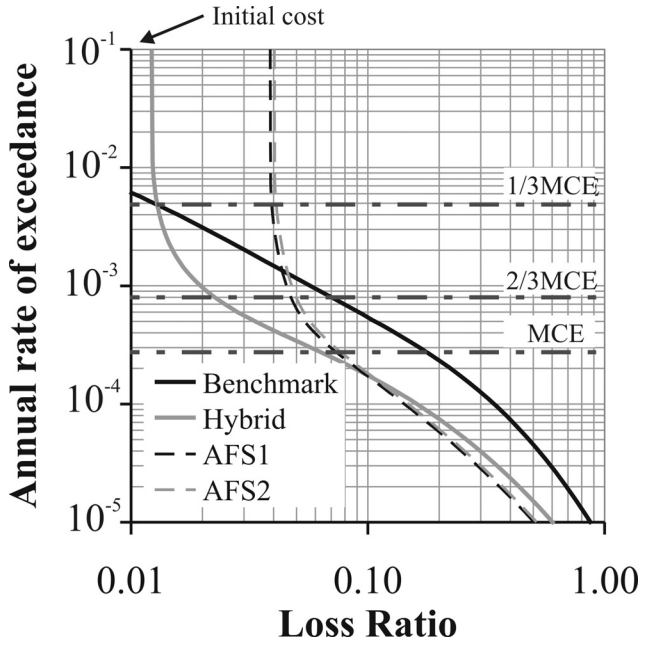

Figure 11.23 Loss-hazard relationship for each bridge system

As discussed in Section 0 the initial cost to construct the hybrid bridge was approximated as an additional 1.22% of the benchmark bridge, while an additional cost of 3.1% (in addition to the post-tensioning expense) was associated with the AFS bridge systems due to the cost of the viscous dampers. This initial cost is indicated by the horizontal offset in loss for the post-tensioned bridges in Figure 11.23. It is clear that the benefits of the hybrid bridge (when compared to the benchmark) are evident when consideration is given to a 1/3MCE event or larger. The discrete loss associated with the 1/3MCE, 2/3MCE and the MCE seismic hazard level is summarised in Table 11.21 for each bridge. The following points are noted:

- The hybrid bridge returns a lower expected loss with respect to the benchmark bridge for annual rates less than 4.89×10^{-3}, i.e. 38.7% in 100 years, which is similar in intensity to the 1/3MCE hazard level.
- There is some benefit to be had from the AFS system (with respect to the benchmark bridge) considering annual rates less than about 1.35×10^{-3}, i.e. 12.6% in 100 years.
- Both Figure 11.23 and Table 11.21 confirm that the AFS bridges provide no financial benefit over a traditional hybrid bridge for all seismic hazards up until the MCE hazard; a marginal benefit is observed for annual rates less than 1.84×10^{-4}, i.e. 1.8% in 100 years.

Table 11.21 Loss-hazard tabulated data for each bridge system presented as loss ratio (monetary value in brackets based on $12.74M benchmark construction cost)

Hazard	Benchmark	Hybrid	AFS1	AFS2
1/3MCE	0.013 ($0.16M)	0.013 ($0.16M)	0.039 ($0.50M)	0.041 ($0.52M)
2/3MCE	0.070 ($0.90M)	0.023 ($0.29M)	0.047 ($0.60M)	0.050 ($0.63M)
MCE	0.178 ($2.27M)	0.063 ($0.81M)	0.074 ($0.94M)	0.077 ($0.98M)

11.10.5. Expected Annual Loss

Integration of the loss-hazard curve results in the Expected Annual Loss (EAL). The EAL considers the loss associated with each point on the loss-hazard curve and is the summation of loss multiplied by the probability of that loss occurring in one year (annual rate of occurrence). EAL, therefore, gives an estimation of the annual loss based on the annual probability of each event. The EAL can be forecasted over the intended operating life of the structure accounting for the time value of money (discount rate) to indicate the expected loss over time.

The EAL for each bridge is computed in Table 11.22. It is expressed as a loss ratio (with respect to the benchmark construction cost), where the monetary value in brackets expresses the loss based on a $12.74M asset value. The EAL computation is based on the loss ratios and dispersion proposed in Section 11.8 for hybrid post-tensioned bridges. Two conclusions can be drawn from these calculations. The first is that there is a significant reduction to the EAL based entirely on the increased ductility capacity of the post-tensioned pier sections. When accounting for the proposed loss ratios and the reduced dispersion associated with the post-tensioned bridges, the EAL is reduced to approximately 71-78% of that computed for the benchmark bridge.

Table 11.22 Expected annual loss: comparison between four bridge systems

	EAL
Benchmark, ductile bridge	0.049% ($6263)
Post-tensioned hybrid	0.018% ($2254)
Post-tensioned AFS1	0.011% ($1406)
Post-tensioned AFS2	0.012% ($1555)

The EAL can be disaggregated into PGA (Figure 11.24). A majority of loss for the benchmark bridge is associated with the frequent events; that is, events having a lower intensity but occurring more often. A majority of the loss for each of the post-tensioned bridges is associated with the intensive, very rare events, causing significant structural damage and/or collapse. By mitigating the damage associated with low-moderate seismic hazard (which occur more frequently), the post-tensioned systems have a significant reduction to the overall computed EAL.

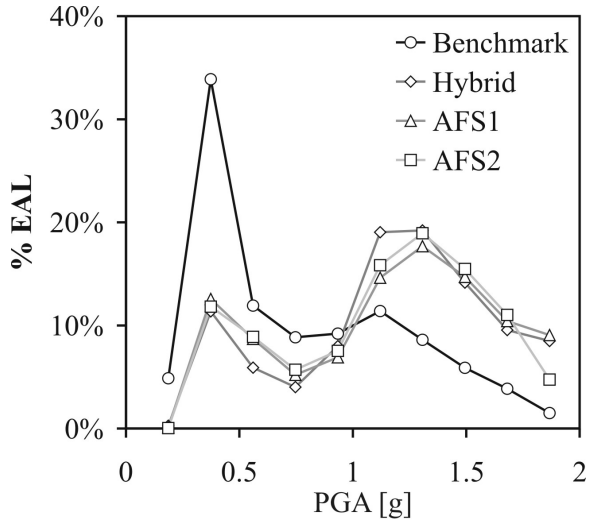

Figure 11.24 Deaggregation of EAL for PGA intensity

11.10.6. Expected Annual Loss Including Initial Cost of Construction

It is meaningless to compare the EAL between the bridges without considering the initial cost of construction. Based on a discount rate of 6%, Figure 11.25 illustrates the comparative loss of each bridge system over the service life of the bridge (as a ratio of construction cost). However, the curves in Figure 11.25 represent each bridge having the same initial cost. ΔL in Figure 11.25 represents the maximum difference between the initial cost of the benchmark and anyone of the post-tensioned bridges before the bridge in question becomes uneconomical (strictly from an EAL point of view). Considering the hybrid bridge, ΔL=0.64%; if the cost to construct the hybrid bridge is greater than 0.64% the construction cost of the benchmark bridge, the hybrid bridge is not a feasible option. It is unlikely that the difference in construction cost would be less than 0.64%, in fact, as discussed in Section 0, the hybrid bridge is likely to be around 1.22% more expensive than the benchmark bridge. This issue is further exasperated for the AFS bridges which have an even larger initial cost associated with the installation of external dampers. Consider AFS1 having ΔL=0.70% and recall the cost to install fluid viscous dampers alone was NZD388,900. Even if a best case scenario is considered in that the overall cost of construction between the AFS and Benchmark Bridge was equal, the total cost of construction would have to equal NZD55.6M before this option became economically feasible. It is unlikely that construction costs for a bridge of this nature would approach this budget.

However, in light of these conclusions, individual stakeholders are less concerned with the EAL as being a primary measure of loss. With reference to the loss-hazard curve in Figure 11.23, for almost any event, the loss far exceeds the computed EAL: this is the high-consequence-low-probability nature of seismic risk. In such situations, decision makers are generally risk averse and consult other forms of financial risk tools over and above the EAL computation such as the loss-hazard relationship.

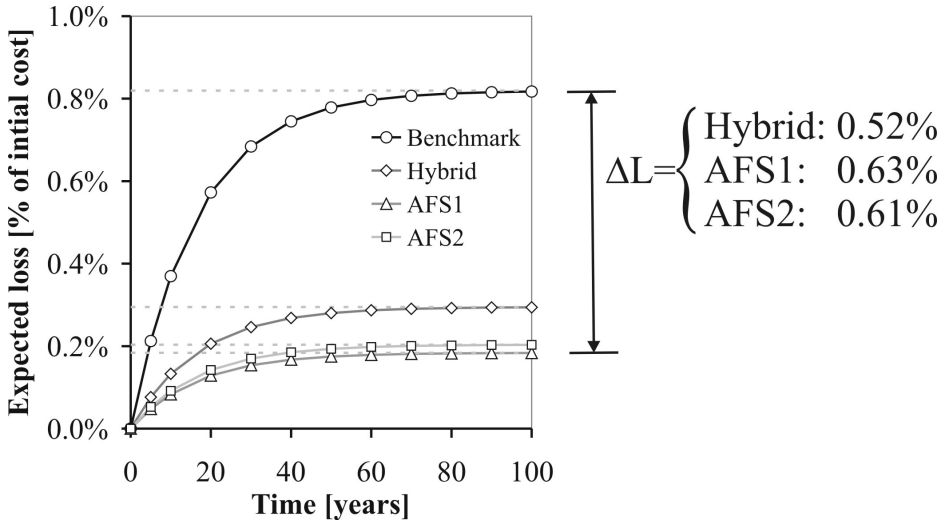

Figure 11.25 Expected loss over time (neglecting initial construction costs)

11.10.7. Loss Associated with Downtime

Throughout this study no consideration was given to any loss associated with downtime as a result of structural repairs/inspection to the bridge following an earthquake event. Downtime is difficult to quantify as it requires an estimate of monetary loss associated with business interruption due to the flow of goods and services in and out of communities. Krawinkler and Miranda [2004] noted "…even if downtime could be quantified with confidence, the associated losses will be highly uncertain and strongly case and scenario specific".

Generally speaking losses are divided into direct and indirect losses. Direct loss is related to bridge damage and the loss directly associated with repairs. Indirect loss is associated with human casualties and downtime. Downtime is defined as economic loss resulting from the reduced functionality of the structure. In particular, Comerio [2006] describes downtime as being made up of *rational* and *irrational* components. The *rational* component includes the time needed to undertake the structural repair work. Irrational components includes the time to secure finance, apply for building permits, relocate human resources, undertake structural inspections, make design decisions, relocate displaced activities, to name a few. Specific to transportation lifelines, Enke et al. [2008] conducted a scenario loss study to assess the loss associated with increased travel time/distance as a result of downtime to damaged bridges: this was determined a partial indirect loss assessment. In this context, loss was related to increased transportation service costs due to the reduced capacity of the highway network system. This ultimately reduces consumer spending and disrupts business operation. The estimated indirect loss (partial) for the study scenario equated to approximately 55% of the direct loss. Losses associated with downtime can be significant, but are scenario specific.

A rapid and relatively crude method was undertaken to account for some loss associated with downtime. With respect to the benchmark bridge, all loss ratios representing the four damage states were multiplied by a factor of 2 to account for some form of downtime for all damage states. Considering the hybrid bridge, the loss ratios for the last two damage states (DS3 and DS4) were multiplied by a factor of 2

recognising that a best case scenario could result in negligible downtime for the first two damage states (DS1 and DS2). Intuitively, the EAL for the benchmark will be simply doubled, resulting in an EAL=0.109% and an expected loss of 1.82% after 100 years of service. An EAL of 0.028% was computed for the hybrid bridge resulting in an expected loss of 0.459% following 100 years of service (not including the initial cost of construction). In this instance, for the hybrid bridge to be an economic solution, the construction cost should not exceed 1.36% of the cost to construct the benchmark bridge. With respect to the cost estimate carried out in Section 0 the use of the traditional hybrid bridge becomes more feasible when considering an EAL computation. However, when the loss-hazard curves are re-computed based on these allowances for downtime the benefit associated with the post-tensioned bridges becomes increasingly more obvious. Considering the hybrid bridge, the loss significantly reduces for the 1/3MCE, 2/3MCE and MCE hazard, however the benefit of the AFS bridges is still relatively minimal with respect to the traditional hybrid bridge system (unless intensities greater than MCE are considered). When compared to the benchmark bridge Table 11.23 indicates that, for the 2/3MCE hazard, a reduction of $1.48M, $1.18M and $1.14M is expected for the hybrid, AFS1 and AFS2 bridges respectively.

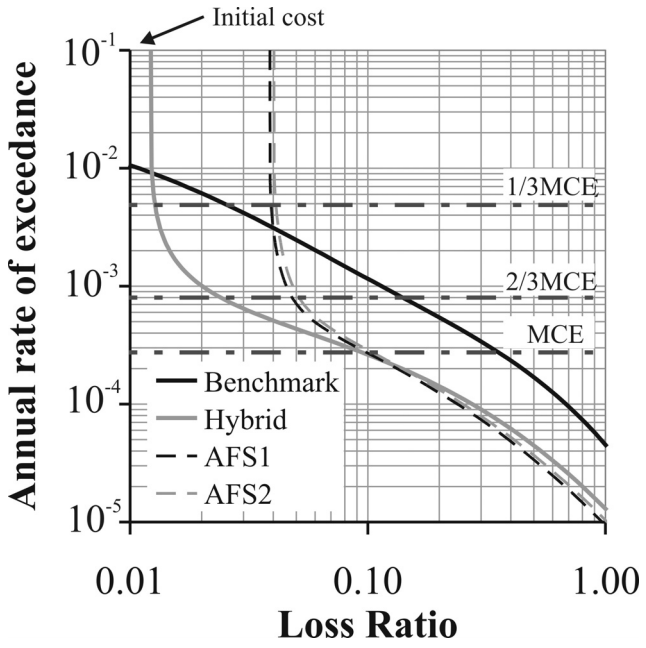

Figure 11.26 Loss-hazard relationship

Table 11.23 Loss-hazard tabulated data considering allowance for downtime loss

	Benchmark	Hybrid	AFS1	AFS2
1/3MCE	0.026 ($0.33M)	0.013 ($0.16M)	0.039 ($0.50M)	0.041 ($0.52M)
2/3MCE	0.140 ($1.79M)	0.024 ($0.31M)	0.048 ($0.61M)	0.051 ($0.65M)
MCE	0.355 ($4.53M)	0.095 ($1.21M)	0.099 ($1.26M)	0.105 ($1.33M)

11.11. LOSS ASSESSMENT OF AN IRREGULAR BRIDGE

To determine whether the results of the loss assessment were specific to the bridge configuration, a second loss assessment was carried out on an irregular bridge. An additional four bridge systems (one monolithic and three post-tensioned systems) were designed and assessed. The configuration of the irregular bridge is illustrated in Figure 11.27, where the geometry of the box-girder bridge deck remained unchanged from the regular configuration. The dimensions of the square piers were increased to 2m.

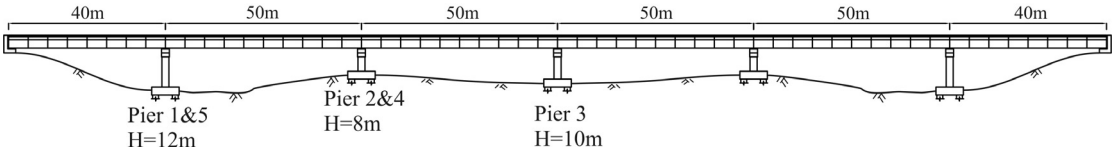

Figure 11.27 Longitudinal elevation of the irregular prototype bridge –symmetric about pier 3.

The target design displacement was dictated by the short 8m piers. The required strength demand was significantly greater for the irregular bridge due to the smaller effective period at the design displacement, hence, requiring the dimensions of the pier to be increased to 2m plus an additional layer of mild steel reinforcement. The results of the detailed design are summarised in Table 11.24. Again, the AFS bridge systems require a significantly lower base shear that their hysteretic counterparts.

Table 11.24 DDBD summary of the irregular bridge prototypes

	Benchmark	**Hybrid(traditional)**	**AFS1**	**AFS2**
Δ_{eq}	0.261m	0.262m	0.260m	0.260m
ξ_{eq}	13.96%	7.27%	11.22%	11.34%
ξ_{hyst}	10.71%	4.93%	4.29%	1.54%
ξ_{FVD}	-	-	4.49%	6.78%
ξ_{el}	3.26%	2.33%	2.44%	3.02%
T_{eff}	1.67s	1.52s	1.80s	1.81s
V_b	22172kN (0.290g)	26863kN (0.351g)	17150kN (0.224g)	16063kN (0.210g)

It was assumed that the cost to construct the benchmark monolithic bridge was unchanged at NZD12.74 million as the increase to the pier dimensions from 1.8m to 2.0m (in addition to more reinforcement within the pier and possibly heavier foundations) would require a more detailed cost evaluation to be carried out. A majority of the cost, in most cases, is attributed to the box-girder superstructure: therefore, this assumption will suffice for the purpose of the study. With that said, the additional post-tensioning steel and anchorages required of the post-tensioned bridges, due to the increase strength demand, were accounted for as these costs could be readily computed.

The tables below summarise the reinforcement details for each of the four bridge systems based on a detailed design and assessment approach.

Table 11.25 Reinforcement contents for the irregular ductile bridge piers

	Longitudinal reinforcement[1]	Transverse reinforcement[1]
Piers 1&5	72-XD32 (1.45%)	XR16@ 200mm crs (1.10%)[2]
Piers 2&4	48-XD32 (1.33%)	
Pier 3	68-XD32 (1.37%)	

[1] XD refers to 500MPa deformed (ribbed) reinforcement, XR refers to 500MPa round (smooth) reinforcement.
[2] Reinforcement ratio calculated by area enclosed by the centreline of the peripheral hoops

Table 11.26 Longitudinal and prestressed reinforcement details for the irregular hybrid bridge

	Prestressed reinforcement	Internally grouted reinforcement
Piers 1&5	183-12.7mm strands (ρ_{pt}=0.46%) with total initial prestressing force of 16,470kN. 1-#3105-31 & 8-#1905-19 BBR anchorage units.	40-XD40 grouted within 90mm diameter Drossbach duct. Provided with 240mm unbonded length. (ρ_s=1.26%)
Piers 2&4	183-12.7mm strands (ρ_{pt}=0.46%) with total initial prestressing force of 14,640kN. 1-#3105-31 & 8-#1905-19 BBR anchorage units.	
Pier 3	183-12.7mm strands (ρ_{pt}=0.46%) with total initial prestressing force of 16,470kN. 1-#3105-31 & 8-#1905-19 BBR anchorage units.	

Table 11.27 Longitudinal reinforcement, prestressing and dissipation details for the irregular AFS1 hybrid pier

	Prestressed reinforcement	Internally grouted reinforcement	External viscous devices
Piers 1&5	80-12.7mm strands (ρ_{pt}=0.20%) with total initial prestressing force of 6,400kN. 4-#3105-20 BBR anchorage units.	24-XD40 grouted within 90mm diameter Drossbach duct. Provided with 240mm unbonded length. (ρ_s=0.75%)	6-Taylor fluid viscous dampers. 220Kip (979kN) device, ±100mm stroke. C_{vd}=8000kNs$^{\alpha}$/m$^{\alpha}$ Non-linearity, α=0.75
Piers 2&4	80-12.7mm strands (ρ_{pt}=0.20%) with total initial prestressing force of 4,400kN. 4-#3105-20 BBR anchorage units.		
Pier 3	80-12.7mm strands (ρ_{pt}=0.20%) with total initial prestressing force of 5,200kN. 4-#3105-20 BBR anchorage units.		

Table 11.28 Prestressing and dissipation details for the irregular AFS2 hybrid pier

	Prestressed reinforcement	External TCY devices	External viscous devices
Piers 1&5	88-12.7mm strands (ρpt=0.22%) with total initial prestressing force of 7,920kN. 4-#3105-22 BBR anchorage units.	6-65mm diameter, Grade 500MPa TCY dampers. Yielding fuse length of 650mm (ρs=0.61%)	6-Taylor fluid viscous dampers. 220Kip (979kN) device, ±100mm stroke. C_{vd}=5000kNs$^{\alpha}$/m$^{\alpha}$ Non-linearity, α=0.75
Piers 2&4	92-12.7mm strands (ρpt=0.23%) with total initial prestressing force of 5,950kN. 4-#3105-23 BBR anchorage units.		
Pier 3	116-12.7mm strands (ρpt=0.29%) with total initial prestressing force of 9,280kN. 4-#3105-29 BBR anchorage units.		

11.12. RESULTS OF THE PROBABLISTIC SEISMIC LOSS ASSESSMENT: IRREGULAR BRIDGE

11.12.1. Irregular Bridge Response when Subjected to the 2/3MCE (Design level) and MCE (Ultimate level) Seismic Intensity

The maximum displacement, maximum shear force and residual displacements for each irregular bridge system (mean envelope of the 22 ground motions) are illustrated in Figure 11.28. The graphs on the left of Figure 11.28, i.e. (a)-(c), presents the mean response when subjected to ground motions scaled to the 2/3MCE hazard level. The graphs on the right of Figure 11.28, i.e. (d)-(f), indicate the mean response when subjected to ground motions scaled to the MCE hazard level. There is relatively minimal variation in the maximum displacement response between each of the four bridges at the 2/3MCE design level: this further confirms the proposed design procedure for the bridge systems with viscous and hysteretic supplementary damping. There is more variation in response between all four bridges at the MCE level, however, with respect to the two AFS systems, the variation here is relatively minimal. The same comment can be made with respect to the two hysteretic systems: the benchmark monolithic and the traditional hybrid bridge system.

It is interesting to note, that for both seismic hazard levels (2/3MCE and MCE) the maximum pier shear in the AFS bridges is less than the benchmark monolithic bridge. This further suggests that the misconception that viscous systems need significant protection against damper over-strength actions may be relaxed in cases having a similar proportion of FVDs as per this study.

Finally, the residual deformations within the post-tensioned piers result from the residual deformations of the abutments, also resulting in residual pier shears. The residual deformations within the benchmark system are clearly more significant and are dramatically larger for the MCE seismic hazard.

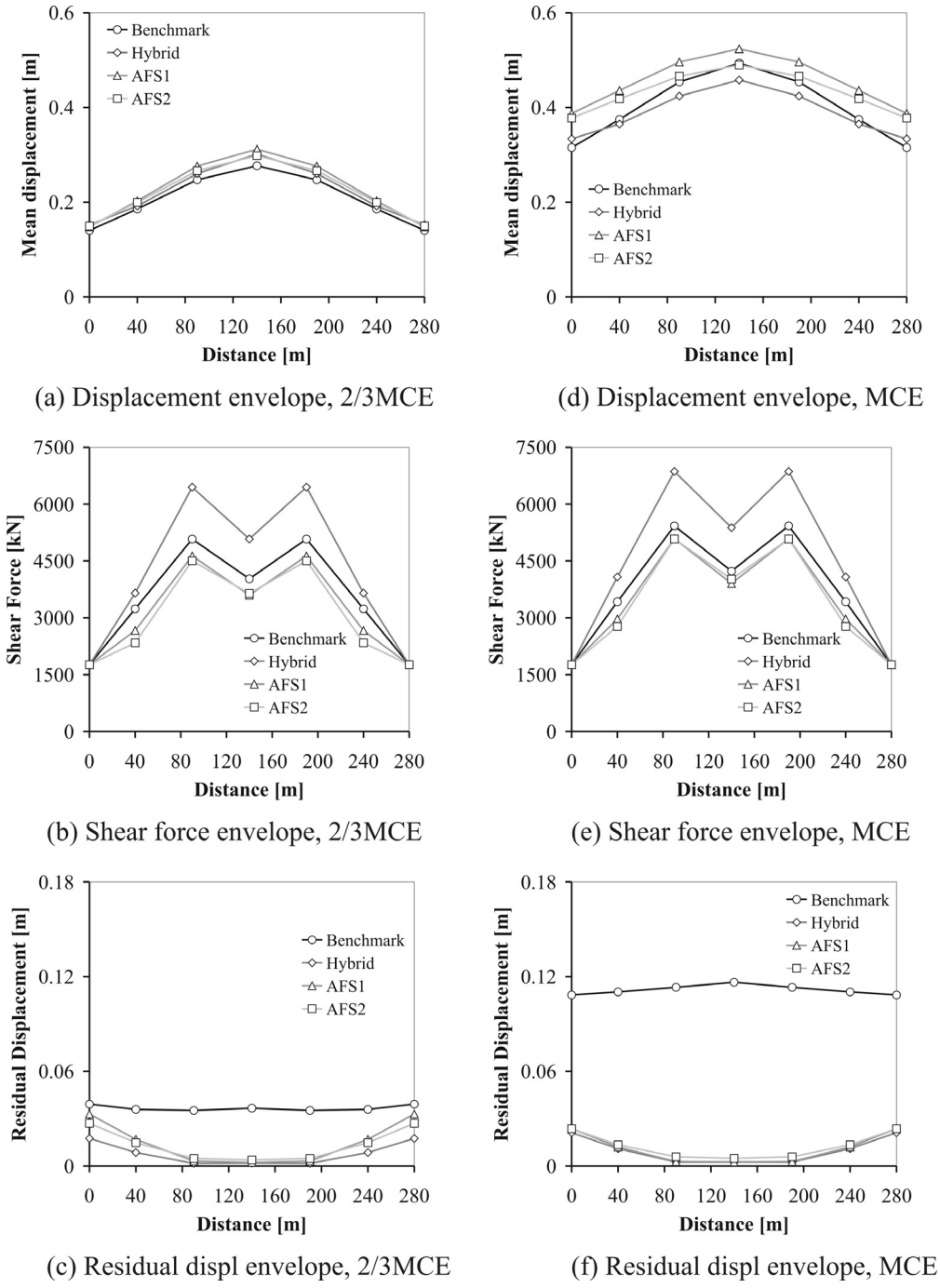

Figure 11.28 Mean displacements, shear force and residual envelopes for the 2/3MCE (a)-(c) and the MCE Seismic Intensity: Irregular Bridge.

11.12.2. Annual Rate and Probability of Global Collapse

The annual probably of global collapse for each of the four irregular bridges is presented in Table 11.29. Similar conclusions to that drawn from the regular bridge can be made: the annual probability of global collapse is reduced by more than 50% for the AFS bridge systems when compared to the benchmark bridge.

Table 11.29 Annual rate and probability of global collapse for the irregular bridge systems

	Benchmark	Hybrid	AFS1	AFS2
Annual rate of global collapse	2.19×10^{-4}	1.41×10^{-4}	0.91×10^{-4}	0.82×10^{-4}
Probability of global collpase[1]	2.16%	1.40%	0.91%	0.82%

[1] within a 100year operating life

11.12.3. Loss-Hazard Relationship

The loss-hazard relationships for each of the irregular bridges are compared in Figure 11.29. The loss-hazard relationship of each irregular post-tensioned bridge is very similar to their regular counterpart systems in Figure 11.23. There is however a significant increase in the loss-hazard relationship for the benchmark system being largely dictated by the response of the central pier.

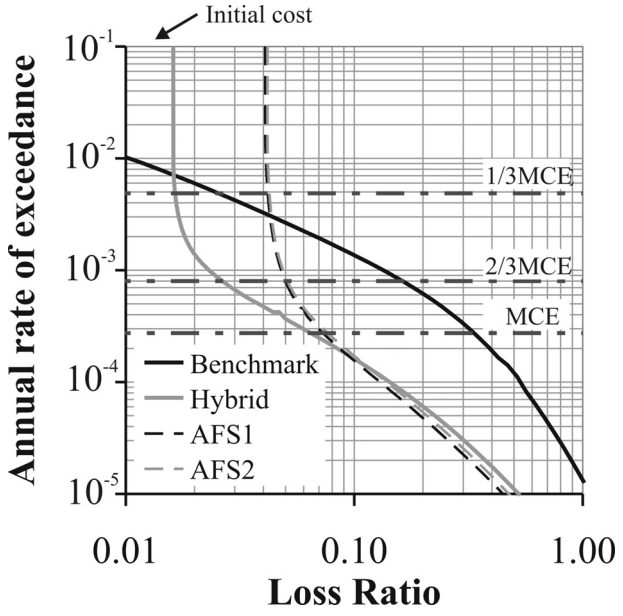

Figure 11.29 Loss-hazard relationship for each irregular bridge system

This benefit of the post-tensioned systems becomes more evident when the tabulated loss-hazard data is investigated in Table 11.30. It is immediately evident that the hybrid bridge provides substantial financial benefit over the benchmark bridge system as the loss is reduced by 84% considering the 2/3MCE seismic hazard. While there is still significant benefit to be had from the AFS bridge systems, the benefit is not as significant as the hybrid system, which is attributed to the greater initial cost to install the FVDs within the AFS bridge system.

Table 11.30 Loss-hazard tabulated data for each irregular bridge system presented as loss ratio (monetary value in brackets based on $12.74M benchmark construction cost)

Hazard	Benchmark	Hybrid	AFS1	AFS2
1/3MCE	0.025 ($0.32M)	0.016 ($0.21M)	0.042 ($0.53M)	0.043 ($0.54M)
2/3MCE	0.163 ($2.08M)	0.026 ($0.34M)	0.050 ($0.64M)	0.051 ($0.65M)
MCE	0.335 ($4.27M)	0.065 ($0.82M)	0.073 ($0.93M)	0.076 ($0.97M)

The loss-hazard data is compared in Table 11.31 between the regular bridge and irregular bridge systems. It is interesting to note that the monolithic bridge suffers greater loss when considering an irregular bridge layout. In contrast, there is no significant increase (or decrease) in loss for each of the post-tensioned systems considering either a regular or irregular bridge layout. This can be attributed to the large displacement capacity of each of the post-tensioned systems and the "tuning" that can be carried out during the design phase to improve the ductility capacity of the pier elements. An example of tuning relates to the initial post-tensioning force within the tendon group; increasing the number of tendons as opposed to increasing the initial prestress will increase the ductility capacity of the section, however, will incur a greater material cost. Further tuning can be carried out on the mild steel reinforcement; in particular, increasing the unbonded length (and bar diameter) of the grouted mild steel reinforcement (to control the longitudinal strains) will increase the ductility capacity of the section, however, at the expense of increasing the flexibility of the pier and a subtle reduction to the overall energy dissipation of the pier section.

Table 11.31 Comparison of the loss-hazard tabulated data between the regular (left column) and irregular bridges (right column), where loss is presented as loss ratio.

Hazard	Benchmark		Hybrid		AFS1		AFS2	
	Reg	Irreg	Reg	Irreg	Reg	Irreg	Reg	Irreg
1/3MCE	0.013	0.025	0.013	0.016	0.039	0.042	0.041	0.043
2/3MCE	0.070	0.163	0.023	0.026	0.047	0.050	0.050	0.051
MCE	0.178	0.335	0.063	0.065	0.074	0.073	0.077	0.076

11.12.4. Expected Annual Loss

Finally, the expected annual loss is tabulated in Table 11.32 and compared between the regular and irregular bridge systems. As expected from the loss-hazard relationship, a significant increase to the EAL is observed for the benchmark monolithic system considering an irregular bridge configuration while little difference is observed for each of the post-tensioned systems (irregular versus regular). From an EAL and loss-hazard point of view, the benefits of the post-tensioned systems are more evident for an irregular bridge configuration.

Table 11.32 Expected annual loss: comparison between four bridge systems

	EAL – Regular bridge	EAL – Irregular bridge
Benchmark, ductile bridge	0.049% ($6263)	0.086% ($10968)
Post-tensioned hybrid	0.018% ($2254)	0.018% ($2353)
Post-tensioned AFS1	0.011% ($1406)	0.014% ($1741)
Post-tensioned AFS2	0.012% ($1555)	0.013% ($1715)

11.13. DISCUSSIONS

11.13.1. Feasibility of Post-tensioned Bridge Systems

Two methods to ascertain the feasibility of a post-tensioned bridge system were presented. The first considered the loss-hazard relationship and associated the loss with each discrete seismic hazard. A reduction in loss was observed for the hybrid bridge when considering seismic events having a 38.7% probability of exceedance within 100 years: this is similar to the 1/3MCE, design basis seismic hazard. No benefit was observed for the AFS bridges (with respect to the hybrid bridge) unless events with a probability of exceedance of 1.8%, or less, within 100 years were considered. This suggested that, of the post-tensioned bridges, the hybrid bridge was the most cost efficient solution and could be seen to be more beneficial than the benchmark bridge. However, while a post-tensioned hysteretic bridge is shown to be the most economic solution, the AFS bridge system will become significantly more advantageous as the cost of fluid-viscous-dampers reduces.

The second method demonstrated that by considering the average annual rate of occurrence for each earthquake and integrating the loss associated with each event (defining the expected loss per annum), the benchmark bridge was the most feasible option.

If the bridge system represents a very significant arterial route with limited alternative bypasses, and the loss due to downtime is determined to well exceed the replacement cost of the structure, then the economic benefit to be had from a post-tensioned hybrid system is further supported. It was noted that even if some proportion of downtime loss is accounted for, from a loss-hazard and EAL viewpoint, there was little benefit to be had when considering an AFS Bridge: the hybrid solution was still the more feasible option in this case.

The results of the loss assessment indicated that there was no significant difference in the loss-hazard relationship between an irregular and regular post-tensioned bridge configuration. In contrast, the benchmark monolithic bridge system showed a significant increase in loss when considering an irregular pier layout. Therefore, the financial benefits were more obvious when considering an irregular bridge layout as the loss of the benchmark pier was largely dictated by that of the short pier elements. The post-tensioned bridge systems allowed some degree of tuning to be undertaken during the design phase, improving the performance of the bridge piers with only minimal increase to the construction cost.

With that said, it is difficult to determine the most feasible solution, or more correctly, how to measure feasibility. Porter and Kiremidjian [2001] demonstrated that a client's risk attitude should be accounted for within risk-management decision-making and questions cost-effectiveness as the key measure for decision making. Furthermore, decision makers are generally risk averse toward low probability (yet high consequence) events, meaning such rare events are given more consideration within the decision making process (Bradley et al. [2008]). A relatively conservative owner may opt to minimise the loss associated with a certain intensity level, assuming that it is entirely likely the event will occur. It is therefore down to the clients risk attitude as to what they consider feasible. It is to this end that the loss-hazard curve appears to be

the most effective tool for decision makers; it allows the client to choose the level of risk (annual probability of exceedance) associated with an acceptable level of loss.

11.13.2. Superstructure, Abutments and Bearing Related Losses

Referring to the IM-EDP relationships in Figure 11.21 it is not possible to argue that damage within the superstructure, abutments, bearings or foundations would differ between any of the bridges. Damage associated with the superstructure, bearings and abutments is directly related to the maximum displacement response of the bridge. As the maximum response between each bridge is very similar (in fact, a slight reduction was observed for the monolithic benchmark bridge) the loss associated with these elements would be very comparable.

11.13.3. Feasibility of an Alternative Post-tensioned Bridge Systems

The option to use an AFS bridge system is more difficult to justify as the cost to install FVDs can out way the reduction in loss associated with the reduced structural damage. With that said, piers 2&4 contributed to a majority of the loss for each of the regular AFS bridge systems. Therefore, to reduce costs associated with the installation of fluid viscous dampers, while still retaining the benefits of an AFS bridge system, an alternative bridge scheme is proposed. The alternative scheme adopts traditional hybrid construction for piers 1, 3 & 5 (refer Figure 11.4 and Figure 11.5 for details) combined with AFS1 piers for 2 & 4 (refer Figure 11.6 and Figure 11.7 for details). This scheme is illustrated in Figure 11.30 below and is intended to reduce the losses associated with piers 2&4 due to the increased deformation capacity and reduced pier damage. The cost of installing FVD at piers 2 & 4 only would reduce the FVD expenses by 60% when compared to AFS1 (and AFS2). The structural response and loss of this alternative bridge is likely to lie somewhere between that of the hybrid bridge and the AFS1 bridge, however, only a modest benefit would be expected when compared to a traditional hybrid solution.

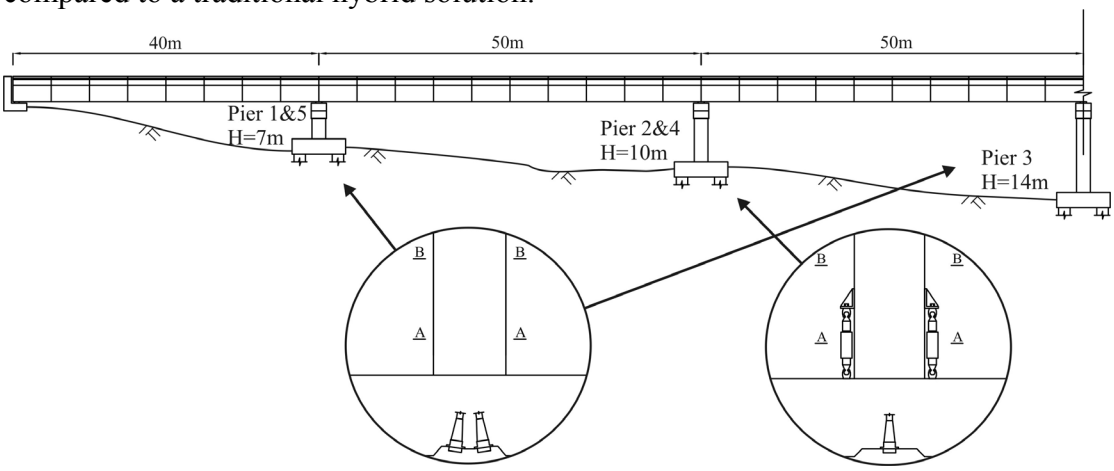

Figure 11.30 Alternative bridge scheme including traditional post-tensioned hybrid piers and AFS piers with fluid viscous dampers.

Another option was also postulated based on post-tensioning alone: that is, no dissipation. Based on the DDBD concept, the base shear would increase significantly, increasing the required number of tendons to satisfy the increased pier moment demands. While there will be savings associated with no internal or external

dissipation, these savings are likely to be outweighed by the greater number of post-tensioning tendons and anchorages required.

11.13.4. The Option to Build High Performance Structures

High performance structures (both buildings and bridges) have been proven to yield a reduction in loss associated with reduced damage. However, insurance companies (at least, with respect to New Zealand) do not recognise building performance when assessing insurance premiums associated with earthquake risk. Is to this end, stake holders may need to take on their own initiative when making such decisions. The choice ultimately comes down to the type of investment the asset represents. That is, property developers are primarily concerned with initial construction costs, as the sole aim is to sell the property and maximise profits. Government funded assets, while still concerned with initial construction cost, may be persuaded to consider life cycle costs if the benefits are conspicuous.

11.14. CONCLUSIONS

A seismic loss assessment was carried out for three post-tensioned bridges and one ductile benchmark bridge. The loss assessment was carried out to quantify the feasibility of a traditional post-tensioned hybrid bridge system and two advanced hybrid bridges. The traditional hybrid bridge piers comprised of internally grouted mild steel reinforcement and unbonded post-tensioned tendons. The first of the advanced hybrid bridge piers (AFS1) was constructed using a combination of externally mounted fluid viscous dampers (FVD), internally grouted mild steel reinforcement and unbonded post-tensioning. The second advanced hybrid bridge (AFS2) was constructed using a combination of externally mounted hysteretic dampers (TCY dampers), externally mounted FVD and unbonded post-tensioning.

The displacement response of all four bridge systems, as the intensity increased, was very similar. In fact, the difference in loss between each bridge was primarily governed by the loss associated with each damage state. The post-tensioned bridges were more ductile and suffered less physical damage than the benchmark bridge; however, initial construction costs were larger.

Two methods were presented to describe the loss associated with each bridge system. The first considered the loss-hazard curve which related the loss associated with discrete ground motions with an annual rate of exceedance. This relationship proved useful in describing the loss at the 1/3MCE, 2/3MCE and MCE hazard levels. At the 2/3MCE level, the hybrid bridge suffered less loss than the benchmark, while at the MCE level all three PT bridges returned a lower loss. However, for these same seismic hazard levels, no reduction in loss was found for the AFS bridges with respect to the hybrid bridge. Therefore, the hybrid bridge could be seen to be the most feasible option in this case. However, as the cost of fluid-viscous-dampers reduces the AFS bridge systems will become significantly more advantageous.

The Expected Annual Loss (EAL) was the second method used to compare loss between each bridge. The EAL considered the loss associated with each point on the loss-hazard curve and is the summation of loss multiplied by the probability of that loss occurring in one year. This gives the expected loss per annum and can be forecasted over the operating life of the structure. While the EAL of each PT bridge was significantly lower than the benchmark bridge, when the additional construction costs of the PT bridges was included, the benchmark bridge was clearly the most feasible option. It was concluded that for bridges located on an important arterial route requiring post-earthquake operation, then a large proportion of loss will be associated with downtime. Unless a significant proportion of loss was associated with downtime (in the order of several multiples of the construction cost), then there is little economic benefit to be had from a post-tensioned bridge (traditional or advanced). In this instance, the benchmark bridge was found to be the most feasible solution when considering an EAL viewpoint.

It was concluded that decision makers are generally risk averse with respect to seismic hazard due to the low-probability-high-consequence stakes involved. It is to this end that decisions should be based on the loss-hazard relationship as apposed to the EAL, therefore, indicating that the feasibility of the hybrid bridge (i.e. the economic benefit

to the client) will be more evident. Furthermore, if the bridge required post-earthquake operation and was to be bounded by minimal downtime following an event, then the hybrid bridge would be the most appropriate solution. Finally, if the sole concern of the client was with regards to collapse prevention, then the AFS bridge systems prevailed.

11.15. REFERENCES

Aslani, H. (2005). "Probabilistic earthquake loss estimation and loss disaggregation in buildings," Stanford University, Stanford.

Basoz, N. and Mander, J. (1999). "Enhancement of the highway transportation lifeline module in HAZUS." National Institute of Building Sciences.

Berry, M. P. and Eberhard, M. O. (2005). "Practical performance model for bar buckling." *ASCE Journal of Structural Engineering*, 131(7), 1060-1070.

Bradley, B. (2008). "SLAT: Seismic Loss Assessment Tool." Christchurch.

Bradley, B., Dhakal, R., Cubrinovski, M., MacRae, G. and Lee, D. "Seismic loss estimation for efficient decision making." *2008 NZSEE conference*, Wairakei, New Zealand.

Carr, A. (2005). "RUAUMOKO." Christchurch, Inelastic Dynamic Analysis.

Comerio, M. C. (2006). "Estimating downtime in loss modeling." *Earthquake Spectra*, 22(2), 349-365.

Cornell, A. C. and Krawinkler, H. (2000). "Progress and challenges in seismic performance assessment." *PEER Center News*, 3.

Deierlein, G. G., Krawinkler, H. and Cornell, A. C. "A framework for performance-based earthquake engineering." *Pacific Conference on Earthquake Engineering*, Christchurch, New Zealand.

Emori, K. and Schnobrich, W. (1980). "Dynamic analysis of reinforced concrete frame-wall structures." *Engineering Structures*, 2(2), 103-112.

Enke, D. L., Tirasirichai, C. and Luna, R. (2008). "Estimation of earthquake loss due to bridge damage in the St Louis Metropolitan Area. II: Indirect Losses." *ASCE Natural Hazards Review*, 9(1), 12-19.

FEMA. (2003). *NEHRP Recommended Provisions for Seismic Regulations for New Buildings and Other Structures: FEMA 450*, Washington, D.C.

Kam, W. Y., Pampanin, S., Carr, A. J. and Palermo, A. "Advanced Flag-Shape Systems for High Seismic Performance including Near-Fault Effects." *NZSEE 2007*, Palermston North.

Krawinkler, H. and Miranda, E. (2004). *Performance-based earthquake engineering* CRC Press, Boca Raton, FL.

Mackie, K. R., Wong, J.-M. and Stojadinovic, B. (2007). "Integrated probabalistic performance-based evaluation of benchmark reinforced concrete bridges." PEER 2007/09, University of California, Berkeley.

Mander, J. B. and Bosoz, N. (1999). "Seismic fragility curve theory for highway bridges in transportation lifeline loss estimation." *Optimising Post-Earthquake Lifeline System Reliability*, TCLEE Monograph No. 16. ASCE.

NZS1170.0. (2002). "Structural Design Actions, Part 0: General Principles." Standards New Zealand, Wellington.

NZS1170.5. (2004). "Structural Design Actions, *Part 5: Earthquake actions*." Standards New Zealand, Wellington.

NZS3101. (2006). "Concrete Structures Standard: Part 1-The Design of Concrete Structures." Standards New Zealand, Wellington.

Otani, S. (1974). "SAKE, A Computer Program for Inelastic Response of R/C Frames to Earthquakes." Report UILU-Eng-74-2029, University of Illinois, Urbana-Champaign.

Palermo, A. (2004). "The Use of Controlled Rocking in the Seismic Design of Bridges," PhD.Thesis, Technical University of Milan, Milan.

Porter, K. A. and Kiremidjian, A. S. (2001). "Assembly-Based Vulnerability of Buildings and its Uses in Seismic Performance Evaluation and Risk Management Decision-Making." T. J. A. B. E. E. Center, ed., Department of Civil and Environmental Engineering, Stanford.

Priestley, M. J. N., Calvi, G. M. and Kowalsky, M. J. (2007). *Displacement-Based Seismic Design of Structures*, IUSS, Pavia.

Priestley, M. J. N., Seible, F. and Calvi, G. M. (1996). *Seismic design and retrofit of bridges*, John Wiley & Sons inc, New York.

Shome, N. and Cornell, A. (1999). "Probabilistic seismic demand analysis of nonlinear structures." Report No. RMS-35, RMS Program, Stanford University, Stanford, CA.

Solberg, K. M., Dhakal, R. P., Mander, J. B. and Bradley, B. A. (2008). "Computational and Rapid Expected Annual Loss Estimation Methodologies for Structures." *Earthquake Engineering and Structural Dynamics*, 37, 81-101.

Stirling, M., McVerry, G. and Berryman, K. (2002). "A new seismic hazard model for New Zealand." *Bulletin of the Seismoligical Society of America*, 92(5), 1878-1903.

TransitNZ. (2003). "Bridge Manual Second Edition." ISBN 0-477-01697-9, New Zealand.

Vamvatsikos, D. and Cornell, A. C. (2002). "Incremental dynamic analysis." *Earthquake Engineering & Structural Dynamics*, 31, 491-514.

Zareian, F. and Krawinkler, H. (2007). "Assessment of probability of collapse and design for collapse safety." *Earthquake Engineering & Structural Dynamics*, 36, 1901-1914.

12. Conclusions and Recommendations for Future Work

12.1. CONCLUSIONS

The high demand placed on engineers and consultants to provide societies with high-performing structures that are able to minimise damage and business interruption following a major earthquake event has been the driving force behind much research over the past two decades. While there is a growing interest within the engineering fraternity given to improved seismic resisting systems, the implementation into mainstream practice is slow due to the lack of design recommendations, lack of understanding of unfamiliar technology, the few existing applications, an impression of high construction costs and additional time-consuming peer-review requirements.

This research has provided a comprehensive experimental and analytical investigation into the behaviour, modelling, design and feasibility of post-tensioned rocking systems for use in regions of high seismicity. The main findings are divided into those relating experimental, modelling and design below.

Experimental response of post-tensioned connections under quasi-static, high-speed cyclic and dynamic loading

- Uniaxial and biaxial cyclic testing of post-tensioned (PT) bridge piers highlighted a superior level of performance when compared to an equivalent monolithic ductile pier. Damage of the PT piers was superficial with most the inelastic deformations confined to the sacrificial energy dissipaters (mild steel). The damage of a PT system with external, replaceable dampers was mitigated altogether: requiring only the external devices to be replaced following a major earthquake event. The suitability of a number of connection typologies for post-tensioned connections is confirmed through testing and constructability.

- Minimal velocity dependency was observed for each of the PT viscous systems due to the high non-linearity of the damper ($\alpha = 0.153$), while mechanical clearances within the connections at each end of the damper reduced their efficiency during cycles of high frequency, low displacement amplitude. Strain-rate effects were found to have little, if any, influence on the strength enhancement of any PT system. A strength enhancement in the order of 10-20% would be further reduced due to the proportion of lateral resistance provided by the steel dampers.

- Dynamic shake-table testing determined that the equivalent viscous damping ratio associated with contact damping was in the range of 2-2.5%, specific to the geometry of this post-tensioned wall.

Modelling the monotonic and cyclic response of post-tensioned rocking connection

- An existing monotonic section analysis procedure was extensively refined and included the following: a method to account for the cyclic behaviour of steel, procedures to estimate the level of confinement in a rocking connection, extension of the procedure include PT systems with external viscous dampers, alternative stress-strain constitutive laws and biaxial loading.

- A technique was presented to accurately calibrate a macro-model utilising multi(axial)-springs at the rocking interface. The calibration was also extended to 3-dimensions with both models returning a very good comparison to the experimental response.

- A damping model is implemented within the macro-model to account for contact damping via a viscous dashpot and friction element. For all practical levels of mechanical damping, the option to ignore contact damping will have little effect on the maximum response of the system. For PT systems with zero (or very low levels of) mechanical damping, the peak response was largely affected by small variations of damping.

Design procedures for post-tensioned viscous systems with viscous and hysteretic damping

- A Direct Displacement-Based Design procedure was developed for SDOF and MDOF post-tensioned bridge systems with viscous and hysteretic dampers. The procedure explicitly accounts for systems located in near-field or far-field seismic regions. The premise behind the procedure is to relate the properties of the viscous dampers to equivalent damping properties at the effective height of the system.

Feasibility of advanced post-tensioned bridge systems

- A probabilistic seismic loss assessment was performed on three post-tensioned bridge systems (two advanced solutions and one traditional solution) and compared to a traditional ductile bridge system. While the initial cost of fluid viscous dampers could not be ignored, there was a cost saving associated with a reduction in the amount of post-tensioning required.

- In all cases, the post-tensioned bridge systems are shown to be more feasible than a traditional ductile bridge system. Overall, the traditional post-tensioned bridge system was found to be the most economical solution. In hind site however, the advanced post-tensioned viscous-hysteretic becomes increasing advantageous as the cost of the fluid viscous dampers reduces.

12.2. RECOMMENDATIONS FOR FUTURE RESEARCH

Contact damping still remains to be a rather undefined parameter for post-tensioned rocking systems. While a level of equivalent viscous damping was computed, and a simple model developed, this solution was specific to this particular system. Further research should be carried out in this area if more comprehensive data is required. In particular geometry aspects, initial post-tensioning, number of tendons, rocking interface are all parameters likely to affect contact damping.

A more extensive parametric analysis is required to provide a better estimate for the axial stiffness of a multi(axial)-spring macro-model. While the method of calibration presented in this research is perfectly valid, a series of design charts to determine the axial stiffness to be assigned to the multi(axial)-spring unit would be more practical

More in-depth probabilistic seismic loss assessments could be carried out to further confirm the cost benefits of not only traditional hybrid systems, but the proposed advanced post-tensioned viscous-hysteretic systems. In particular, the development of more detailed prototype bridge systems to include an itemised costing of the entire construction is likely to help determine the financial benefits of such systems

Appendix A

A1. DISPLACEMENT-BASED DESIGN OF THE PROTOTYPE BRIDGE PIER

The following summarises the DDBD carried out for the monolithic prototype bridge tested in Chapter 4. The New Zealand seismic design spectrum (NZS1170.5 [2004]), specific to the bridge site, is graphed in Figure A.1, while the spectral coordinates are also listed in Table A.1. The design is based on a target drift ratio of 3.4%, i.e., a lateral displacement of $\Delta_d = 3.4\% \cdot 4800mm = 163mm$ and the following seismic hazard properties

- Zone factor, Z=0.33
- Risk Factor, R = 1.7
- Shallow soil
- Amplified PGA = 0.756g
- Structural performance factor, S_p = 1.0
- Site located greater than 20km from known fault, i.e, N(T,D) = 1

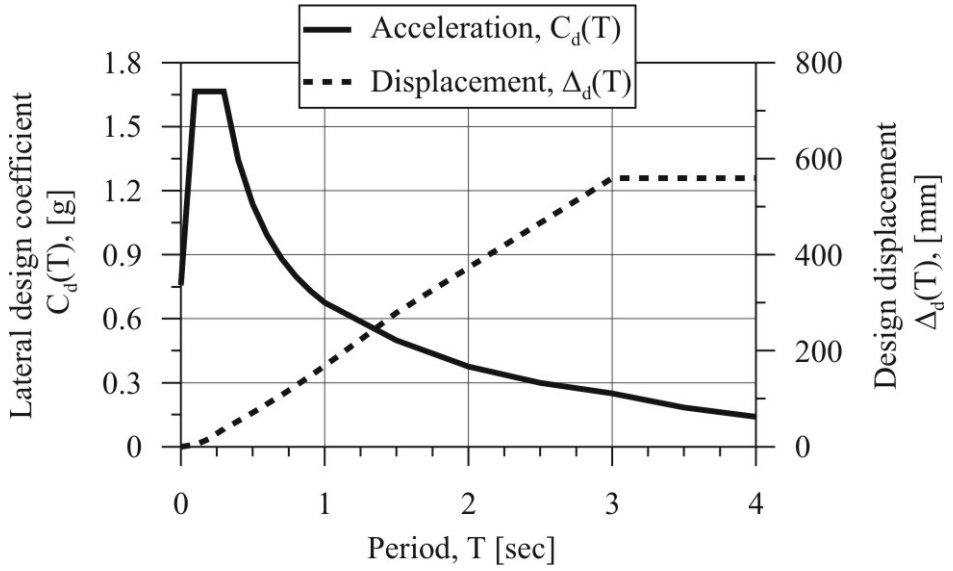

Figure A.1 NZS1170.5 [2004] elastic (5% damped) design spectrum. Zone factor z = 0.33, soil class C, risk factor R_u = 1.7, structural performance factor S_p = 1.0, 20km distance to fault, near-fault factor N(T,D) = 1.0

Table A.1 Coordinates for the elastic (5% damped) design spectrum. Zone factor z = 0.33, soil class C, risk factor R_u = 1.7, structural performance factor S_p = 1.0, 20km distance to fault, near-fault factor N(T,D) = 1.0

Period, T [sec]	$C_d(T)$ [g]	$\Delta_d(T)$ [mm]
0.0	0.756	0
0.1	1.665	4
0.2	1.665	17
0.3	1.665	37
0.4	1.344	53
0.5	1.137	71
0.6	0.991	89
0.7	0.883	108
0.8	0.799	127
0.9	0.731	147
1.0	0.676	168
1.5	0.499	279
2.0	0.375	373
2.5	0.300	466
3.0	0.250	559
3.5	0.184	559
4.0	0.141	559
4.5	0.111	559

Yield curvature

$$\phi_y = \frac{2.1 \cdot \varepsilon_y}{h_c} = \frac{2.1 \cdot 0.0015}{1050mm} = 3 \times 10^{-6} mm^{-1}$$ Priestley [2003]

Yield Displacement

$$\Delta_y = \frac{\phi_y \cdot (h_e + l_{sp})^2}{3} = \frac{\phi_y \cdot (h_e + 0.022 f_y d_b)^2}{3} = 25mm$$

Displacement ductility

$$\mu = \frac{\Delta_d}{\Delta_y} = 6.5$$

Equivalent viscous damping for reinforced concrete bridge piers

$$\xi = 5\% + 95\left[\frac{1 - \mu^{-0.5}}{\pi}\right] = 23.4\%$$ Priestley [2003]

Damping reduction factor

$$\eta = \sqrt{\frac{10}{5+\xi}} = 0.593 \geq 0.55$$ EC8 [2004]

Reading the effective period from the damped design spectrum

T_e=1.48s

Alternatively, scaling up the displacement to allow the 5% damped spectrum to be used

$$\Delta_{5\%} = \frac{\Delta_\xi}{\eta} = 275mm$$

Effective secant stiffness

$$K_e = 4\pi^2 \frac{m_e}{T_e^2} = 3.291MNm^{-1}$$

Base shear

$$V_b = K_e \Delta_d = 3.291MNm^{-1} \cdot 163mm = 540kN$$
$$\frac{V_b}{W_t} = 0.3g$$

A2. DISPLACEMENT-BASED ASSESSMENT PROCEDURE TO EVALUATE THE SEISMIC PERFORMANCE OF AN EXPERIMENTAL TEST

The following method outlines an iterative procedure adopted to assess the performance of a SDOF system from experimental testing.

Step 1. The elastic design spectrum is generated for each seismic hazard level, i.e. R = 0.5, 1.0, 1.5, 1.7 being representative of a return period of 100, 500, 1000, 1425, 2000 years respectively. The elastic design spectrum is converted into an Acceleration Displacement Response Spectrum (ADRS). The experimental response is converted to ADRS units by normalising the lateral load with respect to the effective weight of the SDOF structure.

Step 2. The demand (seismic hazard) is compared with the capacity (experimental response) to determine where the demand intersects the loading envelope (the intersection along the first loading cycle).The "performance point" is defined as the displacement Δ_R where the capacity and demand intersect.

Step 3. The displacement Δ_R defines the damping of the system from the experimental results. Consider the demand-capacity relationship in Figure A.2 (a). The first iteration would consider the 5% damped ADRS curve (or some arbitrary level of damping). The intersection between the demand and capacity would define the displacement $\Delta_{R(i)}$ to be used within experimentally-derived area-based equivalent viscous damping $\xi_{R(i)}$ from Figure A.2 (b). In this study, the 2nd cycle damping-displacement relationship was used.

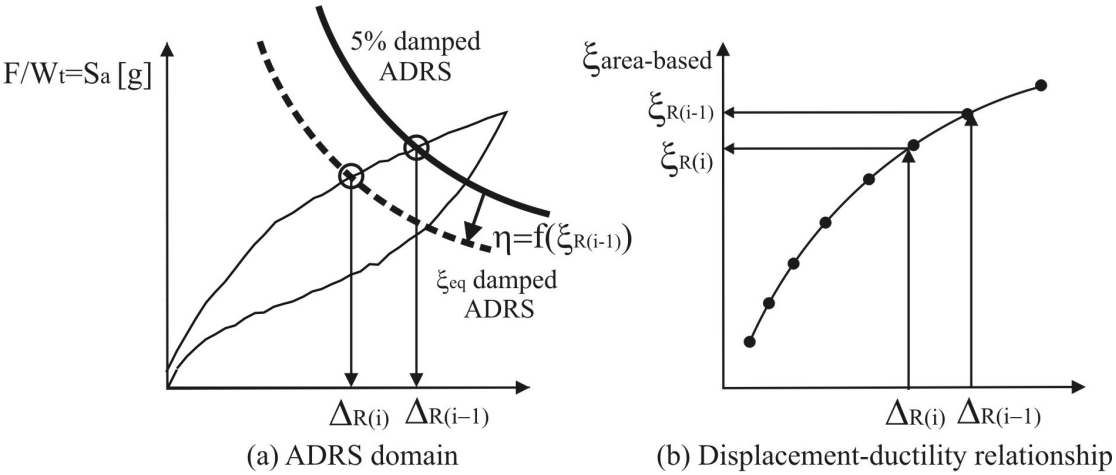

Figure A.2 Evaluation of the performance point

The area-based equivalent viscous damping $\xi_{R(i)}$ is then converted to an equivalent, time-history-calibrated, equivalent viscous damping ξ_{eq}. The spectral reduction factor η is computed according to Eq.(A.1) and the ADRS demand coordinates are reduced according to Eq.(A.2), where ξ_{eq} is expressed as a ratio.

$$\eta = \sqrt{\frac{0.07}{0.02 + \xi_{eq}}} \quad \textbf{A.1}$$

$$\eta = \frac{S_a(T,\xi)}{S_a(T,5\%)} = \frac{S_d(T,\xi)}{S_d(T,5\%)} \quad \textbf{A.2}$$

The performance point, defining the displacement Δ_R, is updated and the procedure is iterated until Δ_R converges.

Conversion of Area-Based Damping to Equivalent Viscous Damping ξ_{eq}.

It is necessary to convert the area-based damping to equivalent viscous damping representing the damped response following dynamic analysis. Priestley et al (2007) provides correction factors (in the form of a graph) as a function of the area-based EVD and the system ductility (Figure A.3 (a)). To avoid reading from the graph, the data was linearised, and expressed as Eq.(A.3).

$$\frac{\xi_{THA}}{\xi_{area-based}} = -0.018 \cdot \xi_{area-based} + \left(0.0875\mu + 0.723\right) \quad \textbf{A.3}$$

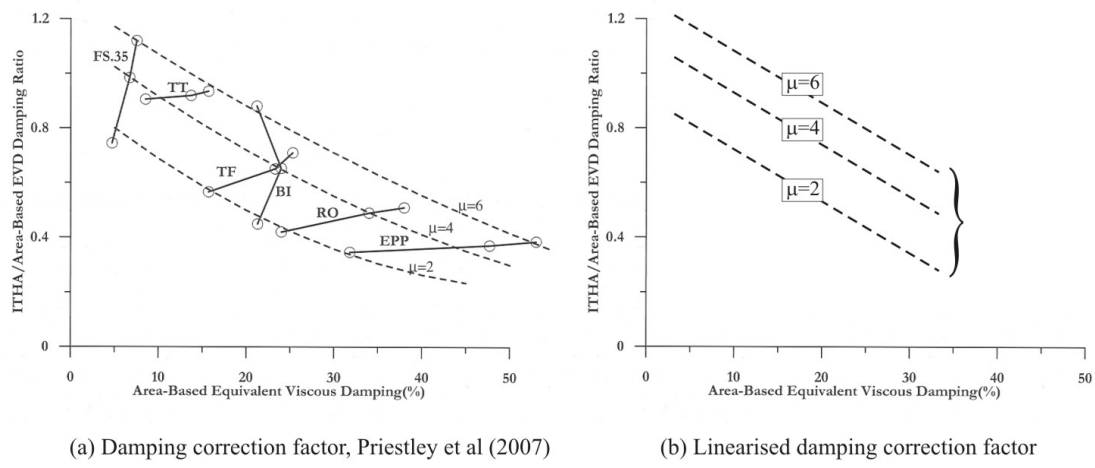

(a) Damping correction factor, Priestley et al (2007) (b) Linearised damping correction factor

Figure A.3 Damping correction factors between area-based and time-history-calibrated EVD

Tangent Stiffness Damping Correction Factor

Studies have shown that the elastic damping is better represented by a tangent stiffness proportional damping model. As Direct Displacement-Based Design (DDBD) utilises an equivalent elastic single-degree-of-freedom (SDOF) substitute structure, damping correction factors are incorporated to convert the elastic (secant stiffness) damping of the structure to a tangent stiffness proportional model. The elastic damping is computed as follows

$$\xi_{el,Tangent} = \mu^{\lambda} \xi_{el,Secant} \quad \textbf{A.4}$$

Where:

μ is the system ductility

λ is a correction factor, equal to -0.378 for a monolithic system (Thin Takeda) and -0.430 for post-tensioned systems (Flag shape with $\beta = 0.35$)

$\xi_{el,Secant}$ is the elastic damping of the system, normally equal to 5% for reinforced concrete structures.

Incorporating the area-based damping correction factor and the elastic damping correction factor, the resultant EVD ξ_{eq} can be written as

$$\xi_{eq} = 5\%\mu^{\lambda} + \xi_{area-based}\left[-0.018 \cdot \xi_{area-based} + \left(0.0875\mu + 0.723\right)\right] \quad \textbf{A.5}$$

A3. REFERENCES

EC8. (2004). "Eurocode 8: Design of structures for earthquake resistance - Part 1: General rules, seismic actions and rules for buildings." CEN/TC 250, Brussels, Belgium.

NZS1170.5. (2004). "Structural Design Actions, *Part 5: Earthquake actions*." Standards New Zealand, Wellington.

Priestley, M. J. N. (2003). *Myths and Fallacies in Earthquake Engineering, Revisited*.

Appendix B

B1. INSTRUMENTATION

The following table outlines the location and type of instrument using in the high-speed and dynamic testing of the post-tensioned walls.

Table B.1 Shake table testing instrumentation

Channel	Device	Instrument ID	Location/Discription	Calibration factor
1	potentiometer	Pot 20	North west dissipater: Viscous damper 1/Mild steel damper	-0.0071558
2	potentiometer	Pot 40	North centre dissipater: Mild steel damper only	-0.0071547
3	potentiometer	Pot 63	North east dissipater: Viscous damper 2/Mild steel damper	-0.0069979
4	potentiometer	Pot 111	South west dissipater: Viscous damper 3/Mild steel damper	-0.0070522
5	potentiometer	Pot 114	South centre dissipater: Mild steel damper only	-0.0071663
6	potentiometer	Pot 124	South east dissipater: Viscous damper 4/Mild steel damper	-0.0070598
7	potentiometer	Pot 4a	North east gap opening	-0.0071488
8	potentiometer	Pot 5a	North centre gap opening	-0.0071868
9	potentiometer	Pot 6a	North west gap opening	-0.0070831
10	potentiometer	Pot 7a	Wall-foundation translation	-0.0070752
11	potentiometer	Pot 106	South east gap opening	-0.0071348
12	potentiometer	Pot 107	South centre gap opening	-0.0071825
13	potentiometer	Pot 108	South west gap opening	-0.0071802
14	potentiometer	Pot 109	Foundation-table translation	-0.0071171
15	potentiometer	Pot A	Wall lateral displacement top	0.0476356
16				
17	Load Cell	LC A	Lateral load (mass-wall)	-0.100784
18	Load Cell	LC B	East tendon	-0.068926
19	Load Cell	LC C	Centre tendon	0.068571
20	Load Cell	LC D	West tendon	-0.068839
21	LVDT	Table LVDT	Shake-table displacement	0.057143
22	Accelerometer	Table Accel	Shake-table acceleration	7.6336E-04
23	Load Cell	LC E	Lateral load (wall-reaction frame)	-0.0208001
24	potentiometer	Table Pot	Shake-table displacement	0.28705
25	Strain gauge	NW1	North west dissipater strain	8.8145
26	Strain gauge	NW2	North west dissipater strain	8.8555
27	Strain gauge	NE1	North east dissipater strain	8.8803

28	Strain gauge	NE2	North east dissipater strain	8.8638
29	Strain gauge	SW1	South west dissipater strain	8.8091
30	Strain gauge	SW2	South west dissipater strain	8.8583
31	Strain gauge	SE1	South east dissipater strain	8.8010
32	Strain gauge	SE2	South east dissipater strain	8.7444
33	Accelerometer	A1	Wall: horizontal acceleration	0.00146742
34	Accelerometer	A2	Wall: vertical acceleration	0.00147644
35	Accelerometer	A3	Mass: out-of-plane horizontal acceleration	0.00140158
36	Accelerometer	A4	Mass: in-plane horizontal acceleration	0.00146522
37	Accelerometer	A5	Mass: vertical acceleration	0.00148589
38				
39				
40				
41	Gyro	Gyro 1	Mass: angular velocity about vertical axis	0.149841
42	Gyro	Gyro 2	Mass: angular velocity about out-of-plane axis	0.152658
43				
44				
45	potentiometer	F1	Foundation flexibility: vertical displacement at east tendon foundation anchorage	0.00356703
46	potentiometer	F2	Foundation flexibility: vertical displacement at west tendon foundation anchorage	0.00349157
47				
48				
49	Strain gauge	SG: A1	East longitudinal bar, 50mm from base of wall	8.8444
50	Strain gauge	SG: A2	East longitudinal bar, 245mm from base of wall	8.7980
51	Strain gauge	SG: A3	East longitudinal bar, 50mm from base of wall	8.7335
52	Strain gauge	SG: A4	East longitudinal bar, 245mm from base of wall	8.8967
53	Strain gauge	SG: C1	West longitudinal bar, 50mm from base of wall	8.8279
54	Strain gauge	SG: C2	West longitudinal bar, 245mm from base of wall	8.8333
55	Strain gauge	SG: C3	West longitudinal bar, 50mm from base of wall	8.9440
56	Strain gauge	SG: C4	West longitudinal bar, 245mm from base of wall	8.7898
57	Strain gauge	SG: S1	North stirrup 100mm from base	8.9273
58	Strain gauge	SG: S2	North stirrup 215mm from base	8.9442
59	Strain gauge	SG: S3	South stirrup 100mm from base	8.9670
60	Strain gauge	SG: S4	South stirrup 215mm from base	9.0178

B2. MARRIOTT, D., PAMPANIN, S. AND BULL, D. (2007). "IMPROVING THE SEISMIC PERFORMANCE OF EXISTING REINFORCED CONCRETE BUILDINGS USING ADVANCED ROCKING WALL SOLUTIONS." NZSEE, PALMERSTON NORTH, NEW ZEALAND.

This paper was published and presented at the 2007 New Zealand Society of Earthquake Engineering annual conference in Palmerston North, New Zealand.

Improving the seismic performance of existing reinforced concrete buildings using advanced rocking wall solutions

2007 NZSEE Conference

D.J. Marriott, S. Pampanin, D. Bull

Department of Civil Engineering, University of Canterbury, New Zealand.

A. Palermo

Dept of Structural Engineering, Politecnico de Milano, Italy.

ABSTRACT: Recent major earthquakes such as Northridge 1994 and Izmit Kocaeli 1999 highlighted the poor performance of existing buildings constructed prior to the early 1970's. Low lateral seismic design coefficients and the adopted "working stress design" methodology (essentially an elastic design) lacked any inelastic design considerations, thus leading to inadequate detailing. Insufficient development lengths, lapping within potential plastic hinge regions, lack, or total absence of joint transverse reinforcement, and the use of plain round reinforcement and hooked end anchorages were common throughout the structure. The behaviour is generally dominated by brittle local failure mechanisms (e.g. joint or element shear failures) as well as possible soft-storey mechanisms at a global level. Amongst several possible retrofit interventions, a typical solution is to provide the structure with additional structural walls i.e. external buttressing or column in-fills.

Extensive developments on precast, post-tensioned, dissipative systems have shown promise for the use of rocking wall systems to retrofit existing poorly detailed frame structures. In this contribution, the feasibility of such a retrofit intervention is investigated. A displacement-based retrofit procedure is developed and proposed, based on targeting pre-defined performance criteria, such as joint shear and/or column curvature deformation limits. A design example, using the proposed retrofit strategy on a prototype frame is presented. A brief overview on experimental work ongoing at the University of Canterbury investigating the dynamic response of advanced rocking walls for retrofit purposes will be provided.

1 INTRODUCTION

It has been well reported that the structural performance of pre 1970's buildings consists of brittle, premature local failure mechanisms leading to possible collapse of the lower or ground floors (Pampanin (2006)). Reasons for such a failure stem from low lateral design coefficients with an expectation that the building will remain elastic. The "elastic" analysis and design, or "working stress" concept, had no allowance for member ductility and hence the structure had insufficient detailing to properly accommodate the inelastic demand due to seismic loadings. Typically, the use of plain round reinforcing bars, lapping of longitudinal bars in potential plastic hinge regions, insufficient development lengths of reinforcing bars, and a lack or total absence of joint transverse reinforcement was common.

Following a brief overview into the performance of existing RC buildings and the advantage of using coupled walls for retrofit applications, the feasibility and efficiency of implementing a rocking/dissipating (PRESSS-technology) wall system is presented. A performance based (displacement-based) retrofit design methodology is developed and presented for poorly detailed (pre-1970's) frame buildings. An example of the design procedure is also given along with an update on the on-going shake-table testing at the University of Canterbury.

2 PERFORMANCE ASSESSMENT OF EXISTING BUILDINGS

Typical joint failure mechanisms for poorly detailed exterior beam-column joints without joint shear reinforcement are shown in

Figure 1 (Priestley (1997); Pampanin, et al. (2003)). Depending on the beam anchorage details different damage mechanisms can occur. When beam bars are bent into the joint (**Figure 1**a, **Figure 1**b) cracking will initiate from dilation of the un-reinforced joint core followed by opening of the hooked anchorages. A more brittle mechanism can be expected if the beam bars are bent away from the joint (**Figure 1**c) as the diagonal compression strut is not adequately "captured" at the anchorages' bent-end preventing the development of a "nodal" point for internal forces. Plain round bars with hooked end anchorages (**Figure 1**d) cause slipping of the reinforcement thought the joint resulting in stress concentrations at the anchorage ends leading to a wedge failure of the joint.

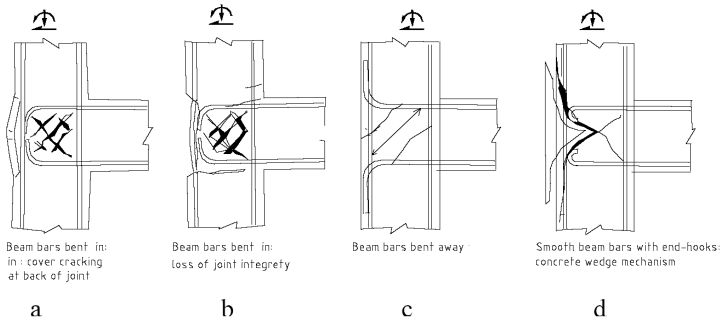

Figure 1: Typical anchorage details for beam-column joints Pampanin, et al. (2003)

Typical details within the pre-1970's building stock are shown in Figure 2a. Lapping within plastic hinge zones, insufficient development lengths, and the low level of transverse reinforcing content were common practice. The expected ductility capacity of these elements will be relatively low due to bar slip, poor confinement, buckling of longitudinal reinforcement and joint shear failure.

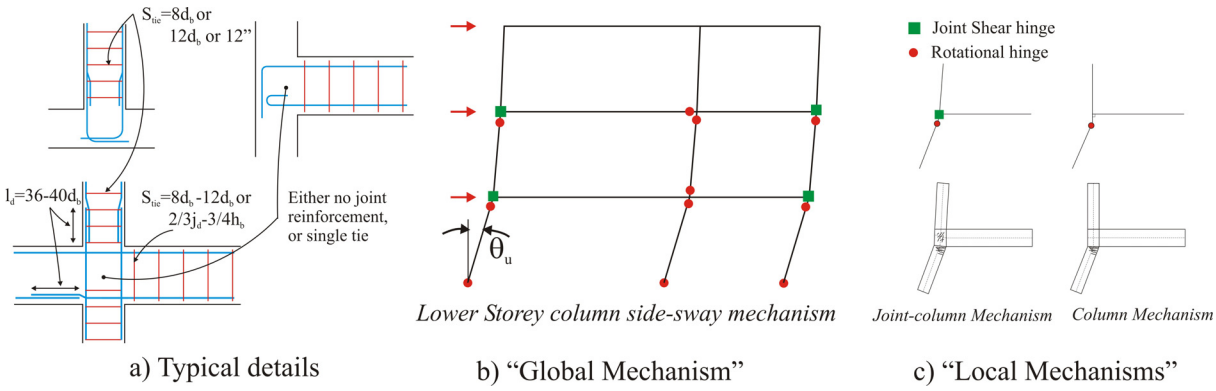

Figure 2: Failure mechanisms and typical NZ detailing

Figure 2b illustrates a soft-storey "global mechanism" for a 3-storey building. The independent, "local mechanisms" are also shown (Figure 2c). In defining the "local mechanism", a comparative strength assessment allows a hierarchy of strength and sequence of events to be evaluated within the beam-column joint subassembly. The capacity of each structural element (beam, column, and joint) is converted to a common-unit, such as an "equivalent column moment", allowing a direct strength comparison to be made within a moment-axial domain (M-N interaction diagram). Both flexure and shear failure modes can be considered as well as strength degradation effects.

2.1 Beam, column, and beam-column joint assessment

An extended literature on the assessment of existing reinforced concrete buildings is available and to some extent, regulated within code previsions e.g. fib (2003), FEMA:356 (2000), NZSEE (2006).

The performance of RC beams and columns are influenced by the type of reinforcing (plain round vs.

deformed), the presence of lap splices within the plastic hinge region, and the amount of transverse reinforcement for confinement, anti-buckling and shear resistance. Plain round bars result in slipping of the longitudinal reinforcement and poor energy dissipation, while lapping within plastic hinge regions will result in premature failure under repeated cyclic loading at low levels of ductility.

The strength and deformation capacity of beam-column joints are more delicate. Joint shear stress and deformation limits are typically provided in assessment guidelines FEMA:356 (2000). However, based on recent experimental investigations, principle tensile stresses have been suggested to be a better indication of damage. Furthermore, strength degradation curves (principal tensile stress vs. joint rotation) have been proposed in literature (Priestley (1997)). Depending on the structural detailing (bars bent into the joint, bars bent out of the joint, hooked anchorage etc), the typology (interior vs. exterior), and of the reinforcing type (plain round vs. deformed) the joint deformation limits can vary significantly (Pampanin, et al. (2003)).

3 FRAME-WALL COUPLED SYSTEMS FOR RETROFIT

Adding either internal or external wall systems is an attractive and common option to retrofit an existing poorly detailed RC frame structure. As a result of the coupling mechanism between the frame and wall, a reasonably stiff, strong system would result, reducing structural deformations (thus deformation related damage) to reasonable limits. The use of monolithic wall systems can however result in significant physical damage and residual deformations, especially when considering the effects of near field events i.e. large velocity pulses. Figure 3 indicates the qualitative performance of a retrofit intervention based on an advanced rocking/dissipating wall when compared to the use of a traditional monolithic wall retrofit. The re-centring capacity of the post-tensioned wall can be used to minimise residual deformations, where deformation of the wall is confined to a "controlled rocking" motion on the foundation, relieving the wall of any physical damage. In addition, more appropriate dissipation techniques can be applied to a rocking system where the advantage of both velocity proportional and displacement proportional devices for near and far field earthquake events respectively, can be utilised.

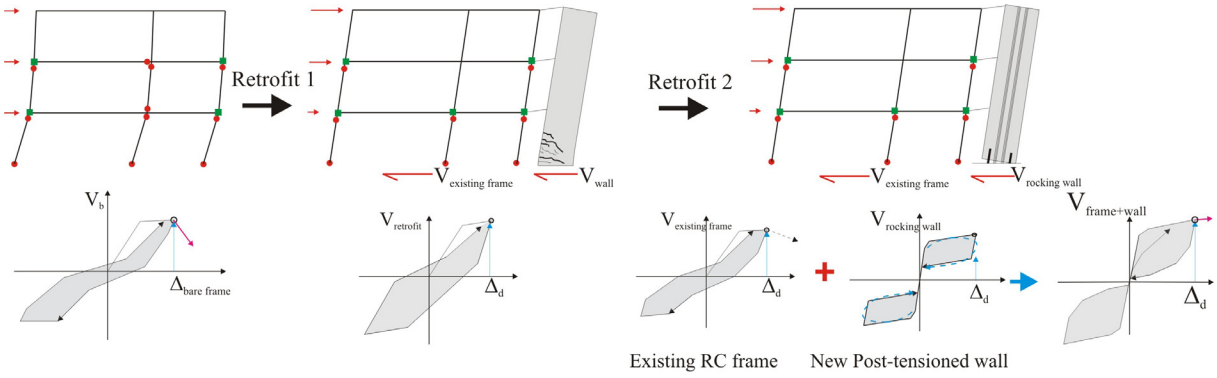

a) Bare frame b) Retrofit with monolithic wall c) Retrofit with advanced rocking wall

Figure 3: Comparison of retrofit intervention having either a monolithic wall or advanced rocking wall

A retrofit intervention based on the introduction of an additional wall system has the advantage of distributing the inelastic demand up the height of the structure, increasing the total strength, stiffness and energy dissipation of the existing bare frame.

The push-over capacity curve in Figure 4 summarises the key concepts for a retrofit intervention of the proposed prototype frame building. The first is that the deformation of the frame is reduced, limited to pre-determined deformation limits of critical elements within the frame. The second, the strength and deformation capacity of the wall alone are substantially improved by simply imposing the frame to deform linearly, redistributing the inelasticity (1); further improved by the additional over-turning capacity provided of the wall (2). Finally, additional energy dissipation (mild steel, friction, viscous, or post-tensioning alone) will provide a more damped structural response (3).

Special attention is required to a number of structural elements within dual systems due to a vertical

displacement incompatibility between the frame and the wall (Paulay (1993)).

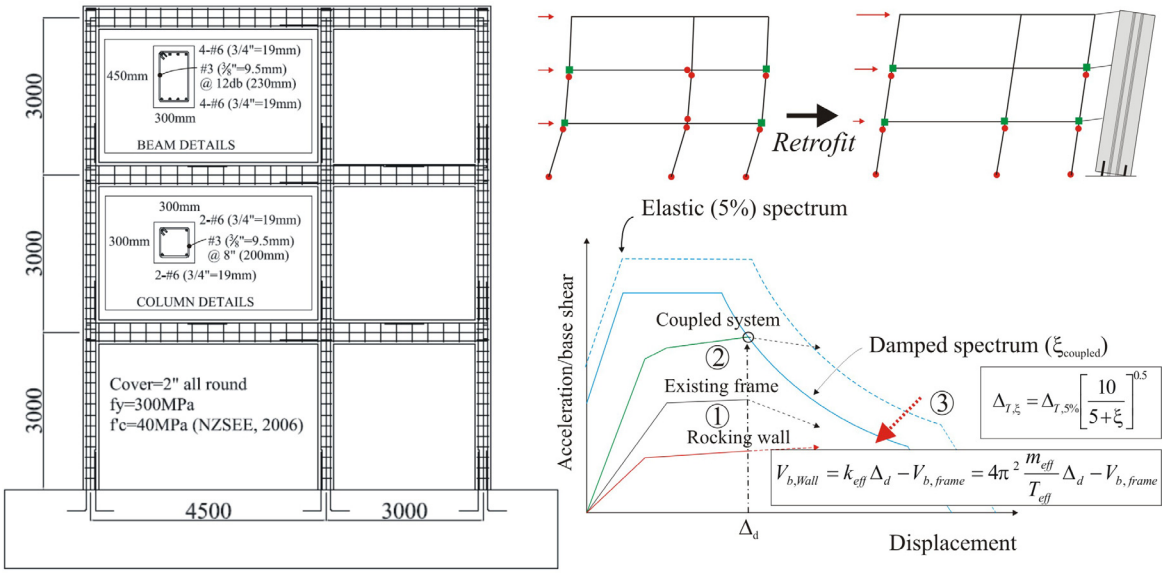

a) Building Details and Geometry

b) Push-over capacity curve

Figure 4: Prototype frame details

The vertical displacement arises from the shift in neutral axis position and the effect of having a "deep" member, resulting in lifting of the tension side of the wall and lowering of the compression side of the wall. This incompatibility can however be properly exploited to activate special yielding elements between two incompatible members (Kurama, et al. (2006)). Displacement-based design procedures have been recently developed for the design of new dual-system structures, including refined damping-ductility relationships (Sullivan, et al. (2006)).

4 ROCKING WALL SYSTEMS WITH ADVANCED DISSIPATION DEVICES

Jointed ductile rocking systems have been widely developed for either frame and wall systems (Priestley (2003), Rahman & Restrepo (2000), Kurama, et al. (2006)). A "controlled rocking" mechanism is developed at the critical interface (i.e. beam-column, pier-foundation interface, etc) and activates two types of reinforcement: prestressed tendons providing re-centring and non-prestressed mild steel dissipation (Figure 5). Rocking systems are characterised by reduced/negligible residual deformations, minimal physical damage (due to a single rotation located at the critical interface), whilst having similar maximum displacements when compared to their equivalently reinforced monolithic counterparts.

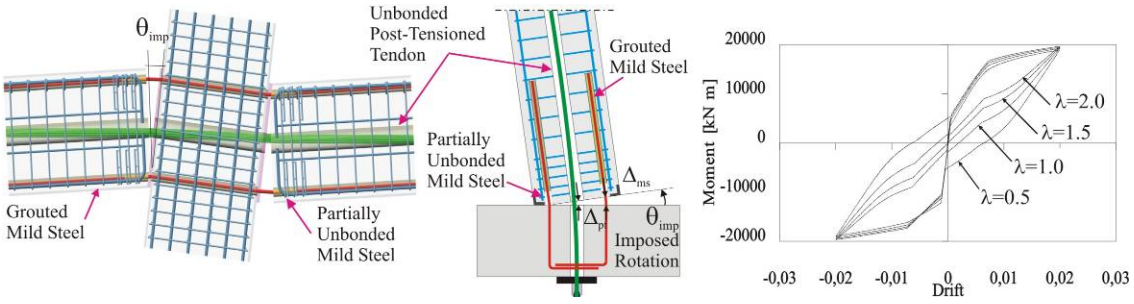

Figure 5: Rocking connection: Left, beam-column joint; Centre, pier/column-foundation connection; Right, cyclic behaviour as function of non-prestressed to prestressed moment ratio (λ).

The behaviour of a "hybrid system" (in terms of maximum and residual displacements) can be defined by a single "design parameter", lambda (λ) (fib (2004), NZS3101:2006 (2006)). Lambda is the moment ratio of the non-prestressed reinforcement (mild steel dissipation) to the prestressed reinforcement and/or axial load respectively, which defines both the energy dissipation and re-centring

capacity of the connection/system (Figure 5).

Controlling structural deformations in existing or new buildings with supplementary dissipation has been extensively studied, including dampers ranging from metallic (elasto-plastic), viscous, visco-elastic, friction etc (FEMA:356 (2000), fib (2003)). More advanced materials include Shape Memory Alloys having "memory" characteristics suitable for use in seismic applications (Dolce, et al. (2000)).

5 PERFORMANCE BASED RETROFIT METHODOLOGY.

Performance-based design approaches are emerging as a more rational design and assessment procedure for the design of new structures and retrofit of existing buildings. Performance-based procedures generally relate performance to damage limit states considering allowable material strains and drift levels (including both maximum and residual). FEMA 356 provides a number of prescriptive performance criteria to be satisfied for the seismic rehabilitation of existing buildings. Indicative limit states, based on maximum and/or residual deformations, are suggested in order to satisfy various structural protection levels.

A displacement based design retrofit procedure is outlined as an extension of the Displacement Based Design Procedure (DDBD) proposed by Priestley (2002). Figure 7 summarises the basic steps within the procedure.

Step 1): A target displacement is defined based on allowable deformation limits of critical elements i.e. joint rotation or member curvatures.

Step 2): The retrofitted system, comprising of a coupled frame-wall (dual system) is converted to an equivalent single degree of freedom (SDOF) elastic system, with secant stiffness to the target displacement at the effective height Figure 7(a) and Figure 7(b).

Step 3): The damping of the coupled system (as built frame plus rocking wall) is evaluated based on a weighting in proportion to the base shear carried by each element Figure 7(c). Limited information is available on damping-ductility curves for poorly detailed buildings when joint damage mechanisms are activated. Equivalent viscous damping ratios in the order of 10% have been suggested by Priestley (1997). Damping-ductility relationships herein have been evaluated using stiffness degrading, pinched hysteresis rules based on previous analytical and experimental works (Galli; (2006), Liu; (2001), Chen; (2006), Sullivan, et al. (2006))

Figure 6 illustrates the ratio between the relative energy dissipation for each of the respective hysteresis rules i.e. slipping/pinching hysteresis vs. Takeda hysteresis. The effects of strength degradation have not been included. Based on this work, a percentage of damping assigned to the as-built frame during design appears to be justified by an amount 40-45% that of a well designed frame.

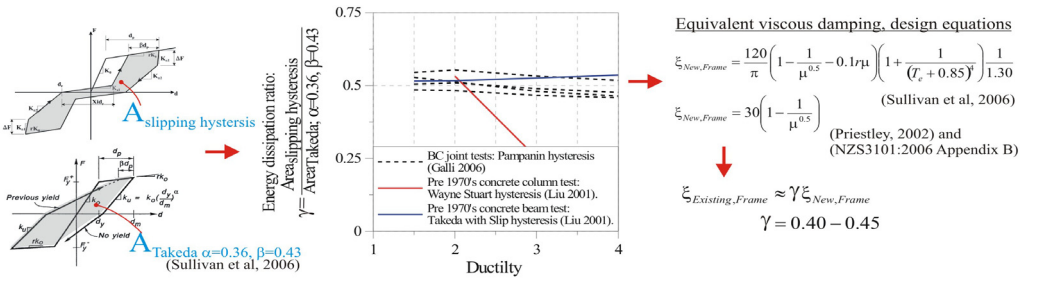

(a) Energy dissipation relationship for existing RC frame

(b) Modification factor for equivalent viscous damping equations

Figure 6: Modified damping relationships for existing buildings

On the other hand, evaluation of the equivalent viscous damping for the rocking wall can be calculated following the guidelines of Appendix B NZS3101 (2006). In principle, the damping is a function of the lambda (λ) ratio mentioned previously. In this case a reasonably high value of λ=1.4-2.0 should be used to guarantee full re-centring of the bare frame, while also counteracting strength degradation and P-Delta effects within the frame.

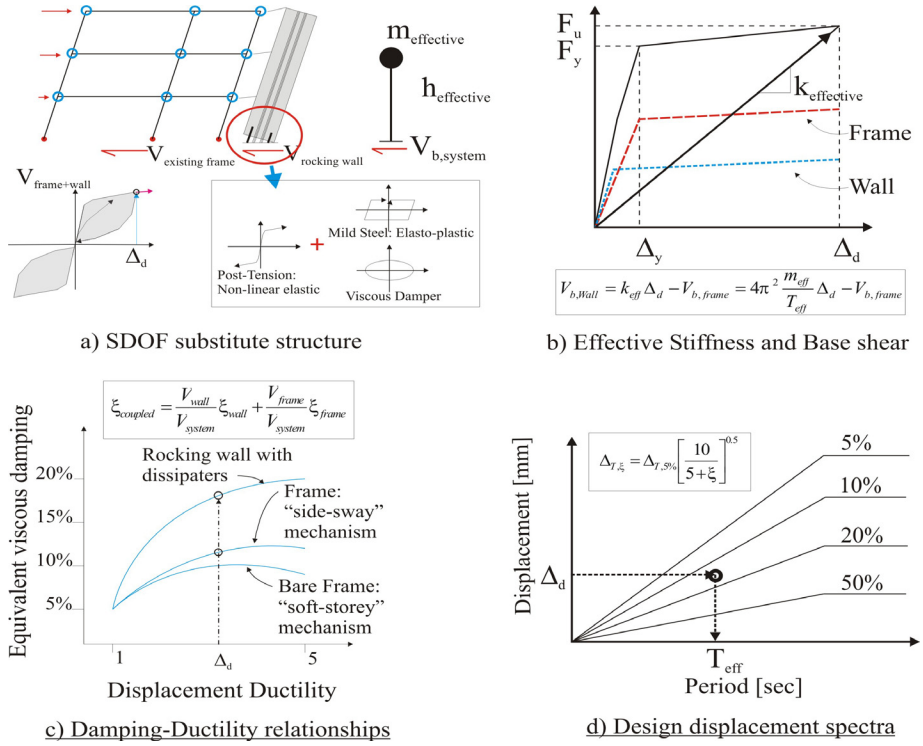

Figure 7: Displacement-based retrofit procedure

Step 4): The displacement response spectrum is used to deduce the effective secant period corresponding to the target displacement (Figure 7(d)). A reduction of the 5% elastic damped spectra is obtained by the η factor adopted in Eurocode 8 (EC8 (2003)).

Step 5): The total required base shear for the coupled system is calculated as $V_{b,total} = k_{eff} \cdot \Delta_d$. The base shear required of the hybrid wall for the retrofit intervention can thus be obtained as the difference between the total system base shear and base shear capacity of the bare frame.

6 NUMERICAL EXAMPLE: DDBD RETROFIT OF A PROTOTYPE BUILDING.

This section briefly outlines a numerical example based on a prototype building intended for testing at the University of Canterbury (Figure 4a). The three storey office building is located in Wellington (on shallow soil) where the retrofit intervention is to bring the capacity of the structure up to 100% of the current seismic loading requirements for new buildings: z = 0.4, R = 1, D = 2km, S_p = 1.

6.1 Design procedure and results.

A "hierarchy of strength" assessment is performed on each joint within each beam-column joint at each storey level, allowing the overall base shear capacity of the bare frame to be determined (in this case, $V_{b,frame}$=*125kN (0.17g)*, where the total frame mass is equal to 73.8tonne)

The deformation capacity of the frame is limited to the most critical elements within the as-built frame (Figure 7b). While the columns have only minimal transverse confinement, reducing their ductility capacity, the detailing of the joints would suggest to limit the allowable drift to 1.0% (limited ductility)

A yield drift of θ_y=*0.80%* (corresponding to equivalent "joint yield", fib (2003)) results in a frame ductility demand of μ=*1.3*. Equivalent viscous damping for the bare frame of ζ=*6.3%* is based on a reduction of γ=*0.4* to damping-ductility relationships presented Figure 6. The wall contributes ξ=*11.9%*, resulting in a total system damping of ξ=*8.0%* (Figure 7c). The total system base shear is determined, defining the required wall capacity: $V_{b,wall}$=*178kN*, at a wall ductility of μ=*5.0* and moment ratio of λ=*1.4*.Table 1 summarises the numerical results of the DDB-retrofit example.

Table 1: Summary of displacement-based retrofit design example

Displacement-based retrofit design results				**Equivalent column moments within frame following a mechanism method of plastic analysis**			
θ_d	1.00%	$V_{b,frame}$	125kN	*Column location*	*Left*	*Centre*	*Right*
Δ_d	68mm	$\xi_{e,frame}$	6.3%	Level 3: Mechanism	column	column	column
h_e	6798mm	$V_{b,wall}$	178kN	Column moment	45kNm	52kNm	46kNm
m_e	63016kg	$\xi_{e,wall}$	11.9%	Level 2: Mechanism	joint	joint	joint
μ_{wall}	5.0	V_b	303kN	Column moment	35kNm	55kNm	38kNm
μ_{frame}	1.3	ξ_e	9.6%	Level 1: Mechanism	joint	joint	joint
T_e	0.75sec			Column moment	40kNm	63kNm	58kNm
K_e	4463kN/m			Ground moment	53kNm	70kNm	68kNm

7 EXPERIMENTAL AND ANALYTICAL WORK ON ROCKING SYSTEMS.

An extensive experimental program at the University of Canterbury is currently investigating the seismic performance of jointed rocking systems with particular emphasis on bridge piers and wall structures. Quasi-static and pseudo-dynamic responses of 1/3-scale precast bridge piers with hybrid connections have been studied and modelled having either internal or external mild steel dissipation Marriott, et al. (2007). Dynamic shake-table testing of 1/3-scale wall specimens involving frequency constant, sinusoidal input motions are currently in progress. Both hysteretic (tension-compression yielding devices) and fluid-viscous (provided by FIP Industriale) are installed external to the wall section.

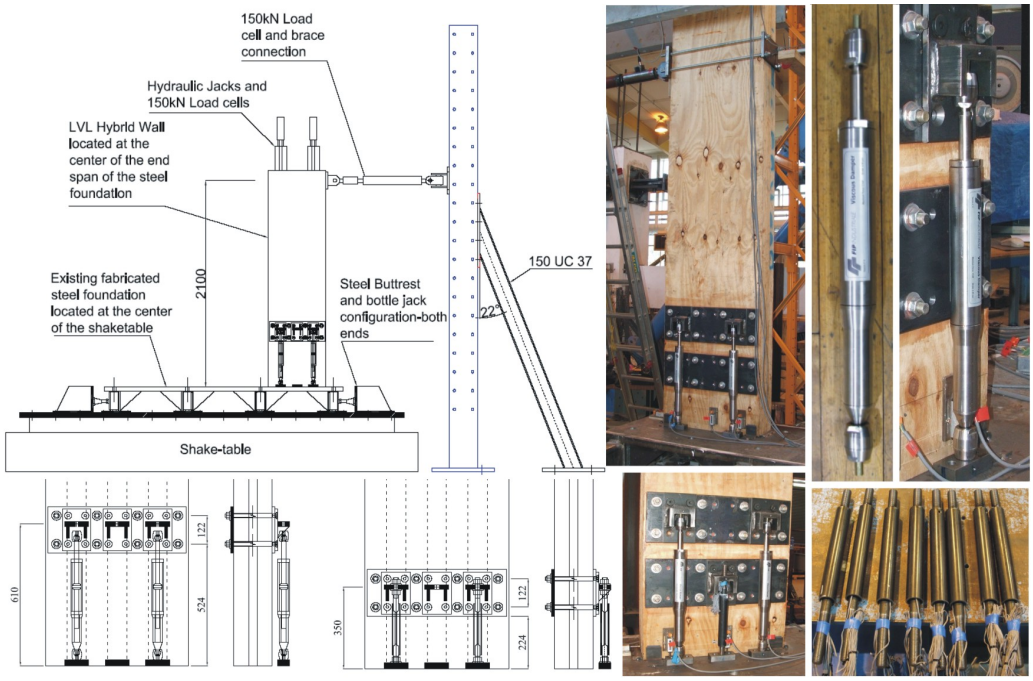

Figure 8: Dynamic wall testing images, Left: Experimental test set-up showing both viscous and mild steel damper arrangement; Right: Actual test rig and location of dissipation devices.

Figure 8 shows a number of images related to the experimental wall test. The studies will investigate the potential benefits of various types of dissipation (hysteretic, viscous, friction etc) used either independently or in combination with respect to either near field (velocity pulse or fling type events) or far field earthquake events. Recent numerical studies on Advanced Flag Shape Systems (Kam, et al. (2006)) have demonstrated that a combination of viscous (velocity proportional dissipation) and hysteretic (displacement proportional dissipation) devices would ensure a superior level of performance in either near field or far field earthquake events.

8 CONCLUSIONS

A conceptual performance-based retrofit design procedure for existing buildings based on the use of a rocking/dissipating (hybrid) wall system has been presented. The rocking wall can add lateral strength and damping to the structural system while controlling the damage in the as-built frame. Global inter-storey drifts for the frame can be limited, in addition to having the inelastic demand distributed up the height of the frame. The displacement-based retrofit procedure targets a pre-defined displacement, limiting deformations within critical structural elements such as joint rotations or member curvatures. Furthermore, residual deformations can also be minimised due to the re-centring capacity of the rocking wall.

Extensive experimental and analytical work is on-going at the University of Canterbury to further investigate the potential benefits of using precast post-tensioned rocking systems for either new design or retrofit solutions. Different dissipation characteristics (displacement or velocity proportional) are adopted and properly combined to improve the structural performance for either far field or near field earthquake events.

9 REFERENCES

Dolce, M., Cardone, D. & Marnetto, R. 2000. Implementation and Testing of Passive Control Devices based on Shape Memory Alloys, *Earthquake Engineering and Structural Dynamics*, Vol 29 (7): 945-968

EC8. *Eurocode 8: Design of Structures for Earthquake Resistance; prEN 1998-1:2003*.

FEMA:356, 2000. *Prestandard and Commentary for the Seismic Rehabilitation of Buildings*. Washington, D.C.

fib, 2003. *Seismic Assessment and Retrofit of Reinforced Concrete Buildings*. Bulletin 24, Lausanne

fib, 2004. *Seismic Design of Precast Concrete Building Structures*. Bulletin 27, Lausanne

Kam, W. Y., Pampanin, S., Palermo, A. & Carr, A. 2006. Advanced Flag-Shaped Systems for High Seismic Performance, *First European Conference on Earthquake Engineering,* Geneva, Switzerland

Kurama, Y., Weldon, B. & Shen, Q. 2006. Experimental Evalutation of Post-tensioned Hybrid Coupled Wall Subassemblages, *ASCE: Journal of Structural Engineering*, Vol 132 (7): 1017-1029

Marriott, D., Pampanin, S. & Palermo, A., 2007. *Seismic Design, Experimental Response, and Numerical Modeling of Rocking Bridge Piers with Hybrid, Post-tensioned Connections*. University of Canterbury Report, ISSN-0110-3326 (2007-01), New Zealand

NZSEE, 2006. *Assessment and Improvement of the Structural Performance of Buildings in Earthquakes*. Wellington

Pampanin, S. 2006. Controversial Aspects in Seismic Assessment and Retrofit of Structures in Modern Times: Understanding and Implementing Lessons from Ancient Heritage, *Bulletin of the New Zealand Society for Earthquake Engineering*, Vol 39 (2): 120-133

Pampanin, S., Magenes, G. & Carr, A. 2003. Modelling of Shear Hinge Mechanism in Poorl Detailed RC Beam-Column Joints, *fib* Athens

Paulay, T., 1993. *Simplicity and Confidence in Seismic Design*. The Fourth Mallet-Milne Lecture, John Wiley & Sons

Priestley, M. J. N. 2002. Direct Displacement-Based Design of Precast/Prestressed Concrete Buildings, *PCI*, Vol 6

Priestley, M. J. N. 1997. Displacement-Based Seismic Assessment of Reinforced Concrete Buildings, *Journal of Earthquake Engineering*, Vol 1 (1): 157-192

Priestley, M. J. N. 2003. *Myths and Fallacies in Earthquake Engineering, Revisited.* Pavia: IUSS Press

Rahman, A. M. & Restrepo, J. I., 2000. *Earthquake Resistant Precast Concrete Buildings: Seismic Performance of Cantilever Walls Prestressed using Unbonded Tendons*. University of Canterbury Research Report-ISSN: 0110-3326 (2000-5),

Sullivan, T. J., Priestley, M. J. N. & Calvi, G. M., 2006. *Seismic Design of Frame-Wall Structures*. Research Report ROSE-2006/02, Pavia

Appendix C

C1. PRECAST WALL CONSTRUCTION DRAWINGS

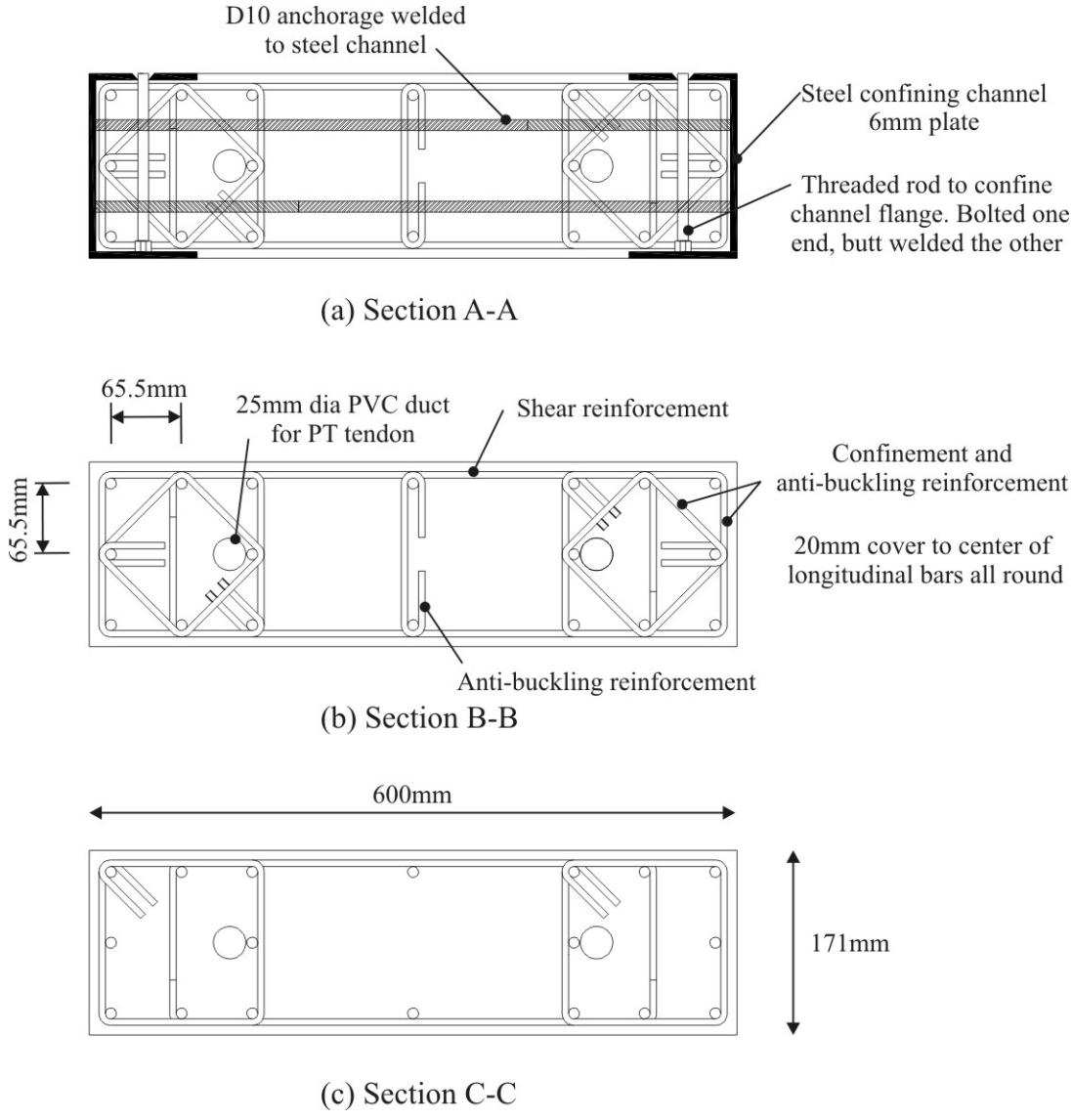

Figure C.1 Section reinforcement details of the precast wall

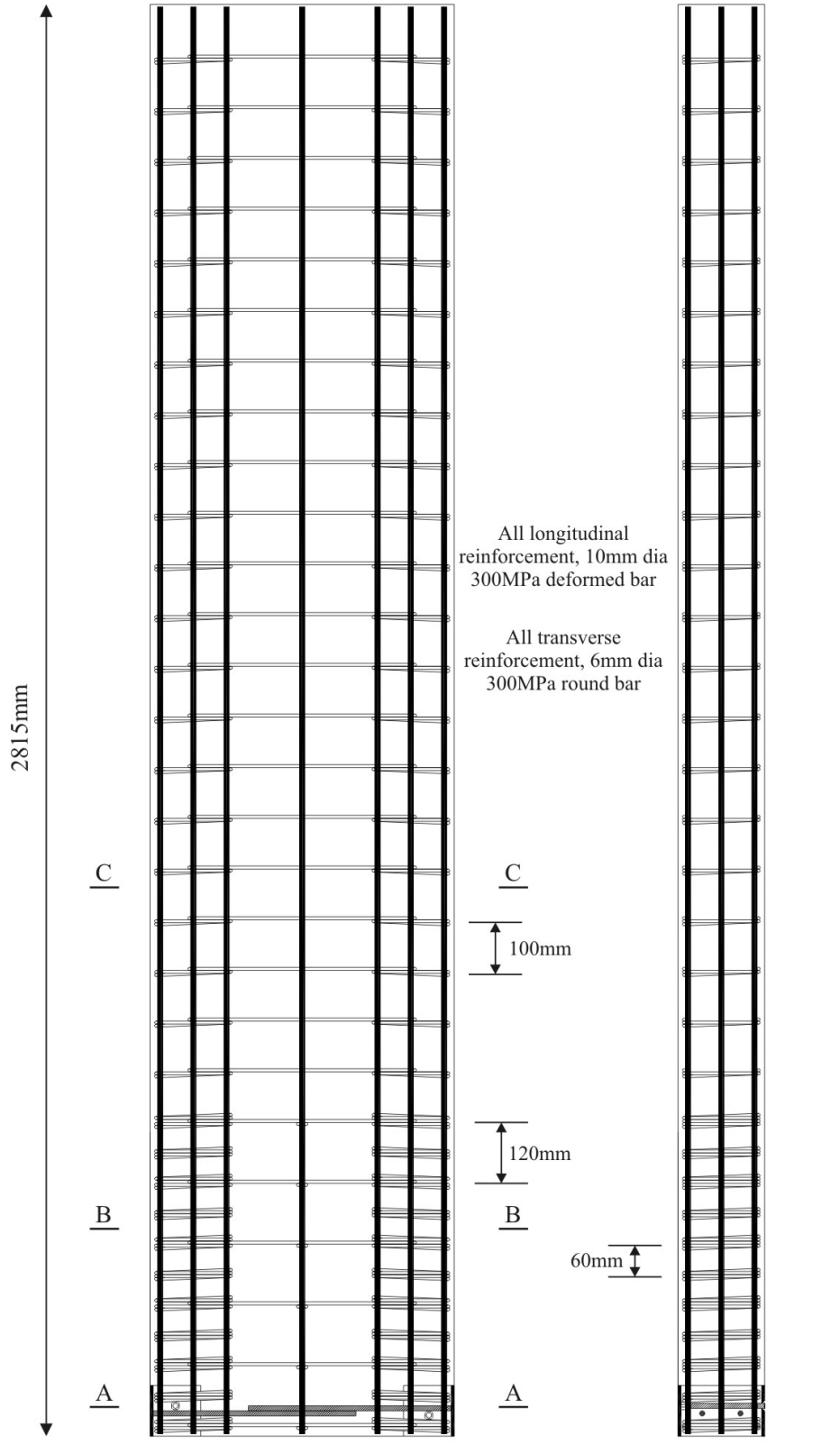

(a) Wall reinforcement, front elevation

(b) Wall reinforcement, end elevation

Figure C.2 Reinforcement layout of the precast wall

C2. RECORD MODIFICATION, METHOD A

The following step-by-step procedure outlines a method to modify an acceleration time-history to limit the peak velocity while retaining the peak acceleration magnitude, Chase et al. [2005].

Step 1 Locate the raw acceleration record $a_{raw}(t)$ (downloaded from PEER or NGA website)

Step 2: Acceleration time history is integrated to obtain the velocity and displacement time history

Step 3: Similitude and spectrum scale factors applied to the time and acceleration ($a_g(t)$)/velocity ($v_g(t)$)/displacement ($x_g(t)$) domains

Step 4: The velocity limitation is imposed while integrating the acceleration time history where $v_{new}(t)$ is the new velocity time history.

$$v_{new}(t) = \begin{cases} \dfrac{dx_g}{dt} & \text{if } \left|\dfrac{dx_g}{dt}\right| \le 230mm/s \\ 230mm/s & \text{if } \dfrac{dx_g}{dt} > 230mm/s \\ -230mm/s & \text{if } \dfrac{dx_g}{dt} < 230mm/s \end{cases}$$

Step 5: The new velocity time history is integrated and differentiated to get the revised displacement and acceleration time history respectively

Step 6: Unless not required, the record was digitized to a time step of $\Delta t=0.005$ using Matlab to improve resolution

Step 7: For non-zero initial velocity and displacements a Cosine displacement function is added to the beginning of the record to ramp-in with appropriate boundary conditions

Step 8: For non-zero final velocities and displacements a 3rd order polynomial is added to the end of the record with appropriate boundary conditions

Step 9: The revised displacement time history is combined with the ramping-in and ramping-out functions. A five point smoothing function is applied over the entire displacement time history to remove any numerically added artificial velocity and/or acceleration spikes

Ramp-In Function

The ramp-in function uses a cosine function, satisfying the initial displacement (x_0) and velocity (v_0) boundary conditions (assuming zero initial acceleration). The displacement velocity ramp-in functions are given as,

$$x_{\text{int},ramp}(t) = x_0\left(1-\cos\left(\frac{2\pi\cdot t}{T_0}\right)\right)$$
$$v_{\text{int},ramp}(t) = \frac{2\pi\cdot x_0}{T_0}\sin\left(\frac{2\pi\cdot t}{T_0}\right)$$

Based on the initial conditions the ramp-in period, T_0 is evaluated as,

$$T_0 = \frac{2\pi\cdot|x_0|}{|v_0|}$$

The ramp in duration, t differs depending on the sign of the initial displacement and velocity.

For $x_0/v_0>0$

$$t = 0:\frac{T_0}{4}$$

For $x_0/v_0<0$

$$t = 0:\frac{3T_0}{4}$$

While this ramp-in function was automated within a Matlab code, in most cases the initial conditions were zero or close to zero and hence the ramp-in was not detectable, or not used.

Ramp-Out Function

The ramp-out function used a 3rd order polynomial using the final displacement x_f and velocity v_f.

$$x(t) = a\cdot t^3 + b\cdot t^2 + v_f\cdot t + x_f$$
$$v(t) = 3a\cdot t^2 + 2b\cdot t + v_f$$

Where the polynomial coefficients ***a*** and ***b*** are defined as,

$$a = \frac{2x_f}{T_f^3} + \frac{v_f}{T_f^2}$$
$$b = -\frac{2v_f}{T_f} - \frac{3x_f}{T_f^2}$$

Here $\boldsymbol{T_f}$ is the duration of the ramp-out function and was generally taken equal to one second, $\boldsymbol{T_f} = 1$.

C3. RECORD MODIFICATION, METHOD B

The following step-by-step procedure outlines a method to modify an acceleration time-history to limit the peak velocity while retaining the peak acceleration magnitude, while minimising the loss of ground motion input energy, Mulligan [2007].

Step 1: Locate the raw acceleration record (downloaded from PEER or NGA website)

Step 2: Similitude and spectral scale factors are applied to the time and acceleration domain, defining the target acceleration time history $a_g(t)$.

Step 3: For each time step the velocity is integrated from the target acceleration time $a_g(t)$ history. The velocity limit is then applied to each time step in turn using the piecewise function,

$$v_{new,1}(t) = \begin{cases} \int_{t=0}^{t=t_i} a_g(t) & \text{if } \left|\int_{t=0}^{t=t_i} a_g(t)\right| \le 230mm/s \\ 230mm/s & \text{if } \int_{t=0}^{t=t_i} a_g(t) > 230mm/s \\ -230mm/s & \text{if } \int_{t=0}^{t=t_i} a_g(t) < 230mm/s \end{cases}$$

Step 4: Given the velocity $\boldsymbol{v_{new,1}(t)}$ at the end of each time step, the resulting acceleration $\boldsymbol{a_{new,1}(t)}$ and displacement $\boldsymbol{x_{new,1}(t)}$ are calculated.

Step 5: The procedure continues for every time step until the end of the acceleration record; the method differs from Method A in that the target acceleration $\boldsymbol{a_g(t)}$ is used at each time step to compute the velocity, as opposed to the revised acceleration $\boldsymbol{a_{new}(t)}$. This has the effect of increasing the velocity immediately following saturation to compensate for the loss in intensity during saturation.

Step 6: A linear velocity baseline correction is generally required for this method, equating to a constant acceleration baseline shift Δa_{base}. This ensures the initial and final velocity is zero. The revised velocity time history is as follows,

$$v_{new,baseline}(t) = v_{new,1}(t) - \left[v_{new,1}(0) + \Delta a_{base} \cdot t\right]$$

Where,

$$\Delta a_{base} = \frac{v_{new,1(final)} - v_{new,1(initial)}}{t_{duration}}$$

The resulting displacement $\boldsymbol{x_{new,2}(t)}$ and acceleration $\boldsymbol{a_{new,2}(t)}$ time histories are then computed from the corrected velocity time history.

Step 7: Similarly a linear displacement baseline correction is also required in order to ensure the initial and final displacement is zero (or, at least equal to each other). This requires a constant velocity baseline shift Δv_{base}.

$$x_{new,baseline}(t) = x_{new,2}(t) - \left[x_{new,2}(0) + \Delta v_{base} \cdot t\right]$$

Where

$$\Delta v_{base} = \frac{x_{new,2(final)} - x_{new,2(initial)}}{t_{duration}}$$

The resulting displacement $x_{new,3}(t)$ and acceleration $a_{new,3}(t)$ time histories are then computed from the corrected displacement time history.

Step 8: In performing a displacement baseline correction, the initial and final velocities are no longer equal to zero. More importantly, the new velocity time history may well now exceed the limiting velocity of 230mm/s. For this reason the resulting acceleration record in *step 7* is used as the target acceleration time history $a_g(t)$ time history in *step 3* and the process repeated until the velocity limit is satisfied.

Step 9: The modified record was digitized to a time step of $\Delta t = 0.005$ using Matlab to improve resolution

Step 10: A 4th order displacement polynomial function is added to the beginning of the record (ramp-in function) to satisfy the appropriate boundary conditions

Step 11: Similarly a 4th order displacement polynomial function is added to the end of the record (ramp-out function) to satisfy appropriate boundary conditions

Step 12: The revised displacement time history is combined with the ramp-in and ramp-out functions. A five point smoothing function is applied over the entire displacement time history to remove any numerically added artificial velocity and/or acceleration spikes. The modified record is compared to the original record to ensure the intensity of the acceleration time-history is maintained.

Ramp-In Function

The ramp-in function used a 4th order polynomial displacement function in order to satisfy the initial velocity (v_0) and acceleration (a_0) boundary conditions. The displacement, velocity and acceleration ramp-in functions are given by,

$$x(t) = a \cdot t^4 + b \cdot t^3$$
$$v(t) = 4a \cdot t^3 + 3b \cdot t^2$$
$$a(t) = 12a \cdot t^2 + 6b \cdot t$$

Solving for the initial velocity and acceleration conditions,

$$a = \frac{a_0}{4T_0^{\,2}} - \frac{v_0}{2T_0^{\,3}}$$

$$b = \frac{v_0}{T_0^{\,2}} - \frac{a_0}{3T_0}$$

Where, $\boldsymbol{T_0}$ is equal to the duration of the ramp-in function, in this case a ramp in duration of $\boldsymbol{T_0} = 1.5s$ was used.

Ramp-Out Function

Similarly, the ramp-out function also uses a 4th order polynomial in order to satisfy the final velocity $\boldsymbol{v_f}$ and acceleration $\boldsymbol{a_f}$ boundary conditions of the earthquake ground motion.

$$x(t) = A \cdot (T_f - t)^4 + B \cdot (T_f - t)^3$$
$$v(t) = 4A \cdot (T_f - t)^3 + 3B \cdot (T_f - t)^2$$
$$a(t) = 12A \cdot (T_f - t)^2 + 6B \cdot (T_f - t)$$

Solving for the final velocity and acceleration conditions,

$$A = \frac{a_f}{4T_f^{\,2}} + \frac{v_f}{2T_f^{\,3}}$$
$$B = -\frac{v_f}{T_f^{\,2}} - \frac{a_f}{3T_f}$$

Where $\boldsymbol{T_f}$ is the duration of the ramp-out function, taken as $\boldsymbol{T_f}=1.5s$. These ramping functions require the displacement at the beginning of the earthquake record to be equal to the displacement at the end of the earthquake record (following the baseline correction in *step 7*). If this was not the case, the final displacement (at the end of the ramp-out) would not equal zero. This was not always possible to satisfy, but generally not too far from zero if not satisfied. A non-zero displacement offset was not considered a problem because the shake table can be manually controlled back to the origin (starting position) at the end of the record.

C4. ENERGY FORMULATIONS

In the equations below *x, v, a* denote displacement, velocity and acceleration respectively while subscript *r, a, g* denotes relative, absolute and ground respectively.

Strain energy

There is no difference between a relative and absolute formation for strain energy. With reference to a SDOF linear-elastic structure having relative displacement x_r, stiffness k and spring force F_r.

$$E_{SE}(t) = \int_0^x F_r(t)dx = \int_0^x [k]\{x_r(t)\}dx = \frac{1}{2}k \cdot x_r(t)^2$$

Or in discrete form,

$$E_{SE}(t+\Delta t) = E_{SE}(t) + \frac{1}{2}\left[\left[F_r(t+\Delta t) + F_r(t)\right]\cdot\left[x_r(t+\Delta t) - x_r(t)\right]\right]$$

Viscous energy

Also, there is no difference between a relative and absolute formulation for viscous energy.

$$E_{SE}(t) = \int_0^x F_d(t)dx = \int_0^x [c]\{v_r(t)\}dx$$

Considering sinusoidal harmonic oscillation, the relationship is non-linear and therefore a discrete form is simpler to manage,

$$E_{VD}(t+\Delta t) = E_{VD}(t) + \frac{1}{2}\left[\left[F_{VD}(t+\Delta t) + F_{VD}(t)\right]\cdot\left[x_r(t+\Delta t) - x_r(t)\right]\right]$$

Kinetic energy

Kinetic energy remains linear and therefore does not require a discrete formulation.

$$E_k^{ab}(t) = \int_0^v \{v_a(t)\}^T[m]dv = \frac{1}{2}\{v_a(t)\}^T[m]\{v_a(t)\} = \frac{1}{2}m \cdot v_a(t)^2$$

Input energy

$$E_{input}^{ab}(t) = \int_0^{x_g} \{a_a(t)\}[m]dx_g = \{x_g(t)\}^T[m]\{a_a(t)\}$$

In discrete form,

$$E_{input}^{ab}(t+\Delta t) = E_{input}^{ab}(t) + \frac{1}{2} m \cdot \left[\left[a_a(t+\Delta t) + a_a(t)\right] \cdot \left[x_g(t+\Delta t) - x_g(t)\right]\right]$$

C5. REFERENCES

Chase, J. G., Hudson, N. H., Lin, J., Elliot, R. and Sim, A. (2005). "Nonlinear Shake Table Identification and Control for near-Field Earthquake Testing." *Journal of Earthquake Engineering. Vol. 9, no. 4, pp. 461-482. July 2005*.

Mulligan, K. (2007). "Experimental and analytical studies of semi-active and passive structural control of buildings," University of Canterbury, Christchurch.

Appendix D

D1. COMPARISON BETWEEN THE EXPERIMENTAL TESTING AND THE MULTI-SPRING MACRO MODEL

Free Vibration Release Testing

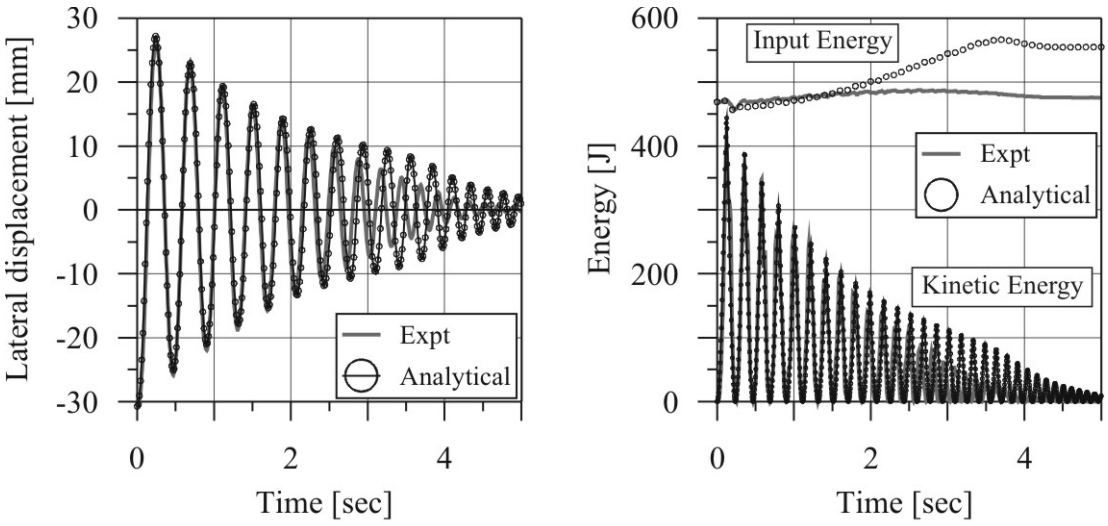

Figure D.1 Free vibration comparison between experimental and macro model at release drift of 1.5% for PC Wall 1 with calibrated contact damping

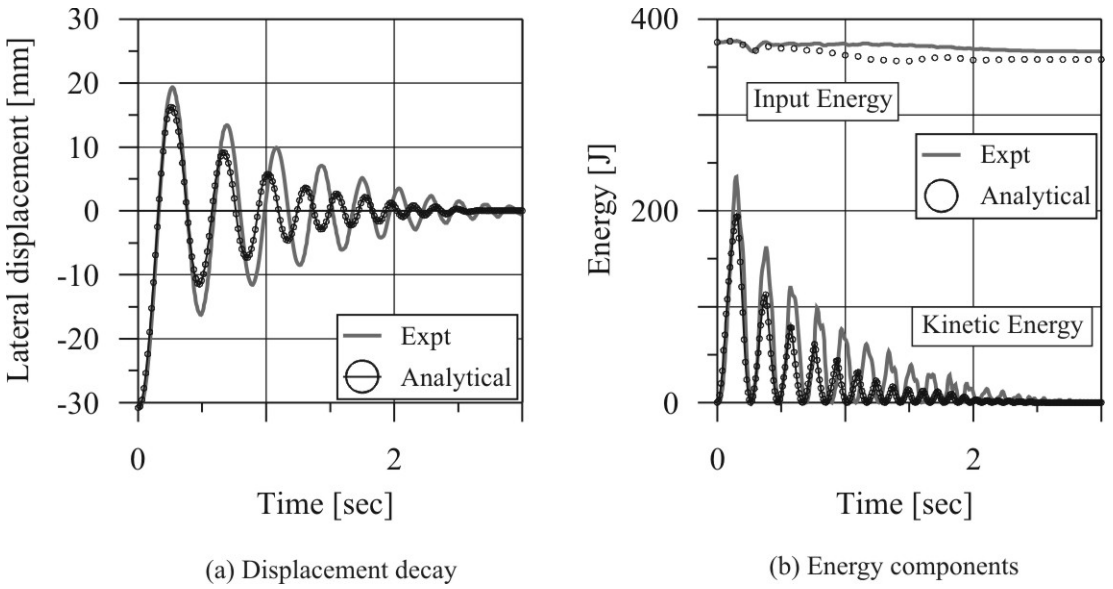

(a) Displacement decay (b) Energy components

Figure D.2 Free vibration comparison between experimental and macro model at release drift of 1.5% for PC Wall 2 with calibrated contact damping

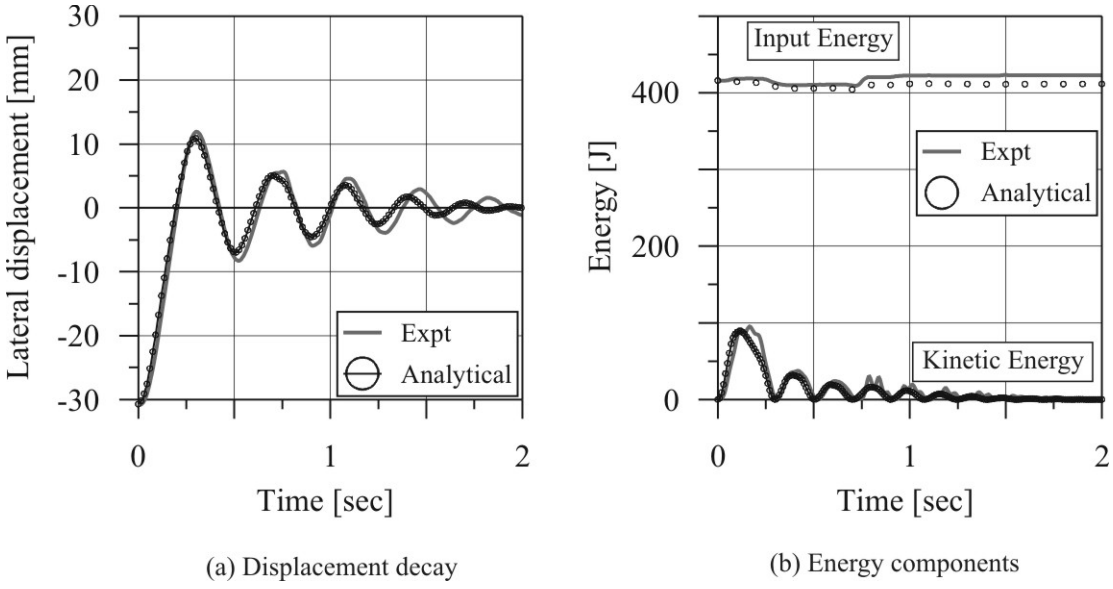

(a) Displacement decay (b) Energy components

Figure D.3 Free vibration comparison between experimental and macro model at release drift of 1.5% for PC Wall 3 with calibrated contact damping

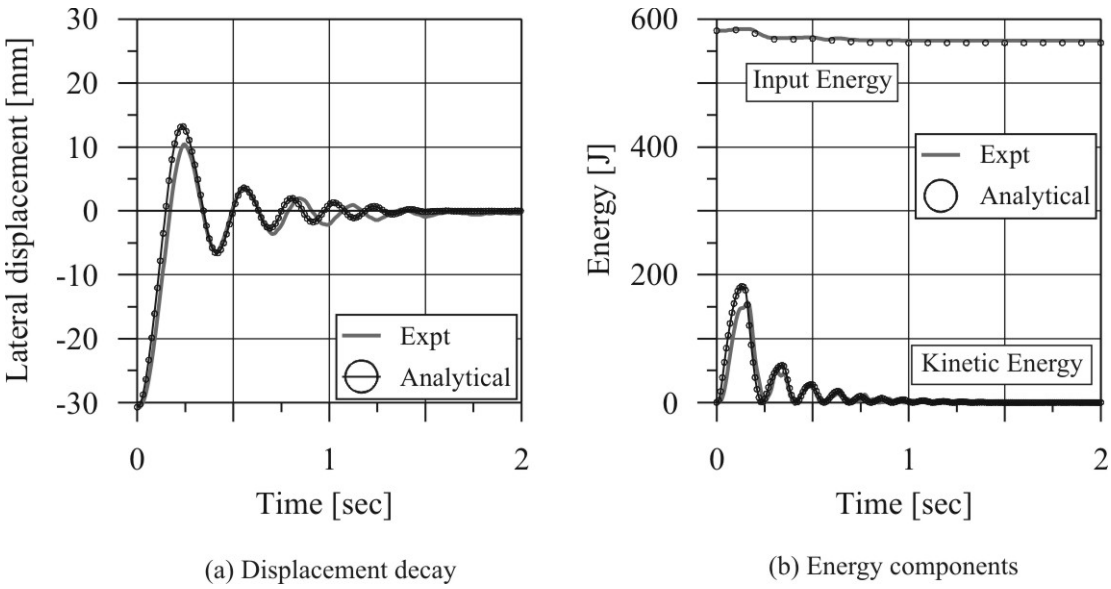

(a) Displacement decay (b) Energy components

Figure D.4 Free vibration comparison between experimental and macro model at release drift of 1.5% for PC Wall 4 with calibrated contact damping

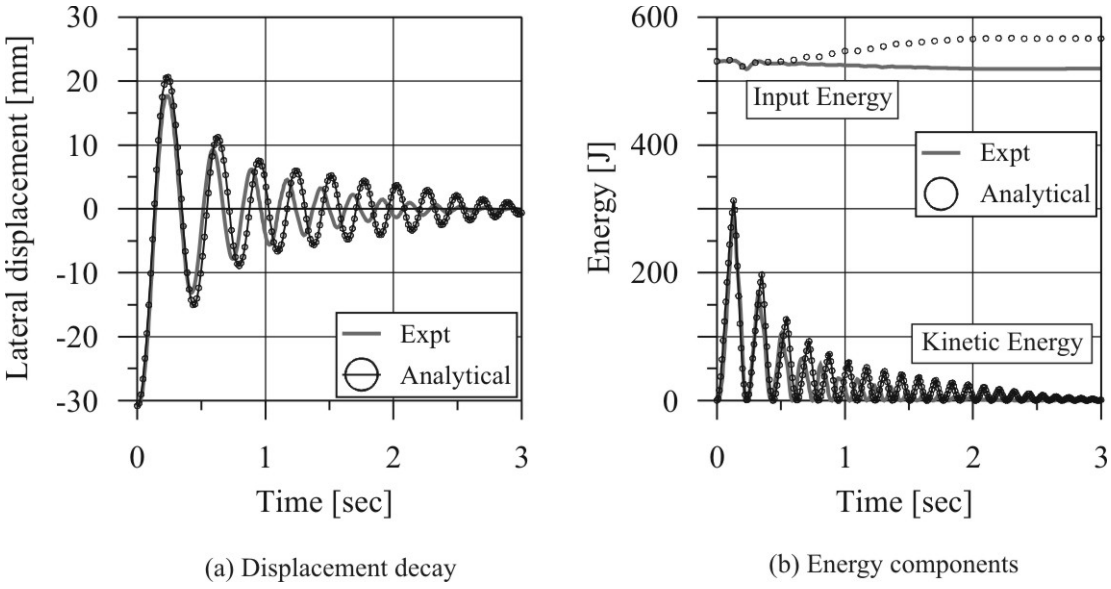

(a) Displacement decay (b) Energy components

Figure D.5 Free vibration comparison between experimental and macro model at release drift of 1.5% for PC Wall 5 with calibrated contact damping

Dynamic Response During Strong Ground Motions

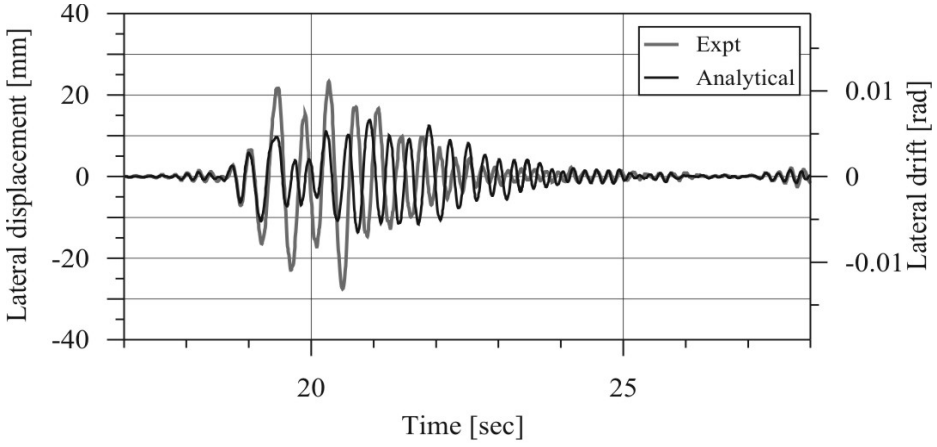

(a) Time history response, calibrated contact damping

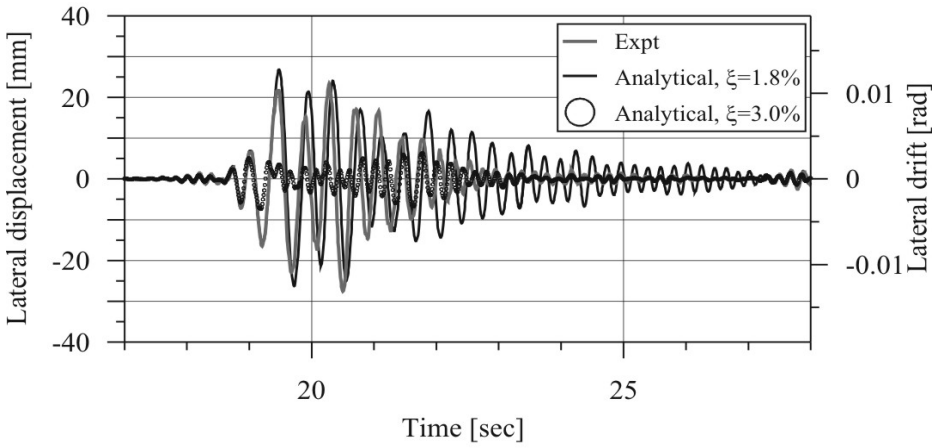

(b) Time history response, ±25% contact damping window

Figure D.6 (a) Experimental and macro model time-history response with calibrated contact damping model, (b) including a variation of ±25% for PC Wall 1, Cape Mendocino record.

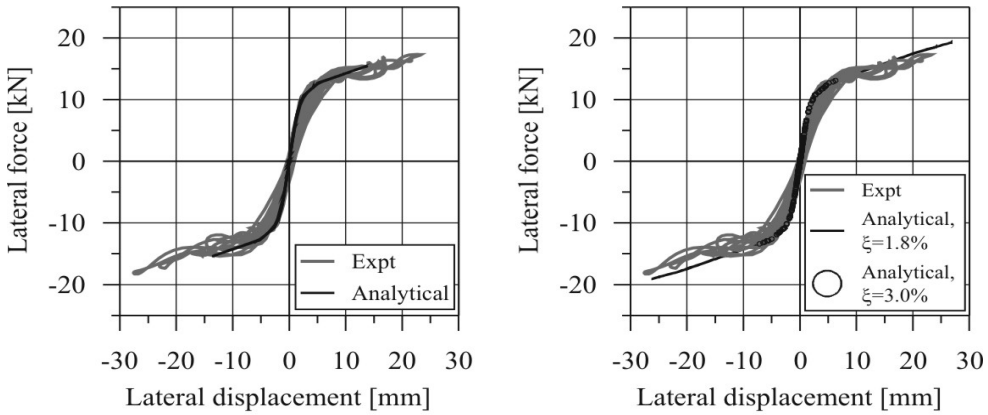

(a) Lateral response, calibrated contact damping

(b) Lateral response, ±25% contact damping window

Figure D.7 (b) Experimental and macro model lateral response with calibrated contact damping model, (b) including a variation of ±25% for PC Wall 1, Cape Mendocino record.

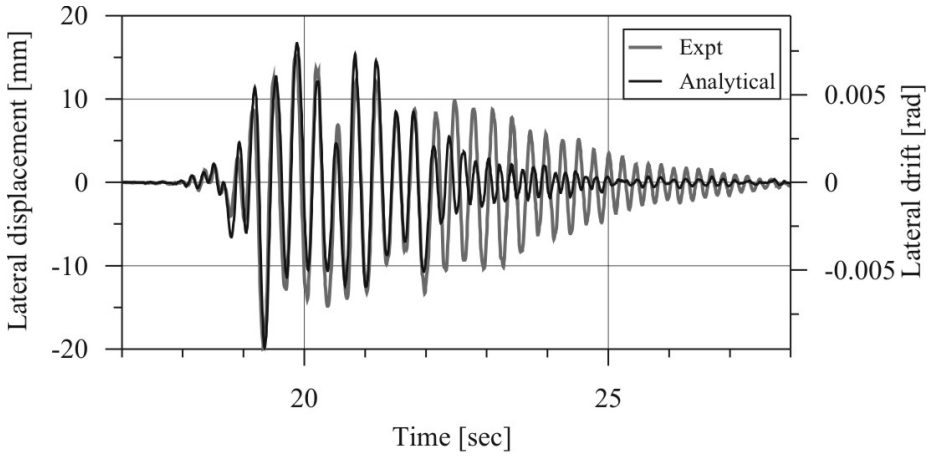

(a) Time history response, calibrated contact damping

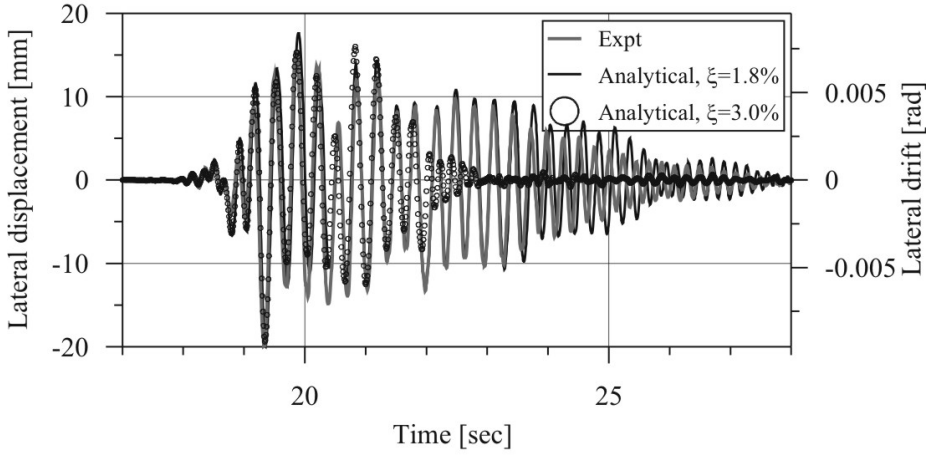

(b) Time history response, ±25% contact damping window

Figure D.8 (a) Experimental and macro model time-history response with calibrated contact damping model, (b) including a variation of ±25% for PC Wall 1, Northridge record.

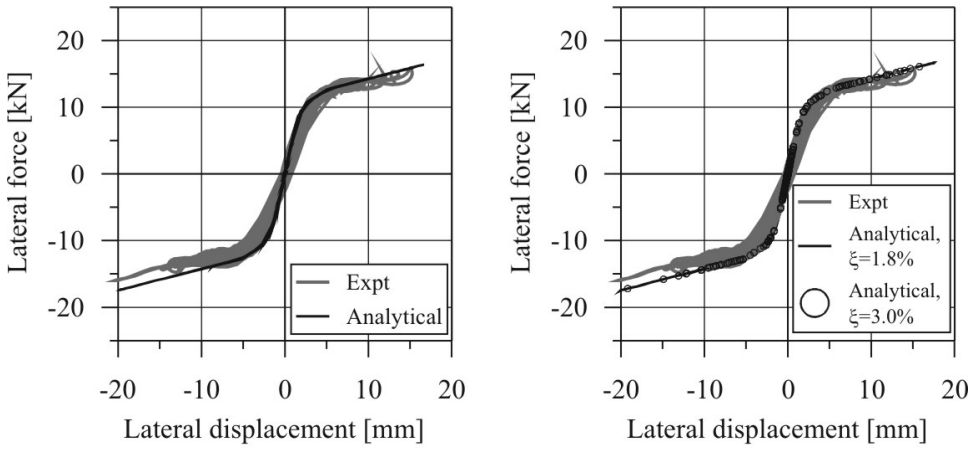

(a) Lateral response, calibrated contact damping

(b) Lateral response, ±25% contact damping window

Figure D.9 (a) Experimental and macro model lateral response with calibrated contact damping model, (b) including a variation of ±25% for PC Wall 1, Cape Mendocino record.

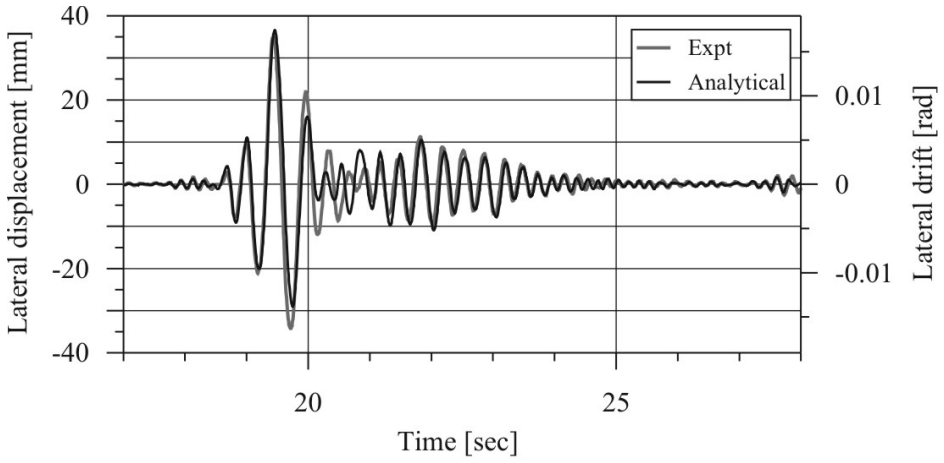

(a) Time history response, calibrated contact damping

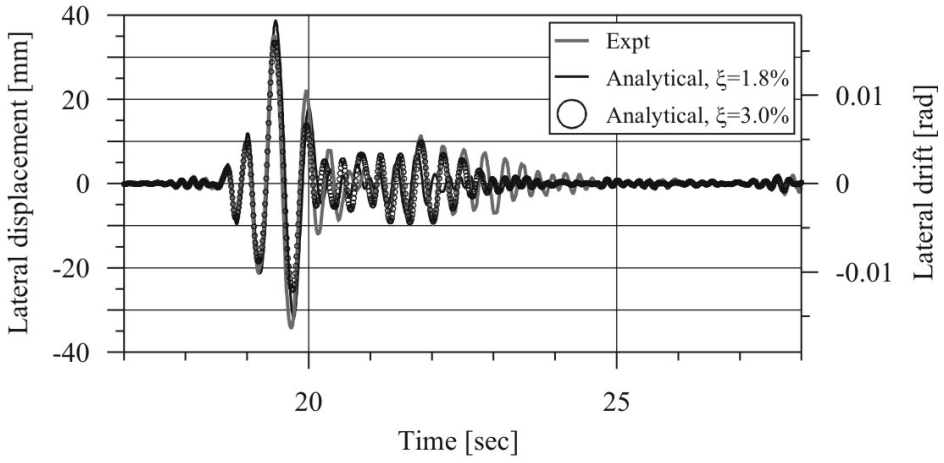

(b) Time history response, ±25% contact damping window

Figure D.10 (a) Experimental and macro model time-history response with calibrated contact damping model, (b) including a variation of ±25% for PC Wall 2, Cape Mendocino record.

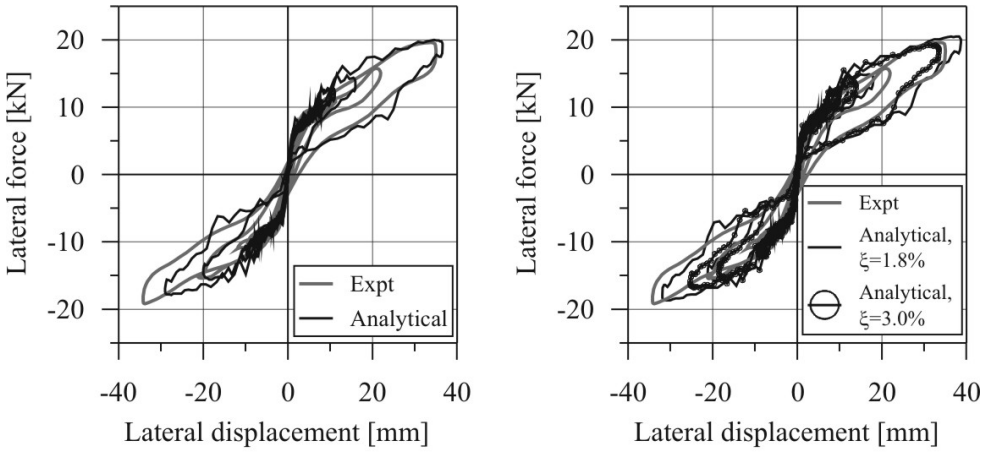

(a) Lateral response, calibrated contact damping

(b) Lateral response, ±25% contact damping window

Figure D.11 (a) Experimental and macro model lateral response with calibrated contact damping model, (b) including a variation of ±25% for PC Wall 2, Cape Mendocino record.

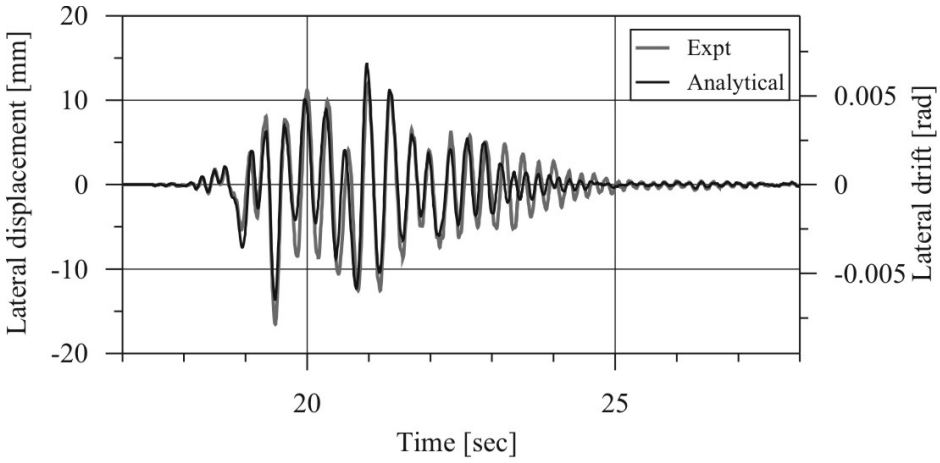

(a) Time history response, calibrated contact damping

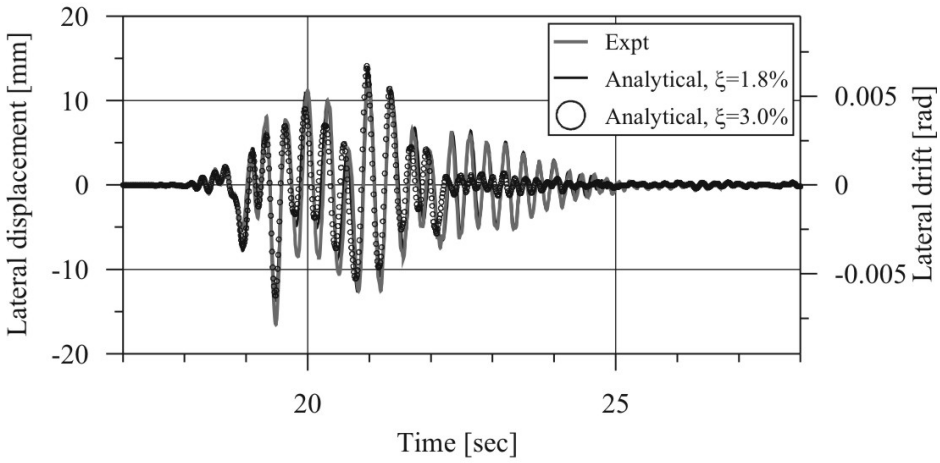

(b) Time history response, ±25% contact damping window

Figure D.12 (a) Experimental and macro model time-history response with calibrated contact damping model, (b) including a variation of ±25% for PC Wall 2, Northridge record.

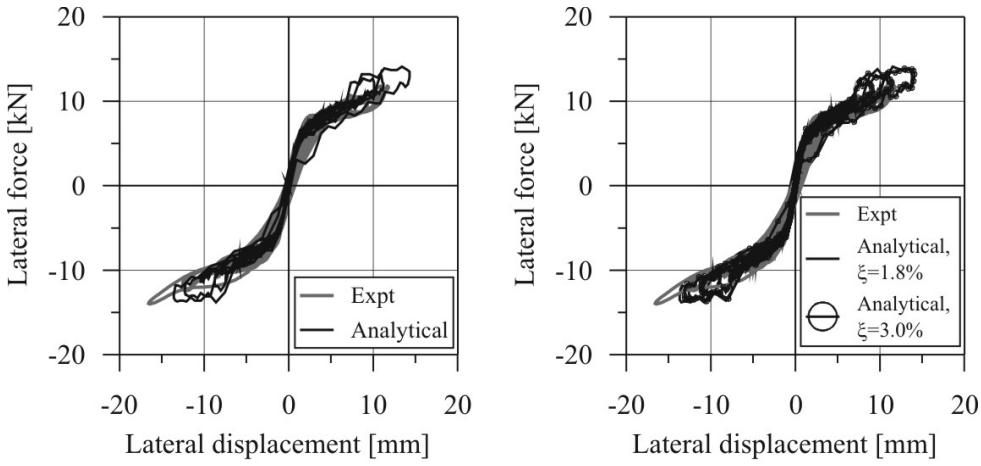

(a) Lateral response, calibrated contact damping

(b) Lateral response, ±25% contact damping window

Figure D.13 (a) Experimental and macro model lateral response with calibrated contact damping model, (b) including a variation of ±25% for PC Wall 2, Northridge record.

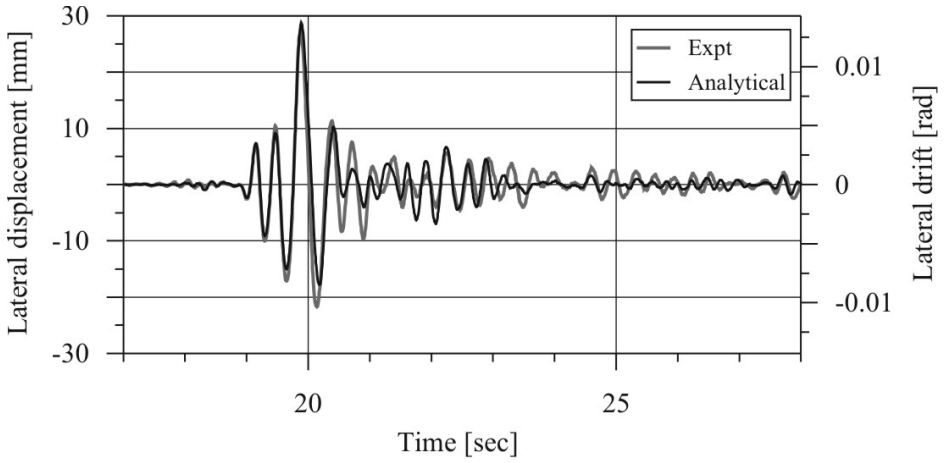

(a) Time history response, calibrated contact damping

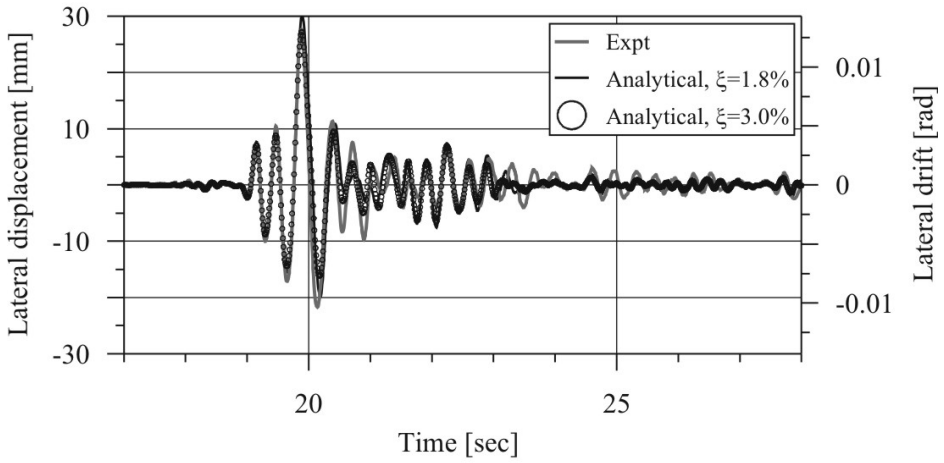

(b) Time history response, ±25% contact damping window

Figure D.14 (a) Experimental and macro model time-history response with calibrated contact damping model, (b) including a variation of ±25% for PC Wall 3, Cape Mendocino record.

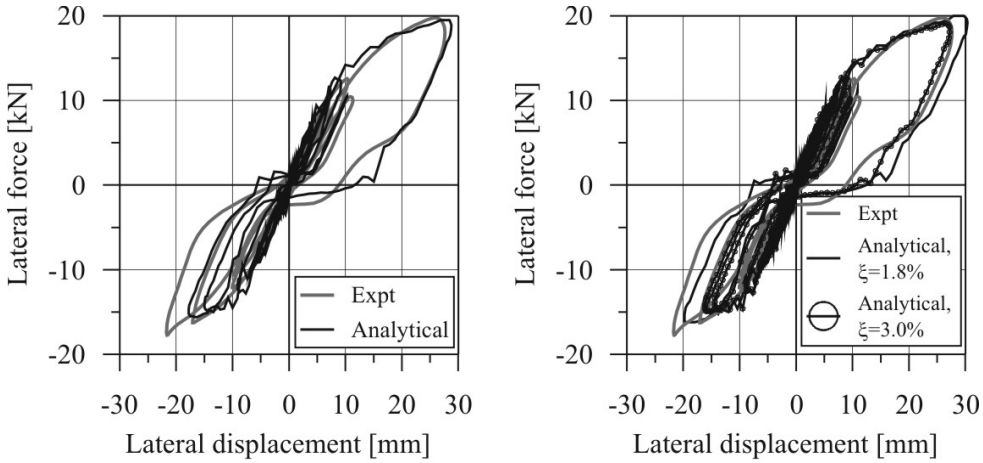

(a) Lateral response, calibrated contact damping

(b) Lateral response, ±25% contact damping window

Figure D.15 (a) Experimental and macro model lateral response with calibrated contact damping model, (b) including a variation of ±25% for PC Wall 3, Cape Mendocino record.

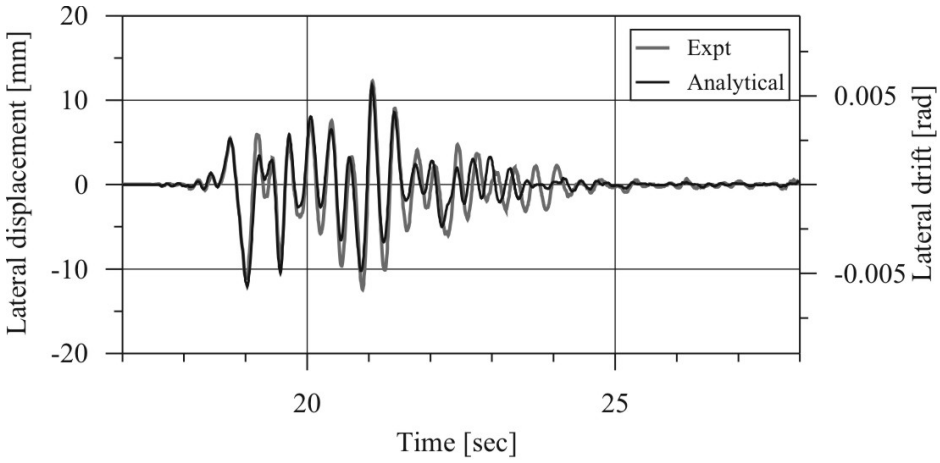

(a) Time history response, calibrated contact damping

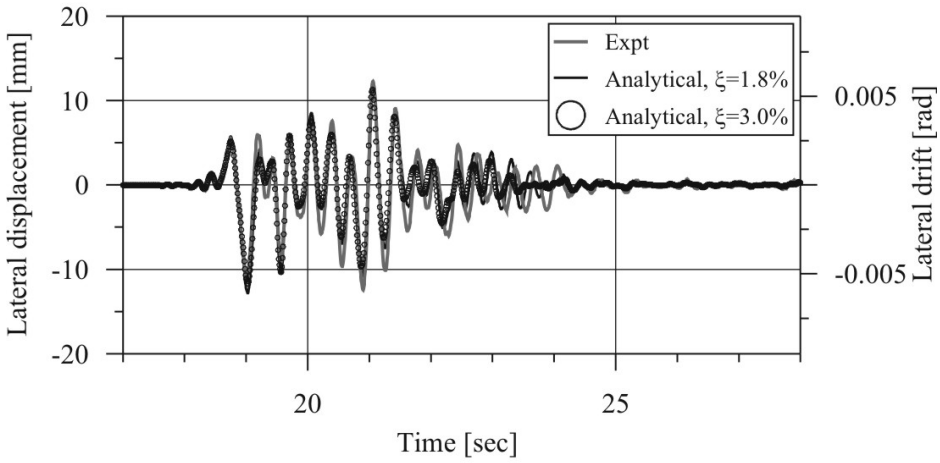

(b) Time history response, ±25% contact damping window

Figure D.16 (a) Experimental and macro model time-history response with calibrated contact damping model, (b) including a variation of ±25% for PC Wall 3, Northridge record.

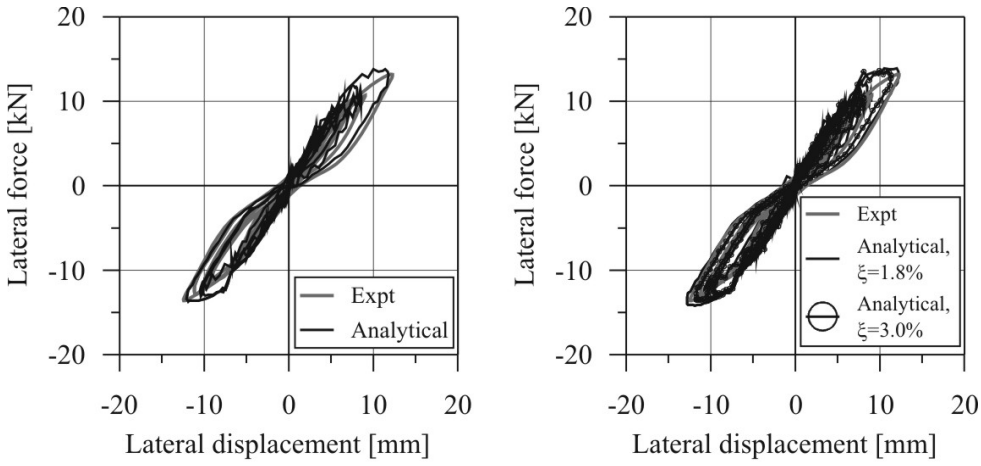

(a) Lateral response, calibrated contact damping

(b) Lateral response, ±25% contact damping window

Figure D.17 (a) Experimental and macro model lateral response with calibrated contact damping model, (b) including a variation of ±25% for PC Wall 3, Northridge record.

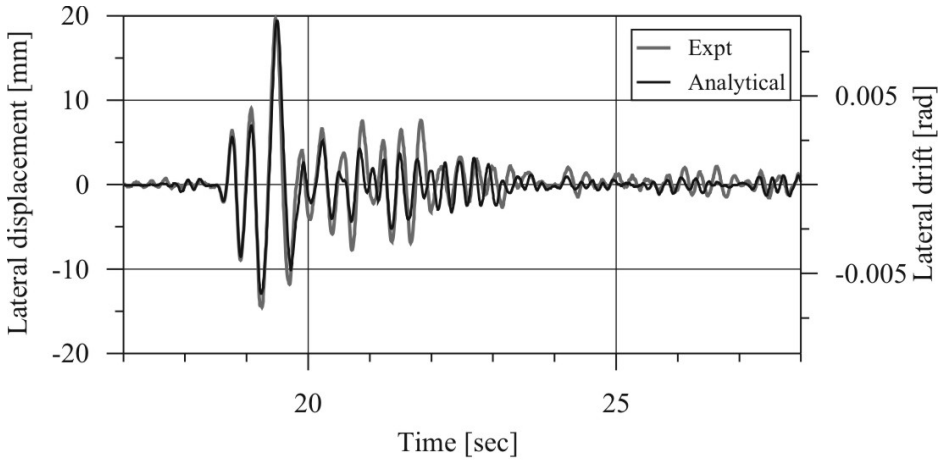

(a) Time history response, calibrated contact damping

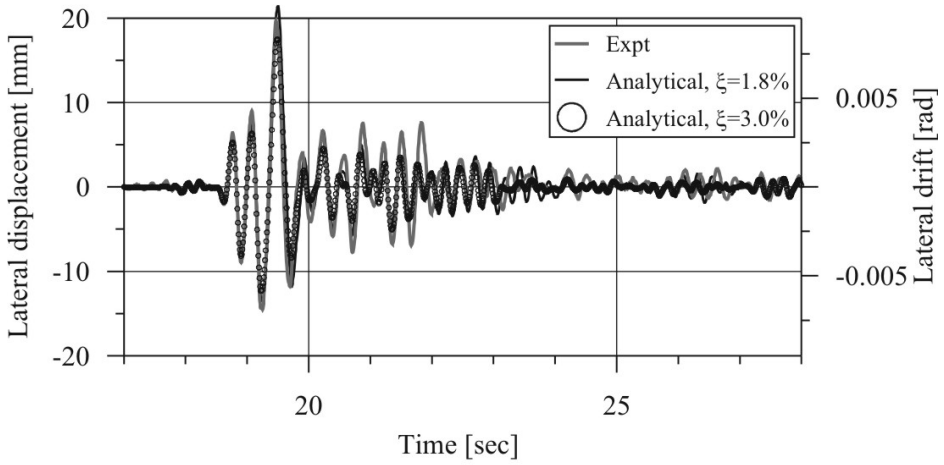

(b) Time history response, ±25% contact damping window

Figure D.18 (a) Experimental and macro model time-history response with calibrated contact damping model, (b) including a variation of ±25% for PC Wall 4, Cape Mendocino record.

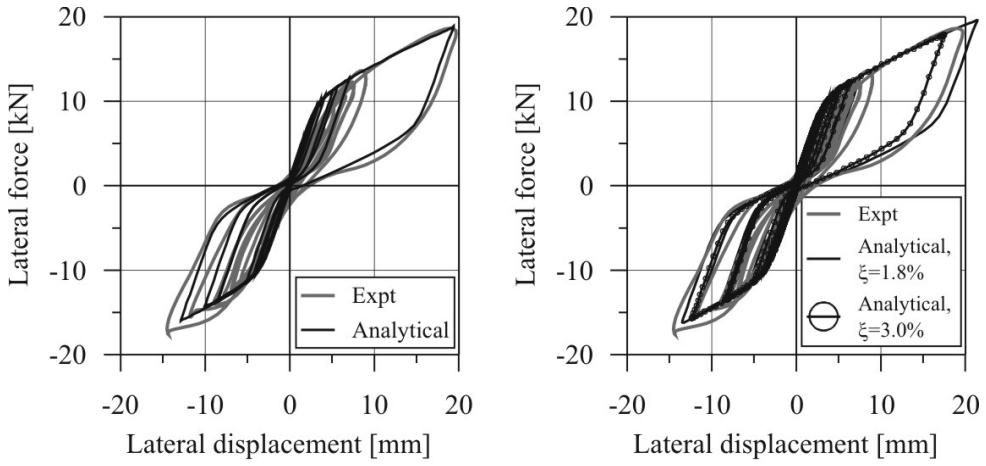

(a) Lateral response, calibrated contact damping

(b) Lateral response, ±25% contact damping window

Figure D.19 (a) Experimental and macro model lateral response with calibrated contact damping model, (b) including a variation of ±25% for PC Wall 4, Cape Mendocino record.

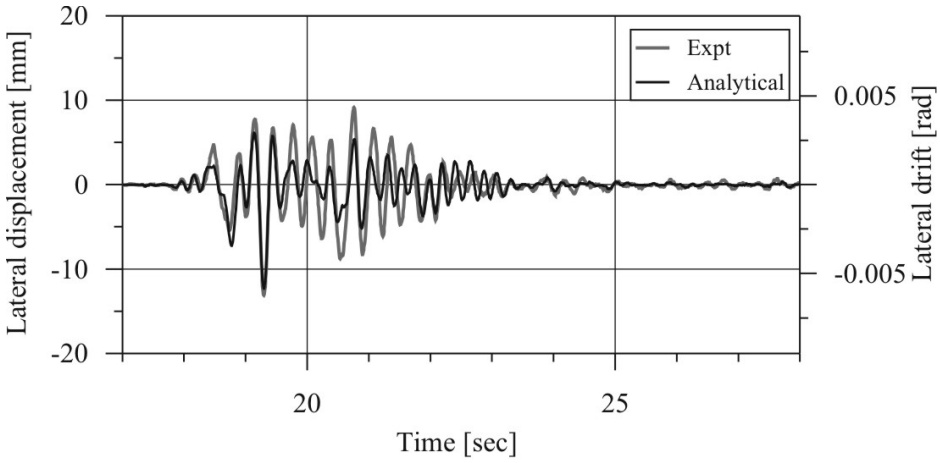

(a) Time history response, calibrated contact damping

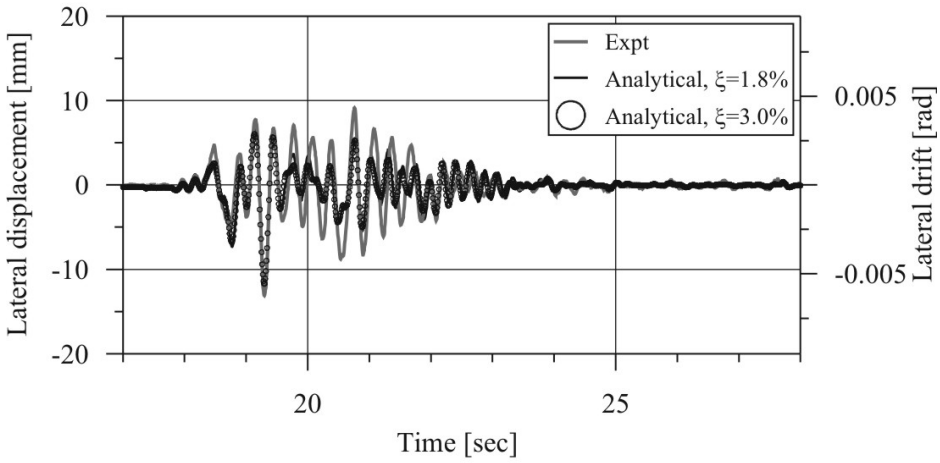

(b) Time history response, ±25% contact damping window

Figure D.20 (a) Experimental and macro model time-history response with calibrated contact damping model, (b) including a variation of ±25% for PC Wall 4, Northridge record.

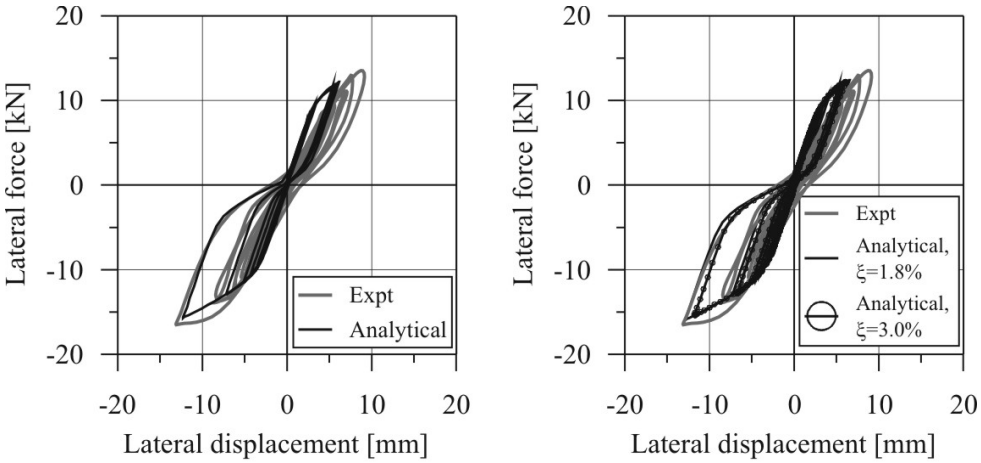

(a) Lateral response, calibrated contact damping

(b) Lateral response, ±25% contact damping window

Figure D.21 (a) Experimental and macro model lateral response with calibrated contact damping model, (b) including a variation of ±25% for PC Wall 4, Northridge record.

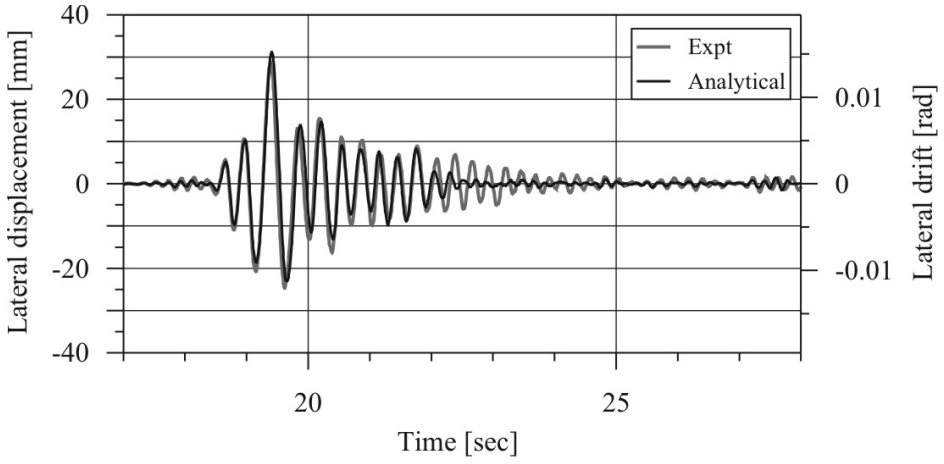

(a) Time history response, calibrated contact damping

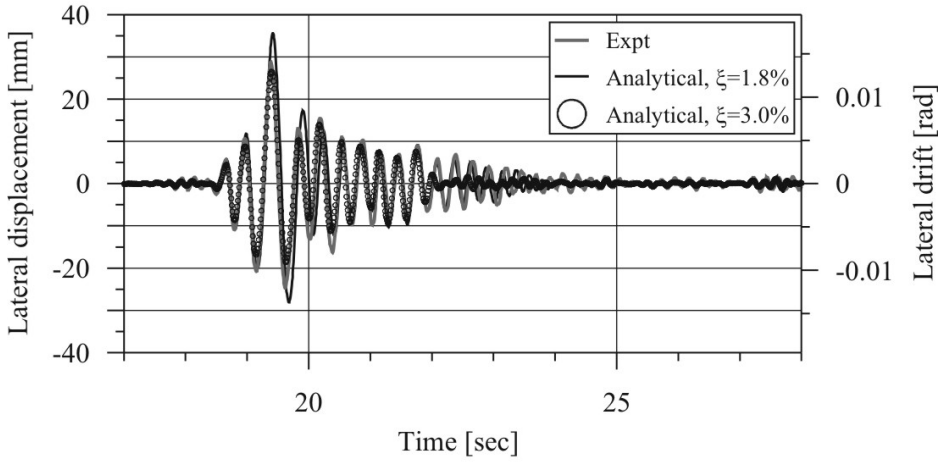

(b) Time history response, ±25% contact damping window

Figure D.22 (a) Experimental and macro model time-history response with calibrated contact damping model, (b) including a variation of ±25% for PC Wall 5, Cape Mendocino record.

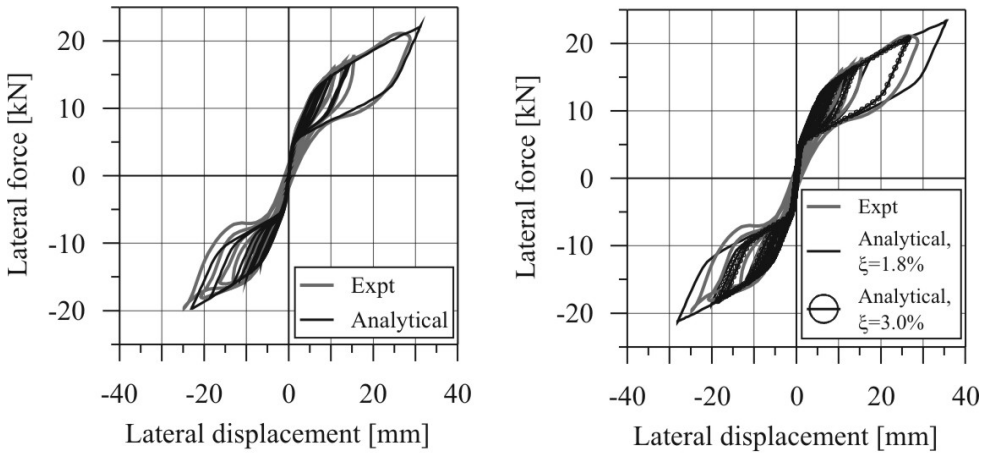

(a) Lateral response, calibrated contact damping

(b) Lateral response, ±25% contact damping window

Figure D.23 (a) Experimental and macro model lateral response with calibrated contact damping model, (b) including a variation of ±25% for PC Wall 5, Cape Mendocino record.

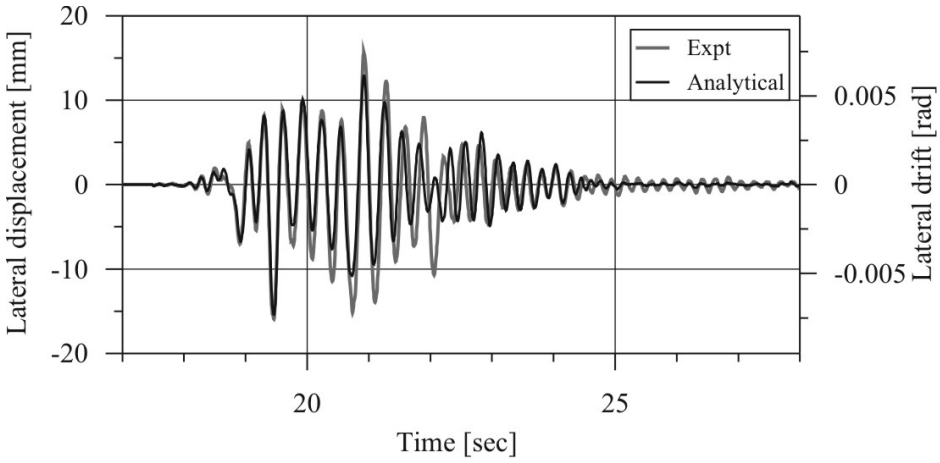

(a) Time history response, calibrated contact damping

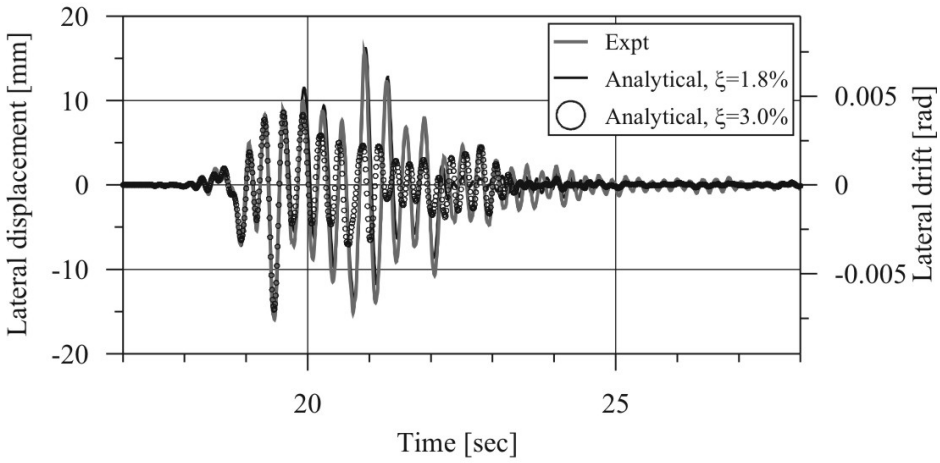

(b) Time history response, ±25% contact damping window

Figure D.24 (a) Experimental and macro model time-history response with calibrated contact damping model, (b) including a variation of ±25% for PC Wall 5, Northridge record.

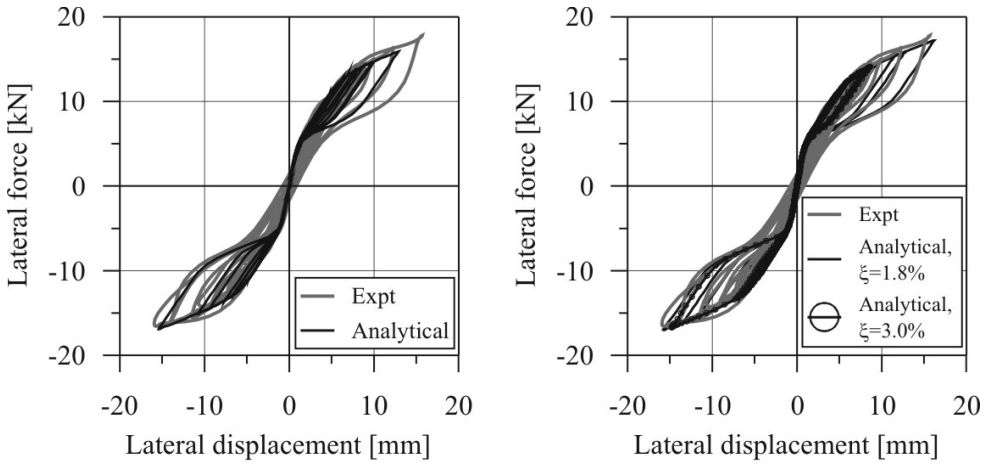

(a) Lateral response, calibrated contact damping

(b) Lateral response, ±25% contact damping window

Figure D.25 (a) Experimental and macro model lateral response with calibrated contact damping model, (b) including a variation of ±25% for PC Wall 5, Northridge record.

D2. STRESS BLOCK FACTORS FOR CONFINED CONCRETE

Stress block factors α and β have been computed for confined concrete. The parameters are computed by numerically integrating the non-linear confined concrete curve proposed by Mander et al. [1988]. The nomenclature is illustrated below, where ε_{cu} is the maximum strain in the concrete.

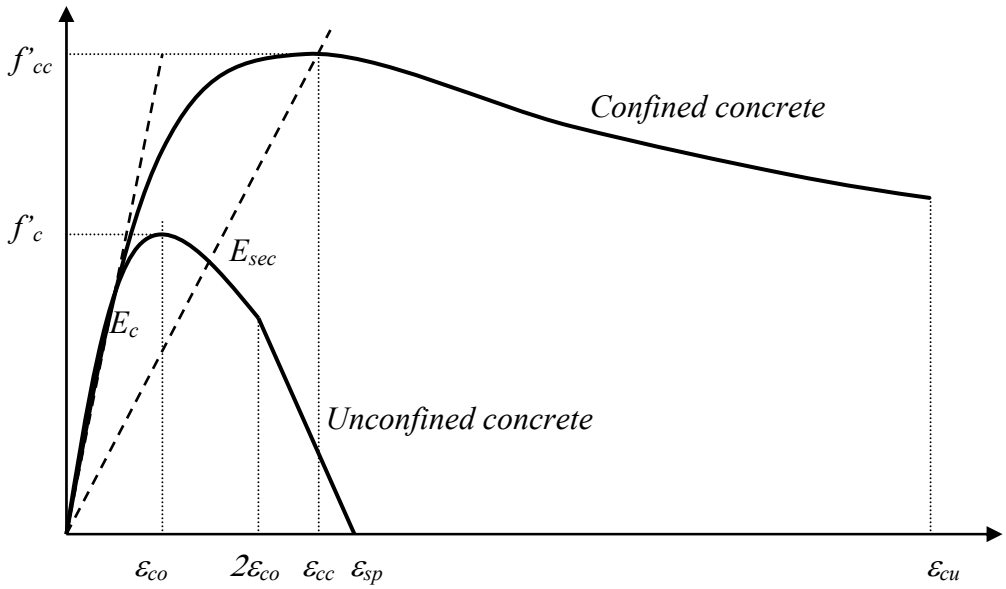

Figure D.26: Nomenclature for concrete stress block factors

For these tables the strain at the peak unconfined compressive stress ε_{co} is given by the following formula, but in general has an approximate value of 0.002.

$$\varepsilon_{co} = \frac{f'_c}{E_c}\frac{n}{n-1}$$

Where,

$$n = 0.8 + \frac{f'_c}{17}$$

Where Young's modulus (in MPa) is given by the following formula with f'_c in MPa.

$$E = 3200\sqrt{f'_c} + 6900$$

Table D.1: Stress block factors for confined concrete $f'_{cc}/f'_c=1.0$

f'_c		Ratio of strain in concrete to strain at maximum compression stress $\varepsilon_{cu}/\varepsilon_{co}$																			
		0.5	**1.0**	**1.5**	**2.0**	**2.5**	**3.0**	**3.5**	**4.0**	**4.5**	**5.0**	**5.5**	**6.0**	**6.5**	**7.0**	**7.5**	**8.0**	**8.5**	**9.0**	**9.5**	**10.0**
20	α	0.644	0.911	0.948	0.906	0.845	0.783	0.727	0.677	0.633	0.595	0.561	0.530	0.503	0.479	0.457	0.438	0.420	0.403	0.388	0.374
	β	0.698	0.763	0.831	0.891	0.942	0.985	1.022	1.053	1.081	1.106	1.128	1.147	1.165	1.181	1.196	1.209	1.222	1.233	1.244	1.254
25	α	0.605	0.900	0.937	0.879	0.800	0.724	0.658	0.600	0.551	0.509	0.473	0.441	0.414	0.389	0.368	0.348	0.331	0.315	0.301	0.288
	β	0.687	0.747	0.820	0.890	0.951	1.004	1.049	1.089	1.123	1.154	1.181	1.206	1.228	1.248	1.266	1.283	1.298	1.313	1.326	1.339
30	α	0.575	0.890	0.928	0.852	0.757	0.669	0.595	0.534	0.482	0.439	0.403	0.372	0.345	0.321	0.301	0.283	0.267	0.252	0.239	0.228
	β	0.681	0.735	0.813	0.892	0.963	1.026	1.079	1.126	1.167	1.203	1.235	1.263	1.289	1.312	1.334	1.353	1.371	1.388	1.403	1.417
35	α	0.552	0.882	0.918	0.826	0.716	0.619	0.540	0.476	0.425	0.382	0.347	0.317	0.292	0.270	0.251	0.235	0.220	0.207	0.196	0.186
	β	0.676	0.726	0.808	0.896	0.978	1.049	1.110	1.163	1.210	1.250	1.286	1.318	1.347	1.373	1.396	1.418	1.437	1.455	1.472	1.488
40	α	0.533	0.875	0.908	0.799	0.676	0.573	0.492	0.428	0.377	0.336	0.302	0.275	0.251	0.231	0.214	0.199	0.186	0.175	0.165	0.156
	β	0.673	0.718	0.804	0.902	0.993	1.073	1.141	1.200	1.251	1.295	1.334	1.369	1.400	1.427	1.452	1.475	1.496	1.515	1.532	1.548
45	α	0.517	0.869	0.899	0.773	0.640	0.532	0.449	0.386	0.337	0.299	0.267	0.242	0.220	0.202	0.186	0.173	0.161	0.151	0.142	0.134
	β	0.671	0.713	0.802	0.909	1.009	1.097	1.172	1.235	1.290	1.337	1.378	1.415	1.447	1.475	1.501	1.524	1.545	1.564	1.582	1.598
50	α	0.504	0.863	0.889	0.748	0.605	0.495	0.413	0.352	0.305	0.269	0.239	0.216	0.196	0.179	0.165	0.153	0.143	0.134	0.125	0.118
	β	0.670	0.708	0.800	0.917	1.026	1.121	1.201	1.269	1.326	1.375	1.418	1.455	1.488	1.517	1.543	1.566	1.587	1.606	1.623	1.639
55	α	0.493	0.858	0.879	0.723	0.573	0.462	0.381	0.323	0.278	0.244	0.217	0.195	0.177	0.162	0.149	0.138	0.128	0.120	0.113	0.106
	β	0.669	0.703	0.800	0.925	1.043	1.145	1.229	1.300	1.359	1.409	1.453	1.490	1.523	1.552	1.578	1.600	1.621	1.640	1.656	1.672
60	α	0.484	0.854	0.870	0.699	0.544	0.432	0.354	0.298	0.256	0.224	0.199	0.178	0.162	0.148	0.136	0.126	0.117	0.110	0.103	0.097
	β	0.669	0.700	0.800	0.934	1.061	1.167	1.255	1.328	1.389	1.440	1.483	1.521	1.553	1.582	1.607	1.629	1.649	1.667	1.683	1.698
65	α	0.476	0.850	0.860	0.676	0.517	0.406	0.331	0.277	0.238	0.208	0.184	0.165	0.150	0.137	0.126	0.117	0.108	0.101	0.095	0.090
	β	0.668	0.697	0.800	0.944	1.077	1.189	1.280	1.354	1.415	1.466	1.509	1.546	1.578	1.606	1.631	1.652	1.672	1.689	1.704	1.719
70	α	0.469	0.846	0.850	0.654	0.492	0.384	0.311	0.260	0.222	0.194	0.172	0.154	0.140	0.128	0.118	0.109	0.101	0.095	0.089	0.084
	β	0.668	0.694	0.801	0.953	1.094	1.210	1.302	1.377	1.439	1.489	1.532	1.568	1.600	1.627	1.651	1.671	1.690	1.707	1.722	1.735

Table D.2: Stress block factors for confined concrete $f'_{cc}/f'_c=1.1$

f'_c		Ratio of strain in concrete to strain at maximum compression stress $\varepsilon_{cu}/\varepsilon_{co}$																			
		0.5	**1.0**	**1.5**	**2.0**	**2.5**	**3.0**	**3.5**	**4.0**	**4.5**	**5.0**	**5.5**	**6.0**	**6.5**	**7.0**	**7.5**	**8.0**	**8.5**	**9.0**	**9.5**	**10.0**
20	α	0.616	0.911	1.025	1.058	1.056	1.037	1.012	0.985	0.958	0.931	0.905	0.881	0.858	0.836	0.816	0.796	0.778	0.761	0.745	0.730
	β	0.702	0.752	0.798	0.838	0.871	0.900	0.925	0.946	0.965	0.981	0.996	1.010	1.022	1.033	1.043	1.053	1.061	1.069	1.077	1.084
25	α	0.577	0.889	1.017	1.053	1.048	1.024	0.993	0.960	0.927	0.895	0.864	0.836	0.809	0.784	0.761	0.739	0.719	0.700	0.682	0.665
	β	0.693	0.739	0.785	0.827	0.864	0.896	0.924	0.948	0.970	0.989	1.007	1.022	1.037	1.050	1.062	1.073	1.083	1.093	1.102	1.110
30	α	0.549	0.872	1.011	1.049	1.042	1.013	0.977	0.938	0.900	0.864	0.830	0.798	0.768	0.741	0.716	0.692	0.670	0.650	0.631	0.613
	β	0.687	0.729	0.775	0.819	0.858	0.893	0.924	0.951	0.975	0.997	1.017	1.034	1.051	1.066	1.079	1.092	1.104	1.114	1.125	1.134
35	α	0.527	0.858	1.005	1.046	1.036	1.003	0.962	0.919	0.876	0.837	0.799	0.765	0.733	0.704	0.677	0.653	0.630	0.608	0.589	0.570
	β	0.683	0.722	0.767	0.813	0.854	0.891	0.925	0.954	0.981	1.005	1.026	1.046	1.064	1.080	1.095	1.109	1.122	1.134	1.146	1.156
40	α	0.510	0.846	1.001	1.043	1.031	0.994	0.948	0.901	0.856	0.813	0.773	0.737	0.704	0.673	0.645	0.619	0.596	0.574	0.553	0.535
	β	0.681	0.716	0.761	0.808	0.851	0.890	0.926	0.958	0.986	1.012	1.035	1.056	1.076	1.094	1.110	1.125	1.139	1.152	1.165	1.176
45	α	0.497	0.837	0.997	1.041	1.026	0.985	0.936	0.886	0.837	0.792	0.750	0.712	0.678	0.646	0.617	0.591	0.567	0.544	0.524	0.505
	β	0.679	0.712	0.756	0.804	0.849	0.890	0.927	0.961	0.991	1.019	1.044	1.066	1.087	1.106	1.124	1.140	1.155	1.169	1.182	1.194
50	α	0.486	0.828	0.994	1.039	1.022	0.978	0.925	0.871	0.820	0.773	0.730	0.690	0.655	0.623	0.593	0.566	0.542	0.519	0.499	0.480
	β	0.677	0.708	0.752	0.800	0.847	0.890	0.929	0.964	0.996	1.025	1.052	1.075	1.097	1.117	1.136	1.153	1.169	1.184	1.198	1.211
55	α	0.476	0.821	0.991	1.037	1.018	0.971	0.915	0.859	0.805	0.756	0.712	0.671	0.635	0.602	0.572	0.545	0.520	0.498	0.477	0.458
	β	0.676	0.705	0.749	0.797	0.845	0.890	0.931	0.968	1.001	1.031	1.059	1.084	1.107	1.128	1.147	1.165	1.182	1.198	1.212	1.226
60	α	0.468	0.815	0.989	1.035	1.014	0.965	0.906	0.847	0.792	0.741	0.696	0.654	0.617	0.584	0.554	0.526	0.502	0.479	0.458	0.439
	β	0.675	0.703	0.746	0.795	0.844	0.890	0.932	0.971	1.006	1.037	1.066	1.092	1.116	1.138	1.158	1.177	1.194	1.210	1.225	1.239
65	α	0.462	0.809	0.987	1.034	1.011	0.959	0.898	0.837	0.780	0.728	0.681	0.639	0.602	0.568	0.537	0.510	0.485	0.463	0.442	0.423
	β	0.674	0.701	0.743	0.793	0.843	0.890	0.934	0.974	1.010	1.042	1.072	1.099	1.124	1.146	1.167	1.187	1.205	1.222	1.237	1.252
70	α	0.456	0.804	0.985	1.033	1.008	0.954	0.890	0.827	0.769	0.716	0.668	0.625	0.587	0.554	0.523	0.496	0.471	0.448	0.428	0.409
	β	0.673	0.699	0.741	0.791	0.842	0.891	0.936	0.976	1.014	1.047	1.078	1.106	1.131	1.155	1.176	1.196	1.215	1.232	1.248	1.263

Table D.3: Stress block factors for confined concrete $f'_{cc}/f'_c=1.2$

f'_c		Ratio of strain in concrete to strain at maximum compression stress $\varepsilon_{cu}/\varepsilon_{co}$																			
		0.5	**1.0**	**1.5**	**2.0**	**2.5**	**3.0**	**3.5**	**4.0**	**4.5**	**5.0**	**5.5**	**6.0**	**6.5**	**7.0**	**7.5**	**8.0**	**8.5**	**9.0**	**9.5**	**10.0**
20	α	0.607	0.917	1.064	1.130	1.157	1.164	1.159	1.148	1.133	1.117	1.101	1.084	1.067	1.051	1.035	1.019	1.004	0.990	0.976	0.963
	β	0.703	0.746	0.785	0.818	0.846	0.869	0.890	0.908	0.923	0.937	0.950	0.961	0.971	0.981	0.989	0.997	1.004	1.011	1.018	1.023
25	α	0.566	0.888	1.048	1.123	1.153	1.159	1.152	1.138	1.121	1.102	1.081	1.061	1.041	1.022	1.003	0.985	0.968	0.951	0.936	0.920
	β	0.695	0.734	0.772	0.806	0.835	0.861	0.883	0.903	0.920	0.936	0.950	0.963	0.975	0.985	0.995	1.004	1.013	1.020	1.028	1.035
30	α	0.537	0.865	1.037	1.118	1.150	1.156	1.147	1.131	1.110	1.088	1.065	1.042	1.020	0.998	0.977	0.957	0.938	0.920	0.902	0.885
	β	0.690	0.726	0.763	0.797	0.828	0.855	0.878	0.900	0.919	0.936	0.951	0.965	0.978	0.990	1.001	1.011	1.020	1.029	1.037	1.045
35	α	0.516	0.848	1.027	1.113	1.147	1.152	1.142	1.124	1.101	1.076	1.051	1.026	1.001	0.978	0.955	0.933	0.912	0.893	0.874	0.856
	β	0.686	0.720	0.756	0.790	0.822	0.850	0.875	0.897	0.918	0.936	0.952	0.967	0.981	0.994	1.006	1.017	1.027	1.036	1.045	1.054
40	α	0.499	0.834	1.019	1.110	1.145	1.150	1.138	1.118	1.093	1.066	1.039	1.012	0.985	0.960	0.936	0.913	0.891	0.870	0.850	0.831
	β	0.684	0.715	0.751	0.785	0.817	0.846	0.872	0.896	0.917	0.936	0.954	0.970	0.984	0.998	1.011	1.022	1.033	1.043	1.053	1.062
45	α	0.486	0.822	1.013	1.107	1.143	1.148	1.135	1.113	1.086	1.057	1.028	0.999	0.971	0.945	0.919	0.895	0.872	0.850	0.829	0.810
	β	0.682	0.711	0.746	0.781	0.813	0.843	0.870	0.894	0.917	0.937	0.955	0.972	0.987	1.002	1.015	1.027	1.039	1.049	1.059	1.069
50	α	0.475	0.812	1.007	1.104	1.142	1.146	1.132	1.108	1.080	1.049	1.018	0.988	0.959	0.931	0.905	0.879	0.856	0.833	0.812	0.791
	β	0.680	0.708	0.742	0.777	0.810	0.840	0.868	0.893	0.916	0.937	0.956	0.974	0.990	1.005	1.019	1.032	1.044	1.055	1.065	1.075
55	α	0.466	0.804	1.002	1.102	1.140	1.144	1.129	1.104	1.074	1.042	1.010	0.979	0.948	0.919	0.892	0.866	0.841	0.818	0.796	0.775
	β	0.679	0.706	0.739	0.774	0.807	0.838	0.867	0.893	0.916	0.938	0.958	0.976	0.993	1.008	1.023	1.036	1.048	1.060	1.071	1.081
60	α	0.459	0.796	0.998	1.100	1.139	1.143	1.126	1.100	1.069	1.036	1.002	0.970	0.939	0.909	0.880	0.854	0.828	0.805	0.782	0.761
	β	0.678	0.704	0.737	0.771	0.805	0.836	0.866	0.892	0.916	0.939	0.959	0.978	0.995	1.011	1.026	1.040	1.053	1.065	1.076	1.087
65	α	0.452	0.790	0.994	1.098	1.138	1.141	1.124	1.097	1.064	1.030	0.996	0.962	0.930	0.899	0.870	0.843	0.817	0.793	0.770	0.749
	β	0.677	0.702	0.735	0.769	0.803	0.835	0.865	0.892	0.917	0.939	0.960	0.980	0.997	1.014	1.029	1.043	1.056	1.069	1.081	1.091
70	α	0.447	0.784	0.991	1.097	1.137	1.140	1.122	1.094	1.060	1.025	0.989	0.955	0.922	0.891	0.861	0.833	0.807	0.782	0.759	0.737
	β	0.677	0.701	0.733	0.767	0.801	0.834	0.864	0.891	0.917	0.940	0.961	0.981	0.999	1.016	1.032	1.046	1.060	1.073	1.085	1.096

Table D.4: Stress block factors for confined concrete $f'_{cc}/f'_c=1.3$

f'_c		Ratio of strain in concrete to strain at maximum compression stress $\varepsilon_{cu}/\varepsilon_{co}$																			
		0.5	**1.0**	**1.5**	**2.0**	**2.5**	**3.0**	**3.5**	**4.0**	**4.5**	**5.0**	**5.5**	**6.0**	**6.5**	**7.0**	**7.5**	**8.0**	**8.5**	**9.0**	**9.5**	**10.0**
20	α	0.605	0.929	1.097	1.186	1.232	1.255	1.264	1.265	1.260	1.252	1.243	1.232	1.220	1.208	1.196	1.184	1.172	1.161	1.149	1.138
	β	0.702	0.742	0.777	0.806	0.831	0.852	0.870	0.886	0.901	0.913	0.925	0.935	0.944	0.953	0.960	0.968	0.974	0.980	0.986	0.992
25	α	0.562	0.893	1.075	1.174	1.226	1.251	1.260	1.260	1.254	1.245	1.233	1.220	1.206	1.192	1.177	1.163	1.149	1.135	1.122	1.109
	β	0.695	0.731	0.764	0.794	0.820	0.842	0.862	0.879	0.895	0.908	0.921	0.932	0.943	0.952	0.961	0.969	0.977	0.984	0.990	0.996
30	α	0.533	0.867	1.058	1.164	1.220	1.248	1.257	1.257	1.249	1.238	1.225	1.209	1.194	1.178	1.162	1.146	1.130	1.115	1.100	1.085
	β	0.690	0.723	0.756	0.785	0.812	0.835	0.855	0.874	0.890	0.905	0.918	0.931	0.942	0.952	0.962	0.971	0.979	0.987	0.994	1.001
35	α	0.511	0.847	1.045	1.157	1.216	1.245	1.255	1.254	1.245	1.233	1.218	1.201	1.183	1.166	1.148	1.131	1.114	1.097	1.081	1.065
	β	0.687	0.718	0.749	0.779	0.805	0.829	0.850	0.870	0.887	0.903	0.917	0.930	0.942	0.953	0.963	0.973	0.981	0.990	0.997	1.005
40	α	0.494	0.831	1.034	1.151	1.213	1.243	1.253	1.251	1.242	1.228	1.211	1.193	1.175	1.156	1.137	1.118	1.100	1.082	1.065	1.048
	β	0.685	0.714	0.744	0.773	0.800	0.825	0.847	0.866	0.884	0.901	0.916	0.929	0.942	0.953	0.964	0.974	0.984	0.992	1.000	1.008
45	α	0.481	0.818	1.025	1.145	1.210	1.241	1.251	1.249	1.239	1.224	1.206	1.187	1.167	1.147	1.127	1.107	1.088	1.069	1.051	1.034
	β	0.683	0.710	0.740	0.769	0.796	0.821	0.843	0.864	0.882	0.899	0.915	0.929	0.942	0.954	0.965	0.976	0.986	0.995	1.003	1.011
50	α	0.470	0.807	1.018	1.141	1.208	1.240	1.250	1.247	1.236	1.220	1.202	1.181	1.160	1.139	1.118	1.098	1.077	1.058	1.039	1.021
	β	0.681	0.708	0.737	0.766	0.793	0.818	0.841	0.862	0.881	0.898	0.914	0.929	0.942	0.955	0.967	0.977	0.988	0.997	1.006	1.014
55	α	0.461	0.797	1.011	1.137	1.206	1.238	1.249	1.245	1.234	1.217	1.197	1.176	1.154	1.132	1.111	1.089	1.068	1.048	1.029	1.010
	β	0.680	0.705	0.734	0.763	0.790	0.815	0.839	0.860	0.879	0.897	0.914	0.929	0.943	0.956	0.968	0.979	0.989	0.999	1.008	1.017
60	α	0.453	0.789	1.006	1.134	1.204	1.237	1.248	1.244	1.232	1.214	1.194	1.172	1.149	1.126	1.104	1.082	1.060	1.039	1.019	1.000
	β	0.679	0.704	0.732	0.760	0.788	0.813	0.837	0.858	0.878	0.896	0.913	0.929	0.943	0.956	0.969	0.980	0.991	1.001	1.010	1.019
65	α	0.447	0.782	1.001	1.131	1.203	1.236	1.247	1.243	1.230	1.212	1.191	1.168	1.144	1.121	1.098	1.075	1.053	1.032	1.011	0.991
	β	0.679	0.702	0.730	0.758	0.786	0.811	0.835	0.857	0.877	0.896	0.913	0.929	0.943	0.957	0.969	0.981	0.992	1.003	1.012	1.022
70	α	0.442	0.776	0.997	1.129	1.201	1.235	1.246	1.241	1.228	1.209	1.188	1.164	1.140	1.116	1.092	1.069	1.046	1.025	1.004	0.983
	β	0.678	0.701	0.728	0.756	0.784	0.810	0.834	0.856	0.876	0.895	0.913	0.929	0.944	0.957	0.970	0.982	0.994	1.004	1.014	1.024

Table D.5: Stress block factors for confined concrete $f'_{cc}/f'_c=1.4$

f'_c		Ratio of strain in concrete to strain at maximum compression stress $\varepsilon_{cu}/\varepsilon_{co}$																			
		0.5	**1.0**	**1.5**	**2.0**	**2.5**	**3.0**	**3.5**	**4.0**	**4.5**	**5.0**	**5.5**	**6.0**	**6.5**	**7.0**	**7.5**	**8.0**	**8.5**	**9.0**	**9.5**	**10.0**
20	α	0.606	0.943	1.129	1.235	1.297	1.333	1.353	1.363	1.366	1.365	1.361	1.355	1.348	1.339	1.331	1.321	1.312	1.303	1.293	1.284
	β	0.701	0.738	0.770	0.797	0.820	0.840	0.857	0.872	0.885	0.897	0.908	0.917	0.926	0.934	0.941	0.948	0.955	0.960	0.966	0.971
25	α	0.562	0.903	1.101	1.218	1.286	1.326	1.348	1.359	1.362	1.360	1.355	1.348	1.339	1.329	1.319	1.308	1.297	1.286	1.275	1.264
	β	0.694	0.728	0.759	0.785	0.809	0.829	0.847	0.863	0.878	0.890	0.902	0.913	0.922	0.931	0.939	0.947	0.954	0.960	0.967	0.972
30	α	0.531	0.873	1.080	1.204	1.278	1.321	1.345	1.356	1.359	1.357	1.351	1.342	1.332	1.321	1.309	1.297	1.284	1.272	1.259	1.247
	β	0.690	0.721	0.750	0.777	0.801	0.822	0.840	0.857	0.872	0.886	0.898	0.909	0.920	0.929	0.938	0.946	0.954	0.961	0.967	0.974
35	α	0.509	0.851	1.064	1.194	1.272	1.317	1.342	1.354	1.357	1.354	1.347	1.337	1.326	1.314	1.301	1.287	1.274	1.260	1.246	1.233
	β	0.687	0.716	0.744	0.771	0.794	0.816	0.835	0.852	0.868	0.882	0.895	0.907	0.918	0.928	0.937	0.946	0.954	0.961	0.968	0.975
40	α	0.492	0.833	1.051	1.185	1.266	1.314	1.340	1.352	1.355	1.351	1.343	1.333	1.321	1.307	1.293	1.279	1.264	1.250	1.235	1.221
	β	0.685	0.712	0.739	0.766	0.789	0.811	0.831	0.848	0.864	0.879	0.893	0.905	0.916	0.927	0.936	0.946	0.954	0.962	0.969	0.976
45	α	0.478	0.819	1.040	1.178	1.262	1.311	1.338	1.351	1.353	1.349	1.341	1.329	1.316	1.302	1.287	1.272	1.257	1.241	1.226	1.211
	β	0.683	0.709	0.736	0.761	0.785	0.807	0.827	0.845	0.862	0.877	0.891	0.903	0.915	0.926	0.936	0.946	0.954	0.963	0.970	0.978
50	α	0.467	0.807	1.030	1.172	1.258	1.309	1.337	1.349	1.352	1.347	1.338	1.326	1.313	1.298	1.282	1.266	1.250	1.234	1.218	1.202
	β	0.682	0.706	0.733	0.758	0.782	0.804	0.824	0.843	0.860	0.875	0.889	0.902	0.914	0.925	0.936	0.946	0.955	0.963	0.971	0.979
55	α	0.458	0.797	1.023	1.166	1.255	1.307	1.336	1.348	1.350	1.345	1.336	1.324	1.309	1.294	1.277	1.261	1.244	1.227	1.211	1.194
	β	0.681	0.704	0.730	0.755	0.779	0.801	0.822	0.841	0.858	0.873	0.888	0.901	0.914	0.925	0.936	0.946	0.955	0.964	0.972	0.980
60	α	0.451	0.788	1.016	1.162	1.252	1.305	1.334	1.347	1.349	1.344	1.334	1.321	1.306	1.290	1.273	1.256	1.239	1.221	1.204	1.188
	β	0.680	0.703	0.728	0.753	0.777	0.799	0.820	0.839	0.856	0.872	0.887	0.900	0.913	0.925	0.936	0.946	0.956	0.965	0.973	0.981
65	α	0.444	0.781	1.010	1.158	1.250	1.304	1.333	1.346	1.348	1.343	1.333	1.319	1.304	1.287	1.269	1.252	1.234	1.216	1.199	1.181
	β	0.679	0.701	0.726	0.751	0.775	0.797	0.818	0.837	0.855	0.871	0.886	0.900	0.912	0.924	0.936	0.946	0.956	0.965	0.974	0.982
70	α	0.439	0.774	1.005	1.154	1.248	1.303	1.333	1.346	1.347	1.342	1.331	1.317	1.301	1.284	1.266	1.248	1.230	1.211	1.194	1.176
	β	0.679	0.700	0.724	0.749	0.773	0.796	0.816	0.836	0.853	0.870	0.885	0.899	0.912	0.924	0.936	0.946	0.956	0.966	0.974	0.983

Appendix E

E1. FORMULATION OF THE BILINEAR, BASE SHEAR REDUCTION FACTOR ϕ_{BL}

Considering Figure E.1 below, the area beneath each bilinear-elastic loading curve is equated as follows

$$E_2 = E_1 = \frac{k_1 \Delta_y^2}{2} + \frac{k_1}{2}\left(\Delta_{BL} - \Delta_y\right)\left[2\Delta_y + r\left(\Delta_{BL} - \Delta_y\right)\right] \qquad \textbf{E.1}$$

Setting the two areas equal and solving for the reduced initial stiffness k_2

$$k_2 = \frac{\frac{k_1 \Delta_y^2}{2} + \frac{k_1}{2}\left(\Delta_{BL} - \Delta_y\right)\left[2\Delta_y + r\left(\Delta_{BL} - \Delta_y\right)\right]}{\frac{\Delta_y^2}{2} + \frac{1}{2}\left(\Delta_d - \Delta_y\right)\left[2\Delta_y + r\left(\Delta_d - \Delta_y\right)\right]} \qquad \textbf{E.2}$$

For far-field ground motions the bilinear reduction factor ϕ_{BL} is defined as

$$\phi_{BL} = \frac{V_b^*}{V_b} = \frac{k_2 \Delta_y + r k_2 (\Delta_d - \Delta_y)}{K_e \Delta_d} \qquad \textbf{E.3}$$

For near-field ground motions, the reduction factor is defined as

$$\phi_{BL} = 0.5\left(\frac{V_b^*}{V_b} + 1\right) = 0.5\left(\frac{k_2 \Delta_y + r k_2 (\Delta_d - \Delta_y)}{K_e \Delta_d} + 1\right) \qquad \textbf{E.4}$$

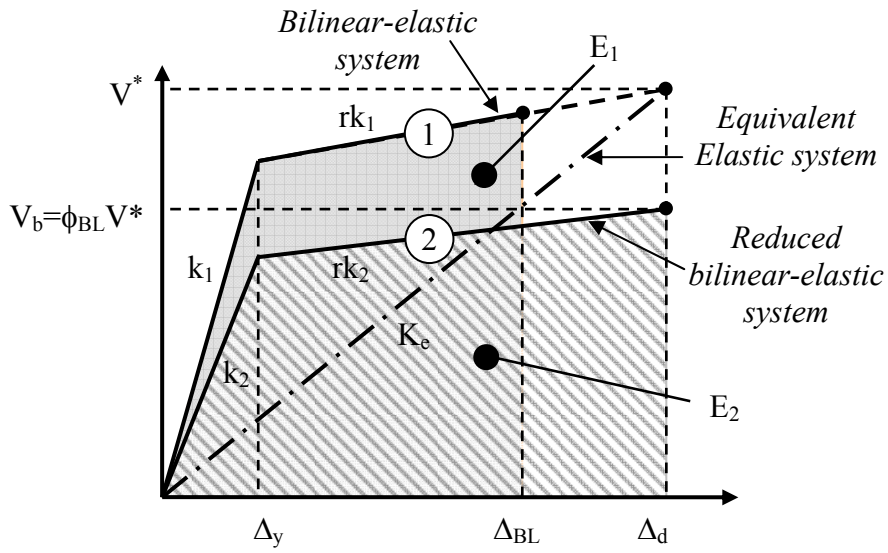

Figure E.1 Bilinear reduction

E2. DAMPED RESPONSE SPECTRA FOR POST-TENSIONED SYSTEMS WITH NON-LINEAR DAMPERS, α = 0.15-0.75

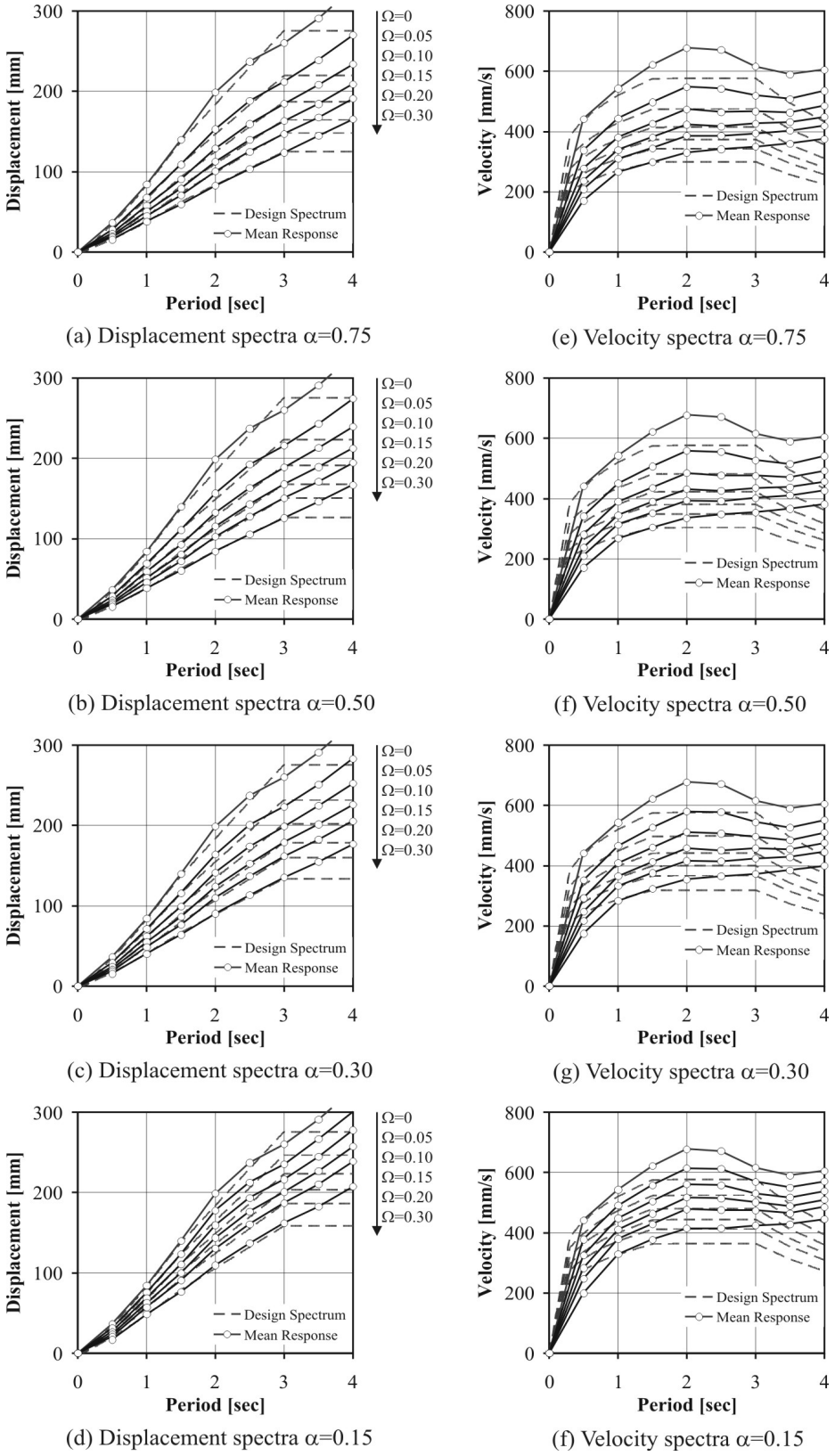

(a) Displacement spectra α=0.75 (e) Velocity spectra α=0.75

(b) Displacement spectra α=0.50 (f) Velocity spectra α=0.50

(c) Displacement spectra α=0.30 (g) Velocity spectra α=0.30

(d) Displacement spectra α=0.15 (f) Velocity spectra α=0.15

Figure E.2 Far-field damped response spectra for displacement (a)-(d) and velocity (e)-(f)

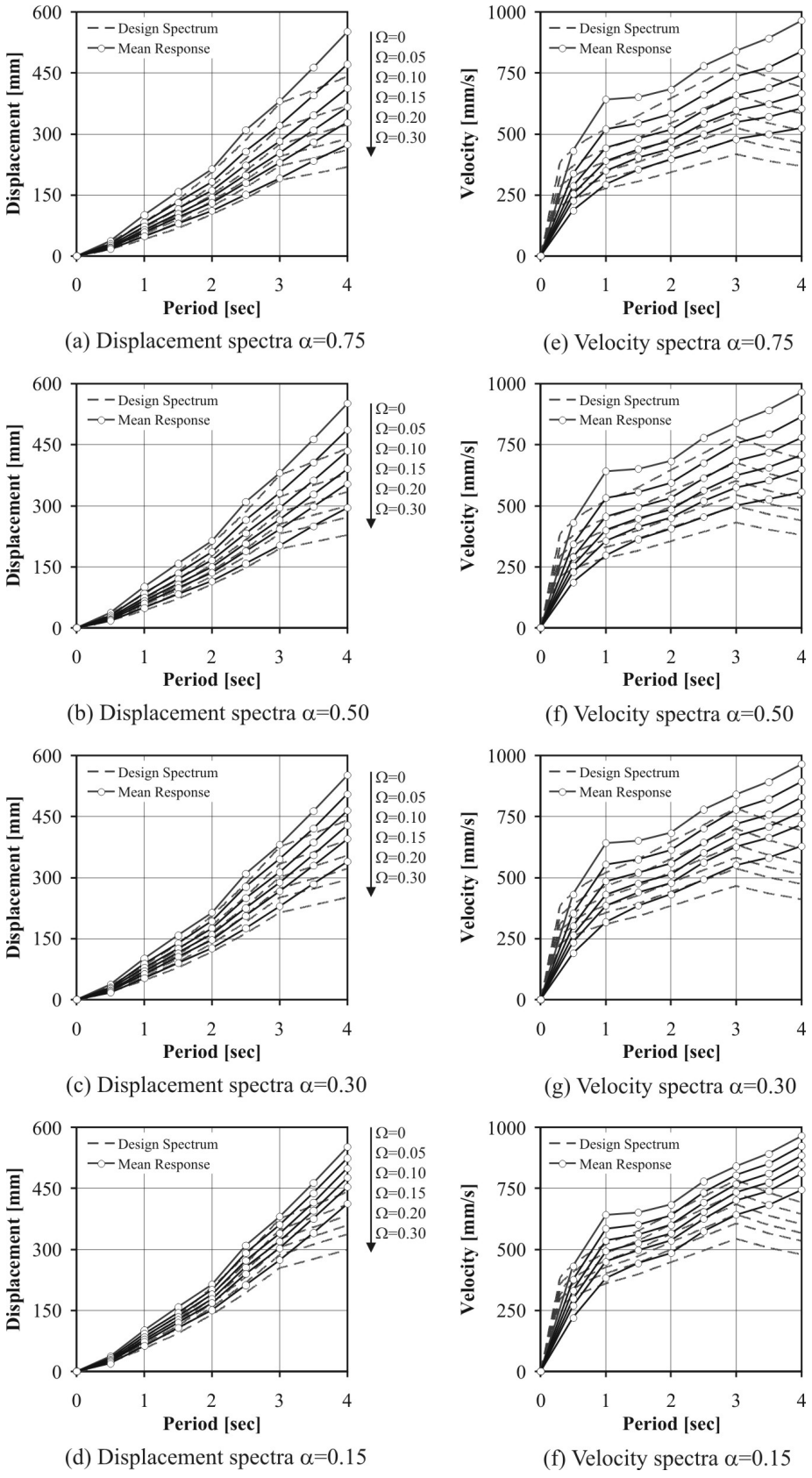

Figure E.3 Near-field damped response spectra for displacement (a)-(d) and velocity (e)-(f)

E3. DERIVATION OF THE INTERNAL LEVER ARM TO THE RESULTANT SUPPLEMENTARY DAMPER FORCE

This section develops an expression for the internal lever arm to the centroid of the resultant viscous damper forces $\Sigma F_{vd,i}$. Consider the system in Figure E.4 below with three viscous damper layers.

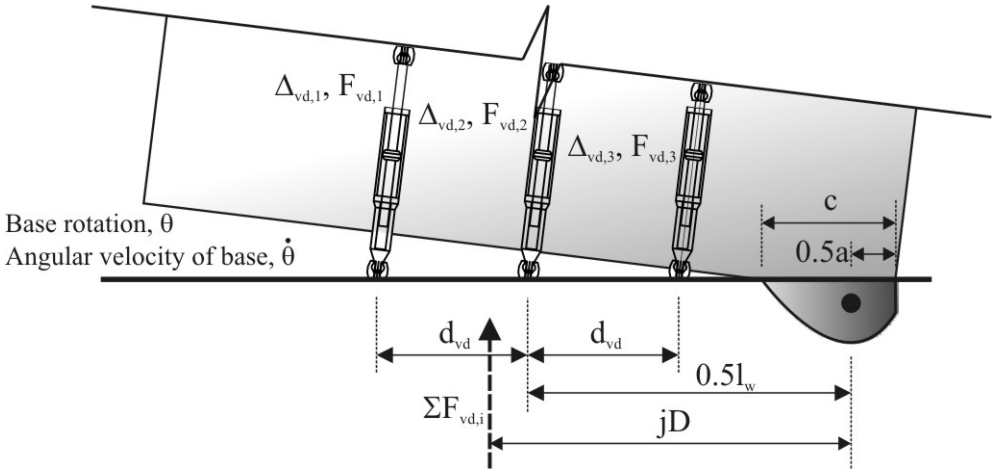

Figure E.4 Distribution of internal viscous damper actions

The ratio between the displacement and velocity of each damper layer can be written as a ratio of their location within the section as follows.

$$\frac{\Delta_1}{\Delta_2} = \frac{v_1}{v_2} = \frac{0.5l_w + d_{vd} - c}{0.5l_w - c} \quad \textbf{E.5}$$

$$\frac{\Delta_2}{\Delta_3} = \frac{v_2}{v_3} = \frac{0.5l_w - c}{0.5l_w - d_{VD} - c} \quad \textbf{E.6}$$

Therefore, the ratio between the forces is written as follows

$$\Phi_{1-2} = \frac{F_{vd1}}{F_{vd2}} = \left[\frac{l_w(0.5-\chi) + d_{vd}}{l_w(0.5-\chi)}\right]^{\alpha} \quad \textbf{E.7}$$

$$\Phi_{2-3} = \frac{F_{vd2}}{F_{vd3}} = \left[\frac{l_w(0.5-\chi)}{l_w(0.5-\chi) - d_{vd}}\right]^{\alpha} \quad \textbf{E.8}$$

The viscous damper moment can be defined using an equivalent internal lever arm to the centroid of the sum of the viscous damper forces.

$$M_{vd} = \sum\left(F_{vd,i}\, jd_{vd,i}\right) = jD\sum F_{vd,i} \quad \textbf{E.9}$$

Where the internal lever arm $\boldsymbol{jd_{vd,i}}$ of each damper set is given by

$$jd_{vd,i} = 0.5l_w(1-\beta\chi) \pm d_{vd} \qquad \textbf{E.10}$$

By substitution, the internal lever arm to the centroid of the viscous damper force ***jD*** can be written as

$$jD = \frac{M_{vd}}{\sum F_{vd,i}} = \frac{\Phi_{1-2}\, jd_{vd,1} + jd_{vd,2} + \Phi_{2-3} \cdot jd_{vd,3}}{\Phi_{1-2} + \Phi_{2-3} + 1} \qquad \textbf{E.11}$$

When the system reduces to two viscous damper sets symmetrically located about the section, ***jD*** reduces to the following

$$jD = \frac{M_{vd}}{\sum F_{vd,i}} = \frac{\Phi_{1-2} \cdot jd_{vd1} + jd_{vd2}}{\Phi_{1-2} + 1} \qquad \textbf{E.12}$$

$$\Phi_{1-2} = \frac{F_{vd1}}{F_{vd2}} = \left[\frac{l_w(0.5-\chi) + d_{vd}}{l_w(0.5-\chi) - d_{vd}}\right]^{\alpha} \qquad \textbf{E.13}$$

When the system reduces to a single viscous damper element ***jD*** reduces to the following

$$jD = jd_{vd,1} \qquad \textbf{E.14}$$

E4. DERIVATION OF THE NET VELOCITY OF THE SUPPLEMENTARY VISCOUS DAMPERS

This section develops an expression to compute the average (or net) velocity $\bar{v}_{vd}$ of the viscous damper group at the centroid of the resultant damper force $\boldsymbol{\Sigma F_{vd,i}}$. Consider the system in Figure E.5 below with three viscous damper layers.

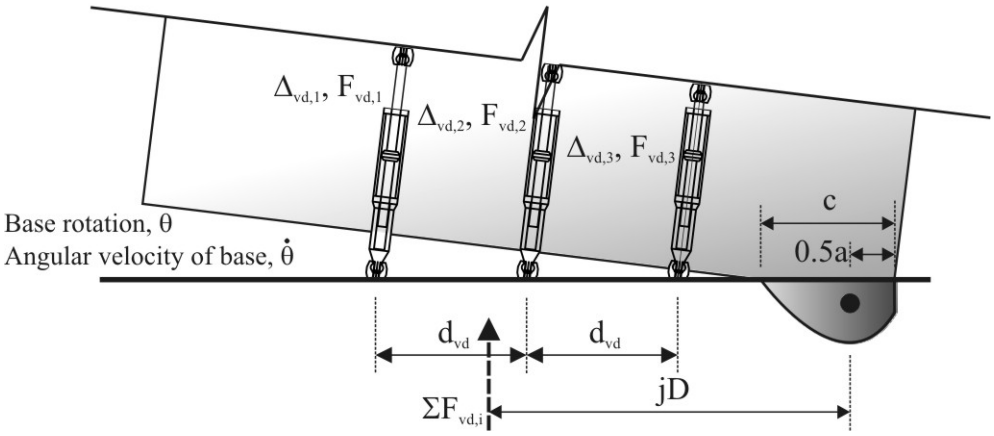

Figure E.5 Distribution of internal viscous damper forces

The sum of all viscous damper forces in the section is equated as follows

$$\begin{aligned}\sum F_{vd,i} =& n_{vd,1}c_{vd}\left(v_{vd,1}\right)^{\alpha} + n_{vd,2}c_{vd}\left(v_{vd,2}\right)^{\alpha} \\ &+ n_{vd,3}c_{vd}\left(v_{vd,3}\right)^{\alpha} = c_{vd}\left(\bar{v}_{vd}\right)^{\alpha}\sum n_{vd,i}\end{aligned} \qquad \textbf{E.15}$$

Where $\boldsymbol{n_{vd,i}}$ is the number of viscous dampers within each layer set (i.e. $\boldsymbol{n_{vd,i}} = 2$ if two dampers are located at each layer). Using geometry to define the velocity at each layer and rearranging for $\bar{v}_{vd}$ yields the following expression

$$\left(\bar{v}_{vd}\right)^{\alpha} = \frac{1}{n_{vis}}\sum_{i=1}^{n}\left[\dot{\theta}\left(l_w(0.5-\chi) \pm d_{vd}\right)\right]^{\alpha} \qquad \textbf{E.16}$$

Finally, the ratio between the velocity of the damper group and the system velocity is given by

$$\frac{\bar{v}_{vd}}{v_r} = \left(\gamma_{vd}\right)^{1/\alpha} = \left(\frac{1}{n_{vis}}\sum_{i=1}^{n}\left[\frac{1}{H_e}\left(l_w(0.5-\chi) \pm d_{vd}\right)\right]^{\alpha}\right)^{1/\alpha} \qquad \textbf{E.17}$$

Alternatively, through geometry recognising rotation about the centroid of the compression block, the following relationship between the lateral displacement and damper displacement can be written

$$\frac{\Delta_{vd}}{\Delta_r} = \frac{jD + l_w\chi(1-0.5\beta)}{H_e} \approx \frac{jD}{H_e} \qquad \textbf{E.18}$$

Hence, the velocity is related in the same way

$$\frac{\bar{v}_{vd}}{v_r} = \frac{jD + l_w\chi(1-0.5\beta)}{H_e} \approx \frac{jD}{H_e} \qquad \textbf{E.19}$$

Therefore the geometric coefficient can be approximated as,

$$\gamma_{vd} = \left(\frac{\bar{v}_{vd}}{v_r}\right)^{\alpha} = \left[\frac{jD + l_w\chi(1-0.5\beta)}{H_e}\right]^{\alpha} \approx \left(\frac{jD}{H_e}\right)^{\alpha} \qquad \textbf{E.20}$$

The two equations give very similar results, however some error can result for the approximation of Eq.(E.20).

E5. DESIGN EXAMPLE OF A POST-TENSIONED WALL SYSTEM WITH VISCOUS DAMPERS

The following presents a worked example of a prototype rocking wall structure located in Wellington dominated by near-fault seismicity in Figure E.6. The seismic design spectrum is shown graphically in Figure E.7, with the numerical coordinates presented in Table E.1. A quick design example and a detailed design example are presented below.

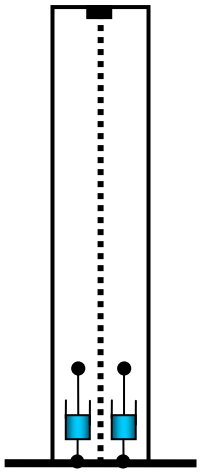

Design details
Design PGA = 0.372 (zone factor **z** = 0.28, soil cat C)
Target inter-storey drift: 1.0%

Structural wall details
$\mathbf{h_w}$ = 15m (5 levels @ 3m)
$\mathbf{l_w}$ = 2.5m
$\mathbf{t_w}$ = 0.25m
Floor mass, $\mathbf{m_i}$ = 20tonne

System damping properties
Total number of dampers, $\boldsymbol{n_{vd}}$ = 4 (2 locations)
Target supplementary damping ratio, $\boldsymbol{\Omega}$ = 15%
Non-linearity, $\boldsymbol{\alpha}$ = 0.50

Figure E.6 Prototype rocking wall for design example

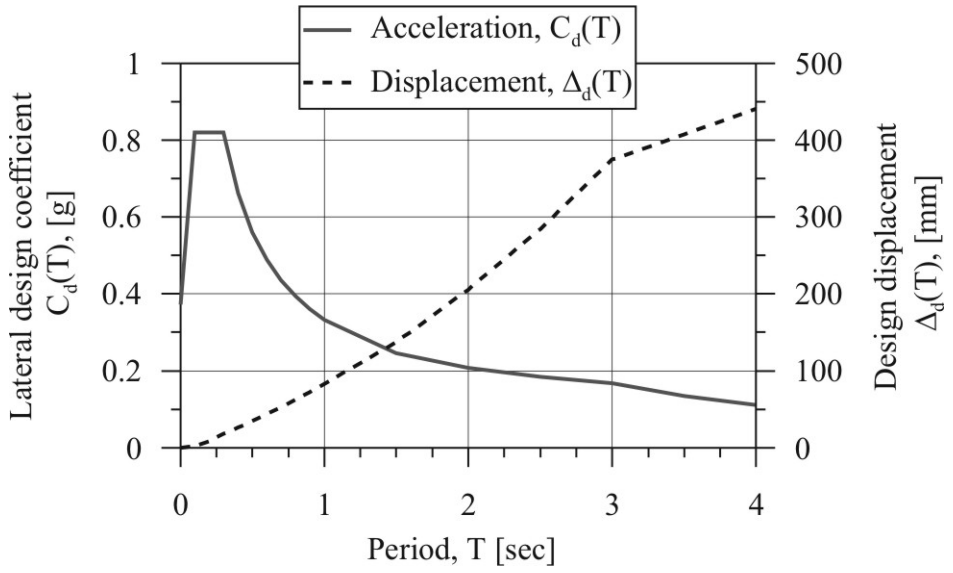

Figure E.7 NZS1170.5 [2004] elastic (5% damped) design spectrum. Zone factor z = 0.28, soil class C, return period 500years R_u = 1, 2km distance to fault, structural performance factor S_p = 1.0

Table E.1 Coordinates for the elastic (5% damped) design spectrum for zone factor z = 0.28, soil class C, return period 500years R_u = 1, 2km distance to fault, structural performance factor S_p = 1.0

Period, T [sec]	$C_d(T)$ [g]	$\Delta_d(T)$ [mm]
0.0	0.372	0
0.1	0.820	2
0.2	0.820	8
0.3	0.820	18
0.4	0.662	26
0.5	0.560	35
0.6	0.488	44
0.7	0.435	53
0.8	0.394	63
0.9	0.360	73
1.0	0.333	83
1.5	0.246	137
2.0	0.207	206
2.5	0.183	285
3.0	0.168	375
3.5	0.134	408
4.0	0.111	441
4.5	0.091	457

In this example, the design is targeting a specified level of damping (or supplementary damping ratio in this case), the Direct Displacement-Based Design for PT viscous systems follows *Design Method A* in Figure 8.31 above.

STEP 1

For simplicity, elastic deformations are ignored in this design example; therefore, the inelastic first mode-shape is linear. The SDOF target displacement is determined from Eq.(8.27)

$$\Delta_{d,\xi} = 110mm$$

The effective mass and effective height are calculated from Eqs.(8.25) and (8.26)

$$m_e = 81,818kg$$
$$H_e = 11000mm$$

STEP 2.

The equivalent viscous damping is determined from Eq.(8.5).

$$\xi_{eq}^{disp} = a_1\Omega + \xi_{el}$$

From Table 8.4, for near-field seismicity and a velocity exponent of $\alpha = 0.50$ the coefficient a_1 is given by

$$a_1 = 0.608$$

Elastic damping is taken as 5%.For simplicity, this design example assumes the elastic damping is proportional to the secant stiffness; therefore, no modification factors are applied to ξ_{el}.

ξ_{el} *=0.05 (5% elastic damping)*

Therefore,

$$\xi_{eq}^{disp} = a_1\Omega + \xi_{el} = 0.608 \cdot 0.15 + 0.05 = 0.1365$$

The damping reduction factor η_{disp} is calculated

$$\eta_{disp} = \left(\frac{0.07}{0.02 + \xi_{eq}} \right)^{0.5} = \left(\frac{0.07}{0.02 + 0.1365} \right)^{0.5} = 0..669$$

STEP 3.
The equivalent 5% damped displacement is given by

$$\Delta_{d,5\%} = \frac{\Delta_{d,\xi}}{\eta_{disp}} = \frac{110mm}{0.669} = 164.5mm$$

Entering the New Zealand 5% design displacement spectrum

T_e *=1.698s*

STEP 4.
The effective stiffness K_e is computed as follows

$$k_e = \frac{4\pi^2 m_e^2}{T_e} = \frac{4\pi^2 \cdot 81{,}818kg}{1.698^2} = 1120kN/m$$

The base shear reduction factor ϕ_{BL}, for $\alpha = 0.50$ and $\Omega = 0.15$, is interpolated from Table 8.6. The interpolation is summarised in Table E.2 below

Table E.2 Interpolated bilinear reduction factor

	α=0.30	α=0.75	α=0.50
	Ω=0.15		Ω=0.15
T_e=1.00s	0.754	0.782	**0.767**
T_e=2.25s	0.809	0.829	**0.818**
T_e=3.50s	0.857	0.870	**0.863**

Interpolating for T_e*=1.698s* results in a bilinear factor of ϕ_{BL}*=0.795*. The design base shear is computed

$$V_b = \phi_{BL} K_e \Delta_d = 0.795 \cdot 1120kN/m \cdot 0.11m = 98.0kN$$

STEP 5.
The critical damping coefficient $\boldsymbol{C_c}$

$$C_c = 2\sqrt{m_e K_e} = 2\sqrt{81{,}818kg \cdot 1120kN/m} = 605.4kNs/m$$

The system damping coefficient required to achieve this particular design is computed below

$$C_{VD} = \Omega \cdot C_c = 0.15 \cdot 605.4kNs^{\alpha}/m^{\alpha} = 90.81kNs^{\alpha}/m^{\alpha}$$

Section Design at the Target Displacement Δ_d
The next series of calculations are not explicitly defined in the design method but are required to determine the specific number of post-tensioned tendons and the initial post-tensioning force required to achieve the design base shear of $\boldsymbol{V_b}$ = 98.0kN. The design of the post-tensioning is carried out at the target design displacement $\boldsymbol{\Delta_d}$ (110mm) where the velocity is zero, hence the viscous damper contribution to the lateral capacity is also zero. To determine the amount of post-tensioning steel required, an estimate on the dimensionless neutral axis depth $\boldsymbol{\chi = c/l_w}$ can be computed from the following expression

$$\chi = \frac{c}{D} = \frac{1}{2\beta}\left[1 - \sqrt{1 - \frac{8\mu}{\alpha}}\right]$$

Where α and β are the stress block coefficients and μ is the dimensionless moment demand

$$\mu = \frac{M}{f_c' BD^2} = \frac{V_b H_e}{f_c' BD^2}$$

The dimensionless neutral axis depth is approximated as χ=*0.1*. Lumping the tendons at the middle of the section and assuming a stress-block coefficient of β=0.67, the internal lever arm is estimated from the following

$$jd_{approx} = 0.5l_w(1 - \beta\chi) = 0.5 \cdot 2.5m(1 - 0.067) = 1{,}166mm$$

The tendon force required to achieve the design lateral capacity is determined

$$T_{pt,req} = \frac{V_b H_e}{jd_{approx}} = \frac{98kN \cdot 11{,}000mm}{1{,}166mm} = 924kN$$

Knowing that the strain in the tendon must not exceed $0.9\varepsilon_y$ (NZS3101 [2006]), the number of tendons required is

$$n_{pt} = \frac{T_{pt,req}}{0.9 f_{pt,y} A_{pt}} = \frac{924kN}{0.9 \cdot 1560MPa \cdot 99mm^2} > 6.6$$

$$\therefore n_{PT} = 8$$

The total initial post-tensioned force is determined as the difference between the tendon force at the design rotation and the tendon force due to gap opening

$$T_{pt,0} = T_{pt,req} - \frac{0.4 l_w \theta}{l_{ub}} E_{pt} A_{pt} n_{pt}$$

$$T_{pt,0} = 924kN - \frac{0.4 \cdot 2{,}500mm \cdot 1.0\%}{15{,}000mm} \cdot 200GPa \cdot 99mm^2 \cdot 8 = 818kN$$

Note that in this example a) the elastic deformation is ignored, and b) the displacement profile is assumed linear; therefore the gap opening is equal to the drift, θ=*1.0%*.

While these parameters may suffice for a quick design, it should be verified by a proper determination of the neutral axis depth involving translation equilibrium. The calculation below is based on the final iteration with a neutral axis depth of c = *289.2mm* (χ = *0.116*), where the initial post-tensioned force is reduced to 809kN. First, the decompression moment and curvature are calculated

$$M_{dec} = T_{pt,0} \frac{l_w}{6} = 809kN \frac{2{,}500mm}{6} = 337kNm$$

$$\phi_{dec} = 3.3 \times 10^{-5} m^{-1}$$

The concrete compression force is calculated from the maximum concrete compression strain of

$$\varepsilon_c = \left(\frac{3\theta}{h_e} + \phi_{dec} \right) c = \left(\frac{3 \cdot 1.0\%}{15{,}000mm} + 3.3 \times 10^{-5} m^{-1} \right) 289.2mm = 0.000798$$

The concrete stress block coefficients are defined and the concrete compression force is calculated,

$$\alpha = 0.75 \frac{4700}{\sqrt{f_c'}} \varepsilon_c = 0.75 \frac{4700}{\sqrt{45}} 0.000798 = 0.419$$

β=*0.67*

$$C_c = \alpha f_c' \beta c t_w = 0.419 \cdot 45MPa \cdot 0.67 \cdot 289.2mm \cdot 250mm = 910kN$$

The elongation in each tendon is determined

$$\Delta_{pt,i} = \theta[l_w(0.5-\chi) \pm d_{pt,i}]$$

$$\Delta_{pt,1} = 1.0\%[2{,}500mm(0.5-0.116)+510mm] = 14.7mm$$

$$\Delta_{pt,2} = 1.0\%[2{,}500mm(0.5-0.116)-510mm] = 4.5mm$$

Similarly, the tendon strain,

$$\Delta\varepsilon_{pt,i} = \frac{\Delta_{PT,i}}{l_{ub}}$$

$$\Delta\varepsilon_{pt,1} = \frac{14.7mm}{15{,}000} = 0.00098 < 0.9\varepsilon_y - \varepsilon_{pt,0}$$

$$\Delta\varepsilon_{pt,2} = \frac{4.5mm}{15{,}000} = 0.00030 < 0.9\varepsilon_y - \varepsilon_{pt,0}$$

The increase in tendon load is thus,

$$\Delta T_{pt,i} = \Delta\varepsilon_{pt,i} E_{pt} A_{pt} n_{pt,i}$$

$$\Delta T_{pt,1} = 0.00098 \cdot 200GPa \cdot 99mm^2 \cdot 4 = 77.7kN$$

$$\Delta T_{pt,1} = 0.00030 \cdot 200GPa \cdot 99mm^2 \cdot 4 = 23.8kN$$

Equating force equilibrium

$$\sum F = T_{pt} - C_c = 809kN + 77.7kN + 23.8kN - 910kN \approx 0$$

The resulting moment capacity,

$$M_n = T_{pt,0} jd_{0.5lw} + \sum_{i=1}^{n} \Delta T_{pt,i} jd_{pt,i}$$

Where the internal lever arms are defined as,

$$jd_{0.5lw} = 0.5l_w(1-\beta\chi) = 0.5 \cdot 2{,}500mm(1-0.67 \cdot 0.116) = 1{,}153mm$$

$$jd_{pt,1} = 0.5l_w(1-\beta\chi) + d_{pt,1} = 1{,}664mm$$

$$jd_{pt,2} = 0.5l_w(1-\beta\chi) - d_{pt,1} = 692mm$$

Therefore,

$$M_n = 809kN \cdot 1{,}153mm + 77.7kN \cdot 1{,}664mm + 23.8kN \cdot 692mm = 1079kN$$

Thus satisfying the required lateral capacity at the target displacement of $\Delta_d = 110mm$

$$P = \frac{M_n}{h_e} = \frac{1079kN}{11{,}000} = 98.1kN > V_b$$

Following the design of the post-tensioned reinforcement, the damper properties must be determined. A quick method (***I***) and a detailed method (***II***) are presented below depending on the level of accuracy required.

I. Design of the Supplementary Dampers (Quick Method)

STEP 6-I.
First, the parameter $\boldsymbol{\beta_{vd}}$ is computed relating the global damping coefficient $\boldsymbol{C_{VD}}$ to a local damping coefficient $\boldsymbol{c_{vd}}$.

$$\beta_{vd} = \frac{C_{VD}}{c_{vd}} = a \cdot n_{vis} \left(A_r\right)^{-(1+\alpha)} = 0.514 \cdot 2 \cdot \left(\frac{11}{2.5}\right)^{-1.5} = 0.111$$

Hence, the local damping coefficient $\boldsymbol{c_{vd}}$ can be computed

$$c_{vd} = \frac{C_{vd}}{\beta_{vd}} = \frac{90.81kNs^{\alpha}/m^{\alpha}}{0.111} = 815kNs^{\alpha}/m^{\alpha} = 25.8kNs^{\alpha}/mm^{\alpha}$$

STEP 7-I.
The EVD damping associated with velocity is computed

$$\xi_{eq}^{vel} = b_1 \Omega + \xi_{el} = 0.608 \cdot 0.15 + 0.05 = 0.129$$

The spectrum reduction factors

$$\eta_{vel} = \sqrt{\frac{0.07}{0.02 + \xi_{eq}^{vel}}} = \sqrt{\frac{0.07}{0.02 + 0.129}} = 0.690$$

Therefore the design velocity $\boldsymbol{v_r}$ (at the intermediate design displacement $\boldsymbol{\Delta_r}$) is calculated as

$$v_r = \Delta_d \frac{2\pi}{T_e}\left(\frac{\eta_{vel}}{\eta_{disp}}\right)\frac{1}{\sqrt{2}} = 110mm \cdot \frac{2\pi}{1.698s}\left(\frac{0.690}{0.669}\right)\frac{1}{\sqrt{2}} = 297mm/s$$

STEP 8-I
The final step estimates the average damper velocity. This allows the damper forces to be estimated for sizing and pricing issues. First, the internal lever ***jD*** arm to the

centroid of the resultant damper force is estimated. To avoid a detailed calculation the neutral axis depth is estimated as $\chi = c/l_w = 0.15$ while a stress block factor of $\beta = 0.7$ is assumed. The resultant damper force is assumed to act at the middle of the section, hence ***jD*** is calculated as

$$jD = 0.5l_w(1-\beta\chi) = 0.5 \cdot 2.5m(1-0.105) = 1.12m$$

The average damper design velocity can be estimated from Eq.(8.20)

$$\bar{v}_{vd} \approx \frac{jD}{H_e} v_r = \frac{1.12m}{11m} \cdot 297mm/s = 30mm/s$$

Hence, the average viscous damper force (in each damper)

$$F_{vd,i} = c_{vd}\left(\bar{v}_{vd}\right)^{\alpha} = 25.8kNs^{\alpha}/mm^{\alpha} \cdot \left(30mm/s\right)^{0.5} = 141kN$$

In summary, following a quick design, a damping coefficient of $c_{vd} = 25.8\text{kNs}^{\alpha}/\text{mm}^{\alpha}$, with a velocity exponent of $\alpha = 0.5$ is required to satisfy the design requirements.

II. Design of the Supplementary Dampers (Detailed Method)

STEP 6-II to STEP 8-II

While the quick design above may suffice in many applications, a detailed design verification based on the actual neutral axis depth of the section should be undertaken. This verification requires a double iteration on the neutral axis depth $\chi l_w = c$ and the local damper coefficient c_{vd}. Iteration on the neutral axis depth $\chi l_w = c$ is required to satisfy force equilibrium while iteration on c_{vd} is required to ensure the system damping C_{VD} is equivalent to that required of design i.e. $C_{VD} = 90.81kNs^{\alpha}/m^{\alpha}$. The final iteration is presented having a neutral axis depth of 409.3mm (χ=0.164) and a local damper coefficient of $c_{vd} = 23.45kNs^{\alpha}/mm^{\alpha}$ (both compare well with the quick design method). Note that the design verification is carried out at an intermediate design displacement of $\Delta_r = \Delta_d/\sqrt{2}$ and therefore the base rotation is also reduced by the same amount i.e. $\theta_r = \theta_d/\sqrt{2}$. The concrete compression strain and stress block factors are calculated,

$$\varepsilon_c = \left(\frac{3\theta_r}{h_w} + \phi_{dec}\right)c = \left(\frac{3 \cdot 0.71\%}{15{,}000mm} + 3.3\times10^{-5}m^{-1}\right)409.7mm = 0.000803$$

$$\alpha = 0.75\frac{4700}{\sqrt{f_c'}}\varepsilon_c = 0.75\frac{4700}{\sqrt{45}}0.000803 = 0.422$$

$$\beta = 0.667$$

The concrete compression force,

$$C_c = \alpha f_c^{'} \beta c t_w = 0.422 \cdot 45MPa \cdot 0.667 \cdot 409.7mm \cdot 250mm = 1296kN$$

The elongation in each tendon is determined

$$\Delta_{pt,i} = \theta[l_w(0.5 - \chi) \pm d_{pt,i}]$$

$$\Delta_{pt,1} = 0.71\%[2{,}500mm(0.5 - 0.164) + 510mm] = 9.6mm$$

$$\Delta_{pt,2} = 0.71\%[2{,}500mm(0.5 - 0.164) - 510mm] = 2.3mm$$

The increase in tendon load is thus,

$$\Delta T_{pt,i} = \Delta\varepsilon_{pt,i} E_{pt} A_{pt} n_{pt,i} = \frac{\Delta_{pt,i}}{l_{ub}} E_{pt} A_{pt} n_{pt,i}$$

$$\Delta T_{PT,1} = \frac{9.6mm}{15{,}000mm} \cdot 200GPa \cdot 99mm^2 \cdot 4 = 50.4kN$$

$$\Delta T_{pt,2} = \frac{2.3mm}{15{,}000mm} \cdot 200GPa \cdot 99mm^2 \cdot 4 = 12.3kN$$

The force in the viscous dampers is related to the angular velocity of the base, which is related to the spectral velocity of the effective mass. The equivalent viscous damping used to reduce the spectral velocity

$$\xi_{eq}^{vel} = a_1 \xi_{vd,sys} + \xi_{el}$$

Where for α=0.50 and a near-fault rupture mechanism

$$a_1 \quad = 0.602$$

with,

$$\xi_{el} \quad = 0.05 \text{ (5\% elastic damping)}$$

Therefore,

$$\xi_{eq}^{vel} \quad = 0.1271$$

The damping reduction (velocity) factor (η_{vel}) is calculated,

$$\eta_{vel} = \left(\frac{0.07}{0.02 + \xi_{eq}^{vel}} \right)^{0.5} = \left(\frac{0.07}{0.02 + 0.1271} \right)^{0.5} = 0.690$$

The design velocity (at the reduced level of displacement) is calculated

$$v_r = \Delta_d \frac{2\pi}{T_e}\left(\frac{\eta_{vel}}{\eta_{disp}}\right)\frac{1}{\sqrt{2}} = 110mm\frac{2\pi}{1.698}\left(\frac{0.690}{0.669}\right)\frac{1}{\sqrt{2}} = 296.9mm/s$$

The corresponding rotational velocity of the base is equal to (ignoring elastic deformations),

$$\dot{\theta}_r = \frac{v_r}{H_e} = \frac{296.9mm}{11m} = 0.027rad/s$$

The velocity of each damper layer is calculated as,

$$v_{vd,i} = \dot{\theta}(l_w(0.5-\chi) \pm d_{vd})$$

$$v_{vd,1} = 0.027(2{,}500mm(0.5-0.164)+510mm) = 36.5mm/s$$

$$v_{vd,2} = 0.027(2{,}500mm(0.5-0.164)-510mm) = 8.9mm/s$$

Therefore, the force within each damper layer,

$$F_{vd,i} = n_{vd,i}\cdot c_{vd}\cdot\left(v_{vd,i}\right)^{\alpha}$$

$$F_{vd,1} = 2\cdot 23.45kNs^{\alpha}/mm^{\alpha}\cdot\left(36.5mm/s\right)^{0.5} = 283.2kN$$

$$F_{vd,2} = 2\cdot 23.45kNs^{\alpha}/mm^{\alpha}\cdot\left(8.9mm/s\right)^{0.5} = 140.1kN$$

Finally force equilibrium,

$$\sum F = \sum \Delta T_{pt,i} + T_{pt,o} + \sum F_{vd,i} - C_c$$
$$\sum F = 62.7kN + 809kN + 423.3kN - 1296kN \approx 0$$

While the calculation of the lateral capacity is not explicitly required, it will be useful to ensure capacity design of the precast wall element. The internal lever arms to each component is as follows,

$$jd_{0.5lw} = 0.5l_w(1-\beta\chi) = 0.5\cdot 2{,}500mm(1-0.67\cdot 0.164) = 1{,}113mm$$

$$jd_{pt,1} = jd_{vd,1} = 0.5l_w(1-\beta\chi) + d_{pt,1} = 1{,}623mm$$

$$jd_{pt,2} = jd_{vd,2} = 0.5l_w(1-\beta\chi) - d_{pt,1} = 603mm$$

Finally, the moment capacity

$$M_n = T_{pt,0} jd_{0.5lw} + \sum_{i=1}^{j} \Delta T_{pt,i} jd_{pt,i} + \sum_{i=1}^{j} F_{vd,i} jd_{vd,i}$$

$$M_n = 809kN \cdot 1113mm + (50.4kN + 283.2kN) \cdot 1623mm$$
$$+ (12.3kN + 140.1kN) \cdot 603mm = 1{,}534kNm$$

This next verification/iteration confirms that the system damping is consistent with that required of design i.e. $C_{VD} = 90.81 kNs^{\alpha} / m^{\alpha}$.This is based on a rigorous analysis of the relationship between the system damping coefficient and the local damping coefficient (detailed calculations are presented in Appendix E),

$$\beta_{vd} = \frac{C_{VD}}{c_{vd}} = n_{vd} \left(\frac{jD}{h_w} \right) \cdot \gamma_{vd}$$

From Eq.(E.12), for a rocking system with two sets of viscous dampers the net internal lever arm to the resultant viscous damper force is defined as,

$$jD = \frac{M_{vd}}{\sum F_{vd,i}} = \frac{\Phi_{1-2} \cdot jd_{vd,1} + jd_{vd,2}}{\Phi_{1-2} + 1}$$

With

$$\Phi_{1-2} = \frac{F_{vd1}}{F_{vd2}} = \left[\frac{l_w (0.5 - \chi) + d_{vd}}{l_w (0.5 - \chi) - d_{vd}} \right]^{\alpha}$$
$$\Phi_{1-2} = \left[\frac{2{,}500(0.5 - 0.164) + 510}{2{,}500(0.5 - 0.164) - 510} \right]^{0.5} = 2.021$$

Therefore

$$jD = \frac{\Phi_{1-2} \cdot jd_{vd,1} + jd_{vd,2}}{\Phi_{1-2} + 1} = \frac{2.021 \cdot 1{,}623mm + 603mm}{2.021 + 1} = 1286mm$$

The geometric velocity coefficient (γ_{vd}) is defined from Eq.(E.17) and reproduced below

$$\gamma_{vd} = \frac{1}{n_{vis}} \sum_{i=1}^{n} \left[\frac{1}{H_e} \left(l_w (0.5 - \chi) \pm d_{vd} \right) \right]^{\alpha} = \left(\frac{v_{vd}}{v_r} \right)^{\alpha}$$
$$\gamma_{vd} = \frac{1}{2} \left[\frac{1}{11{,}000mm} \left(2{,}500mm(0.5 - 0.164) + 510mm \right) \right]^{0.5}$$
$$+ \frac{1}{2} \left[\frac{1}{11{,}000mm} \left(2{,}500mm(0.5 - 0.164) - 510mm \right) \right]^{0.5}$$
$$\gamma_{vd} = 0.262$$

Therefore the ratio between the average damper velocity and the system velocity is equal to,

$$\frac{\overline{v}_{vd}}{v_r} = \left(\gamma_{vd}\right)^{\frac{1}{\alpha}} = 0.262^2 = 0.069$$

Finally the system damping coefficient is computed from the local damping coefficient and compared with the value required from design.

$$\beta_{vd} = n_{vd}\left(\frac{jD}{h_w}\right)\cdot\gamma_{vd} = 4\left(\frac{1.286m}{11m}\right)\cdot 0.262 = 0.123$$

$$C_{VD} = \beta_{vd}c_{vd} = 0.123\cdot 23.45 kNs^{\alpha}/mm^{\alpha} = 2.872 kNs^{\alpha}/mm^{\alpha} = 90.81 kNs^{\alpha}/m^{\alpha}$$

Convergence is satisfied as the actual system damping coefficient compares with that required of design.

E6. REFERENCES

NZS1170.5. (2004). "Structural Design Actions, *Part 5: Earthquake actions*." Standards New Zealand, Wellington.

NZS3101. (2006). "Concrete Structures Standard: Part 1-The Design of Concrete Structures." Standards New Zealand, Wellington.

Appendix F

F1. MANIPULATION OF THE SPECTRAL REDUCTION FACTOR FOR NEAR-FIELD COMPATIBILITY

The exponent α in the spectral reduction factor of η in Eq.(F.1) takes on a value of $\alpha = 0.5$ for far-field seismicity and 0.25 for near-field seismicity. The idea to manipulate this equation is to be able to use Eq.(F.1) with $\alpha = 0.5$ for the design of near-field and far-filed ground motions: thus, utilising a common spectral reduction factor η.

$$\eta = \left(\frac{0.07}{0.02 + \xi_{eq}} \right)^{\alpha} \qquad \textbf{F.1}$$

Equating the two spectral reduction formulations to include only the hysteretic EVD

$$\left(\frac{0.07}{0.07 + \xi_{hyst,DDBD}} \right)^{0.25} = \left(\frac{0.07}{0.07 + \xi_{hyst}} \right)^{0.5} \qquad \textbf{F.2}$$

Where:

$\xi_{hyst,DDBD}$ = the EVD as calculated following the DDBD formulations of Eq.(9.8)

ξ_{hyst} = the manipulated EVD to be used within the spectral reduction formulation of Eq.(F.1) with $\alpha = 0.5$

By rearranging Eq.(F.2), the hysteretic component of EVD becomes

$$\xi_{hyst} = \left[0.07 \left(0.07 + \xi_{hyst,DDBD} \right) \right]^{0.5} - 0.07 \qquad \textbf{F.3}$$

Note, when $\xi_{hyst,DDBD}$ is equal to zero, ξ_{hyst} is also equal to zero.

F2. DESIGN EXAMPLE OF A POST-TENSIONED ROCKING SYSTEM WITH VISCOUS AND HSYTERETIC DAMPERS

The following presents a worked example of a prototype rocking wall structure located in Wellington dominated by near-fault seismicity in Figure F.1. The seismic design spectrum is shown graphically in Figure F.2, with the numerical coordinates presented in Table F.1. A quick design example and a detailed design example are presented below.

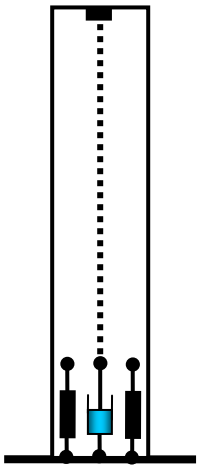

Design details
Design PGA = 0.372 (zone factor **z** = 0.28, soil cat C)
Target inter-storey drift: 1.5%

Structural wall details
h_w=15000mm (5 levels @ 3000mm)
l_w=2500mm
t_w=250mm
Seismic mass, m_i=20tonne

Viscous damping properties
Total number of viscous dampers, $\boldsymbol{n_{vd}}$=2 (1 location)
Damping coefficient $\boldsymbol{c_{vd}}$=450kNs$^{\alpha}$/m$^{\alpha}$
Non-linearity, $\boldsymbol{\alpha}$=0.50

Hysteretic damping properties
Total number of hysteretic dampers, $\boldsymbol{n_{ms}}$=4 (2 locations)
Target moment ratio $\boldsymbol{\lambda}$=1.0

Figure F.1 Details of the prototype wall, worked example

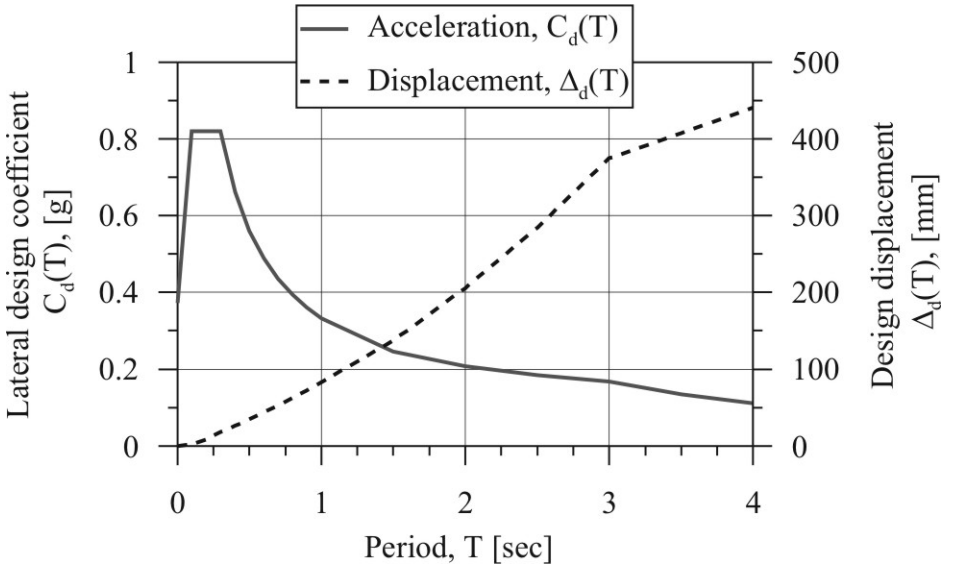

Figure F.2 NZS1170.5 [2004] elastic (5% damped) design spectrum. Zone factor z = 0.28, soil class C, return period 500years R_u = 1, 2km distance to fault, structural performance factor S_p = 1.0

Table F.1 Coordinates for the elastic (5% damped) design spectrum for zone factor z = 0.28, soil class C, return period 500years R_u = 1, 2km distance to fault, structural performance factor S_p = 1.0

Period, T [sec]	$C_d(T)$ [g]	$\Delta_d(T)$ [mm]
0.0	0.372	0
0.1	0.820	2
0.2	0.820	8
0.3	0.820	18
0.4	0.662	26
0.5	0.560	35
0.6	0.488	44
0.7	0.435	53
0.8	0.394	63
0.9	0.360	73
1.0	0.333	83
1.5	0.246	137
2.0	0.207	206
2.5	0.183	285
3.0	0.168	375
3.5	0.134	408
4.0	0.111	441
4.5	0.091	457

In this example, the design specifies a particular local damper properties, i.e. c_{vd} and α. The Viscous-DDBD follows *Design Method B* in Figure 9.4 above.

STEP 1

For simplicity, elastic deformations are ignored in this design example; therefore, the inelastic first mode-shape is assumed to be linear: the SDOF target displacement is determined as

$$\Delta_{d,\zeta} = 165mm$$

The effective mass and effective height are calculated

$$m_e = 81{,}818kg$$
$$H_e = 11000mm$$

STEP 2

The local-to-global damping constant β_{vd} is first determined from Eq.(9.12)

$$\beta_{vd} = a \cdot n_{vis} \left(A_r\right)^{-(1+\alpha)}$$

For $\alpha = 0.50$

$$a = 0.514$$
$$\beta_{vd} = 0.514 \cdot 1\left(4.4\right)^{-(1+0.5)} = 0.056$$

Following iteration and a more detailed calculation (discussed in Chapter 8), it is found that β_{vd}=0.0606 (an initial error of 6.7%). The revised value of β_{vd} is used here on.

The global damping coefficient is computed from below

$$C_{VD} = \beta_{vd} c_{vd} = 0.0606 \cdot 450 kNs^{\alpha} / m^{\alpha} = 27.3 kNs^{\alpha} / m^{\alpha}$$

STEP 3

An estimate of the base shear ($K_e\Delta_d$, not including $\phi_{BL,sys}$) is required to determine the critical damping C_c. An initial estimate of $0.1W_t$ provides a good first estimate; however, the converged value of $0.123W_t$ is used. The effective stiffness and hence critical damping is computed:

$$K_e = \frac{V_b}{\Delta_d} = \frac{120.4kN}{0.165m} = 730 kN/m$$

$$C_c = 2\sqrt{m_e K_e} = 488.6 kNs/m$$

Therefore the SDR Ω is defined from Eq.(9.11)

$$\Omega = \frac{C_{VD}}{C_c} = \frac{27.3kNs^{\alpha}/m^{\alpha}}{488.6kNs/m} = 0.0558$$

STEP 4

The viscous damping component of EVD ξ_{vd} is determined from Eq.(9.10)

$$\xi_{vd} = a_1\Omega$$

From Table 9.1, for $\alpha = 0.50$ and near-fault seismicity, the coefficient $a_1 = 0.602$. Therefore the viscous component of EVD

$$\xi_{vd} = a_0 + a_1\Omega = 0.602(0.0558) = 0.034$$

STEP 5

The hysteretic damping component of EVD ξ_{hyst} is defined from the displacement ductility μ_{Δ} of the section using Eq.(9.6):

$$\mu_{\Delta} = \frac{\theta_d D}{K_{\theta,yield}\varepsilon_y H} = \frac{0.015 \cdot 2.5m}{0.48 \cdot 0.0015 \cdot 11m} = 4.73$$

Hence, ξ_{hyst} is determined from Eq.(9.14):

$$\xi_{hyst} = \frac{1}{1+\lambda}\left[a\left(1-\frac{1}{\mu^b}\right)\left(1+\frac{1}{(T_e+c)^d}\right)\right]$$

While hysteresis parameters corresponding to a Ramberg-Osgood rule would normally be recommended for externally mounted steel yielding devices, the non-liner time-history verification is carried out with an elastic-perfectly-plastic (EPP) rule. Therefore, EPP parameters are used for ξ_{hyst} (note, iteration is required on the effective period, T_e)

λ = 1.0
a = 0.224
b = 0.336
c = -0.002
d = 0.250
T_e = 2.10s (confirmed later)

$$\xi_{hyst} = \frac{1}{1+1.0}\left[0.224\left(1-\frac{1}{4.73^{0.336}}\right)\left(1+\frac{1}{(2.10-0.002)^{0.25}}\right)\right] = 0.083$$

The hysteretic damping is further reduced for near-field seismicity following Eq.(9.17).

$$\xi_{hyst} = \left[0.07(0.07+0.083)\right]^{0.5} - 0.07 = 0.034$$

STEP 6

The elastic component of EVD ξ_{el} would normally be computed using Eq.(9.9); however, a constant damping model is used within the non-linear time-history verification. The elastic damping ξ_{el} is equal to 0.05 of critical damping, specified at the secant stiffness K_e to the target displacement.

$$\xi_{el} = 0.05$$

Therefore, the total EVD ξ_{eq}:

$$\xi_{eq} = 0.05 + 0.034 + 0.034 = 0.118$$

The spectral reduction factor η:

$$\eta = \sqrt{\frac{0.07}{0.02 + \xi_{eq}}} = \sqrt{\frac{0.07}{0.02 + 0.118}} = 0.743$$

STEP 7

The equivalent 5% damped displacement

$$\Delta_{d,5\%} = \frac{\Delta_{d,\xi}}{\eta} = \frac{0.165m}{0.743} = 0.222m$$

Entering the 5% damped displacement spectrum to define the effective period

$$T_e = 2.10\,\text{sec}$$

STEP 8

The effective stiffness is computed

$$k_e = \frac{4\pi^2 m_e^2}{T_e} = \frac{4\pi^2 \cdot 81{,}818kg}{2.10^2} = 730kN/m$$

The system base-shear reduction factor $\phi_{BL,sys}$ is weighted based on the proportion of the viscous and hysteretic component of EVD. The un-weighted base-shear reduction ϕ_{BL} for near-field ground motion is interpolated form Table 9.5: the interpolation is summarised in Table F.2 below.

Table F.2 ϕ_{BL} interpolation of Error! Reference source not found.

	α=0.30	α=0.75	α=0.50
	Ω=0.056		Ω=0.056
T_e=1.00s	0.724	0.747	**0.734**
T_e=2.25s	0.777	0.787	**0.781**
T_e=3.50s	0.841	0.853	**0.846**

From Table F.2 the un-weighted reduction factor for $T_e = 2.10$s, $\alpha = 0.5$ and $\Omega = 0.0558$ is equal to $\phi_{BL} = 0.776$. Therefore, the weighted reduction factor $\phi_{BL,sys}$ is given by Eq.(9.25)

$$\phi_{BL,sys} = \phi_{BL} + (1-\phi_{BL})\frac{\xi_{hyst}}{\xi_{hyst}+\xi_{vd}} = 0.776 + (1-0.776)\frac{0.034}{0.034+0.034} = 0.908$$

Finally, the design base shear is computed

$$V_b = \phi_{BL,sys} K_e \Delta_d = 0.908 \cdot 730kN/m \cdot 0.165m = 109kN$$

STEP 9

The critical damping ratio is re-computed and compared with the estimation in *Step 1*. The procedure is iterated until convergence is acceptable. The final iteration has been presented in this example

$$C_c = 2\sqrt{m_e K_e} = 488.6kNs^{\alpha}/m^{\alpha}$$

This compares with the value used in *Step 3*.

Section Design at the Target Displacement Δ_d

The next series of calculations are not explicitly described in the design method but are required to determine the specific number of post-tensioned tendons, the initial post-tensioning force and the amount of mild steel required to achieve the design base shear of $V_b = 109.0$kN and moment re-centring ratio $\lambda = 1.0$ at the target displacement Δ_d. Recalling that the velocity is zero at the target displacement; therefore, the viscous damper forces are zero. To determine the number of tendons, initial post-tensioned force and the mild steel reinforcement content required, an estimate on the dimensionless neutral axis depth $\chi = c/l_w$ can be computed from the following expression

$$\chi = \frac{c}{D} = \frac{1}{2\beta}\left[1 - \sqrt{1 - \frac{8\mu}{\alpha}}\right]$$

Where α and β are the compression stress block coefficients and μ is the dimensionless moment demand defined as

$$\mu = \frac{M}{f_c^{'} BD^2} = \frac{V_b H_e}{f_c^{'} BD^2} = \frac{109kN \cdot 11m}{45MPa \cdot 0.25m \cdot (2.5m)^2} = 0.01711$$

The dimensionless neutral axis depth is approximated as $\chi = 0.1$. Lumping the tendons and mild steel at the middle of the section and assuming a stress-block coefficient of $\beta = 0.67$, the internal lever arm is estimated from the following

$$jd_{approx} = 0.5l_w(1 - \beta\chi) = 1166mm$$

The tendon force required to achieve the required lateral capacity is determined from the over-turning moment $V_b H_e$ and the required moment ratio λ

$$T_{pt,req} = \frac{V_b H_e}{jd_{approx}}\left(\frac{\lambda}{1+\lambda}\right) = \frac{109kN \cdot 11{,}000mm}{1{,}166mm}\left(\frac{1}{1+1}\right) = 516kN$$

Knowing that the strain in the tendon must not exceed $0.9\varepsilon_y$ (NZS3101 [2006]), the number of required tendons is estimated based on two tendons ducts

$$n_{pt} = \frac{T_{pt,req}}{0.9 f_{pt,y} A_{pt}} = \frac{505kN}{0.9 \cdot 1560MPa \cdot 99mm^2} > 3.7$$
$$\therefore n_{PT} = 4$$

The total initial prestress T_{pt0} is determined as the difference between the tendon force at the design rotation and the tendon force due to gap opening

$$T_{pt,0} = T_{pt,req} - \frac{(0.5 - \chi)l_w \theta}{l_{ub}} E_{pt} A_{pt} n_{pt}$$

$$T_{pt,0} = 516kN - \frac{0.4 \cdot 2{,}500mm \cdot 1.5\%}{15{,}000mm} \cdot 200GPa \cdot 99mm^2 \cdot 4 = 436kN$$

The total required mild steel force is estimated from the over-turning moment demand and target moment ratio within the section.

$$T_{ms,req} = \frac{V_b H_e}{jd_{approx}}\left(\frac{1}{1+\lambda}\right) = \frac{109kN \cdot 11{,}000mm}{1{,}166mm}\left(\frac{1}{1+1}\right) = 516kN$$

Given that 4 steel devices are located within the section, and assuming that all are yielding, the required bar diameter is calculated assuming a 15% increase in steel yield strength to account for strain hardening of the material.

$$d_b = \sqrt{\frac{T_{ms,req} 4}{N_{ms} \pi \cdot 1.15 f_{yms}}} = \sqrt{\frac{516kN \cdot 4}{4\pi \cdot 1.15 \cdot 300MPa}} = 0.022m$$

Note that in this example a) the elastic deformation is ignored, and b) the displacement profile is assumed linear; therefore the gap opening is equal to the drift, $\theta=1.5\%$.

While the computed design parameters above may suffice for a quick design, it should be verified by a proper determination of the neutral axis depth involving translation equilibrium. The calculation below is based on the final iteration with a neutral axis depth of $c=254mm$ ($\chi=0.103$), where the initial prestress was reduced to 420kN.
First, the decompression moment and curvature are calculated

$$M_{dec} = T_{pt,0}\frac{l_w}{6} = 420kN\frac{2{,}500mm}{6} = 175kNm$$

$$\phi_{dec} = 1.60\times10^{-5}m^{-1}$$

The concrete compression force is then calculated from the maximum concrete compression strain of

$$\varepsilon_c = \left(\frac{3\theta}{h_e}+\phi_{dec}\right)c = \left(\frac{3\cdot1.5\%}{11{,}000mm}+1.60\times10^{-5}m^{-1}\right)254mm = 0.00104$$

The concrete stress block coefficients are defined and the concrete compression force is calculated,

$$\alpha = 0.75\frac{4700}{\sqrt{f_c^{'}}}\varepsilon_c = 0.75\frac{4700}{\sqrt{45}}0.00104 = 0.520$$

$\beta=0.67$

$$C_c = \alpha f_c^{'}\beta c t_w = 0.520\cdot45MPa\cdot0.67\cdot254mm\cdot250mm = 1017kN$$

The elongation in each tendon is determined (each tendon duct is located 510mm from the centreline of the wall section)

$$\Delta_{pt,i} = \theta[l_w(0.5-\chi)\pm d_{pt,i}]$$

$$\Delta_{pt,1} = 1.5\%[2{,}500mm(0.5-0.103)+510mm] = 22.6mm$$

$$\Delta_{pt,2} = 1.5\%[2{,}500mm(0.5-0.103)-510mm] = 7.3mm$$

Similarly, the tendon strain,

$$\Delta\varepsilon_{pt,i} = \frac{\Delta_{PT,i}}{l_{ub}}$$

$$\Delta\varepsilon_{pt,1} = \frac{22.6mm}{15{,}000} = 0.00151 < 0.9\varepsilon_y - \varepsilon_{pt,0}$$

$$\Delta\varepsilon_{pt,2} = \frac{7.3mm}{15{,}000} = 0.00049 < 0.9\varepsilon_y - \varepsilon_{pt,0}$$

The increase in tendon load is thus,

$$\Delta T_{pt,i} = \Delta\varepsilon_{pt,i} E_{pt} A_{pt} n_{pt,i}$$

$$\Delta T_{pt,1} = 0.00151 \cdot 200GPa \cdot 99mm^2 \cdot 2 = 59.7kN$$

$$\Delta T_{pt,1} = 0.00049 \cdot 200GPa \cdot 99mm^2 \cdot 2 = 19.3kN$$

Without going into the detail of calculating the displacement and elongation of the hysteretic dampers (mild steel TCY devices), the entire steel group is lumped at the centre of the section and assumed to have a yield capacity of $1.15\boldsymbol{f_{yms}}$.

$$T_{ms} = N_{ms} A_{ms} 1.15 f_{yms} = 4\frac{\pi \cdot 0.022^2}{4} 1.15 \cdot 300MPa = 517kN$$

Equating force equilibrium

$$\sum F = T_{pt} + T_{ms} - C_c = 420kN + 59.7kN + 19.3kN + 517kN - 1017kN \approx 0$$

The resulting moment capacity,

$$M_n = T_{pt,0} jd_{0.5lw} + \sum_{i=1}^{n} \Delta T_{pt,i} jd_{pt,i} + T_{ms} jd_{0.5lw}$$

Where the internal lever arms are defined as,

$$jd_{0.5lw} = 0.5l_w(1 - \beta\chi) = 0.5 \cdot 2{,}500mm(1 - 0.67 \cdot 0.103) = 1{,}164mm$$

$$jd_{pt,1} = 0.5l_w(1 - \beta\chi) + d_{pt,1} = 1{,}674mm$$

$$jd_{pt,2} = 0.5l_w(1 - \beta\chi) - d_{pt,1} = 654mm$$

Therefore,

$$M_n = 420kN \cdot 1{,}164mm + 59.7kN \cdot 1{,}674mm$$
$$+ 19.3kN \cdot 654mm + 517kN \cdot 1164mm = 1203kNm$$

Thus, satisfying the required lateral capacity at the target displacement

$$P = \frac{M_n}{h_e} = \frac{1203kN}{11{,}000} = 109kN > V_b$$

And satisfying the moment ratio required of design

$$\lambda = \frac{M_{pt} + M_N}{M_{ms}} = \frac{601kNm}{602kNm} = 1.0$$

I. Design of the Supplementary Dampers (Quick Method)

STEP 10-I.

The EVD damping associated with velocity is computed from Eq.(9.19)

$$\xi_{eq}^{vel} = \xi_{el} + \xi_{hyst} + b_1\Omega$$

The coefficient b_1 is listed in Table 9.1. For a = 0.5 and near-field seismicity, b1 = 0.526, hence

$$\xi_{eq}^{vel} = 0.05 + 0.034 + 0.526 \cdot 0.0558 = 0.113$$

The spectral velocity reduction factor is defined by Eq.(9.21)

$$\eta_{vel} = \sqrt{\frac{0.07}{0.02 + \xi_{eq}^{vel}}} = \sqrt{\frac{0.07}{0.02 + 0.113}} = 0.738$$

Therefore, the design velocity v_r (at the intermediate design displacement Δ_r) is calculated from Eq.(9.21)

$$v_r = \Delta_d \frac{2\pi}{T_e}\left(\frac{\eta_{vel}}{\eta_{disp}}\right)\frac{1}{\sqrt{2}} = 165mm\frac{2\pi}{2.10}\left(\frac{0.738}{0.743}\right)\frac{1}{\sqrt{2}} = 346mm/s$$

STEP 11-I

The final step estimates the average damper velocity. This allows the damper forces to be estimated for sizing and pricing issues. First, the internal lever jD arm to the centroid of the resultant damper force is estimated. To avoid a detailed calculation the neutral axis depth is estimated as $\chi = c/l_w = 0.15$ while a stress block factor of $\beta = 0.7$ is assumed. The resultant damper force is assumed to act at the middle of the section, hence jD is calculated as

$$jD = 0.5l_w(1 - \beta\chi) = 0.5 \cdot 2.5m(1 - 0.105) = 1.12m$$

The average damper design velocity can be estimated from Eq.(9.24)

$$\bar{v}_{vd} \approx \frac{jD}{H_e}v_r = \frac{1.12m}{11m} \cdot 346mm/s = 35mm/s$$

Hence, the average viscous damper force (in each damper)

$$F_{vd,i} = c_{vd}\left(\bar{v}_{vd}\right)^{\alpha} = 450kNs^{\alpha}/m^{\alpha} \cdot \left(0.035m/s\right)^{0.5} = 84kN$$

In summary, following a quick design, a damper coefficient of $\boldsymbol{c_{vd}} = 450\text{kNs}^{\alpha}/\text{m}^{\alpha}$, with a velocity exponent of $\boldsymbol{\alpha} = 0.5$ is required to satisfy the design requirements.

I. Design of the Supplementary Dampers (Detailed Method)

STEP 10-II to STEP 11-II

The method to design the supplementary dampers for a hysteretic-viscous system is slightly different to a pure viscous post-tensioned system presented in Chapter 8 for two reasons: 1) the addition of the mild steel dampers must be considered within the section equilibrium, 2) the design has a specified value of damping, $\boldsymbol{c_{vd}} = 450\text{kNs}^{\alpha}/\text{m}^{\alpha}$ as opposed to a specified supplementary damping ratio $\boldsymbol{\Omega}$. With this said, the procedure requires iteration to ensure that the global damping coefficient $\boldsymbol{C_{VD}}$ used in the design calculations of *Step 2-Step 9* is compatible with that computed following a detailed section analysis. That is, following a detailed section analysis the global damping coefficient $\boldsymbol{C_{VD}}$ must agree with that used during design in *Step 2*.

The following calculations step through the section analysis based on a converged neutral axis depth of χ=0.126 (314mm). Note that the design verification is carried out at an intermediate design displacement of $\Delta_r = \Delta_d/\sqrt{2}$, therefore, the base rotation is reduced by the same amount i.e. $\theta_r = \theta_d/\sqrt{2}$. The concrete compression strain and stress block factors are calculated,

$$\varepsilon_c = \left(\frac{3\theta_r}{h_e} + \phi_{dec}\right)c = \left(\frac{3 \cdot 1.06\%}{11{,}000mm} + 1.6\times10^{-5}m^{-1}\right)314mm = 0.00091$$

$$\alpha = 0.75\frac{4700}{\sqrt{f_c^{'}}}\varepsilon_c = 0.75\frac{4700}{\sqrt{45}}0.00091 = 0.48$$

$$\beta = 0.67$$

The concrete compression force,

$$C_c = \alpha f_c^{'}\beta c t_w = 0.48 \cdot 45MPa \cdot 0.67 \cdot 314mm \cdot 250mm = 1119kN$$

The elongation in each tendon is determined

$$\Delta_{pt,i} = \theta[l_w(0.5-\chi) \pm d_{pt,i}]$$

$$\Delta_{pt,1} = 1.06\%[2{,}500mm(0.5-0.126)+510mm] = 15.3mm$$

$$\Delta_{pt,2} = 1.06\%[2{,}500mm(0.5 - 0.126) - 510mm] = 4.5mm$$

The increase in tendon load is thus,

$$\Delta T_{pt,i} = \Delta\varepsilon_{pt,i} E_{pt} A_{pt} n_{pt,i} = \frac{\Delta_{pt,i}}{l_{ub}} E_{pt} A_{pt} n_{pt,i}$$

$$\Delta T_{PT,1} = \frac{15.3mm}{15{,}000mm} \cdot 200GPa \cdot 99mm^2 \cdot 2 = 40kN$$

$$\Delta T_{pt,2} = \frac{4.5mm}{15{,}000mm} \cdot 200GPa \cdot 99mm^2 \cdot 2 = 12kN$$

Again, the force contribution of the mild steel dampers is computed assuming the stress in the mild steel is equal to $1.15\boldsymbol{f_{yms}}$

$$T_{ms} = N_{ms} A_{ms} 1.15 f_{yms} = 4\frac{\pi \cdot 0.022^2}{4} 1.15 \cdot 300MPa = 517kN$$

The force in the viscous dampers is related to the angular velocity of the base, which is related to the spectral velocity of the effective mass. The equivalent viscous damping used to reduce the spectral velocity differs from that used to reduce the spectral displacement and is discussed in Chapter 8. For spectral velocity, the viscous component of EVD ξ_{vd}^{vel} is computed

$$\xi_{vd}^{vel} = b_1 \Omega$$

Where for $\boldsymbol{\alpha} = 0.50$ and a near-fault rupture mechanism

$$b_1 = 0.526$$

Therefore, the viscous damping component of EVD to reduce the velocity spectrum,

$$\xi_{vd}^{vel} = 0.526(0.0558) = 0.029$$

The total EVD used to reduce the velocity spectrum,

$$\xi_{eq}^{vel} = 0.05 + 0.029 + 0.034 = 0.113$$

The spectral velocity reduction factor $\boldsymbol{\eta_{vel}}$ is calculated,

$$\eta_{vel} = \left(\frac{0.07}{0.02 + \xi_{eq}^{vel}}\right)^{0.5} = \left(\frac{0.07}{0.02 + 0.113}\right)^{0.5} = 0.738$$

The design velocity (at $\boldsymbol{\Delta_r}$) is calculated,

$$v_r = \Delta_d \frac{2\pi}{T_e}\left(\frac{\eta_{vel}}{\eta_{disp}}\right)\frac{1}{\sqrt{2}} = 165mm\frac{2\pi}{2.10}\left(\frac{0.738}{0.743}\right)\frac{1}{\sqrt{2}} = 346mm/s$$

The corresponding rotational velocity of the base is equal to,

$$\dot{\theta}_r = \frac{v_r}{h_e} = \frac{346mm/s}{11000mm} = 0.0315rad/s$$

The velocity of each damper layer is calculated as,

$$v_{vd,i} = \dot{\theta}(l_w(0.5-\chi) \pm d_{vd})$$

$$v_{vd,1} = 0.0315(2{,}500mm(0.5-0.126)) = 21mm/s$$

Therefore, the force within each damper layer,

$$F_{vd,i} = n_{vd,i} \cdot c_{vd} \cdot (v_{vd,i})^{\alpha}$$

$$F_{vd,1} = 2 \cdot 450kNs^{\alpha}/m^{\alpha} \cdot (21mm/s)^{0.5} = 130kN$$

Finally, force equilibrium,

$$\sum F = T_{pt,o} + \sum \Delta T_{pt,i} + T_{ms} + \sum F_{vd,i} - C_c$$
$$\sum F = 420kN + 40kN + 12kN + 517kN - 1119kN \approx 0$$

While the calculation of the lateral capacity is not explicitly required, it will be useful to ensure capacity design of the precast wall element is satisfied. The internal lever arm to each component is as follows,

$$jd_{0.5lw} = 0.5l_w(1-\beta\chi) = 0.5 \cdot 2{,}500mm(1-0.67 \cdot 0.126) = 1{,}144mm$$

$$jd_{pt,1} = jd_{vd,1} = 0.5l_w(1-\beta\chi) + d_{pt,1} = 1{,}654mm$$

$$jd_{pt,2} = jd_{vd,2} = 0.5l_w(1-\beta\chi) - d_{pt,1} = 634mm$$

Finally, the moment capacity

$$M_n = T_{pt,0}jd_{0.5lw} + \sum_{i=1}^{j}\Delta T_{pt,i}jd_{pt,i} + T_{ms}jd_{0.5lw} + \sum_{i=1}^{j}F_{vd,i}jd_{vd,i}$$

$$M_n = (420kN + 517kN + 130) \cdot 1144mm + 40kN \cdot 1654mm$$
$$+ 12kN \cdot 634mm = 1{,}293kNm$$

This next verification confirms that the system damping is consistent with used in *Step 2* of design, i.e. $\Omega = 0.0558$. The procedure and equations used have been presented in detail in Appendix E and discussed in Chapter 8. The global-to-local damping constant is given below

$$\beta_{vd} = \frac{C_{VD}}{c_{vd}} = n_{vd}\left(\frac{jD}{h_w}\right)\cdot\gamma_{vd}$$

The supplementary damping ratio, SDR is given by

$$\Omega = \frac{C_{VD}}{C_c} = \frac{\beta_{vd}c_{vd}}{C_c}$$

For a rocking system with a single layer of viscous dampers the internal lever arm to the centroid of the damper force is trivial,

$$jD = jd = 0.5l_w(1-\beta\chi) = 0.5\cdot 2500mm(1-0.67\cdot 0.126) = 1143mm$$

The geometric velocity coefficient γ_{vd} is defined in Chapter 8 and reproduced below

$$\gamma_{vd} = \frac{1}{n_{vis}}\sum_{i=1}^{n}\left[\frac{1}{H_e}\left(l_w(0.5-\chi)\pm d_{vd}\right)\right]^{\alpha} = \left(\frac{v_{vd}}{v_r}\right)^{\alpha}$$

$$\gamma_{vd} = \frac{1}{1}\left[\frac{1}{11{,}000mm}\left(2{,}500mm(0.5-0.126)\right)\right]^{0.5} = 0.292$$

While not required, the ratio of the system velocity to the damper velocity can be computed

$$\frac{v_{vd}}{v_r} = \left(\gamma_{vd}\right)^{\frac{1}{\alpha}} = 0.292^2 = 0.085$$

The local-to-global damping constant β_{vd} is computed

$$\beta_{vd} = n_{vd}\left(\frac{jD}{h_w}\right)\cdot\gamma_{vd} = 2\frac{1143}{11000}0.292 = 0.0606$$

Finally, the SDR Ω is computed and compared with that used during design

$$\Omega = \frac{\beta_{vd}c_{vd}}{C_c} = \frac{0.0606\cdot 450kNs^{\alpha}/m^{\alpha}}{488.6kNs/m} = 0.0558$$

Convergence is therefore satisfied as the actual SDR compares with the value used in design.

F3. REFERENCES

NZS1170.5. (2004). "Structural Design Actions, *Part 5: Earthquake actions*." Standards New Zealand, Wellington.

NZS3101. (2006). "Concrete Structures Standard: Part 1-The Design of Concrete Structures." Standards New Zealand, Wellington.

Appendix G

G1. DESIGN EXAMPLE OF A POST-TENSIONED ROCKING BRIDGE SYSTEM WITH VISCOUS AND HYSTERETIC DAMPERS

The six span system of Bridge 5 is designed for a near-field seismic hazard. The piers contain non-linear viscous dampers and hysteretic dampers.

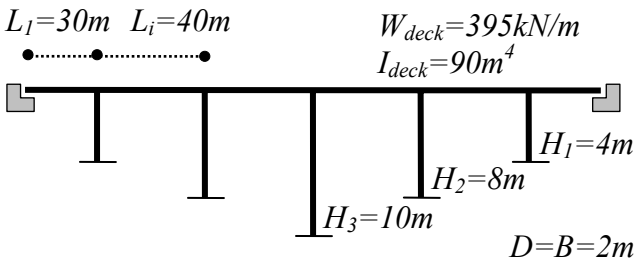

1. Non-linear viscous dampers properties:

Damping coefficient of the fluid viscous dampers (FVD's), c_{vd}=7500kNs$^{\alpha}$/m$^{\alpha}$
Damper linearity, α=0.5
Total number of fluid viscous dampers at each rocking section, n_{vd}=4
Number of damper layers at each rocking section, n_{vis}=2

2. Hysteretic damper properties:

Target moment ratio, λ=1.0

The target displacement is governed by the 8m pier corresponding to an arbitrary lateral drift of 1.64%. While the design procedure is iterative, only the final iteration is presented. In fact, the full procedure requires a triple iteration: the first iteration deals with the deformed shape of the bridge, the second considers the proportion of base-shear resisted by the superstructure, while the third iteration uses the converged value of critical damping to determine the viscous damper contribution to EVD. A computer code is written in *Matlab* to deal with such an iterative procedure.

The converged proportion of base-shear resisted by the superstructure is x=0.097, while the converged displaced shape is given by:

$$\phi = \langle 0 \quad 0.383 \quad 0.822 \quad 1 \quad 0.822 \quad 0.383 \quad 0 \rangle$$

This corresponds to a displaced shape of:

$$\Delta_i = \begin{bmatrix} 0 & 0.0689 & 0.1479 & 0.18 & 0.1479 & 0.0689 & 0 \end{bmatrix} m$$

The mass along the bridge:

$$m_i = \begin{bmatrix} 604 & 1409 & 1611 & 1611 & 1611 & 1409 & 604 \end{bmatrix} tonne$$

The displacement of the effective mass:

$$\Delta_d = \frac{\sum m_i \Delta_i^2}{\sum m_i \Delta_i} = 0.1416 m$$

The effective mass:

$$m_e = \frac{\sum m_i \Delta_i}{\Delta_d} = 6783 kg$$

Elastic component of EVD

The elastic damping of the superstructure and of the piers is taken as $\xi_{ss} = \xi_{el,piers} = 0.05$. Therefore, the elastic damping is trivial:

$$\xi_{el} = 0.05$$

Calculation of the equivalent viscous damping

From the local damping properties (c_{vd}, α), the global damping coefficient is determined for each pier at the location of the effective mass $C_{VD,i}$ and weighted to define the total system damping coefficient C_{VD} to be used in the calculation of the EVD. The aspect ratio of each pier is first computed:

$$A_r = \begin{bmatrix} 2 & 4 & 5 & 4 & 2 \end{bmatrix}$$

The damping constant β_{vd} is computed for each pier from Eq.(10.21):

$$\beta_{vd} = a \cdot n_{vis} \left(A_r \right)^{-(1+\alpha)}$$

For $\alpha = 0.5$ the coefficient $a = 0.514$, therefore:

$$\beta_{vd,i} = \begin{bmatrix} 0.363 & 0.129 & 0.092 & 0.129 & 0.363 \end{bmatrix}$$

It should be recognised, following the design of the bridge, a section analysis should be carried out on each pier to confirm the actual value of $\beta_{vd,i}$ as outlined in the worked example of Chapter 8. The damping coefficient at the effective height of each pier is computed from Eq.(10.20):

$$\beta_{vd,i} = \frac{C_{VD,i}}{c_{vd,i}}$$

Therefore:

$$C_{VD,i} = \begin{bmatrix} 2726 & 964 & 690 & 964 & 2726 \end{bmatrix} kNs^{\alpha} / m^{\alpha}$$

The system damping coefficient is weighted according to Eq.(20.22):

$$C_{VD} = \frac{\sum_{i=1}^{i=piers} C_{VD,i} \left(\Delta_i\right)^{\alpha+1}}{\left(\Delta_d\right)^{\alpha+1}} = 4895 kNs^{\alpha} / m^{\alpha}$$

The effective stiffness $\boldsymbol{K_e}$ is required to compute the critical damping $\boldsymbol{C_c}$ of the system. This can be computed by estimating the base shear of the system (not including $\boldsymbol{\phi_{BL}}$). Recalling, an initial estimate of $0.1\boldsymbol{W_t}$ will provide a good first estimate to compute the effective stiffness $\boldsymbol{K_e}$. The converged value of $\boldsymbol{K_e}$ = 60826kN/m is used.

$$K_e = 60826 kN / m$$

$$C_c = 2\sqrt{m_e K_e} = 40623 kNs / m$$

The supplementary damping ratio is computed

$$\Omega = \frac{C_{VD}}{C_c} = \frac{4895 kNs^{\alpha} / m^{\alpha}}{40623 kNs / m} = 0.120$$

Finally, the viscous component of EVD can be computed from Eq.(20.23). For $\boldsymbol{\alpha}$=0.5 and near-field ground motions, the coefficient is equal to $\boldsymbol{a_1}$=0.602.

$$\xi_{vd} = a_1 \cdot \Omega = 0.602 \cdot (0.120) = 0.0722$$

Calculation of the hysteretic component of EVD

First, the displacement ductility is computed for each pier from Eq.(10.14) with $\boldsymbol{K_{\theta,yield}}$ = 0.50 and $\boldsymbol{\varepsilon_y}$ = 0.0015:

$$\mu_i = \begin{bmatrix} 11.5 & 6.2 & 4.8 & 6.2 & 11.5 \end{bmatrix}$$

The hysteretic component of EVD is determined from Eq.(10.25) with the following:

$$\xi_{hyst,i} = \frac{1}{1+\lambda_i}\left[a\left(1 - \frac{1}{\mu_i^b}\right)\left(1 + \frac{1}{\left(T_e + c\right)^d}\right)\right]$$

$\boldsymbol{\lambda}$ = 1.0
$\boldsymbol{a}$ = 0.224

$\boldsymbol{b}$ = 0.336
$\boldsymbol{c}$ = -0.002
$\boldsymbol{d}$ = 0.250
$\boldsymbol{T_e}$ = 2.10s (confirmed later)

Resulting in:

$$\xi_{hyst,i} = \begin{bmatrix} 0.0437 & 0.0371 & 0.0338 & 0.0371 & 0.0437 \end{bmatrix}$$

The hysteretic damping is weighted based on the proportion of shear resisted by each pier. This is distributed according to $\boldsymbol{1/H}$ and the proportion of base shear resisted by the superstructure $\boldsymbol{x}$.

$$\xi_{hyst} = \frac{\dfrac{(1-x)}{\sum(1/H_i)}\sum_{i=1}^{n}(1/H_i)\Delta_i\xi_{hyst,i}}{\dfrac{(1-x)}{\sum(1/H_i)}\sum_{i=1}^{n}(1/H_i)\Delta_i} = 0.0859$$

A near-field damping reduction is applied using Eq.(10.26):

$$\xi_{hyst} = \left[0.07\left(0.07 + \xi_{hyst,DDBD}\right)\right]^{0.5} - 0.07 = 0.0341$$

Therefore, the total EVD $\boldsymbol{\xi_{eq}}$:

$$\xi_{eq} = \xi_{el} + \xi_{hyst} + \xi_{vd} = 0.05 + 0.0341 + 0.0667 = 0.151$$

The spectral reduction factor $\boldsymbol{\eta}$:

$$\eta = \sqrt{\frac{0.07}{0.02 + \xi_{eq}}} = \sqrt{\frac{0.07}{0.02 + 0.151}} = 0.64$$

The equivalent 5% damped displacement:

$$\Delta_{d,5\%} = \frac{\Delta_{d,\xi}}{\eta} = \frac{0.1416m}{0.64} = 0.221m$$

Entering the 5% damped displacement spectrum, the effective period is determined:

$$T_e = 2.10\,\text{sec}$$

The effective stiffness is computed:

$$k_e = \frac{4\pi^2 m_e^2}{T_e} = \frac{4\pi^2 \cdot 6783tonne}{2.10^2} = 60826kN/m$$

The critical damping ratio can be computed and compared with that used to calculate the SDR above.

$$C_c = 2\sqrt{m_e K_e} = 40623 kNs^{\alpha} / m^{\alpha}$$

The value of $\boldsymbol{C_c}$ compares with that used above. The applied loads are computed from Eq.(10.10):

$$P_i = K_e \Delta_d \frac{m_i \Delta_i}{\sum m_i \Delta_i}$$

Where:

$$P_i = [871 \quad 2137 \quad 2600 \quad 2137 \quad 871] kN$$

The loads are applied to a structural model representing the effective stiffness at the target displacement. The effective stiffness of each pier is computed from Eq.(10.12) and Eq.(10.13):

$$K_i = \frac{V_i}{\Delta_i} = (1-x)\frac{K_e \Delta_d}{\Delta_i}\left(\frac{1/H_i}{\sum_{i=1}^{n} 1/H_i}\right)$$

$$K_i = [29265 \quad 6814 \quad 4480 \quad 6814 \quad 29265] kN/m$$

The structural model is constructed as follows:

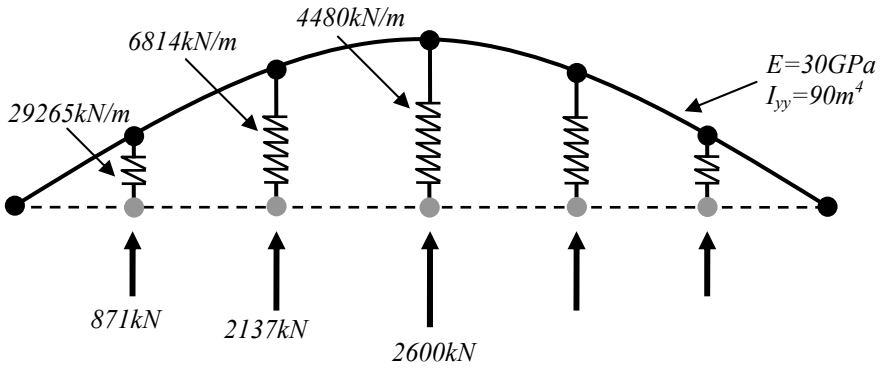

Figure G.1 Structural model of Bridge 5

From the output of the structural analysis the displaced shape is extracted and verified/updated with that used in the initial stages of design.

$$\Delta_i = [0 \quad 0.0689 \quad 0.1479 \quad 0.18 \quad 0.1479 \quad 0.0689 \quad 0] m$$

Furthermore, the total reaction force at the abutments is extracted and found to equal 0.097***Vb***, that is, ***x***=0.097. Convergence is satisfied as all three iteration parameters have converged, i.e. the critical damping ratio C_c, the displaced shape Δ_i and the reactions at the abutments ***x***.

Base shear reduction factor

The base shear reduction factor $\phi_{BL,sys}$ is weighted based on the proportion of the viscous and hysteretic component of EVD and on the proportion of base shear resisted by the superstructure ***x***. The un-weighted base-shear reduction factor ϕ_{BL} factor for near-field ground motion is reproduced from Chapter 8 below in Table G.1. The interpolation of Table G.1 for $\Omega = 0.120$ and $\alpha = 0.50$ is given below in Table G.2.

Table G.1 Base shear reduction factors ϕ_{BL}: Near-field

	α=0.30		α=0.75	
	Ω=0.05	**Ω=0.30**	**Ω=0.05**	**Ω=0.30**
Te=1.00s	0.722	0.803	0.745	0.838
Te=2.25s	0.775	0.861	0.784	0.896
Te=3.50s	0.840	0.882	0.852	0.898

Table G.2 ϕ_{BL} interpolation of Table G.1

	α=0.30	α=0.75	α=0.50
	Ω=0.120		Ω=0.120
T_e=1.00s	0.745	0.771	**0.757**
T_e=2.25s	0.799	0.816	**0.807**
T_e=3.50s	0.852	0.865	**0.858**

Hence, the un-weighted base-shear reduction factor ϕ_{BL} from Table G.2 with T_e=2.10s is given

$$\phi_{BL} = 0.800$$

The weighted system base shear reduction factor $\phi_{BL,sys}$ is computed from Eq.(10.36):

$$\phi_{BL,sys} = \left[\phi_{BL} + (1-\phi_{BL}) \frac{\xi_{hyst}}{\xi_{hyst} + \xi_{vd}} \right] (1-x) + x$$

$$\phi_{BL,sys} = \left[0.800 + (1-0.800) \frac{0.0341}{0.0341 + 0.0667} \right] (1-0.097) + 0.097$$

$$\phi_{BL,sys} = 0.881$$

Finally, the design base-shear V_b of the system is computed:

$$V_b = \phi_{BL,sys} K_e \Delta_d = 0.881 \cdot 60826 kN/m \cdot 0.1416 m = 7586 kN$$

The final shear distribution within each of the piers, representing the design shear, is given by Eq.(10.12):

$$V_i = (1-x)\phi_{BL,sys} K_e \Delta_d \left(\frac{1/H_i}{\sum_{i=1}^{n} 1/H_i} \right) = (1-0.097) \cdot 7586 kN \left(\frac{1/H_i}{\sum_{i=1}^{n} 1/H_i} \right)$$

$$V_i = \begin{bmatrix} 2016 & 1008 & 806 & 1008 & 2016 \end{bmatrix} kN$$

The shear at the abutments is given by:

$$V_{abut} = 0.5 x V_b = 0.5 \cdot 0.097 \cdot 7586 kN = 366 kN$$

A summary of this design is presented in Table G.3

Table G.3 Summary of bridge design

	Abut 1	**Pier 1**	**Pier 2**	**Pier 3**	**Pier 4**	**Pier 5**	**Abut 2**	**Sum =**
Hi		4	8	10	8	4		
mi	604	1409	1611	1611	1611	1409	604	8858
Δi		0.0689	0.1479	0.180	0.1479	0.0689		
A_r		2	4	5	4	2		
β_{vd}		0.363	0.129	0.092	0.129	0.363		
c_{vd}		2726	964	690	964	2726		
							C_{VD} =	4895
							ξ_{vd} =	0.0667
μ_i		11.5	6.2	4.8	6.2	11.5		
$\xi_{hyst,i}$		0.0437	0.0371	0.0338	0.0371	0.0437		
							ξ_{hyst} =	0.0341
V_i	366	2016	1008	806	1008	2016	366	7586

G2 DERIVATION OF THE WEIGHTING FUNCTION TO DETERMINE THE SYSTEM DAMPING COEFFICIENT C_{VD}

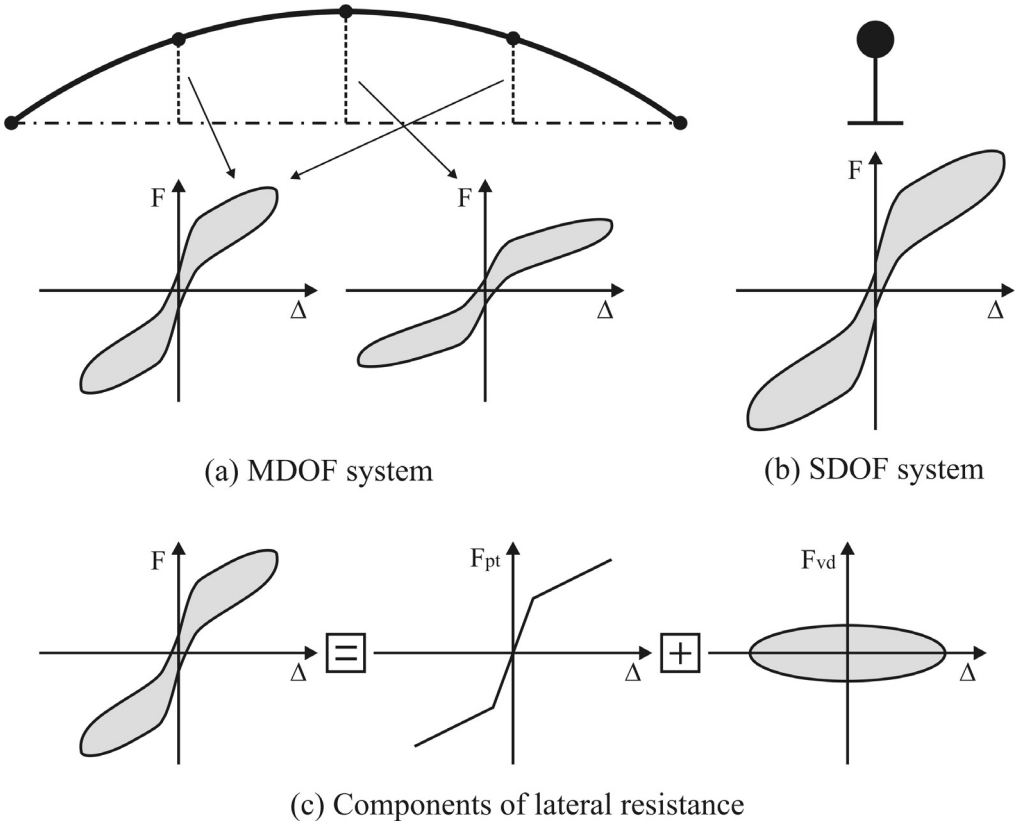

Figure G.2 Equating the work done between MDOF and SDOF system

The energy dissipated within each pier is the integral of the viscous force-displacement response over one cycle.

$$E_i = 4\int_{\Delta=0}^{\Delta=\Delta_i} F_{vd,i}(t)\,d\Delta = \int_{t=0}^{t=T_e} F_{vd,i}(t)\,\dot{\Delta}(t)\,dt \qquad \text{G.1}$$

Where

$\boldsymbol{F_{vd,i}(t)}$ is the viscous component of lateral resistance of pier ***i*** at time ***t***.

$\boldsymbol{\Delta_i}$ is the maximum displacement of pier ***i***.

$\dot{\Delta}(t)$ is the velocity of pier ***i*** at time ***t***.

$\boldsymbol{T_e}$ is the effective period of the system.

Equating the dissipated energy of the MDOF system to the dissipated energy of the SDOF system

$$E_{MDOF} = \sum_{1}^{piers} \int_{t=0}^{t=T} F_{vd,i}(t) v(t) dt = 4 \sum_{1}^{piers} \int_{t=0}^{t=T/4} F_{vd,i}(t) v(t) dt$$
$$E_{MDOF} = 4 \sum_{1}^{piers} \int_{t=0}^{t=T/4} C_{VD,i} \left[v(t) \right]^{\alpha+1} dt \qquad \text{G.2}$$

Considering harmonic motion, the velocity of pier ***i*** at time ***t*** is given by

$$v(t) = \Delta_i \omega \cdot \cos(\omega \cdot t) \qquad \text{G.3}$$

Therefore, by substitution into Eq.(G.2) and some rearrangement

$$E_{MDOF} = 4 \sum_{1}^{piers} \int_{t=0}^{t=T/4} C_{VD,i} \left[\Delta_i \omega \cdot \cos(\omega \cdot t) \right]^{\alpha+1} dt$$
$$E_{MDOF} = 4 \cdot \left[\sum_{1}^{piers} C_{VD,i} \left(\Delta_i \omega \right)^{\alpha+1} \right] \cdot \int_{t=0}^{t=T/4} \left[\cos(\omega \cdot t) \right]^{\alpha+1} dt \qquad \text{G.4}$$

Similarly, for the SDOF system

$$E_{SDOF} = 4 C_{VD} \left(\Delta_d \omega \right)^{\alpha+1} \int_{t=0}^{t=T/4} \left[\cos(\omega \cdot t) \right]^{\alpha+1} dt \qquad \text{G.5}$$

Equating the energy between the MDOF and SDOF system defines the weighted damping coefficient $\boldsymbol{C_{VD}}$ of the system.

$$C_{VD} = \frac{\sum_{i=1}^{i=piers} C_{VD,i} \left(\Delta_i \right)^{\alpha+1}}{\left(\Delta_d \right)^{\alpha+1}} \qquad \text{G.6}$$

G3. DETAILS AND FORMULATION OF AN ELASTIC DAMPING, DASHPOT MODEL

The main idea for implementing a physical damping model consisting of viscous dashpots at each DOF, as opposed to a traditional damping model, was to isolate any errors between the proposed design procedure and the THA response to the specific calibration carried out in this research. That is, if the design of the prototype bridges is undertaken accounting for the elastic damping correction factors proposed by Grant et al. [2005] combined with the THA being carried out using a tangent stiffness damping model, it would be difficult to ascertain how much error is associated with the elastic damping calibration of Grant et al. [2005] (if any) and how much is associated with the calibration associated with this research.

Generalised versus Effective SDOF Parameters

Before going into the details of the damping model, a number of key relationships are presented relating the *effective* and *generalised* SDOF parameters. The inelastic first mode shape $\boldsymbol{\phi}$ in Eq.(G.7) is normalised such that the largest term in the vector is equal to 1.0 (this normalisation is different to that used in the DDBD procedure where $\boldsymbol{\phi_i} = 1.0$ at the location of the critical pier). The inelastic displacement profile is therefore defined as:

$$\{\Delta\} = \{\phi\} Y \qquad \textbf{G.7}$$

Where, $\boldsymbol{Y}$ is the displacement of the largest term in the vector $\{\boldsymbol{\Delta}\}$. The displacement of the effective mass is given by:

$$\Delta_d = \frac{\sum m_i \Delta_i^2}{\sum m_i \Delta_i} = \frac{\sum m_i \phi_i^2}{\sum m_i \phi_i} Y = \frac{Y}{\Gamma} \qquad \textbf{G.8}$$

Where, $\boldsymbol{\Gamma}$ is the participation factor of the $\boldsymbol{i^{th}}$ mode (in this case, the inelastic first mode), which can be explicitly defined as:

$$\Gamma = \frac{\{\phi\}^T [M] \{r\}}{\{\phi\}^T [M] \{\phi\}} \qquad \textbf{G.9}$$

Where, $\{\boldsymbol{r}\}$ is the influence vector. The effective mass $\boldsymbol{m_e}$ is given by:

$$m_e = \frac{\sum m_i \Delta_i^2}{(\Delta_d)^2} = \frac{\sum m_i \phi_i^2}{(\Delta_d)^2} Y^2 = \Gamma^2 \sum m_i \phi_i^2 \qquad \textbf{G.10}$$

Hence, the relationship between the *effective mass* $\boldsymbol{m_e}$ and the *generalised mass* $\boldsymbol{M^*}$ is given by:

$$m_e = \Gamma^2 M^* \qquad \textbf{G.11}$$

Similarly, the *effective stiffness* $\boldsymbol{K_e}$ is related to the *generalised stiffness* $\boldsymbol{K^*}$ by:

$$K_e = \frac{\sum k_i \Delta_i^2}{(\Delta_d)^2} = \frac{\sum k_i \phi_i^2}{(\Delta_d)^2} Y^2 = \Gamma^2 \sum k_i \phi_i^2 = \Gamma^2 K^* \qquad \textbf{G.12}$$

This is further confirmed through the following:

$$\omega^2 = \frac{K^*}{M^*} = \frac{K_e}{m_e} = \frac{K_e}{\Gamma^2 M^*} \qquad \textbf{G.13}$$

Therefore:

$$K_e = \Gamma^2 K^* \qquad \textbf{G.14}$$

Finally, the effective damping is related to the generalised damping in the following way

$$C_e = \lambda 2\sqrt{m_e K_e} = 2\lambda\sqrt{\Gamma^2 M^* \Gamma^2 K^*} = \lambda \Gamma^2 C_c^* = \Gamma^2 C^* \qquad \textbf{G.15}$$

Therefore, the *effective* SDOF parameters ($\boldsymbol{m_e}$, $\boldsymbol{K_e}$, $\boldsymbol{C_e}$) are related to the *generalised* SDOF parameters ($\boldsymbol{M^*}$, $\boldsymbol{K^*}$, $\boldsymbol{C^*}$) by the participation factor squared $\boldsymbol{\Gamma^2}$.

Elastic Damping, Dashpot Model

In this method a Rayleigh damping matrix (Chopra [2001]) is computed; the diagonal terms are extracted and manipulated such that the effective damping $\boldsymbol{C_e}$ of the MDOF system is equivalent to the damping of the SDOF substitute structure.

Two modes need to be specified to generate the Rayleigh damping matrix; the first mode is the inelastic first mode (effective properties specified at the target displacement), while the second mode is the elastic (fundamental) mode (note $\boldsymbol{T_e > T_1}$). At each mode a percentage of critical damping must be specified. The percentage of critical damping within the effective mode $\boldsymbol{T_e}$ is specified as the elastic damping of the bridge $\boldsymbol{\xi_{el}}$, while the percentage of critical damping in the fundamental mode $\boldsymbol{T_1}$ is computed such that the effective damping coefficient in the fundamental mode $\boldsymbol{C_1}$ is equal to the effective damping coefficient in the effective mode $\boldsymbol{C_e}$. That is:

$$C_1 = C_e = 2 \cdot \xi_e \cdot m_e \frac{2\pi}{T_e} \qquad \textbf{G.16}$$

Therefore, the damping ratio in the fundamental mode is computed as:

$$\xi_1 = \frac{m_e}{M_1^* \Gamma_1} \frac{T_1}{T_e} \xi_e \qquad \textbf{G.17}$$

It should be recognised that $M_1^* \Gamma_1$ is the effective mass in the fundamental mode $\boldsymbol{T_1}$. The Rayleigh damping matrix is computed from the well known formulation:

$$[C] = a_1[M] + a_2[K] \qquad \textbf{G.18}$$

The Rayleigh damping coefficients a_1 and a_2 are computed from the following:

$$\begin{Bmatrix} a_1 \\ a_2 \end{Bmatrix} = 2\begin{bmatrix} 1/\omega_e & \omega_e \\ 1/\omega_1 & \omega_1 \end{bmatrix}^{-1} \begin{Bmatrix} \xi_e \\ \xi_1 \end{Bmatrix} \qquad \textbf{G.19}$$

The diagonal terms are extracted from [$\boldsymbol{C}$] resulting in the diagonal matrix [$\boldsymbol{C}$]$_{\text{diag}}$. Isolating the diagonal terms in the damping matrix takes on a similar form to mass proportional damping. By extracting only the diagonal terms within the damping matrix, some damping can be lost if the off-diagonal terms C_{ij} are similar in magnitude to the diagonal terms C_{ii} . Therefore, to account for the possible reduction in effective damping, the factor c_{damp} is computed as a ratio of the damping within the SDOF substitute structure C_e to the effective damping formed from the diagonal damping matrix [$\boldsymbol{C}$]$_{\text{diag}}$ within the MDOF system.

$$c_{damp} = \frac{C_e}{\{\phi\}^T [C]_{diag} \{\phi\} \Gamma^2} \qquad \textbf{G.20}$$

Where, ϕ is the inelastic first mode shape. Finally, the diagonal Rayleigh damping matrix representing the elastic damping of the structure is computed from:

$$\begin{bmatrix} C_{el,1} \\ C_{el,2} \\ C_{el,i} \\ C_{el,n} \end{bmatrix} = \{r\} \cdot [C]_{diag} \cdot c_{damp} = \{1 \quad 1 \quad 1 \quad 1\} \begin{bmatrix} C_{1,1} & 0 & 0 & 0 \\ 0 & C_{2,2} & 0 & 0 \\ 0 & 0 & C_{i,i} & 0 \\ 0 & 0 & 0 & C_{n,n} \end{bmatrix} \cdot c_{damp} \qquad \textbf{G.21}$$

Where $C_{el,i}$ is the elastic damping coefficient located at DOF i. It can be appreciated that this formulation gives a distribution of damping which is similar to the proportion of mass along the system.

G4. REFERENCES

Chopra, A. (2001). *Dynamics of Structures*, Prentice Hall, Upper Saddle River.

Grant, D. N., Blandon, C. A. and Priestley, M. J. N. (2005). *Modelling Inelastic Response in Direct Displacement-Based Design*, IUSS, Pavia.